Dynamic monitoring of photosynthesis in light-acclimated organisms

Aliénor Lahlou

Sorbonne Université

École doctorale 388

Chimie Physique et Chimie Analytique de Paris Centre

Département de Chimie – École Normale Supérieure PSL

et

Sony Computer Science Laboratories – Paris

Dynamic monitoring of photosynthesis in light-acclimated organisms

Par Aliénor Lahlou

Thèse de doctorat de Chimie Physique

Dirigée par Ludovic Jullien

Présentée et soutenue publiquement le 18 septembre 2023 devant un jury présidé par M. Thomas Walter et composé de :

M DEDECKER Peter	Professeur	Rapporteur
Mme MATUSZYŃSKA Anna	Professeure	Rapportrice
Mme PEEK Nadya	Professeure	Examinatrice
M WALTER Thomas	Directeur de Recherche	Président et Examinateur
M JULLIEN Ludovic	Professeur	Directeur de Thèse
M HANAPPE Peter	Directeur de Laboratoire	Responsable Industriel
M BAILLEUL Benjamin	Chargé de Recherche	Invité
M COLLIAUX David	Chercheur	Invité Industriel
M Le SAUX Thomas	Maître de conférence	Invité

Abstract

This CIFRE PhD work between ENS and Sony CSL Paris led to designing a new instrument and new protocols to characterize photosynthetic organisms' physiological status. This objective was addressed at the single-cell level to quantify three light-stress response mechanisms in the microalgae *Chlamydomonas reinhardtii*. This PhD work further lays the grounds for the European project DREAM, addressing its constraints in terms of generalization and applicability.

Chapter 1 describes the specifications for an epi-fluorescence microscope developed during the project. A strong accent was put on modularity and automation. The long-term DREAM objective to provide an affordable portable device was also taken into account in the design and hardware choices. The calibration and quality control of the instrument is described. The calibration of light intensity led to an extended work on the use of fluorescent actinometers in the visible spectrum, in 1D, 2D and 3D. It resulted in an accepted manuscript entitled "Fluorescence to measure light intensity" (*Nature Methods*, 2023).

Chapter 2 introduces the role of chlorophyll fluorescence (ChlF) in remote sensing of photosynthesis. The concept of de-excitation pathways of the energy harvested by the photosynthetic organisms is described, allowing to introduce the classical methods in ChlF remote sensing. The article manuscript "Leaves to measure light intensity" is introduced to describe the diversity of light-dependent phenomena in plants. The challenge of adapting the current protocols to an imaging system with a CMOS camera at the single-cell algae level was lifted using a new light protocol, and validated.

In Chapter 3, a manuscript under writing details the case study of the light-stress response in *Chlamydomonas reinhardtii* after an introduction to the key concepts in the biological process studied and the computational methods used. The experiments consist in collecting a video of ChlF time traces, and retrieving the individual responses by image segmentation. The three elementary light-stress responses studied are entangled and have dynamic signatures that overlap within the ChlF time trace. A machine learning framework is introduced to convert the ChlF traces into stress scores. A reference dataset was constructed to train the framework, relying on biological protocols involving mutant strains and pre-conditioning. These protocols were used to individually explore the three elementary components and establish the reference populations within the dataset. The framework consists of two parts. Dictionary Learning first reduces the dimension of the ChlF traces with optimized reconstruction. It is followed by a dimension reduction using Linear Discriminant Analysis to maximize the separability of the annotated classes. This combination allows to project a general stress response in a 3-dimensional space where each axis represents the amplitude of an elementary stress-response. This method can unmix the stress responses within the ChlF traces of wild-type strains. An emphasis is put on the reconstruction capability of the pipeline, which can be used as a criterion to validate the hypothesis made to build the training dataset, or to identify new stress-responses.

Chapter 4 presents a third draft manuscript. It describes the open-source hardware reproduction of the epi-fluorescence microscope, demonstrating the reproducibility of the work but also providing instructions to allow the targeted community to reproduce it. It also introduces tools to control in a modular way several devices and to implement a database system which can be helpful when designing Data Management Plans.

Acknowledgements

Tout d'abord, je souhaite remercier mon directeur de thèse Pr. Ludovic Jullien, pour s'être adonné à la construction de ce sujet nouveau et ambitieux et m'avoir permis d'y participer. J'ai été profondément inspirée par ta démarche consistant à te lancer dans des questions très pluridisciplinaire qui nécessitent de nouvelles collaborations, tout comme ta prise assumée de risques pour la mise en place de techniques innovantes. Merci de m'avoir donné beaucoup de liberté tout au long de mon projet, dans le choix des démarches et des interlocuteurs. Merci d'avoir eu confiance dans mes intuitions et mes propositions, et d'avoir su si bien les enrichir et guider leur concrétisation. Enfin, merci tout particulièrement pour toutes les heures dédiées à m'enseigner les rouages de la rédaction d'articles et du processus de publication, permettant d'ajouter beaucoup de structure et de valeur aux travaux.

Je remercie Dr. Thomas Le Saux, mon co-encadrant académique, pour toutes les connaissances en expérimentation et en instrumentation partagées avec générosité. Elles nous ont permis de mener à bout les développements instrumentaux en naviguant efficacement entre les contraintes. Si peu de problèmes te résistent ! Merci aussi pour toutes les discussions sur la science, sur le monde académique, et sur tout le reste, qui m'ont si bien guidée.

Je remercie Dr. Peter Hanappe, mon directeur industriel, pour toute sa confiance accordée au long de ce travail et pour avoir toujours sû être le manager qui correspondait à mes besoins. Merci aussi pour ton aisance en C^{++} et en conception 3D qui ont tant amélioré les développments instrumentaux. Enfin, merci pour avoir été le phare qui résiste aux aléas des semaines, en conservant toujours un point de vue d'ensemble et terre-à-terre, indispensable pour un projet si pluridisciplinaire.

Enfin, je remercie Dr. David Colliaux, mon co-encadrant industriel, pour son accompagnement complet ces dernières années, au sens scientifique tout comme humain. Merci d'avoir enrichi les développements par tes idées originales, en particulier en Machine Learning. Merci aussi d'avoir organisé chaque semaine les séminaires &inCSL sur des thèmes si variés qu'ils apportaient chaque fois de nouvelles idées, à l'image de chaque discussion avec toi.

Je souhaite aussi remercier mes collaborateurs, en particulier en biologie, un domaine très nouveau pour moi. Sans leur guidage, le travail qui suit n'aurait pas été possible. Merci à Dr. Benjamin Bailleul pour les nombreuses réunions menées avec Dr. David Colliaux qui ont permis d'aboutir aux dévelopements expérimentaux et analytiques du Chapitre 4. Ta façon de formuler les questions a profondément enrichi le travail, mais aussi ma façon d'y réfléchir et de le présenter. Merci à Sandrine Bujaldon pour son partage de riches connaissances sur les microalgues. Je remercie aussi Pr. Dusan Lazár et Dr. Ladislav Nedbal pour les nombreuses discussions qui ont mené aux développements des chapitres 2 et 3.

Je remercie aussi mes autres co-auteurs Dr. Hessam Sepasi Tehrani, Dr. Ian Coghill, Yuriy Shpinov, Dr. Mrinal Mandal, Marie-Aude Plamont, Dr. Isabelle Aujard, Dr. Yuxi Niu, Dr. Pierre Mahou, Dr. Willy Supatto, Dr. Emmanuel Beaurepaire, Isabelle Eisenmann, Dr. Nicolas Desprat, Dr. Raphaël Jeanneret, Marcelo Orlando, Dr. Raja Chouket, Dr. Agnès Pellissier-Tanon, Dr. Agathe Espagne, Dr. Ruikang Zhang, Dr. Annie Lemarchand pour tous les dévelopements que nous avons menés ensemble. Un remerciement particulier à Dr. Vincent Croquette pour son soutien et pour m'avoir mise en contact avec Ludovic et Thomas. Je remercie aussi mes stagiaires Ali Ruyer-Thompson et Alec Cochard pour leurs contibutions au chapitre 5.

Je remercie l'ANRT qui a contribué au financement de ce travail, ainsi que l'ED 388 et la Sorbonne université pour leur accompagnement.

Merci à tous les collègues de l'ENS pour tous les bons moments passés ensemble. Tout d'abord le groupe de la mezzanine des canapés, avec Marc et Valentine et nos vendredis en musique, Ian et Pierre-Louis et nos discussions de très grands sportifs et Yoan et nos exercices Python. Sans oublier les autres mezzanines avec les joyeux Fat Friday et nos discussions de cuisine et jardinage: Audrey, Lucas, Hélène, Emma, Laura, Léonard, Pauline, Chems, Hessam, Mrinal, Yuriy, Damien, Annamaria. Merci en particulier à Marie-Aude, pour toutes nos tentatives de boutures et tes messages chaleureux pendant la période de rédaction. Un grand merci au cycliste de l'équipe, Fabien, pour toutes les discussions velo (et bien d'autres), c'était un grand plaisir de partager ta salle de manips et nos passions ! Merci enfin au groupe déjeuner, Hélène, Isabelle et Eliora, le rayon de soleil de la semaine qui est vite devenu indispensable.

Merci à tous les collègues de Sony CSL pour tous les bons moments, autour de bières, à écumer les restaurants du quartier, en off-site, ou parfois même à vélo: Mike, Pratik, Inès, Martina, Pietro, Giulio, Remi, Cyran, Amaury, Alain, Javier, Gabriel, Nidham, Michael, Emmanuel, Matthias, Stefan, Cristina, Sophie, Alessandro, Vittorio, Tim, Lisa, Aurèle, Nabil, Doug, Mona, Fred et Joe.

Thanks also to the Sony colleagues for the Rookie project, always a pleasure to disconnect from the PhD to meet up with such a nice team: Sebastiana, Matti, Seki, Yoko, Gabriele, Matthias, Hideaki, Allison et Filip.

Merci maintenant à tous mes amis qui ont été présents tout au long de la thèse.

Un grand merci aux cyclistes pour les longues séances de déconnexion le week-end, que ce soit avec Neurchi de Biclou, les Jean Gentils, les Rouleurs du Dimanche et tous les autres. Un grand merci aux amis que je ne peux pas tous citer, pour toutes les occasions de déconnecter du travail. Merci à celles et ceux du collège et lycée, de colonie de vacances, de prépa, de l'ESPCI, du MVA, des conférences, pour être toujours motivés pour des déjeuners, des verres, des jeux de société, de la cuisine et du sport. Merci de vous être déplacés si nombreux le jour de ma soutenance, j'étais si heureuse de vous voir toutes et tous réunis ! Merci tout particulier à celles et ceux qui ont vécu l'expérience de la thèse en parallèle pour tous nos échanges et soutien mutuel. Même s'il est court, ce paragraphe de remerciements est le plus important pour moi, mais si j'entrais dans les détails, cela risquerait de rajouter un nouveau chapitre à ce manuscrit déjà très long.

Merci à mon parrain et ma marraine, et aux membres de ma famille pour avoir toujours été présents et encourageants. Merci à mes grands-parents, oncles, tante, cousins et cousines pour nos vacances et nos déjeuners ensemble. Merci à toi Alex pour les déjeuners, verres, voyages, formations et conversations passionnantes qu'on a partagés. Merci à mes deux parents, les superviseurs discrets, pour tous les bons conseils dans le cadre du travail et de la thèse, ainsi que des relectures, ils ont été si utiles. Merci d'avoir toujours su me remonter le moral et me remettre les idées en place. Merci pour tous les dîners partagés, les soirées 7 parnassiens, les week-end hors de Paris et les randonnées improvisées.

Enfin, merci à toi Maxime, mon conjoint et meilleur ami, pour ton soutien si fondamental. Merci d'avoir toujours été si compréhensif, à l'écoute, positif, et d'avoir apporté tes conseils et ta confiance infaillible dans les hauts comme dans les bas. Merci aussi pour nos discussions scientifiques, il y a plusieurs traces de toi dans ce manuscrit. Et surtout, merci d'avoir pavé de tant de bons souvenirs tout le chemin de la thèse: allons vite savourer la suite !

Finally, thanks to Pr. Peter Dedecker, Pr. Anna Matuszyńska, Pr. Nadya Peek and Pr. Thomas Walter for accepting to participate in the jury of my PhD defense and thanks for your valuable feedback reading the manuscript.

Glossary

Application Programming Interface (API):

An Application Programming Interface (API) is a set of rules and protocols that allows different software applications to communicate with each other. It defines the methods, data structures, and protocols that developers can use to interact with a particular software component, service, or platform.

Camera or Photodetector:

In this PhD work, the camera or photodetector captures the emitted fluorescence light from the sample. It converts the light photons into electrical signals that can be further processed and displayed as an image.

Chlorophyll a/b:

Chlorophyll (Chl) a/b are primary pigments found in plants, algae, and cyanobacteria. They play a vital role in photosynthesis by absorbing light energy and initiating the conversion of light energy into chemical energy. They differ slightly in their absorption spectrum: Chl a absorbs red and purple light while Chl b absorbs blue and orange light. Chl a has a methyl group attached to the C-3 position of the porphyrin ring, where chlorophyll-b has an aldehyde group.

Chlorophyll Fluorescence:

Chlorophyll fluorescence is the emission of light by chlorophyll molecules when they return to their ground state from an excited state. It is used as a non-invasive and sensitive tool to study various aspects of photosynthetic processes and plant stress responses.

Clustering:

A technique that groups similar data points together based on their inherent similarities, aiming to discover underlying patterns or clusters in the data. It allows for unsupervised identification of groups or clusters, which can be useful for tasks such as pattern identification.

Dichroic Filter (Beam Splitter):

Optical device that selectively transmits or reflects light based on its wavelength or color. It consists of multiple layers of thin films with varying optical properties, allowing it to separate light into different spectral components by reflecting or transmitting specific wavelengths while blocking others.

Dictionary Learning:

Dictionary learning is an unsupervised learning approach that aims to learn a dictionary of basis elements (atoms) to represent the data in a sparse and efficient manner. It seeks to find a set of dictionary atoms or basis functions that can reconstruct the data with the minimum number of non-zero coefficients.

Dimension Reduction:

Dimension reduction is the process of reducing the number of input features or variables while preserving important information and structure in the data. It helps to simplify the data representation and remove irrelevant or redundant features.

Driver:

A device driver is a computer program that operates or controls a hardware device attached to a computer.

Electron Transport Chain:

The electron transport chain is a series of redox reactions that occur during photosynthesis, involving the transfer of electrons from water molecules to $NADP^+$ to produce NADPH, which is used in the synthesis of carbohydrates.

Emission Filter:

The emission filter is a wavelength filter that allows only the emitted fluorescence light to pass through to the detector. It blocks the excitation light and selects the specific wavelength range of the emitted fluorescence to be detected.

Emission Spectrum:

The emission spectrum represents the relative emission of fluorescence photons over a range of wavelengths emitted by a fluorophore when it transitions from an excited state to a lower energy state. It provides information about the specific wavelengths of light emitted by a fluorophore and is usually measured using a spectrophotometer.

Excitation Energy:

Excitation energy is the energy absorbed by chlorophyll molecules during the excitation process. This energy is temporarily stored and is subsequently used in photosynthetic reactions.

Excitation Filter:

The excitation filter is a specific wavelength filter that allows only the desired excitation light to pass through to the sample. It selects the appropriate wavelength of light to excite the fluorophores present in the sample.

Excitation Light:

Excitation light refers to the light energy that is absorbed by chlorophyll molecules and other pigments to initiate photosynthesis. It is typically provided by a specific wavelength of light.

FD:

Direct fluorescence, collected in response to actinic light ($FD_{actinic}$) or saturating pulse (FD_{sat}). To compare it to the fluorescence classically described in chlorophyll fluorescence literature F_S (resp F_M), it has to be divided by the excitation light intensity corrected by the absorption spectrum, and normalized.

Filters:

Filters are optical components used to selectively transmit or block specific wavelengths of light.

Filter Cubes:

Filter cubes are assemblies that contain multiple filters, including the excitation filter, dichroic mirror, and emission filter, all positioned in the correct alignment for fluorescence microscopy.

Fluorescence Emission:

Fluorescence emission refers to the light emitted by fluorescent molecules as they return to their ground state from an excited singlet state. The emitted light has a longer wavelength than the absorbed light and can be detected and measured.

Fluorescence Excitation Spectrum:

The fluorescence excitation spectrum shows the range of wavelengths at which a fluorophore becomes excited. It is obtained by measuring the fluorescence intensity while scanning the excitation wavelengths.

Fluorescence Induction/Transient/Rise:

Fluorescence induction is a commonly used technique to study the kinetics of chlorophyll fluorescence. It involves measuring the changes in fluorescence emission intensity over time after the application of a short high-light pulse to a dark-adapted sample.

Fluorescent Labels or Fluorophores:

Fluorophores are specific molecules or dyes that absorb light at a certain wavelength and emit light at a different, longer wavelength. They are used to label specific structures or molecules of interest within the sample for visualization under fluorescence microscopy.

Fluorescent Dye:

Chemical compound that absorbs light in a wavelength range and can convert part of the absorbed energy by emitting light in another wavelength range. These dyes are designed to selectively bind to specific molecules or structures in biological samples, allowing them to be visualized under fluorescence microscopy. Fluorescent dyes are commonly used as labels in various applications, such as immunostaining, cell tracking, and molecular imaging.

Fluorescent Protein:

A fluorescent protein is a protein that naturally exhibits fluorescence. These proteins are derived from organisms such as jellyfish, coral, or bacteria, which produce these proteins. Fluorescent proteins are widely used in biological research as genetic tags or markers to label specific proteins or structures within cells or organisms. They can be genetically encoded and expressed in living systems, enabling real-time visualization and tracking of cellular processes.

Fluorescence Yield:

Fluorescence yield is the amount of fluorescence emission produced relative to the amount of excitation energy absorbed. It is often expressed as the quantum yield, which represents the efficiency of the fluorescence process.

Fluorophore:

A fluorophore refers to a molecule or a portion of a molecule that exhibits fluorescence (see Fluorescent dye/protein).

Image Analysis Software:

Image analysis software is used to analyze, process, and quantify the acquired images. It may provide tools for image segmentation, feature extraction, colocalization analysis, and other image-processing tasks.

Image Processor:

The image processor is responsible for processing and enhancing the acquired images. It may perform tasks such as noise reduction, contrast adjustment, and image analysis.

k_F, k_P, k_{NPQ}, k_o:

Rate constants of the fluorescence, photosynthesis, non-photochemical quenching, and other competitive phenomena (including intersystem-crossing and internal conversion) for the deexcitation of P680*.

KD-tree:

A KD-tree (short for k-dimensional tree) is a data structure used for organizing multi-dimensional data in computer science and computational geometry. It provides efficient searching of nearest neighbors in a multi-dimensional space. A KD-tree recursively divides the data points along orthogonal axes, creating a binary tree structure. This allows for faster search operations by selectively traversing the tree based on the distance to the query point. KD-trees are commonly used in applications like k-nearest neighbor search, range searches, and spatial indexing.

K-Means:

K-means is an unsupervised machine learning algorithm used for clustering analysis. It aims to partition a dataset into K distinct clusters, where each data point belongs to the cluster with the nearest mean (centroid). The algorithm iteratively assigns data points to clusters based on their proximity in the feature space and updates the centroids until convergence.

Light Source:

The light source provides illumination for the sample. In epifluorescence microscopy, commonly used light sources include mercury lamps, xenon lamps, or LED light sources.

Light-Harvesting Complex (LHC):

The Light-Harvesting Complex (LHC) is a group of proteins and pigments found in photosynthetic organisms. Its primary function is to capture and transfer light energy to the photosynthetic reaction centers. The LHC acts as an antenna system, efficiently absorbing light of various wavelengths and funneling it to the reaction centers, where the process of photosynthesis initiates.

Linear Discriminant Analysis (LDA):

A supervised dimension reduction technique that seeks to find a linear combination of features that maximizes class separability. It aims to project the data onto a lower-dimensional space while maximizing the differences between classes and minimizing the variations within each class.

Lumen:

The lumen is the internal space within the thylakoid membrane of the chloroplast. It is involved in the accumulation of protons (H^+) during photosynthesis, which generates a proton gradient used in ATP synthesis.

Maximum Quantum Yield (Fv/Fm):

The maximum quantum yield represents the maximum efficiency of photosystem II (PSII) in converting light energy into chemical energy. It is calculated as the ratio of variable fluorescence (Fv) to maximum fluorescence (Fm) and serves as an indicator of the overall health and photosynthetic performance of plants.

Non-Photochemical Quenching (NPQ):

Non-photochemical quenching refers to the protective mechanisms employed by plants to dissipate excess absorbed light energy as heat, reducing the potential for damage to the photosynthetic apparatus.

NoSQL Database (see SQL database):

A noSQL (not only SQL) database is a type of database management system that provides a flexible approach to storing and retrieving data. Unlike SQL databases, noSQL databases do not rely on a fixed schema and can handle unstructured, semi-structured, or polymorphic data.

Objective Lens:

The objective lens collects and focuses the light from the sample onto the detector. It determines the resolution and magnification of the captured image. High numerical aperture (NA) objectives are commonly used in epifluorescence microscopy to maximize the collection of emitted fluorescence light.

OJIP curve:

See **Fluorescence transient/induction/rise**.

Overfitting:

Overfitting is a phenomenon that occurs in machine learning when a model becomes excessively tailored to the training data, resulting in poor performance on unseen or new data. It happens when a model learns noise or irrelevant patterns in the training set, rather than the underlying generalizable patterns.

$\phi_{\mathbf{F}}$, $\phi_{\mathbf{P}}$, $\phi_{\mathbf{NPQ}}$:

Quantum yield of fluorescence, photosynthesis and non-photochemical quenching (see **Quantum yield**).

Principal Component Analysis (PCA):

PCA is an unsupervised dimension reduction technique that transforms the data into a new set of uncorrelated variables called principal components, ordered by their importance in explaining the variance in the data. It captures the most significant information in the data while reducing its dimensionality.

Photosynthesis:

Photosynthesis is the process by which plants, algae, and some bacteria convert light energy into chemical energy, utilizing chlorophyll and other pigments to capture sunlight and convert carbon dioxide and water into glucose and oxygen.

Photosystem II (PSII):

Photosystem II is a protein complex located in the thylakoid membranes of chloroplasts. It is responsible for capturing light energy and initiating the electron transport chain in photosynthesis.

Photosystem I (PSI):

Photosystem I is another protein complex located in the thylakoid membranes of chloroplasts. It functions to absorb light energy and pass electrons to $NADP^+$ to produce NADPH, which is used in the synthesis of carbohydrates.

Plastoquinone Pool:

The plastoquinone pool is a collection of plastoquinone molecules that serve as electron carriers in the electron transport chain of photosynthesis. They shuttle electrons between photosystem II (PSII) and the cytochrome b6f complex.

P680,P700 (see Reaction center):

$P680^*$ and $P700^*$ represent the excited states.

qA and qB:

qA and qB are temporary electron acceptors in photosystem II (PSII). They receive electrons from the reaction center of PSII and transfer them to the plastoquinone pool.

Reversible Switchable Fluorescent Protein (RSFP):

RSFP defines a class of engineered fluorescent proteins derived from tetrameric Pectiniidae coral fluorescent protein [1]. It can be reversibly toggled between different states of fluorescence using specific wavelengths of light. These proteins exhibit the ability to switch back and forth between "on" and "off" states, providing researchers with control over their fluorescence emission.

Reaction Center P680:

The Reaction Center P680 is a chlorophyll a dimer located in the photosystem II (PSII) complex of plants, algae, and cyanobacteria. The "P" stands for pigment, and "680" indicates the peak absorption wavelength of this chlorophyll pigment at around 680 nm. The P680 chlorophyll molecule plays a central role in capturing light energy and initiating the primary photochemical reaction of photosynthesis within the photosystem II complex.

Reaction center P700:

Reaction Center P700: The Reaction Center P700 is a chlorophyll a dimer located in the photosystem I (PSI) complex of plants, algae, and some bacteria. Similar to P680, the "P" represents pigment, and "700" refers to the peak absorption wavelength of this chlorophyll pigment at around 700 nm.

Structured Query Language (SQL):

An SQL database is a type of relational database management system (RDBMS) that uses a structured approach for organizing and managing data. It employs a tabular structure where data is stored in tables consisting of rows and columns. SQL databases follow a predefined schema, which defines the structure, relationships, and constraints of the data.

Stage:

The stage is a platform that holds the sample in place and allows precise movement and positioning. It enables scanning or imaging of different areas of the sample.

Sun-Induced Fluorescence (SIF):

The SIF is the endogeneous fluorescence emitted by photosynthetic organisms in response to sunlight. It is used up to the kilometer scale to monitor vegetation. Multiple fitness indexes derive from SIF.

Supervised Learning:

A machine learning approach where the algorithm learns from labeled training data to make predictions or decisions on unseen data. It involves mapping input features to known target labels, allowing the algorithm to learn the underlying patterns and relationships in the data.

Stroma:

The stroma is the fluid-filled region inside the chloroplast, surrounding the thylakoid membranes. It plays a role in various metabolic processes, including the synthesis of carbohydrates during photosynthesis.

t-Distributed Stochastic Neighbor Embedding (t-SNE):

t-SNE is a dimension reduction and visualization technique that emphasizes the local structure and preserves pairwise similarities between data points. It constructs a low-dimensional representation of the data where similar instances are modeled as nearby points, allowing for effective visualization and clustering analysis.

Time series:

A time series is a sequence of data points collected or recorded in chronological order. Time series data is characterized by its temporal dependency, meaning that the value of each data point is influenced by its previous values.

UMAP (Uniform Manifold Approximation and Projection):

UMAP is a dimension reduction and visualization technique that preserves both local and global structure in the data. UMAP constructs a low-dimensional representation of the data while respecting both the local and global data relationships, making it useful for visualizing high-dimensional datasets with complex structures.

Unsupervised Learning:

A machine learning approach where the algorithm learns patterns or structures from unlabeled data without explicit guidance or labels. It aims to discover hidden patterns, group similar data points, or find meaningful representations of the data without any predefined output labels.

Water-Splitting Complex:

The water-splitting complex, also known as the oxygen-evolving complex, is a part of photosystem II (PSII) responsible for oxidizing water molecules, releasing oxygen, and providing electrons for the electron transport chain.

Wide-field microscope:

In a wide field microscope, the whole sample is exposed to the light source through a microscope objective. The image is viewed by the observer either via a camera or the microscope's eyepieces.

Contents

Chapter 1

Introduction

Managing the agriculture system in times of population growth and climate change will be a major challenge of the 21^{st} century. The IPCC's special report of 2019 [2] reiterated the ambivalent role of the food system, contributing to climate change by accounting for 21-37% of yearly greenhouse gas emissions but also experiencing significant impacts, such as heightened vulnerability of crops to more frequent extreme weather events (as evident already). One approach to address the current challenges is to mitigate the contribution of agriculture to climate change, while the other is to adapt the agricultural practices to incoming changes. These strategies are investigated by international agencies such as the Food and Agriculture Organization (FAO) or the Intergovernmental Panel on Climate Change (IPCC), which provide detailed reports as well as summaries for decision-makers. While executives in relevant organizations or government bodies may be the primary recipients of these summaries, they are also valuable for policymakers, funding agencies, researchers, and private companies involved in making strategic decisions related to the addressed challenges.

The Sony Computer Science Laboratories (CSL) is a blue skies research laboratory, which allows employees to work on research topics of their choice. The Sony CSL in Paris hosts a Sustainability division (Peter Hanappe, David Colliaux and I) that focuses on sustainable agriculture strategies, with research questions aligned with the problems described in the summaries for executives.

On the other hand, the team of Ludovic Jullien and Thomas Le Saux (Ecole Normale Supérieure) has been active in imaging the dynamic response of photoactive fluorophores to time modulated illuminations. More recently, they applied their developments for harnessing the exogenous fluorescence of genetically-modified plants to evaluate their stress level. After meeting specialists of photosynthesis (notably in the Institute Bio Phy Chem - IBPC in Paris), they reached the conclusion that their skillset would be relevant to address the same questions using the endogeneous fluorescence of plants with remote sensing, which allows avoiding GMOs. In relation to agriculture, this fluorescence which comes from chlorophyll is of high interest because its signature carries information on the health status of the plant, as will be described in details.

We initiated a collaboration between Sony CSL and Ludovic Jullien to launch the PhD work described in this manuscript. Rapidly, Ludovic Jullien took it to another level by preparing a European project proposal with complemented partners that was funded in 2021. The research strategy proposed was deemed radically new and matching the current societal questions in agriculture, addressing both the capacity to mitigate the contribution of agriculture to climate change and to adapt to climate change's consequences.

I will begin by summarizing the current challenges identified in agriculture and selectively evoke some solutions that resonate with the research project. Then I will introduce the various actors and their projects related to agriculture. It will enlight how the complementarities between Sony CSL Paris and ENS brought us to write a PhD proposal between an industrial partner and an academic

partner (CIFRE grant[1]). Finally, I will introduce the plan of work followed throughout the PhD project and detailed in the following chapters with their respective introductions.

1.1 Current challenges in agriculture

This section synthesizes the main challenges in agriculture in terms of contribution to greenhouse gas (GHG) emissions, as it is the current method to evaluate impact on climate change. Unlike other sectors where CO_2 is the main contributor, two major outputs of the agrifood sector are gases with a higher warming potential than CO_2: methane (CH_4) and nitrous oxide (N_2O). The warming power corresponds to how the presence of the gas in the atmosphere changes the radiative balance between the energy received by the Earth from the Sun and the energy outgoing from Earth [3, 4]. Some contributions to GHG emissions can also be specific to countries and/or management practices. It includes deforestation [5], but also specific cases, such as artificial lightning in greenhouses. Reducing GHG emissions is not the only challenge in agriculture. The management practices have numerous consequences on the natural cycles and the biodiversity and need to be addressed.

1.1.1 Greenhouse Gas Emissions from the agrifood sector

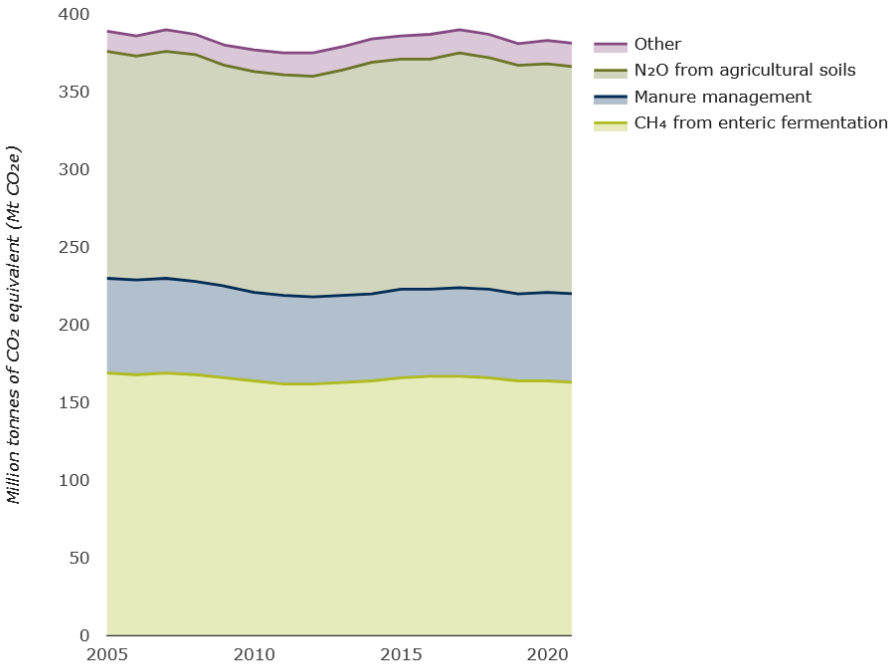

Figure 1.1: EU GHG emissions in the agriculture sector by source. Adapted from [6].

Enteric fermentation and methane

The digestion process of ruminant livestock such as cattle principally involves microbial anaerobic fermentation. The major fermentation pathway is methanogenesis, which is evolved by hosted

[1]Industrial Research Training Agreements

methanogen microorganisms [7] and leads to methane emissions. They contribute to 30% of the global emissions of methane and 40% of the agricultural GHG emissions in Europe (Figure 1.1). Several proposed solutions to reduce enteric fermentation involve, for example, modifying the diets of either humans or livestock. In particular, studies have shown potential in complementing the cattle diet with anti-methanogenic compounds, including microalgae [8].

Chemical fertilizer and nitrous oxide

Conventional agriculture practices rely on additive fertilizer of nutrients that cannot be regenerated by the soil, in particular nitrogen (N), phosphorus (P) and potassium (K). Since 1961, the usage of nitrogen-based chemical fertilizers was multiplied by nine, correlated with an increase in N_2O emissions [4]. Overall they contribute to a significant part of emissions (Figure 1.1). The gas emission is a result of nitrogen-evolving microbial processes in the soil [9–11]. A part of the N_2O emissions also come from manure spread over the fields [10]. The imbalance between nitrogen added to the soil compared to harvested nitrogen is quantified as Nitrogen surplus (N-surplus) [12]. These surpluses that are not absorbed by the crops are washed off by rains and end up polluting rivers and sea. These flows contribute to the development of algal blooms [13] or dead zones [14], both phenomena altering the local ecosystem balance. A more balanced fertilizer use combined with improved nitrogen assimilation could help reduce these emissions [15]. The other chemicals are also a matter of concern, such as phosphates and the disrupted phosphate cycle [16]. ENS has been granted from the national research agency (ANR) for a project of phosphate farming with algae to clean up water (2022 - ANR Phosphalgue [17]).

Artificial lighting

It is worth noting that in some countries, national agriculture strategies also have an environmental cost. It is the case in the Netherlands, where greenhouses are widely spread. They depend on electricity-powered illumination and heat and have a significant impact on the GHG emissions of the country [18] (Figure 1.2). Indeed, the electricity generation of the country mainly comes from gas (52%) and coal (27%) (numbers from 2018 [19]). Improving the efficiency of indoor farming illumination to drive photosynthesis would result in energy savings in this scenario.

1.1.2 Farming footprints: the consequences of agricultural management practices

GHG is not the only way to measure the impact of agriculture on the Earth's geochemical cycles. The management of resources and the impact of farming practices on the soil also have a significant impact.

Water use

Although it does not appear in the carbon footprint, the water use was multiplied by two since 1961 [15]. It is bound to keep increasing if the global temperature increases, due to evaporation. Efficient water management practices are a primary target to equilibrate the water cycle in crops. Among the solutions come irrigation techniques, satellite monitoring, soil management and conservation, water harvesting, crop selection. The solutions also include decontamination of water by micro-organisms such as algae, for which Sony CSL has received funds starting in November 2023 (Mi-Hy).

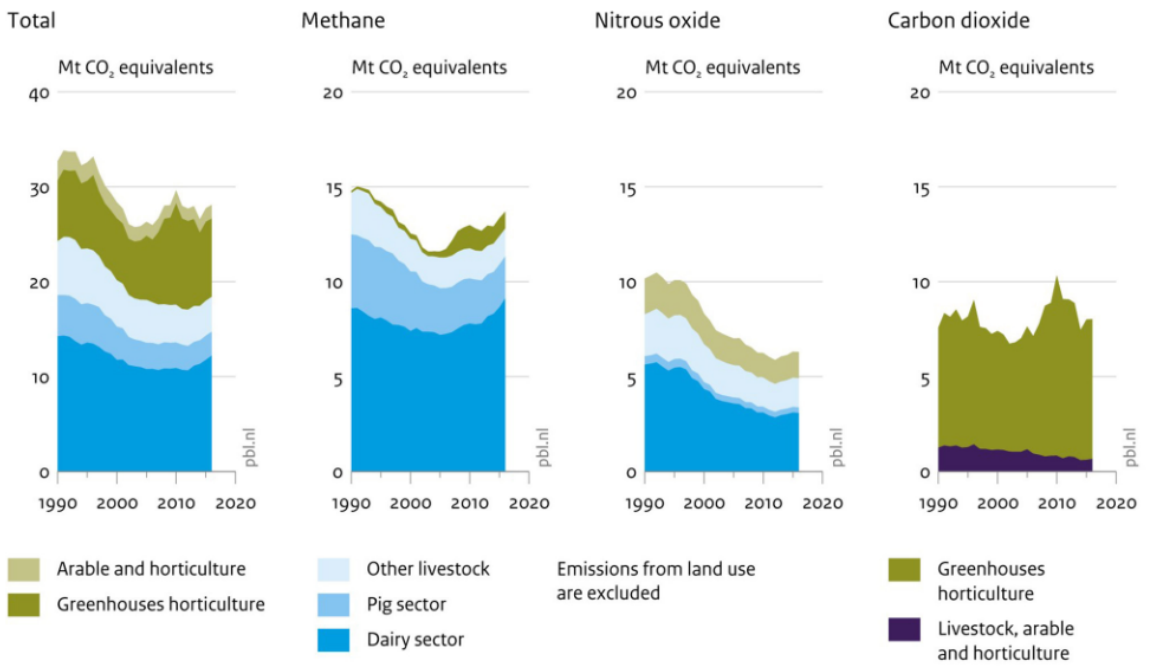

Figure 1.2: Netherlands GHG emissions in the agriculture sector by source. Adapted from [18].

Pest control

Pest control plays a crucial role in modern agriculture by minimizing pest damage while reducing the use of harmful chemicals. It is achieved through cultural practices, resistant varieties, and proactive monitoring [20] to regulate pest populations and maintain a balance between economic and environmental factors. A well balanced and living soil is often beneficial to reduce pathogen attacks [21].

Land erosion

Soil erosion is one major consequence of industrial farming. It refers to the process of soil being washed from its original location, leading to the loss of fertile topsoil. Some agricultural practices are associated with long-term exposure of the soil to rainfalls, while the use of cover crops [22], agroforestery [23], and hedgerows [23] can help mitigate soil erosion with other benefits: increasing water-holding capacity, reduced nutrient loss, increased nutrient absorption by plants [22, 23].

Biodiversity

It is necessary to stress that these management practices highly affect biodiversity. In 2021, the Intergovernmental Science-Policy Platform on Biodiversity and Ecosystem Services (IPBES) was created in order to enable and promote, among other, the conservation and sustainable use of biodiversity.

As the ecological challenges continue to grow, there is an urgent need for sustainable solutions that can balance agricultural productivity with environmental preservation while addressing the issues described above. Sustainable farming, with its focus on responsible resource management, regenerative practices, and reduced chemical usage, stands as a promising set of solutions to mitigate the adverse effects of conventional farming and spread more resilient and ecologically balanced strategies.

1.2 Sustainable farming to restore natural cycles balance and biodiversity

1.2.1 History of sustainable farming

The publication of Rachel Carson's book "Silent Spring" in 1962 [24] brought attention to the negative impact of synthetic chemical products on the environment, sparking discussions on natural farming. This led to the formation of the International Federation of Organic Agriculture Movements (IFOAM) in 1972, which played a crucial role in the development of organic farming regulations, including the EU "Certified organic food" label [25]. Around the same time in Australia, David Holmgren and Bill Mollison introduced Permaculture [26, 27], a holistic approach to sustainable design principles that found resonance among non-professional farmers seeking self-sufficiency.

In the late 1970s, researchers such as Altieri and Gliessman in South America explored sustainable farming systems, contributing to the emergence of agroecology [28, 29]. Agroecology encompasses the scientific study and practice of sustainable agriculture, focusing on the use of ecosystem services instead of chemical inputs. It has also expanded to include the study of the entire food system, incorporating ecological, economic, and social dimensions. Various specific approaches have gained recognition within agroecology, such as agroforestry (integrating trees in crops and pasture) and intercropping (mixing cereals and leguminous plants).

Where organic farming's main characteristic is the absence of chemical inputs, agroecology focuses on the use of services provided by the ecosystem. A trivial example of such an ecosystem service is the fertilization of fruit trees by pollinators.

1.2.2 Comparison between conventional and sustainable agriculture practices

In conventional agriculture, the farmer follows a set of well-defined processes, starting with a plowed land, the seed selection, the application of fertilizer, the mechanical seeding of a single crop, the irrigation and pest control, to obtain a consequent crop at the end of the season with a controlled risk of crop losses. Despite their efficiency, these practices have caused several imbalances that sustainable farming aims to correct. Yet farming is not a natural process: most of the products of the agrifood sector would not grow in the wild. As a consequence, replacing chemical inputs with ecosystem services while keeping high crop yields is a significant challenge.

In small-scale, vegetable production in moderate climates, excluding staple crops, dairy, livestock, and fisheries, most of the abiotic stresses are relatively well mastered. Nutrient stress can be overcome by the use of organic fertilizer to compensate for the export of nutrients through the sales of the vegetables. Automated irrigation is effective against drought stress, although does not avoid flooding and damage from hail. However, a soil management that pays careful attention to the soil's aggregate structure and carbon content can improve water retention, infiltration and flood control [30, 31][2]. Techniques to deal with chilling temperatures are well integrated into the practices of small vegetable farming [33], however increasing climate variability exposes farmers to prolonged periods of high temperatures. Adapted forms of agroforestry (e.g. combining fruit trees and vegetable production) have been proposed to reduce the risk of heat and light stress [34, 35].

However, it is the abiotic stresses (viral, bacterial, or fungal plant diseases, aggressors including nematodes, insects, molluscs and weeds) that pose the highest risks and against which, in the absence of chemical perticides, there is often little to protect the plants. This explains why organic farmers often rely on a catalog of sometimes heuristic methods to control pests [36] and why copper-based fungicides are still tolerated in organic agriculture [37]. On the previously mentioned stresses, the simplest is the management of weeds, which can be done mechanically after visual inspection. Technological advances can provide automated tools to reduce the drudgery and time spent weeding. For

[2]Minimal soil disturbance is one of the key focus points of conservation agriculture [32].

the other stresses, in agroecology and organic agriculture, the focus is shifted from curative measures to disease prevention in order to obtain reliable yields. Techniques such as crop associations [38], habitat management [39], and selective plant breeding [40] have known benefits to limit the potential of attacks of bioaggressors, however it is difficult to generalize as their study faces a combinatorial explosion and depends on environmental conditions. When a pest does invade, early stress detection is essential, both for conventional or organic agriculture [41]. Although the literature in agroecology is abundant on pest prevention, little has been written on mitigation. However, the earlier that farmers can detect an invasion, the easier it is to remove infected leaves or plants, or manually remove aggressors, in the hope of reducing the spreading of the pest. Plant status monitoring through fluorescence has also proved to be a useful method to anticipate risks [42].

The debate on whether organic agriculture sustains higher losses or has lower yields is very lively [43, 44]. What should be obvious from the above discussion is that the agroecological approach is more complex (in the sense of complex systems) because it takes into account the crop production in its relation to the multitude of highly variable and often little-understood ecosystem services. Its study necessarily combines know-how from multiple scientific fields [45]. Reintroducing diversity and variability in the crop field increases the complexity of the management. Novel approaches to measure, model, and predict agroecosystems may be beneficial to help spread sustainable practices.

1.3 The collaborative frame of the Cifre PhD

1.3.1 Industrial partner: Sony Computer Science Laboratories – Paris

SONY is a multinational consumer electronics Japanese company based in Tokyo, Japan. Established in 1946 initially as a repair store, the team swiftly transitioned into manufacturing their own products. Sony's first products on the market came in 1955: transistors, six years after their invention in the US. Sony is now renowned for its innovations, among them the Walkman, the Compact Disk (CD), the Blue-Ray and many more. It is also well-known today for the audio-visual products, smartphones, video games and consoles (PlayStation), as well as the music and film industry (Spider-Man, Men in Black...).
The company has kept a strong spirit of research and innovation and the best example was the creation of the Sony Computer Sciences laboratories in Japan in 1988. The inspiration of the laboratory was to host researchers to work on their personal project, with the condition that their work would be different from mainstream research. Historically the research was focused on operating systems and the Internet, but the range has expanded to bioinformatics, economics, cooking, agriculture, music and artificial intelligence. The daughter lab Sony CSL Paris was established in 1996, while Sony CSL Kyoto and Sony CSL Rome opened in 2022. On the side, Sony AI was opened in 2020 in order to meet the competition pressure in artificial intelligence lead by Google, Meta, Open AI and numerous new actors, leaving the upstream research to Sony CSL.

Sustainability team

The four topics of research in CSL Paris at the moment are Sustainability, Creativity, Music and Language, and they are all fueled by tools from artificial intelligence. The music team develops generational models for music creation and collaborates with Sony Music France and artists. They work on developing modular tools to generate synthetic music on demand and with flexibility. The Language team works on the emergence and evolution of language through robotics and simulations, as well as language generation and aid for speech and reading disabilities. The Creativity team studies complex systems such as social networks, city organization, to question the emergence of creativity. The Sustainability team builds open-source and open-hardware tools to answer challenges in agriculture. It is currently focused on developing robotic platforms for organic gardening farms and research centers, which started with the European project ROMI (Robotics for Microfarms). We

concentrate mostly on organic, diversified market farms. In addition, we take inspiration from the 19th century Parisian jardiniers-maraîchers who developed techniques to optimise vegetable production both in space (no soil remains unused, apply mixed intercropping) and time (overlapping growth cycles), and to grow vegetables out-of-season [46, 47]. It should also be noted that Sony CSL in Tokyo works on the topic of Synecoculture, elaborated by Masa Funabashi [48, 49]. This approach is inspired by Complex Systems and combines hundreds of different edible species randomly on small plots with the objective to find an ecological niche in which the plants can thrive. It is well adapted to re-created ecosystems on degraded soils.

The ROMI project

Between conventional and organic market farming lies a fertile field for sustainable innovation. Sony CSL proposes smart robotic platforms developed for small organic market gardening farms [50, 51]. They are intended to improve the working conditions of farmers while respecting the complexity of diversified agriculture. Our main contributions rely on imaging techniques using computer vision. It was the objective of the H2020 ROMI project (Robotics for Microfarms) which was funded from 2017 to 2022. The outcome was the development of an automated robot designed for field work, a robot held on a line cable to monitor the crops, and a 3D plant scanner to monitor growth. The robotic developments continue with the Centrinno project (New CENTRalities in INdustrial areas as engines for inNOvation and urban transformation - H2020 2020-2024). The tools are aimed at maintaining crops by regular weeding and 2D/3D-monitoring (Figure 1.3). The tools developed can also be used in academic research [52].

Figure 1.3: Romi Rover in the field of the Parc la Villette (Paris) for the FabCity Summit

The field-robot is able to distinguish weeds from crops with imaging techniques, and compute a path to mechanically remove the weeds. To enhance the functionality of the ROMI rover, the development of a technique to perform direct and non-invasive diagnostic of the stress status of the plant before any damage is visible was a highly desired target. The idea to use fluorescence as a reporter of photosynthesis was given by Ludovic Jullien and Thomas Le Saux at Ecole Normale Supérieure (ENS) when I met them.

1.3.2 Academic partner: Chimie Physique et Biologique de la Matière Vivante

Ludovic Jullien and Thomas Le Saux are members of the group Chimie Physique et Biologique de la Matière Vivante (CPBMV[3]) which is hosted by the Processus d'Activation Sélectif par Transfert d'Energie Uni-électronique ou Radiative (PASTEUR[4]) laboratory of the Chemistry department of ENS. It is a pluridisciplinary laboratory where a wide range of expertise is present, from analytical chemistry to optical developments.

Fluorescent proteins

The group has worked on a collection of fluorescent dyes and proteins with a particular attention on the dynamic fluorescence response to light stimulation and environmental changes. In recent years, a focus was given to the study of Reversible Photoswitchable Fluorescent Proteins (RSFP) (see Chapter 2). These proteins switch from a bright fluorescent state to a dark state upon illumination. The illumination provokes a photochemical reaction, whose kinetic constant is related to the illumination intensity. To exploit the RSFPs properties, further developments implying specific harmonic illumination strategies were implemented to leverage the tools of chemical kinetics and Fourier analysis. The objective is to exploit the alternative representation of the fluorescence signals, either through a kinetic model or a Fourier transform, to perform an analysis of the data that could not be possible with time series alone.

The OPIOM strategy [53] allows to unmix fluorescence from background fluorescence using demodulation. It allows to better image a signal of interest lost within the background noise that can come from unwanted fluorescent entities. The RSFPs respond with a phase-delay to the input oscillating light. Therefore, retaining only the out-of-phase (delayed) component on the fluorescence leads to discarding the background whose response is in phase with the excitation light.

The HIGHLIGHT [54] strategy aims at identifying RSFPs within a sample by exploiting the non-linearity of their fluorescence response. When excited by a sinusoidal signal, a non-photoactive fluorophore will emit a fluorescent signal at the same fundamental frequency. Instead, the non-linear response of the RSFPs produce a signal with multiple harmonics, whose frequencies are multiples of the fundamental frequency. By measuring the amplitude of the Fourier transform of the signal at these specific frequencies, it is possible to distinguish RSFPs from fluorophores that are not distinguished by the OPIOM protocol.

The LIGHTNING [55] strategy exploits the difference of kinetic response to the same input pattern. Each RSFP has a specific photochemical constant. Therefore, it is possible to unmix different RSFP tags by measuring their kinetic properties. It enables multi-labelling with up to 20 different – but spectrally similar – RSFPs (10 in a biological sample), while classical spectral discriminations based on wavelength allow using a maximum of 3-4 spectrally distinct markers.

Fluorescent plants

In the midst of these projects, the group came to develop an imaging system that was used to monitor the stress response to water or iron deficiency of plants by genetically expressing an RSFP under the control of a stress-related gene. Although the results were very promising, enabling to monitor stress in response to water and iron deficiency [56], the group met resistance when searching for institutional financial support because it required genetic modification of the crops. This first encounter with plants led them to consider using the endogeneous fluorescence of plants as a reporter of stress instead of inducing the expression of external probes.

[3]Physical and Biological Chemistry of Living Matter

[4]Selective Activation Process by Uni-electronic or Radiative Energy Transfer

1.4 Remote sensing of plants using chlorophyll fluorescence

1.4.1 A centenarian method to probe plants health

In Chapter 3, I detail the origin and the interpretation of the endogeneous fluorescence in plants and how it can report on their physiological status. It has been used as a tool to monitor the photosynthetic chain since the first studies more than 90 years ago [57]. It is now used in multiple scales, from micrometer (single-cell algae monitoring) to kilometers (forest monitoring). The objective is to establish a health status of the photosynthetic organisms, be it a young plant shoot for selection in a laboratory, or a canopy from a satellite. It relies on the collection of the photosynthetic organisms' endogenous fluorescence, emitted in response to light stimulation, whether artificial or solar (Sun-Induced Fluorescence, Figure 1.4). Remote sensing technologies can provide rapid and comprehensive assessments of vegetation status over extensive areas, with the example of the FLEX (Fluorescence Explorer) program, which aims at launching a satellite in 2025 with the objective to quantify photosynthetic activity of the terrestrial vegetation [58]. They can also be used at the field or laboratory scales, with multiple companies developing instruments for that purpose (Walz, PSI, LICOR, PhotosynQ, and more). They implement specific artificial illumination protocols, such as Pulse-Amplitude Modulated (PAM) fluorescence [59] which forces the photosynthetic chain into specific regimes to probe its status. By utilizing technologies like remote sensing and imaging, plant stressors can be identified before they become visible to the naked eye or a camera [60, 61]. This enables targeted application of inputs and reducing energy-intensive practices associated with excessive fertilizer use. Furthermore, non-invasive methods can aid in optimizing irrigation practices, conserving water and energy resources by delivering water only when and where needed based on plant stress indicators. This capability facilitates early detection of stress conditions, enabling farmers and agronomists to implement timely interventions and prevent widespread crop losses. Remote sensing also allows for the identification of spatial variations in plant health, aiding in site-specific management practices and resource allocation [62]. Plant sensing using fluorescence is a fertile field to bring new insights from the fluorescence kinetics in chemistry – a topic of interest for the team of Ludovic Jullien and Thomas Le Saux at ENS, described below.

By bringing together the drive to contribute to the development of sustainable agriculture from Sony CSL and the scientific expertise of Ludovic Jullien and Thomas Le Saux, we built the project of the PhD work presented in this manuscript. Although Sony CSL usually works with plants, we also decided to work on microalgae. Indeed the species *Chlamydomonas reinhardtii* we used is a reference organism in photosynthesis research, and an easy one to cultivate.

1.4.2 Presentation of the PhD project (Cifre)

The PhD proposal we wrote stated that the objective was to design a new protocol to study the fluorescence response of photosynthetic organisms to changes in illumination. The protocol would generate a significant amount of data, from which robust and independent parameters would be extracted. These parameters would be processed using machine learning methods, which would enable the differentiation of photosynthetic organisms and the determination of their physiological status based on fluorescence response. In the long term, the optical instrument developed could be implemented on a prototype robot intended to assist organic vegetable farmers. I will show how I addressed these questions at the microscopic scale on microalgae.

From the beginning of the project, we consolidated collaborations with previous collaborators from the group of CPBMV. In particular with Ladislav Nedbal (Forschungszentrum Jülich) who has been involved in the stimulation of photosystems using oscillating light for several years [64], with Dusan Lazár (Palacky University Olomouc) who developed kinetic models of the photosynthetic apparatus [61, 65], and with Benjamin Bailleul (Institut de Biologie Physico-Chimique) who brought his expertise on microalgae mutants and stress-response [66, 67]. We have collaborated to write several publications, but the collaboration was brought further with the initiative from Ludovic Jullien to

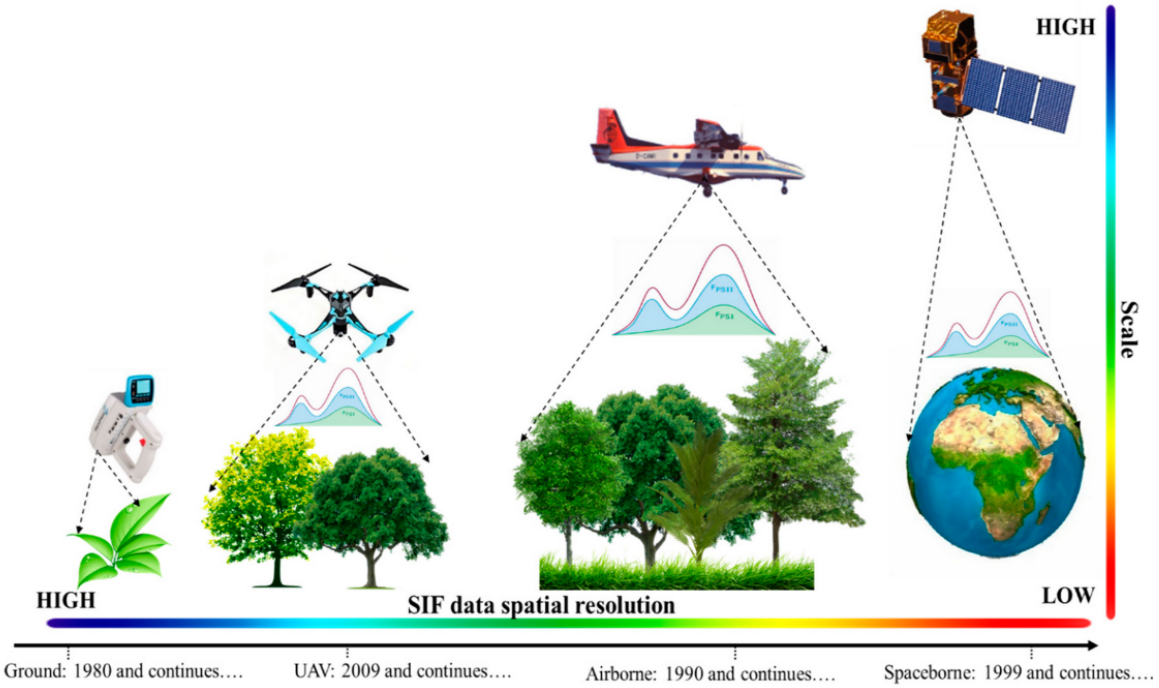

Figure 1.4: The different scales at which the SIF (Sun-Induced Fluorescence) is measured: from leaf to canopy. Adapted from [63].

take the lead on a European Union funding proposal called DREAM (Dynamic contrast for Remote sensing and EnvironmentAl Monitoring). In particular, the DREAM project follows up on the work at the microscopic scale to bring it to the macroscopic scale on plants by using oscillating light excitation. The consortium was complemented by the teams of Shizue Matsubara (Forschungszentrum Jülich) for Plant Studies, Leyla Özkan (Eindhoven University of Technology) for System Identification, Jacques Fattacioli (ENS) for Microfluidics, and Gilles Charvin (Institut de génétique, biologie moléculaire et cellulaire) for photosynthesis enhancement. Below, the DREAM project is briefly introduced, as an additional background for reading out the present PhD work. The DREAM project was granted by EIC Pathfinder in 2021, one year after the beginning of my PhD thesis. I will highlight how the development of my PhD project contributed to the objectives of DREAM.

1.4.3 Presentation of the DREAM project (EIC Pathfinder)

To cope with environmental fluctuations (e.g. light), photosynthesis regulation involves multiple reactions over the 10^{-3} – 10^{3} s range (from tuning electron transfers to driving syntheses/degradations) [68–70]. The DREAM project aims at enabling its exploitation for production in controlled environments and hence, offer a complementary and synergistic strategy to genome engineering for improving plant cultivation [71, 72].

To reach this goal, DREAM will dissolve the traditional boundaries between sciences (e.g. electrical engineering and chemistry) and realize science-towards-technology breakthroughs on the following aspects:

Novel protocols to probe the photosynthetic apparatus

In photosynthesis sensing, most practices apply a continuous (or a series of) actinic light and detecting pulses or pulse amplitude-modulated – PAM – methods on preliminarily dark-acclimated

organisms. The response of endogenous chlorophyll fluorescence to this type of stimulation yields parameters that lack selectivity [61, 65]. In the DREAM project we will introduce modulated illuminations that are much closer to natural environmental light conditions, to enable sensing, even on light-acclimated photosynthetic organisms. Moreover, beyond chlorophyll fluorescence, DREAM will exploit luminescent nanosensors, which have seldom been used to interrogate photosynthetic organisms [73]. Hence, DREAM will yield a multi-parameter optically readable fingerprint reporting on the dynamics of photosynthesis regulation with much improved sensing selectivity over the current approaches[74, 75].

Global server

The strategy will be validated for sensing on a few organisms under standardized conditions of laboratories and greenhouses. In the perspective to extend acquisition and processing of data for sensing a wide variety of algae and plants under environmental conditions relevant to the future of cultivation in controlled environments, we will implement a server incrementally improving its diagnosis from data collected by multiple participants [76]. The project members will be the first participants, and the species investigated will start from *Chlamydomonas reinhardtii* and progressively extend to *Arabidopsis thaliana* and a crop species – the tomato.

Portable device

We aim to provide a miniaturized device to record and process the response of reporters of the dynamics of photosynthesis regulation in microalgae or plants. The extracted rich kinetic data will be sent to the server, where they will be processed with the tools of non-linear system identification and control. Fed by the participative action of multiple end users, the server will benefit from kinetic information gathered from a wide range of organisms and environmental conditions. Hence, it can harness the extracted kinetic data for delivering selective categorization of the physiological status as well as modulated illumination for lighting enhancement. These specific protocols will enable the end-users for sustainable production in controlled environments by reducing their demands of resources.

Optimizing illumination

Photosynthesis enhancement has been reported by exposing photosynthetic organisms to flashing light, as compared to the same photon dose under continuous light [77]. However, this phenomenon has remained only partially understood from adopting a linear perspective, which contradicts the obviously non-linear dynamics of photosynthesis regulation (e.g. oscillations [78]). Following theoretical and experimental reports showing that the periodic excitation of non-linear dynamic systems can improve the yield of energy conversions by up to several tens of percent [79, 80], we will exploit this non-linear dynamics and tailor modulated illuminations, which optimise the photon budget for driving photosynthesis.

1.5 Description of the PhD work

The consortium was rich with knowledge on photosynthesis, fluorescence kinetics, machine learning and instrumental development. To reach the objectives of the PhD project, I had to leverage each of these aspects in order to build an instrument to induce and read the fluorescence, and develop methods to extract biologically significant data from the collected fluorescence. At ENS, IBPC and Sony CSL, it is traditional to build specific instruments for addressing new research questions, rather than relying on already-existing instruments. This perspective allows to be independent of the hardware and software limitations. For example, it allows to select a specific and desired combination of light sources to probe the fluorescence of plants and that of luminescent nanosensors. It allows to

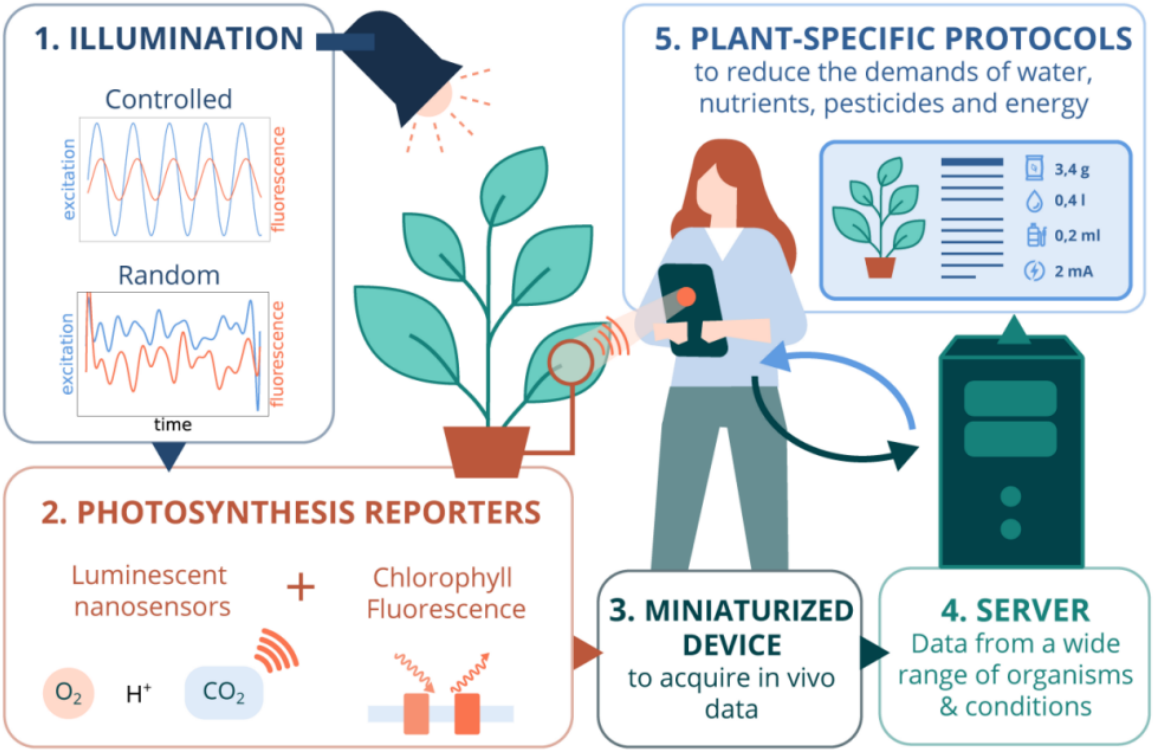

Figure 1.5: *The DREAM vision.*

design illumination sequences without pre-imposed pattern. It allows to work with modular equipments and easily change camera, light sources, filters, stage, objective, etc. Finally, I will show that it allows also to control the whole design and be able to reduce it and miniaturize it while keeping the same software.

Given the collaboration with IBPC and the proximity of IBPC, ENS and Sony CSL, all within a three minutes walk, we decided to focus on *Chlamydomonas reinhardtii* for which IBPC holds a wide collection of strains [81]. The reasons for this choice are detailed in Chapter 4.

I developed an automated microscope instrument to study algae at the single-cell level, for long-term observations. The requirements were to collect the endogeneous fluorescence of photosynthetic organisms but also comply with the potential use of nanosensors, which required a combination of selected exciting wavelengths for the light source, and appropriate filtering techniques for the fluorescence collection. The instrument was built keeping in mind that the methods developed should be transferable to an affordable portable system.

It gave rise to a list of specifications described in **Chapter 2**. Following this specification list, I justify the choice of hardware and software we made, and compare them to the choices made in several state-of-the-art instruments. In particular, I insisted on modularity, automation, open-source and the ability to persistently record experimental results, characteristics not found in the instruments of the literature. The final set-up and its characterization are presented.

This chapter also describes a method to calibrate the light intensity used to stress the algae, which is necessary to study the distribution of responses within a sample. The method is based on monitoring the kinetic evolution of fluorescent actinometers exposed to the input light. It resulted in the development of a general method transferable to multiple fields to calibrate light sources at various wavelengths, in a broad intensity range. Furthermore, performing the protocol under a microscope allows to measure the light distribution within a sample. These protocols address the work-packages

identified by the QUAREP-LiMi group (Quality Assessment and Reproducibility for Instruments & Images in Light Microscopy [82]). This part of the PhD resulted in producing an accepted manuscript for *Nature Methods*. It is introduced in Appendix 2.6 because its scope is broader than the chapter's topic.

Chapter 3 describes the origin of the endogenous fluorescence of photosynthetic organisms and explain step-by-step how it can be used to obtain information on the status of the photosynthetic chain, and in consequence the stress level of the whole organism, since the photosynthetic chain is the root process of their metabolism.

This chapter then includes a manuscript explaining the various actinometric processes in leaves, happening at different time scales. It allows to demonstrate the diversity and complexity of the dynamic system studied while introducing the various phenomena tackled in the manuscript.

Then the validation of the home-built instrument against a collaborator's instrument is described. A PAM-like protocol was implemented in the instrument and modified to meet the sensitivity constraints imposed on the home-built set-up. We performed the same experiment on both instruments with the same sample and obtained statistically similar results.

This preliminary work allowed us to identify the potential and limits of our instrument and the specifications for a first case study of stress-response of single-cell algae. We deemed it important to select a question that had already been explored at the population level. That way we could evaluate the performances of our analysis in comparison to results from the literature. I will detail the various aspects that led us to select the response to high-light stress which is named NPQ (for Non-Photochemical Quenching, introduced in Chapter 3).

Chapter 4 describes how the home-built instrument was used to perform fluorescence experiments by exposing algae to light stress. The experiments consisted in collecting a video of fluorescence time traces, and retrieving the individual responses after image segmentation. The three light-stress responses studied are entangled and have dynamic signatures that overlap within the fluorescence time trace. We established a biological protocol including mutant strains and sample preparation to probe the stresses separately. These separate responses were used to build a reference dataset to train a machine learning framework. This framework relies on two dimension-reduction steps. First, Dictionary Learning is used to reduce the dimension of the fluorescence traces with optimized reconstruction, and it is followed by a dimension reduction using Linear Discriminant Analysis to maximize the separability of the annotated classes. This combination allows to represent a general stress response along three dimensions, each axis representing one single stress response.

This methodology allowed quantifying the stress response of wild-type strains and unmix the stress responses within the fluorescence traces. I also show how putting emphasis on the reconstruction capability of the pipeline allows identifying outliers in the input data.

In **Chapter 5** I detail how I developed an open hardware version of our home-built microscope, to complement the open-software and open-data approach used for the instrument presented in Chapter 2. I present how I used the optics open-hardware library OpenUC2 to 3D-print the system in a modular way. The software part of both instruments is described in this chapter, with an introduction of the independent modules to control the lights, the camera and the motors. I also put emphasis on the database system implemented to collect the experimental parameters, the code, and the outputs of each experiment in a database. This database was borrowed from computer science experimentalists and to my knowledge, was never used for laboratory experiments before.

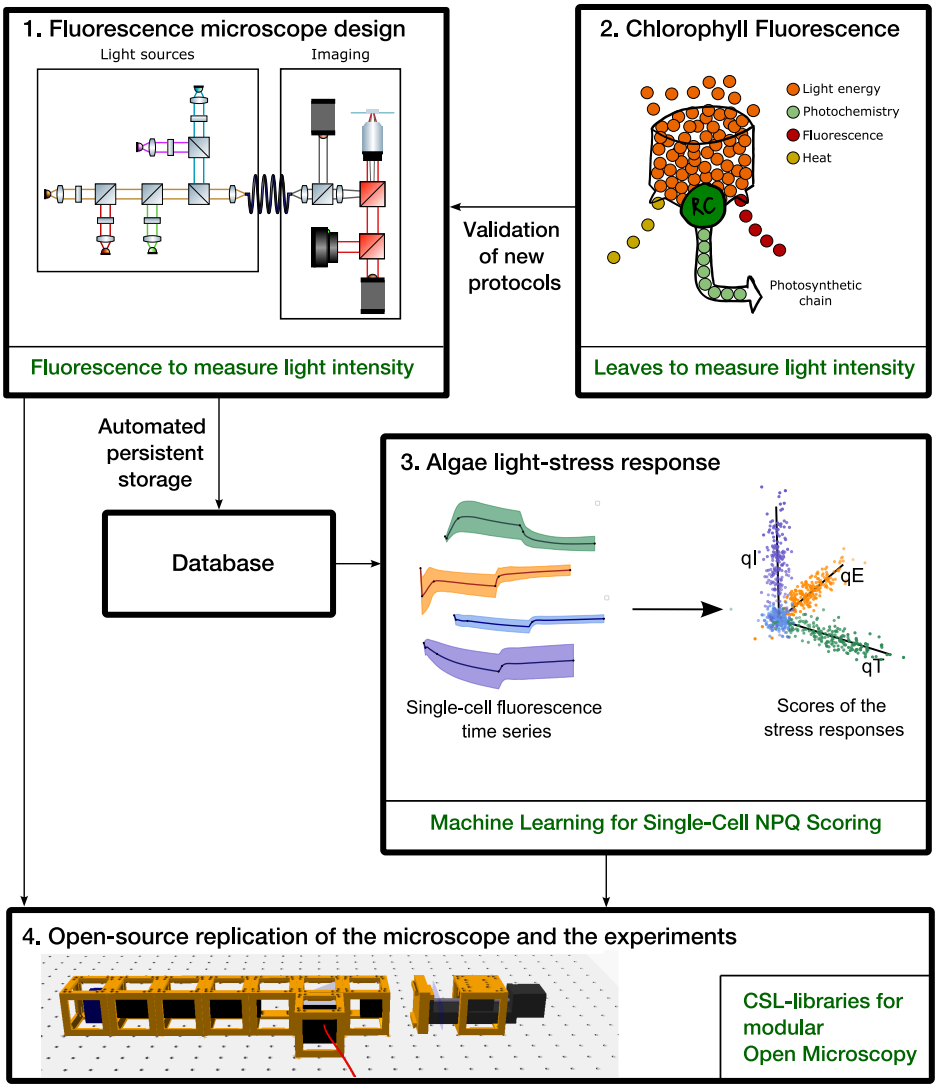

Figure 1.6: *Summary of the PhD work and prepared manuscripts.*

Chapter 2

Fluorescence microscope design

2.1 Background and motivations to build a new instrument

Chlorophyll fluorescence (ChlF) corresponds to the emission of fluorescence photons by photosynthetic organisms in the range 650-750 nm as a consequence of excitation by any light from the visible spectrum below 750 nm. It is detailed specifically in the next Chapter. Multiple instruments to probe ChlF already exist in the literature (including imaging: [83–88]) and on the market (Walz, PSI, PhotosynQ, LI-COR...). However, they are proprietary black-boxes which limits their use when developing new protocols, or they are limited in their configuration possibilities because they are not modular. For these reasons, and by relying on these instruments to develop our specification list, we decided to build a new instrument, keeping a high modularity as a general frame. Another aspect which led us to build our own instrument is that, in ChlF research, one critical protocol aspect requires to be sensitive enough to record the fluorescence response to a low-intensity short light pulse (called measuring pulse, see Chapter 3). This becomes a major challenge in imaging, which has led to multiple compromises (averaging, long integration times, coupling of the camera with a photon counter). The compromises are made in accordance to the camera noise sensitivity, and often involve buying an expensive Peltier-cooled camera (see [84] for a review). At the start of the project, the measurement method we envisioned did not rely on measuring pulse but rather oscillating actinic light of various amplitudes, leveraging the possibility to demodulate the signal based on its frequency content. We were also planning to transfer the technology to non-academic users, adding the necessity to provide an affordable and accessible design. Therefore, we relaxed this high-sensitivity constraint when building our setup and developed new protocols requiring no measuring pulse.

The following sections begin by a description of the requirements we set for the instrument with Ludovic Jullien and Thomas Le Saux. I then move forward with the instrument specifications we derived to describe the epifluorescence microscope we needed. Finally, I present the setup we built with Thomas Le Saux following these specifications and various characterizations I performed. One of the characterizations led to an extended work on calibration of light intensity, accepted in *Nature Methods* and included in the Appendix 2.6 of this Chapter. The consequent Supplementary Materials are integrated in the Appendix A.1 at the end of the manuscript.

2.2 Instrument requirements for ChlF experiments

2.2.1 An imaging scale adapted to single-cell studies

As this work marked the inaugural exploration of ChlF in both ENS and Sony laboratories, we needed to take a decision regarding the organism with which to commence our study. Although the collaboration between Sony CSL and PASTEUR had started based on the topic of small-scale

farming, beginning the study with higher plants was not ideal because of the lack of experience of either team in lab-grown plants. Furthermore, the growth time was not compatible with the high rate of experiences necessary to enrich our knowledge on the organisms and to develop the various sensing protocols. On the other hand, the unicellular algae *Chlamydomonas reinhardtii* is a reference organism to study photosynthesis [89, 90]. The team of ENS had previously been in contact with the IBPC (Institut de Biologie Physico-Chimique) which owns the largest collection of *Chlamydomonas reinhardtii* [81], including mutants with known alterations of the photosynthetic pathway. The research field of *Chlamydomonas reinhardtii* has also worked on the parallels and differences with higher plants, which will allow us to predict the transferability of our results to higher plants.

We wanted to use an imaging system for two reasons. On the one hand, as the robot is autonomous, it would need to be able to image the fluorescence to get spatial information on the fluorescence emitter (even identify the plant type with classical imaging [91]). In that sense it would differ from portable commercial instruments in the field which are used manually by the farmers to clip the leaves and probe them (e.g. MultispeQ (PhotosynQ), FluorPen (PSI), PAM-2500 (Walz)). The second reason is that we wanted to study the distribution of response to stress within a population. It involved studying a statistically significant population, with more than 50 individuals.

The typical radius of a *Chlamydomonas reinhardtii* cell is 5 μm [89], which is why we decided to build a microscope. A 10x magnification allows imaging hundreds of algae in the field of view while keeping a cellular resolution. Interestingly, it does not limit the study to algae: it is still possible to observe leaves under the microscope, with several cells in the field of view [92]. We built a wide-field epifluorescence microscope where the excitation light flows through the same objective as the collected fluorescence. The fluorescence emission by the sample is isotropic, and a fraction is collected by the objective to be transferred to the imaging system. The wavelength of fluorescence being higher than excitation light (with one-photon excitation), it is possible to drive the fluorescence light through a different pathway using a filter that reflects these higher wavelengths towards a collection instrument able to read the fluorescence (photon counter, camera).

2.2.2 Modularity to enable exploratory research

As it was an exploratory project, we planned that we would need to keep a lot of flexibility in the instrument design in order to be able to adapt to the various constraints to come. For this reason we built the instrument with Thorlabs modules, allowing to structure and modify the setup easily (affordability of these modules is discussed in Chapter 5). Knowing the photon budget was a limit presented in the literature [84], I anticipated that I would face difficulties with imaging. Therefore, I introduced the possibility to split the fluorescence collection path into two, one part reaching the camera and the other reaching a photon counter (similar to [93]). I also introduced a diaphragm to select individual samples (for example alga cell) manually. Once the diaphragm is closed around the individual object, the fluorescence collected by the imaging circuit originates from this object only. This allows to collect the fluorescence from a single object fluorescence with the photon counter as in [59], with more sensitivity and time-resolution than with the camera.

2.2.3 Accessibility and affordability to enable reproduction

The ROMI rover is fully open-hardware and open-software. We aimed as a long term goal to develop an embarked instrument respecting this philosophy. It is also a desired specificity for a cheap and portable prototype related to the DREAM project. To pursue this goal, considerations such as the cost of materials, ease of assembly, and availability of components were taken into account when building the specifications.

Still, for the epifluorescence microscope, I relaxed some aspects in order to build an instrument that would not limit my investigations. Where I could, I built the automated modules, but to speed up the prototyping I also relied on more expensive and closed-systems (from NI or Thorlabs, IDS)

using APIs (control protocols) provided by the manufacturer. These parts were rearranged in Chapter 5 when I built a fully open-source version of instrument.

2.2.4 Open-Source software to enable modification and reproduction

Providing open-source software allows new users to modify and improve the microscope's functionality, develop new analysis algorithms, and contribute to the overall advancement of the instrument. That is why I added a layer in Python to control all the instruments, and allow the next developers and users to work on a unified code rather than the multiple APIs of the different manufacturers. As this development was intermediary between open and closed-source, and because I have later developed a fully open-source version, I did not detail it in this manuscript. Instead, I present the full open-source version in Chapter 5. The extra Python layer allowed to fully automate the instrument. The two advantages were that, in times of Covid, I could work remotely on the instrument and write and test protocols from home, when traveling to work was forbidden. It also allowed me to run experiments when I was in conferences and during the nights. The other advantage is the considerate minimization of user-based errors by using scripted protocols to fix the experimental parameters. Special care was given not to depend only on automation: all the automated modules can be controlled manually in parallel, to ease debugging and be independent of the software for quick trials.

It differentiates our instrument from the state-of-the-art, where ChlF instrument software are proprietary or depend on proprietary software, and are not made available [83, 86, 87, 93].

2.2.5 Database system to store data and metadata

Often it comes that, when investigating a new experimental topic, the trial data to reach conclusive protocols are lost in the computer folders and never reused. I wanted to avoid this scenario, and for this reason I got inspired by Machine Learning research. The training of machine learning algorithms involves multiple trials with different hyperparameters to obtain a performing transformation algorithm, for example a convolution neural network able to classify images. Often, large designs of experiments are launched to run for several hours on remote computers to test the hyperparameters. In order to easily visualize and analyze the output of the trainings, several tools have been developed which provide dashboard interfaces with the different parameters and outputs (Tensorboard, Sacred, Neptune). I had the idea to leverage the developments of one of these tools, Sacred (called this way because "all experiments are sacred") to run and save the microscope experiments. An extract of Sacred website says:

> Sacred is a tool to help you configure, organize, log and reproduce experiments. It is designed to do all the tedious overhead work that you need to do around your actual experiment in order to:
>
> - keep track of all the parameters of your experiment
> - easily run your experiment for different settings
> - save configurations for individual runs in a database
> - reproduce your results
>
> Sacred achieves this through the following main mechanisms:
>
> - **Config Scopes** A very convenient way of storing the local variables in a function to define the parameters your experiment uses.
> - **Config Injection** You can access all parameters of your configuration from every function. They are automatically injected by name.
> - **Command-line interface** You get a powerful command-line interface for each experiment that you can use to change parameters and run different variants.

- **Observers** Sacred provides Observers that log all kinds of information about your experiment, its dependencies, the configuration you used, the machine it is run on, and of course the result. These can be saved to a noSQL database (for example MongoDB), for easy access later.
- **Automatic seeding** helps to control the randomness in your experiments, such that the results remain reproducible.

Further details about Sacred are provided in Chapter 5. A comparable strategy has been developed in one of the instruments of the literature (PhotosynQ project [94]) and has demonstrated its validity by gathering a large community online.

2.3 Hardware specifications for the epifluorescence microscope

When building a fluorescence microscope, several optical considerations need to be taken into account to ensure optimal imaging and detection of fluorescence signals. These considerations play a crucial role in maximizing sensitivity, resolution, and signal-to-noise ratio. I had to leverage them with the long-term goal of embarked affordable instrument. The next sections describe the various aspects taken into account for the instrument specifications. For ease of read, I separated the specifications from the list of hardware.

2.3.1 Light sources to excite the fluorescence

Selecting an appropriate excitation light source is critical for fluorescence imaging. Common choices include light-emitting diodes (LEDs), laser diodes, or arc lamps. In our case, we needed to produce light up to an intensity equivalent to the maximal sunlight irradiance on Earth's surface (thousands of μmol(photons) $\cdot\, \mathrm{m}^{-2} \cdot \mathrm{s}^{-1}$) to shine the field of view of a 10x microscope. We evaluated that we could use single high-power LEDs to reach this maximal light level [95]. LEDs exhibit remarkable durability, requiring no costly electronics, and enabling microsecond-scale switching. Moreover, they offer a narrow bandwidth while being accessible across the UV/Vis/NIR spectrum. It is compatible with our affordability and accessibility constraints while numerous proofs can be found in the literature that they are suitable for microscopy (to cite only [96]). We could also have used lasers, but working with incoherent light of the LEDs allows avoiding speckle patterns due to interferences, polarization and higher costs.

In our case, since we also wanted to be able to measure the fluorescence of nanosensors for the DREAM project, we selected a set of wavelengths for the specific applications. In order to probe the fluorescence of pH and O_2 sensors, we aimed to excite the photosynthetic organisms with green light which is minimally absorbed by photosynthetic organisms (see Chapter 3). To measure the fluorescence of CO_2 probes and possibly NADPH, we aimed to excite the systems with purple light. We also introduced two red lights in order to excite separately P680 and P700 (see Chapter 3). Finally, we introduced a blue LED for it is highly absorbed by the Chlorophyll and because multiple photoreceptors of photosynthetic organisms are light-sensitive (see Chapter 4 and [97]). Eventually, we incorporated multiple LEDs with different wavelengths (purple, blue, green, red, far red). Note that having all these LEDs allows to probe the fluorescence of complex system such as leaves with more possibilities. Indeed, the absorbance of the leaves depends on the wavelength (Chapter 3). LEDs are commonly used in ChlF imaging instruments [83, 86, 87]. However, they are often arranged in crowns in order to reach a high light intensity over a wide surface, which leads to inhomogeneous patterns. Further, it makes the LED filtering more complex by relying on large filter plates [86]. In [87] however, a liquid light guide is used to channel the light coming from multiple sources and probably contributes to homogenize the light flux (no specific build details are provided by the manufacturer). We also used a light guide (silicon optical fiber) to homogenize the intensity in the field of view as described in the next section.

The LEDs have narrow bandwidths but were still filtered with band-pass filters to avoid any leak over other wavelengths, in particular over the fluorescence emission spectrum.

We collimated the LEDs and combined them as displayed in Figure 2.1 with different dichroic filters. We will show later that in some protocols, we needed two light sources with different intensities. We could have used different LEDs of the same wavelength with different opacity filters in front to have the two intensities. However, it is easier to combine with dichroic filters light fluxes coming from different sources if they have different wavelengths. For example, to combine λ_1 and λ_2 we can use a filter that fully transmits λ_1 and fully reflects λ_2. If the light sources are arranged at 90^o and oriented towards the dichroic, the resulting beam will be in the direction of the λ_1 source and combine the intensity from λ_1 and λ_2. If we wanted to use the same color, we would have used semi-reflecting filters, which would have resulted in loss of intensity, because only part of the light would have been reflected.

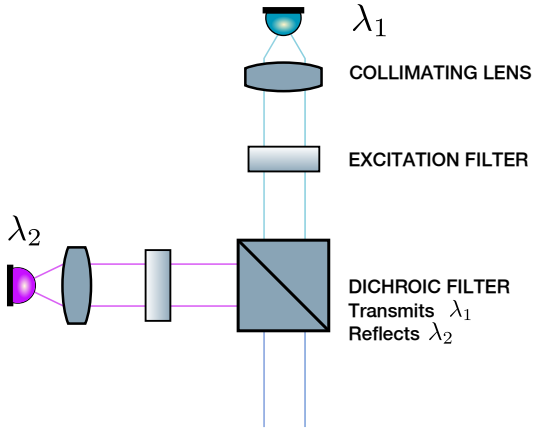

Figure 2.1: *Principle of LED combination with a dichroic filter.*

2.3.2 Filter wheel to reach four orders of magnitude of illumination intensity

In front of the LED used to excite the photosystem to perturb it, I placed an automated filter wheel. It allows reaching with high precision light levels from 1 μmol(photons) $\cdot$ m^{-2} $\cdot$ s^{-1}to 10000 μmol(photons) $\cdot$ m^{-2} $\cdot$ s^{-1}, accessing the whole spectrum of protocols found in ChlF research. This costly wheel could be reproduced in open source using a Nema motor and 3D printing if needed.

2.3.3 Light injection to illuminate the sample

One crucial parameter of the illumination in the field of view of the microscope is the homogeneity of the spot. A high-power LED is actually made of a grid of smaller LEDs. Using them to illuminate directly an imaging system results in an heterogeneous illumination in the field of view. To address this issue, I opted to direct the LED light into a large-core multimode optical fiber. By doing so, the fiber effectively blends the light by allowing the various excited modes to mix as the light travels through the fiber, resulting in a more uniform illumination [98]. I could have used a liquid light guide as in [87], but the core is ten times wider than optical fibers which requires larger optics to collimate the output. Large optics are more expensive and rarer than one-inch optics which is a standard compatible with large-core optical fibers.

The light from the LEDs is injected in the fiber with a microscope objective of matching numerical aperture. The size of the LED chip is 1 mm, I selected an objective magnification and an optical

fiber core size such that the whole chip image is injected into the fiber. The output of the fiber is collimated by a similar microscope objective.

A strong advantage of this method is to decouple the light sources from the imaging system. It allows to switch the light source easily. I used this feature to inject a white light source when I demonstrated how to calibrate a large-spectrum white LED with a fluorophore (see 2.6) or a leaf (see 3.4).

2.3.4 Light sources control

The microscope LEDs are controlled by a Thorlabs LED controller, highly expensive, but also highly responsive (see below for the response time characterization). It is controlled partly serially with Python (to set the maximal levels) and partly by an analog signal (to control the signal evolution with time). This control analog signal is generated in two different ways depending on the application. When sending light pulses of short duration (miliseconds) to different synchronized LEDs, I used an Arduino with a custom code developed inn the ROMI project (described in Chapter 5), exploiting the Arduino internal clock to generate ON-OFF control signals up to the kHz. When generating complex signals such as sinusoids, or any signal that can be written as a Python array, I used a National Instrument Data Acquisition (DAQ) card at 3 MHz to generate and read signals. Power switches are used to channel the signal from either the Arduino or the DAQ card to the LED controller. On the topic of light source control, I added a glass slide on the path of the excitation light in order to reflect a fraction towards photon counter. It allows to measure the photons sent to the system and make experimental controls. It is only shown in Figure 2.4. Note that only four LEDs can be controlled simultaneously by the Thorlabs controller. This set of choices, especially the pulse control and the fast controller response, allowed me to reproduce results from the literature as shown in Chapter 3 and 4, as well as to design new protocols.

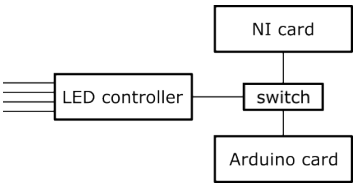

Figure 2.2: LED control system.

Dichroic mirror to split the light excitation path from the fluorescence emission path

A dichroic mirror, also known as a beam splitter, reflects the excitation light towards the sample while transmitting the emitted fluorescence. The selection of an appropriate dichroic mirror depends on factors such as the excitation and emission spectra of the fluorophores and the desired separation of excitation and emission light. The filters were selected in order to reflect all the wavelengths above the higher excitation wavelength used (Figure 2.3). Since the wavelength of fluorescence emission is always higher than the excitaion wavelengths in the cases we studied, this constraint was not a problem. For example, to measure green fluorophores, we only used blue and purple light excitation and a dichroic filter cut-off wavelength below the green wavelength and above the blue wavelength.

Fluorescence emission filter

The emission filter is used to selectively transmit the fluorescence emitted by the fluorophores while blocking the excitation light and other unwanted wavelengths. Different emission filters are used depending on the fluorophores observed.

2.3.5 Imaging objective lens

The choice of objective lens affects the resolution and image quality in fluorescence microscopy. We selected a high numerical aperture (NA) objective to collect a greater amount of emitted fluorescence light, improving sensitivity. The NA also determines the spatial resolution of the microscope, which we chose to match the algae size and be able to capture one algae image on multiple pixels. We chose the magnification of the objective in order to collect the response of hundreds of algae on the camera sensor to acquire simultaneously a significant amount of data per experiment. For simplicity of use, the microscope has a large working distance (a few centimeters) and the imaging medium between the objective and the sample is air.

2.3.6 Detectors to read the fluorescence

I developed a dual detection system (Figure 2.3), allowing to switch between a camera and a photon counter or use both simultaneously. We chose an accessible camera in terms of cost (CMOS camera, 500 €), compromising on the photon sensitivity and the frame rate but respecting the requirement of accessible prices for an embarked or portable solution. This is the principal difference with the literature, where we do not use an amplified camera, nor an high-speed camera, nor a cooling system nor a gating system [84, 86–88]. On the other hand we used a highly sensitive amplified multi-photon counter (MPPC) for point detection, to use in scenarios where the camera was not sensitive enough, as described in other systems (e.g. [93]).

The camera is connected by USB-3 cable and I modified the Python API provided by the manufacturer to control it freely. The two photon counters are connected to the DAQ card which is used for both reading and writing signals (with the possibility to read and write at distinct rates). I developed over a couple of months a code to control the DAQ card with Python using the library NI-DAQmx[1] provided by National Instruments.

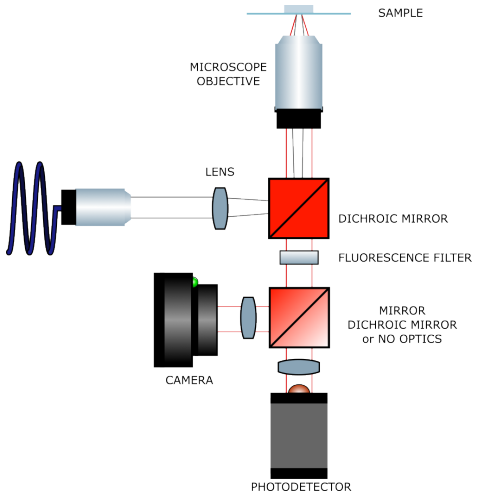

Figure 2.3: Imaging part of the microscope with dual detection system.

Sample Preparation

Regarding leaves, the sample preparation is direct: I fix the leaf between two glass slides allowing gas diffusion. For algae, multiple protocols are found in the literature to avoid part or all of the problems faced with samples: dry-out, limited gas exchanges, temperature increase, sedimentation,

[1] nidaqmx-python.readthedocs.io

motility. There are sample preparation in flat glass capillaries [93], cooled chambers with cellophane interface for gaz exchange and medium pumping system with gas bubbling [85, 99], metal plate (for the instrument described in [86]), microfluidic device [88, 100]. I investigated two protocols. I started with microfluidic traps in order to trap each alga individually and allow a constant influx of renewed medium. With the difficulties met, I chose a simpler design to fix the algae on an agarose pad, and validated it.

2.4 Detailed list of hardware components

The final instrument is pictured in Figure 2.4. In the following we present the technical choices for the illumination and the imaging parts, and the instrument controls. For the frame, we chose Thorlabs optical plates to easily (un-)screw the parts. We built the microscope in three stages combined with thick Thorlabs posts to maximize the stability of the setup.

2.4.1 Light part

The five light sources (Table 2.1) are high-power LEDs mounted on cages (*CXY1 - Thorlabs*). They are collimated by lenses with a focal distance of 16 mm (*ACL25416U - Thorlabs*) then filtered by band-pass filters (Table 2.1). A SWP 650 nm filter was added in front of the green LED L5 because it also emits in the red. The lights are combined by dichroic filters (Table 2.1) to be merged and injected into an optical fiber ($\emptyset = 400\ \mu m, NA = 0.5$ - *M45L02 Thorlabs*) through a microscope objective (*Plan APO 20X/0.75 DIC N2 - Nikon*). A filter wheel (*FW102C - Thorlabs*) is set in front of the blue LED allowing to explore a range of intensity from 1 μmol(photons) $\cdot\, \mathrm{m}^{-2} \cdot \mathrm{s}^{-1}$to 10000 μmol(photons) $\cdot\, \mathrm{m}^{-2} \cdot \mathrm{s}^{-1}$. The LEDs are controlled by a voltage to intensity converter (*DC4100 - Thorlabs*). It can power four LEDs and is controlled by four voltage inputs. Depending on the type of signal expected, a different controller is used to send the voltage inputs, and a switch allows to keep the signals into two separate circuits. A National Instruments Data Acquisition Card *SCB68A* with *PCI 6374* generates time signals written as Python arrays, or an *Arduino Uno* controller generates precisely-timed pulses of light.

2.4.2 Imaging part

The optical fiber output is connected to a microscope objective (*Plan 10x/.25 - Olympus*). A fraction of the illumination flux is reflected towards a photon counter by a microscope glass plate D6 installed on the light path. It allows to monitor the intensity of the LEDs for a given voltage input with Photodetector 1 (*Multi-Pixel Photon Counter C13366 - Hamamatsu*). The light path crosses a tunable diaphragm and a lens (*focal length 150 mm, AC254-150-A-ML - Thorlabs*). A dichroic filter D7 (Table 2.1) reflects the excitation light towards a microscope objective (*Objective Fluae 10x-0.50-M27 - Zeiss*). The objective can easily be changed for another magnification, with a flexibility in the working distance in the range of several centimeters, thanks to Thorlab rings stacking. The objective is mounted on a plate that moves in the z-direction to control the focus (*NFL5DP20/M - Thorlabs*). The plate can also be controlled by a piezoelectric (*KPZ101 - Thorlabs*, and we added the possibility to use a motor controlled by an Arduino to move the stage with a coarser precision[2]). The diaphragm is conjugated with the microscope plane and allows to reduce the diameter of the excitation light, and excite a limited area in the sample. The sample is mounted onto an automated platform with x and y movements[3] that we built with Ali Ruyer-Thompson and Peter Hanappe. The fluorescence is collected by the same microscope objective and is transmitted by the dichroic filter D8 (Table 2.1) and a fluorescence filter F6 (Table 2.1) towards the measuring devices. The fluorescence light can be either collected on a camera (*Ueye 3060CT-M - IDS*) conjugated with a tube lens (2 inches, focal

[2]SonyCSLParis/Motorized-stage
[3]SonyCSLParis/Motorized-stage/XY-stage

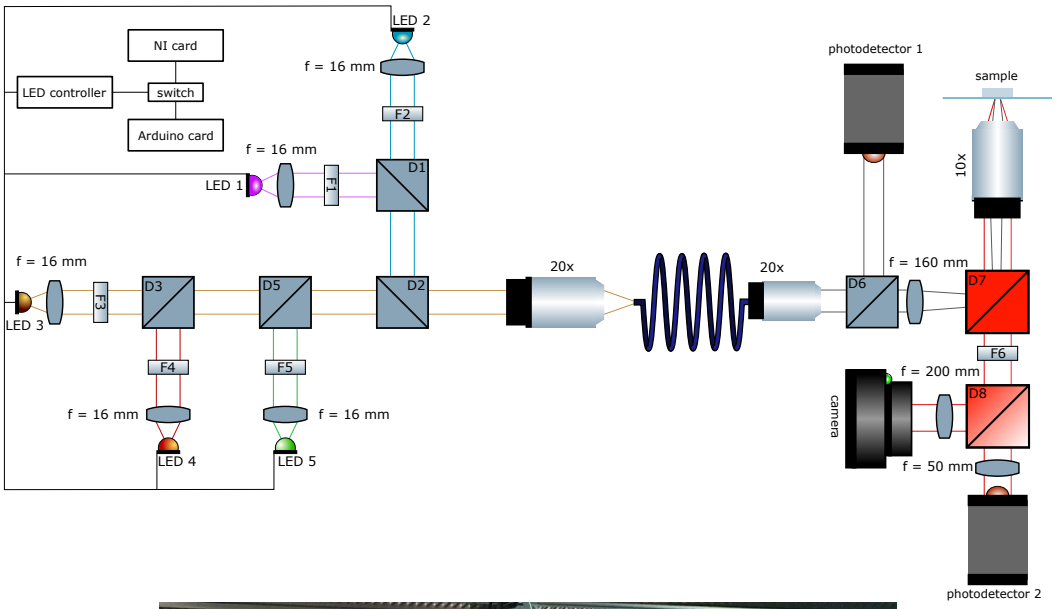

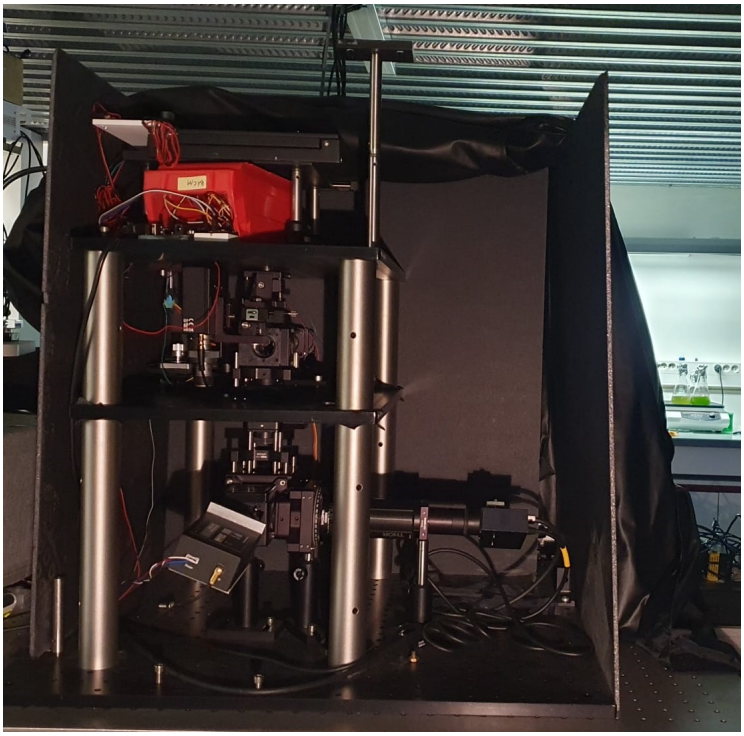

Figure 2.4: *Optical setup* **a**: Scheme of the optical setup. LEDs and band filters: 1: 405 nm, 2: 480 nm, 3: 690 nm, 4: 659 nm, 5: 550 nm; Dichroic high-pass filters: D1: 425 nm (to combine 405 nm and 480 nm), D2: 700 nm, D3: 665 nm (to combine 690 nm and 659 nm), D5: 560 nm; D6: glass plate to reflect incident light on detector, D7: 506 nm (to send light excitation towards the sample and collect the fluorescence), D8: 699 nm (cuts-off in the middle of the ChlF spectrum to split the signal between the photodetector and the camera - can be removed or replaced by a mirror); **b**: Picture of the setup.

length 200 mm, to maximally collect the photons), or a Photodetector 2 (*Multi-Pixel Photon Counter C13366 - Hamamatsu*) conjugated with a lens of focal length 50 mm. We can also collect the signal

name	quality	wavelength	reference	supplier
L1	high power LED	purple	LHUV0-405-A065	Lumileds
L2	high power LED	blue	LXZ1-PB01	Lumileds
L3	high power LED	far-red		Roithner Lasertechnik
L4	high power LED	red	LXM3-PD01	Lumileds
L5	high power LED	green		Lumileds
F1	band-pass filter	405/20	ZET405/20x	Chroma
F2	band-pass filter	479/40	FF01-479/40-25	Semrock
F3	band-pass filter	690/8	FF01 690/8	Semrock
F4	band-pass filter	650/13	FF01-650/13	Semrock
F5	band-pass filter	550/15	ET550/15x	Chroma
F6	band-pass filter	775/140	FF01 775/140	AHF
F6bis	band-pass filter	675/90	675/90 ET	AHF
D1	long-pass dichroïc filter	425	t425lpxr	Chroma
D2	long-pass dichroïc filter	700	FF700-Di01	Semrock
D3	long-pass dichroïc filter	665	FF665-Di02	Semrock
D5	long-pass dichroïc filter	560	FF01 560 Di01	Semrock
D6	glass microscope plate	NA		
D7	long-pass dichroïc filter	506	FF506-Di03	Semrock
D8	long-pass dichroïc filter	699	FF699-FDi01	Semrock

Table 2.1: Illumination equipment. D7 can be replaced by D8 to excite the photosynthetic organisms with the green and red LEDs (fluorescence emission: 650-750 nm).

on both, depending on the filter used use: mirror, dichroic filter D8 whose cut-off is in the middle of the fluorescence spectrum (Table 2.1), or no filter. The camera has adaptable gain and exposure time and is triggered internally or externally depending on the experiment. Unless specified, the camera was neither binned nor sub-sampled and the image size is 1936×1216 pixels^2.

2.4.3 Instrument control

The automated instruments (filter wheel, $x - z$ displacements, LED controller, LED switch) are controlled by serial communication with Python codes I wrote to based on their APIs. The excitation signals are sent either through an Arduino Uno microcontroller or a DAQ National Instruments card (*SCB68A* with *PCI 6374*). The fluorescence signals are acquired through a camera (*UEye 3060CT-M - IDS*) controlled with Python or through the MPPC signals collected with the DAQ card. For each experiment, the codes and the results are saved in a database MongoDB with the Python library Sacred [101]. The experiments are accessible with the interface Omniboard [102] which allows to compare the results. The codes are described in Chapter 5.

2.5 Calibration and characterization

2.5.1 Characterization of the response time of the LEDs

A record of the light jump with the photodetector 1 allows to compute the rising and falling edge time dynamics. The response of the LEDs to an offset has a characteristic time that depends on the input voltage. The characteristic time varies by a tenfold depending on the input voltage (Figures 2.5-2.6), and is always lower than 10 μs, which is sufficient for our experiments because our maximal acquisition frequency is 100 kHz (period 10 μs).

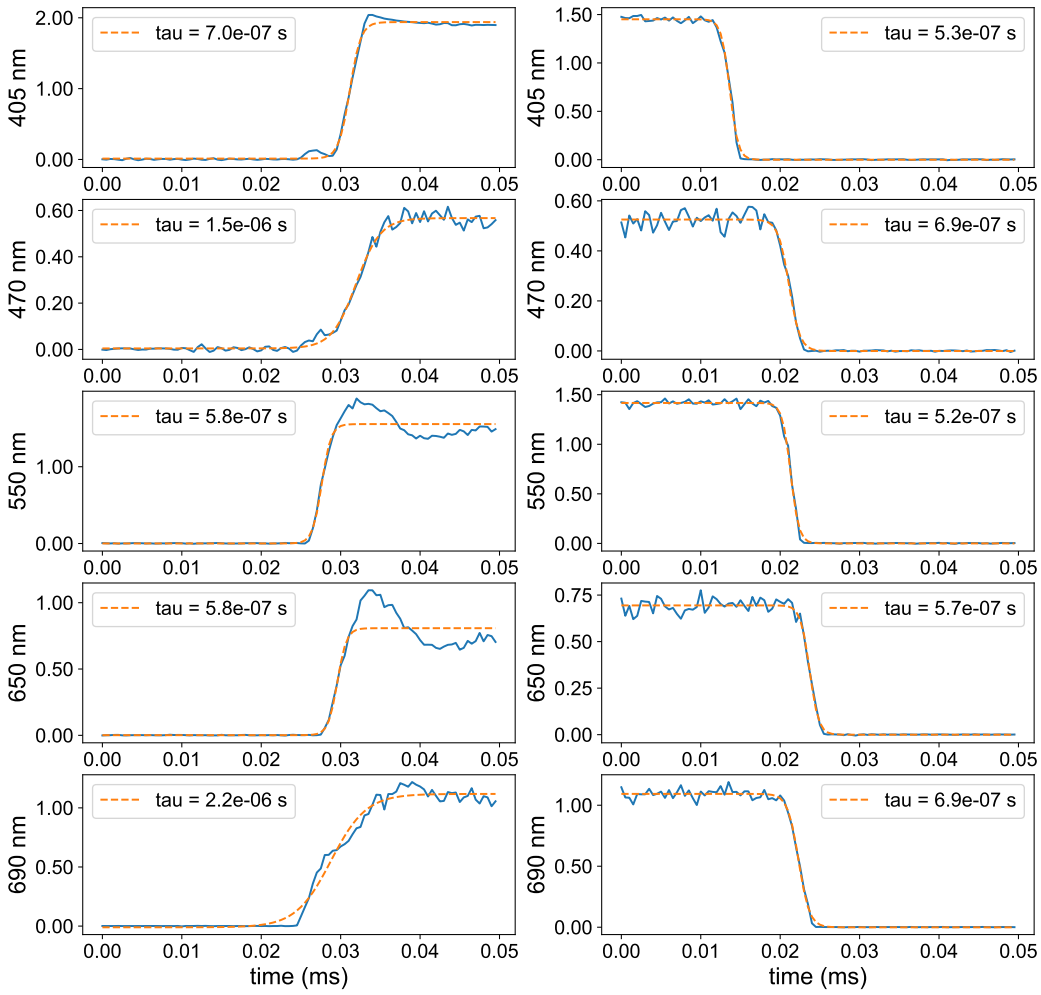

Figure 2.5: Characterization of the response-time of the LEDs to a high voltage input (5 V) for the five LEDs, with a sigmoidal fit to evaluate the response time (inserts) for the ON and OFF response.

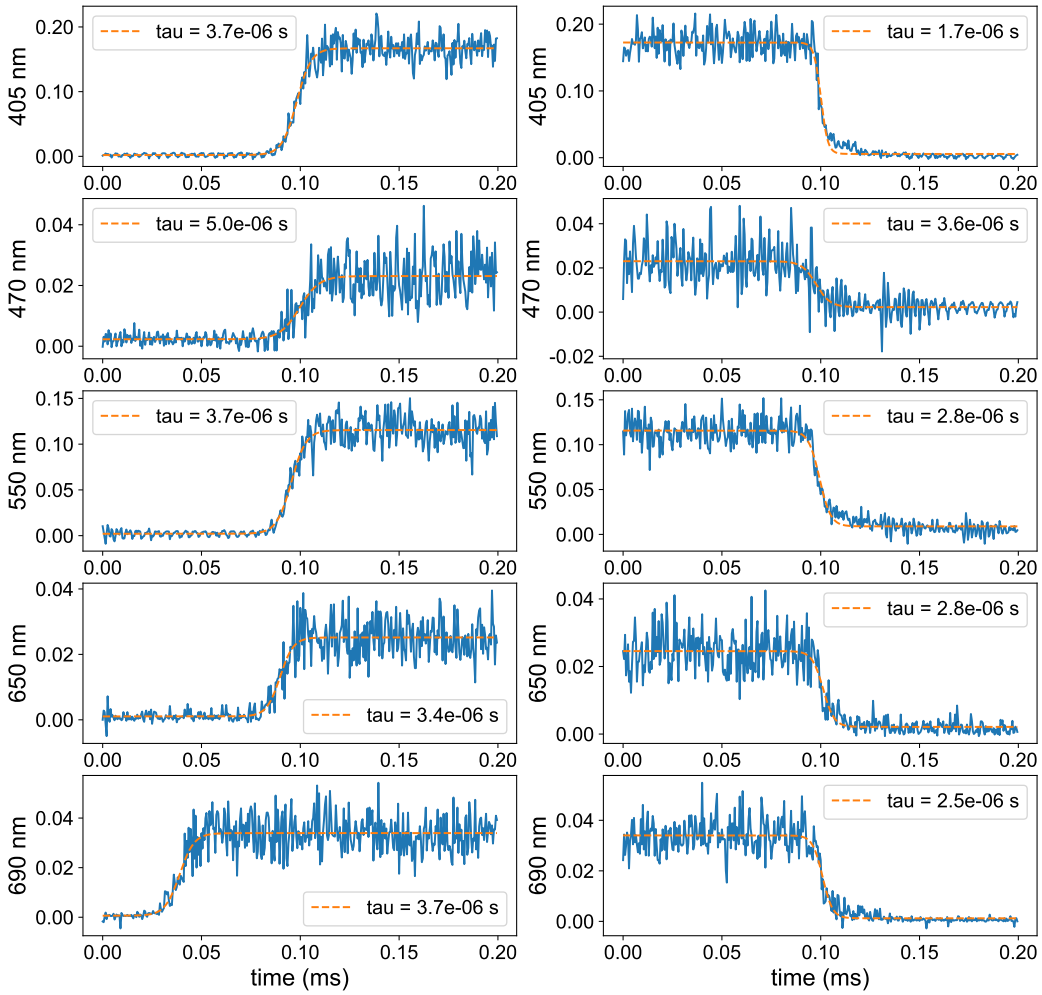

Figure 2.6: Characterization of the response-time of the LEDs to a high voltage input (0.05 V) for the five LEDs, with a sigmoidal fit to evaluate the response time (inserts) for the ON and OFF response.

2.5.2 Calibration of light intensities

The work on light calibration has led to a manuscript which goes beyond the scope of this Chapter and was placed in Appendix 2.6. Although the techniques developed at ENS had already been described in the literature, I suggested that it could have an impact for the community of optical microscopists and beyond, and was worth describing in details and with further exploration. In the manuscript, we address how to calibrate light intensity using the actinometric properties of a selection of fluorophores covering the whole visible spectrum. We add one fluorophore with a broad absorption spectrum that can be used to transfer a calibration to another wavelength. We use these systems to calibrate the light intensity of commercial instruments, the light intensity in the field of view of wide-field and confocal microscopes (in 2D and in 3D), and to calibrate a broad-spectrum light source.

For the work presented in the following Chapters, only the purple and the blue LEDs were used. Therefore, I investigated more in depth their calibration. The other LEDs have also been calibrated for the purpose of two publications ("Fluorescence to measure light intensity" in Appendix 2.6 and "Leaves to measure light intensity" in Section 3.4), and their calibration is described in the corresponding Supplementary Materials.

Blue and Purple LEDs

The following text is written after [56] and the manuscript in Appendix 2.6.

The light calibration relies on the photoswitching kinetics of a photochemically well-characterized RSFP (**Dronpa-2** at pH 7.4) for measuring light intensities at which the kinetics is well-accounted for with a two-state model. Such an actinometric measurement is photochemically reliable up to 10 μmol(photons) $\cdot\, \mathrm{m}^{-2} \cdot \mathrm{s}^{-1}$ light intensity at the wavelengths $\lambda_1 = 470$ nm and $\lambda_2 = 405$ nm respectively.

The calibration of the light intensities exploits light jumps on **Dronpa-2** samples (typically a 10 μM **Dronpa-2** solution in pH 7.4 PBS buffer):

- As a preliminary step of the calibration protocol, the **Dronpa-2** solution is illuminated with the 405 nm LED ($I_2 = 0.01$ μmol(photons) $\cdot\, \mathrm{m}^{-2} \cdot \mathrm{s}^{-1}$ for 2 min) to ensure that **Dronpa-2** is initially in its thermodynamically stable state;

- Then the sample is illuminated at constant light intensity I_1 at $\lambda_1 = 470$ nm (this first illumination is associated with the exponent I) and the evolution of the fluorescence signal is collected. The decay is adjusted by:

$$I_F^{\mathrm{I}} = I_F^{\mathrm{I}}(0) + A^{\mathrm{I}} \left[1 - \exp\left(-\frac{t}{\tau^{\mathrm{I}}} \right) \right] \tag{2.1}$$

  The time τ^{I} is used as a fitting parameter and the intensity I_1 is retrieved according to

$$I_1 = \frac{\dfrac{1}{\tau^{\mathrm{I}}} - k_{21}^{\Delta}}{\sigma_1} \tag{2.2}$$

  where the reference values of the rate constant for thermal return after reversible fluorescence photoswitching ($k_{21}^{\Delta} = 0.014\ \mathrm{s}^{-1}$) and the sum of the photoswitching cross-sections ($\sigma_1 = 196$ $\mathrm{m}^2\mathrm{mol}^{-1}$) at the wavelength λ_1 are given in reference [53];

- In a second step, while maintaining constant illumination I_1 at the wavelength $\lambda_1 = 470$ nm, the sample is submitted to a light jump of intensity I_2 at the wavelength $\lambda_2 = 405$ nm (this second illumination protocol is associated with the exponent II). The exponential fluorescence recovery is recorded and adjusted using

$$I_F^{\mathrm{II}} = I_F^{\mathrm{II}}(0) + A^{\mathrm{II}} \left[1 - \exp\left(-\frac{t}{\tau^{\mathrm{II}}} \right) \right] \tag{2.3}$$

where the time τ^{II} is used as a fitting parameter and the intensity I_2 can be retrieved from

$$I_2^{\mathrm{II}} = \frac{\frac{1}{\tau^{\mathrm{II}}} - \sigma_1 I_1 - k_{21}^{\Delta}}{\sigma_2} \tag{2.4}$$

where the reference value of the sum of the photoswitching cross sections ($\sigma_2 = 413$ m^{2}mol^{-1}) at the wavelength λ_2 is given in reference [53].

Figure 2.7 shows an example of the evolution of the fluorescence for a given pattern of light input: constant blue light and oscillating purple light. The fluorescence is collected by photodetector 1. Here I did not give the population the time to fully relax for display reasons. However, when performing the calibration, the relaxation is allowed to be complete in order to have a better fit.

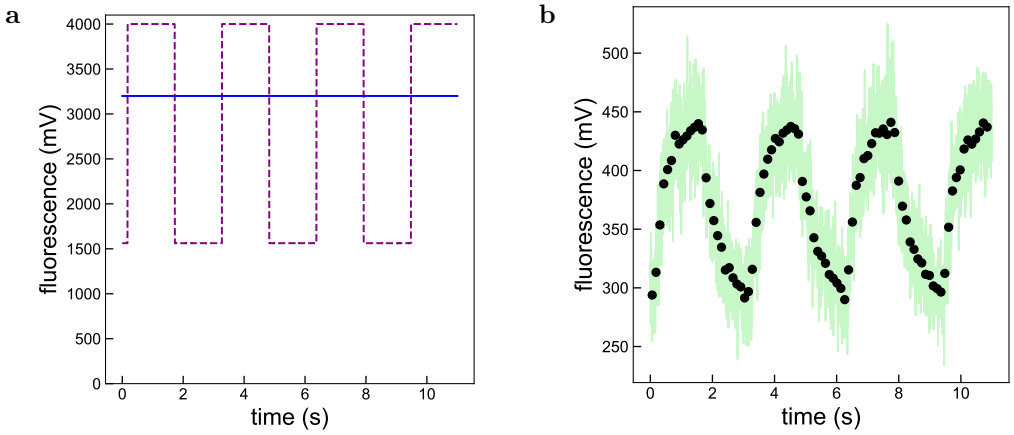

Figure 2.7: *Kinetic evolution of the fluorescence of* ***Dronpa-2*** *for a given light input pattern.* **a**: Intensity of the blue (solid line) and purple LED (dotted line) with time (here, the y-scale of light intensity was obtained thanks to the calibration procedure); **b**: Fluorescence of **Dronpa-2** collected by the photodetector 2. The transparent background corresponds to the full trace acquired at 300 Hz and the markers are the result of a window averaging (size 40).

I ran this procedure for various levels of intensity of the blue and purple LED (Figure 2.8). To expand the range of accessible light levels, I used density filters and characterized their optical density at the wavelengths of interest. In practice, I needed the optical density only in front of the 470 LED for the experiments.

Green and Red LEDs

These lights were calibrated with a powermeter (PM100A, Thorlabs, NJ) using the camera to evaluate the spot size. They were also calibrated with complementary actinometers. These calibrations are described in Appendix 2.6.

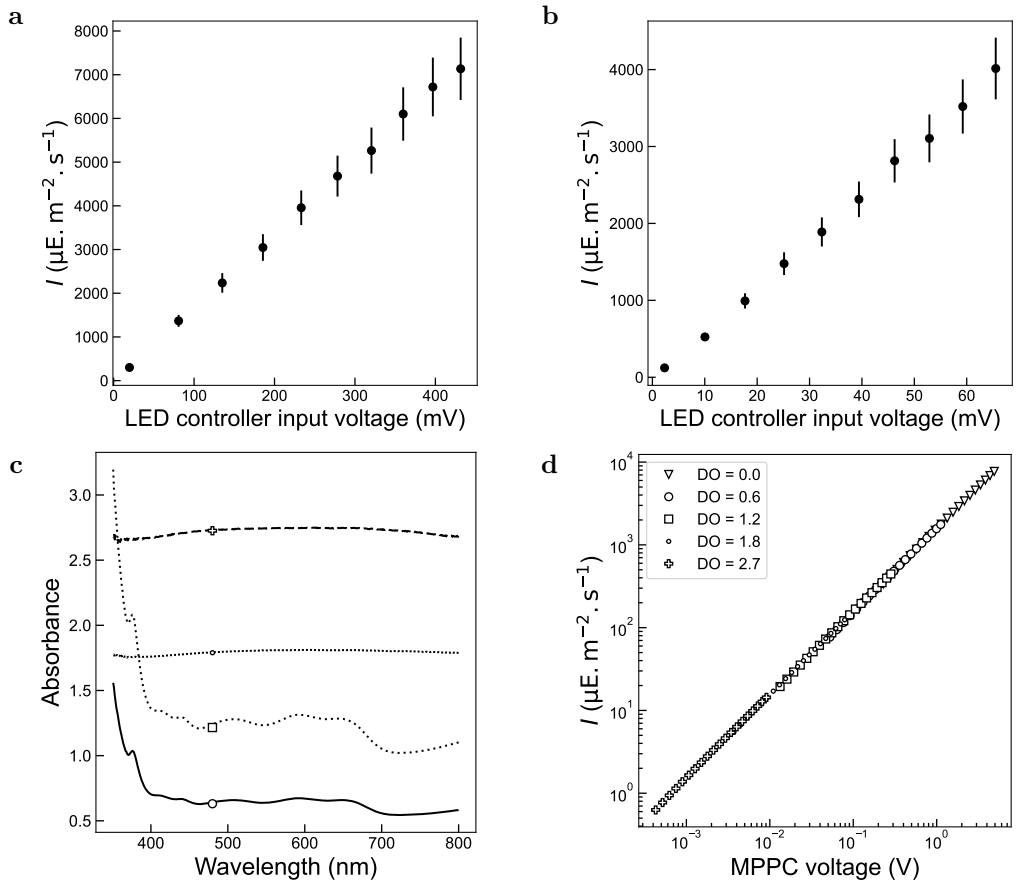

Figure 2.8: *Calibration of the blue and purple light sources.* **a-b**: Intensity of the 470 (resp. 405) LED in the focal plane calibrated with **Dronpa-2** for different voltage inputs of the LED controller. The error comes from the ±10% uncertainty on the value of σ_{470} (resp. σ_{405}); **c**: Absorbance spectra of the optical densities. Markers placed at 470 (circle: DO=0.7, square: DO=1.2, dot: DO=1.8, cross: DO=2.7); **d**: Extrapolated light intensity of the 470 LED in the field of view when the optical density is in place.

Homogeneity of the spot

To study the homogeneity of the field of illumination I performed the calibration process described in 2.5.2 and in Appendix 2.6, and recorded the fluorescence with the camera (5 Hz). I analyzed the temporal response of the fluorescence of **Dronpa-2** extracted from the movie. Figure 2.9a shows a frame of the movie where the blue and purple LEDs are ON, while Figure 2.9b shows a slide where only the blue LED is on, evidencing the transition to a dark state. A 3×3 pixel averaging is applied to obtain macro-pixels on which the curve fitting to extract the relaxation times is ran. The map of intensities derived from the relaxation times using Eq. 2.4 for the blue LED and the purple LED are shown in Figure 2.9c,d. The distribution of intensities present a narrow distribution (Figures 2.9e,f). There is a 20% variation of light intensity in the field of view for the two light sources. In Figure 2.9a, the mean pixel value is 40 and the standard deviation is 20. This demonstrates that the initial frame image gives a misleading characterization of the heterogeneity in the field of view, because it is affected by optical aberrations and camera sensitivity in the observation pathway. It demonstrates that **Dronpa-2** is a useful tool to characterize this heterogeneity.

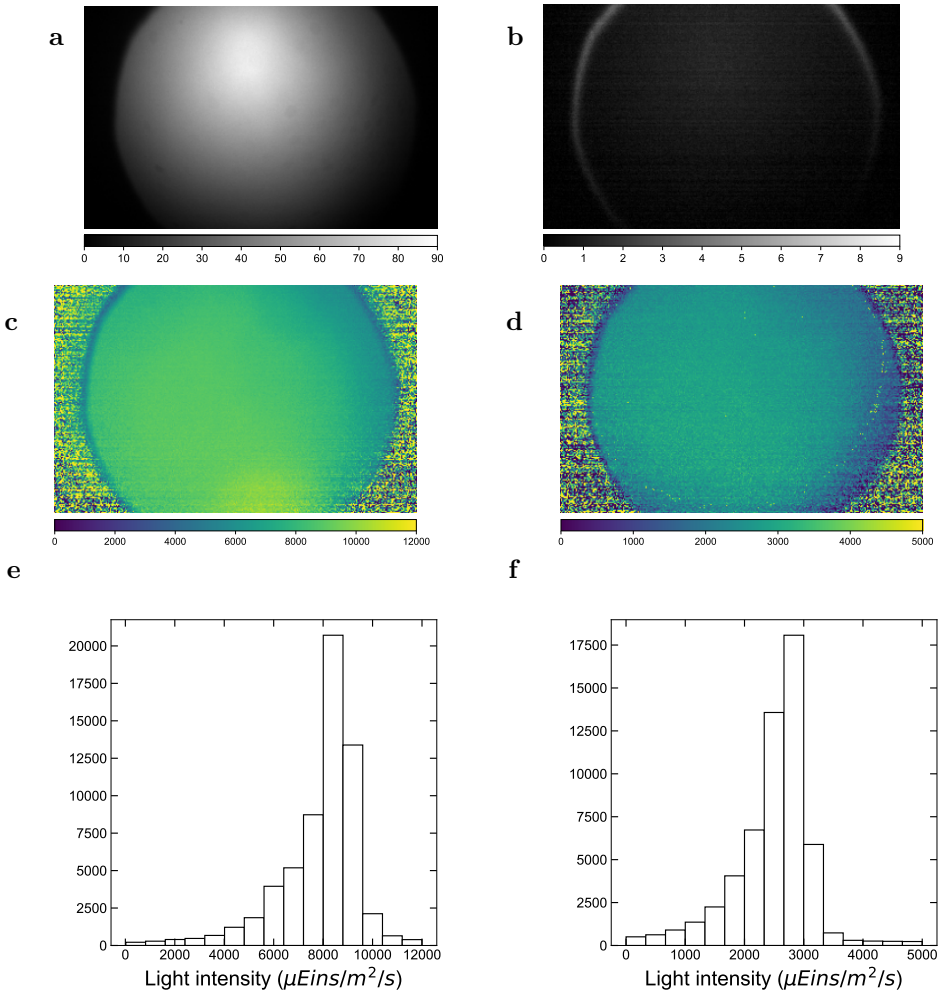

Figure 2.9: *Calibration of the light sources.* **a,b**: Intensity map of the 470 (resp. 405) LED in the focal plane calibrated with **Dronpa-2** for voltage inputs of the LED controller 400 mV (resp. 250 mV); **c,d**: Histogram of the intensity values, $(\mu, \sigma) = (8200,900)$ (resp. $(2500,380)$ μmol(photons) $\cdot\, \mathrm{m}^{-2} \cdot \mathrm{s}^{-1}$).

2.5.3 Autofocus

In the protocols described in Chapter 4, experiments can last several hours and the sample can move under the microscope and lose focus. With a motor controlled by an Arduino I wrote a routine to operate an autofocus step at low light before each start of four consecutive measurements. The motor moves until the image captured presents a maximal Laplacian variance [103]. The detailed method is described in Section 5.6.4.

2.5.4 Sample preparation

I began by exploring the possibility to use a microfluidic device to trap the algae in a trap matrix with hundreds of traps in the field of view for the duration of the experiment. The device allowed a thermally regulated medium to flow and renew the nutrient content throughout the experiment thanks to a pumping system. I borrowed the device from [104, 105]. The traps were designed for larger cells, so it would trap multiple cells at once. When inverting the flow I could isolate a single cell on a trap lump, which was unstable. I managed to isolate algae and image the algae separately, as well as use the diaphragm to collect their individual fluorescence (Figure 2.10). However, the complexity of the logistic of the flow, and the heavy work required to build new traps led me to select a simpler and straightforward sample preparation.

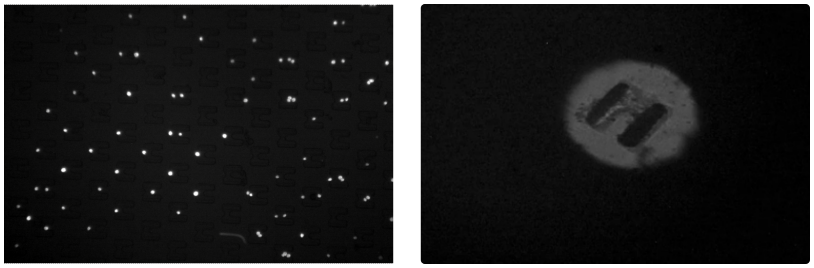

Figure 2.10: *Microfluidic traps.* Left: Full field fluorescence image of the algae trapped in the microfluidic device; Right: Image of the microfluidic trap, example of how the diaphragm is used to select a single trap (no algae in the image).

The final protocol is the following:

In all experiments, the culture is collected in exponential phase (from 5×10^5 to 5×10^6 cells/mL), centrifuged (2500 rpm for 8 min) and transferred in **MIN** medium. The algae are deposited on agarose pads for observations based on a protocol described in [55]. A 1 % suspension of agarose in **MIN** medium was heated to dissolve the agarose (800 W - 40 s). The agarose pads were prepared by dropping 175 µL of melted agarose onto a glass slide holding a spacer (AB-0578 ThermoFisher). To make its surface flat, the pad was covered with a thick microscope glass slide and left for 5 min at 4^oC for hardening. The cover slide was removed, and the preparation was left for 10 min to allow thermal adaptation and evaporation of excess humidity. It results in a single sparse layer of algae. About 5 µL of algae suspension was dropped onto the agarose and left to evaporate for 10 min. Finally, a coverslip was gently placed over the agarose pad for observation.

I validated the sample format by being able to reproduce experiments from another fluorometer (Chapter 3 – Pulse-Amplitude Modulated fluorometry) and from a publication (Chapter 4 – Non-Photochemical Quenching measurement). I also left the algae to grow with intermittent 15 min HL/15 min dark (HL: 400 μmol(photons) $\cdot\, m^{-2} \cdot s^{-1}$, 470±10 nm) for several days and showed the growth was not limited by the sample preparation. In Figure 2.11 we show the algae after a first division (B). They divide into four cells every division which is consistent with the literature stating that each cell can divide into two up to thirty-two cells depending on the environmental conditions [106]. Figure 2.11C shows the same sample after four and a half day. The surface occupied by

algae was multiplied by 14 between the two images. It corresponds to a doubling rate of 7.7 hours, consistent with the literature for unstressed algae [107, 108].

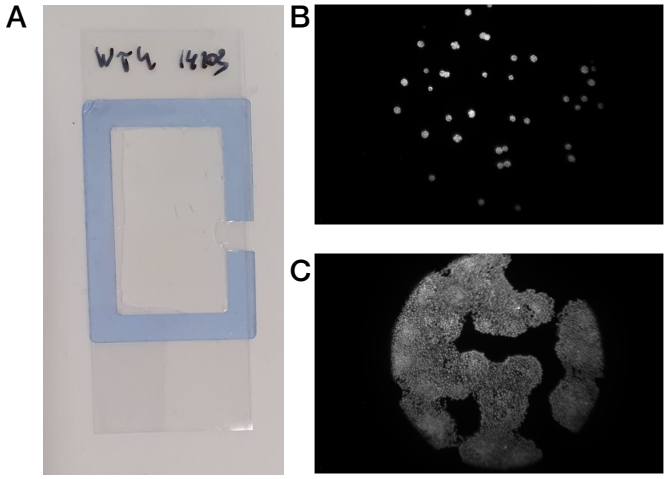

Figure 2.11: **a**: Sample preparation: the medium mixed with agarose is spread on a pad and solidified. A drop of algae is deposited on the agar mix and covered by a microscope slide. **b,c**: Demonstration of the viability of the cells on the agarose pad. Fluorescence images of wild-type strain taken four and a half days apart. The surface occupied by the algae is multiplied by 14, corresponding to a doubling rate between seven and eight hours.

This chapter described the motivations to build a new epifluorescence microscope to probe ChlF and the design choices were justified. The epifluorescence microscope characterization was presented (response time, precision). In particular the light intensity calibration led to an extended side work in the form of an article (Appendix 2.6). It is introduced in the appendix of the Chapter. Finally, the sample preparation was discussed, initially involving microfluidic circuits but quickly replaced with straightforward and validated agarose pad preparation. The next Chapter explains in details how ChlF can be used as a reporter of the photosynthetic chain status. It describes how the epifluorescence microscope was used to set in place the various protocols used in the rest of the manuscript and compare our approach to the literature.

2.6 Appendix Manuscript: Fluorescence to measure light intensity

2.6.1 Main Text

Fluorescence to measure light intensity

Aliénor Lahlou,[1,2,*] Hessam Sepasi Tehrani,[1] Ian Coghill,[1] Yuriy Shpinov,[1] Mrinal Mandal,[1] Marie-Aude Plamont,[1] Isabelle Aujard,[1] Thomas Le Saux,[1,*] Ludovic Jullien[1,*]

Yuxi Niu,[3] Ladislav Nedbal[3,4]

Dusan Lazár[4]

Pierre Mahou,[5] Willy Supatto,[5] Emmanuel Beaurepaire[5]

Isabelle Eisenmann,[6,7] Nicolas Desprat,[6,7] Vincent Croquette,[6,7] Raphaël Jeanneret[6,7]

[1] PASTEUR, Département de chimie, École normale supérieure, PSL University, Sorbonne Université, CNRS, 24, rue Lhomond, 75005 Paris, France.

[2] Sony Computer Science Laboratories, Paris, France.

[3] Institute of Bio- and Geosciences/Plant Sciences, Forschungszentrum Jülich, Wilhelm-Johnen-Straße, D-52428 Jülich, Germany.

[4] Department of Biophysics, Faculty of Science, Palacký University, Šlechtitelů 27, 783 71 Olomouc, Czech Republic.

[5] Laboratory for Optics and Biosciences, Ecole polytechnique, CNRS, INSERM, IP Paris, 91128, Palaiseau Cedex, France.

[6] Laboratoire de Physique de l'École normale supérieure, ENS, Université PSL, CNRS, Sorbonne Université, Université Paris Cité, F-75005 Paris, France.

[7] Institut de Biologie de l'ENS (IBENS), École Normale Supérieure, CNRS, INSERM, Université PSL, 75005, Paris, France.

Abstract

Quantitative measurement of light intensity is required in many fields of biology, chemistry, engineering, and physics. The available protocols necessitate specific equipment and expertise, and suffer from limitations in their scope. Here we report on two protocols, which exploit fluorescence to enable the retrieval of the light intensity even in the depth of samples, with spatial distribution information, over wide ranges of wavelengths and intensities, and in a quick, inexpensive, and simple manner. The first protocol relies on species whose fluorescence intensity decays/rises in a mono-exponential fashion when constant light is applied. The second protocol relies on a broad-absorbing photochemically inert fluorophore to back-calculate the light intensity from one wavelength to another. As a demonstration of their use, the protocols are applied to quantitatively characterize the spatial distribution of light of various fluorescence imaging systems, and to calibrate illumination of commercially available instruments and light sources.

Introduction

Photochemistry deals with chemistry driven by light. Involved in key mechanisms of living systems (e.g. photosynthesis and vision), it has found multiple applications at micro- and macro-scales extending from the production of molecules and materials[1] to the design of medical protocols (e.g. photodynamic therapy[2]). More recently, its scope has been extended. In bioimaging, optical microscopists balance light intensity to get optimal signals without phototoxicity. In optogenetics, biologists use photons for triggering physiological processes at the cellular level.[3] In photocatalysis,[4] chemists exploit photons as reactants driving the synergetic action of light-absorbing and metallic catalysts. Nowadays, a vast community of biologists, chemists, engineers, and physicists are concerned with delivering precise numbers of photons.

Illumination systems require accurate quantitative characterization in order to enable a fair comparison of results obtained by various research groups as well as to ensure reproducibility,[5] or to rationally choose parameters, such as duration of light application for delivering the right number of photons to a sample. Here we address one important aspect of illumination system characterization: light intensity – more precisely irradiance which is a surfacic power ($W.m^{-2}$) – alternatively denominated photon flux density with $mol.m^{-2}.s^{-1}$ (or $E.m^{-2}.s^{-1}$; See Supporting Information) units which we will use in the following as it is wavelength independent.

Several tools are helpful to measure light intensity.[6,7] Light meters provide a fast response over a wide range of wavelengths and intensities.[8,9] However their detectors integrate light over their surface and do not yield any information on the spatial distribution of light. A further measurement of the area of the illuminated surface is required to retrieve the light intensity. Fluorescent microscope slides are commonly used to reveal the spatial profile of illumination in imaging systems. Yet, the image read-out of the fluorescence intensity is affected by optical aberrations and detection efficiency of the imaging system and therefore cannot be relied upon for the retrieval of accurate spatial information. Moreover, they do not provide quantitative information on light intensity. On top of the latter issues, light meters and fluorescent microscope slides sense light at sample surfaces only and experience geometrical constraints from relying on large and rigid sensing elements.

An alternative approach involves the use of an actinometer. An actinometer is a system which can be used to directly measure light intensity by knowing the quantum yield of its photo-conversion, and following the time-course of the reaction extent on the application of light.[10] This approach can further yield spatial information when used with an imaging system. Moreover, since they take the form of liquid solutions, actinometers can measure light in samples of various sizes and geometries. However, most established and newly reported actinometers have relied on absorbance as an indicator of reaction extent[10,11,12] - an observable which is not very sensitive, and is not easily accessible in imaging systems. Furthermore, they are generally restricted for the ranges of wavelengths and light intensities.

Fluorescence is a more sensitive observable than absorbance[13] and is accessible to imaging systems. Harnessing fluorophore photobleaching has been proposed for quantitative measurement of light intensity.[14] The drawbacks of such an approach include the fact that the kinetics can be complex and exhibit environmental dependence, and that it is limited to use in situations of high light levels or long time periods since most fluorophores are strongly resistant to photobleaching.

In this work, we demonstrate the use of synthetic and genetically encoded fluorescent systems capable of efficient light-driven conversions which we have previously reported[15,16,17,18,19] as actinometers, whereby fluorescence is used for reporting on reaction extent. Such conversions proceed much more rapidly than in the case of photobleaching, and thus these systems can be used in weak-light situations (or short time periods). In order to allow for measurement over a wider range of wavelengths, we complement our proposed method, with a broad-absorbing photochemically inert fluorophore which enables light intensity at one wavelength to be used to calculate light intensity at a second wavelength. In this manuscript, we report on the relevant features of these systems for measuring light intensity and demonstrate their use in characterizing illuminations systems at both microscopic and macroscopic scales with samples of various sizes and geometries.

Results

A first protocol to measure light intensity (Figure 1a). It exploits molecular actinometers, which react upon absorbing the excitation light to be characterized (see Supporting Information). The absorbance of their solution is adjusted low enough in order to ensure that light intensity is essentially constant along the optical path (below 0.15, an easily met threshold). The protocol begins with the sudden exposure of the actinometer solution to illumination, set at the level of light intensity to be measured. One subsequently collects the time evolution of the fluorescence emission signal, which reports on

the actinometer photoconversion extent. It is processed by the fitting of a mono-exponential curve, to enable the retrieval of the associated characteristic time τ (see Supporting Information), which evaluates the time scale of the actinometer photoconversion. In an appropriate range of light intensity *I* (see Supporting Information), *I* is inversely proportional to the product $\sigma\tau$ where σ is the photoconversion cross section (a measure of the molecular surface leading to the actinometer photoconversion after light absorption) (see Figure 1a). A general estimate of the achievable measurement uncertainty on *I* is 20% (see Supporting Information). Where photoconversion occurs rapidly, on a timescale where molecular motion is minimal, it is possible to retrieve a map of the spatial distribution of light intensity. However, if the molecules can visit the whole irradiated area at the timescale of the actinometer photoconversion, only mean light intensity values can be obtained.[16]

The choice of the reported actinometers has been guided by different considerations. First, we wanted to illustrate two different mechanisms to enable fluorescence to be used as an indicator of their photoconversion. In the first one, the actinometer and/or its photoproducts are intrinsically fluorescent: the fluorescence intensity changes in accordance with the actinometer photoconversion and the actinometer alone is sufficient to retrieve *I*. This mechanism is simple but its implementation relies on specific features, which led us to identify appropriate candidates. Indeed, photoconversion and fluorescence emission are generally competitive deexcitation processes from an excited state. By contrast, when the actinometer and its photoproducts are non-fluorescent, the actinometer photoconversion only drives a change of absorbance. Here, a photochemically inert fluorophore can be added to report, through fluorescence, on the time evolution of the absorbance at the excitation wavelength by the inner filter effect (see Supporting Information). In this latter mechanism, the absorbance is advantageously adjusted around 0.15 to increase the amplitude of the time variation of the fluorescence signal, and thus sensitivity. Then we wanted to make fluorescent actinometers accessible to different communities of end users. Hence, we report on easily synthesized chemicals for the chemists, whereas we propose to use proteins and photosynthetic organisms for end users with access to biological techniques. Eventually, the five reported actinometers cover the entire UV-Vis wavelength range for measurement of light intensity (Figure 1c; see Supplementary Information):

- Two actinometers for the UV A wavelength range (relevant for decontamination of materials,[20] evaluation of environmental radiation,[21] photoactivation of many caged molecules in optogenetics,[22] photocatalysis with metal complexes,[4] etc): (i) The dark (E)-3-(3,5-dibromo-2,4-dihydroxyphenyl) acrylic acid ethyl ester (**Cin**),[15,23] which irreversibly converts under illumination between 350 and 420 nm into the bright 6,8-dibromo-7-hydroxycoumarin fluorescing between 400 and 550 nm in Tris pH 7 buffer; (ii) The dark α-(4-diethylamino)phenyl)-N-phenylnitrone (**Nit**),[24] which irreversibly converts under illumination between 320 and 430 nm into the dark N-(p-dimethylaminophenyl)formanilide in ethanol.[25] The photochemically inert rhodamine B (**RhB**) emitting fluorescence between 550 and 650 nm is selected here for optimally reporting on **Nit** photoconversion by inner filter effect;

- One actinometer for the blue wavelength range (important in optogenetics for photoactivating opsins, FAD CRY, FAD BLUF, and FMN LOV systems,[3] or driving photosynthesis[26]): A bright reversibly photoswitchable fluorescent protein **Dronpa-2** (or M159T),[27] contained within *Escherichia coli* or eucaryotic cells, or in buffered solution or polyacrylamide gel, emitting fluorescence between 500 and 600 nm, which reversibly converts into a dark photoisomerized state under illumination between 400 and 550 nm;

- One actinometer for the green to red wavelength range (important for photoactivating opsins or bilin PHY[3] in optogenetics, or driving photosynthesis[26]): In acetonitrile, the donor-acceptor Stenhouse dye **DASA**[17] emitting fluorescence extending up to 675 nm reversibly converts into a dark state under illumination between 530 and 670 nm;

- Since the width of the absorption band of the preceding fluorescent actinometers is limited which necessitates to have several of them to cover the whole range of wavelengths, we eventually report on the last actinometer, the photosynthetic apparatus of algae (denoted **PA**), which can provide an estimate of light intensity for the entire visible range of wavelengths. In oxygenic photosynthetic organisms, a few percent of collected sunlight energy is released as fluorescence in the 650-800 nm range.[28] When exposed to constant light at sun-like light intensity, the fluorescence of dark-adapted photosynthetic organisms rises in less than 1 s from a minimum to a maximum via intermediate steps.[29,30] The rate constant of the fastest step linearly depends on the light intensity.[31,32] Usefully, its value does not significantly depend on the type of photosynthetic organism.[33]

Characterization and validation of the five above-mentioned actinometers as well as specific protocols for their use are reported in the Supporting Information. The end users can exploit the reported parameters to reliably measure light intensity as long as they follow the reported measurement protocols. Table 1 provides information to facilitate the selection of the most optimal actinometer to use for specific scenarios. To further facilitate the use of these actinometers, we further provide an online access to the actinometer properties[34] and to codes and user-friendly applications to process the acquired data without specific installation.[35]

A second protocol to measure light intensity (Figure 1c). Envisioned as a complementary tool to face the often limited width of the absorption band of the fluorescent actinometers, it exploits a photochemically inert fluorophore exhibiting a broad absorption band to transfer information on light intensity from one wavelength, measured with a fluorescent actinometer as reported above, to another (see Supporting Information). Below a value of 0.15 for the absorbance of its solution, the fluorophore emits fluorescence at an intensity proportional to light intensity of the illumination system. By recording the fluorescence emitted when the fluorophore solution is exposed to light at a wavelength (λ_1) where the light intensity (I_1) is known, and a wavelength (λ_2) where the light intensity (I_2) is unknown, the unknown light intensity (I_2) can be determined (see Figure 1c).

As demonstrated in Supporting Information, 7-hydroxy-9H-(1,3-dichloro-9,9-dimethylacridin-2-one) (**DDAO**) is a suitable photochemically inert light intensity-transferring fluorophore (see Figure 1d). It is commercially available. It absorbs light between 450 and 650 nm and emits fluorescence between 640 and 700 nm in neutral aqueous solutions.[3637] These features are particularly attractive for light calibration in the orange and red wavelength range where actinometers are scarce and often exhibit a poor quantum yield of fluorescence. Eventually, its quantum yield of fluorescence does not depend on the excitation wavelength as evidenced by the similarity of its absorption and normalized fluorescence excitation spectrum.

Measurement of light intensity in fluorescence imaging systems. Accurate measurement of light intensity is vital in many fluorescence bioimaging studies. It can, for example, allow for phototoxicity on live biological samples to be limited;[38] quantitative analysis in long timelapse[39] or ratiometric[40] studies; or optimal conditions to be ensured (e.g., in single molecule localization[41] and dynamic contrast[16,42] dependent experiments). Hence, we demonstrate here the use of fluorescent actinometers for the measurement of light intensity at the focal plane of multiple wide-field and light-scanning fluorescence imaging systems. **Dronpa-2** has been used here for this.

In wide-field imaging, the **Dronpa-2** actinometer has been first implemented in epifluorescence microscopy. A **Dronpa-2** aqueous solution sandwiched between two glass-slides was imaged (Figure 2a) and submitted to a jump of homogeneous light at 470 nm. Figure 2b evidences the relevance of a monoexponential fit of the resulting temporal fluorescence decay over the field of view. We additionally retrieved the map of the characteristic time τ at each pixel (Figure 2c) and built the histogram of the τ values (Figure 2d). The map (Figure 2e) and the corresponding histogram (Figure 2f) of light intensity at 470 nm were subsequently computed from using the photoconversion cross section of **Dronpa-2** in Table 1. We further exploited a patterned illumination at 470 nm (Figure 2g).

Hence, we established that the map of light intensity was obtained at lower spatial resolution when **Dronpa-2** was in solution (Figure 2h) than when it was embedded in a polyacrylamide gel (Figure 2i). This result was anticipated from molecular diffusion occurring at the time scale of **Dronpa-2** photoconversion, which generates blurring (see Supporting Information).

For quantitative validation, **Dronpa-2** was then implemented in fluorescence macroimaging on an original optical setup (see Supporting Information), whose illumination is not homogeneous but instead contains a gradient of light intensity across the field of view (Figure 2j). The sandwiched **Dronpa-2** solution was submitted to a jump of light at 470 nm to extract the map of the characteristic time τ, which was eventually converted into the map of light intensity. This latter map was validated by favorable comparison of the direction of the linear gradient of light intensity, either experimentally observed (Figure 2k) or computed from an optical simulation (Figure 2l; see Supporting Information). The lines along the direction of the gradient of light intensity were found to be different from each other only by an angle of 3°.

A similar protocol was applied in confocal microscopy. A series of images of the **Dronpa-2**-labeled nucleus of a fixed U-2 OS cell were acquired in raster scanning mode with a pulsed laser at 488 nm (Figure 3a). The dwell time was used to convert the observed fluorescence decay on the number of frames into a fluorescence drop over time. Figure 3b displays the average drop over a nucleus. It also shows that a **Dronpa-2** aqueous solution sandwiched between two glass-slides yields a similar kinetic signature upon properly restricting analysis to a central portion of the overall image to limit the interference of molecular diffusion on the results (see Supporting Information). Maps of the characteristic time τ (Figure 3c) and light intensity (Figure 3e), and the corresponding histograms (Figure 3d and f, respectively), were obtained. The mean light intensity retrieved was shown to be consistent with that calculated using the photon flux measured with a power meter, combined with area measurements of the beam waist of the laser beam, evaluated by raster image correlation spectroscopy[43] or imaging a fluorescent bead (see Supporting Information). The same series of experiments and validations were performed using a confocal microscope equipped with a continuous, rather than pulsed, laser (see Supporting Information). The results of which confirmed the ability of this protocol to retrieve light intensity with both modes of laser scanning.

In order to further examine the ability of this technique to measure light intensity, not just at the surface, but *in situ*, deep within samples, we performed measurements with cells with and without a layer of gel between them and the imaging system, and compared the results. In this, **Dronpa-2**-labeled Escherichia Coli bacteria cells were deposited on the surface of a 2% agarose gel sandwiched between glass-slides (Figure 3g). Light was applied with the deposited layer facing the objective, and then again after the sample was flipped, such that the light had to cross the gel before reaching the cells. The maps of light intensity for both orientations, provided in Figure 3h, show that it is possible to measure light intensity in bacteria cells even when buried behind the agarose gel, supporting the idea that this protocol can be useful for measurement deep within samples.

Calibration of the setting scale of light intensity in optical instruments. Many optical instruments do not provide information to the user on the absolute light intensity, but rather just the percentage of the maximum possible light. Such a fact presents issues for those who require the absolute value to be known. These issues include that the light level may not be linear with respect to the percentage scale, and the maximum may change with time as the light source ages. Thus, the second application envisioned for the fluorescent actinometers is their use in calibrating the light intensity in such instruments. As a demonstration, we applied the **Dronpa-2** and **PA** actinometers for the calibration of the percentage scales of a confocal microscope and a fluorometer respectively.

Using a **Dronpa-2** aqueous solution sandwiched between glass-slides, we measured the light intensity of a confocal microscope equipped with a pulsed laser at 488 nm at different percentages of the maximal laser power, using the same protocol detailed above for confocal systems. The resulting

calibration graph is provided in Figure 4a. Following this, we generated the same type of calibration graph (Figure 4b) for a fluorometer, this time by analyzing the **PA** fluorescence kinetics of a dark-acclimated suspension of microalgae exposed to its illumination light at 625 nm (see Supporting Information). These experiments demonstrated that this protocol can enable such a calibration graph to be obtained, allowing end-users to determine the light intensity, in absolute terms, based on the percentage value indicated on the instrument, and the verification of linearity in the range of settings investigated.

Spectral measurement of light intensity. Photons at different wavelengths drive photoconversion of actinometers to differing degrees. As an example, in regard to the use of **PA** as the actinometer, green photons are approximately seven times less efficient than blue or red photons for driving its photoconversion. This, in combination with the fact that light sources often do not emit at a single wavelength but rather over a spectrum of wavelengths, means that in order to obtain accurate measurements of light intensity for such sources, the spectral characteristics must be considered. Thus, in this section, we demonstrate an extension of our protocol to take into account the spectral characteristics of the light source. Moreover, since it is often desired, we show that we can retrieve information in the form of spectral light intensity.

This extended protocol begins with matching the excitation spectrum of the actinometer with the emission spectrum of the light source made available by the manufacturer or measured with a spectrophotometer (see Supporting Information). Then, in the same manner as before, the time course of the fluorescence intensity is obtained. The retrieved characteristic time is then used in conjunction with the integral of the action spectrum, the convolution of the normalized emission spectrum of the light source with the excitation spectrum of the actinometer, to quantitatively enable the retrieval of the spectral light intensity (see Supporting Information).

As preliminary validation, we used **Nit** and **PA** to characterize the illumination from purple and red-orange Light Emitting Diodes (LEDs), respectively, which are relevant colors in photocatalysis and optogenetics, and in studies of photosynthesis (see Supporting Information). Then we turned to the more challenging task of measuring the spectral light intensity of a white LED upon using the broad band absorbing **DDAO** fluorophore and implementing the protocol for transferring information on light intensity (Figure 5a) (see Supporting Information). We measured the **DDAO** fluorescence intensity when illuminated by a blue LED previously calibrated with the **Dronpa-2** actinometer, and by the white LED. The ratio of the fluorescence signals obtained was used, in combination with the known light intensity of the blue LED, to infer the light intensity of the white LED. The light intensity was then spectrally corrected by using the integral of the normalized action spectrum between the white LED and **DDAO**, whose spectral information is provided in Figure 5b. This experiment was repeated for a range of different LED current settings, and the integrated light intensities recorded at each (Figure 5c). Figure 5d displays the spectral light intensity of the white LED at a specific current setting.

Discussion

In this manuscript, we addressed two topics, which have been identified as key by the QUAREP-LiMi community (Quality Assessment and Reproducibility for Instruments & Images in Light Microscopy; https://quarep.org/):[6] (i) The measurement of the absolute flux of light at the sample (Working Group 1); (ii) The assessment of the uniformity of illumination (Working Group 3). Specifically, we showed that fluorescent actinometers (synthesized, genetically encoded, and even a natural photosynthetic organism) were relevant for quantitatively measuring light in widespread imaging modalities from wide-field fluorescence micro and macroimaging to confocal microscopy.

Compared to alternative methods for quantitatively measuring the light intensity which have been implemented here for validation purposes, these fluorescent actinometers have the advantage of (i) direct access to the information sought for independently on their concentration and without the

need for any further measurement (e.g the illuminated surface). In particular, they can measure light intensities at the surface of samples as well as in their depth as illustrated with the measurement of light intensity in **Dronpa-2**-labeled bacteria embedded in a light scattering gel. This information is difficult to obtain by any other method and it makes possible to use gels with similar refractive index as biological tissues to mimic thicker samples and calibrate irradiance with depth; (ii) a high signal-to-noise ratio (thanks to the use of fluorescence); (iii) an easy online access to the actinometer properties[34] and to codes and user-friendly applications to process their data;[35] (iv) an easy transfer of know-how to end users, which in our experience takes less than one hour from sample preparation to data processing.

Furthermore, the kinetics-based protocol of measurement of light intensity with fluorescent actinometers is robust with respect to the parameters generally affecting a fluorescence signal from the sample[44] and the instrument[45] side.[13] Hence, it can be noticed that the quantum yield of fluorescence of the fluorescent actinometer does not enter into the expression of the relaxation time τ. Hence, any possible variation of its value over the range of wavelengths of its light absorption is not detrimental for properly measuring light intensity as long as the wavelength of light excitation remains constant over the measurement. Similarly, as long as the experiment is performed under isothermal conditions, its temperature dependence is not significant for altering the extraction of the light intensity. In fact, this dependence may become only significant in the presence of strong spatial temperature gradients (in line with the 20% estimate of the achievable measurement uncertainty, typically a spatial gradient of 20 °C over the distance overcome by the reporting fluorophore - e.g. rhodamine B[46] - during the photoconversion time of the fluorescent actinometer). Eventually, our previous exploitation of quantitative photoconversions on other setups (e.g. single plane illumination microscopes,[47] fluorescence endoscopes[48]) suggests that the scope of these fluorescent actinometers could eventually be extended to other optical imaging systems.

However, the time resolution of the fluorescent actinometers is governed by the kinetics of their photoconversion, which imposes a lower limit on both the measurement duration (still short, 300 ms – 30 min) and the ability to analyze time evolving profiles of light intensity. Moreover, the mechanisms underlying their photoconversion often involve multiple steps and the mechanistic reduction making relevant monoexponentially fitting the time evolution of their fluorescence response to illumination deserves thorough attention.[16] Hence, we investigated the light intensity-dependence of the characteristic time τ to define ranges of light intensity in which the light-driven step of the photoconversion mechanism is constant and rate limiting so as to make this protocol of data processing reliable.

Moreover, two aspects must be kept in mind when implementing them for the characterization of spatially inhomogeneous light profiles: (i) As illustrated by the imaging of a Petri dish containing a solution of **Dronpa-2** being illuminated by a surrounding radial array of LEDs (a commonly used device in photocatalysis; see Supporting Information), a 3D-inhomogeneous light profile cannot be retrieved from the 2D-map of the characteristic time τ of the fluorescent actinometer. Nevertheless, one can still retrieve a useful information on the light intensity averaged over the sample thickness; (ii) As shown in Figure 2g-i, the motion of the fluorescent actinometer molecules can further introduce blurring in the retrieved 2D light profile. However, this phenomenon does not introduce any significant deviation modifying the order of magnitude of the measured light intensity as long as molecular diffusion remains spatially limited at the time scale of the actinometer photoconversion. Moreover, this phenomenon can be efficiently limited by using a medium (e.g. a gel) in which molecular diffusion is reduced. Key is here to choose the right embedding medium. For the water-soluble fluorescent actinometers, a polyacrylamide gel is a good choice. Here, low mesh size and gel sealing after sandwiching between glass slides ensure both low molecular diffusion and absence of water loss respectively. Immobilization of the synthetic fluorescent actinometers in organic media would require some more developments either by modifying their molecular structure (by adding

anchoring groups to graft them on a surface) or by embedding them in a highly viscous (e.g. a polymer) or solid organic matrix. However, one would have then to characterize their photochemical properties in those media, which has not been covered during the present study.

Author contribution statements

Conceptualization: A.L., T. L. S., L. J.; Methodology: A.L., L. N., T. L. S., L. J.; Software: A.L., I. C., T. L. S.; Validation: A. L., H. S. T., I. C., D. L.; Formal analysis: A. L., H. S. T., I. C., T. L. S., L. J.; Investigation: A. L., H. S. T., I. C., M. M., Y. N., I. E., R. J., P. M., T. L. S.; Resources: A. L., I. C., Y. S., M.-A. P., I. A., Y. N., L. N., P. M., W. S., E. B., I. E., N. D., V. C., R. J.; Data Curation: A. L., I. C., Y. N., P. M., T. L. S.; Writing - Original Draft: A. L., H. S. T., I. C., L. N., D. L., T. L. S., L. J.; Writing - Review & Editing: A.L., T. L. S., L. J.; Visualization: A.L., H. S. T., T. L. S., L. J.; Supervision: A.L., T. L. S., L. J.; Project administration: L. J.; Funding acquisition: T. L. S., L. J.

Online methods

The Supporting Information starts with a list, which indicates the (sub)sections associated with the calls “See Supporting Information” of the Main Text, as well as details on statistical parameters and image processing. It is then divided in two parts: (i) The sections 1–3 are dedicated to end-users, who are willing to directly implement the reported fluorescent actinometers; (ii) The Appendix has six sections A–F, which contain more advanced information as well as the complete validation of the reported fluorescent actinometers. Codes and metadata for the Figures of the Main Text can be found online, as well as user-friendly tools and how to use them: https://github.com/DreamRepo/light_calibration and in a mirror Zenodo repository (10.281/zenodo.7665939).

Data availability statement

The datasets generated during and/or analysed during the current study and that are not in the online repository are available from the corresponding author on request.

Code availability statement

The codes that require several steps to reproduce the data analysis have been made available online: https://github.com/DreamRepo/light_calibration and in a mirror Zenodo repository (10.281/zenodo.7665939).

Table 1: *Key parameters for choosing a fluorescent actinometer.* λ_{exc}, [λ_{em}], $\sigma(\lambda_{exc})$, and [$I(\lambda_{exc})$] respectively designate the excitation wavelength, the range of emission wavelengths, the cross section, and the range of reliably measurable light intensity associated to the actinometer photoconversion at λ_{exc}. $5\,\tau_{min}$ is the minimum measurement duration at the highest measurable light intensity. See Supplementary Information.

Actinometer (availability)[a]	λ_{exc} (nm)	[λ_{em}] (nm)	$\sigma(\lambda_{exc})$ (±10%;$m^2.mol^{-1}$)	[$I(\lambda_{exc})$] ($E.m^{-2}.s^{-1}$($W.m^{-2}$))[b]	$5\,\tau_{min}$ (s)
Cin	350		940	[0-1.6] 10^{-5}([0-5.5])	332
(S)	365		1200	[0-1.4] 10^{-5}([0-4.6])	298
	380	[400-550]	1000	[0-1.7] 10^{-5}([0-5.3])	294
	405		184	[0-5.0] 10^{-5}([0-15])	543
	420		49	[0-1.3] 10^{-4}([0-37])	785
Nit	365		960	[0-11] 10^{-4}([0-360])	4.7
(S)	380	[550-650]	1200	[0-7.2] 10^{-4}([0-230])	5.8
	405		1100	[0-7.0] 10^{-4}([0-200])	6.5
	420		850	[0-12] 10^{-4}([0-340])	4.9
Dronpa-2	445		140 (192)[c]	[3 10^{-4}-18]([80-4.8 10^6])	2.0 10^{-3}
(GE)	480	[500-600]	198 (251)[c]	[2 10^{-4}-10]([50-2.5 10^6])	2.5 10^{-3}
	500		128 (151)[c]	[3 10^{-4}-13]([72-1.0 10^6])	3.0 10^{-3}
DASA	530		255	[8-290] 10^{-5}([18-660])	6.8
(S)	560		530	[4-150] 10^{-5}([9-320])	6.3
	600	[530-670]	885	[2-72] 10^{-5}([4-140])	7.8
	632		1135	[2-60] 10^{-5}([4-110])	7.3
	650		575	[3-140] 10^{-5}([6-260])	6.2
PA	405		2.0 (±0.4)10^6	[0-10^{-2}]([0-3000])	1[d]
(B)	470	[650-800]	2.0 (±0.4) 10^6	[0-10^{-2}]([0-2600])	1[d]
	650		1.1 (±0.4)10^6	[0-10^{-2}]([0-1900])	1[d]

[a] S: easily synthesized; GE: genetically encoded; B: photosynthetic organism available for sale (chlamycollection.org). See Supporting Information; [b] The conversion between the units mol of photon.$m^{-2}.s^{-1}$ – $E.m^{-2}.s^{-1}$ – and $W.m^{-2}$ is given in Section A in the Supporting Information; [c] The first and second numbers provide the values to be used in the **Dronpa-2** solution and in the **Dronpa-2** labeled fixed cells, and in the **Dronpa-2** labeled bacteria respectively; [d] $5\tau_{min}$ is here the time requested to record the whole **PA** fluorescence rise.

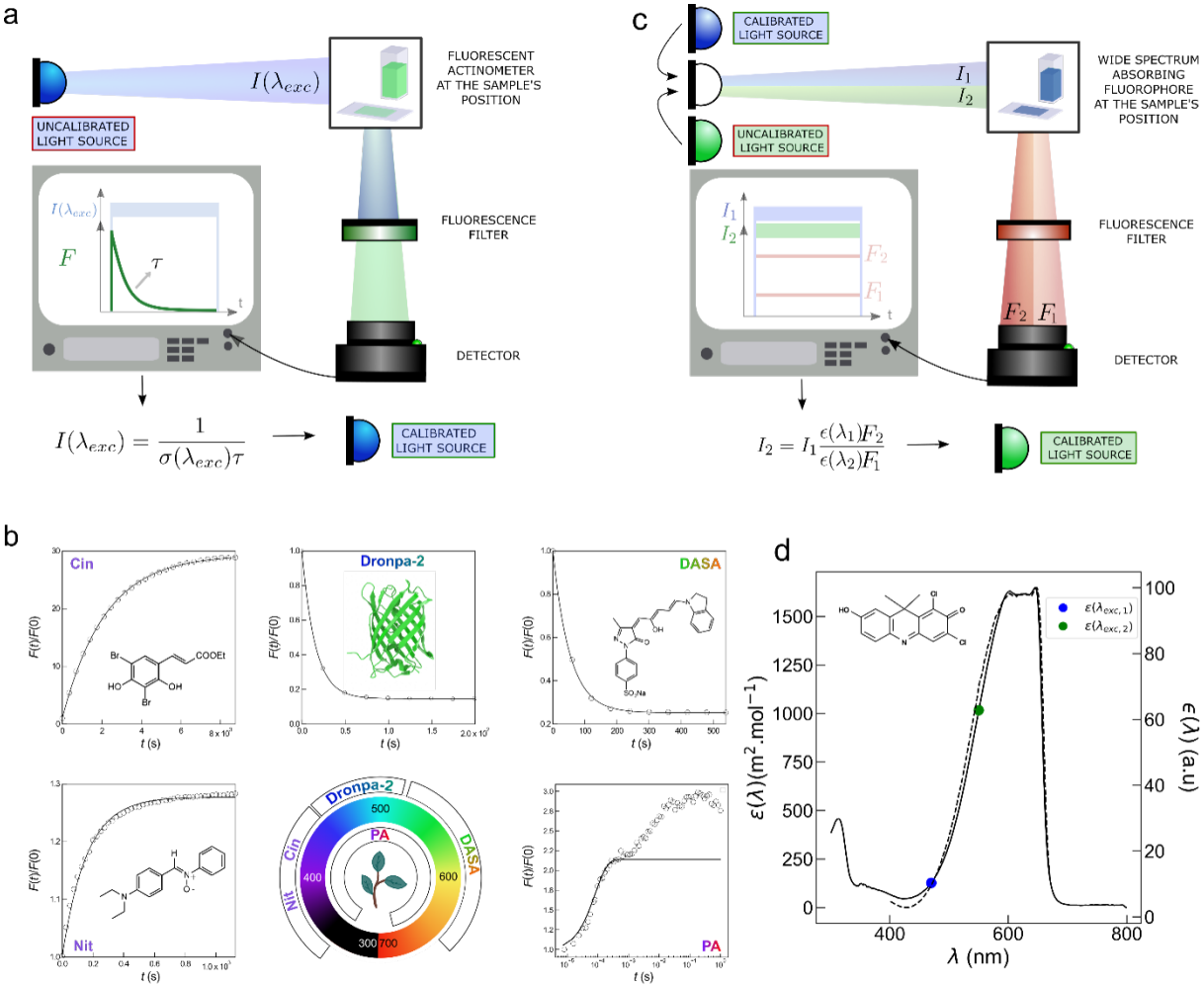

Figure 1: *Fluorescence reporting for retrieving light intensity*. **a**: *First protocol with a fluorescent actinometer.* A jump of constant light I is applied onto the actinometer. The time evolution of its fluorescence signal F is recorded and fit with a mono-exponential curve to extract its characteristic time τ. I is retrieved from τ by using the photoconversion cross section σ of the actinometer; **b**: *Five fluorescent actinometers covering the UV-Vis range in action*. Monoexponential fit of the time evolution of the normalized fluorescence signal *F(t)/F(0)* provides τ. See Table S3 in Supporting Information; **c**: *Second protocol with a fluorophore to transfer information on light intensity from one wavelength to another.* Lights at wavelengths λ_1 (with intensity I_1 - known) and λ_2 (with intensity I_2 - to be measured) are successively applied onto the fluorophore and the associated fluorescence signals F_1 and F_2 are recorded at a same emission wavelength. I_2 is extracted from F_1 and F_2 by using I_1 and the tabulated fluorescence excitation spectrum $\epsilon(\lambda)$ of the fluorophore; **d**: *Absorption ($\varepsilon(\lambda)$; dotted line) and normalized fluorescence excitation ($\epsilon(\lambda)$; solid line) spectra of* ***DDAO***. $\varepsilon(\lambda_1)$ and $\varepsilon(\lambda_2)$ indicated by blue and green disks respectively are used to retrieve $I(\lambda_2)$ in **c**. See Text and Supporting Information.

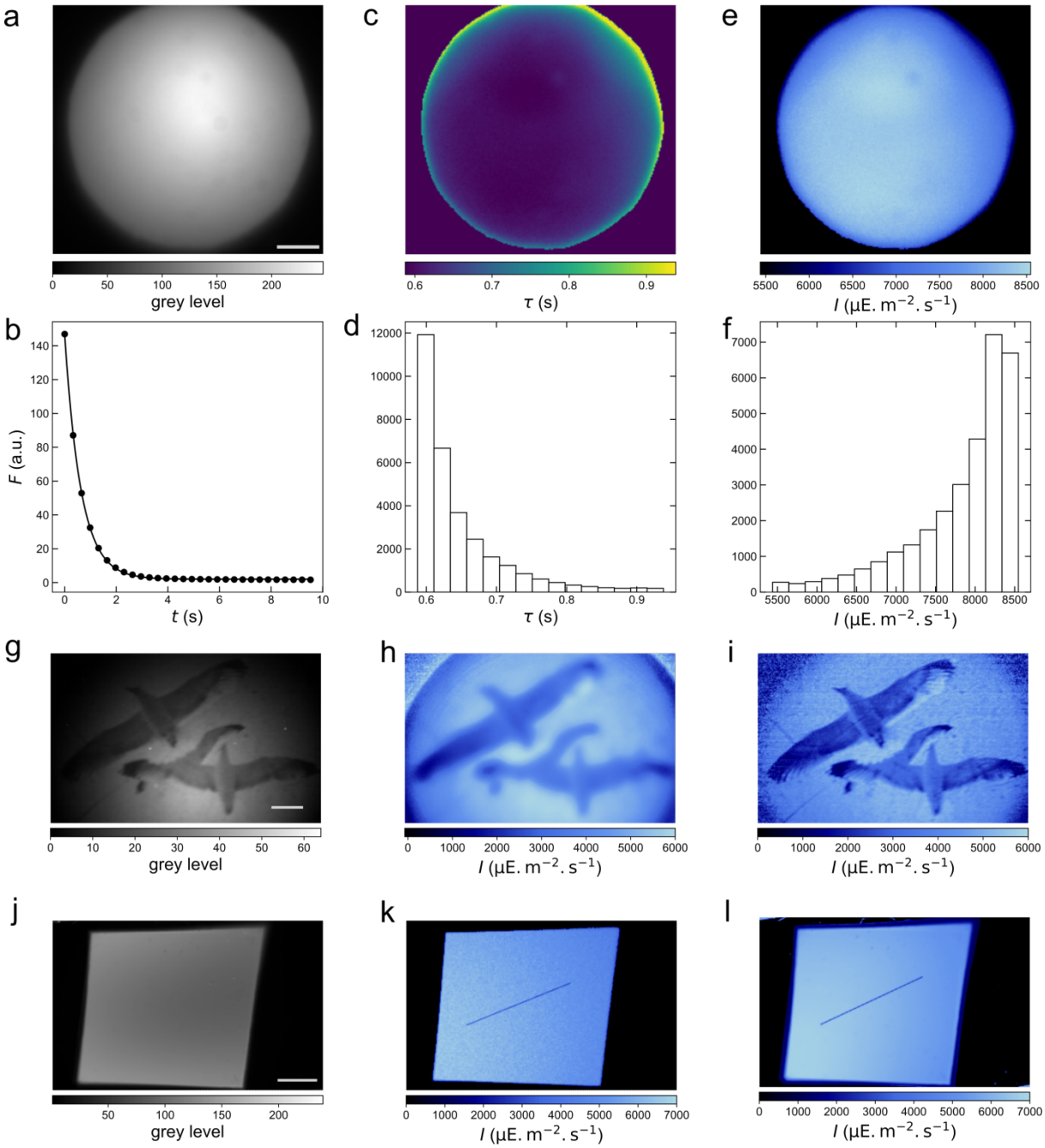

Figure 2: ***Dronpa-2*** *for characterization of illumination in wide-field fluorescence imaging.* **a-i**: Epifluorescence microscopy. **a**: Initial image of the **Dronpa-2** solution under homogeneous illumination; **b**: time fluorescence response (τ = 0.63 s), maps of the characteristic time τ (**c**), light intensity (**e**), and corresponding histograms (**d**,**f**) in the field of view; Initial image (**g**) and maps of light intensity (**h**,**i**) of **Dronpa-2** in solution (**h**) or in polyacrylamide gel under patterned illumination; **j**-**l**: Macroscopic fluorescence imaging. **j**: Initial image of the **Dronpa-2** solution and experimental (**k**) and simulated (**l**) maps of light intensity. The blue line shows the angle of the linear light gradient; the angle between the simulated gradient and the measured one is 3°. **a**-**f**, **h**, **j**-**l**: 10 µM **Dronpa-2** solution or 19% polyacrylamide gel in Tris buffer pH 7.4 (50 mM Tris, 150 mM NaCl); scale bar: 100 µm in **a**,**c**,**e**, **g**-**h**, 3 mm in **j**-**l**; *T* = 293 K. λ_{exc} = 470 nm; λ_{em} = 550 nm. See Text and Supporting Information.

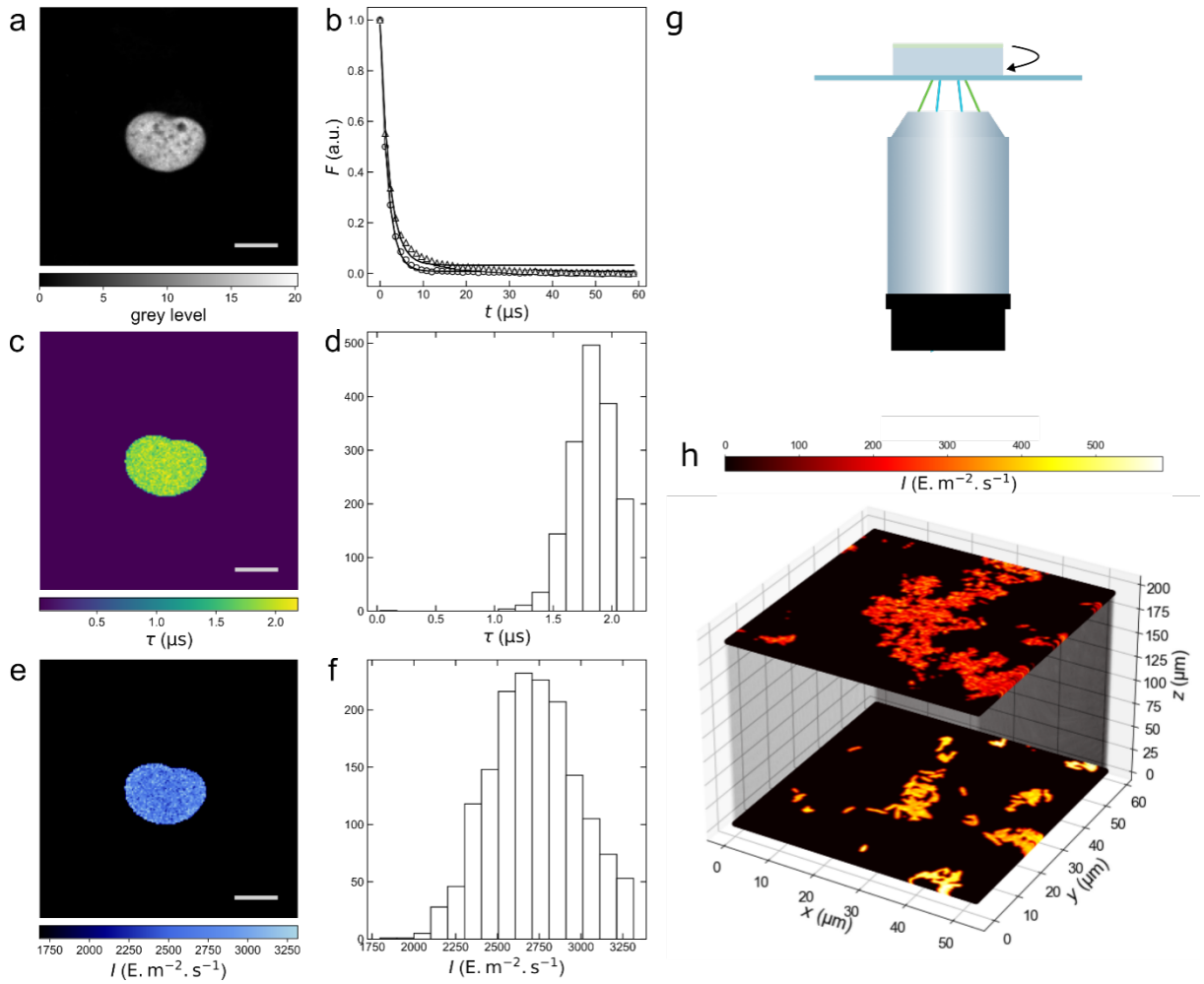

Figure 3: ***Dronpa-2*** *for characterization of illumination in confocal microscopy equipped with a pulsed laser in the raster scanning mode.* **a-f**: **Dronpa-2**-labeled nucleus of a fixed U-2 OS cell. **a**: Initial image; **b**: Time evolution of the averaged fluorescence over the whole nucleus (circles: experimental data; solid line: monoexponential fit, τ = 1.87 µs). The corresponding evolution from a central portion of the overall image of a 10 µM **Dronpa-2** solution sandwiched between two glass-slides is shown with triangles (τ = 2.08 µs); **c**-**f**: Maps of the characteristic time τ (**c**) and light intensity (**e**), and corresponding histograms (**d**,**f**). See Table S3 in Supporting Information; **g**,**h**: Setup (**g**) and map of light intensity retrieved from **Dronpa-2**-labeled E. Coli bacteria imaged at the surface or through a 2 % agarose pad by changing the sample orientation (**h**). Solvent: Tris buffer pH 7.4 (50 mM Tris, 150 mM NaCl); T = 293 K. λ_{exc} = 488 nm; 500 nm < λ_{em} < 550 nm; scale bar: 12 µm in **a**,**c**,**e**; See Text and Supporting Information.

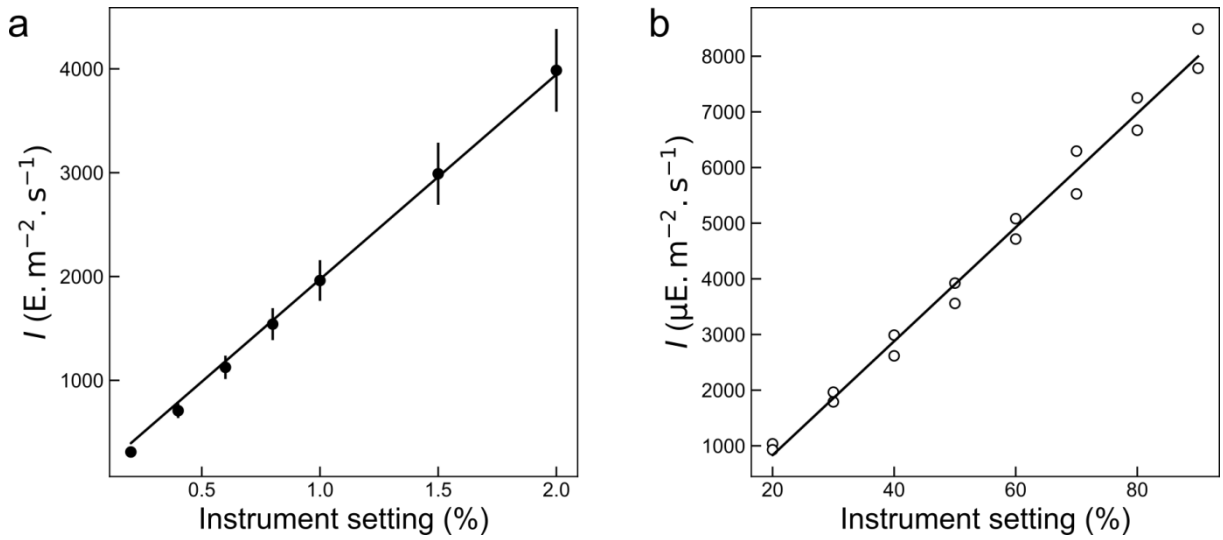

Figure 4: *Calibration of optical instruments.* The dependence of the light intensity at 488 (**a**) and 625 (**b**) nm on the percentage scale available on the instruments (confocal microscope with pulsed laser in **a** and fluorometer in **b**) has been established with the **Dronpa-2**-labeled nucleus of a fixed U-2 OS cell (SD are propagated from the error on $\sigma(488)$) and **PA** actinometers respectively. T = 293 K. See Text and Supporting Information.

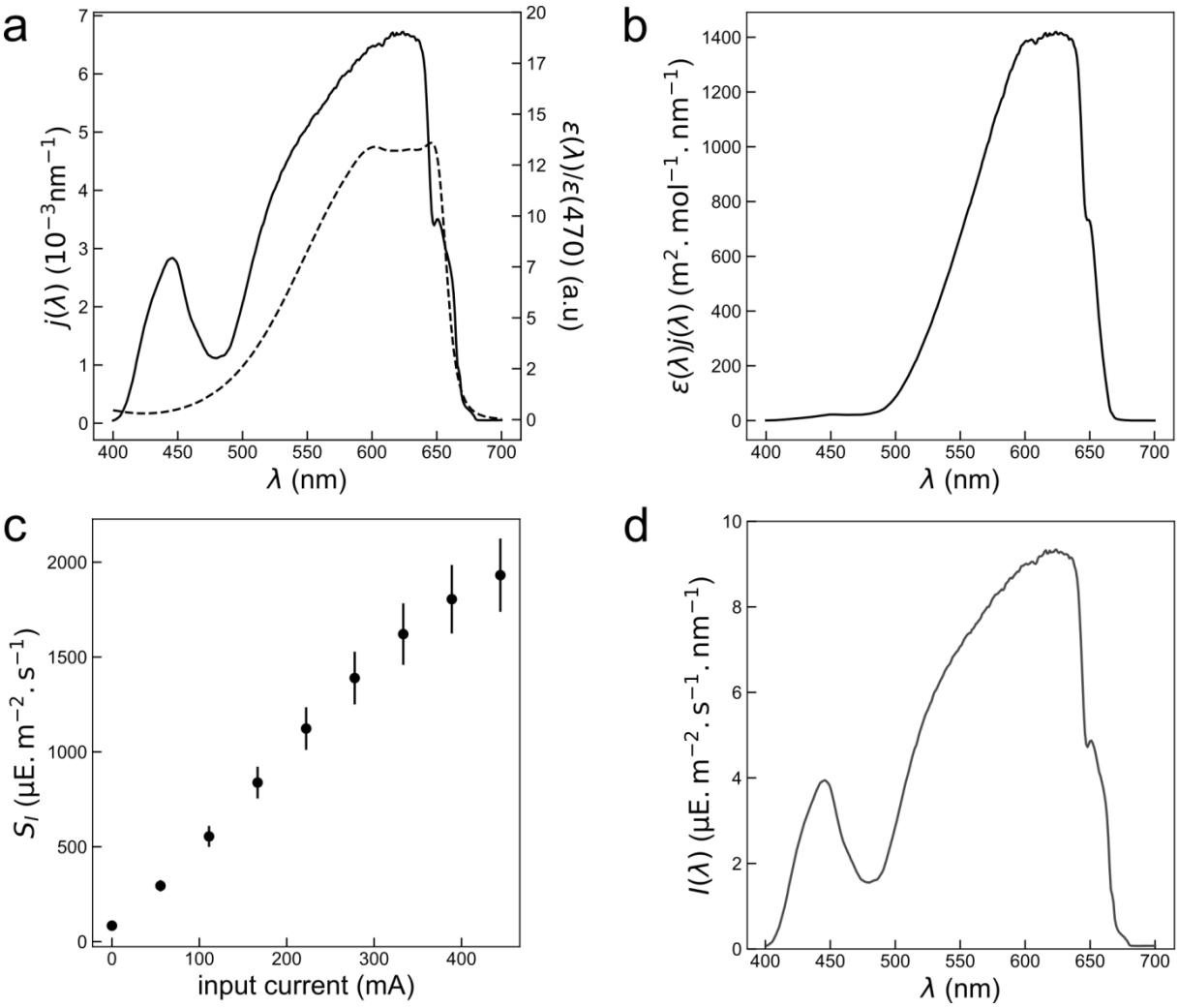

Figure 5: *Characterization of the spectral light intensity of a white LED by **DDAO**-mediated measurement*. **a**: Emission spectrum of the white LED normalized by its integral (solid line), absorbance spectrum of **DDAO** normalized at 470 nm (dashed line); **b**: Action spectrum of the white LED on **DDAO**; **c**: Dependence of the integral light intensity S_I emitted by the white LED on the input currents as measured with spectral transfer of **DDAO** fluorescence intensity (SD are propagated from the error on $\sigma(470)$); **d**: Incident spectral light intensity $I(\lambda)$ of the white LED fed with 277 mA current as retrieved with **DDAO** (S_I = 1.40 mE.m^{-2}.s^{-1}). See Text and Supporting Information.

Acknowledgement

The authors thank N. Gagey for providing **Cin**, S. Bujaldon for providing *Chlamydomonas reinhardtii* strains, S. Lahlou for the seagull picture used for patterning the light, and A. Jawahar for useful discussions on the protocol implementation. D. Bensimon, C. Boccara, P. Dedecker, G. Ellis-Davies, and L. Fensterbank are acknowledged for manuscript reading and discussions. This work was supported by the ANR (France BioImaging - ANR-10-INBS-04, Morphoscope2 - ANR-11-EQPX-0029, IPGG - ANR-10-IDEX-0001-02 PSL, ANR-10-LABX-31, and ANR-19-CE11-0005) (for T. L. S. and L. J.), the Federal Ministry of Education and Research of Germany (BMBF) within the YESPVNIGBEN project (03SF0576A) (for Y. N.), the European Regional Development Fund project 'Plants as a tool for sustainable global development' (no. CZ.02.1.01/0.0/0.0/16_019/0000827) (for D. L. and L. N.), and the EIC Pathfinder Open DREAM (GA number 101046451) (for all authors).

[1] D. Cambié, C. Bottecchia, N. J. W. Straathof, V. Hessel, T. Noël, Applications of continuous-flow photochemistry in organic synthesis, material science, and water treatment, *Chem. Rev.* **2016***, 116*, 10276–10341.

[2] T. J. Dougherty, C. J. Gomer, B. W. Henderson, G. Jori, D. Kessel, M. Korbelik, J. Moan, Q. Peng, Photodynamic Therapy, *J. Nat. Can. Inst*., **1998**, *90*, 889-905.

[3] A. Gautier, C. Gauron, M. Volovitch, D. Bensimon, L. Jullien, S. Vriz, How to control proteins with light in living systems, *Nat. Chem. Biol.*, **2014**, *10*, 533-541.

[4] D. Ravelli, D. Dondi, M. Fagnoni and A. Albini, Photocatalysis. A multi-faceted concept for green chemistry, *Chem. Soc. Rev*., **2009**, *38*, 1999–2011.

[5] Md. A. Hoque, M. I. Guzman, Photocatalytic Activity: Experimental Features to Report in Heterogeneous Photocatalysis, *Materials*, **2018**, *11*, 1990.

[6] Boehm, U., Nelson, G., Brown, C.M. *et al.* QUAREP-LiMi: a community endeavor to advance quality assessment and reproducibility in light microscopy. *Nat Methods,* **2021**, *18*, 1423–1426.

[7] O. Faklaris, L. Bancel-Vallée, A. Dauphin, B. Monterroso, P. Frère, D. Geny, T. Manoliu, S. de Rossi, F. P. Cordelières, D. Schapman, R. Nitschke, J. Cau, T. Guilbert, Quality assessment in light microscopy for routine use through simple tools and robust metrics, *J Cell Biol*., **2022**, 221, e202107093.

[8] U. Megerle, R. Lechner, B. König, E. Riedle, Laboratory apparatus for the accurate, facile and rapid determination of visible light photoreaction quantum yields, *Photochem. Photobiol. Sci.* **2010**, *9*, 1400–1406.

[9] D. Grünwald, S. M Shenoy, S. Burke, R. H Singer, Calibrating excitation light fluxes for quantitative light microscopy in cell biology, *Nat. Protocols*, **2008**, *3*, 1809–1814.

[10] H. J. Kuhn, S. E. Braslavsky, and R. Schmidt, Chemical Actinometry (IUPAC Technical Report), *Pure Appl. Chem*., **2004**, *76*, 2105–2146.

[11] M**.** Reinfelds, V**.** Hermanns, T**.** Halbritter, J**.** Wachtveitl, M**.** Braun, T**.** Slanina, A**.** Heckel**,** A Robust, Broadly Absorbing Fulgide Derivative as a Universal Chemical Actinometer for the UV to NIR Region, *ChemPhotoChem*, **2019**, *3*, 441-449.

[12] A. Roibu, S. Fransen, M. E. Leblebici, G. Meir, T. Van Gerven, S. Kuhn, An accessible visible-light actinometer for the determination of photon fux and optical pathlength in flow photo microreactors, *Sci. Rep*., **2018**, *8*, 5421.

[13] B. Valeur, M.-N. Berberan-Santos, Molecular Fluorescence: Principles and Applications 2nd Edition, Wiley, 2012.

[14] J. M. Zwier, G. J. Van Rooij, J. W. Hofstraat, G. J. Brakenhoff, Image calibration in fluorescence microscopy, *J. Microscopy*, **2004**, *216*, Pt 1, 15–24.

[15] N. Gagey, P. Neveu, C. Benbrahim, B. Goetz, I. Aujard, J. – B. Baudin, L. Jullien, Two-photon uncaging with fluorescence reporting: Evaluation of the o-hydroxycinnamic platform, *J. Am. Chem. Soc.*, **2007**, *129*, 9986-9998.

[16] R. Chouket, A. Pellissier-Tanon, A. Lahlou, R. Zhang, D. Kim, M.-A. Plamont, M. Zhang, X. Zhang, P. Xu, N. Desprat, D. Bourgeois, A. Espagne, A. Lemarchand, T. Le Saux, L. Jullien, Extra kinetic dimensions for label discrimination, *Nat. Commun*., **2022**, *13*, 1482.

[17] Y Shpinov, A Schlichter, P Pelupessy, T Le Saux, L Jullien, B Adelizzi, Unexpected acid-triggered formation of reversibly photoswitchable Stenhouse salts from Donor-acceptor Stenhouse adducts, *Chemistry–A European Journal*, **2022**, *28*, e202200497.

[18] M. Emond, T. Le Saux, S. Maurin, J.-B. Baudin, R. Plasson, L. Jullien, 2-Hydroxy-Azobenzenes to Tailor pH Pulses and Oscillations with Light, *Chem. Eur. J.*, **2010**, *16*, 8822-8831.

[19] P. F. Wang, L. Jullien, B. Valeur, J.-S. Filhol, J. Canceill, J.-M. Lehn, Multichromophoric Cyclodextrins. 5. Antenna-induced Unimolecular Photoreactions. Photoisomerization of a Nitrone, *New J. Chem.*, **1996**, *20*, 895-907.

[20] Su, A.; Grist, S.; Geldert, A.; Gopal, A.; Herr A., Quantitative UV-C dose validation with photochromic indicators for informed N95 emergency decontamination, *Plos One* **2021**, *16*, e024355.

[21] Berces, A.; Fekete, A.; Gaspar, A.; Grof, P.; Rettenberg, P.; Ronto, G., Biological UV dosimeters in the assessment of the biological hazard from environmental radiation, *Photochem. Photobiol. B*, **1999**, *53*, 36-43.

[22] P. Klan, T. Solomek, C. G. Bochet, A. Blanc, R. Givens, M. Rubina, V. Popik, A. Kostikov, and J. Wirz. Photoremovable protecting groups in chemistry and biology: Reaction mechanisms and efficacy. *Chem. Rev.*, **2013**, *113*, 119–191.

[23] N. Gagey, P. Neveu, and L. Jullien. Reporting two-photon uncaging with the efficient 3,5-dibromo-2,4-dihydroxycinnamic caging group, *Angew. Chem. Intl. Ed*., **2007**, *46*, 2467-2469.

[24] P. R. West, G. C. Davis, The synthesis of diarylnitrones, *J. Org. Chem***.,** **1989**, *54,* 5176-5180.

[25] P. F. Wang, L. Jullien, B. Valeur, J.-S. Filhol, J. Canceill, J.-M. Lehn, Multichromophoric Cyclodextrins. 5. Antenna-induced Unimolecular Photoreactions. Photoisomerization of a Nitrone, *New J. Chem.*, **1996**, *20*, 895-907.

[26] Maxwell, K., & Johnson, G. N., Chlorophyll fluorescence—a practical guide. *Journal of experimental botany*, **2000**, *51*(345), 659-668.

[27] Stiel, A. C., et al. 1.8 Å bright-state structure of the reversibly switchable fluorescent protein Dronpa guides the generation of fast switching variants, *Biochem J*, **2007**, *402*, 35 – 42.

[28] Mirkovic, T., Ostroumov, E. E., Anna, J. M., van Grondelle, R., Govindjee, & Scholes, G. D., Light Absorption and Energy Transfer in the Antenna Complexes of Photosynthetic Organisms, *Chemical Reviews,* **2017***, 117*, 249–293.

[29] D. Lazar, The polyphasic chlorophyll a fluorescence rise measured under high intensity of exciting light, *Funct. Plant Biol.*, **2006**, *33*, 9-30.

[30] Stirbet, A., & Govindjee, On the relation between the Kautsky effect (chlorophyll a fluorescence induction) and Photosystem II: Basics and applications of the OJIP fluorescence transient, *J. Photochem. Photobiol. B: Biology,* **2011***, 104*, 236–257.

[31] R. Delosme, Étude de l'induction de fluorescence des algues vertes et des chloroplastes au début d'une illumination intense, *Biochim. Biophys. Act*., **1967**, *143*, 108-128.

[32] R. J. Strasser, A. Srivastava, G. Govindjee, Polyphasic chlorophyll a fluorescence transient in plants and cyanobacteria, *Photochem. Photobiol*., **1995**, *61*, 32-42.

[33] D. Joly, R. Carpentier, Sigmoidal reduction kinetics of the photosystem II acceptor side in intact photosynthetic materials during fluorescence induction, *Photochem. Photobiol. Sci.*, **2009**, *8*, 167–173.

[34] https://chart-studio.plotly.com/~Alienor134/#/

[35] https://github.com/DreamRepo/light_calibration

[36] D. Warther, F. Bolze, J. Lonéard, S. Gug, A. Specht, D. Puliti, X.- H. Sun, P. Kessler, Y. Lutz, J.-L. Vonesch, B. Winsor, J.-F. Nicoud, M. Goeldner, Live-Cell One- and Two-Photon Uncaging of a Far-Red Emitting Acridinone Fluorophore, *J. Am. Chem. Soc.*, **2010**, *132*, 2585-2590.

[37] R. Labruère, A. Alouane, T. Le Saux, I. Aujard, P. Pelupessy, A. Gautier, S. Dubruille, F. Schmidt, L. Jullien, Self-immolation for uncaging with fluorescence reporting, *Angew. Chem. Int. Ed.*, **2012**, *51*, 9344-9347.

[38] J. Icha, M. Weber, J. C. Waters, C. Norden, Phototoxicity in live fluorescence microscopy, and how to avoid it, *Bioessays*, **2017**, *39*, 1700003.

[39] D. L. Coutu, T. Schroeder, Probing cellular processes by long-term live imaging – historic problems and current solutions, *J. Cell. Sci.,* **2013**, *126*, 3805–3815.

[40] D. W. Piston, G.-J. Kremers, Fluorescent protein FRET: the good, the bad and the ugly, *Trends. Biochem. Sci*., **2007**, *32*, 407-414.

[41] M. Lelek, M. T. Gyparaki, G. Beliu, F. Schueder, J. Griffié, S. Manley, R. Jungmann, M. Sauer, M. Lakadamyali, C. Zimmer, Single-molecule localization microscopy, *Nat. Rev., Methods Primers*, **2021**, *1*, 39.

[42] J. Quérard, R. Zhang, Z. Kelemen, M.-A. Plamont, X. Xie, R. Chouket, I. Roemgens, Y. Korepina, S. Albright, E. Ipendey, M. Volovitch, H. L. Sladitschek, P. Neveu, L. Gissot, A. Gautier, J.-D. Faure, V. Croquette, T. Le Saux, L. Jullien, Resonant out-of-phase fluorescence microscopy and remote imaging overcome spectral limitations, *Nat. Commun.*, **2017**, *8*, 969.

[43] C. M. Brown, R. B. Dalal, B. Hebert, M. A. Digman, A. R. Horwitz, E. Gratton, Raster image correlation spectroscopy (RICS) for measuring fast protein dynamics and concentrations with a commercial laser scanning confocal microscope, *J. Microscopy*, **2008**, *229*, 78–91.

[44] U. Resch-Genger, Paul C. DeRose, Fluorescence standards: Classification, terminology, and recommendations on their selection, use, and production (IUPAC Technical Report)*, *Pure Appl. Chem.*, **2010**, *82*, 2315-2335.

[45] U. Resch-Genger, Paul C. DeRose, Characterization of photoluminescence measuring systems (IUPAC Technical Report), *Pure Appl. Chem*., **2012**, *84*, 1815-1835.

[46] D Ross, M Gaitan, L E Locascio, Temperature measurement in microfluidic systems using a temperature-dependent fluorescent dye, *Anal. Chem*., **2001**, *73*, 4117-4123.

[47] J. Querard, T.-Z. Markus, M.-A. Plamont, C. Gauron, P. Wang, A. Espagne, M. Volovitch, S. Vriz, V. Croquette, A. Gautier, T. Le Saux, L. Jullien, Photoswitching kinetics and phase sensitive detection add discriminative dimensions for selective fluorescence imaging, *Angew. Chem. Int. Ed.*, **2015**, *54*, 2633-2637.

[48] R. Zhang, R. Chouket, A. G. Tebo, M.-A. Plamont, Z. Kelemen, L. Gissot, J.-D. Faure, A. Gautier, V. Croquette, L. Jullien, T. Le Saux, *Optica*, **2019**, *6*, 972-980.

2.6.2 Contributions

This work is the result of years of research by the team of Ludovic Jullien and Thomas Le Saux. I suggested summarizing this work into a publication targeting the community of bioimaginig in life sciences interested in assessing the instruments quality and reproducibility. Ludovic Jullien and Thomas Le Saux introduced the various actinometric strategies. With Ludovic Jullien and Thomas Le Saux, we designed the epiflorescence setup and the set of experiments displayed in the main text, and the complementary characterizations required. I mainly focused on the experiments using **Dronpa-2**, **DDAO** and *Chlamydomonas reinhardtii*. I made all the figures from the Main Text except Figure 2j-l made by Ian Coghill. Ian Coghill also performed the 3D simulations presented in the Supplementary Materials. Hessam Sepasi Tehrani performed the experiments on **Nit**, **DASA** and **Cin**. The actinometers were synthesized by Marie-Aude Plamont, Hessam Sepasi Tehrani and Yuriy Shpinov. Hessam Sepasi Tehrani performed the characterizations of these fluorophores presented in the Supplementary Materials. Ludovic Jullien developed the models and computations for the kinetics, as well as the model for the estimations of light intensity under the confocal microscopes. The confocal experiments were performed by Hessam Sepasi Tehrani, Pierre Mahou, Thomas Le Saux and me, and were analyzed by me for the **Dronpa-2** images and Thomas Le Saux for fluorescent beads, which he complemented with the RICS experiments and their analysis (Supplementary Materials). The experiments on *Chlamydomonas reinhardtii* were performed by Yuxi Niu, Ladislav Nedbal and me and I ran the analysis. I wrote the codes and applications addressed to the users and shared on Github. Ludovic Jullien wrote the first drafts of the manuscript and supplementary materials.

Chapter 3

Remote sensing of chlorophyll fluorescence

3.1 Introduction

This Chapter describes the principles at the root of photosynthesis remote sensing. I used three books [89, 92, 109] and a seminar from Christian Frankenberg at the Keck Institute for Space Studies (2017) as references.

Fluorescence refers to the phenomenon in which a system that reached a singlet excited state by the absorption of light energy re-emits this energy in the form of visible light. In one-photon absorption, the emission wavelength is longer than the excitation wavelength because a fraction of the absorbed energy is relaxed by internal vibrations. When excited by light, the reaction centers of the photosynthetic chain respond by dissipating a fraction of the excitation as fluorescence photons that can be measured remotely. The rest of the exciting light is used in the photosynthetic chain or dissipated, principally as heat. Probing the fluorescence brings information on these competitive pathways: photosynthesis and heat dissipation, in particular active heat dissipation, which intervenes dynamically when the plant is stressed.

Before detailing these pathways, I give an overview of the photosynthetic chain and its structure within the leaf architecture. Although this specific part focuses on leaves, for the rest of the work the comments are valid for leaves and algae, as the phenomena described are well-preserved among photosynthetic species.

Then, the pathways that an absorbed photon can follow are described. I introduce a thought experiment to clarify the key parameters used in chlorophyll fluorescence (ChlF) research. It consists in applying a high-light jump to a plant previously left in the dark, to fill its photosynthetic chain until saturation. This thought experiment, which is actually a whole branch of photosynthesis research – fluorescence transient –, can enlight the complexity of the dynamics of the fluorescence response.

At this point I introduce a manuscript that we plan to submit to Advanced Science in September 2023. This manuscript shows that within the dynamic ChlF response, the very first part is kinetically dependent on the light intensity. As the photosystem activity is well-preserved among photosynthetic organisms, we introduced a method to exploit this phenomena to calibrate a light intensity using a leaf randomly collected from a garden.

The publication discusses other light-dependent phenomena that could be measured to characterize the excitation light. They happen over longer time-scales and further away from the initial photon absorption step. As a consequence, they not only integrate information on light, but also on the plant's inner biochemistry (stress, synthesis, etc). Therefore, we focus only on the initial step of the fluorescence transient for actinometry. In the following part of the work, we will not be interested to use the slower processes as actinometers. On the contrary, we will use them as reporters

of the photosynthetic organism status, precisely the objective of remote sensing. I will show how, by exploiting the light calibration methods described principally in Appendix 2.6, it is possible to unmix the light amplitude effect from the fluorescence response and focus on the contribution of the plant's inner biochemistry. I demonstrate and validate a new protocol to perform fluorescence remote sensing in imaging at the micrometer scale. For this, we ran experiments with Benjamin Bailleul, Eliora Israelievitch and Marcelo Orlando on their instrument at IBPC and the epifluorescence microscope simultaneously.

3.2 Light capture in photosynthetic organisms

3.2.1 Description of the photosynthetic chain

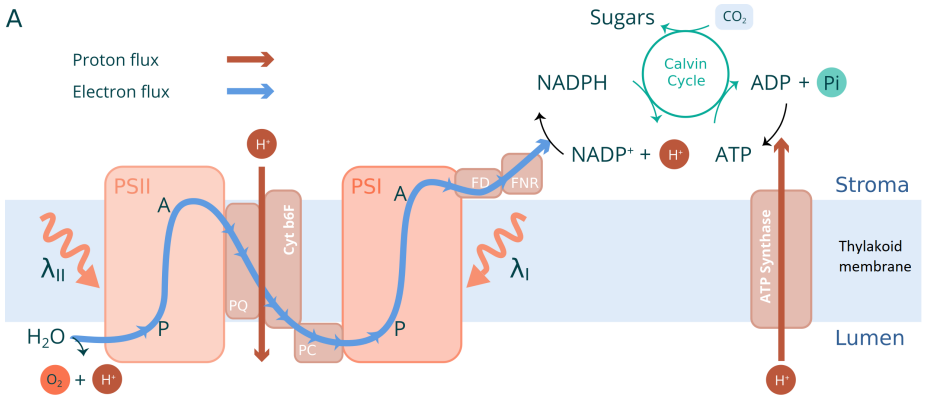

Figure 3.1: *Scheme of the photosynthetic chain*, displaying the photosystems PSII and PSI (P) playing the motive role in the light reaction in combination with the redox agents, plastoquinone (PQ), cytochrome b6f (Cyt b6f), plastocyanin (PC), ferredoxin (FD), Ferredoxin–$NADP^+$ reductase, and the dark reaction site (Calvin cycle). Absorption of light by the photosystems initiates a series of electron transfers from a first (PSII) photosystem - releasing oxygen from water - to a second photosystem (PSI), which releases strong reductants ending up at NADPH; an electrochemical potential across the membrane coupling a H^+ gradient to ATP production. NADPH and ATP subsequently enable fixation of carbon dioxide and production of sugars. Photosynthesis regulation manages excess of light and balances the serial operation.

Photosynthesis is the vital process of plants, algae, and some bacteria. These photosynthetic organisms convert carbone dioxyde (CO_2) and water (H_2O) into sugars ($C_6H_{12}O_6$) and dioxygen (O_2) through the following reaction: $6\,CO_2 + 6\,H_20 \longrightarrow C_6H_{12}O_6 + 6\,O_2$.

This reaction is fueled by light from the whole visible spectrum. It is absorbed by specialized pigments whose absorption bands cover the wavelength range from 400 nm to 750 nm. The pigments are located in the chloroplasts within cells and act as antennas: they transfer the excitation energy to reactions centers (RC), where the photosynthetic chain operates.

The photosynthesis process can be divided into two main steps: the light-dependent reactions and the dark reactions, also known as the Calvin cycle. In the light-dependent reactions, solar energy is captured by the pigments and transferred as an exciton to the RC driving the photosynthetic chain [110]. The pigment-protein complexes are called Photosystems. There are two types of photosystems, Photosystem II (PSII) and Photosystem I (PSI) which work synchronously to convert light energy into chemical energy. Their activity is combined with a series of biomolecules where oxydo-reduction reaction take place to transfer the excited energy throughout the chain, as explained in the following. The light transferred from the antennas is absorbed by Photosystem II (PSII), specifically by the chlorophyll a (Chl a) molecules in the reaction center called P680. As a result of light absorption, P680 reaches an excited state, and an electron is transferred from P680 to the primary electron

acceptor (Figure 3.1). This process leaves P680 in an oxidized state, which is subsequently restored by extracting electrons from water molecules. This extraction of electrons from water is facilitated by the water-oxidizing enzyme known as the Oxygen-Evolving Complex (OEC) [111]. Through a series of redox reactions, the OEC catalyzes the splitting of water molecules, releasing electrons, protons (H^+), and molecular oxygen (O_2) as byproducts. The electrons released from the water molecules are then used to replenish the electron hole in the oxidized P680, allowing it to continue participating in the electron transport chain of PSII. The same principle happens with PSI and its reaction center core molecule P700, where the electrons reoxydizing P700 come from P680 and subsequent redox reactions. In the rest of the manuscript, PSI will seldom be mentioned as the fluorescence at room temperature mainly emerges from PSII [112] and therefore reflects principally P680 activity.

The extracted electrons travel through an electron transport chain, involving electron carriers and protein complexes within PSII and PSI. These exchanges contribute to the formation of adenosine triphosphate (ATP) and nicotinamide adenine dinucleotide phosphate (NADPH), which are reagents of the dark-reaction. In particular, the protons from the OEC and from cytochrome b6f transfer reaction contribute to building up a gradient of proton across the thylakoid membrane, driving the ATP-synthase (Figure 3.1).

In the dark reactions, the ATP and NADPH generated in the previous stage are utilized to convert carbon dioxide into glucose through a series of enzymatic reaction, in particular carbon fixation by RubisCO (ribulose-1,5-bisphosphate carboxylase/oxygenase), it is the Calvin Cycle [113].

Let us now focus on the light reaction, as it allows understanding how light affects the plant status, and how to get information from fluorescence. I begin by describing the leaf structure to describe the pathway of an input solar photon within the leaf and highlight how the characteristics of the input light can affect the fluorescence measurements.

3.2.2 Leaves structure optimizing light capture

The structure of leaves is designed to maximize the absorption of light. Leaves consist of several layers, each serving a specific purpose in capturing and utilizing sunlight effectively. The outermost layer, the epidermis, acts as a protective barrier and is transparent to allow light to pass through. Within the epidermis are tiny openings called stomata, which regulate gas exchange, including the intake of carbon dioxide.

Beneath the epidermis lies the mesophyll, the primary site of photosynthesis. The mesophyll is composed of two layers: the palisade mesophyll and the spongy mesophyll. The palisade mesophyll cells are elongated and tightly packed, occupying the upper part of the leaf (Figure 3.2a). They contain a high concentration of chloroplasts, where photosynthesis takes place. The spongy mesophyll, located below the palisade layer, has more air spaces, allowing for gas exchange and facilitating the movement of water and nutrients.

The large surface area of leaves allows for more exposure to sunlight, maximizing the chances of light absorption. The chloroplasts within the mesophyll are motile, and their arrangement depends on the incident light level. In low light they are randomly distributed, in shade they are evenly distributed to maximize light absorption, with the largest cross-section oriented perpendicular to the light flux, and in high light they stack in columns parallel to the flux, to benefit from collaborative shading. They adapt their position to the light level by chloroplast relocation over tens of minutes [117, 118]. A part of the fluorescence response signal will mirror this motility.

3.2.3 Thylakoids hosting the photosynthetic chain

The chloroplasts contain thylakoids which are the sites of photosynthesis. They are flattened, disc-like membranous sacs that are stacked on top of each other to form structures called grana (Figure 3.2c).

The photosystems (reaction centers and connected pigment antennas) are embedded into the thylakoid membrane. The membrane separates the lumen from the stroma and allows in particular

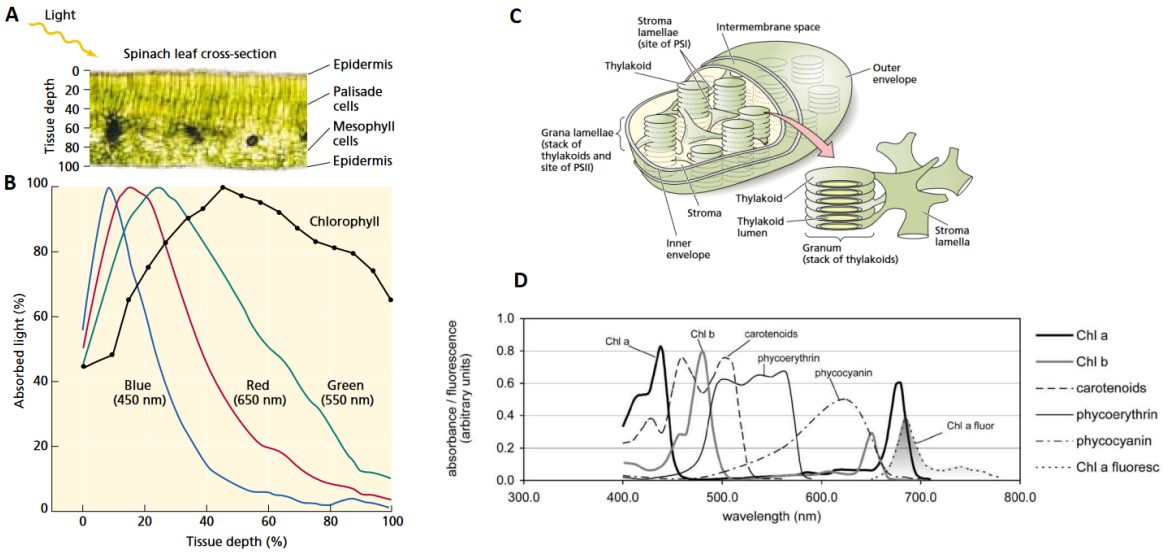

Figure 3.2: Leaf architecture, from cells to pigments. a,b:Distribution of absorbed light in spinach sun leaves. Irradiation with blue, green or red light results in different profiles of absorbed light in the leaf. The micrograph above the graph shows a cross-section of a spinach leaf, with rows of palisade cells occupying nearly half of the leaf thickness. The shapes of the curves are in part a result of the unequal distribution of Chlorophyl within the leaf tissues [114, 115]. **c**: Schematic picture of the overall organization of the membranes in the chloroplast displaying the thylakoid, the stroma, the lumen and the grana. **d**: In vivo absorption spectra of selected photosynthetic pigments from plants, algae and cyanobacteria, and fluorescence spectrum of Chl a. Carotenoid absorption spectrum is an estimated in vivo absorption spectrum in green algae. Phycoerythrin and phycocyanin absorption spectra are unpublished spectra from Govindjee's laboratory. Chl a fluorescence spectrum is from spinach chloroplasts [92, 116].

a proton build-up fueled by the light reaction at the level of Cytochrome b6f to drive the ATP-synthase which feeds the Calvin cycle with ATP. The arrangement of thylakoids in grana is crucial for maximizing the efficiency of light capture. By stacking the thylakoid membranes, more Chlorophyl molecules can be packed into a smaller space, increasing the surface area available for light absorption.

3.2.4 Pigments and reaction centers fueling the photosynthetic chain

The primary pigments involved in photosynthesis are chlorophylls and carotenoids (Figure 3.3a). Chlorophylls, specifically chlorophyll a (Chl a) and chlorophyll b (Chl b), are the main pigments responsible for absorbing light energy in the visible spectrum. Carotenoids, such as beta-carotene and xanthophylls, complement chlorophylls by alternatively extending the range of light absorption and providing protection under excess light energy. The pigments have different absorption spectra (Figure 3.2d), and their combined spectra show a maximum of absorption in the blue and red, while the green light is mainly reflected and transmitted. Therefore, the distribution of absorbed light varies within the leaf's depth, making it relevant to use different wavelengths to probe the apparatus (Figure 3.3b). Interestingly, Chl a and Chl b present shifted absorption spectra. The Chl a/Chl b ratio is higher in PSI than PSII, making it more sensitive to far red light [119, 120].

The core of the reaction centers of PSII and PSI consist in a pair of Chl a molecules which reach an excited state when they receive the exciton energy coming from the antennas. There are two layers of antennas, the core antennas that are consistently connected to the reactions centers, and the Light Harvesting Complex (LHC) antennas, that are mobile and can detach from the Photosystems. As there are two peaks in absorption, the reaction center can be excited from a wider span of light and an internal conversion rapidly occurs to reach the lower and most stable excited-state (internal

conversion - IC). It is why it is relevant to measure the incoming light energy in terms of moles of photons per unit of surface and time (*einstein* - E) rather than W/m², because no matter the wavelength, as long as it is absorbed and transferred to the reaction center, a photon will lead to the same excited state (Figure 3.3b). The natural deexcitation pathway for this pigment complex would be fluorescence, but several quenching pathways occur in competition, the prominent being photosynthesis (Photochemical Quenching), described in 3.2.1.

The rate constants of the deexcitation pathways in competition with fluorescence depend on numerous factors and are time-dependent. Their study is at the core of the research on remote sensing using fluorescence, in particular in the establishment of protocols to probe photosynthetic organisms' status dynamically.

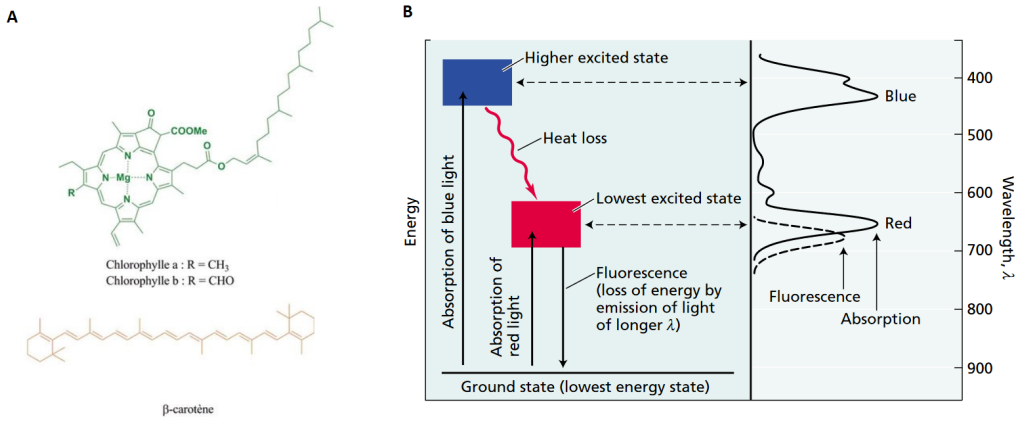

Figure 3.3: **a**: Structure of Chlorophyll a,b and β-carotene; **b**: Excited states of Chlorophyll a. Adapted from: [92].

Light dependency of the photosynthetic chain

The principal actor which affects the quantum yields evolution is the incoming light. Indeed, the photosynthetic capacity of an organism is dictated by its photon absorption capacity, but also the capacity of the photosynthetic chain to process the energy input and accomplish the full reaction. A way to picture these constraints is to see the photosynthetic chain as a chain of workers. The light and the reagents are the raw products, while the photosystems, the oxydizing agents and the Calvin cycle act as the workers. A sortage of raw material will leave the workers free and ready to absorb a full workload when the raw material flows back in. On the other hand, if the flow of raw material is high, each worker will reach saturation at a different rate, and the overall chain will be blocked at different stages.

In particular, the enzymatic capacity of the Calvin Cycle is limited, which is schemed in Figure 3.4a. When increasing the incoming light, the photosynthetic capacity reaches a saturation point after which the Calvin cycle becomes limiting. This transition light level depends on the growth light level of the photosynthetic organism. Indeed, the growth light received drives different long-term synthesis strategies to optimally use the light, in particular for the photosystems and the chloroplast structure [121].

Non-Photochemical Quenching (NPQ)

When the system is exposed to saturating light, excess photon energy builds up and can lead to photo-toxicity. To reuse the work chain metaphor, the raw material (photon energy) is in excess and since the chain cannot handle it, it overflows elsewhere, where it is not desired. When the pathway of

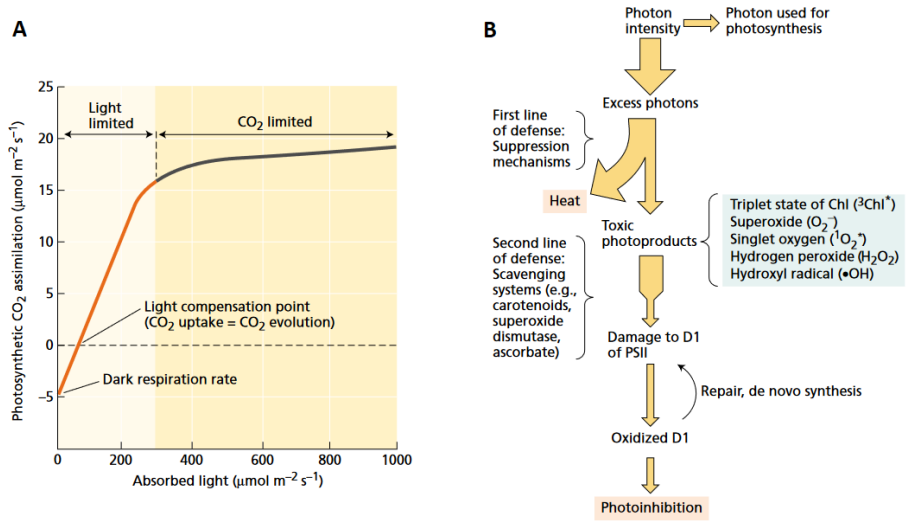

Figure 3.4: *Light-dependent response of the photosynthetic chain* **a**: Dependence of photosynthesis on the light level evaluated as CO_2 assimilation. A minimal light threshold is required to compensate the respiration. The light compensation point is reached when photosynthetic CO_2 assimilation equals the amount of CO_2 evolved by respiration. Above this point, the photosynthesis rate increases proportionally with light, indicating a light-limited electron transport rate, which in turn is limited by the amount of available light. Further increases in photosynthesis are eventually limited by the carboxylation capacity of RubisCO or the metabolism of triose phosphates. This part of the curve is referred to as CO_2 limited. Adapted from: [92]; **b**: Photon pathway under excess light conditions. There are several layers of photodamage protection. The first line of defense is the quenching of excess excitation as heat (NPQ). If this defense is not sufficient and toxic photoproducts form, various scavenging systems come into play to eliminate these reactive photoproducts. Should this second line of defense also prove ineffective, the photoproducts have the potential to cause damage to the D1 protein present in photosystem II, resulting in photoinhibition. The D1 protein is then excised from the PSII reaction center and degraded. A newly synthesized D1 is reinserted into the PSII reaction center to form a functional unit. Adapted from: [92, 122].

the photosynthetic chain is blocked because the forward electron transfer is limited by a step along the chain, the electron can recombinate with the reaction center, in particular P680 (inside PSII). In this scenario it has been shown that the probability of conversion of P680 to P680* triplet state (inter-system crossing - ISC) is increased [123–126]. From the triplet state the emission is called phosphorescence, and has a much longer lifetime (sometimes up to seconds). For this reason the triplet state is much more likely to undergo an excited state chemical reaction and react with oxygen (a natural triplet), forming damaging Reactive Oxygen Species (ROS). The first defense mechanism developed throughout evolution is active heat dissipation of the photon energy to decrease the triplet conversion probability by offering the exciton another deexcitation pathway (Figure 3.4). It is referred to as Non-Photochemical Quenching (NPQ) and enters in the processes competitive with fluorescence and photosynthesis (Photochemical Quenching). Alternative path not shown in the figure include movement to avoid light: chloroplast relocation or leaf motion for higher plants, phototaxis for motile algae equipped with flagella. When the excess energy cannot be evacuated, it resolves in damaging the proteins at the core of PSII by ROS. It involves a modification of the damage and repair rates of photosystems which are continuous mechanisms [127]. This phenomena is called photoinhibition and is generally included in the NPQ mechanisms.

3.3 Deexcitation pathways of the excited state

Equipped with this range of phenomena, we can now address the question of quantum yields with more clarity. Figure 3.5 depicts the different deexcitation pathways mentioned previously and their respective rate constants (assumed to be first order). k_T designates the Photochemical Quenching, k_F the fluorescence, k_Q the NPQ, k_{IC} the conversion to the thermally relaxed excited-state (IC, see Figure 3.3), and k_{ISC} the singlet-to-triplet conversion (ISC). It also includes photobleaching k_{PB} which occurs when the excited triplet state reacts with oxygen to form singlet oxygen and damages the RC proteins, leading to the quenching of the RC. We have previously included this process in k_Q. These competitive mechanisms affect the fluorescence life-time ($\sim$ 1 ns [112]) and the quantum yield of fluorescence, giving two strategies to measure them. We focused on the quantum yield of fluorescence as it requires less sensitive and rapid instruments, which is more compatible with our instrument specifications. The yield of a given process is the rate constant of the process divided by the sum of all the rate constants.

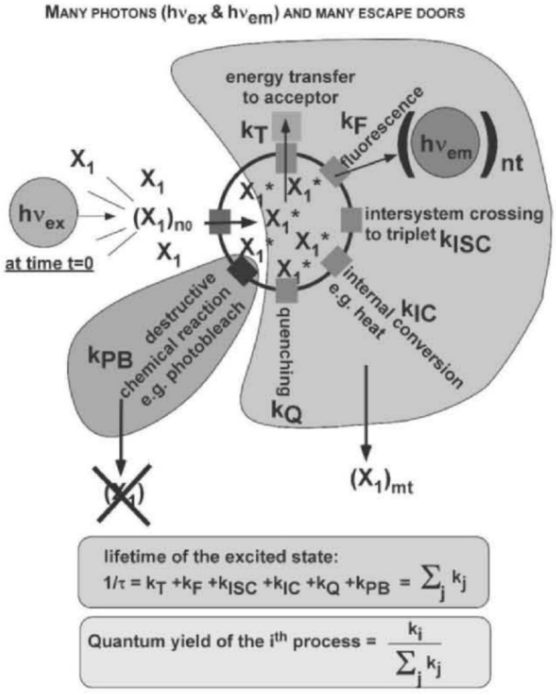

Figure 3.5: *Deexcitation pathways of the reaction center excited state.* The excited state is depicted as a circle in which the excited molecules are confined. Each molecule that is in the excited state has an asterisk (X*). The entrance to the excited state takes place through excitation with a photon of energy $h\nu_{ex}$. The excited molecules can leave the excited state through several pathways: energy transfer (k_T), fluorescence emission (k_F), intersystem crossing (k_{ISC}), internal conversion (k_{IC}), quenching (k_Q), or photolysis (k_{PB}). Every time a molecule leaves the excited state by the fluorescence emission pathway it emits a photon of energy $h\nu_{em}$. Except for the photobleach pathway (from which the molecule is irreversibly chemically destroyed) and intersystem crossing, every molecule that exits from the excited state returns to the ground state, and can be excited again. Adapted from: [109]

3.3.1 Quantum yield of photochemistry

I will now show an example of how fluorescence can report on one of the competitive quantum yields (ϕ_P - photosynthesis) to give the reader an insight of the problem complexity and the approach

taken in the literature. Considering k_O (for "other") the rate constants of the processes other than P, F and Q (which we will call NPQ), the quantum yield of photochemistry is:

$$\phi_P = \frac{k_P}{k_P + k_F + k_{NPQ} + k_O} \tag{3.1}$$

If a leaf is left in the dark for some time, the photosynthetic chain is completely empty, and has the capacity to convert light into energy at its maximal capacity because all the electron acceptors are oxidized: $k_P = k_{P,max}$ In these conditions we write the minimal quantum yield of fluorescence F_0:

$$\phi_{F_0} = \frac{k_F}{k_P + k_F + k_{NPQ} + k_O} \tag{3.2}$$

If a strong pulse of light is applied to the leaf, the photosynthetic chain will fill-up until all the actors are reduced. In these conditions the quantum yield of photochemistry becomes $k_P = k_{p,min} = 0$. At saturation, the quantum yield of fluorescence is called ϕF_M and equals:

$$\phi_{F_M} = \frac{k_F}{k_F + k_{NPQ} + k_O} \tag{3.3}$$

F_M designates the fluorescence level at saturation and F_0 the initial fluorescence value when the light is turned on. Assuming the pulse light is constant, that there are no changes in the light absorption during the illumination, and that the saturation is reached before k_{NPQ} and k_O start to be affected by the excess light (they remain constant), the proportionality constant c between the fluorescence yields and the measured fluorescence is constant: $F_M = c\phi_{F_M}$ and $F_0 = c\phi_{F_0}$. Then we can develop:

$$\frac{F_M - F_0}{F_M} = \frac{\phi_{F_M} - \phi_{F_0}}{\phi_{F_M}} = 1 - \frac{\phi_{F_0}}{\phi_{F_M}} \tag{3.4}$$

When replacing the rate constants:

$$1 - \frac{k_F + k_{NPQ} + k_O}{k_P + k_F + k_{NPQ} + k_O} = \frac{k_P}{k_P + k_F + k_{NPQ} + k_O} = \phi_P \tag{3.5}$$

Resulting in:

$$\frac{F_M - F_0}{F_M} = \phi_P = 1/k_P \tag{3.6}$$

This shows how to obtain ϕ_P from the fluorescence measurement of F_0 and F_M.

3.3.2 Fluorescence transient to measure the quantum yield of photochemistry

This thought experiment which explains how to obtain the maximal yield of photochemistry (around 83% for an healthy leaf, equivalent to $F_M \approx 5F_0$) is easy to perform experimentally. A light jump is applied to a dark-adapted leaf, and the fluorescence dynamics is collected. F_0 is the fluorescence measured at the beginning of the trace[1] and F_M as the global maxima. Its investigation forms a whole branch of photosynthesis research because more information can be obtained from this curve [61]. The saturation can be reached in less than 1 s for a light above 1000 μmol(photons) $\cdot$ m^{-2} $\cdot$ s^{-1}[61]. It is called fluorescence transient, fluorescence induction or Kautsky effect. As the chain fills up, the fluorescence displays local inflection points which report on the

[1] $\sim$ 50 μs after the light onset, to make sure that the dynamics of the light source does not overlap with the leaf kinetics. In the epifluorescence microscope setup, the LEDs characteristic time is below 10 μs.

successive reduction of the electron acceptors. The curve is often named after the letters attributes to each maxima (OJIP - Figure 3.6). When the light is left on for longer, the other mechanisms come into play, in particular k_{NPQ} changes dynamically as the leaf reacts in defense to the saturating light (see 3.2.4).

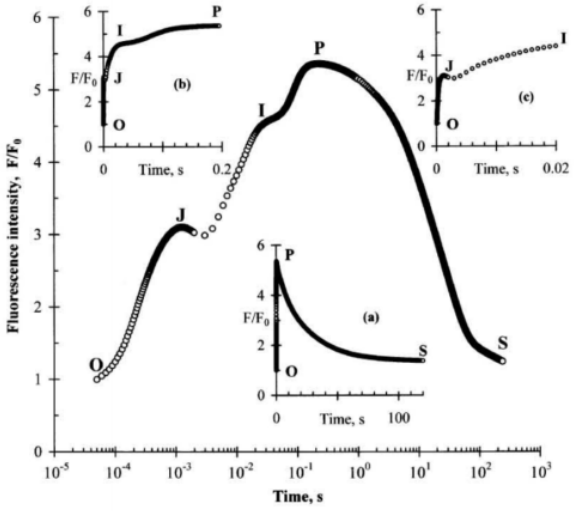

Figure 3.6: A typical Chl a fluorescence transient (induction/Kautsky/OJIP curve) measured in response to a saturating red light pulse (650 nm, 3200 μmol(photons) $\cdot$ m^{-2} $\cdot$ s^{-1}) applied to a dark-adapted pea leaf. Fluorescence values are expressed as F/F_0, where F_0 is the initial fluorescence (at 50 μs). The O-J-I-P fluorescence rise is followed by a decline to a steady-state S. Inserts show the same transient on different linear time scales: (a; center) up to 120 s, (b; top left) up to 200 ms and (c; top right) up to 20 ms. Adapted from: [109].

Interestingly, the primary phase of the fluorescence transient reflects the light-limited reaction (reduction of the electron acceptor Q_a). It has been shown that its rate constant is linearly dependent on the excitation light intensity. As light calibration was one of our research focus, I suggested writing a manuscript on how to use leaves to calibrate a light source. Note that it was also evoked with a work done on algae presented in Appendix 2.6. Here we use fluorescence as a means to learn about our instrument exciting light before diving into how fluorescence can give information about the photosynthetic system. When probing the system as close as possible to photon absorption, we obtain information on the absorption process. But the further we probe, the more phenomena affect the fluorescence quantum yield, leading to richer information, but also more complex unmixing strategies to identify the origin of the signal dynamics.

3.4 Manuscript: Leaves to measure light intensity

Leaves to measure light intensity

Aliénor Lahlou Dusan Lazar* Thomas Le Saux* Ludovic Jullien**

A. Lahlou, Dr. T. Le Saux, Prof. Dr. L. Jullien
PASTEUR, Département de chimie, École normale supérieure, PSL University, Sorbonne Université, CNRS, Paris, France
Email Address: Alienor.Lahlou@ens.psl.eu, Thomas.Lesaux@ens.psl.eu, Ludovic.Jullien@ens.psl.eu.

A. Lahlou
Sony Computer Science Laboratories, Paris, France
Email Address: Alienor.Lahlou@sony.com

Prof. Dr. D. Lazar
Department of Biophysics, Faculty of Science, Palacký University, Olomouc, Czech Republic Email Address: dusan.lazar@upol.cz

Keywords: *Photoactive materials, Green materials, Light intensity, Irradiance, Actinometry, Fluorescence*

Quantitative measurement of light intensity is a key step in ensuring the reliability and the reproducibility of scientific results in many fields of physics, biology and chemistry. The protocols presented so far use various photoactive properties of manufactured materials. Here we introduce leaves as an easily accessible green material to calibrate light intensity. The measurement protocol consists in monitoring the chlorophyll fluorescence of a leaf while it is exposed to a jump of constant light. The inverse of the characteristic time of the initial chlorophyll fluorescence rise is shown to be proportional to the light intensity received by the leaf over a wide range of wavelengths and intensities. Moreover, the proportionality factor is stable across a wide collection of plant species, which makes the measurement protocol accessible to users without prior calibration. This favorable feature is finally harnessed to calibrate a source of white light from exploiting simple leaves collected from a garden.

1 Introduction

Quantitative measurement of light intensity is presently highly demanded by physicists, biologists and chemists involved in fields as diverse as production of molecules and materials, design of medical protocols, optical bioimaging, optogenetics, or photocatalysis.[1, 2, 3, 4] Indeed this measurement is essential to compare scientific results from different sources and to ensure their reproducibility.

Materials exhibit multiple interactions with light thereby altering the material properties or the incoming electromagnetic field such as (non)linear optics, photorefractivity, photochromism, photovoltaics, photocatalysis, magneto-optics... [5, 6, 7, 8, 9]. Hence, they provide various designs for measuring light intensity. Selenium and silicon light meters use photovoltaic sensors generating

a voltage proportional to light exposure whereas cadmium sulfide light meters exploit a photoresistor sensor whose electrical resistance changes proportionately to light exposure. As an alternative method, actinometers are photoactive materials, which measure light intensity from extracting a time after optically analyzing the time course of the extent of a photochemical reaction with a known quantum yield.[10]

Light meters and actinometers are powerful tools but they suffer from limitations.[11, 12] Measuring light intensity with light meters is fast and can be achieved over a wide range of wavelengths and incident light intensities. Yet, this measurement requires a specific instrument and the independent determination on the illumination spot size.[13, 14] Actinometers often rely on the low sensitive absorbance for reporting and their accessibility is limited for most end-users.[10] Here, we are interested in studying a light-measuring system, which combines the attractive features of light meters and actinometers while addressing some of their limitations.

Plant leaves are abundant green materials. They have been considered to produce silica or other chemicals[15] or as a source of components.[16] They have also been important actors of bioinspiration (e.g. in relation to specific wettability properties[17, 18]). More generally, photosynthetic organisms have been harnessed to produce living materials.[19] However, although strongly photoactive and sensitive to light, they have never been considered for quantitative measurement of light intensity. Here, we show that they act as widely accessible fluorescent actinometers, which are relevant to quantitatively measure light over the whole 400–650 nm visible light window in a broad range of light intensities covering two to three orders of magnitude, without spot size calibration.

2 Results

2.1 Principle of the measurement of light intensity

In oxygenic photosynthetic organisms, sunlight is collected with an efficient antenna absorbing light in the whole visible wavelength range.[20, 21] The absorbed energy is conveyed to the photosystem II and photosystem I, where it drives a charge separation accompanied by water splitting leading to oxygen evolution, followed by assimilation of carbon dioxide to produce sugars. However, a small part of the absorbed energy (a few percent) is released as fluorescence emission (mostly by chlorophylls, Chl) spanning the 650–800 nm range with an emission maximum around 680 nm and a smaller peak at about 730 nm at room temperature.

When a dark-adapted leaf is exposed to continuous constant light, the Chl a fluorescence (ChlF) intensity shows characteristic changes.[22] It first rises during about a second. Following on from this step, the ChlF level decays over a few minutes as a consequence of several events (changes in redox states of components of the linear electron transport flow, involvement of alternative electron

routes, build-up of a transmembrane pH difference and membrane potential, activation of different nonphotochemical quenching processes, activation of the Calvin–Benson cycle,...).[23, 24, 25, 26, 27]

Here, we focus on the fast ChlF rise called OJIP rise,[28] which primarily reports on the successive reduction of the electron acceptors of the photosynthetic electron transport chain. The ChlF intensity rises in less than 1 s from a minimum level (the O level) to a maximum level (P). Depending on the light level and the experimental conditions, it exhibits one, two or three intermediate steps identified as local maxima labeled K, J and I. The first step systematically reflects the light-limited reaction (reduction of the electron acceptor Qa). Interestingly, the rate constant of this so-called photochemical phase has been reported to linearly depend on the intensity of the exciting light[29, 30] and to not significantly depend on the nature of the photosynthetic organism,[31, 32] in order to facilitate obtaining samples for light measurement. Yet, the reported facts do not presently enable to exploit green leaves for quantitative measurement of light intensity, which is the purpose of the present work.

Considering that the ChlF emission from a leaf is a side-product of the light-driven process of charge separation, the rate constant driving the initial step of the ChlF rise is the product of two terms: the cross section for photoactivation of the photosystem II denoted σ which reflects the capacity to absorb light, and the light intensity I (more precisely irradiance) which is a surfacic power ($W.m^{-2}$) alternatively denominated photon flux density (with mol (photon).m^{-2} .s^{-1} or E.m^{-2}.s^{-1}; see Experimental Section). Provided that this rate constant k – or similarly its characteristic time $\tau = 1/k$ – can be retrieved from the time evolution of the ChlF rise, I can be measured if σ is known since all these parameters are linked in Eq.(1).

$$I = \frac{1}{\sigma\tau} \quad (1)$$

Therefore the goal of this work has first been to measure the value of $\sigma(\lambda_{exc})$ over a wide span of excitation wavelengths λ_{exc} covering the near UV-visible wavelength range. In order to proceed, we first validated an automated protocol for extraction of τ from the initial step of the ChlF rise on a wide variety of green leaves (61 samples). Then we explored two complementary approaches to extract $\sigma(\lambda_{exc})$: (i) we first directly measured the values of $\sigma(\lambda_{exc})$ at four selected wavelengths spanning the UV-Vis wavelength range; (ii) we subsequently established an average ChlF excitation spectrum, which has been shown to be relevant for extrapolating the value of $\sigma(\lambda_{exc})$. As a final application, we harnessed a leaf for characterizing a light source exhibiting a broad spectrum of light emission.

2.2 Protocol for measuring the cross section associated to the initial step of the ChlF rise

In a first step, we established an automated protocol for measuring the cross section associated to the initial step of the ChlF rise in leaves by using continuous illumination. The leave samples are prepared according to the protocol described in the Experimental Section. They are first submitted to darkness for 15 min before starting the illumination experiments. This preliminary step empties the photosynthetic electron transport chain and enables to get a reference state of the leaf. After the latter dark acclimation, the face of the bifacial leaves that is not directly exposed to sunlight (abaxial) is exposed to time constant light at wavelength λ_{exc} in the [400 nm; 650 nm] wavelength range, and the ChlF intensity is collected. 680 nm is the maximum of ChlF emission of the photosynthetic apparatus. However, any wavelength between 650 and 750 nm can be used for ChlF reporting, albeit with a lower fluorescence signal.

Fluorescence recording is started before turning on illumination (typically 10 ms in our experiments) and the collected ChlF signal $F(\lambda_{\text{exc}},\lambda_{\text{em}},t)$, is recorded as a function of time over 1 s. The acquisition frequency has to be high enough in order to enable satisfactory sampling of the initial step of the ChlF rise (typically 3 MHz in our experiments). The time evolution of the ChlF signal is then automatically processed (a downloadable application is accessible online with instructions for implementation available at https://github.com/Alienor134/OJIP-fit and in the Experimental Section). The fitting algorithm exploits the approach of Joly & Carpentier[31] to obtain a preliminary estimation of the parameters of the whole ChlF rise. After identifying the onset of the ChlF response (F_0) and the maximum of ChlF (F_M), the algorithm iteratively estimates the parameters of the initial step of ChlF rise:

- In a first step, the algorithm applies an unsupervised fit with Eq.(2)

$$F(t) = F_0 + A_1\left(1-e^{-t/\tau_1}\right)^{s_1} + A_2\left(1-e^{-t/\tau_2}\right)^{s_2} + A_3\left(1-e^{-t/\tau_3}\right)^{s_3} \quad (2)$$

  in order to retrieve a first estimate τ_1 of the value of the characteristic time associated to the initial step of the ChlF rise. In this step the ChlF curve is pre-processed with a smoothing (typically window size 10) and logarithmic subsampling (typically 200 samples per decade);

- In a second step, it restricts the time window to $[0;3\tau_1]$ and applies the fit given in Eq.(3) to the time evolution of the ChlF emission

$$F(t) = F_0 + A\left(1-e^{-t/\tau}\right)^{s} \quad (3)$$

  upon fixing $s = 1.24$ [31] in order to retrieve a second estimate of the value of the characteristic time τ associated to the initial step of the ChlF rise;

- In the last step, it restricts the time window to [0;5τ], applies a fitting function given in Eq.(4)

$$F(t) = F(0) + A\left(1 - e^{-t/\tau}\right)^{s} \quad (4)$$

to the time evolution of the ChlF emission upon adopting the values of parameters extracted during the second step as starting values, and retrieves the final value of the characteristic time τ associated to the initial step of the ChlF rise.

The light intensity sought for can eventually be extracted by introducing τ and the relevant value of the cross section of photoconversion $\sigma(\lambda_{\text{exc}})$ in Eq.(1).

As a solid criterion allowing end-users to establish the relevance of their measurement of light intensity, we eventually suggest exploiting the ratio $(F_{\text{m}} - F_{\text{o}})/F_{\text{m}}$, which involves the minimal (F_{o}) and maximal (F_{m}) values gathered from the time evolution of the ChlF signal F from the illuminated leaf over a second. The ratio reflects the maximum quantum yield of PSII photochemistry [**?**] and a fully developed and healthy plant exhibits a ratio of about 0.75 – 0.84.[33] Consequently, only measurements leading to ratios above 0.75 should be retained to reliably extract light intensity by using our reported average value of the cross section for photoactivation of the photosynthetic apparatus.

2.3 Measurement of the cross section associated to the initial step of the ChlF rise at 470±10 nm

The relevance of the latter measurement protocol and iterative fitting algorithm of the initial step of the ChlF rise has first been evaluated at 470±10 nm on a dark acclimated thin and young leaf from the genus *Chelidonium*, no later than 1 h after its collection. The leaf has been observed under an epifluorescence microscope equipped with a silicon photomultiplier as detector (see Experimental Section). Figure 1a displays representative time evolutions of the normalized fluorescence emission at various intensities of constant light. The fitting protocol was found relevant as displayed in Figure 1a (see also Figure 3a) illustrating different rises of ChlF. As shown in Figure 1b, the inverse of the characteristic time of the photoconversion associated to the initial step of the ChlF rise linearly depends on the light intensity over the whole investigated range. This behavior demonstrates that the process driving the initial step of the ChlF rise evolution is photochemical at least up to 10^{-2} E.m^{-2}.s^{-1} light intensity. It also enabled us to retrieve the value of (1.30±0.05)×10^{6} m^{2}.mol^{-1} from the slope as a first estimate of the cross section of photoconversion at 470±10 nm associated to the initial step of the ChlF rise. With respect to typical orders of magnitude encountered for small photoactive molecules, the later value is extremely high. It is a consequence of the large surface of the antenna over which light is collected and its energy conveyed toward the reaction center of the photosystem II at which charge separation occurs with a very high efficiency.

Then the iterative fitting algorithm has been successfully applied at different light intensities, on dark acclimated green leaves from sixty-one samples of plants reflecting a wide variety of photosynthetic species families, of shapes, growth conditions, soils, and microclimates (see Experimental Section). We noticed that the leaves that were not green (*Oxalis triangularis*, purple areas of *Columnea guttata*) were the only ones not responding properly to the protocol, probably due to high amount of epidermal anthocyanines. Although anthocyanines absorb mostly green light, they also absorb blue and red light [34], which decreases absorption of chlorophylls. Thus, they were removed from the dataset and we focused on green leaves. Figure 1c displays the dependence of the inverse of their characteristic time τ associated to the initial step of the ChlF rise and Figure 1d shows the associated distribution of the retrieved cross sections. The results enabled us to conclude that using a cross section $(1.1 \pm 0.8) \times 10^6$ $m^2.mol^{-1}$ for measuring light intensity at 470±10 nm gives an accurate value within a factor 2.5 whatever the exploited leaf. Such a low dispersion of the cross section was anticipated since the process of light-induced photochemical reaction in the reaction center of PSII which is at the core of our protocol for measuring light intensity involves the same molecular structures of the photosynthetic apparatus in all the green plants independently on the climate zone.

The preceding derivation of the cross section σ associated to the initial step of the ChlF rise at 470±10 nm relied on measurements on leaves conditioned with a standardized protocol detailed in the Experimental Section. Hence, we addressed the robustness of its value by examining the impact of the leaf development stage and of the time lag between the leaf collection and the measurement (see section 2 in the Supplementary Information). We concluded that the leaf development stage does not impact the cross section value, and that it is preferred to prepare the sample and perform the measurement within one hour after the leaf collection.

2.4 Minimal set-up for light calibration

The preceding series of validating experiments has been performed with an epifluorescence microscope. However, such an equipment is not necessitated to apply our protocol for measuring light intensity with a leaf.

To support this statement, we first designed an easy-to-build-up setup. Its principal part consists in an optical fiber that can reach the side of the sample to collect the ChlF through a red filter, and a photon detector such as a photon counter or a photodiode (Figure 2a,b), which are classically used to collect the ChlF rise upon illumination.[35, 36]. As displayed in Figure 2c, we could extract the characteristic time τ from analyzing the initial step of the ChlF rise from dark acclimated leaves upon constant illumination at 470±10 nm and show that it provided consistent values of the light intensity: 18 ± 1 $mE.m^{-2}.s^{-1}$ (4.6×10^3 in $W.m^{-2}$) light intensity was retrieved from the τ measurement by using $\sigma = 1.1 \times 10^6$ $m^2.mol^{-1}$ whereas 11 $mE.m^{-2}.s^{-1}$ was estimated

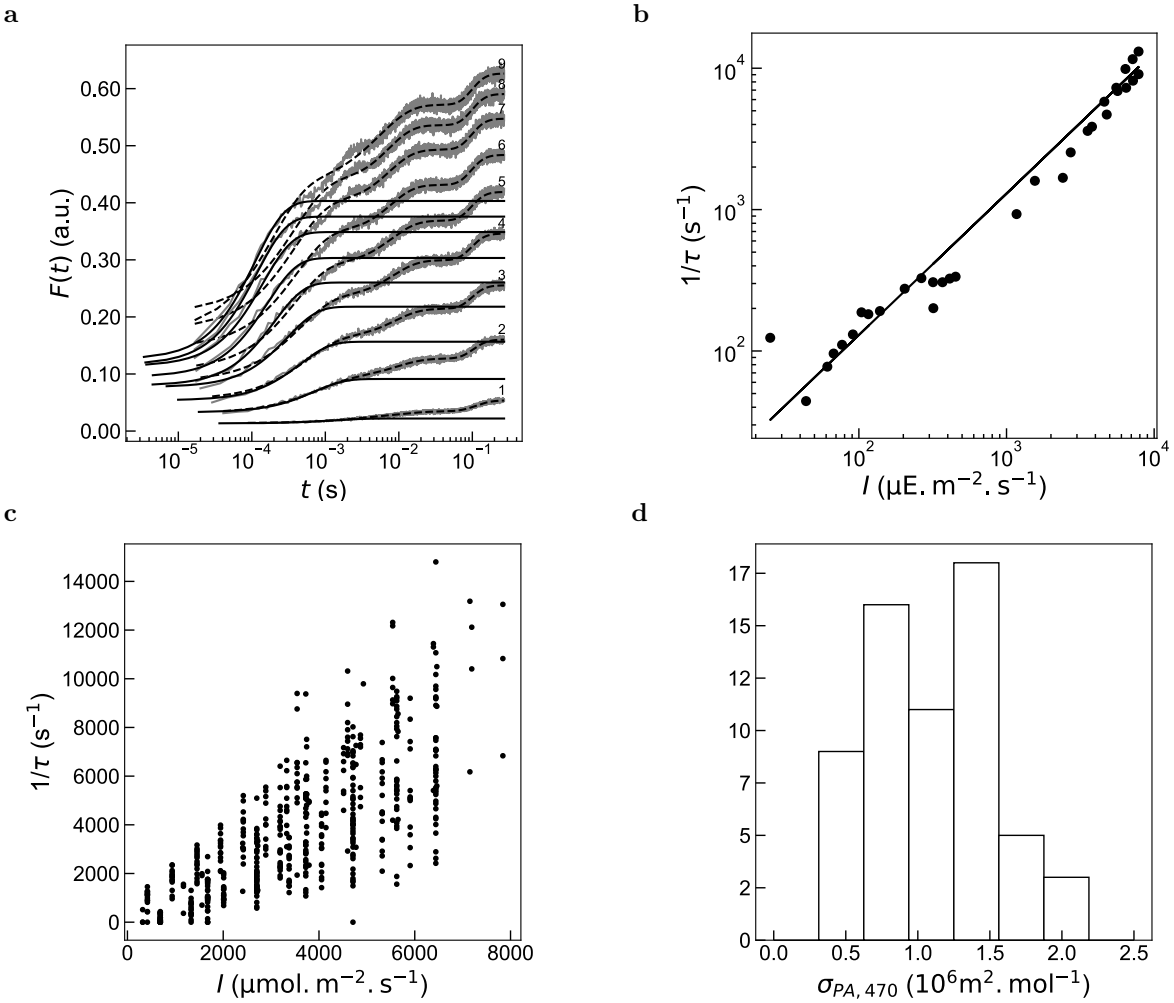

Figure 1: *Validation of an automated protocol for extraction of τ from the initial step of the ChlF rise and determination of the cross section associated to the initial step of the ChlF rise from dark acclimated leaves upon constant illumination at 470±10 nm.* **a**: Time evolution of the ChlF emission from a dark acclimated leaf (genus *Chelidonium*) upon illumination at various light intensities (from 1 to 9 in mE.m^{-2}.s^{-1} (in W.m^{-2}): 0.3 (75), 1.2 (305), 2.4 (610), 3.5 (890), 4.6 (1200), 5.5 (1400), 6.4 (1600), 7.2 (1800), 7.8 (2000)). A moving average was applied on the experimental data (grey lines) before subsampling with window sizes of 50 and 10 for the fits given in Eq.(2) (dashed lines) and (3) (solid lines) respectively; **b**: Dependence of the inverse of the characteristic time τ associated to the the initial step of the ChlF rise from a dark acclimated leaf (genus *Chelidonium*) retrieved from the monoexponential fit on the light intensity in the range 20–8000 μE.m^{-2}.s^{-1} (5–2000 W.m^{-2}). Markers: Experimental data; Solid line: Linear fit. The extracted slope is (1.30±0.05)×10^6 m^2.mol^{-1} where the uncertainty is the standard deviation of the regression coefficient for an ordinary least square regression; **c**: Dependence of the inverse of the characteristic time τ associated to the initial step of the ChlF rise retrieved from the monoexponential fit on the light intensity for various dark acclimated leaves picked-up from endemic and imported species grown in different soils, under different illuminations and microclimates over the January 2022 – September 2023 period (61 samples); **d**: Distribution of the cross section associated to the initial step of the ChlF rise from the dark acclimated leaves displayed in **c**. The extracted average of the distribution is (1.1±0.8)×10^6 m^2.mol^{-1}.

from a calibration relying on a powermeter at the position of the leaf and a ruler to recover the illumination spot size.

On another aspect, the acquisition frequency of the photodetector has to match the dynamics of the initial step of the ChlF rise to yield meaningful information on the light intensity. For blue

light in the range 50–10000 μE.m^2.s^{-1} (10–2500 W.m^2), the characteristic time τ varies between 50 ms and 50 μs. During the preceding microscope experiments, we used a data acquisition card to collect the ChlF and subsequently extract the cross section for photoactivation of the photosystem II from processing its time evolution. Since this equipment might not be available for fast acquisition of the fluorescence signal, we alternatively used an oscilloscope to collect the initial step of the ChlF rise. A *Robinia* leaf was placed under the epifluorescence set-up and illuminated at 470 nm. We measured the output of the detector collecting the fluorescence signal, which was connected to both an oscilloscope (37 Hz) and the data acquisition card (3 MHz) during the same experiment. As displayed in Figure 2d,e, we observed an accurate match between the outputs for three different values of the current input (Figure 2e), which demonstrates that an oscilloscope can be used to perform the light calibration with a leaf.

Hence, our simple protocol for measuring light intensity with a randomly picked leaf can be implemented with a setup comprising an optical fiber, a red optical filter, a photon detector, and an oscilloscope. Most of these elements can be found in almost every laboratory and do not require extra investments.

2.5 Dependence of the cross section associated to the initial step of the ChlF rise on the excitation wavelength

2.5.1 Direct measurement

The absorption spectrum of the photosynthetic apparatus is broad, which is favorable to make measurements of light intensity over a wide range of wavelengths. Hence, the dependence of the cross section associated to the initial step of the ChlF rise on the excitation wavelength has been investigated with the epifluorescence setup equipped with four different LEDs emitting at 405±7 nm, 470±10 nm, 550±6 nm, and 630±9 nm with collection of emitted fluorescence at 775±70 nm.

Figure 3a displays representative time evolutions of the normalized fluorescence emission at various light intensities of the four LEDs from a dark acclimated leaf (genus *Robinia*) observed with the photodetector under the epifluorescence microscope. These time evolutions have been fitted with the preceding iterative fitting algorithm in order to retrieve the characteristic time τ associated to the initial step of the ChlF rise. Figure 3b displays the dependence of the inverse of τ retrieved from processing the corresponding evolutions. It was again found linear over the whole range of investigated light intensities. We extracted $(1.54\pm 0.07)\times10^6$ m^2.mol^{-1}, $(1.65\pm 0.07)\times10^6$ m^2.mol^{-1}, $(0.31\pm 0.02)\times10^6$ m^2.mol^{-1}, and $(0.60\pm 0.02)\times10^6$ m^2.mol^{-1} for the cross sections $\sigma_{\text{leaf}}(\lambda_{\text{exc}})$ associated to the purple, blue, green, and red-orange lights respectively.

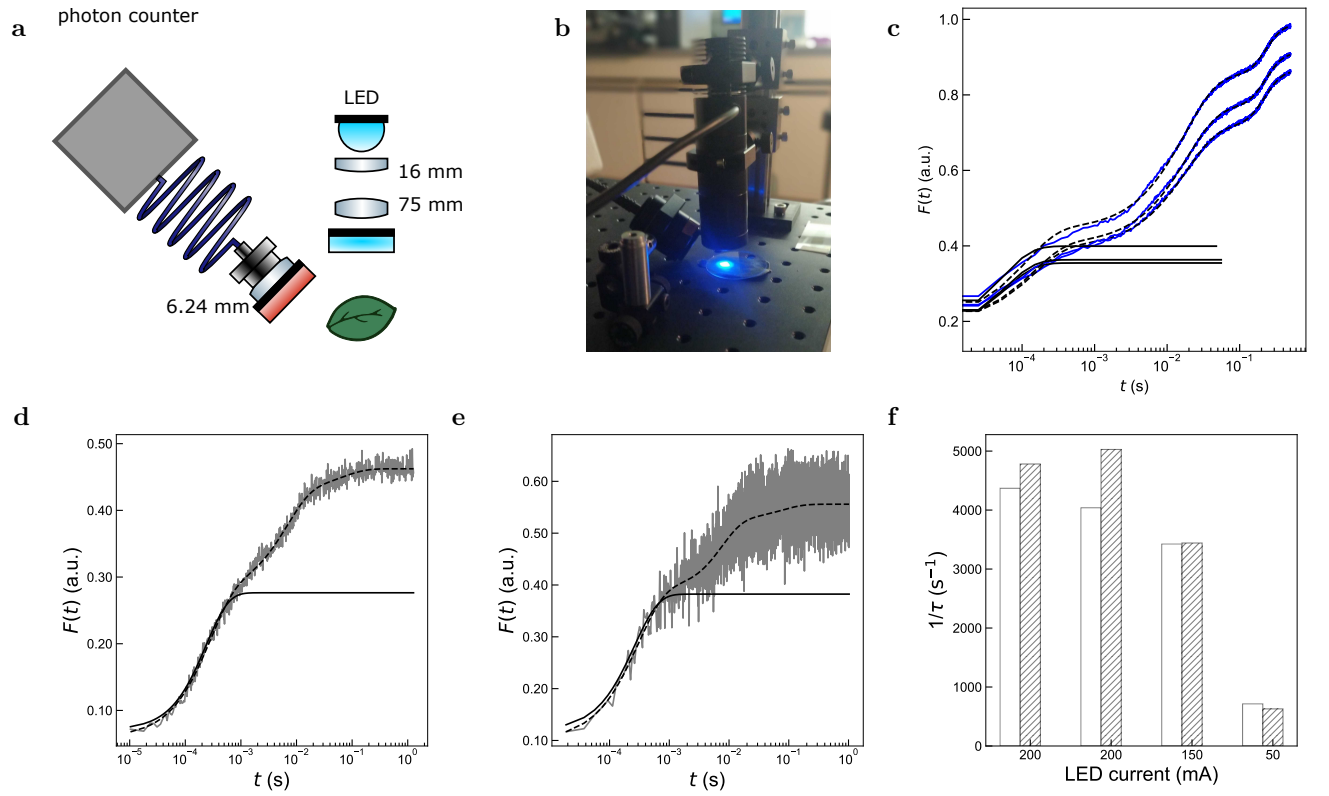

Figure 2: *Adapting the protocol for measurement of light intensity with a leaf to alternative optical setups.* **a-c**: Measurement with a simplified set-up. **a,b**: Scheme (**a**) and picture (**b**) of the simplified set-up. It consists in an optical fiber equipped with a red fluorescence filter (775/140) connected to a photon detector to access the sample and collect the ChlF. Here the light source to calibrate is simulated by a collimated and filtered LED (470/40 nm); **c**: Example of ChlF rise obtained with the simplified set-up. A moving average was performed on the experimental data (grey lines) with window size of 10 followed by a logarithmic subsampling. Applying the fits given in Eq.(2) (dashed lines) and (3) (solid lines) respectively yielded $\tau = (5.1, 5.2, 4.7) \times 10^5$ s^{-1}. Leaf species: genus *Lonicera*. **d-f**: Measurement with an oscilloscope. Fit of the initial step of the ChlF rise performed on the ChlF response acquired with the data acquisition card (**d**; τ=209 μs) or the oscilloscope (**e**; τ=229 μs). A moving average was performed on the experimental data (grey lines) with window size of 10 (**d**) or 2 (**e**) followed by a logarithmic subsampling for the fits given in Eq.(2) (dashed lines) and (3) (solid lines) respectively; **f**: Values of $1/\tau$ retrieved from fitting the time evolution of the ChlF signal collected with the oscilloscope (white) or data acquisition card (striped) for various LED currents (including a repeat at 200 mA). $T = 293$ K.

2.5.2 Exploitation of the fluorescence excitation spectrum of the photosynthetic apparatus

To further expand the range of wavelengths at which the cross sections associated to the initial step of the ChlF rise from a dark acclimated leaf would be available, we used fluorescence excitation spectra.

We first recorded the fluorescence excitation spectrum of the photosynthetic apparatus of a leaf from the genus *Robinia*. As shown in Figure 3c, it exhibits strong values in the purple-blue and red wavelength ranges and a minimum at green wavelengths. Upon assuming the quantum yield driving the initial step of the ChlF rise to not depend on the excitation wavelength, we then used the fluorescence excitation spectrum of the leaf to compute the wavelength dependence of the cross

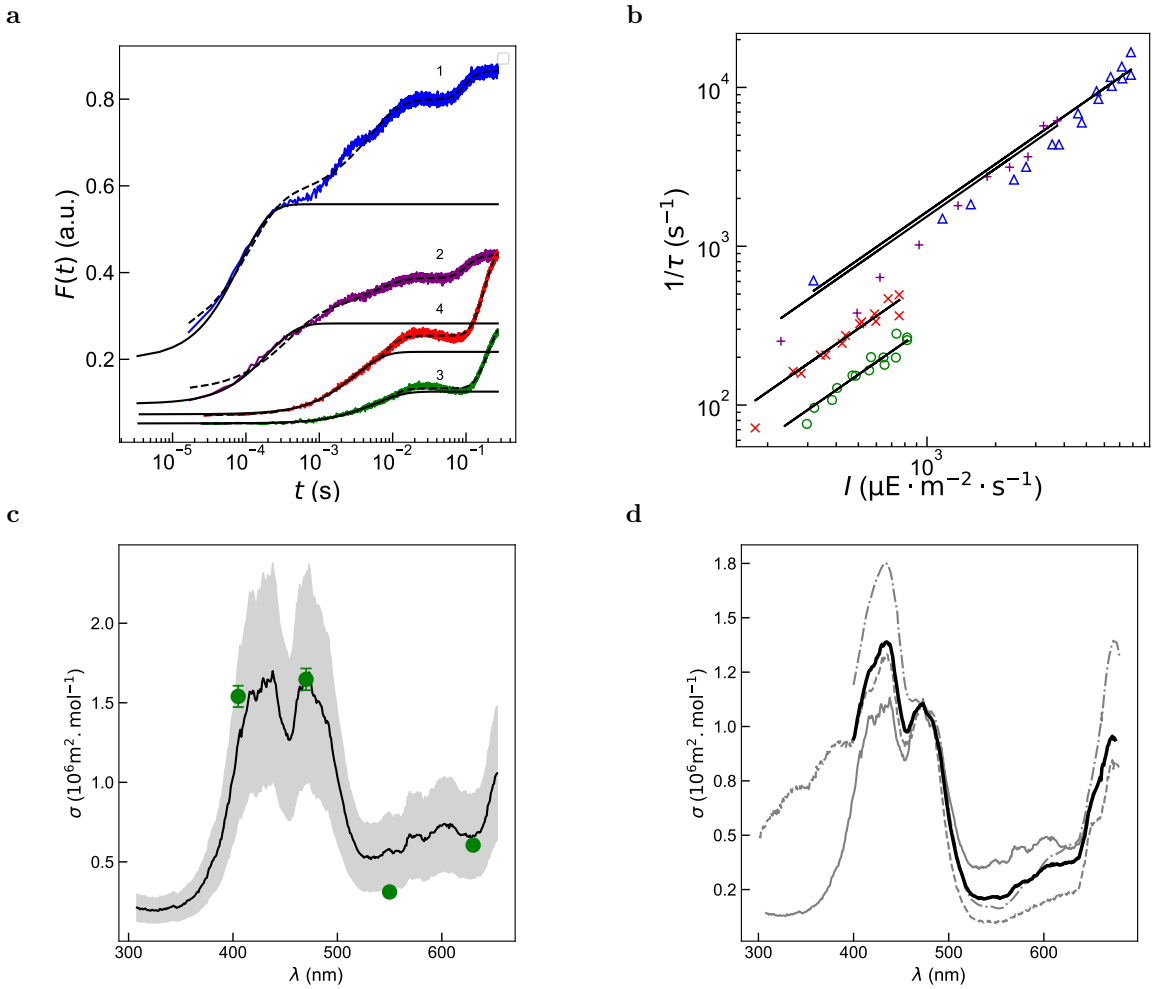

Figure 3: *Dependence of the cross section associated to the initial step of the ChlF rise from a dark acclimated leaf on the excitation wavelength.* Direct determination upon constant illumination at various wavelengths (**a**,**b**). **a**: Time evolution of the ChlF emission from a dark acclimated leaf (genus *Robinia*) upon illumination at various light intensities (from 1 to 4 in mE.m^{-2}.s^{-1}: 7.2, 3.2, 0.73, 0.60) at 470±10 nm (1), 405±7 nm (2), 550±6 nm (3), and 630±9 nm (4). A moving average was performed on the experimental data (grey lines) before subsampling with window sizes of 50 and 10 for the fits given in Eq.(2) (dashed lines) and (3) (solid lines) respectively; **b**: Dependence of the inverse of the characteristic time τ associated to the initial step of the ChlF rise retrieved from the monoexponential fit on the light intensity at 405±7 nm (pluses), 470±10 nm (triangles), 550±6 nm (circles), and 630±9 nm (crosses). Markers: Experimental data; Solid line: Linear fit. The extracted slopes are $\sigma_{\text{leaf}}(405)=(1.54\pm0.07)\times10^6$ m^2.mol^{-1}, $\sigma_{\text{leaf}}(470)=(1.65\pm0.07)\times10^6$ m^2.mol^{-1}, $\sigma_{\text{leaf}}(550)=(0.31\pm0.02)\times10^6$ m^2.mol^{-1}, and $\sigma_{\text{leaf}}(630)=(0.60\pm0.02)\times10^6$ m^2.mol^{-1} where the uncertainties are the standard deviation of the regression coefficient for an ordinary least square regression; Indirect determination from exploiting the fluorescence excitation spectrum of the photosynthetic apparatus (**c**,**d**). **c**: Wavelength dependence of the cross section $\sigma(\lambda_{\text{exc}})$ associated to the initial step of the ChlF rise for a *Robinia* leaf as extracted from exploiting its fluorescence excitation spectrum (the grey background reflects a 30% error bar). The graph values are accessible online. Green markers: $\sigma_{\text{leaf}}(\lambda_{\text{exc}})$ as measured in **b** (genus *Robinia*). $T = 293$ K; **d**: Fluorescence excitation spectra of the photosynthetic apparatus from three different photosynthetic organisms. The fluorescence excitation spectra ϵ_{norm} ($\lambda_{\text{em}} = 690 \pm 2$ nm) have been normalized at 470 nm using the value $\sigma=1.1\times10^6$ m^2.mol^{-1} extracted from Figure 1d. Semi-dotted grey line: leaf (genus *Robinia*); dotted grey line: *Chlamydomonas reinhardtii (cc124)*; solid grey line: spinach thylakoid.[37] The averaged fluorescence spectrum built from the three preceding fluorescence excitation spectra is displayed with a thick black solid line.

section $\sigma_{leaf,exc}(\lambda_{exc})$ associated to the initial step of the ChlF rise by fixing the value of the cross section to 1.65×10^6 $m^2.mol^{-1}$ at 470 nm as a reference (value measured for the *Robinia* leaf – Figure 3b). At 405, 550, and 630 nm, we obtained $(1.2\pm 0.4)\times10^6$ $m^2.mol^{-1}$, $(0.6\pm 0.2)\times10^6$ $m^2.mol^{-1}$, and $(0.7\pm 0.4)\times10^6$ $m^2.mol^{-1}$ respectively, which were in line with the measured values $\sigma_{leaf}(\lambda_{exc})$ reported above (Figure 3c and Table 1). Thus, this reasonable agreement has suggested that the knowledge of the fluorescence excitation spectrum and one σ value at a given wavelength would be sufficient to predict the σ value at any wavelength within the action range (between 400 and 650 nm).

To evaluate the variance of the fluorescence excitation spectrum of the photosynthetic apparatus among photosynthetic organisms, we further recorded the fluorescence excitation spectrum from a culture of microalgae (*Chlamydomonas reinhardtii cc124* in exponential growth phase) and superposed the reported fluorescence excitation spectrum from a spinach thylakoid solution.[37] As displayed in Figure 3d, the three fluorescence excitation spectra exhibit similar shapes. Hence, we built an average fluorescence excitation spectrum of the photosynthetic apparatus (Figure 3d), which has been subsequently used for extracting estimates of the light intensity over a wide range of wavelengths (accessible online).

Altogether, the preceding agreements have suggested that the average fluorescence excitation spectrum could be exploited to compute an estimate of the wavelength dependence of the cross section associated to the initial step of the ChlF rise at any wavelength between 400 and 650 nm from the value measured at 470 nm. Hence, upon using the average value 1.1×10^6 $m^2.mol^{-1}$ of the cross section at 470 nm determined in Figure 1d as a reference, we eventually used the normalized fluorescence excitation spectrum shown in Figure 3d to build an average wavelength dependence of the cross section $\sigma(\lambda_{exc})$ associated to the initial step of the ChlF rise (see Figure 3d). Table 1 sums up the relevant parameters which have to be used for measuring the light intensity at various wavelengths with a leaf.

2.6 Application: Characterization of the spectral light intensity of a white light source

Manuscripts exploiting photochemistry often report on the power of light sources together with geometrical indications of their position with respect to the samples. However, this information is limited to quantitatively retrieve the incident light intensities, which drives the kinetics of the photochemical reactions. Moreover, even when the latter is provided, its spectral distribution may be lacking. Hence, an attractive application envisioned for a leaf is to measure the incident spectral light intensity of a light source at a sample. More precisely, we addressed the challenging calibration of a white LED by benefiting from the broad light absorption of the photosynthetic apparatus, which covers the whole visible range (Figure 3c).

Table 1: *Photoconversion parameters associated to the initial step of the ChlF rise in a leaf.* The normalized excitation coefficient $\epsilon_{\text{norm}}(\lambda_{\text{exc}})$ was extracted from the average fluorescence excitation spectrum displayed in Figure 3d by fixing the value to one at 470 nm. The cross sections $\sigma_{\text{leaf}}(\lambda_{\text{exc}})$, $\sigma_{\text{leaf,exc}}(\lambda_{\text{exc}})$, and $\sigma(\lambda_{\text{exc}})$ have respectively been measured (see Figure 3) and computed at 405, 550, and 630 nm from using respectively the excitation spectra of the leaf and the average excitation spectrum of various photosynthetic organisms displayed in Figure 3c upon fixing the value of the cross section of the photoconversion to 1.65 10^6 $m^2.mol^{-1}$ (for $\sigma_{\text{leaf,exc}}(\lambda_{\text{exc}})$) or 1.1 10^6 $m^2.mol^{-1}$ (for $\sigma(\lambda_{\text{exc}})$) at 470 nm. $I_{\text{sup}}(\lambda_{\text{exc}})$ indicates the upper light intensity tested and relevant for a reliable measurement.

λ_{exc} (nm)	$\epsilon_{\text{norm}}(\lambda_{\text{exc}})$	$\sigma_{\text{leaf}}(\lambda_{\text{exc}})$ ($10^6 m^2 mol^{-1}$)	$\sigma_{\text{leaf,exc}}(\lambda_{\text{exc}})$ ($10^6 m^2 mol^{-1}$)	$\sigma(\lambda_{\text{exc}})$ ($10^6 m^2 mol^{-1}$)	$I_{\text{sup}}(\lambda_{\text{exc}})$ ($E.m^{-2}.s^{-1}$ ($W.m^2$))
405	1.0 ± 0.2^a	1.54 ± 0.07^b	1.2 ± 0.6^c	1.1 ± 0.8^d	$10^{-2}(3000)^e$
470	1.0 ± 0.2^a	1.65 ± 0.07^b	1.65 ± 0.6^c	1.1 ± 0.8^d	$10^{-2}(2600)^e$
550	0.2 ± 0.1^a	0.31 ± 0.03^b	0.6 ± 0.3^c	0.22 ± 0.16^d	$10^{-2}(2200)^e$
630	0.4 ± 0.1^a	0.60 ± 0.04^b	0.7 ± 0.4^c	0.44 ± 0.32^d	$10^{-2}(1900)^e$

[a] The error on the average fluorescence excitation spectrum $\epsilon_{\text{norm}}(\lambda_{\text{exc}})$ arises from the analysis of the data displayed in Figure 3d.
[b] The error on σ_{leaf} is given by the standard deviation of the linear coefficient using an ordinary least squares regression.
[c] The error on $\sigma_{\text{leaf,exc}}(\lambda_{\text{exc}})$ has been computed by taking into account the propagation of the error on the fluorescence excitation spectrum of the leaf used for the experiment, which has been evaluated to 30% of the value at 470 nm.
[d] The error on $\sigma(\lambda_{\text{exc}})$ has been computed by taking into account the distribution of the σ values displayed in 1d and the error on the average spectrum.
[e] Extracted from the value of $I_{\text{sup}}(\lambda_{\text{exc}})$ by using $I_{\text{sup}}(\lambda_{\text{exc}}) = I_{\text{sup}}(\lambda_{\text{exc,ref}}) \times \frac{\epsilon(\lambda_{\text{exc,ref}})}{\epsilon(\lambda_{\text{exc}})}$ where $\lambda_{\text{exc,ref}}$ designates the wavelength at which the extraction of the cross section of photoconversion has been performed ($\lambda_{\text{exc,ref}} = 470$ nm).

In a first step, we recorded the unscaled emission spectrum $S(\lambda)$ of the LED (filtered above 665 nm to avoid spectral overlap with the fluorescence emission of the leaf), which has been normalized by its integral to yield the normalized emission spectrum $j(\lambda) = S(\lambda)/S$ displayed in Figure 4a. The average $\sigma_{\text{leaf}}(470 \text{ nm})$=1.1×$10^6$ $m^2.mol^{-1}$ cross section associated to the initial step of the ChlF rise from dark-acclimated leaves retrieved from Figure 1d was used to scale the average excitation spectrum displayed in Figure 3d and generate the scaled fluorescence excitation spectrum $\sigma_{\text{leaf}}(\lambda)$. The resulting scaled spectrum $\sigma_{\text{leaf}}(\lambda)$ was multiplied by the normalized emission spectrum $j(\lambda)$ to generate the action spectrum of the white LED on the photosynthetic apparatus of the leaf, $\sigma_{\text{leaf}}(\lambda) \times j(\lambda)$ (Figure 4b). Then we submitted the leaf to illumination with the white LED at different current inputs and recorded the rises of its fluorescence emission at 775±70 nm as a function of time. Each characteristic time τ associated to the initial step of the ChlF rise was used to retrieve the scaling parameter S_I for the corresponding current input (see Experimental section). Figure 4c displays the resulting stack of scaled emission spectrum of the white LED.

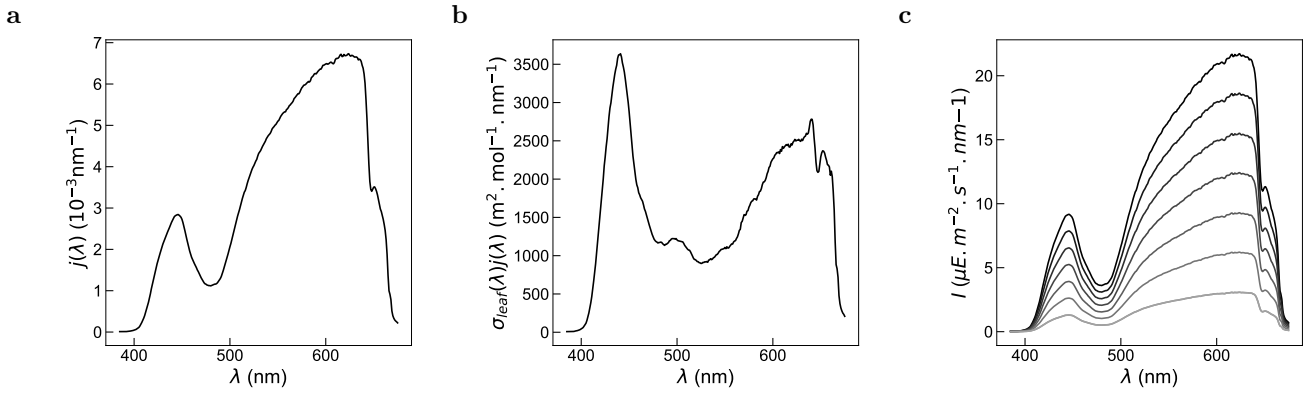

Figure 4: *Characterization of the spectral light intensity of a white LED by a leaf-mediated measurement.* **a**: Normalized emission spectra ($j(\lambda)$=$S(\lambda)/S$) of the white LED; **b**: Product of the scaled spectrum $\sigma_{\mathrm{leaf}}(\lambda)$ by the normalized emission spectrum $j(\lambda)$ to generate the action spectrum of the white LED on the photosynthetic apparatus of the leaf, $\sigma_{\mathrm{leaf}}(\lambda)\times j(\lambda)$; **c**: Scaled spectral photon flux of the white LED for current levels 55, 111, 166, 222, 277, 333, 388 mA (light to dark) predicted from $S_I = (\tau \int_{\lambda_{min}}^{\lambda_{max}} \sigma_{leaf}(\lambda) j(\lambda) d\lambda)^{-1}$. The corresponding S_I values are 0.5, 0.9, 1.4, 1.8, 2.3, 2.7, 3.2 mE.m^{-2}.s^{-1}. $T = 293$ K. See Experimental Section.

3 Discussion

Leaves are subjected to multiple processes driven by light,[23, 24, 25, 26, 27] which are prone to produce images.[38, 39, 40, 41] These processes span over various time scales. The closer the process is to the driving photon absorption, the faster it is to measure and the more reliable it is for measuring light intensity. First, the processes get slower when they become farther in the metabolism of photosynthesis. Hence, to use slower processes for reporting on light intensity would take longer time and reduce the range of measurable light intensity since the photochemical step has to determine the overall kinetics. Moreover, as the processes become farther in the metabolism of photosynthesis, they integrate other factors than the sole input of light to govern their extent, which would affect the robustness of the measurement of light intensity.

When a dark-adapted leaf is exposed to continuous constant light, the redox reactions of the photosynthetic apparatus are significantly reflected in the initial ChlF rise only for the first second. They are essentially conserved among photosynthetic organisms so as to ensure robustness of the present protocol for measuring light intensity. In particular, the variable chlorophyll fluorescence (ChlF) can be modeled by considering that illumination leads to the reversible formation of Q_a^-, the reduced first quinone electron acceptor in photosystem II (PSII), and that it is proportional to the fraction of reduced Q_a.[22] At its turn, Q_a^- then reduces Q_b, which is the second quinone electron acceptor in PSII. After accumulation of two electrons at Q_b and Q_b^{2-} protonation by two protons from the stroma, the resulting protonated doubly reduced Q_bH_2 is released to the plastoquinone pool as PQ_{red}. The vacant place in the Q_b-pocket of PSII is then filled back by a molecule from the oxidised part of the plastoquinone pool, PQ_{ox}, forming thus Q_b in PSII. The associated

kinetic scheme neglecting protonation of doubly reduced Qb is displayed in Figure 5a.[42, 43] Under constant illumination of the initial state Q_aQ_b (the O level of the ChlF rise) at light intensity I, the time evolution of ChlF evidences several kinetic regimes. Upon assuming that ChlF rise only reflects Q_a^- accumulation, they are associated with the successive accumulations of the states $Q_a^-Q_b$ (J step), $Q_a^-Q_b^-$ (I step), and $Q_a^-Q_b^{2-}$ (P step) respectively, which result from the decrease of the rate constants k_i and k_{-i} when i increases. When the light intensity I decreases, one progressively observes the disappearance of the fastest steps. The initial rise of ChlF is rate limited by a photochemical activation associated with the rate constant σI. Hence, at the slowest time scale, the time evolution of the ChlF signal can be reliably accounted for with the two-state kinetic model displayed in Figure 5b.

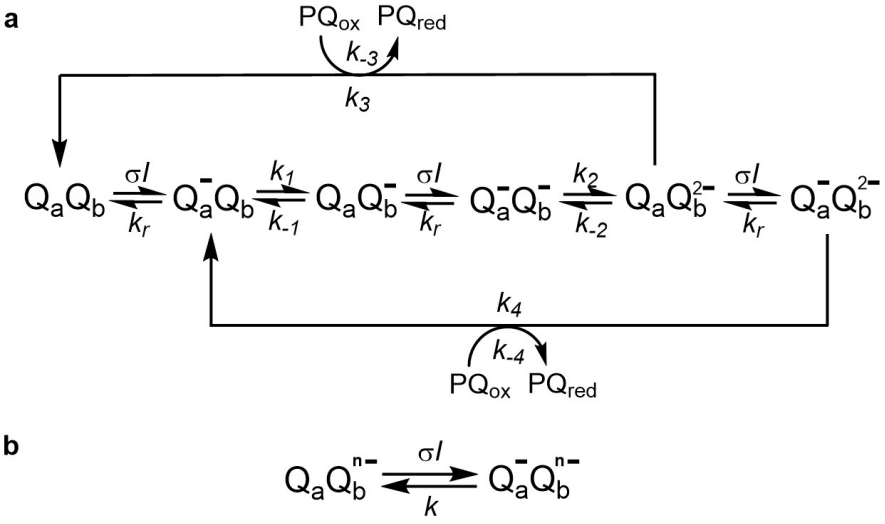

Figure 5: *Mechanisms accounting for the time evolution of ChlF.* **a**: *Complete kinetic model.* Illumination at light intensity I drives the reversible reduction of Q_a^-, the reduced first quinone electron acceptor in photosystem II (PSII). In turn, Q_a^- then reduces Q_b, which is the second quinone electron acceptor in PSII. After accumulation of two electrons at Q_b and Q_b^{2-} protonation by two protons from the stroma, the resulting protonated doubly reduced Q_bH_2 is released to the plastoquinone pool as PQ_{red}. The vacant place in the Q_b-pocket of PSII is then filled back by a molecule from the oxidised part of the plastoquinone pool, PQ_{ox}, forming thus Q_b in PSII. Order of magnitude of the rate constants:[43, 44] $\sigma \simeq 1\ 10^6\ m^2.mol^{-1}$, $k_r \simeq 1\ 10^4\ s^{-1}$, $k_1 \simeq 5\ 10^3\ s^{-1}$, $k_{-1} \simeq 2\ 10^2\ s^{-1}$, $k_2 \simeq 1.5\ 10^3\ s^{-1}$, $k_{-2} \simeq 5\ 10^1\ s^{-1}$, $k_3 = k_4 \simeq 1\ 10^2\ s^{-1}$, $k_{-3} = k_{-4} \simeq 5\ 10^1\ s^{-1}$; **b**: *Reduced kinetic model.* It involves the rate constants σI – where σ designates the cross section associated with the photoactivation – and k – which reports on the back reaction (k_r) and the relevant electron transfer to Q_b (k_n; $n = 1$ or 2) at the considered light intensity.

On a longer time scale, other light-driven phenomena affect the leaf ChlF. In typically 30 s, (non-) photochemical quenching first decreases ChlF emission.[45] However, it is leaf species- and physiological state-specific. Moreover, it cannot be made quantitative without a preliminary calibration. As a result of a longer light exposure, one can observe photoinhibition, which results from the photodegradation of PSII. Hence, the ChlF decreases at the most illuminated zones.[46] Interestingly, a linear relationship has been established between the rate-constant of photoinhibition and light intensity when the leaves are treated with lincomycin, which inhibits the repair of the photodegraded PSII.[47, 48, 49]. However, as for non-photochemical quenching, it is expected

to be specific and requesting a demanding calibration. At the 30-min and longer time scale, blue light further makes chloroplasts to stack on the side of the cells of leaves to minimize their light exposure (avoidance).[50, 51] As a consequence, a light beam crossing the leaf is less absorbed than when the chloroplasts are equally distributed in the cell. In practice, the three latter phenomena overlap each-other as illustrated in Figure 6, in which we used a projector to imprint an image of the overall reaction of photosynthesis.[41] Among the slowest processes, it is eventually worth to mention starch production. Here light exposure generates contrasted sizes and numbers of starch grains, which has early been used to produce images after extraction of the leaf pigments and iodine staining.[38, 39] However, the photoproduction and staining of starch is slow (day time scale). Moreover, its robustness has not been investigated and it is not quantitative, which forbids its use for measuring light intensity.

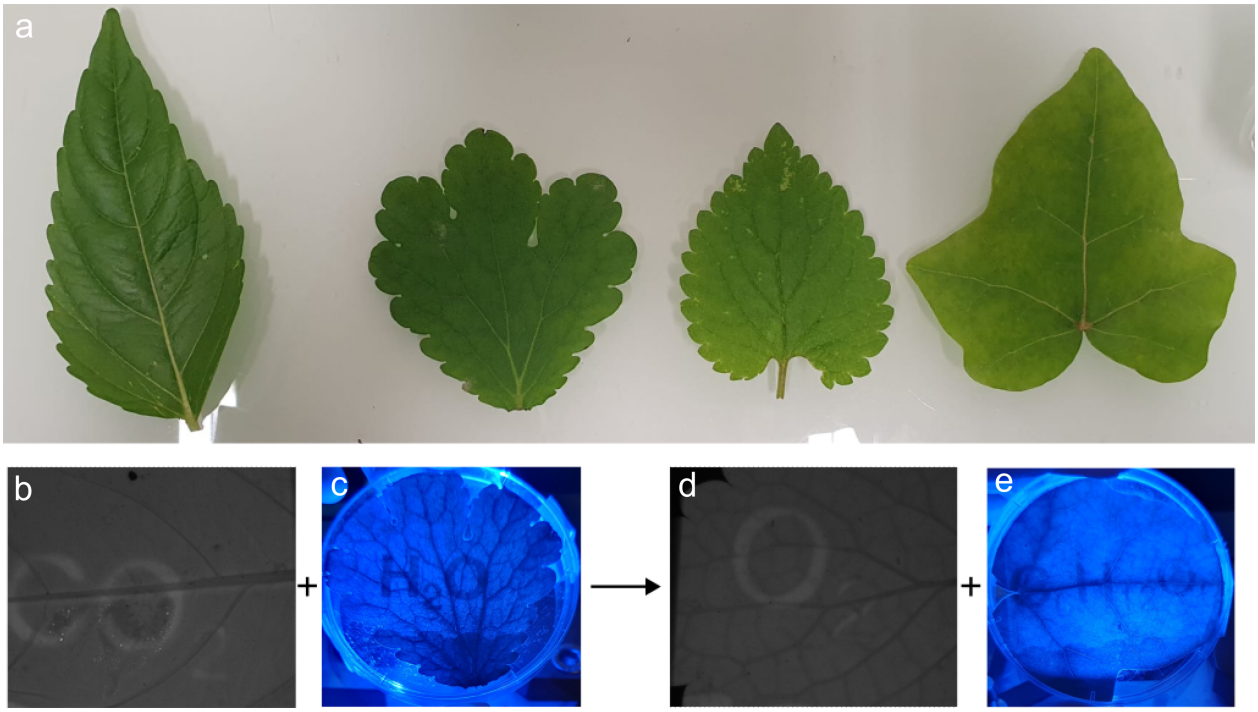

Figure 6: *Regulation processes leading to the formation of images.* Four leaves picked-up from the ENS garden (**a**) have been illuminated for 2 h with a videoprojector, which projected the overall reaction of photosynthesis in black letters against a white background. Then we exposed them to blue light from the back and took a picture of the transmitted light with a cell-phone camera (**c**,**e**), or with collimated blue light and took a picture with a fluorescence filter (**b**,**d**). We observe that on the highly-illuminated areas, the transmission is higher in accordance with chloroplast relocation. The ChlF level is also lower than on the areas not exposed (letters and numbers). This could be due to photoinhibition or non-photochemical quenching, but also to chloroplast relocation because chloroplasts are responsible for ChlF.

4 Conclusion

The experiments reported in this manuscript demonstrate that the fast light-driven step of ChlF rise occurring at the subsecond time scale in leaves can be robustly harnessed to quantitatively

evaluate light intensity. Despite the diversity of leaves which have been evaluated, similar cross sections associated to the initial step of the ChlF rise have been measured, which illustrates the convergence of the primary process of charge separation in higher plants. Hence, provided that it has been well-acclimated in darkness, a simple fully-functional green leaf randomly chosen in a garden is endowed to yield a good quantitative estimate of light over wide ranges of wavelengths and intensities.

5 Experimental Section

Materials :
We performed several rounds of experiments by selecting leaves of endemic and imported species over two years at different time periods (January, May, July, August and September), grown in different microclimates and with different soil compositions, under different light exposure, at different ages, to average the diversity of the chloroplasts.

Forty leaves were collected in the surroundings of Ecole Normale Supérieure (45 rue d'Ulm, 75005 Paris), both endemic and imported species, under different shadings, identified with the mobile application PlantNet (Figure 7a – genus *Trifolium, Chelidonium, Hedera, Robinia, Parietaria, Cotoneaster, Malus, Acer, Liriope, Athyrium, Lonicera, Hesperocyparis, Ginkgo, Plectranthus, Taxus, Platycladus, Oxalis, Olea, Lavandula, Vitis* or family *Poacae*). The leaves were collected and analyzed within one hour after their collection. They were cleaned with MilliQ water, dried with absorbing paper, and eventually sandwiched between two 150 μm-thick glass slides (24×60 #1 cover slips – Epredia), which were taped together for the microscope observation. The leaves were always illuminated from below (abaxial – the surface not directly exposed to sunlight on the plants).

To increase the variety of leaves, we collected twenty-one supplementary samples in the botanic garden of the Museum National d'Histoire Naturelle of Paris (Figure 7b), where imported specimen were grown under different microclimates and growth conditions (controlled humidity levels, light levels, temperature levels, soil composition, and controlled plant competition and watering frequency). These microclimates included arid desert, warm and humid tropical forest, temperate tropical forest, shadowed pond, alpine climate, with various soil structures including acidic, calcic, rocky and ultramafic soils. The genus of the species collected correspond to *Selaginella, Dictymia, Sinningia, Columnea (green areas), Dischida, Pittosporum, Bocquillonia, Hereroa, Adenium, Monophyllaea, Begonnia, Graptopetalum, Optunia, Gentiana, Tulipa, Minuartia, Saxifraga, Eremogone, Ramonda, Wollfia, Optunia* and *Lunularia*. In this later case, the samples were collected between 9.30 am and 11.30 am and stored in Petri dishes with humid cottons to preserve humidity (tap water). The two leaves collected from the arid microclimate were kept in a Petri dish without humidity. The measurements were performed between 12 am and 7 pm the same day. Each

leaf was left in the humid Petri dish in the dark until 20 min before the experiment to allow sample preparation (glass slide preparation presented above) and dark-adaptation.

All the samples have been submitted to darkness for 15 min before starting the illumination experiments. Then, a time-lag of 1 min was left between each measurement at different light intensity on the same leaf.

Fluorescence spectrometer:
The fluorescence measurements were acquired on a LPS 220 spectrofluorometer (PTI, Monmouth Junction, NJ), equipped with a TLC50 cuvette holder (Quantum Northwest, Liberty Lake, WA) thermoregulated at 25 °C.

We recorded the fluorescence excitation spectrum of the leaf as follows. The leaf was taped on a glass slide and introduced inside a 1×1 cm^2 quartz cuvette at 45 ° from the incident light beam. The fluorescence emission was collected at 690 nm. The acquired excitation spectrum was corrected from the response of the detector to the glass slide only and it was smoothed with a moving window.

The emission spectra of the LEDs have been recorded by sending the light emitted from the LEDs filtered above 665 nm into the emission pathway of the fluorometer with reduced slits opening.

Simplified set-up:

The epifluorescence microscope as well as the reference light calibration strategy of the equipment to retrieve the calibrated cross section associated to the initial step of the ChlF rise is described in Section 1.1 of the Supplementary Information. Here we provide the description of the simplified set-up that will allow the user to calibrate a light source using the tabulated cross sections.

The illumination part consists in a LED (M470L4, Thorlabs, NJ) collimated with a 16 mm lens (ACL25416U-A, Thorlabs, NJ) and converging with a 75 mm lens (LBF254-075, Thorlabs, NJ) filtered with a 470/40 nm filter (FF01-479/40-25, Semrock, Rochester, NY). The collection part consists in an optical fiber (M29L05, NA = 0.39, 600 µm core diameter, Thorlabs) that harvests the light intensity through a red filter (FF01-775/140, Semrock) and a 6.24 mm lens (F110SMA-780, NA=0.37, Thorlabs, NJ). The output of the fiber is collected by a photon counter (MPPC C13366-3050GA Hamamatsu, Hamamatsu, Japan) connected to an oscilloscope (RTB2004, Rhode & Schwarz, Munich, Germany) and a data acquisition card (PCI 6374, National Instruments, Austin, TX).

Protocol for measuring the cross section associated to the initial step of the ChlF rise:

The measurement consisted in exposing the conditioned leaves to at least seven different light intensity levels and measuring the ChlF rise over 1 s at 3 MHz. Under blue illumination, it was per-

Figure 7: Samples of leaves used to evaluate the distribution of the cross section associated to the initial step of the ChlF rise. **a**: Leaves from the surroundings of Ecole Normale Supérieure (40 samples in total) used to collect the rise of ChlF. They were placed between two microscope slides taped together. The genus of the leaves shown in the picture were identified with the mobile application PlantNet[52]: *Trifolium, Chelidonium, Hedera, Robinia, Parietaria, Cotoneaster, Malus, Acer, Liriope, Athyrium, Lonicera, Hesperocyparis, Ginkgo, Plectranthus, Taxus, Platycladus, Oxalis, Olea, Lavandula, Vitis* or family *Poacae*. **b**: Leaves collected in the different microclimates engineered at the botanic garden of the Museum National d'Histoire Naturelle of Paris (21 samples in total) used to measure the rise of ChlF. They were kept in a humid Petri dish until 20 min before the measurement to allow sample preparation between two glass slides and 15 min dark-adaptation. The genus of the species collected correspond to *Selaginella, Dictymia, Sinningia, Columnea (green areas), Dischida, Pittosporum, Bocquillonia, Hereroa, Adenium, Monophyllaea, Begonnia, Graptopetalum, Optunia, Gentiana, Tulipa, Minuartia, Saxifraga, Eremogone, Ramonda, Wollfia, Optunia* and *Lunularia*.

formed over a range of intensities between 50 μE.m^{-2}.s^{-1} (13 W.m^{-2}) and up to 10^{-2} E.m^{-2}.s^{-1} (2600 W.m^{-2}) with a time lag of 1 min between each acquisition. Then the initial step of the ChlF rise was fitted with the iterative algorithm to retrieve a relaxation time for each intensity level. The fitness level is evaluated by selecting the ChlF level F_0 at the light onset, and F_M at the ChlF maximum. The $\frac{F_M-F_0}{F_M}$ ratio reflects the maximal quantum yield of PSII photochemistry [**?**] and can be used as a measure of healthness of the leaves. If $\frac{F_M-F_0}{F_M}$ is below 0.75, the datapoint is considered unfit and discarded. The inverse of the relaxation time was fitted against the light intensity with a linear model. To ensure the validity of the fit, we performed a first fit, test for outlier data points (threshold based on the z-score: two standard deviations). Then a second fit was performed on the remaining data to obtain the final σ value. In practice only one leaf was removed due to an average fitness level of 0.5, and no more than two data points per leaf were removed, either between the first and the second linear fit or due to a low $\frac{F_M-F_0}{F_M}$.

Implementation of an application to retrieve the light intensity from the ChlF kinetics :
After acquiring the ChlF kinetics as described in subsection 2.2, the user can implement an application we provide online to retrieve the light intensity without needing to manually proceed with the fitting algorithm. In order to execute the application for automated data processing of the time evolution of the ChlF signal from a darkness-acclimated leaf exposed to constant illumination:

- Open the address http://127.0.0.1:8050 on a web browser;
- Drag-and-drop the data in .csv format;
- Select the time and fluorescence columns. Then, the data curve, the fits and the extracted τ value of the initial step of ChlF will be displayed;
- Select the excitation wavelength used in the experiment, which gives access to the photoactivation cross section σ. Then the light intensity sought for I is computed using τ and σ, and it appears on the screen with a factor 2 error.

Possible troubleshootings of the protocol for measuring light intensity :
We list below three possible troubleshootings of the present protocol for measuring light intensity:

- The ChlF rise starts decaying after reaching the maximum. The tri-exponential fit must be stopped at the maximum for better accuracy;
- Upon calibrating a red light source, exclude the excitation light from the detected light by using a bandpass filter to collect ChlF that is far enough away from the wavelength range of the emission source (for example using a 700 nm filter to calibrate a 650 nm LED);

- Check that the observed rise time of the ChlF signal is not driven by the rise time of the light source (e.g. due to heating in LEDs; generally in the μs range[53]) or of the photodetector by preliminarily analyzing the rise time of the fluorescence signal from a photochemically inert fluorophore upon turning on light.[53]

Conversion of energy units :
In this manuscript, we provide the values of the light intensities in $\mathrm{E.m^{-2}.s^{-1}}$ (or mol. of $\mathrm{photons.m^{-2}.s^{-1}}$). This unit is currently used in actinometry. However, it is not often used in other fields such as optical microscopy, in which the researchers prefer to adopt $\mathrm{W.m^{-2}}$. Here, we provide the conversion between both units [54]. We consider a monochromatic light of wavelength λ_{exc}. Its values in $\mathrm{E.m^{-2}.s^{-1}}$ and $\mathrm{W.m^{-2}}$ are respectively denoted as $I(\lambda_{\mathrm{exc}}, \mathrm{E.m^{-2}.s^{-1}})$ and $I(\lambda_{\mathrm{exc}}, \mathrm{W.m^{-2}})$. The relation between $I(\lambda_{\mathrm{exc}}, \mathrm{E.m^{-2}.s^{-1}})$ and $I(\lambda_{\mathrm{exc}}, \mathrm{W.m^{-2}})$ is given in Eq.(5)

$$I(\lambda_{\mathrm{exc}}, \mathrm{W.m^{-2}}) \;=\; \frac{hcN_A}{\lambda_{\mathrm{exc}}} \times I(\lambda_{\mathrm{exc}}, \mathrm{E.m^{-2}.s^{-1}}) \approx 0.12 \times \frac{\mathrm{I}(\lambda_{\mathrm{exc}}, \mathrm{E.m^{-2}.s^{-1}})}{\lambda_{\mathrm{exc}}\,(\mathrm{m})} \tag{5}$$

with the Planck constant $h = 6.63\ 10^{-34}\ \mathrm{m^2.kg.s^{-1}}$, speed of light in a vacuum $c = 3.00\ 10^{8}\ \mathrm{m.s^{-1}}$, the Avogadro number $N_A = 6.02\ 10^{23}\ \mathrm{mol^{-1}}$, and where λ_{exc} is in m.

Characterization of the spectral light intensity of a white light source:
We consider a light source associated with a spectral light intensity $I(\lambda)$ (expressed in $\mathrm{E.m^{-2}.s^{-1}.nm^{-1}}$) spread over $[\lambda_{\mathrm{min}};\lambda_{\mathrm{max}}]$ (with the wavelength expressed in nm). It perpendicularly illuminates a leaf associated to a scaled excitation spectrum leading to its light absorption $\epsilon(\lambda)$ (expressed in $\mathrm{m^2.mol^{-1}}$). The rate constant k for the **PA** photoactivation as well as the associated characteristic time τ obey Eq.(6)

$$k = \frac{1}{\tau} = 2.3 \int_{\lambda_{\mathrm{min}}}^{\lambda_{\mathrm{max}}} \epsilon(\lambda)\phi(\lambda)I(\lambda)d(\lambda) = \int_{\lambda_{\mathrm{min}}}^{\lambda_{\mathrm{max}}} \sigma(\lambda)I(\lambda)d(\lambda) \tag{6}$$

where $\phi(\lambda)$ and $\sigma(\lambda)$ designate the quantum yield (supposed to be independent on the excitation wavelength) and the cross section associated with the **PA** photoactivation.

We introduce the normalized emission spectrum $j(\lambda) = I(\lambda)/S_I$ of the light source, where S_I designates the integral of $I(\lambda)$ over $[\lambda_{\mathrm{min}};\lambda_{\mathrm{max}}]$ (Eq.(7))

$$\int_{\lambda_{\mathrm{min}}}^{\lambda_{\mathrm{max}}} I(\lambda)d(\lambda) \;=\; S_I \tag{7}$$

and the integral of $j(\lambda)$ over the same wavelength range is equal to one (Eq.(8))

$$\int_{\lambda_{\mathrm{min}}}^{\lambda_{\mathrm{max}}} j(\lambda)d(\lambda) \;=\; 1 \tag{8}$$

Eq.(6) yields Eq.(9)

$$k = \frac{1}{\tau} = 2.3 S_I \int_{\lambda_{\min}}^{\lambda_{\max}} \epsilon(\lambda)\phi(\lambda)j(\lambda)d(\lambda) = S_I \int_{\lambda_{\min}}^{\lambda_{\max}} \sigma(\lambda)j(\lambda)d(\lambda) \tag{9}$$

From computing the integral of the action spectrum AS of the light source given in Eq. (10)

$$AS = \int_{\lambda_{\min}}^{\lambda_{\max}} \sigma(\lambda)j(\lambda)d(\lambda) \tag{10}$$

and measuring the characteristic time τ, one can extract the integral $S_I = 1/(\tau AS)$ and retrieve the scaled spectral light intensity $I(\lambda) = S_I \times j(\lambda)$ sought for.

In practice, one has the dependence of $\sigma(\lambda)$ on the wavelength and an unscaled emission spectrum of the light source $S(\lambda)$ (expressed in arbitrary unit) and the goal is to scale it to retrieve the spectral light intensity $I(\lambda)$ (expressed in E.m^{-2}.s^{-1}.nm^{-1}) at the sample. The scaling step first involves the normalization of the unscaled emission spectrum $S(\lambda)$ by its integral S (Eq.(11))

$$\int_{\lambda_{\min}}^{\lambda_{\max}} S(\lambda)d(\lambda) = S \tag{11}$$

to yield the normalized emission spectrum $j(\lambda) = S(\lambda)/S$. Then one proceeds as reported above to first compute the integral of the action spectrum AS of the light source given in Eq.(10), and then retrieve the scaled spectral light intensity $I(\lambda) = S_I \times j(\lambda)$ sought for from the measured characteristic time τ and the integral $S_I = 1/(\tau AS)$.

Acknowledgements

This work was supported by the ANR (France BioImaging - ANR-10-INBS-04, Morphoscope2 - ANR-11-EQPX-0029, IPGG - ANR-10-IDEX-0001-02 PSL, ANR-10-LABX-31, and ANR-19-CE11-0005) (for T. L. S. and L. J.), the European Regional Development Fund project 'Plants as a tool for sustainable global development' (no. CZ.02.1.01/0.0/0.0/16_019/0000827) (for D. L.), and the EIC Pathfinder Open DREAM (GA number 101046451) (for all authors).

References

[1] T. J. Dougherty, C. J. Gomer, B. W. Henderson, G. Jori, D. Kessel, M. Korbelik, J. Moan, Q. Peng, *JNCI: Journal of the national cancer institute* **1998**, *90*, 12 889.

[2] D. Ravelli, D. Dondi, M. Fagnoni, A. Albini, *Chemical Society Reviews* **2009**, *38*, 7 1999.

[3] A. Gautier, C. Gauron, M. Volovitch, D. Bensimon, L. Jullien, S. Vriz, *Nature chemical biology* **2014**, *10*, 7 533.

[4] D. Cambie, C. Bottecchia, N. J. Straathof, V. Hessel, T. Noel, *Chemical reviews* **2016**, *116*, 17 10276.

[5] T. W. Ebbesen, *Accounts of chemical research* **2016**, *49*, 11 2403.

[6] J.-Y. Shan, M. Ye, H. Chu, S. Lee, J.-G. Park, L. Balents, D. Hsieh, *Nature* **2021**, *600*, 7888 235.

[7] N. J. Borys, C. Argyropoulos, L. Ye, *APL Materials* **2022**, *10*, 6 060401.

[8] N. Kamely, *Journal of Electronic Materials* **2022**, *51*, 3 953.

[9] A.-L. Leistner, Z. L. Pianowski, *European Journal of Organic Chemistry* **2022**, *2022*, 19 e202101271.

[10] H. Kuhn, S. Braslavsky, R. Schmidt, *Pure and Applied Chemistry* **2004**, *76*, 12 2105.

[11] U. Boehm, G. Nelson, C. M. Brown, S. Bagley, P. Bajcsy, J. Bischof, A. Dauphin, I. M. Dobbie, J. E. Eriksson, O. Faklaris, et al., *Nature methods* **2021**, *18*, 12 1423.

[12] O. Faklaris, L. Bancel-Vallée, A. Dauphin, B. Monterroso, P. Frère, D. Geny, T. Manoliu, S. de Rossi, F. P. Cordelières, D. Schapman, et al., *Journal of Cell Biology* **2022**, *221*, 11 e202107093.

[13] D. Grünwald, S. M. Shenoy, S. Burke, R. H. Singer, *Nature protocols* **2008**, *3*, 11 1809.

[14] U. Megerle, R. Lechner, B. König, E. Riedle, *Photochemical & Photobiological Sciences* **2010**, *9*, 10 1400.

[15] R. Ragni, S. Cicco, D. Vona, G. Leone, G. M. Farinola, *Journal of Materials Research* **2017**, *32*, 2 279.

[16] J. J. Kaschuk, Y. Al Haj, O. J. Rojas, K. Miettunen, T. Abitbol, J. Vapaavuori, *Advanced Materials* **2022**, *34*, 6 2104473.

[17] E. Tredenick, H. Stuart-Williams, T. G. Enge, *Frontiers in Plant Science* **2022**, *13*.

[18] V. Andrei, G. M. Ucoski, C. Pornrungroj, C. Uswachoke, Q. Wang, D. S. Achilleos, H. Kasap, K. P. Sokol, R. A. Jagt, H. Lu, et al., *Nature* **2022**, *608*, 7923 518.

[19] S. Balasubramanian, K. Yu, A. S. Meyer, E. Karana, M.-E. Aubin-Tam, *Advanced Functional Materials* **2021**, *31*, 31 2011162.

[20] T. Mirkovic, E. Ostroumov, J. Anna, R. V. Grondelle, G. Scholes, *Chemical reviews* **2017**, *117*, 2 249.

[21] D. Lazár, A. Stirbet, L. O. Björn, G. Govindjee, et al., *Photosynthetica* **2022**, *60*, SPECIAL ISSUE 2022 25.

[22] D. Lazár, *Biochimica et Biophysica Acta (BBA)-Bioenergetics* **1999**, *1412*, 1 1.

[23] K. Maxwell, G. N. Johnson, *Journal of experimental botany* **2000**, *51*, 345 659.

[24] A. Stirbet, Govindjee, *Journal of Photochemistry and Photobiology B: Biology* **2011**, *104*, 1-2 236.

[25] H. M. Kalaji, V. Goltsev, K. Bosa, S. I. Allakhverdiev, R. J. Strasser, *Photosynthesis Research* **2012**, *114* 69.

[26] A. Porcar-Castell, E. Tyystjärvi, J. Atherton, C. Van der Tol, J. Flexas, E. E. Pfündel, J. Moreno, C. Frankenberg, J. A. Berry, *Journal of experimental botany* **2014**, *65*, 15 4065.

[27] A. Stirbet, G. Y. Riznichenko, A. Rubin, *Biochemistry (Moscow)* **2014**, *79* 291.

[28] D. Lazár, *Functional Plant Biology* **2006**, *33*, 1 9.

[29] R. Delosme, *Biochimica et Biophysica Acta (BBA)-Bioenergetics* **1967**, *143*, 1 108.

[30] R. Strasser, A. Srivastava, Govindjee, *Photochemistry and photobiology* **1995**, *61*, 1 32.

[31] D. Joly, R. Carpentier, *Photochemical & Photobiological Sciences* **2009**, *8*, 2 167.

[32] N. Khan, J. Essemine, S. Hamdani, M. Qu, M.-J. A. Lyu, S. Perveen, A. Stirbet, G. Govindjee, X.-G. Zhu, *Photosynthesis Research* **2021**, *150* 137.

[33] D. Lazár, J. Nauš, *Photosynthetica* **1998**, *35*, 1 121.

[34] M. Landi, G. Agati, A. Fini, L. Guidi, F. Sebastiani, M. Tattini, *Plant, Cell & Environment* **2021**, *44*, 4 1119.

[35] K. J. Appenroth, J. Stöckel, A. Srivastava, R. J. Strasser, *Environmental Pollution* **2001**, *115*, 1 49.

[36] H. Bates, A. Zavafer, M. Szabó, P. J. Ralph, *Photosynthesis Research* **2019**, *142*, 3 361.

[37] R. Pedrós, Y. Goulas, S. Jacquemoud, J. Louis, I. Moya, *Remote Sensing of Environment* **2010**, *114*, 1 155.

[38] H. Molisch, *Ueber die Herstellung von Photographien in einem Laubblatte*, Hölder, **1914**.

[39] H. Gest, *Photosynthesis Research* **1991**, *30*, 1 49.

[40] L. Ning, B. E. Petersen, G. E. Edwards, L. S. Daley, J. B. Callis, *Applied spectroscopy* **1997**, *51*, 1 1.

[41] R. P. Hangarter, H. Gest, *Photosynthesis Research* **2004**, *80* 421.

[42] B.-D. Hsu, *Biochimica et Biophysica Acta (BBA)-Bioenergetics* **1992**, *1140*, 1 30.

[43] P. Tomek, P. Ilık, D. Lazár, M. Štroch, J. Nauš, *Plant Science* **2003**, *164*, 4 665.

[44] D. Lazár, *Journal of Theoretical Biology* **2003**, *220*, 4 469.

[45] X.-P. Li, O. BjoÈrkman, C. Shih, A. R. Grossman, M. Rosenquist, S. Jansson, K. K. Niyogi, *Nature* **2000**, *403*, 6768 391.

[46] B. Osmond, O. Schwartz, B. Gunning, *Functional Plant Biology* **1999**, *26*, 7 717.

[47] E. Tyystjärvi, K. Ali-Yrkkö, R. Kettunen, E.-M. Aro, *Plant Physiology* **1992**, *100*, 3 1310.

[48] E. Tyystjärvi, P. Mäenpää, E.-M. Aro, *Photosynthesis Research* **1994**, *41* 439.

[49] E. Tyystjärvi, E. Aro, *Proceedings of the National Academy of Sciences* **1996**, *93*, 5 2213.

[50] M. Wada, *Proceedings of the Japan Academy, Series B* **2016**, *92*, 9 387.

[51] B. Baránková, D. Lazár, J. Nauš, *Remote sensing of environment* **2016**, *174* 181.

[52] H. Goëau, P. Bonnet, A. Joly, V. Bakić, J. Barbe, I. Yahiaoui, S. Selmi, J. Carré, D. Barthélémy, N. Boujemaa, J.-F. Molino, G. Duché, A. Péronnet, In *Proceedings of the 21st ACM international conference on Multimedia*. ACM, **2013** URL `https://doi.org/10.1145/2502081.2502251`.

[53] R. Chouket, A. Pellissier-Tanon, A. Lahlou, R. Zhang, D. Kim, M.-A. Plamont, M. Zhang, X. Zhang, P. Xu, N. Desprat, D. Bourgeois, A. Espagne, A. Lemarchand, T. L. Saux, L. Jullien, *Nature communications* **2022**, *13*, 1 1.

[54] A. Walter, H. Schöbel, *Photosynthesis Research* **2023**, *156*, 3 325.

Table of Contents

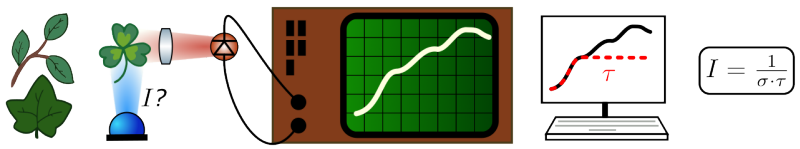

Leaves provide an easily accessible green material to robustly calibrate light intensity. Under exposure to a jump of constant light, their ChlF exhibits a fast evolution at a characteristic time, which is inversely proportional to the light intensity received by the leaf over a wide range of wavelengths and intensities. This favorable feature is harnessed to calibrate a source of white light.

3.5 Supplementary Materials for "Leaves to measure light intensity"

Supplementary materials: Leaves to measure light intensity

Aliénor Lahlou Dusan Lazar* Thomas Le Saux* Ludovic Jullien**

A. Lahlou, Dr. T. Le Saux, Prof. Dr. L. Jullien
PASTEUR, Département de chimie, École normale supérieure, PSL University, Sorbonne Université, CNRS, Paris, France
Email Address: Alienor.Lahlou@ens.psl.eu, Thomas.Lesaux@ens.psl.eu, Ludovic.Jullien@ens.psl.eu.

A. Lahlou
Sony Computer Science Laboratories, Paris, France
Email Address: Alienor.Lahlou@sony.com

Prof. Dr. D. Lazar
Department of Biophysics, Faculty of Science, Palacký University, Olomouc, Czech Republic Email Address: dusan.lazar@upol.cz

Keywords: *Photoactive materials, Green materials, Light intensity, Irradiance, Actinometry, Fluorescence*

Contents

1 Complement to the Experimental Section

1.1 Epifluorescence microscope

The measurements of the cross sections associated to the initial step of the ChlF rise from a dark acclimated leaf and of the incident spectral light intensity of a white LED have been performed on a home-built inverted epifluorescence microscope (Figure S1).

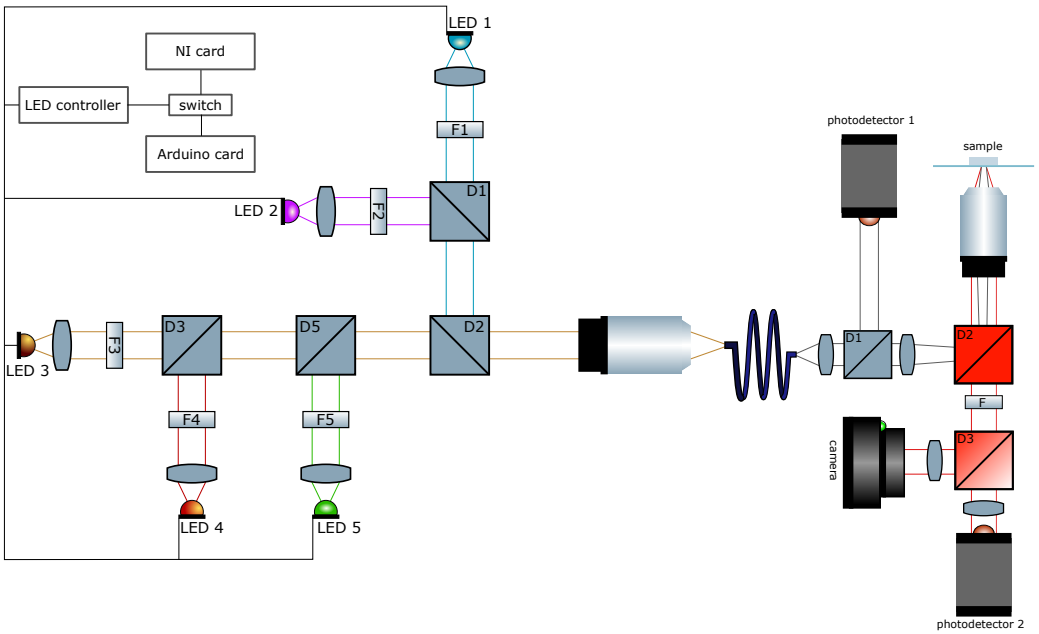

Figure S1: Schematic representation of the epifluorescence microscope.

To illuminate the samples, the lights from high power LEDs (LXZ1-PB01, LHUV-405, LXZ1-PX01, LXM3-PD01; Lumileds, NL) are collimated by high-NA condensers (ACL25416U-A, $f = 16$ mm, Thorlabs, NJ) and filtered by band pass filters (ET405/20x, ET550/15x; Chroma Technology, VT and FF01-479/40-25, FF01-650/13, Semrock, US) to avoid spectral overlaps. The white LED (LXML-PWN1-0080, Lumileds, NL) was filtered with a short-pass 694 filter (FF01-694/SP, Semrock, Rochester, NY) to eliminate the LED signal that could overlap with the fluorescence of the photosynthetic apparatus.

The quasi-parallel beams are combined with dichroic mirrors (T425LPXR, T505LPXR Chroma Technology, VT and FF01 560 Di01, Semrock, NY) and injected in a 400 μm-core optical fiber using a 20× objective (Nikon, NA = 0.75) to further homogenize the light beams. Light at the output of the fiber is collimated with a 10× objective (Olympus, NA = 0.5) and focused with $f = 150$ mm lens (AC254-150-A Thorlabs, NJ) at the back focal plane of a 10× imaging objective (Zeiss, NA = 0.5) after being reflected by a dichroic mirror (Di-FF506, Semrock, US). With the white LED at different current inputs, the rise of the fluorescence emission has been recorded with a 775±70 nm band-pass filter (775/140 single band-pass, Semrock, US).

The LEDs are powered by an LED driver (DC4104, Thorlabs, NJ) controlled by an Arduino Uno card or a DAQ card (PCI 6374, National Instruments, US) depending on the applications. The DAQ card also collects the output signals from detectors. The fluorescence signal has been collected by a photodetector (MPPC C13366-3050GA Hamamatsu, JP). Another photodetector (MPPC C13366-3050GA) is used to collect part of the light excitation that reaches the sample. For the experiment exploiting the measurement with the oscilloscope, we connected the output of the MPPC measuring ChlF flurorescence to both the oscilloscope (RTB2004, Rohde and Schwarz, DE) and the DAQ card (PCI 6374, National Instruments, US) and measured the output on both detectors during the same experiment (see Figure 2 in the Main Text). The acquisition rates of the DAQ card and the oscilloscope are 3 and 8 MHz respectively. However, after the data export, it results in a 37 kHz sampling rate.

Two protocols have been used to calibrate the coloured LEDs of the optical setup at its focal plane:

- The purple and blue LEDs respectively emitting at 405±7 nm and 470±10 nm have been calibrated with a solution of Dronpa-2 actinometer.[1] They have been used in the range 250–4000 μE.m^{-2}.s^{-1} (80–1200 W.m^{-2}) and 50–8000 μE.m^{-2}.s^{-1} (250–2000 W.m^{-2}) respectively;
- The green and red-orange LEDs respectively emitting at 550±6 nm and 630±9 nm have been calibrated with a powermeter (PM100A, Thorlabs, NJ). Its probe (*S170C* Thorlabs, NJ) was placed at the position of the sample and the excitation wavelength was selected. The collected output is given in Watt. To estimate the surfacic power (W/m^2), we further recorded a scaled image of the illumination spot at the sample position to measure the spot surface (0.25 mm^2 in our configuration where the illumination was narrowed by a diaphragm). The green and red-orange LEDs have been used in the range 250–900 μE.m^{-2}.s^{-1} (50–200 W.m^{-2}) and 200–800 μE.m^{-2}.s^{-1} (40–150 W.m^{-2}).

The rise-time of the LEDs is always faster than a few μs[1] while the dynamics of the initial step of the ChlF rise is in the tenths of microseconds range. Therefore the rise time of the LEDs does not interfere with the recording of the fluorescence rise dynamics.

2 Robustness of the cross section associated to the initial step of the ChlF rise at 470±10 nm

2.1 Impact of the leaf development stage

We first collected and analyzed similarly conditioned ivy leaves (genus *Hedera*) of different ages (Figure S2a,b). We derived σ values ranging between 0.72 and 1.40×10^6 m^2.mol^{-1} (Figure S2c) from analyzing the light intensity-dependence of the inverse of τ retrieved from the fluorescence

kinetics in response to increasing light intensity levels (Figure S2d). Hence, we concluded that the leaf age does not significantly impact the σ value beyond the expected error range.

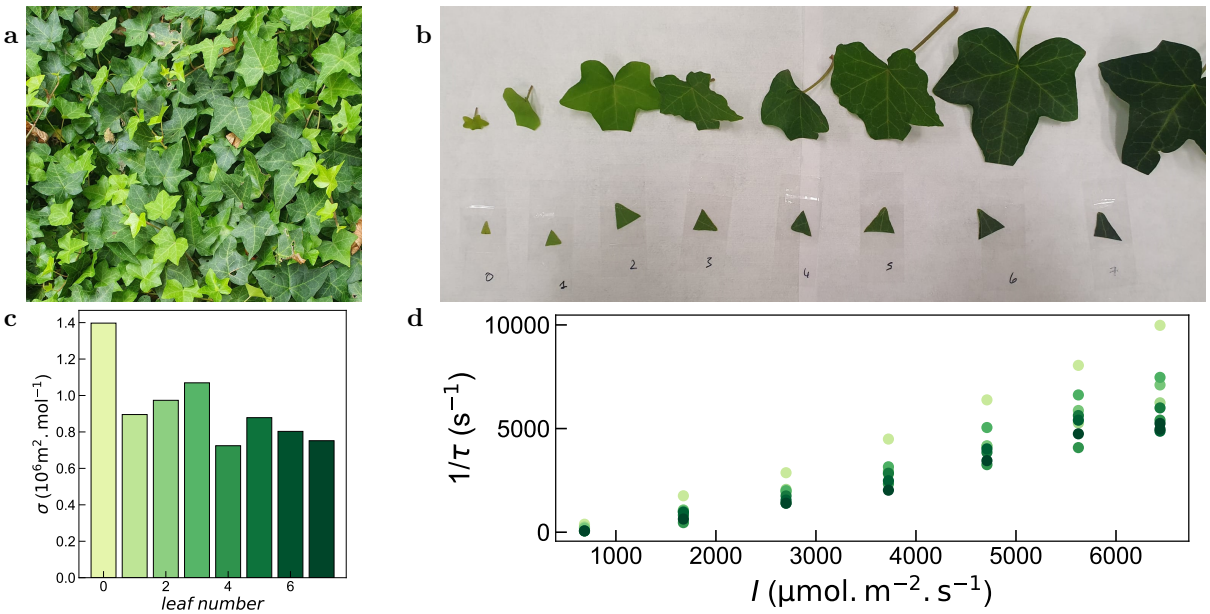

Figure S2: *Evaluation of the impact of the leaf age on the cross section associated to the initial step of the ChlF rise at 470±10 nm.* **a**: Parcel from which the ivy leaves were collected over 1 m^2 at the surface, therefore exposed to the same light intensity. Each leaf was collected and analyzed less than 20 min after being collected to allow sample preparation and 15 min dark-adaptation. **b**: Leaf ordering based on color and size (respectively light-green to dark-green and small to large, to ensure a gradual representation of increased growth time) to correspond to increasing age for increasing leaf number. The apex of each leaf was cut-off with a box cutter and used for the analysis. **c**,**d**: Derivation of the σ value for each collected leaf. The average $\langle\sigma\rangle = 0.94 \pm 0.20\times10^6$ $m^2.mol^{-1}$ has been retrieved from the σ values of all the examined leaves (**c**), which have been extracted from analyzing the dependence of $1/\tau$ on the light intensity for each leaf (**d**; coded by the color in **c**).

2.2 Impact of the time lag between the leaf collection and the measurement

Then we performed two tests to evaluate whether the time lag between the leaf collection and the measurement impacts the σ value. The first was to collect a leaf, prepare the sample and perform the measurement loop to acquire σ once every hour for seven hours. Figure S3a shows that the value of σ of five distinct leaves of different species does not display any significant variation that could be attributed to the time lag. The second test was performed on twenty one leaves, which were kept in a humid Petri dish before preparing the sample and performing the measurement loop to acquire σ. Figure S3b evidences a slow decay of the σ value on the time lag between the leaf collection and the sample preparation and the measurement.

From the whole series of experiments, we concluded that it is most appropriate to prepare the sample and take the measurement in the hour following the leaf collection.

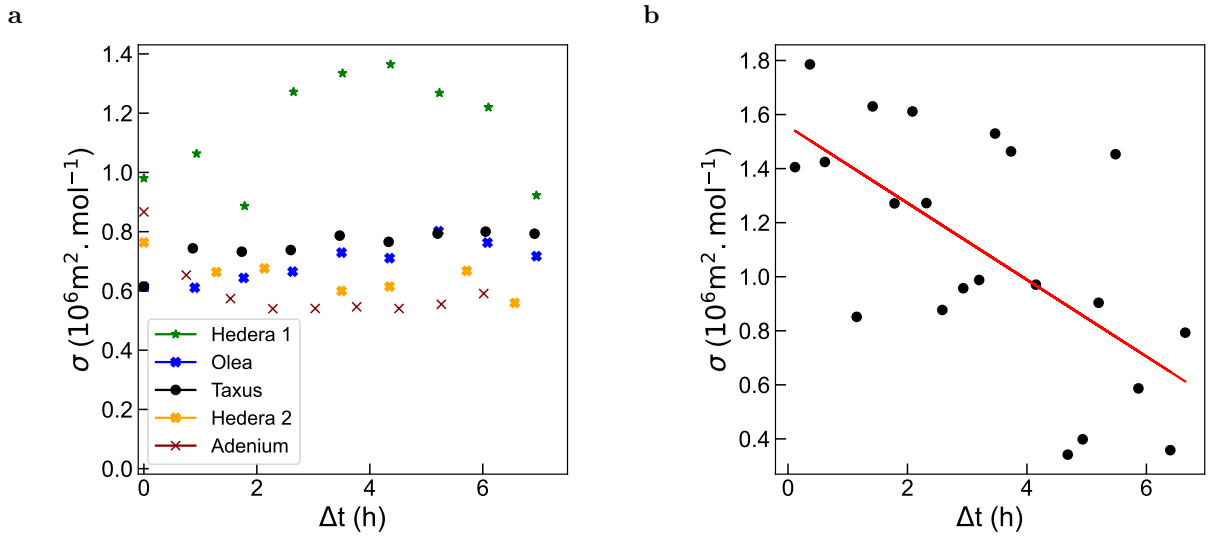

Figure S3: *Evaluation of the impact of the time lag between the leaf collection and the measurement of the cross section associated to the initial step of the ChlF rise at 470±10 nm.* **a**: Evolution of the σ value on the time lag Δt for five samples prepared less than one hour after the leaf collection (from the genus *Hedera* – two different samples, *Olea, Taxus, Adenium*) and exposed to the measurement protocol once every hour for seven hours; **b**: Evolution of the σ value for the twenty-one leaves collected in the Jardin des Plantes (see Figure 7 in the Main Text) and kept in humid Petri dishes in the dark until 20 min before the measurement to allow sample preparation and 15 min dark-adaptation. The linear fit yields $\sigma = 1.41 - 0.11\Delta t$ where σ and Δt are expressed in 10^6 m^2.mol^{-1} and hour respectively.

References

[1] R. Chouket, A. Pellissier-Tanon, A. Lahlou, R. Zhang, D. Kim, M.-A. Plamont, M. Zhang, X. Zhang, P. Xu, N. Desprat, D. Bourgeois, A. Espagne, A. Lemarchand, T. L. Saux, L. Jullien, *Nature communications* **2022**, *13*, 1 1.

3.6 Protocols to measure the quantum yields of the de-excitation pathways

3.6.1 Measuring pulses to inspect the status of the photosynthetic chain

As mentioned in 3.3.1, having access to the fluorescence quantum yield ϕ_{F_0} of a dark-acclimated leaf is important to solve the equations for the quantum yields of interest. However, probing the system requires light, which in turns affects the fluorescence quantum yield as it induces a dynamic evolution of competitive (non-)photochemical quenching processes. Therefore, probing the dark state of a photosynthetic apparatus with light is a challenge. With the fluorescence rise, the strategy is to send saturating light and collect the fluorescence at the very onset of the signal (around 50 μs), before it has time to respond actively to the light. Another strategy that forms another branch in chlorophyll fluorescence research (and development) is the use of measuring pulses. Measuring pulses are short (few ms) and low-intensity (few μmol(photons) $\cdot\, \mathrm{m}^{-2} \cdot \mathrm{s}^{-1}$) light pulses repeated frequently (several times per second). Their role is to probe the system at a given time t by sending n photons (always the same quantity) and collect the fluorescence F corresponding specifically to the response induced by the n photons. They can be seen as inspectors: they should not affect the system, but still be able to report on its status and make the report accessible to a user.

The evolution of the value of F mirrors the evolution of the quantum yield of fluorescence ϕ_F, as the energy input quantity n is constant. The measuring pulse allows to probe the photosynthetic organism in the dark, and the quantity n is so low that it is assumed to not perturb the photosynthetic chain. This allows also to probe the yield dynamically while the photosynthetic chain is being perturbed with other light sources. These include actinic light – mimicking the effect of the sun–, or saturating light flashes that drive the photochemistry rate to $k_P = 0$ (saturating level similar to the light level used in OJIP).

3.6.2 Pulse-Amplitude Modulated (PAM) fluorometry

In the literature using this approach, two strategies are used to unmix the photons emitted in response to the measuring pulses and the ones provoked by the other light sources. The approach used in Pulse-Amplitude Modulated fluorometry (PAM) [128, 129] is to send the measuring pulses on top of the other light sources (actinic and saturating) at a known frequency f and unmix the total fluorescence signal by using demodulation (Figure 3.7a). In general the demodulation consists in substracting the fluorescence received just before a measuring pulse is applied from the fluorescence received during the measuring pulse [128, 130]. The other strategy developed in the laboratory of IBPC (Institut de Biology Physico-Chimique) by Frederic Joliot and Daniel Beal consists in turning all the light sources off when a measuring pulse is applied (experimental result in Figure 3.7b). The fluorescence level in response to the measuring pulses in the dark is called F_0, the one collected to probe the response to a saturating pulse is called F_M, while the measuring pulses fluorescence response collected to probe the response to actinic light is called F_S.

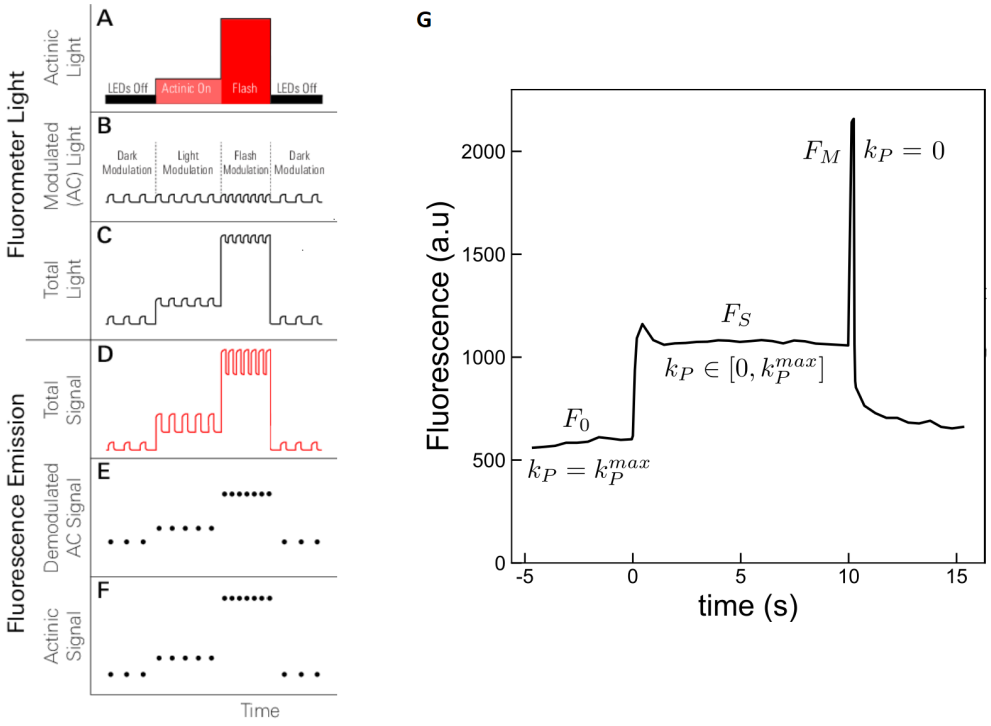

Figure 3.7: *PAM protocols.* **A**: Depiction of actinic light driving the photochemistry; **B**: Measuring pulses to inspect the chain status; **C**: Total excitation light (sum of A and B) **D**: Resulting total chlorophyll a fluorescence collected by a sensor in response to C; **E**: Demodulated fluorescence; **F**: Actinic (direct) fluorescence signals; **G**: Fluorescence signal in response to measuring pulses. The actinic light and saturating pulses are turned off durng the application of the measurinig pulses ($\sim$10 μs) using Joliot protocol with the value of the rates at different stage depending on the exciting light intensity (sample: non-motile *Chlamydomonas reinhardtii* PHUN 325 #3 in MIN, growth conditions described in Table 3.3).

3.6.3 Limit of measuring pulses: photon count

This methodology can find limitations when working with imaging. Indeed, I have derived computations to simulate the number of photons that the camera could collect per chloroplast (Figure 3.8). This computation works for algae and higher plants, but I present the estimations based on algae to simplify the problem and because our sample for the rest of the work will be algae. I used values from algae evaluated under intermediate growth light corresponding to our growth conditions (5 μmol(photons) $\cdot$ m^{-2} $\cdot$ s^{-1}, white LED) and described in Table 3.1.

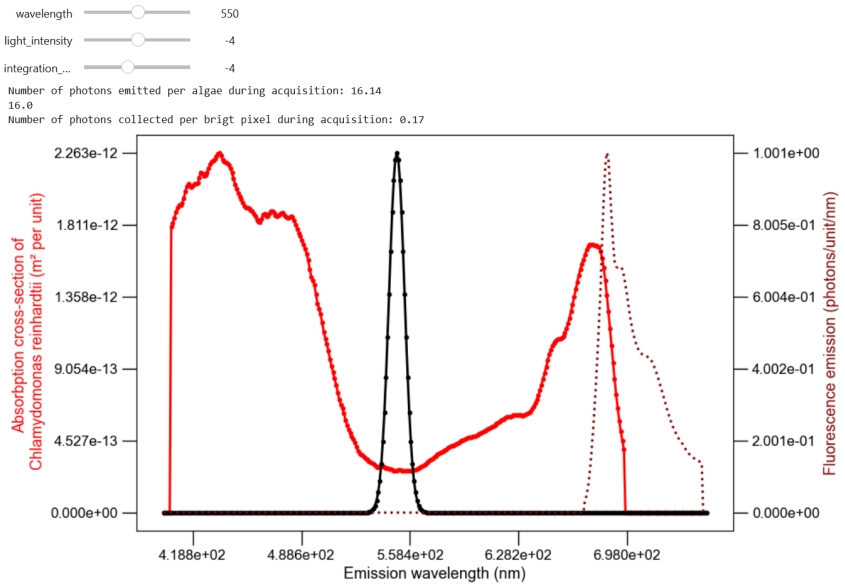

Figure 3.8: *Python simulation to estimate the number of fluorescence photons emitted by an algae during a frame acquisition for a given light excitation (wavelength and amplitude).* The number of photons emitted is computed from the excitation light spectrum and the absorption section spectrum of *Chlamydomonas reinhardtii*, the quantum yield of fluorescence, the intensity of the excitation light and the integration time. The number of photons collected by the camera takes the objective angle collection and the camera sensitivity into account.

Parameter	Annotation	Value	Source
fluorescence quantum yield	ϕ_F	0.01	[131]
absorption cross-section per RC (596 nm)	σ_{RC}	60 Å^2	[132]
chlorophyll per cell	N_{chl}	$3 \cdot 10^{-16} mol/cell$	[132]
chlorophyll per reaction center	$N_{chl/RC}$	260	[132]
chloroplast cross-section	S	10-20 μm^2	[133]

Table 3.1: Values used to evaluate the quantity of fluorescence photons emitted by an algal cell similar to our *Chlamydomonas reinhardtii* samples (*Chlorella vulgaris* growth conditions: 5 μmol(photons) $\cdot$ m^{-2} $\cdot$ s^{-1}, white LED)

The cross-section for light absorption per cell at 596 nm is given by $\sigma_{cell}^{596} = \sigma_{RC} N_{chl}/N_{chl/RC} = 0.41 \cdot 10^{-12} m^2$. This value allows to scale the excitation spectra of algae presented in Chapter 2 (Figure 3.8). At the maximum of absorption around 440 nm, $\sigma = 2.3\ \mu m^2$. In comparison, the physical cross-section of a chloroplast is approximately 10-20 μm^2, which is very close. With a classical fluorophore, for example the ones displayed in Appendix 2.6, the cross-section for light absorption

corresponds to approximately 1% of the molecular surface, highlighting that the absorbing matter is mainly transparent. In the case of chloroplasts, a higher fraction is reached for two reasons: the antenna system is designed to maximally extend the absorption cross-section of the reaction centers, and the grana organization of the thylakoids allows for stacking the absorbing antennas. When a photon crosses the chloroplast, it eventually gets absorbed by one of the antenna systems. Due to the multiple layers of these complexes, the photon is eventually absorbed by one of them: it is called the inner-filter effect (see Appendix 2.6 and Appendix A.1).

I then compute how many photons are collected by a microscope objective with a numerical aperture of 0.5, which represents a collection angle of 60^o. I used the simulation to compute the values for different wavelengths, light levels and integration times. I made the hypothesis that the fluorescence filter encompasses the whole fluorescence spectrum between 660 nm and 750 nm and that the excitation light is an LED with a bandwidth of 10 nm (these conditions make the calculation relevant only below 650 nm when considering the tail of the LED spectrum). For the camera mounted on the epifluorescence setup (*Ueye 3060CT-M - IDS*), a minimum of 50 photons per pixel per frame must be acquired to reach a consistent signal-over-noise ratio. I used the specifications of the camera to estimate the number of photons collected on each pixel for specific excitation lights. The pixel surface is 30 μm^2 and the overall magnification of the system is 10x[2]. Table 3.2 displays the estimate

λ ms	duration ms	intensity μmol(photons) $\cdot$ m^{-2} $\cdot$ s^{-1}	photons per alga	photons per pixel	name
550	3	5	25	0.25	measuring pulse
470	3	5	170	1-2	measuring pulse
470	3	40	1350	14	actinic light
470	60	40	$3{\cdot}10^4$	300	actinig light
470	170	450	$8{\cdot}10^5$	$9{\cdot}10^3$	saturating light
405	170	1300	$1.3{\cdot}10^6$	$1.5{\cdot}10^4$	saturating pulse

Table 3.2: Number of photons emitted by the algae and received by pixel under different configurations.

of the photon integration for short measuring pulses (3 ms) and the frame duration (60 ms-170 ms) with a CMOS camera within an accessible price range (500 €). These are the typical integration times used in the experiments described in the manuscript. It appears clearly that using the fluorescence emitted as a response to actinic and saturating light is easier than collecting light from the measuring pulses with a camera, because the signal-over-noise ratio will be much higher. For this reason I have adapted the PAM protocol by removing the measuring pulses and only collecting the direct fluorescence photons (the ones emitted in response to actinic and saturating light perturbations). Since I benefit from a precise calibration of the excitation light, it becomes simple to correct the direct fluorescence ($FD_{actinic}$ or FD_{sat}) collected by the excitation light level ($I_{actininc}$ or I_{sat}) in order to yield a proxy of the fluorescence yield, similar to the one obtained with the measuring pulses: $F_S \propto FD_{actinic}/I_{actinic}$ and $F_M \propto FD_{sat}/I_{stat}$. The value that can be obtained for F_0 is the minimal value of F_S that can be read when the actinic light is decreased, for a given signal-over-noise ratio. It is higher than the measuring pulse light intensity, and may perturb the system, therefore it will only provide an estimate of the yields usually derived from F_0, such as ϕ_P.

3.6.4 Direct fluorescence to inspect the status of the photosynthetic chain

In order to validate this approach, we reproduced synchronously the experiment displayed in Figure 3.7 with two instruments: the fluorometer of IBPC (pump-probe fluorometer [134]) measuring

[2]The simulation is detailed in Alienor134/html_widget. The number of photons emitted is computed from the excitation light spectrum and the absorption section spectrum of *Chlamydomonas reinhardtii*, the quantum yield of fluorescence, the intensity of the excitation light and the integration time. The number of photons collected by the camera takes the objective angle collection and the camera sensitivity into account.

the fluorescence response to measuring pulses from an algae solution with a photodiode, and the epifluorescence microscope capturing a video of the algae fluorescence. We used the strain PHUN 325 #3 of non-motile algae for this experiment. The growth condition and experimental parameters are described in Table 3.3. The sample is more concentrated for the microscope observation to get multiple algae in the field of view. Note that the light levels have been calibrated to match each other when corrected by the absorbance of algae in green and blue (actinic light). The sequence corresponds to the one displayed in Figure 3.7b, and is repeated with 2 min 30 dark intervals with different actinic light levels (the levels increase from 0 to 1000 μmol(photons) $\cdot\, m^{-2} \cdot s^{-1}$ (green) or 100 μmol(photons) $\cdot\, m^{-2} \cdot s^{-1}$ (blue) and decrease back to zero). We performed two repeats of the experiment on the pump-probe on the same sample in a row to obtain more data.

Parameter		**pump-probe fluorometer**		**Epifluoresnce Microscope**
strain		PHUN 325 #3		
concentration		10^6		10^7
growth conditions		12/12 dark-light cycle		
growth light		white LED - 80 μmol(photons) $\cdot\, m^{-2} \cdot s^{-1}$		
growth temperature		25^oC		
growth medium		TAP		
experiment medium		MIN		
experimental sample		algae in solution agitated manually between each measurement sequence		algae deposited on agarose pad between two glass slides
actinic light	wavelength	520 nm		470 nm
	duration	10 s		10 s
	range	0-1120		0-100
saturating pulse	wavelength	520 nm		405 nm
	duration	250 ms		200 ms
measuring pulse	wavelength	520 nm		NA
	period when shone during:	dark	500 ms[1]	
		saturating pulse	50 ms[2]	
		actinic	500 ms[3]	
	duration	10-20 μ s	10-20 μ s	

Table 3.3: *Experimental parameters for the validation of the direct fluorescence method.* In the pump-probe fluorometer, the actinic and saturating lights are turned off during a measuring pulse application. In practice there is a 250 μs delay before the application of the measuring pulse to allow the detector to relax between the high lights and the low measuring light.
[1]: shorter period right after the saturating pulse to capture the kinetics of the relaxation;
[2]: shorter period at the light onset to capture the kinetics of the first seconds precisely;
[3]: first pulse after 150 ms to allow the ChlF to reach its maximum (OJIP induction). Then 3 points are collected every 50 ms.

For the analysis of these experiments, I introduce how to evaluate the Non-Photochemical Quenching. When the leaf is dark-adapted for a long-enough period (15 min) and has not experienced high-light stress over the past hours, the NPQ is fully relaxed: $k_{NPQ} = 0$. When a saturating pulse is shone to excite a plant in this state, we have $k_{NPQ} = 0$ and $k_P = 0$ (see 3.3.1, the photosynthetic chain is saturated): it is the fluorescence $F_M(0)$. When the light is turned on, the NPQ mechanisms come into play gradually and their evolution can be monitored by following the fluorescence of saturating pulses $F_M(i)$ of the consecutive repeats of the experiment with increasing actinic light. We can develop:

$$\phi_{F_M(0)} = \frac{k_F}{k_F + k_O} \tag{3.7}$$

$$\phi_{F_M(i)} = \frac{k_F}{k_F + k_{NPQ} + k_O} \tag{3.8}$$

Then:

$$\frac{F_M(0) - F_M(i)}{F_M(i)} = \frac{\phi_{F_M(0)} - \phi_{F_M(t)}}{\phi_{F_M(i)}} = \frac{\phi_{F_M(0)}}{\phi_{F_M(i)}} - 1 \tag{3.9}$$

As opposed to ϕ_P, ϕ_{NPQ} is not derived directly from this equation. Instead, the derivations in photosynthesis literature follow from the conversion of this equation into a Stern-Volmer quenching function. The quenching mechanism assumed between the excited state and a quencher can be represented as [109]:

$A^* + Q \longrightarrow A + Q$

The kinetics of this mechanism obey the equation of Stern-Volmer:

$$\frac{I_{f^0}}{I_f} = 1 + kp\tau[Q] \tag{3.10}$$

Where:

- I_{f^0} is the fluorescence intensity without the quencher;
- I_f is the fluorescence intensity in the presence of the quencher;
- p is the collision probability;
- k is the collision rate constant;
- τ is the fluorescence lifetime in absence of the quencher;
- $[Q]$ is the quencher concentration;

With these assumptions,

$$\frac{F_M(0)}{F_M(i)} = 1 + kp\tau[Q](i) \tag{3.11}$$

And according to equation (3.9):

$$NPQ = \frac{F_M(0) - F_M(i)}{F_M(i)} \propto [Q](i) \tag{3.12}$$

Monitoring this ratio called NPQ enables in theory to monitor the evolution of the quenching process. Although the hypothesis that the NPQ mechanisms indeed follow a Stren-Volmer relationship has been questioned [135], the ratio remains widely spread in the community to evaluate NPQ.

I also introduce the quantum yield of photochemistry $\phi_P = \frac{F_M - F_S}{F_M}$ which follows the same derivations as described in 3.3.1, but using F_S, the fluorescence measured during the actinic light exposition. As compared to F_0, we do not obtain the maximal quantum yield of fluorescence (see Figure 3.7), but acquiring F_0 requires a very low light, too low to be sensed by our camera.

The experimental results are displayed in Figure 3.9. The single algae data are displayed in terms of mean and one standard deviation, while two consecutive repeats of the experiment were performed for the experiment on the pump-probe fluorometer. We show, because of the range of values falling mainly within the deviation range, that the two protocols provide the same results in

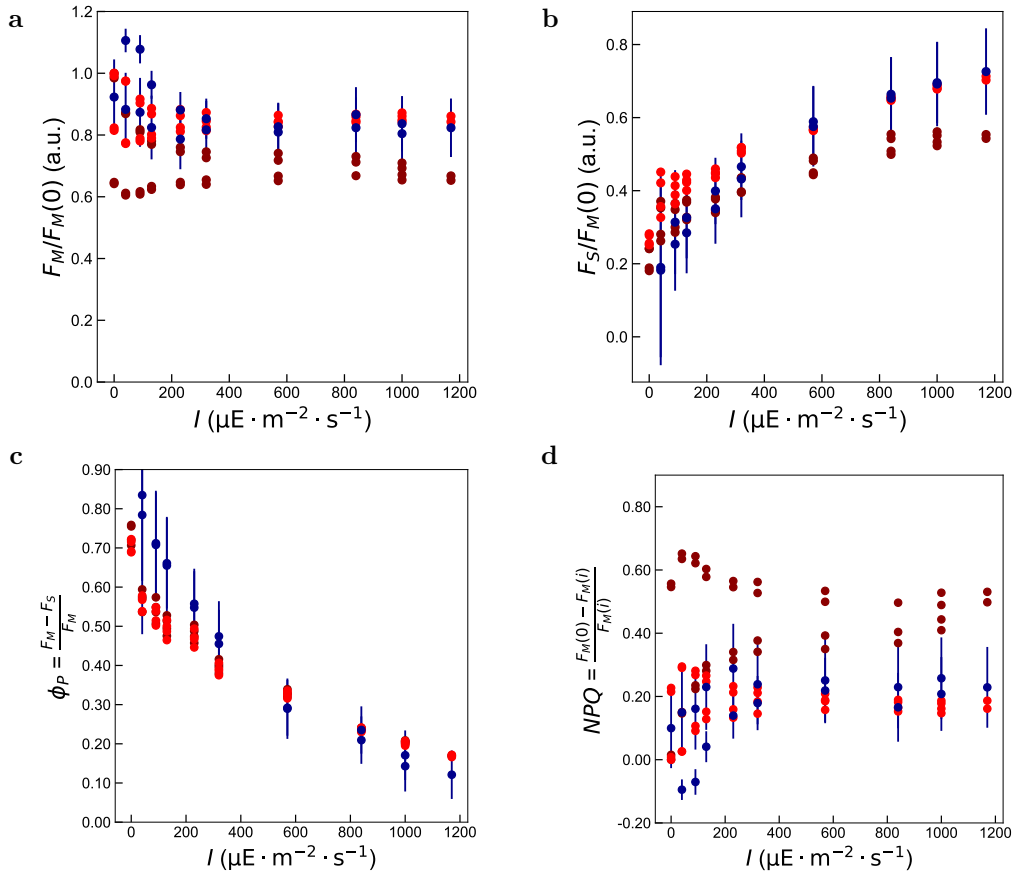

Figure 3.9: *Validation of the direct fluorescence light protocol.* Measuring pulse experiments (pump-probe fluorometer - darkred: first repeat, red: second repeat) *vs* direct fluorescence (calibrated fluorescence microscope - blue - M ± SD) The actinic light is applied for 10 s, allowing to measure the variable fluorescence F_S, and is immediately followed by a saturating pulse, from which F_S is derived. The experiment is reproduced for increasing then decreasing actinic levels spaced by 2 min 30 dark intervals. **a**: F_M, **b**: F_S, **c**: ϕ_P, **d**: ϕ_{NPQ}.

terms of F_M, F_S, ϕ_P and hysteresis (Figure 3.9), which validates the direct fluorescence protocol. We find a discrepancy in the values of NPQ which could be due to a difference of biological status of the algae in each instrument and small discrepancies in the precise application of the two protocols. Indeed, the two repeats of the protocol under pump-probe show high discrepancies, demonstrating that NPQ is a very sensitive parameter in this experiment.

3.7 Conclusion

In this Chapter, I detailed the various deexcitation mechanisms of the reaction centers and explained why ChlF could be used to report on them. I demonstrated how light intensity was a key player in understanding the various protocols introduced in the literature. Then, I introduced a manuscript detailing the use of leaves as actinometers. It describes how the fluorescence dynamics related to a phenomenon directly linked to the photon absorption can be used as an actinometer. I showed that processes that happen further away from light absorption integrate the internal biochemistry. They also have actinometric properties, but are more interesting to study from the viewpoint of biochemistry. In that sense, I have implemented a protocol that allows to probe the response of

algae to increasing light level applied for a short time. I present a protocol different from those presented in the literature, but yielding comparable results. I used the successful comparison to validate the protocol and the home-built microscope. In the next chapter, I will describe how fluorescence can report on biochemistry and how we used it to build a computational framework to transform a fluorescence response into a stress-response score.

Chapter 4

Scoring of light-stress response in *C. reinhardtii*

4.1 Introduction

This chapter focuses on describing the implementation of a novel machine learning framework to quantify stress responses using chlorophyll fluorescence (ChlF) data that we derived. The single-cell input ChlF data were acquired with the homemade microscope discussed in Chapter 2. The research conducted in this study centers around investigating a widely studied stress-response mechanism, drawing upon established protocols from the literature (outlined in Chapter 3). We adapted these protocols after discussions with the team of IBPC and utilized them as a reference to evaluate the performance of the new framework. To implement the methodology, I built a dataset of ChlF traces corresponding to various phenotypes that were fed to the machine learning framework. This work is described in a manuscript under preparation introduced in Section 4.4.

Before the manuscript, I justify the choice of the organism, *Chlamydomonas reinhardtii*, and the mechanism monitored, Non-Photochemical Quenching (NPQ). I will explain how I used them to build a training dataset. In particular, I detail how to segment each alga from fluorescence movies. Then I introduce several concepts in machine learning, and describe specifically the methods employed in the framework (Dictionary Learning and Linear Discriminant Analysis).

4.2 *C. reinhardtii*, a model for ChlF remote sensing

4.2.1 *C. reinhardtii*, a reference organism in photosynthesis

We chose to focus on the system *Chlamydomonas reinhardtii*, a unicellular algae which is a model organism to study photosynthesis [136]. It is fast and easy to grow in the laboratory with little risk of contamination. The population doubles in less than a day, and it can be grown heterotrophically, allowing severely photosynthesis-impaired mutants to still grow. Its unicellular nature allows for easy experimental manipulation, precise measurements, and the possibility to study individual cells.

Chlamydomonas reinhardtii is also well-suited for classical genetics, thanks to its haploid genome that allows loss-of-function mutations to be immediately expressed. In consequence, *Chlamydomonas reinhardtii* has a well-established and accessible genetic toolkit. The IBPC holds a collection of more than 500 different strains of *Chlamydomonas reinhardtii* [81]. Among them, mutant strains have been obtained by UV or chemical mutagenesis, or gene transformation (nucleus or chloroplast). Despite being a unicellular organism, *Chlamydomonas reinhardtii* shares many fundamental aspects of photosynthesis with higher plants [89]. It possesses chloroplasts, the cellular organelles responsible for photosynthesis, and carries out similar biochemical processes such as light absorption,

electron transport, and carbon fixation. Studying *Chlamydomonas reinhardtii* provides valuable insights into the basic principles of photosynthesis applicable to a broader range of organisms. We used *Chlamydomonas reinhardtii* grown under low-light (10-100 μmol(photons) $\cdot$ m^{-2} $\cdot$ s^{-1}). A light above 300 μmol(photons) $\cdot$ m^{-2} $\cdot$ s^{-1} is considered stressful for our populations, while a light above 1200 μmol(photons) $\cdot$ m^{-2} $\cdot$ s^{-1} saturates the photosynthetic chain [90]. In comparison, the sunlight can irradiate up to 8000 μmol(photons) $\cdot$ m^{-2} $\cdot$ s^{-1} on Earth's surface.

4.2.2 Light-stress responses in *Chlamydomonas reinhardtii*

The previous Chapter introduced the NPQ components. As these phenomena can be measured through fluorescence using well-described protocols, it has been extensively studied in the literature. It has been the topic of multiple publications at the population level, summarized in two chapters of the *Chlamydomonas reinhardtii* SourceBook, Volume 2 [90]. In particular, the NPQ induction provoked by light-stress response and its relaxation in the dark are very practical to implement experimentally. Although there are other light-stress responses, such as electron transfer pathways, phototaxis, antioxidant defenses and changes in gene expression [90], we have focused on three phenomena that induce Non-Photochemical Quenching on the time-scale from minutes to hours under high-light exposure. The time scale of the kinetics of the NPQ components for *Chlamydomonas reinhardtii* is displayed in Figure 4.1 along with the time scale of the underlying biological processes.

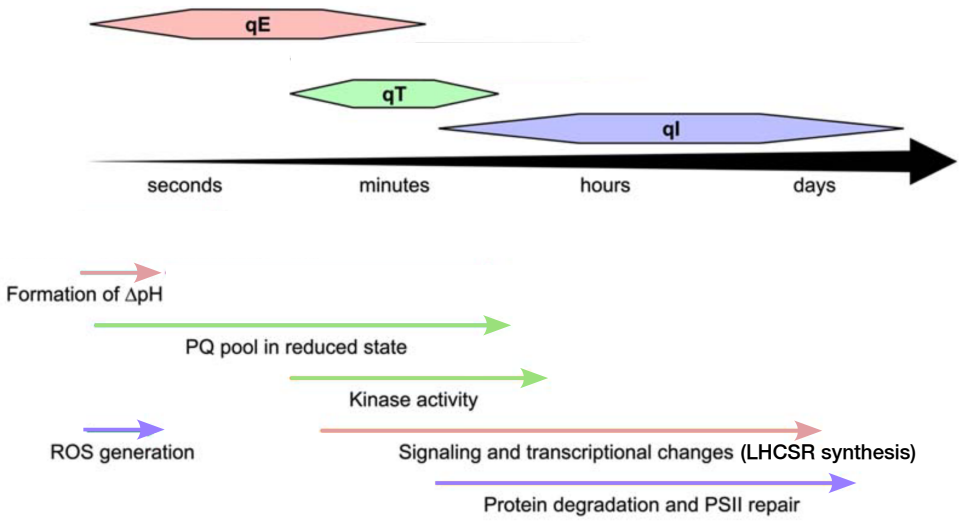

Figure 4.1: Time scale of the light-stress response in *Chlamydomonas reinhardtii*. NPQ components are displayed on the top, whereas the underlying biological processes are displayed on the bottom. Adapted from: [90].

Energy-dependent quenching (qE)

Under high-light, photosynthetic electron transport results in the accumulation of protons in the thylakoid lumen. The acidic pH drives the protonation of lumenal domains in specific photosystem antennas. This protonation induces the conversion of these antennas from exciton transporter to exciton quencher. This phenomenon is called energy-dependent quenching, and appears in the fluorescence trace as a quick decay of fluorescence (seconds to minutes). When the lumenal pH increases (under the action of regulation processes or because the light is turned off), the LHCSRs deprotonate

and recover their energy-transfer capacity. This results in an increase of fluorescence with similar rate constants.

This process is the main light-stress response in plants, where the PSII subunit S (PsbS) is the pH-sensitive protein promoting the quenching [137]. In *Chlamydomonas reinhardtii*, the pH-sensitive antennas are called Light Harvesting Complex Stress-Related (LHCSR). There are three genes encoding the expression of LHCSRs (LHCSR3.1, LHCSR3.2 and LHCSR1) producing two types of antennas, LHCSR3 and LHCSR1, with corresponding mutants *npq4* and *lhcsr1*. The LHCSRs are not constitutively expressed under low-light growth conditions. However, a protocol was developed to induce their expression by stimulating the transcription using a prolonged high-light exposure (>400 μmol(photons) $\cdot$ m^{-2} $\cdot$ s^{-1}, 2-6 h) [97]. This induction, called qE-activation, is enhanced by blue light, which explains why we used the blue LED in the following manuscript [138, 139]. An illustration of the qE component is displayed in Figure 4.3.

State-transition quenching (qT)

The next NPQ component we studied regulates the amount of energy transferred to the photosystems, by modifying the size of the connected antenna supercomplex. The State Transitions regulate the binding of mobile LHCII antennas to PSI and PSII, balancing their energy input. They are driven by the actions of phosphatases and a kinases that respectively phosphorylate and dephosphorylate the antennas, modifying their binding properties to the reaction centers (Figure 4.2). When the electron carrier plastoquinone (PQ) becomes highly reduced (PQH2) it binds to the Q_o site of the cytochrome b_6f, which activates the kinase STT7 (STN in plants) [140]. STT7/STN dephosphorylates LHCII proteins, which then bind to PSII. The phosphatase PPH1 and PBCP (counterparts of STL1 phosphatase in plants) mechanisms are less known but they contribute to the binding of mobile LHCII antennas to PSI. In particular, when a light that is preferably absorbed by PSI (light 1 [119]) is used to illuminate the organism, the mobile antennas will favor binding to PSII to enhance its light collection and equal the rate of PSI: it is called state 1 (for light-1 state). When light favoring PSII is used (light 2), the antennas bind preferentially to PSI, which is called state 2 (for light-2 state) [141]. When the antennas transition to state 1 (binding to PSII), the fluorescence increases because most of the fluorescence comes from PSII[1] and the state-transition increases its light-collection capacity. When the antennas detach from PSII, the fluorescence decreases. In *Chlamydomonas reinhardtii*, 80% of the antennas are mobile, compared to 20% in plants [142, 143]. In the manuscript below, we illuminated with high-light a *Chlamydomonas reinhardtii* culture grown in low-light and transferred to a MIN medium[2]. Interestingly, a transition to state-1 is observed. This is counter-intuitive because the kinase STT7 is expected to dephosphorylate the antennas when PQ is reduced (a consequence of high-light illumination). The hypothesis that the kinase STT7 is inhibited by high-light has been suggested [144–146]. The state transitions take place over minutes to tens of minutes (Figure 4.1) and the mechanism centered on PSII is depicted in Figure 4.3.

Photoinhibition quenching (qI)

Reaction centers experience a significant turnover of excitation and de-excitation when exposed to light. Two key proteins of the reaction center, D1 and D2, which bind together the essential components of PSII (in particular P680 and the electron acceptor pheophytin) [147], have been shown to be degraded and repaired under light exposure [148, 149]. The degradation and repair rates are dependent on the light intensity [149]. Under high-light, the degradation rate outpaces the repair rate[3]. It results in an overall degradation of the photosystems on the time scale of minutes to hours (Figures 4.1, 4.3), which recovers more slowly in the dark [149]. As a consequence, if the system is

[1] see Chapter 3.

[2] The MIN medium contain salts and trace elements, but lacks organic carbon sources or other nutrients that would be used as a direct food source for the algae.

[3] D1 degradation is more sensitive than D2 [148]. Therefore, it is often mentioned alone in publications.

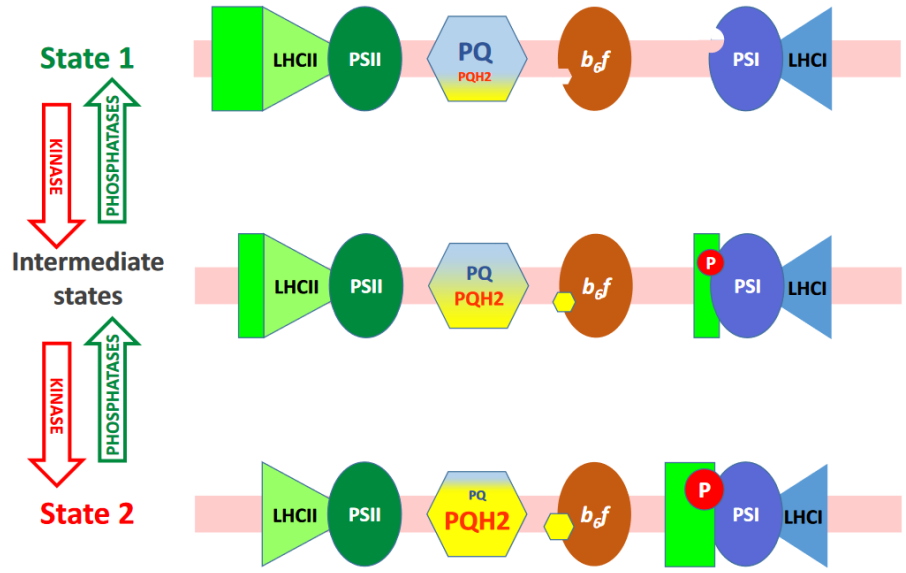

Figure 4.2: State transitions. The reversible binding of mobile LHCII antennas to PSI and PSII allows to channel the harvested energy to either photosystems. It is driven by the kinase STT7 (dephosphorylation, favors binding to PSII) and the phosphatases PPH1 and PBCP (phosphorylation, favors binding to PSI). The action of the kinase and phosphatase are multi-phenomena-dependent, sensitive to the reduction of PQ to PQH_2 and high-light intensity. After [90].

exposed to intense light for a specific period and then kept in darkness for an equal duration, the fluorescence level at the end of the experiment will not reach its initial fluorescence level.

As these three phenomena have entangled dynamics with overlapping time-scales (Figure 4.1), the fluorescence response to high-light exposure of a dark-adapted *Chlamydomonas reinhardtii* is complex. We developed a methodology to unmix the NPQ components that shape a fluorescence trace obtained after applying a light protocol of 15 min of high-light followed by 15 min of dark. As we were interested in quantifying the stresses and observing their diversity of expression among individuals, we ran single-cell experiments using the microscope. The data analysis of those experiments required the computational methods described below.

4.3 Computational methods

4.3.1 Image segmentation of fluorescence movies

I acquired fluorescence movies of single-algae to collect the evolution of their response to high-light stress. I adapted my code written at the beginning of the PhD for the project LIGHTNING [55] initially designed to segment bacteria expressing RSFPs. The following is an excerpt of the Supplementary Materials I wrote for the publication [55].

Processing fluorescence movies

All the movies were processed and analysed with in-house routines written in Python 3 (the codes are available on Github[4]) using the Scikit-image library [153]. We used the

[4]The codes for processing the images are available at Alienor134/image_segmentation [152].

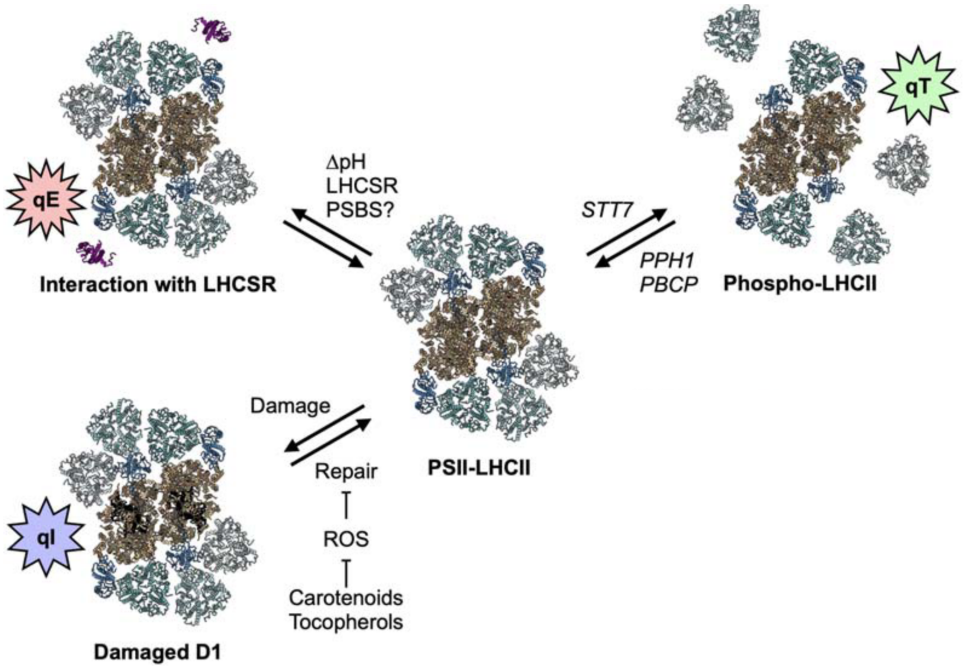

Figure 4.3: Non-photochemical quenching components in *Chlamydomonas reinhardtii*. The reaction centers are displayed in dark brown, the LHCII antennas are displayed in grey, the LHCSR are displayed in purple. **qE**: The pH in the lumen drives the state of the LHCSRs that either transfer the exciton or quench it when they are protonated due to low luminal pH. **qT**: The state-transition corresponds to the binding and unbinding of secondary antennas to the PSII upon the dephosphorylation by pph1-pbcp and phosphorylation by STT7. Antenna binding to PSII increases the fluorescence level by increasing the energy transfer to the reaction center. **qI**: The excess of energy that is not dissipated through the previous mechanisms induces photo-oxidative damage to the D1 subunit of PSII, forbidding the energy transfer to PSII. After [90]. Note: The slow (tens of minutes) relaxing component of NPQ in Chlamydomonas is composite. The existence of a zeaxanthin-dependent but pH-independent component of NPQ in *Chlamydomonas reinhardtii* was recently proposed, very similar to the qZ component described in plants [150]. We cannot exclude that a qZ contribution is present in our work. However, given that the relaxation of the slow NPQ component in *Chlamydomonas reinhardtii* is sensitive to inhibitors of the chloroplast protein synthesis and require the activity of the protease FtsH for D1 repair [151], we decided to call the slowest relaxing component in our analysis qI and did not represent qZ here.

high quality video as a reference to perform the segmentation of the bacteria, and the binned movies to extract the time evolution of the fluorescence from the RSFP-labeled bacteria under the different illuminations.

Segmentation of bacteria

For all acquired movies, we assumed that the bacteria positions did not vary throughout the recording. Hence we first selected and summed frames with high dynamics and contrast from the high-quality movie to generate an information-rich single reference image F_r (Figure 4.4a). More precisely, we computed $S_i = \sum_{x_i,y_i} p_{x_i,y_i}$ in the image i for a movie of n frames ($i \in I = [1, ..., n]$) where x_i, y_i designate the coordinates of the pixels with signal level p_{x_i,y_i}. After identifying $S_{max} = \max\{S_i\}$, we extracted the set $M = \{i, S_i > 0.8 \times S_{max}\}$. The reference image F_r, $p_{x_r,y_r} = \sum_{i \in M} p_{x_i,y_i}$, is the sum of the images of the M set.

The first step of the segmentation was to process the reference image F_r by applying operations based on mathematical morphology[154]:[5] (i) the *rank.enhance_contrast* filter on the one hand. We obtained a first image with enhanced contrast of the bacteria against the background (Figure 4.4b); (ii) the *rank.autolevel* filter on the other hand.[6] We retrieved a second image with sharpened frontiers of the bacteria against the background (Figure 4.4c). Both grey-level images were binarized by using the local threshold method of Otsu (Figure 4.4d,e)[155]. The intersection of the generated two masks was used to generate a final mask sharpening the distinction between the background and the bacteria (Figure 4.4f): this mask is white on the pixels where bacteria are present and black on the background pixels. The new reference image for the segmentation (Figure 4.4g) was obtained from masking the reference image F_r behind the final mask in Figure 4.4f.

When the bacteria were isolated in the reference image F_r, the white areas in Figure 4.4f corresponded to single bacteria with a single maximum (the brightest point of the segmented area, displayed in Figure 4.5a). In contrast, when bacteria were grouped (e.g. two bacteria emerging from division of a mother bacteria), the white areas corresponded to multiple cells with multiple maxima. To further split these white areas, we applied the Watershed Segmentation method [154] on Figure 4.4g,[7] which resulted in the image displaying segmented individual bacteria in 4.5b.

The parameters of the segmentation algorithm are the size of the kernels and the thresholds selected for binarization. We tested several sets of parameters and selected a common set that segmented most objects in all of the experiments, without selecting parts of the background, and with a granularity of segmentation corresponding to the bacteria size. The segmentation can miss bacteria whose fluorescence expression level is low in each set of bacteria. We detected an overall low expression level for bacteria expressing protein **2**, **16** and **21**, which resulted in poor segmentation.

Registration of bacteria

The image processing of the high-quality video allowed to segment each bacterium individually on the high-quality movie. They had to be subsequently identified in the binned movies acquired at high frame-rate under the regimes of low- and high-light illuminations I and II. To spatially associate the bacteria to their position in each binned video, we first cross-correlated a down-scaled version of F_r (obtained by binning four pixels in the F_r image; see Figure 4.6a) and the first frame of the binned movie (Figure 4.6b). Then the segmented pixels in the high-quality image were attributed to the binned pixels (see Figure 4.6c).[8] To avoid signal mixing, we subsequently discarded binned pixels

[5]Morphological image processing relies on the use of kernels - small patches of pixels - to modify the features in the image. One way to visualize morphological image processing is to consider the image as a 3D landscape where the value of a pixel represents its elevation in the third dimension. Morphological operations would consist in modifying the elevation locally with small tools like shovels and pickaxes. For all the operations we used (see Figure 4.4), the parameters were the size and shape of the kernel – a disk of radius varying between two pixels and seven pixels in our case.

[6]The auto-leveling consists in stretching the histogram of the pixels covered by the kernel to locally increase the dynamics.

[7]The Watershed Segmentation method consists in flooding the negative of the image Figure 4.4g from the position of the local maxima.

[8]We observed slightly different shifts in the two movies recorded under low- and high-light illuminations. Therefore, a bacterium segmented in the high-quality movie might be represented by $k_{N,low}$ pixels in the low-light movie and by $k_{N,high}$ pixels in the high-light movie, with $k_{N,low} \neq k_{N,high}$.

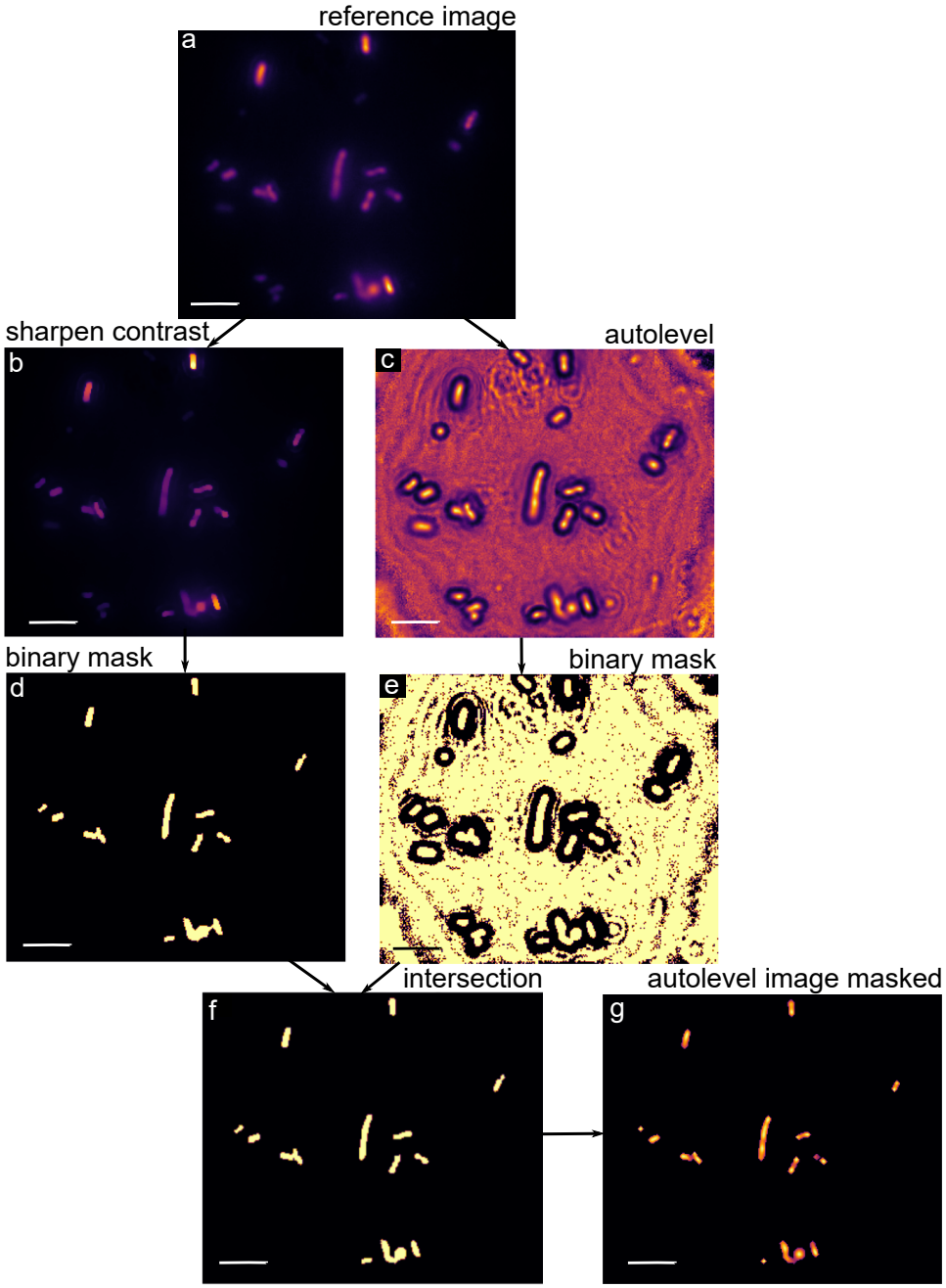

Figure 4.4: **a**: Reference image F_r; **b**, **d**: Application of the *rank.enhance_contrast* filter on the reference image F_r to yield an image with enhanced contrast (**b**), which is subsequently binarized (**d**); **c**, **e**: Application of the *rank.autolevel* filter on the reference image F_r to yield an image with sharpened frontiers of the bacteria (**c**), which is subsequently binarized (**e**); **f**: Intersection of the images **d** and **e**; **g**: Image obtained by masking the image **c** with the intersection mask **f**. Scaling bar = 5 μm.

corresponding to areas where two bacteria were present in the high definition image (see Figure 4.6d).

The segmentation allowed us to collect the fluorescence value at each pixel belonging to a bac-

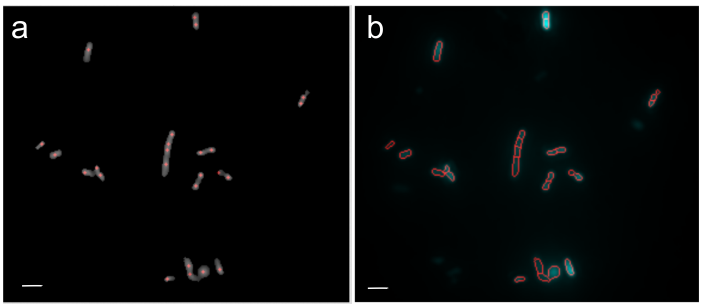

Figure 4.5: **a**: Image exhibiting the positions of the local maxima, source of flooding by the Watershed Segmentation method; **b**: Resulting segmented contours of the items. Scaling bar = 5 μm.

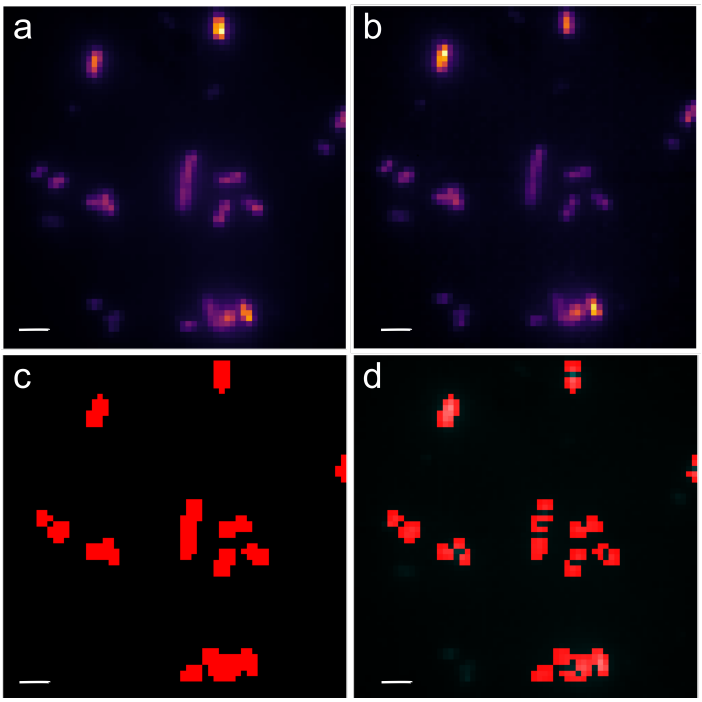

Figure 4.6: **a**: Downscaled version of the reference image F_r after 4×4 binning; **b**: First image of a binned video acquired at high frame-rate; **c**: Segmented pixels on the binned image; **d**: Segmented pixels without bacteria overlaps. Scaling bar = 5 μm.

terium in each frame. From the movie we extract the fluorescence response of each algae by summing the signal corresponding to the pixels in the algae, the time stamp of each frame, and the position and size (number of pixels) of each algae. The evolution of the ChlF signal over time is usually called a time series in machine learning, however since we will identify it as a pattern rather than exploiting the time dependence between consecutive values, we will later refer to them as "traces".

The adaptation of the segmentation code to single-cell algae is described in the Supplementary Materials. I also tried to use StarDist [156] without fine-tuning. It showed very similar results with sparse images of algae, but failed when the images displayed cells that underwent multiple cell-cycle divisions (as in Figure 2.11). Fully exploiting StarDist would have therefore required manual annotations, but since the morphological segmentation algorithm was already working I kept the presented solution. The segmentation could be improved by using Segment Anything [157] and single-shot fine-tuning, although a quick trial on the online demo gave poor results.

4.3.2 Machine learning key concepts

Supervised learning

Supervised learning involves training a model using labeled data, where the input variables (features) and their corresponding outputs (labels) are known. This approach aims to generalize patterns and relationships in the data to make accurate predictions or classifications on new data. Supervised learning allows to leverage existing knowledge and labeled data to build models that can interpret new similar yet unlabeled data. However, its main limitation is the need of labeled data, which may be time-consuming and costly to obtain (for example manual annotation of images for a segmentation task). Additionally, the models produced by supervised learning can suffer from overfitting if the training data does not adequately represent the true underlying distribution of the data. An overfitting model will perform very well on the training set but not generalize to new data.

Unsupervised learning

In contrast, unsupervised learning operates on unlabeled data, aiming to discover underlying patterns, structures, and relationships within the dataset. It involves techniques such as clustering, dimension reduction, and anomaly detection. Supervised learning is able to reveal hidden insights and structures within complex datasets without relying on prior knowledge or labeled data. This makes it particularly useful in scenarios where the data lacks labels or when the goal is to gain a deeper understanding of the dataset. However, the lack of labeled data in unsupervised learning raises a challenge when evaluating the quality and interpretability of the results. For example, the relationship between data form the same group identified by unsupervised clustering often requires further investigation.

Metric selection

Metric optimization refers to the process of selecting and tuning a performance metric that best represents the desired outcome or objective of a learning algorithm. It involves choosing a specific metric to evaluate the performance of the task completion, and then optimizing the model's parameters or architecture to maximize or minimize that metric.

Different machine learning tasks, such as classification, regression, and clustering, require specific metrics to assess their performance. For example, in the segmentation task described in the following manuscript, I used the F1 metric to evaluate the morphological segmentation's performance. If I had trained a segmentation neural network instead, I would have used this metric to guide the training of the network, using back-propagation[9].

If the training converges, it converges towards a local minima of the loss-function which maximizes or minimizes the metric on the training set. In regression tasks, metrics like mean squared error (MSE) or R-squared are often employed. For example, I used MSE in the light calibration articles to fit fluorescence curves with mathematical models (Chapters 2, 3). These metrics quantify the predictive accuracy, robustness, or other relevant characteristics of the models.

Metric selection involves selecting the most appropriate metric based on the problem domain and the desired outcome. Once the metric is chosen, the machine learning algorithm is trained to optimize the selected metric. In our case, we chose two consecutive models optimizing two different metrics (reconstruction and separability) and trained them separately.

Linear dimension reduction

Dimension reduction techniques aim to reduce the dimensionality of high-dimensional datasets while keeping the essential information. Reduction dimension techniques suffer from the risk to

[9]Back-propagation allows to update the model parameters in order to minimize a loss-function that is built from the definition of the metric.

discard atypical (yet significant) patterns in new data, as they were not trained to give them weight. I address this issue in the following manuscript.

Linear dimension reduction techniques, such as Principal Component Analysis (PCA - unsupervised) and Linear Discriminant Analysis (LDA - supervised), project the data onto a lower-dimensional space with projection matrices. In single-cell studies, linear dimension reduction methods offer several advantages, including interpretability[158, 159]. They are well-suited for datasets where linear relationships dominate and can effectively capture the global structure of the data. For this reason, I used a linear technique in the machine learning framework. However, linear techniques may struggle to capture complex nonlinear relationships, which I also investigate in the following manuscript.

Non-linear dimension reduction

Nonlinear dimension reduction techniques, on the other hand, are designed to capture and represent complex nonlinear relationships in the data. Methods such as t-distributed Stochastic Neighbor Embedding (t-SNE [160] - unsupervised) and Uniform Manifold Approximation and Projection (UMAP [161] - unsupervised) have gained popularity in analyzing biological single-cell data due to their ability to uncover intricate cellular heterogeneity. Nonlinear techniques allow to preserve local structures, enabling the identification of rare cell populations and revealing detailed cellular interactions. However, the outputs are often less interpretable than linear techniques. Interpretation and analysis of the results require careful consideration and validation, as nonlinear dimension reduction methods can introduce distortions and artifacts in the representation of the original data.[158]

Clustering

Clustering is an unsupervised technique used to group similar data points or objects together based on their inherent characteristics or patterns. The goal of clustering is to partition a dataset into distinct groups, called clusters, where the objects within each cluster are more similar to each other than to those in other clusters. The similarity or dissimilarity between data points is typically measured using distance metrics, such as Euclidean distance. Clustering algorithms aim to find the optimal arrangement of clusters by minimizing the intra-cluster distance and maximizing the inter-cluster distance. Some popular clustering algorithms include K-means [162], Density-Based Spatial Clustering of Applications with Noise (DBSCAN - [163]), and Gaussian mixture models (GMM) [162]. K-means clusters together points that project near each-other in a K-dimensional space. I made use of K-means on several occasions in the following part of the PhD thesis, in order to evaluate the separability performance of unsupervised dimension methods on our dataset. I also used it when I reproduced the experiments on a second microscope in Chapter 5: I evaluated if a clustering algorithm trained on the results in the following manuscript would properly classify data from the experiments ran on the second microscope.

Before detailing the elements used in the machine learning framework, I will introduce key concepts in machine learning.

4.3.3 Machine learning tools for analysis of fluorescence traces

Details on the level of supervision

I constructed a dataset where each fluorescence trace was attributed a label (qE, qT, qI, or 0). The label 0 corresponds to absence of qE, qT and qI simultaneously. The dataset was used to train a machine learning framework able to output stress scores from fluorescence traces. These scores quantify the contribution of qE, qT and qI developed by the plant in response to high-light. With David Colliaux and Benjamin Bailleul, we decided to train a machine learning framework relying on the biological knowledge we had of the processes that induce qE, qT and qI.

To build the training dataset, we selected a set of mutant and wild-type strains, and conditioned them to express only one stress response at maximum (qE, qT, qI, or no response). We were guided by Sandrine Bujaldon and Francis-André Wollman in this task. To be more precise, we chose a mutant of stt7, the gene coding for STT7, for the negative control of state-transition (qT absent), and the wild-type with the same genetic background for the population expressing the trait. Instead of using a mutant for qE, I suggested to use the strains before qE-activation for the negative control of energy-dependent quenching (qE absent), and after activation for the population expressing the trait. Finally, I designed how to use populations taken from growth light for the population expressing qI, and exposed them to high-light until they reached a steady state of degradation and repair.

Yet, we did not attribute a score to these traces, which would have been a stronger information. There are methods that could have been used to attribute a score, since many studies have addressed this question, in particular for plants where the kinetics of the three NPQ processes are less entangled in the fluorescence traces than in algae. This method relied on identifying three specific points corresponding to the full relaxation of each kinetic response consecutively, and deriving NPQ metrics from these points [164]. There are also some metrics derived for NPQ in *Chlamydomonas reinhardtii*[146, 165]. In our case, we decided to use these metrics rather to support our method (which requires less biological knowledge) *a posteriori*.

Details on the choice of metrics: reconstruction and separability

In our case, we used the hypothesis that the kinetics of the elementary processes would be preserved when expressed together, and therefore studying the elementary kinetics to train the machine learning algorithm is sufficient to later investigate the phenotype with the combined kinetics (wild-type). To test this hypothesis, we introduced a dimension reduction step optimized under a reconstruction metric. We used dictionary learning that captures the underlying structure or patterns in the data by adaptive selection of a set of basis functions (called atoms). For this method, the labels are not required because the model identifies specific patterns in the ChlF traces. Once the model was trained, we fed it with the wild-type traces. Being able to reconstruct the fluorescence trace properly as a linear combination of the basis atoms would validate the hypothesis. On the other hand, a large reconstruction error would mean that the processes in the wild-type are expressed differently when they co-occur, and the hypothesis is wrong. Dictionary learning also provides significant information to identify new phenotypical traits that give rise to a high reconstruction error.

The final objective is to output scores for each trait. To achieve this goal, I applied a second dimension reduction technique that requires the labels to optimize the separation of the classes. The method used is Linear Discriminant Analysis, which aims at projecting the data in a space where each population with the same label is clustered together and each cluster can be separated by hyperplanes [162]. This method is often followed by clustering in order to build a model that can be used to classify the new data. In the study, I rather took advantage of the linearity of the method transformation combined with the specific construction of the dataset to use the low-dimension space as an NPQ-space, where each axis represents an NPQ component.

In the following I detail the mathematical models of Dictionary Learning and Linear Discriminant Analysis, and later introduce the manuscript describing the experimental work.

Reconstruction step: Dictionary learning

In order to perform data reconstruction, or data approximation, a model of the data is needed. The most common reconstruction methods are Fourier methods, which allow to decompose a periodic function as a sum of trigonometric functions (Fourier series), with an extension to non-periodic functions (Fourier transform). Related, the Wavelet transform allows to represent an input as a combination of wavelets taken from described datasets (e.g. Haar [166], Daubechies [167]). They are dimension reduction methods: an image of dimension N^2 can be approximated by a sparse set of M coefficients that weight the wavelets. Wavelet transforms are often used in data compression

because they allow to build a lighter representation of a sound, an image, a video, etc. It is a materialization of dimension reduction. In those methods, the underlying model of the data is known (Fourier base, wavelets set). The underlying model can also be a parametric function and the aim of the representation is to find the parameters. This strategy will be used in the DREAM project, but for this work we decided to evaluate what level of information could be retrieved using an agnostic method. The underlying model can also be learned from a training set, for example with Dictionary Learning. The objective is to learn a dictionary of M basis elements that best reconstructs the dataset through weighted linear combinations [168]. These M basis elements are called atoms, designated as D_i for $i \in [0, M]$. Then, new data can be reconstructed as a linear combination of the atoms (Figure 4.7). A sparsity constraint is added on the coefficients, so that new data is represented with a minimal number of atoms. It is important to describe the data with a low amount of coefficients when the dictionary size is big, but also to avoid overfitting the signals with multiple summed atoms. The idea of learning a sparse code over a large collection of dictionary elements was initially proposed in [169] when building a theory of computation in primary visual cortex based on the observation that natural images can be seen as a composition of many primitive elements. The labels are not required to learn the dictionary.

We used the dictionary learning method introduced by Mairal et al [168], which is in an online method: the training set is fed sequentially (sample by sample or subset per subset) to the algorithm which updates gradually the dictionary by minimizing a cost function. This cost function includes a penalty on the mean-squared error of reconstruction and the sparsity of the linear coefficients, detailed in the Methods of the manuscript under writing at the end of this Chapter.

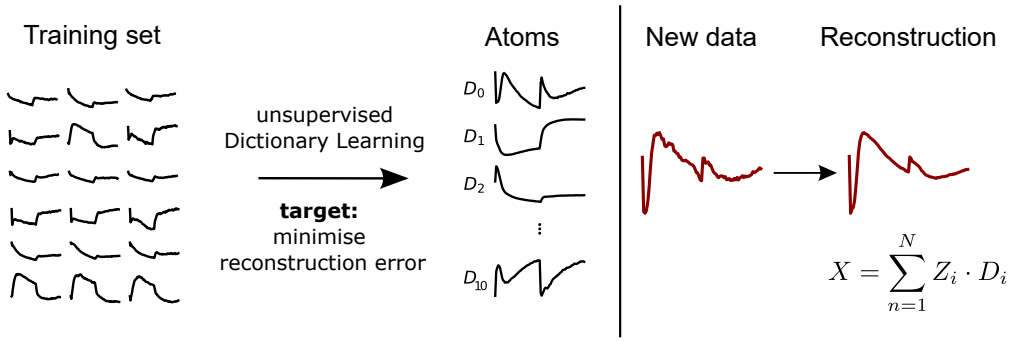

Figure 4.7: *Principle of Dictionary learning.* A set of M atoms is learned from a training set of unlabeled data. The metric optimized is the quality of reconstruction of the traces, with a sparsity penalty. The dictionary can be used to build a reconstruction of a new signal as a linear combination of the atoms.

Classes separation: Linear Discriminant Analysis

The Linear Discriminant Analysis (LDA) is a supervised dimension reduction method that allows to separate data with distinct labels in the low-dimension space. It was historically introduced by Fisher [170] with an example applied to classify Iris species based on the taxonomy of their petals and sepals. I will introduce the principle of LDA with the case of two classes in d-dimensions based on the derivations presented in"Pattern Classification"[10]. I will also summarize the multiclass problem in order to explain the dimensionality constraint on the projected space that led us to chose four classes to reach a 3-dimensional space of the NPQ components.

We define a set of n samples $\mathbf{x_1}, ..., \mathbf{x_n}$ in the d-dimensional space $\mathbb{R}^d$ split into two classes: ω_1 and ω_2. They define two groups, Ω_1 and Ω_2. Let $\mathbf{w}$ be a projection matrix from $\mathbb{R}^d$ to $\mathbb{R}$. We define the projection of the vector $\mathbf{x_i}$ in the 1-dimensional space $\mathbb{R}$ as:

[10]"Pattern Classification" [162], Chapter 3.8 "Fisher Linear Discriminant".

$$y_i = \mathbf{w}^t \mathbf{x}_i \tag{4.1}$$

The two groups Y_i correspond to the projections of the groups Ω_i.

The objective of the LDA is to find the projection $\mathbf{w}$ that allows to best separate Y_1 from Y_2 in the projection space $\mathbb{R}$. Figure 4.8 presents the outcome of the projection by two different matrices $\mathbf{w}$, one that allows well to separate the classes and the other not.

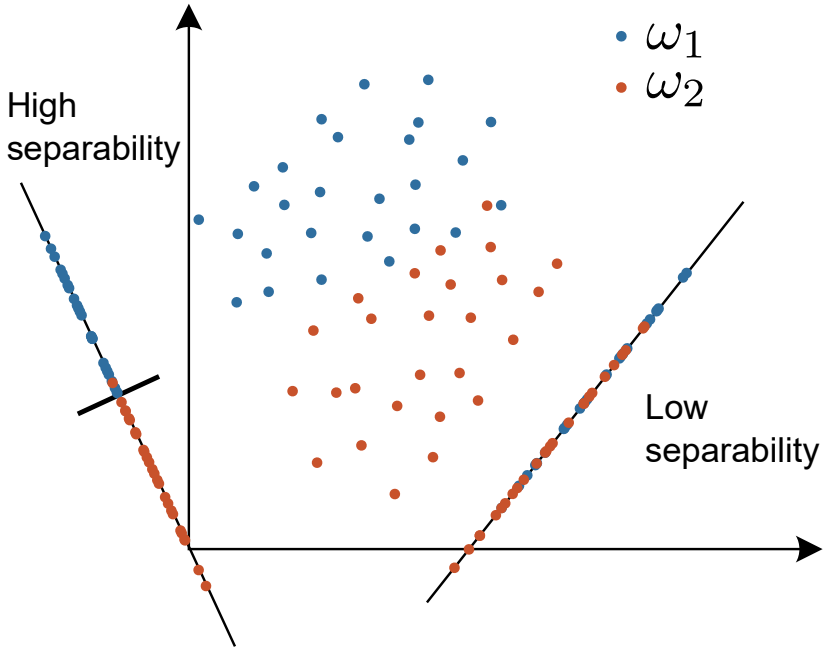

Figure 4.8: *Principle of Linear Discriminant Analysis* (simplification: $d = 2$). The two classes labeled ω_1 and ω_2 are projected on a one-dimension line. The direction of the line enables the best separation of the data points belonging to different classes.

A measure of the separation between the projected points is first the difference of the sample means. The d-dimensional mean of the samples belonging to class ω_i (n_i samples) is named m_i and given by:

$$\mathbf{m}_i = \frac{1}{n_i} \sum_{x \in \Omega_i} \mathbf{x} \tag{4.2}$$

The average of the projections y_i is given by:

$$\widetilde{m}_i = \frac{1}{n_i} \sum_{x \in \Omega_i} \mathbf{w}^t \mathbf{x} = \mathbf{w}^t \frac{1}{n_i} \sum_{x \in \Omega_i} \mathbf{x} = \mathbf{w}^t \mathbf{m}_i \tag{4.3}$$

which is the projection of $\mathbf{m}_i$.

The distance between the projected means is:

$$|\widetilde{m}_1 - \widetilde{m}_2| = |\mathbf{w}^t (\mathbf{m}_1 - \mathbf{m}_2)| \tag{4.4}$$

Second, the separability is characterized by the variance within projected data with the same class. To simplify, if the distance between the means is greater than the intraclass variance, the data are easily separable. The LDA method introduces the *scatter* defined as the sum squared distance to the class mean:

$$\widetilde{s}_i^2 = \sum_{y \in Y_i} |y - \widetilde{m}_i|^2 \tag{4.5}$$

Thus, $(1/n)(\widetilde{s}_1^2 + \widetilde{s}_2^2)$ is an estimate of the variance of the pooled data, and $\widetilde{s}_1^2 + \widetilde{s}_2^2$ is called the total within-class scatter of the projected samples.

As such, the objective of the LDA is to maximize the criterion function:

$$J(\omega) = \frac{|\widetilde{m}_1 - \widetilde{m}_2|^2}{\widetilde{s}_1^2 + \widetilde{s}_2^2} \tag{4.6}$$

To obtain J as an explicit function of w, we introduce $S_B = (\mathbf{m}_1 - \mathbf{m}_2)(\mathbf{m}_1 - \mathbf{m}_2)^t$ when we develop the expression:

$$|\widetilde{m}_1 - \widetilde{m}_2|^2 = |\mathbf{w}^t(\mathbf{m}_1 - \mathbf{m}_2)|^2 \tag{4.7}$$
$$= \mathbf{w}^t(\mathbf{m}_1 - \mathbf{m}_2)(\mathbf{m}_1 - \mathbf{m}_2)^t\mathbf{w} \tag{4.8}$$
$$= \mathbf{w}^t\mathbf{S_B}\mathbf{w} \tag{4.9}$$

Similarly, we develop the expression of the scatters $\widetilde{s}_i^2$:

$$\widetilde{s}_i^2 = \sum_{x \in \Omega_i} (\mathbf{w}^t\mathbf{x} - \mathbf{w}^t\mathbf{m}_i)^2 \tag{4.10}$$
$$= \sum_{x \in \Omega_i} \mathbf{w}^t(\mathbf{x} - \mathbf{m}_i)(\mathbf{x} - \mathbf{m}_i)^t\mathbf{w} \tag{4.11}$$

We introduce the notation $S_i = \sum_{x \in \Omega_i}(\mathbf{x} - \mathbf{m}_i)(\mathbf{x} - \mathbf{m}_i)^t$ so that $\widetilde{s}_i^2 = \mathbf{w}^t S_i \mathbf{w}$

As such,

$$\widetilde{s}_1^2 + \widetilde{s}_2^2 = \mathbf{w}^t(S_1 + S_2)\mathbf{w} \tag{4.12}$$

We introduce the notation $\mathbf{S_W} = S_1 + S_2$. $\mathbf{S}_W$ is called the *within-class scatter matrix* and $\mathbf{S}_B$ is called the *between-class scatter matrix*. Interestingly, we notice that $\mathbf{S}_B$ is the outer product of two vectors, therefore its rank[11] is at most one.

In terms of $\mathbf{S}_B$ and $\mathbf{S}_W$, the criterion function J(·) can be written as:

$$J(\omega) = \frac{\mathbf{w}^t\mathbf{S}_B\mathbf{w}}{\mathbf{w}^t\mathbf{S}_W\mathbf{w}} \tag{4.13}$$

The multi-class problem is also described with $\mathbf{S}_B$ and $\mathbf{S}_W$.

They are computed following:

$$S_B = \sum_{i=1}^{c} n_i(\mathbf{m}_i - \mathbf{m})(\mathbf{m}_i - \mathbf{m})^T$$

Where S_B has dimension $d \times d$.

- $\mathbf{c}$ is the number of classes,
- $\mathbf{n_i}$ is the number of samples in class i,

[11]The rank represents the maximum number of linearly independent rows or columns in the matrix. It represents the level of information brought by each rank/column. For example, if a column is the linear combination of two other columns, it does not bring new information.

- $\mathbf{m_i}$ is the mean vector of class i in the input space,
- $\mathbf{m}$ is the overall mean vector of all the data points,

$$\mathbf{S}_W = \sum_{i=1}^{c} \sum_{\mathbf{x} \in X_i} (\mathbf{x} - \mathbf{m}_i)(\mathbf{x} - \mathbf{m}_i)^T$$

Where S_W has dimension $d \times d$.

- $\mathbf{c}$ is the number of classes,
- $\mathbf{\Omega_i}$ represents the set of data points belonging to class i in the input space,
- $\mathbf{x}$ is a data point in the input space,
- $\mathbf{m_i}$ is the mean vector of class i,

It can be shown [162] that the solution corresponds to solving:

$$\mathbf{S}_B \mathbf{w}_i = \lambda_i \mathbf{S}_W \mathbf{w}_i \tag{4.14}$$

where $\mathbf{w}_i$ represent the columns of the projection $\mathbf{w}$ for each dimension of the output space and λ_i a variable. It becomes an eigenvalue problem if $\mathbf{S}_W$ is invertible. $\mathbf{S}_B$ is a sum of c-matrices of rank one or less. Since $\mathbf{m}$ is a linear combination of the $\mathbf{m}_i$, only c-1 of these matrices are independent. Therefore, $\mathbf{S}_B$ is of rank c-1 or less. Thus, $\mathbf{S}_W^{-1}\mathbf{S}_B$ rank's is no more than c-1. At most c-1 eigenvalues are nonzero, and the desired eigenvectors correspond to these nonzero eigenvalues. As a consequence, the larger dimension of the projection space is c-1. It explains why I used four classes to reach a 3-dimensional NPQ space.

4.4 Manuscript: Scoring of NPQ components in *C. reinhardtii*

4.4.1 Abstract

Understanding the regulation processes of photosynthesis at the single-cell level has become crucial to better exploit photosynthetic organisms. This work explores the potential of single-cell studies to reveal cellular heterogeneity and identify correlations in photosynthetic traits. By leveraging single-cell imaging, we propose a novel machine-learning framework that analyzes temporal chlorophyll fluorescence responses to effectively separate and quantify co-occurring stress-response mechanisms, offering valuable insights into the functional response and stress adaptation of photosynthetic organisms. Our study focuses on the dynamic light-stress response of the unicellular green alga *Chlamydomonas reinhardtii*, demonstrating the power of this approach in advancing phenotypic characterization and complementing single-cell omics approaches.

4.4.2 Introduction

The biomass of photosynthetic organisms is a key resource for producing food, feed, energy, and materials. The current organisms and cultivation practices necessitate significant resources and exert major environmental impacts. Moreover, Earth experiences climate evolution. Thus it is relevant and timely to bring new insights that would enable the selection or design of new photosynthetic organisms and enable their parsimonious cultivation [171].

Most of the existing knowledge on photosynthesis has been derived from measurements at the organism or tissue level for plants, and bulk measurements for unicellular organisms [172]. These measurements reflect the combined behavior of multiple cells, smoothing out their individual contributions. Although having revealed major insights into the biology of photosynthesis, those studies cannot demonstrate cellular heterogeneity, which is observed even within monoclonal populations [173, 174]. In contrast, single cell studies are relevant to access the distribution of biophysical traits and evidence their correlations. It is a prerequisite to increase the proportion of a population endowed with a favorable trait on the basis of understanding the underlying process controlling those traits.

There has recently been a surge in the development of single-cell sequencing technologies probing "omics" data from genomics, proteomics, metabolomics, lipidomics and glycomics [158]. A new challenge is to integrate them with physiological data and connect changes in genes expression and proteins, sugar and fat synthesis with physiological changes. For this purpose, being able to quantify a physiological process from a biological observation becomes necessary.

This has been a goal of a few reported studies of unicellular photosynthetic organisms at the single cell level [85, 87, 99, 100, 107, 175–183]. Most of them have relied on endogenous chlorophyll fluorescence (ChlF), an approach with a century-long history [109, 184]. After absorption by the antenna pigments of the chloroplast, light energy is funneled to the reaction center of PSI or PSII, which gets excited. Its deexcitation mostly involves electron transfers to the closest acceptor in the photosynthetic chain. However, it also occurs through competitive pathways: heat and fluorescence. Hence, the fluorescence level is a proxy of photochemical (effective photosynthesis) and non-photochemical (dissipation as heat) quenching, which makes it to be widely used for reporting on the efficiency of the photosynthesis realization.

Photosynthesis is tightly coupled to the metabolism of photosynthetic organisms and it benefits from an efficient regulation occurring over multiple time scales [68–70]. Consequently, the ChlF response detected under application of tailored temporal sequences of illumination mirrors the kinetics of realization of numerous biological processes. Thus, it contains rich and specific information on the functional response of the system, which makes it a favorable asset of the physiological state and a good candidate to evaluate biotic and abiotic stress responses in a perspective of phenomics [60, 61].

Yet, an appropriate metric has to be harnessed to fully exploit the temporal ChlF response in the latter purpose. Well-established metrics have been empirically derived from basic mathematical

processing of specific values in the ChlF traces (timestamps, inflection points or local extrema) [109, 146, 185–187]. However, the ChlF trace is the result of overlapping contributions from several co-occuring biological processes associated with their respective amplitudes and characteristic times of the kinetics: a ChlF point on the trace intricately reflects the combination of these contributions. Untangling the contributions of the co-occuring processes can be achieved by introducing complementary observables. Nevertheless, this strategy comes at the cost of complexifying the instruments and protocols (for instance the fluorescence lifetime can be measured along the fluorescence [165]). In this report, we alternatively introduce a new computational method to analyse the complex ChlF trace and effectively separate the contributions of the co-occuring processes.

This computational method relies on the construction of a low-dimension space in which the ChlF traces are projected, allowing to interpret the biological processes they reflect. It relies on the exploitation of training populations expressing the elementary processes that define the axis of the base of the low-dimension space. In this report, we make the hypothesis that the kinetic behavior of a population of wild type individuals (expressing multiple processes simultaneously) can be satisfactorily accounted for by a referential of populations expressing the different elementary processes separately. We take advantage of a study at the single cell level to test this hypothesis. Thus, we can overcome a description relying on a phenomenological exploitation of the ChlF trace and use the latter to assign an unambiguous, agnostic phenomic score relying on biological processes.

To illustrate our perspective, we selected the response of photosynthetic organisms to light stress as a case study. In natural media, the intensity and wavelength distribution of sunlight exhibit strong fluctuations over time scales expanding from the second to the month [77, 188]. Photosynthetic organisms have evolved several processes to cope with these fluctuations, which enable them to dissipate the excess of energy when the light intensity peaks and maximize the photon intake when the light reaches a low [68]. The study of the light-stress response has become critical in photosynthesis research as it is the main adapting process effected by the plants and algae [90, 189] and is easy to implement quantitatively.

In this study, we focus on regulating processes manifesting as nonphotochemical quenching of ChlF (NPQ) [190, 191], which are driven by light fluctuations from seconds to hours driven by factors such as surface wave movement, vertical movement of phytoplankton, overlapping and shifting leaves, as well as clouds passing overhead [77, 188]. Governing the NPQ kinetics is presently debated for improving several aspects of photosynthetic efficiency [192–196].

For our case study, we addressed the dynamic light-stress response in a reference organism of photosynthesis research: the unicellular green alga *Chlamydomonas reinhardtii* [89, 90, 197]. After a specific activation protocol [97], *Chlamydomonas reinhardtii* exhibits significant amplitudes of three extensively studied NPQ components: qE, qT, and qI. The fastest NPQ component is energy-dependent quenching, abbreviated qE. Taking place at the timescale of second to minutes, it originates from a pH-dependent change of conformation of the stress-related Light Harvesting Complexes (LHCSR). Under low light, these antennas absorb light and transfer it to reaction centers to perform photosynthesis. Under light excess, a proton gradient builds-up accross the thylakoid membrane and the pH of the lumen decreases, which drives the protonation of LHCSR residues exposed to the lumen [189, 198]. The LHCSR then become quenchers and dissipate the absorbed excitation through heat rather than propagating it to the reaction centers. The second NPQ component is state-transition, and is called qT. It happens within minutes and involves the reversible binding of the secondary light-harvesting antennas to the reaction centers of PSI and PSII. The reversible binding is driven by their phosphorylation by the kinase STT7 and dephosphorylation by PBB1-PCSB [199, 200]. Depending on binding, the antennas preferentially channel energy to PSII (state 1) or PSI (state 2), to balance the energy input of the photosynthetic chain. Photoinhibition is the last NPQ component known as qI. It is induced over tens of minutes to hours and relaxes even more slowly. It occurs due to a light-induced modification in the equilibrium of the continuous degradation-and-repair process of the reaction centers involving the protein D1 [201, 202]. Under high-light, the repair rate slows down because D1 is damaged. As a consequence, less energy fuels the photosynthetic chain. Under exposure to high-light of 15 minutes to one hour, the co-occurring NPQ components qE, qT and qI

simultaneously shape the ChlF time response of wild-type strains with their characteristic signatures.

Moreover, it is easy to control the extent of the qE, qT and qI components in *Chlamydomonas reinhardtii* either by adopting mutants or specific conditioning protocols. Hence, it is a favorable system to evaluate the relevance of our perspective to deliver quantitative phenotypic information from the dynamical NPQ traces. To accomplish this goal, a machine learning algorithm has been trained on a biological dataset consisting of reference populations of mutants and pre-conditioned strains, each exhibiting at maximum one NPQ component (qE, qT, qI or no response). The training enabled the algorithm to learn how to project a ChlF trace in a lower-dimension (3-dimensional) space, where each axis represents one of the three NPQ component. Once the transformation method was learned, it has been applied to the ChlF trace of a wild-type strain.

4.4.3 Results

A favorable observable to probe photosynthesis at the single-cell level: chlorophyll fluorescence

ChlF is interrogated by applying constant or time-modulated light for perturbing the photosystem and measuring its response [128]. In the conventional method of Pulse-Amplitude Modulated (PAM) fluorometry [129], the photosynthetic organism that has been dark-adapted is exposed to a sequential pattern of light intensities. This pattern first includes light resembling sunlight (actinic light, tens to hundreds of μmol(photons) $\cdot\, \mathrm{m}^{-2} \cdot \mathrm{s}^{-1}$) and high-intensity light that saturates the photosynthetic chain (saturating pulse, $>$ 1000 μmol(photons) $\cdot\, \mathrm{m}^{-2} \cdot \mathrm{s}^{-1}$, 0.2-1 s), whose purpose is to bring the plant to different saturation states of the photosynthetic chain. These components are complemented by short pulses with low intensity (measuring pulses, $<$ 10 μmol(photons) $\cdot\, \mathrm{m}^{-2} \cdot \mathrm{s}^{-1}$, shorter than 10 ms) that probe the state of the photosystem without perturbing it. In particular, PAM allows to assess the quantum yield of photosynthesis, denoted as ϕ_{PSII}, and NPQ, which measures the dissipation as heat.

Harnessing PAM in fluorescence microscopy for imaging a population down to the single cell level is a major challenge due to low photon count [88, 100, 175, 203–205]. No more than one fluorescence photon per pixel is emitted in response to the measuring pulses when using a 10x objective lens to image a cell [206] (adapted from [86] for a single *Chlamydomonas reinhardtii* cell with the correction made for the field of view size). This value is comparable to the noise level of a camera. To tackle this limitation, different strategies have been implemented in single-cell instruments, often at the cost of using stronger or longer measuring pulses that perturb the system [84].

As validated below, the direct ChlF response to the saturating pulses can advantageously replace the weak one from the measuring light to study NPQ. Accordingly, we built a Python-based fully automated microscope for applying versatile light-protocols to photosynthetic organisms (leaves, algae) with sub-cellular imaging resolution (see Section 4.5.1 of the SI). It enabled us to perform long-term experiments to study NPQ on the same cells by measuring the time evolution of their ChlF response to a repeated saturating pulse of fixed high light intensity, while exposing the system to high actinic light or relaxing it in the dark. More precisely, we modified an illumination protocol inducing simultaneously qE, qT and qI [146, 185] to study the high-light response. It involves four consecutive repetitions of a 30 min-long basic pattern consisting in strong actinic blue light (400 μmol(photons) $\cdot\, \mathrm{m}^{-2} \cdot \mathrm{s}^{-1}$, 470$\pm$10 nm) for 15 min followed by 15 min of dark with simultaneous application of a saturating pulse every 20 seconds (1300 μmol(photons) $\cdot\, \mathrm{m}^{-2} \cdot \mathrm{s}^{-1}$, 405$\pm$7 nm, 200 ms) (see Section 4.5.2 of the SI). The actinic light is turned off during the saturating pulse. Hence the measured ChlF level (F_M) originates from the application of the saturating pulse only. The camera records a movie during each basic pattern and a segmentation algorithm allows to retrieve the ChlF temporal trace of each algae, from which the response to saturating pulses are retrieved (F_M).

Presentation of the reference dataset

The diversity and complexity of the F_M traces collected from individual algae of a wild-type strain submitted to our illumination protocol is shown in Figure 4.9a. In order to identify the contribution of each NPQ component to the F_M trace, we designed a set of strains displaying only one of the three elementary stress-response component, or no stress-response (see Table 4.1 and Methods):

- **qE** Two strategies can be used to study qE. One is to use mutants of the two types of antennas contributing to qE (LHCSR3 and LHCSR1 [97]), the strains (*npq4*) and LHCSR1 (*lhcsr1*) or the double-mutant *npq4-lhcsr1*. The other is to take advantage of the inducible expression of these antennas. In *Chlamydomonas reinhardtii*, the latter are only synthesized in response to prolonged high-light exposure [97]. We selected the second option, exploiting the negligible level of LHCSR expression under low growth-light conditions to study strains without qE, and forcing the LHCSR expression upon 2–8 h exposure to high-light [97] (later referred as qE-activation). qE-activated cells are identified with the symbol *. The qE-activation was directly performed under the microscope, which allowed us to monitor the same cells before and after the expression of LHCSR.

- **qT** A common mutant to study state-transition is *stt*7 which lacks the kinase STT7. In the wild-type, the protonation of this kinase drives unbinding of the mobile LHCII antennas from PSII (state 1-to-state 2) [90]. In consequence, the mutant *stt*7 is blocked in state 1. We used the non-leaky mutant *stt7-1* [200] as a negative control of state transition (qT absent) and wild-types as positive controls (qT present).

- **qI** There is no mutant specifically for qI. Instead, we rely on the changing dynamics of qI, as follows. Both qE-activation and high-light exposure for observing NPQ induce photo-inhibition. In order to attenuate the contribution of photo-inhibition to the ChlF dynamics, we repeated four times in a row our basic pattern of illuminations before and after qE-activation. The first occurrences of the basic pattern induces non-stationary photo-inhibition but in the last two repeats the photodamage-repair rates are at equilibrium [202], which has been evidenced by the equivalent level reached by the first and last saturating pulses F_M of the basic pattern. When the damage and repair rates are at equilibrium, we consider the cell to be photoinhibited (symbol ^{i}).

Since no triple-mutant *stt7-1-npq4-lhcsr1* has yet been obtained to our knowledge, we further exploited the culture of *stt7-1* before qE-activation as a double-negative control for qE and qT.

Generation of the reference dataset

After selecting the mutants and experimental conditions, we generated the reference dataset for our machine learning framework. It was made of a collection of four sets of F_M traces acquired from movies of hundreds of algae cells (Figures 4.9b,c), where each population either displays a single elementary light-stress response (qE, qT or qI) or no light-stress response at all (see Table 4.1, Methods and 4.5.2 of the SI for a description of the sample preparations).

Figure 4.9c further shows the average responses computed from the dataset collections of individual traces. They compare well with the measuring pulses fluorescence traces from the same populations conditioned in liquid state, submitted to the same actinic and saturating pulse sequence, and observed under a fluorescence macro-imaging system (Speedzen MX, JBeamBio, France) (see Figure 4.9d) [86, 146]. The corresponding agreement validates our exploitation of the direct fluorescence with respect to protocols based on measuring pulses.

As observed in previous works [146, 165, 207], we identified five phases (I – V) on the fluorescence traces, indicated in Figure 4.9c,d. a fast (<30 s - *Phase I*) decay of ChlF at the light onset for the population ***stt7***^{i}. It is a consequence of the increase of the lumen pH under high-light: the LHCSRs

Name	total experiments	total algae	qT	qE	qI
stt7^{i}	3	433			
stt7	3	453			✓
****stt7***^{i}	3	480		✓	
wt4^{i}	4	936	✓		

Table 4.1: *Dataset description.* Strains, conditioning, and acquisition: ***stt7***^{i}: not qE-activated, third repeat of the basic pattern: photoinhibited (no qI), lacks qT, lacks qE; ***stt7***: not qE-activated, first repeat of the basic pattern: exhibits qI, lacks qT, lacks qE; ****stt7***^{i}: qE-activated, last repeat of the basic pattern: photoinhibited (no qI), lacks qT and exhibits qE; ***wt4***^{i}: not qE-activated, last repeat of the basic pattern: photoinhibited (no qI), exhibits qT and lacks qE. Name code: **stt7**: mutant lacking STT7 (qT absent) **wt4**: wild-type expressing STT7 (qT present) , ^{i}: photoinhibited by consecutive exposures to the basic pattern (qI absent), *: qE-activated by prolonged exposure to high-light, expressing LHCSRs (qE present). Shaded cells: NPQ component absent, checkmark: NPQ component present.

get protonated and do not anymore act as antennas but as quenchers. We observe a fast (<2 min, *Phase IV*) relaxation when the light turns off as a consequence of the recovery of the dark lumen pH. Interestingly, we also observe a relaxation of the quenching over 2-5 min (*Phase II*) following the light onset which could be attributed to a relaxation of qE. The ***wt4***^{i} population displays an increase in the ChlF response at the light onset, corresponding to the dephosphorylation of the LHCII antennas and their consequent binding to PSII, increasing its photon collection capacity. Time-wise, this bump overlaps with the increase of ChlF in *Phase II* in the ****stt7***^{i} population, which makes them hard to be discriminated when both qE and qT are expressed. When the light is turned off, the ChlF decays slowly (*Phase V*), revealing the unbinding of the LHCII antennas from PSII. In the ***stt7*** population, the high light induces a decay of the ChlF exhibiting the degradation of the reaction centers by photoinibition. The ChlF does not fully recover in the dark, resulting in an overall decay of F_M before and after the basic pattern exposure. The three mechanisms co-occur between 5 and 10 minutes (*Phase III*).

Two other remarks arise from the elementary traces (Figure 4.9c): the algae from the ***stt7***^{i} population show a slight drop in ChlF at the light onset characteristic of qE although they are expected to display no stress-response. This can be explained by the lack of state-transition capacity during the growth which could result in a quicker capacity to express qE under high light. This led us to select the third repeat of the basic pattern, which presents less qE than the fourth repeat, for ***stt7***^{i} of the fourth to build the dataset since less (see Figure 4.17 in the SI for a visual understanding of the experimental data). The second observation is that ***stt7*** display a smaller photoinhibition response than wild-type (see the photoinhibition of wild type *wt4* in Figures 4.18c and 4.27 of the SI), probably because they are already photoinhibited by the growth light. Finally, the photoinhibition equilibrium is not completely reached for the ***stt7***^{i} and ***wt4***^{i} population which could alter the performance of the following machine learning algorithm. The photoinhibition mechanism is distinct from qE and qT because our controls are not ideal since the qI is present in all the strains although we tried to minimize its contribution by waiting for the equilibrium to be reached between the damage and repair rates (photoinhibited populations). We kept it to build the 3D NPQ space and deconvolve its effect from the other stresses, but later on focused only the analysis and interplay of qE and qT using photoinhibited strains (^{i}, qI absent).

From the reference dataset to a base of elementary NPQ components in a 3D space

We used the reference dataset with a machine learning framework to build a base in a 3D NPQ space where the axes x, y, and z are associated to elementary biological processes driving the NPQ components qE, qT, and qI respectively. The framework performs two consecutive steps of dimension reduction to transform the F_M traces into a 3D vector that can be interpreted from a biological

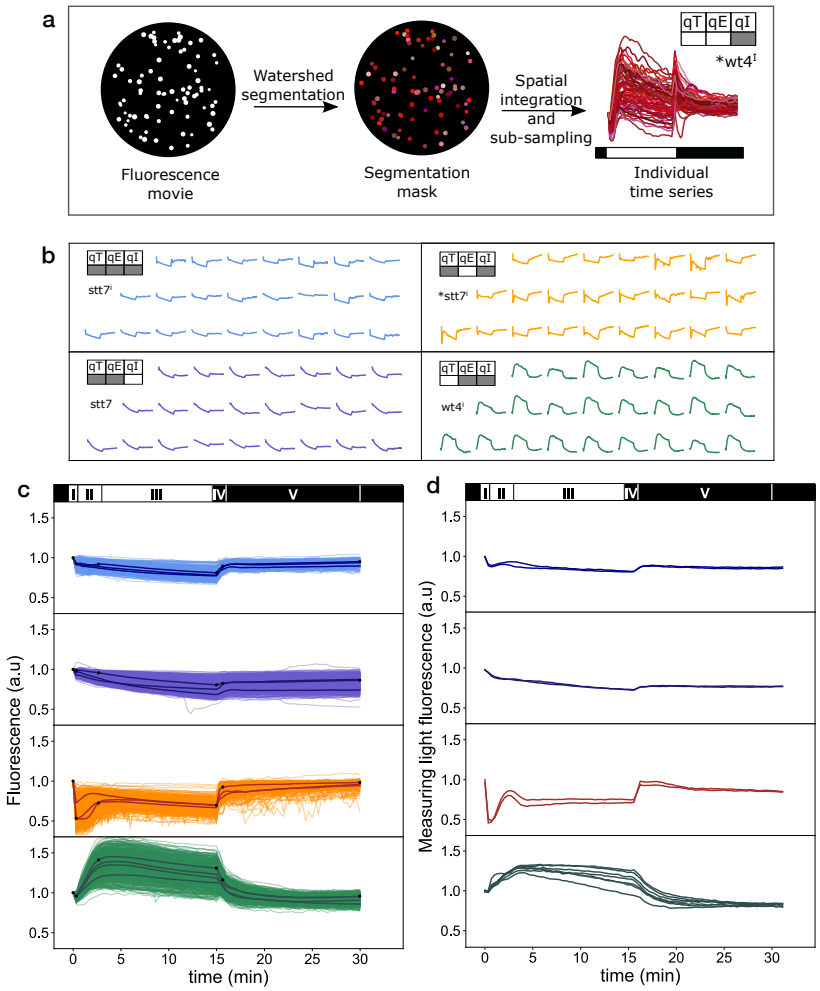

Figure 4.9: *Steps towards acquisition of the reference dataset for quantitative phenomic scoring of NPQ relying on biological processes.* **a**: *Extraction of the ChlF time traces F_M from single algae cells imaged in fluorescence microscopy.* Watershed segmentation is used to compute a segmentation mask, which is applied to each frame of the recorded movie to collect the temporal ChlF response of each segmented alga. Sample: population of a wild type strain, which expresses qE and qT (***wt4***^{i}: qE-activated, photoinhibited); **b**: *Randomly sampled F_M traces of the four populations used to build the reference dataset.* ***stt7***^{i}: not qE-activated, photoinhibited; ***stt7***: not qE-activated, dark-adapted; ****stt7***^{i}: activated, photoinhibited; ***wt4***^{i}: not qE-activated, photoinhibited. One population (***stt7***^{i}) expresses none of the stress-responses whereas the other ones express only one of the elementary stress responses (either qI – ***stt7***, qE – ****stt7***^{i}or qT – ***wt4***^{i}) during the experiment; **c**: *Average (dark lines) and accumulated (light lines) F_M traces of the four populations used to build the reference dataset.* From top to bottom: ***stt7***^{i} (3 experiments – 433 algae), ***stt7*** (3 experiments – 453 algae), ****stt7***^{i} (3 experiments- - 480 algae), ***wt4***^{i} (4 experiments – 936 algae); **d**: *Validation of the microscope setup.* Overall F_M traces from the four populations used to build the reference dataset obtained from bulk measurements by using the MacroSpeedZen. From top to bottom: ***stt7***^{i} (2 repeats), ***stt7*** (2 repeats), ****stt7***^{i} (2 repeats), ***wt4***^{i} (5 repeats). In **c** and **d**, the ChlF data are normalized to $F_M(0)$, and the illumination regime (HL or dark) is identified on the top and the five phases I–V used for *ad hoc* NPQ evaluation are identified as blocks (and further as points on the F_M traces in **c**).

viewpoint. Each step learns to optimize a different metric. The first step aims at learning how to reconstruct a ChlF trace in a lower-dimension space with a minimal reconstruction error. It

ensures that the pipeline will be able to interpret new data as a combination of the waveforms learned in the training phase. Any failure to reconstruct the trace will either invalidate our working hypothesis or demonstrate the outbreak of a new phenotype in the input data. It is followed by a supervised dimension reduction, where the aim is to maximize the separability of the annotated training populations. This second step learns a matrix used to project the output of the first step onto a 3D space. Thus, a new F_M trace given as input to the framework is first reduced to a vector of coefficients that describe the linear combination of basic waveforms to reconstruct the F_M trace. Then, this vector is projected on a 3D space with axes x, y, and z, which we denominated qT-0-0, 0-qE-0, and 0-0-qI (Figure 4.10a).

As a first step, we implemented Dictionary Learning (Figure 4.10a) [168], which decomposes any complex series of data into pre-learned arbitrary waveforms that capture its most important features. The training phase is unsupervised: it exploits all the F_M traces from the four training populations of the dataset without any label. It learns to identify characteristic patterns in the ChlF traces that are stored in a dictionary of basic waveforms (called atoms). Its metric is the accuracy of reconstruction of a ChlF trace as a linear combination of the atoms. The dictionary convergence depends on hyper-parameters such as the sparsity level, number of atoms, and training set size. After investigating their influence on the reconstruction error (see Figure 4.21 in the SI), we selected a reconstruction threshold ($2{\cdot}10^{-4}$) corresponding to 10 atoms D_i (Figure 4.10b).

As a second step, we used a method based on Linear Discriminant Analysis (LDA), an algorithm that shares similarities with Principal Component Analysis (PCA) for they are both linear dimension reduction techniques [162, 208]. The metric used to train the LDA is the separability of the training populations. The separability is maximized by minimizing the distance between data points within the same training population while maximizing the separation between different training populations. Hence, since the labels of the training populations are here required, it is a supervised training. The LDA learns a projection matrix from the output space of the dictionary (dimension 10) to a 3-dimensional (3D) space by identifying three hyperplanes that effectively separate the four training populations. This inherent dimensionality constraint of LDA explains why we had to select four classes to build the reference dataset in the first place. Once we obtained the 3D projection, we could define the final 3D base of elementary NPQ components by assigning the x, y and z axes to the direction along which the training populations ***wt4***^{i}, ****stt7***^{i} and ***stt7*** are spread (principal components) and redefining its origin. As a consequence, each training population's point cloud is spread along a distinct axis. Then, by construction, since each of the training populations represents an elementary stress-response, the x, y and z axes based on the corresponding components have been named: qT-0-0, 0-qE-0 or 0-0-qI (see Methods).

Figure 4.10c,d,e display the 2D projections resulting from application of our machine learning framework on the dataset. The four training populations project along a given axis as expected: (i) the point clouds of the population expressing the NPQ component spreads along this axis only; (ii) the point clouds of the ones not expressing the component overlap at the origin (e.g. in the (qT-0-0, 0-qE-0) representation, the ***stt7*** and ***stt7***^{i} populations overlap since they both exhibit neither qE nor qT).

We notice that the distance from the origin of ***stt7*** is higher, but not significantly higher, than the other training populations. This is due to the already highly photoinhibited status of ***stt7*** even under growth light [90], and the slightly incomplete photoinhibition of the other populations of the reference dataset as described earlier. As a consequence, we now focus on qE and qT, and use photoinhibited populations (^{i}) for the following investigations to discard qI.

We further compared the outcome of the machine learning framework with the one relying on *ad hoc* metrics, which have been used in the literature to quantitatively measure the stress levels [146, 185, 207]. The latter are based on the variation of F_M over phases I–V (see Figure 4.9c,d), which have been *ad hoc* identified as representative of elementary NPQ phenomena [146].

Figure 4.11a-b shows the box-plots of the *ad hoc* metrics used to quantify the NPQ in each population of the reference dataset. The ****stt7***^{i} and ***wt4***^{i} distributions are statistically distinct from the others, which are grouped on the axis origin. This result demonstrates that the *ad hoc* metrics

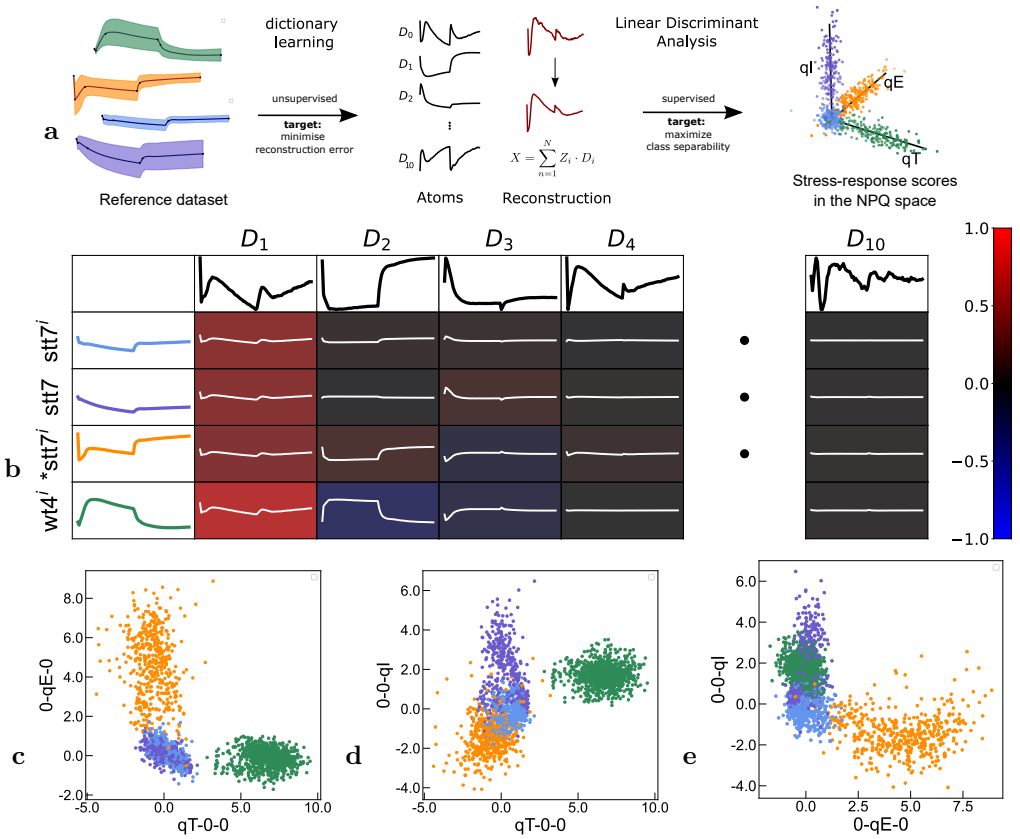

Figure 4.10: *From the reference dataset to a base of elementary NPQ components in a 3D space.* **a**: Flow of the process. All the reference dataset traces are first used to perform unsupervised training of an algorithm of dictionary learning. The resulting basis traces (atoms) are then combined with the labels of the four training populations in order to perform a Linear Discriminant Analysis. It results in an output in a 3D space, where each axis corresponds to a population of the reference dataset expressing an elementary stress; **b**: The atoms D_i are the learned representation of the dataset. Each element of the dataset can be reconstructed as a linear combination of the atoms D_i. In the table, the first column shows the reconstruction of the average trace of each population in the reference dataset. In each table cell, the color scales Z_i while the trace is $Z_i \times D_i$; **c, d, e**: 2D projections of the reference dataset onto the 3D NPQ space after performing Linear Discriminant Analysis on the atom code from applying dictionary learning. **c**: (qT-0-0, 0-qE-0), **d**: (qT-0-0, 0-0-qI), **e**: (0-qE-0, 0-0-qI).

built on populations where the stress response is elementaryly expressed are satisfactory indicators of the expression of the NPQ components. Figure 4.11c-d displays the box-plots of the machine learning scores which did not rely on prior kinetic knowledge. The ***stt7***^{i} and ***wt4***^{i} training populations are equally – if not better – distinguishable from the other training populations. This result supports the LDA relevance for separating the training populations while encompassing the underlying NPQ components so as to enable us to classify populations developing distinct NPQ components.

To further explore the performance of the machine learning framework, we plotted the *ad hoc* metrics against the machine learning scores. As shown in Figure 4.11e, there is a clear correlation between 0-qE-0 and NPQ(*Phase I*) for the ***stt7***^{i} population (p-value: 10^{-122}), whereas the other populations show little spread along both axes as they do not express qE. Such a correlation is similarly observed between qT-0-0 and NPQ(*Phase V*) for the ***wt4***^{i} population (Figure 4.11b - p-value: 10^{-145}). The *ad hoc* metrics from the literature allow to quantify the amplitude of the NPQ components. The correlation between the *ad hoc* metrics and the machine learning scores

demonstrates that the machine learning approach is able not only to classify, but also to quantify the stress responses using only the class labels.

We notice that the qT value computed with the *ad hoc* method is not zero for the mutants of state-transition (*stt7-1*), whereas the machine learning scores fall on zero, which represents better the absence of qT in the non-leaky mutant *stt7-1*.

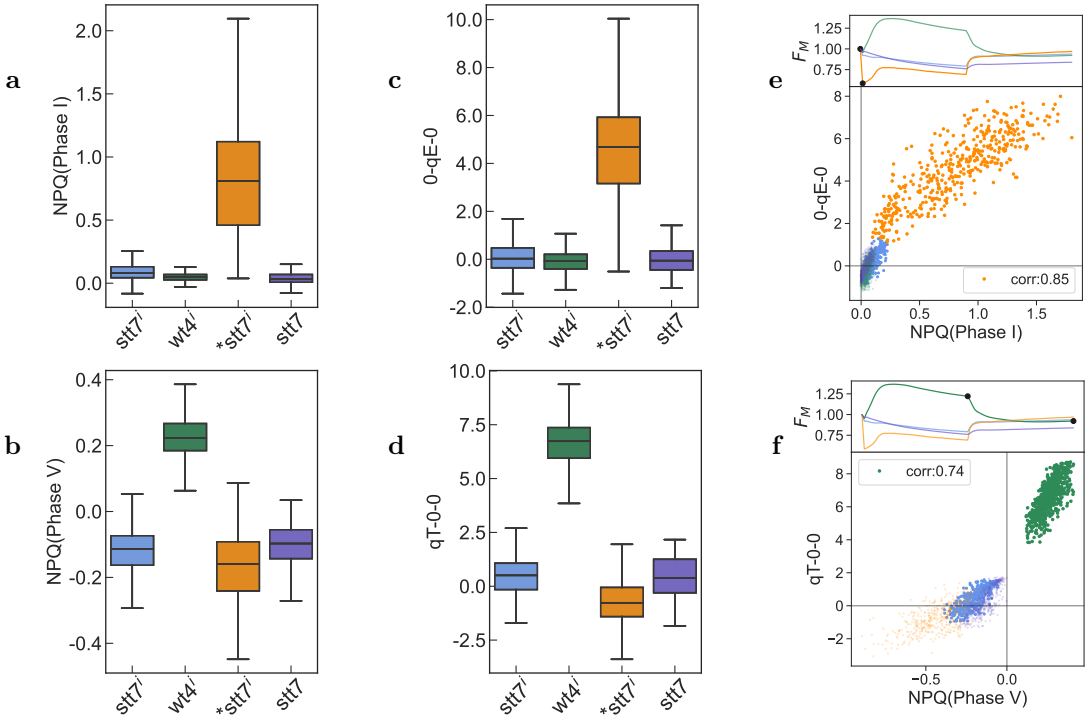

Figure 4.11: *Comparison of the bases originating from the machine learning framework and well-established metrics [146, 185, 207].* For each alga cell, the F_M trace has been processed by using the machine learning metric (0-qE-0 or qT-0-0) and the NPQ metric computed from $NPQ(t_n) = \frac{F_M(0)-F_M(t_n)}{F_M(t_n)}$ where 0 and t_n refer to the beginning and the end of the phases I–V (see Figure 4.9c,d) [146]. **a** and **b** respectively display the box-plot of the NPQ over *Phase I* and *Phase V* whereas **c** and **d** respectively display the box-plot of the projection of axis 0-qE-0 and qT-0-0. **e** and **f** respectively display the average ChlF F_M trace of the population from ***stt7***^{i} and ***wt4***^{i} (the black points identify the limit of each phase on the F_M trace) and the correlations between the axes 0-qE-0 and NPQ of *Phase I* ($p - value = 10^{-122}$), and qT-0-0 and NPQ *Phase V* ($p - value = 10^{-145}$) for all the populations.

The variation of the 0-qE-0 and qT-0-0 values appears to be more significant in the populations expressing qE and qT respectively. This observation led us to question to which extent the data distribution reflected an underlying biological diversity. To address this, we performed a series of complementary experiments, which aimed to distinguish the distributions originating from biological cell-to-cell variation and from instrumental noise or reconstruction artifacts by the dictionary.

Our microscope set-up allows us to apply the illumination protocol on a same sample kept in a same position. We exploited this feature to compare the NPQ response of the same algae from two consecutive identical repeats. Indeed, provided their state remains identical, any variation of the NPQ-response between both repeats is a signature of other factors (fluorescence noise, instrumental noise, inaccurate dictionary reconstruction) than the physiological state. To evaluate whether these other contributions were significant and could explain alone the variance of the distributions, we exploited the NPQ coordinates of all imaged cells to calculate the distribution of pairwise distances of each algae in the two experiments to themselves ($D_{i,i}$) and to all other algae ($D_{i,j}$). Similar distance

distributions $D_{i,i}$ and $D_{i,j}$ would suggest that the experimental noise governs the NPQ distributions. On the contrary, a narrower distance distribution for $D_{i,i}$ than for $D_{i,j}$ would suggest that two algae with a same biological status are statistically closer in the NPQ space and point on biological variance to drive the variance of the distribution of NPQ scores.

To perform the latter experiments, we selected monoclonal synchronized algae of $\boldsymbol{wt4}^i$ and $\boldsymbol{*stt7}^i$ in order to minimize the genetic diversity and the contribution of the cell cycle to the variance of the distribution (see Methods). We collected the F_M traces by applying the same illumination protocols as those used to build the training populations of $\boldsymbol{wt4}^i$ and $\boldsymbol{*stt7}^i$ and we retrieved the NPQ scores using the machine learning framework initially trained on the reference dataset.

We first evidenced that the distributions of the NPQ scores after two consecutive identical repeats were similar (Figure 4.12b,e), which supported that the cellular state remained identical (in Figure 4.25 of the SI, we show the distribution of the remaining scores and the statistical equality tests). Then we showed that the distance distribution was twice narrower for $D_{i,i}$ than for $D_{i,j}$ (Figure 4.12a,d; a statistical test validated that the distribution variances are different). Eventually, we interrogated the influence of the illumination heterogeneity in the field of view of the microscope and found no significant correlation to the value along each NPQ-axis (see Section 4.5.6). Hence, we concluded that the experimental noise does not alone explain the variance of the NPQ scores.

The latter investigations support that the variance of the NPQ-scores must have a biological origin. From the distributions displayed in Figure 4.12b,e, 40 and 20% have been retrieved for characterizing the biological cell-to-cell variation of qE and qT respectively, as computed from the standard deviation relative to the mean. As shown in Figure 4.12c,f, these variation coefficients are not statistically different from those of the non-monoclonal synchronized algae for the reference dataset, which supports that the distribution is not governed by a genetic diversity. We further showed that the cell surface measured in the field of view does not alone explain the variance either (see 4.5.6).

Projection of wild type strains in the generated 3D NPQ space of elementary NPQ components

Equipped with a 3D base of elementary NPQ components, we could analyze the outcome of the projection of the F_M traces collected at the single cell level from wild type strains. We first studied the wild type *wt4*, which has the same genetic background as *stt7-1* used in the reference dataset for the population exhibiting qE, and is already used in the population $\boldsymbol{wt4}^i$ (prior to qE-activation).

As a preliminary experiment, the monoclonal population $\boldsymbol{wt4}^i$ was qE-activated for 4 h and photoinhibited. It resulted in the population $\boldsymbol{*wt4}^i$ which is expected to display a stationary qI, and both qE and qT. Its F_M traces were processed as above. The $D_{i,i}$ distribution was narrower than the $D_{i,j}$ one as observed above (Figure 4.13a). Figures 4.13b,c evidence simultaneous expression of qE and qT with Gaussian distributions (normality test: p-value $< 10^{-6}$). They exhibit a dispersion much similar to the one observed for the training populations expressing only one of the traits (44% for qE, 21% for qT in 4.13b,c) although upon expression in a lesser extent, which is in agreement with a lower expression level of qE in wild-types compared to *stt7-1* previously reported in the literature [200, 209, 210].

We then investigated the dynamics of the well-studied qE-activation process [97] by applying three sequential high-light exposure of 2 h with measurements of the F_M traces after each interval. The time evolution of the cell coordinates in the base (qT-0-0, 0-qE-0) is displayed in Figure 4.13d. The gradual increase of 0-qE-0 with high-light exposure time (Figure 4.13d,f) is in line with reported results displaying the evolution of qE, where a few hours of exposure allow to reach a steady qE level [146]. We also observed a gradual decrease of the amplitude of qT-0-0 (Figure 4.13d,i). The two phenomena qE and qT appear to be correlated, both at the level of the point cloud centroids but also at the single-cell level (Figure 4.13d), as shown by the alignment of the respective affine fit in Figure 4.13d. This observation is compatible with the synergistic action of both qE and qT to respond to high light stress raised in the literature [90, 165].

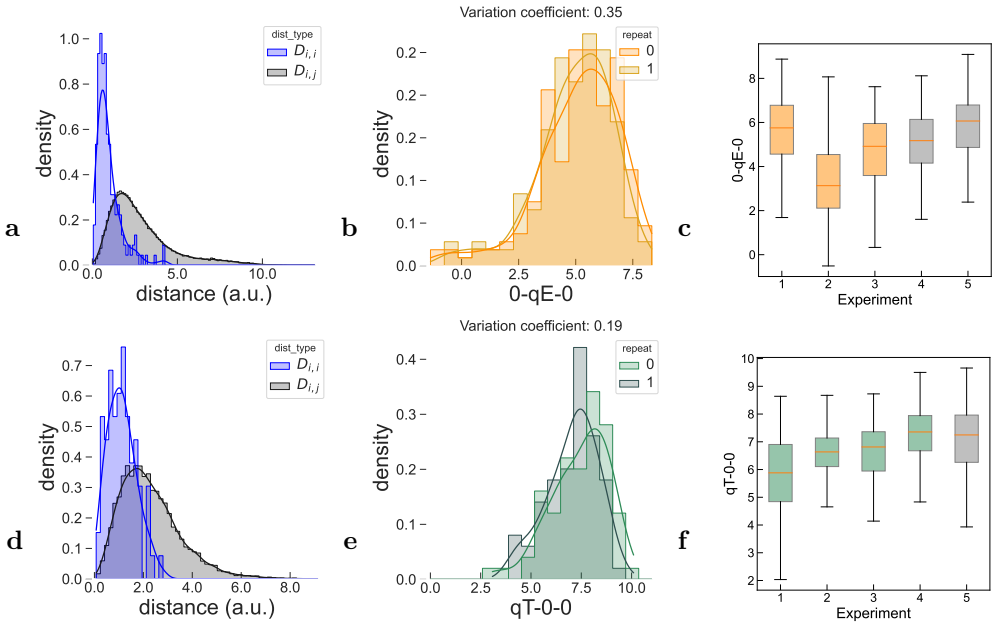

Figure 4.12: *Characterization of the dispersion of the NPQ traits within isogenic synchronised populations.* **a**,**d**: Distributions of the cell-to-cell ($D_{i,i}$ – blue, SD: 0.7 (**a**), 0.5 (**d**)) *vs* cell-to-population ($D_{i,j}$ – black, SD: 1.8 (**a**), 1.2 (**d**)) distances in the 3D NPQ space retrieved from **a**: two isogenic ***stt7***^{i} populations (2 consecutive repeats; 176 algae); **d**: two isogenic ***wt4***^{i} populations (**d**; 2 consecutive repeats; 77 algae); **b**,**e**: Distribution of the 0-qE-0 (**b**) and qT-0-0 (**e**) values of the ***stt7***^{i} (***wt4***^{i}) populations in **a** (**d**); **c**: Dispersion of the 0-qE-0 values collected from the training set (orange) and in experiments with isogenic synchronized populations (grey); **f**: Dispersion of the qT-0-0 values collected from the training set (green) and in experiments with isogenic synchronized populations (grey).

Figure 4.13e demonstrates that our machine learning framework effectively sorted the NPQ component-rich F_M traces initially observed in Figure 4.9a. Indeed, as the 0-qE-0 score increases, the characteristic drop in *Phase I* becomes significant, while as the amplitude of the qT-0-0 score decreases, so does the amplitude of *Phase V*.

We performed the same experiments with another wild-type strain: wild type *cc124*. As for wild type *wt4*, the time evolution of the point cloud qualitatively shows a continual increase of the amplitude of 0-qE-0 along the y-axis (Figure 4.13f) and a continual decrease of the amplitude of qT-0-0 along the x-axis (Figure 4.13i). However, as opposed to wild type *wt4*, although the correlation appears at the population level, it is not present within the point cloud (Figure 4.13g). Indeed, the affine fitting curve of the point cloud centroids is not aligned with the respective affine fit of each point cloud (Figure 4.13g). When the traces are displayed in the grid (Figure 4.13h) we observe phenotypes where both qE and qT are significant, that were absent in wild type *wt4* (Figure 4.13e).

Figure 4.13f,i shows the time evolution of the distribution of the cell coordinates for each stain, and the means of the boxes correspond to the information that a study at the population level would have yielded. It is interesting to notice that both populations have apparent similar evolutions. Yet, we have identified different synergies between qE and qT in the individual cell traces.

Evidence for the outbreak of a new phenotype

Our machine learning framework has learned how to identify traits of interest for its optimization tasks and discard the noise. However, its dimension reduction could miss significant features from a new population absent from the training dataset. In fact, this limitation may turn as an advantage when it comes validate the initial working hypothesis that a ChlF response corresponding to

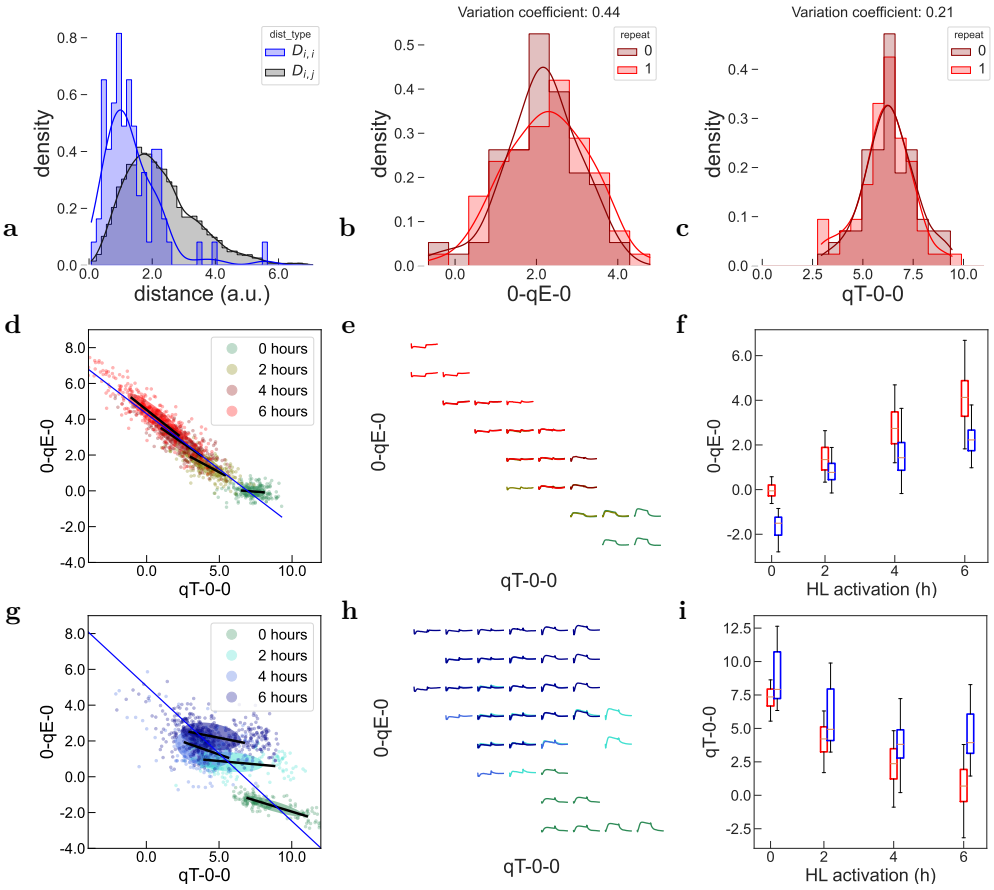

Figure 4.13: *Evolution of the distribution of wild type populations throughout qE-activation.* **a**: Distribution of cell-to-cell distance ($D_{i,i}$ – blue) vs cell-to-population distances ($D_{i,j}$ – black) in the 3D NPQ space corresponding to experiment in **b,c** (see Section 4.5.7 for the statistical tests). **b**: Distribution of the 0-qE-0 values of two monoclonal ***wt4***^{i} populations (2 consecutive repeats - 77 algae) Variation coefficient: 44%; **c**: Distribution of the qT-0-0 values of two monoclonal ***wt4***^{i} populations (2 consecutive repeats - 77 algae) Variation coefficient: 20%; **d**: Wild type *wt4* population taken from the growth light not qE-activated and photoinhibited (***wt4***^{i}) exposed to three consecutive qE-activation protocols of 2 h to promote the expression of LHCSR proteins and induce qE. The blue line indicates the direction of the affine fitting curve of the point cloud centroids while the black line indicates the affine curve fit of each point cloud elementaryly; **e**: Grid projection of the F_M traces from **d**. The axis limits have been adjusted to the point cloud and a trace is represented in the grid only if two or more datapoints fall within the box; **f**: Amplitude of the trait along the 0-qE-0 axis throughout the qE-activation of wild type *wt4* (experiment **d,e** - red and **g,h** - blue) **g**: Wild type *cc124* population taken from the growth light not qE-activated and photoinhibited exposed three consecutive qE-activation protocols of 2 h to promote the expression of LHCSR proteins and induce qE. The blue line indicates the direction of the affine fitting curve of the point cloud centroids while the black line indicates the affine curve fit of each point cloud elementaryly; **h**: Grid projection of the F_M traces from **g**. The axis limits have been adjusted to the point cloud and a trace is represented in the grid only if two or more datapoints fall within the box; **i**: Amplitude of the trait along the qT-0-0 axis throughout the qE-activation of wild type *wt4* (experiment **d,e** – red) and wild type *cc124* (experiment **g,h** – blue).

co-occuring light-stress responses can be reconstructed from combining the elementary fluorescence kinetics reflecting these responses. It can also be used to evidence the presence of a phenotype endowed with atypical traits. To illustrate these perspectives, we applied our machine learning framework to new sets of data.

In the previous section we studied the qE-activation of wild-type strains *wt*4 and *cc*124. Except from $\boldsymbol{wt4}^i$, such data have never been seen in the training phase of the Dictionary Learning. Figure 4.14a demonstrates that the main features of the F_M traces are well accounted for, validating the working hypothesis. Accordingly, as shown in Figure 4.14i, the reconstruction errors are within the order of magnitude of the reconstruction threshold defined in the training phase (2-4). We also investigated another mutant absent from the reference dataset: *npq*4, the mutant for LHCSR3 which is supposed to express no qE, and show a phenotype similar to $\boldsymbol{wt4}^i$ before and after activation. Although the responses are similar before activation (Figure 4.14c), they differ after activation (Figure 4.14g), as *npq*4 displays qE (probably coming from an over-expression of LHCSR1 [211], explaining why we did not use it as a negative control of qE). The Dictionary generalizes well to this mutant as it is able to reconstruct the traces properly and the reconstruction error is low (Figure 4.14i).

Then, we investigated another culture of wild type *wt4*, which was left to grow on a Petri dish for several months. Figure 4.14h already evidences that recurrent features are not satisfactorily accounted for by the projection. This discrepancy yields a reconstruction error an order of magnitude above the training threshold (Figure 4.14i). It expresses an uncommon stress response, which does not correspond to qE, qT nor qI and most probably originates from an unknown phenotypical trait with a strong characteristic signature.

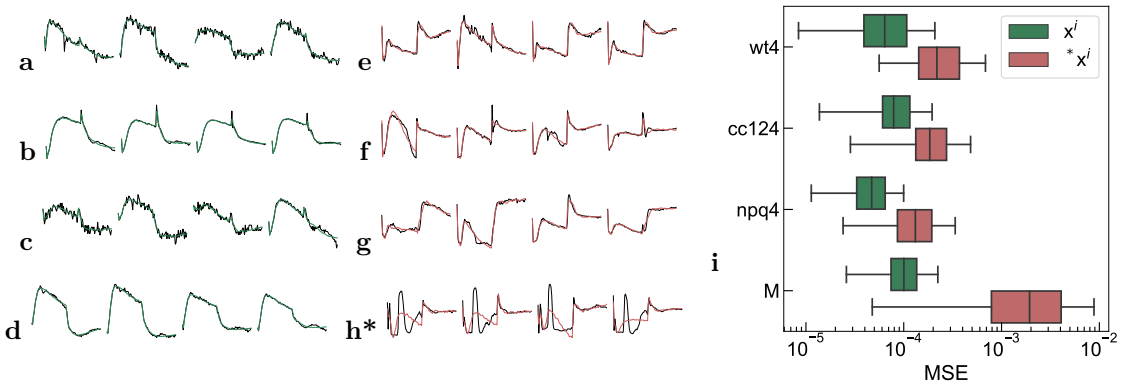

Figure 4.14: *Dictionary learning reconstruction for phenotypes absent from the training set.* **a-d**: Raw (black) and reconstructed (green) traces of x^i with the dictionary. **a**: *wt*4, **b**: *cc*124, **c**: *npq*4, **d**: M; **e-h**: Raw (black) and reconstructed (red) traces of $^*x^i$ with the dictionary. **e**: *wt*4, **f**: *cc*124, **g**: *npq*4, **h**: M; **i**: Distribution of the reconstruction mean squared error from experiments displayed in **a-h**. *wt*4: 185 algae, *cc*124: 192 algae, *npq*4: 98 algae, M: 443 algae. The traces plotted in **a-h** have the highest reconstruction error among all the algae in the experiment.

4.4.4 Discussion

In this report, we developed a microscope and an acquisition protocol to record the complex ChlF trace of *Chlamydomonas reinhardtii* in response to high-light stress at the single cell level. The traces have been analyzed with a new machine learning framework. It enabled us to achieve a dimension reduction to define a three-dimensional NPQ space and to effectively separate and quantify the contributions of the co-occuring NPQ components, including in several strains absent from the training set. In the following, we first adopt a methodological perspective and compare the outcome of our analysis with established protocols of ChlF processing. Then we are concerned with the biological aspects of our results and discuss the level and origin of the observed heterogeneity in the extracted distributions of the NPQ scores as well as the correlation between the qE and qT scores. Eventually, we discuss the scope of our approach to analyze the ChlF trace in the broader context of phenomics.

Methodological perspective

About the machine learning framework: qualitative and quantitative evaluation
The ChlF traces contains rich kinetic information reflecting the realization of multiple biological processes. In order to perform the mechanistic analysis and to extract the most informative waveforms in the trace, it is necessary to introduce an appropriate framework for data processing. In the present work, we harnessed a two steps machine learning framework combining Dictionary Learning and LDA to disentangle and quantify the respective contribution of the NPQ components to the ChlF trace. To evaluate its relevance, this framework has been challenged by established or alternative approaches for processing the ChlF data.

We verified that the NPQ scores obtained with the machine learning framework were both qualitatively and quantitatively related to the *ad hoc* metrics used in the literature to evaluate the NPQ components amplitude. By observing the evolution of the shapes of the F_M traces together with their projection in the NPQ space, we were able to derive interpretations of the dimension reduction process (see Figure 4.23 in the SI). We also verified that the evolution of the qE score obtained throughout qE-activation reflected the well-established gradual genetic expression of LHCSRs quenchers [97, 146].

Alternatively, we exploited our dataset to test other approaches, which could have been used to reduce the dimension of the data. In these tests, we did not introduce the intermediary Dictionary Learning step and used the functions provided in the library SciPy (v1.8.0) [212] with their default parameters.

We first evaluated the performances of PCA (non-supervised, linear), using as input the F_M traces without the labels (see Figure 4.28 in the Supporting Information). The PCA creates two clusters from the single ***stt7**^{i}* class. Apart from the mixed half of the *stt7-1* point cloud, it manages to properly distinguish the training populations in 3D. Whereas the evolution along the qT-0-0 axis seems to relate to qT (only the ***wt4**^{i}* population spreads along it), both 0-qE-0 and 0-0-qI axis mix qE and qI (both ***stt7**^{i}* and ***stt7*** are spread along them). Hence, although non-supervised linear PCA achieves to create clusters from unlabeled data, it does not yield a fully meaningful biological interpretation as opposed to our framework.

Then we evaluated t-SNE [213] and UMAP,[214] which are unsupervised non-linear dimension reduction algorithms often used in single-cell research, in particular RNA-sequencing. Both algorithms take as input the F_M traces and project them onto a 2-dimensional space with the aim to reflect similarities between the input traces through the distance between their projection (see Figure 4.30 in the SI). We observed that they perform well at reducing the dimension to enable a classification of the populations as long as the population expressing no-stress response is removed from the training dataset (compare Figure 4.30 and Figure 4.31 of the SI). However, it is not straightforward to retrieve a biological meaning from these projections, as opposed to our framework.

About the machine learning framework: test of the working hypothesis

Another methodological aspect concerns the evaluation of our working hypothesis that the kinetic response of a variety of strains could be satisfactorily accounted for in a referential built from the

kinetic responses of properly conditioned strains and mutants. In particular, we have demonstrated that the ChlF trace of strains co-expressing multiple NPQ components is well accounted for by a framework that was only trained on populations expressing an elementary NPQ component. We showed that the Dictionary Learning step is not necessary to build a meaningful NPQ space (see Figures 4.29 in SI). Yet we demonstrated the relevance to introduce it in our framework when it comes to comparing the reconstruction of the traces. The introduction of an intermediary reconstruction step with Dictionary Learning enabled us to introduce a test on the Mean-Squared error to evaluate the reconstruction quality of an F_M trace by using a linear combination of the atoms, to validate or reject the hypothesis. As shown in Figure 4.14, we demonstrated that this working hypothesis is relevant to account for a wide range of strains, which have not been included in the training set and which do not share the same genetic background. We found an order of magnitude difference in the reconstruction quality between data compatible with the training set ($\boldsymbol{*wt4}^i$) and outlier data ($^*\mathrm{M}^i$ - 3 repeats). In fact, the failure observed in Figure 4.14h probably reveals the emergence of a new mechanism acting on the ChlF trace which is not encompassed in the reference dataset, and that has not, to our knowledge, been reported in the literature. Performing the reconstruction is also possible by retrieving the pseudo-inverse of the LDA projection. Yet, the reconstruction performances of the LDA are not as discriminative as the Dictionary (Figure 4.32 in the SI).

About the machine learning framework: identifying loss of meaningful data thanks to the reconstruction step

We can take advantage of this test criterion to identify such atypical behaviors in new data, even from a single cell among a population. This task is usually a challenge in classical dimension reduction algorithm, which tend to discard information irrelevant in the training set but that can be relevant in new data. To support this claim, we evidenced that none of the dimension reduction methods we tested were able to distinguish the $^*\mathbf{M}^i$ data from the wild types in the NPQ space if they had not been included in the training set (see Figure 4.32 and Figure 4.33 in the SI).

Biological perspective

Extent and origin of the dispersion

The purpose of our investigation at the single cell was to access the dispersion and correlations originating from the diversity of biological status, which we demonstrated to be higher than the one originating from the instrumental noise or the data analysis (Figure 4.12). In the present investigation, we paid attention to control the external parameters, which could generate dispersion. Hence, we adopted monoclonal cultures of 12/12 synchronized cells cultivated on a Petri dish under a level of growth light set to have a 12 h doubling rate. Furthermore, we could not evidence any systematic deviation that would originate from the distribution of light intensity or of the position in the measurement chamber (Figures 4.24 in the SI). Thus we concluded that the observed dispersion was of biological origin.

Since causal relationships between size and photosynthetic activity have been reported [215], we examined whether the NPQ score depended on the cell size. As displayed in Figure 4.24 in the SI, we did not observe any significant correlation between the cell size and the NPQ score. The possible sources for cell diversity may lay in disparities during the growth on the Petri dish, the growth under agitation, the centrifugation phase provoking diversity in the biological status, or from stochastic gene expression [216, 217].

We observe that population-averaged values of qE and qT anti-correlate during the qE-activation in both wild-types. For one of the two wild-types, *wt*4, this correlation was confirmed within a population: cells with a higher qE have the tendency of having a lower qT. However, for *cc*124, it was not the case: no such positive correlation was observed within the population. This is a typical illustration of the Yule-Simpson paradox where a correlation appearing at the population level may or may not reflect a causal relationship at the level of the individuals forming this population [218].

In the case of *wt*4, an hypothesis for the negative correlation between qE and qT (chosen positive when moving from state II to state I) after high-light treatment is a mechanistic coupling via the Cyclic Electron Flow around PSI. Indeed, state II favors cyclic electron flow around PSI and the acidification of the lumen, which in turns could activate qE. Another hypothesis is that the LHCSRs quench the energy transferred by the new LHCII antennas biding to PSII during transition to state-I. The fluorescence increases in a lesser extent because it is partly quenched.

It is also possible that the correlation seen at the population level, as acclimation time in high light increases, does not correspond to a mechanistic link between the two, but instead to two independent effects of the high light treatment on qE and qT. From this point of view, it is well known that the effector of qE, the protein LhcSR3 is expressed in high light.

Finally, the direction of correlation which differs in *wt*4 and *cc*124 and not always match the correlation at the population level could reveal another complementary interplay between qE and qT, possibly involving mechanisms that have evolved differently in the two wild-types. One hypothesis previously observed is the phosphorylation of LHCSRs by the kinase STT7 [200, 219].

Extension to new observables, stresses, and biological questions

Scoring the physiological state of living organism is demanded in multiple fields, which extend from remote sensing to environmental monitoring. Indeed, an efficient score acting as an integrator could fruitfully complement or replace a set of physicochemical parameters possibly endowed with a demanding acquisition. In this report, we introduced a framework for building a score, which proved to be efficient. It is now examined in the perspective to be extended to addressing phenomics.

Our machine learning framework relies on a first step of training. It necessitates a proper observable and training populations representative of phenotypes to be scored. In this study, we exploited ChlF as expressing the kinetic response of the photosynthesis metabolism to a light stress. We further adopted training populations made of mutants and properly conditioned strains, which have been selected to express an elementary mechanism giving rise to specific features. In principle, our framework could as well apply to ChlF possibly complemented with other time series of observables and alternative sets of training populations, pending verification of the working hypothesis, which can be experimentally tested.

4.4.5 Conclusion

We demonstrated that our machine learning framework is able to predict a stress-response level without *a priori* knowledge of the temporal phases, but taking into account only the dynamics of the signal. As the framework is agnostic to the biological question, it is expandable to other experimental datasets. Furthermore, the machine learning approach on single-cell allows, with a small number of experiments, to derive information on the heterogeneity of the stress-response within a given population, and identify statistically significant correlation between the stress-responses, highlighting an underlying biological interplay. By design, this agnostic method will be applicable to other single-cell phenotyping problems involving kinetic responses.

4.4.6 Methods

Microscope set-up

A Python-based fully automated microscope instrument was designed to study single cells over time. An Arduino board controls the 470±10 nm and 405±7 nm LEDs at the millisecond precision. The blue LED is used for the high actinic light, the qE-activation and the relaxation, and the purple LED is used for the saturating pulses. These two wavelengths were chosen because it is possible to calibrate the distribution of light intensity at the level of the cell to ensure an homogeneous illumination. A Python algorithm [55, 152] segments each cell from the first frame of the movie (Figure 4.9a) to extract its individual temporal fluorescence response over the time frames and create a database of F_M traces for statistical analysis. A thorough description of the set-up is provided in the Supplementary Information.

Optical calibration

LED ON-OFF dynamics The dynamics of the LEDs switching is dependent on the input voltage on the LED controller, and is systematically lower than 10 μs (Figure 2.5,2.6 in Supplementary Information).

Calibration of the light intensity The blue and purple LEDs were calibrated using the point detector (MPPC). The relaxation time associated to the conversion between ON and OFF state of the Reversible Photoswitchable Protein (RSFP) Dronpa-2 was monitored, according to the protocol described in Appendix 2.6. We repeated the protocol for different LED current levels. We used a 525/30 filter to collect Dronpa-2 fluorescence. The calibration curves are displayed in Supplementary Information.

Calibration of the light intensity in the field of view
To compare the fluorescence responses of the algae, they must be exposed to the same light intensity in the field of view. To ensure the homogeneity, we performed the light calibration of the 470 and 405 LEDs with Dronpa-2 and used a camera instead of a single-point detector to measure the fluorescence's response dynamics. The video was downsized by a 10×10 averaging kernel to improve signal-to-noise ratio. The 470 LED was kept constant and the 405 one was switched ON and OFF four times for 6 s every 24 s. The first response was discarded due to the difference of response of the dark state of Dronpa-2.[220] The mask of the illuminated area was evaluated with a threshold on the intensity image and the following operations were performed only on the unmasked pixels. Monoexponential fits were performed on each ON-OFF and OFF-ON phase and the retrieved characteristic times were averaged. From the extracted characteristic times, the light intensity in μmol(photons) $\cdot\, \mathrm{m}^{-2} \cdot \mathrm{s}^{-1}$ was computed for each pixel using the molecular action cross-sections for photoisomerisation of Dronpa-2 [220]. The mean value of light intensity in the field in the given conditions is 8200 and 2500 μmol(photons) $\cdot\, \mathrm{m}^{-2} \cdot \mathrm{s}^{-1}$ for the 470 and 405 LEDs respectively. The histograms demonstrate the homogeneity of the illumination, respectively 10 and 15%.

Biological samples

Cells and mutants The *Chlamydomonas reinhardtii* strains *wt*4A^-, *cc*124, *stt7-1* and *npq*4 were from the ChlamyStation [81] collection. *stt7-1* originates from *wt*4A^-. It is a clone allelic to *stt*7 [140] and non-leaky compared to *stt7-9.*[200].

The strains were synchronized in a 12/12 light cycle (9 AM to 9 PM: 15 $\mu\mathrm{E}\cdot\mathrm{m}^{-2}\cdot\mathrm{s}^{-1}$ – white LED pannels, 23^{o}C) and grown in mixotrophic conditions (TAP medium [221]). The synchronized strains grown on Petri dish were diluted in liquid medium on Fridays and left to grow for agitation over the

weekend. The culture was diluted with fresh TAP medium on Mondays and every following days. The experiments were always performed in the exponential phase, between Tuesdays and Fridays. For each experiment, the whole illumination protocol started at 11 AM.

Sample preparation In all experiments the culture is collected in exponential phase (from 5×10^5 to 5×10^6 cells/mL), centrifuged (2500 RPM for 8 min) and transferred in **MIN** medium[12]. The algae are deposited on agarose pads for observations based on protocol from [55]. A 1% suspension of agarose in MIN medium was heated to dissolve the agarose. The agarose pads were prepared by dropping 175 µL of melted agarose onto a glass slide holding a spacer *(AB-0578 ThermoFisher)*. To make its surface flat, the pad was covered with a thick microscope glass slide and left for 5 min at 4^oC for hardening. The cover slide was removed and the preparation was left for 10 min to allow thermal adaptation and evaporation of excess humidity. About 5 μL of algae suspension was dropped onto the agarose and left to evaporate for 10 min. Finally, a coverslip was gently placed over the agarose pad for observation.

Light protocols

Basic pattern The algae are exposed to 15 min of 400 μmol(photons) $\cdot\, m^{-2} \cdot s^{-1}$, 470±10 nm and 15 min of dark. Throughout the whole experiment, saturating pulses are shone every 20 s (1300 μmol(photons) $\cdot\, m^{-2} \cdot s^{-1}$, 405±7 nm, 200 ms). The whole fluorescence is collected with a camera, but only the response specific to saturating pulses, F_M, is analyzed.

qE activation The algae are exposed to 400 μmol(photons) $\cdot\, m^{-2} \cdot s^{-1}$, 470±10 nm for 2–8 h under the microscope. The activation is followed by 45 min of 40 μmol(photons) $\cdot\, m^{-2} \cdot s^{-1}$, 470±10 nm. More details are provided in the Supplementary Information.

Photoinhibition To reach a steady-state of photoinhibition, the basic pattern is repeated four times in a row. The last two repeats are considered photoinhibited because the F_M level at the begining of the exposure equals the F_M level at the end of the exposure.

Data analysis

Dictionary Learning We used the sparse coding method to decompose the data into a linear combination of atoms from a dictionary [168] implemented in *scikit-learn* [222]. Given a F_M trace, the algorithm optimizes its reconstruction with a linear combination of the waveforms (atoms) of the dictionary. The coefficients weighting the atoms form a feature vector. The dimension of this feature vector is lower than the dimension of the original F_M trace (91) and is equal to N_D, the number of atoms in the dictionary. To build the dictionary, the randomly-sampled equilibrated dataset containing $n_{samples}$ F_M traces from ***stt7**^{i}*, ***stt7***, ***stt7**^{i}* and ***wt4**^{i}* was used as a training set and fitted with least angle regression following [168]. The metric optimized is the reconstruction fidelity with a penalty on the sparsity level, by minimizing the following function:

$$\min_{\mathbf{D},\mathbf{X}} \frac{1}{2}||\mathbf{Y} - \mathbf{D}\mathbf{X}||_2^2 + \lambda||\mathbf{X}||_1, \tag{4.15}$$

Where:

- $\mathbf{Y}$ is the input data matrix of dimension $91\times$ $n_{samples}$,
- $\mathbf{D}$ is the dictionary matrix with N_D atoms of dimension 91(normal matrix),
- $\mathbf{X}$ is the coefficient matrix of dimension N_D,
- $||\mathbf{Y} - \mathbf{D}\mathbf{X}||_2^2$ is the squared Euclidean norm of the reconstruction error,

[12] www.chlamycollection.org/methods/media-recipes/tap-and-tris-minimal/

- $||\mathbf{X}||_1$ is the L1 norm (sum of absolute values) of the coefficients,
- λ is the regularization parameter that controls the sparsity level.

We explored several parameters detailed in the Supplementary Information, including the normalization of the F_M traces prior to the training. For the analysis described in the Main Text, we selected $N_D = 10$, $n_{samples}$=300, $\lambda = 10^{-6}$, and normalized by the sum of the F_M to obtain a probability distribution.

Linear Discriminant Analysis The dimension reduction algorithm, multiclass Linear Discriminant Analysis [170] (LDA) finds the best linear combinations of input features that maximizes the separability among differently-labelled data. The metric optimized is derived from two matrices, S_B and S_W which represent respectively the separation between (B) the means of the classes and the dispersion of the datapoints within (W) each class. We obtain a projection from a space of dimension 10 to a space of dimension $c-1$ where c is the number of classes (in our case $c = 4$, ***stt7***^{i}, ****stt7***^{i}, ***wt4***^{i} and ***stt7***). The LDA is solved by Singular Value Decomposition (scikit-learn Python library [222]). Once the projection $\mathbf{T} \in 10 \times 3$ is obtained, we have to operate a transformation to align the significant axis with the canonical space (x, y, z) for easier analysis. The first step is to identify the principal directions of each class in the dataset and associate it to an axis by collecting the corresponding eigenvector (using Principal Component Analysis ([162])). They form a transfer matrix $\mathbf{R}$ which allows to change the base of the space. Then, the origin is identified by using biological knowledge. The average of the point clouds representing ****stt7***^{i}, ***stt7***^{i} and ***stt7*** is expected to show no qT as the strain is lacking STT7 gene: it is the origin of the qT-0-0 axis. The average of the point cloud ***stt7*** is expected to show no qE because it has only been exposed to growth light. It is set as the origin of the axis 0-qE-0. The average of the photoinhibited point clouds ***wt4***^{i}, ***stt7***^{i} and ****stt7***^{i} are supposed to show stationary photoinhibition and are therefore used as the zero reference for the 0-0-qI axis.

Monoclonal experiments

Samples and preparation

The synchronized monoculture of ****stt7***^{i} was obtained by the streak plate protocol[223]. The cultures were taken from the growth-light incubator (15 μmol(photons) $\cdot\, \mathrm{m}^{-2} \cdot \mathrm{s}^{-1}$, white LED panels, 23^oC), prepared according to "Sample preparation" in subsection 4.4.6, dark-adapted for 15 min and exposed to the basic pattern: four consecutive exposures 15 min HL-15 min dark. Then followed 4 h of qE-activation (400 μmol(photons) $\cdot\, \mathrm{m}^{-2} \cdot \mathrm{s}^{-1}$, 470±10 nm), 45 min of low light to partly relax the photoinhibition (40 μmol(photons) $\cdot\, \mathrm{m}^{-2} \cdot \mathrm{s}^{-1}$, 470±10 nm), 15 min dark and another set of four consecutive exposures to the basic pattern. The last two repeats were used for building Figure 4.12a,b. For the synchronized monoclonal ***wt4***^{i} population, the cultures were taken from growth light, prepared according to "Sample preparation" in subsection 4.4.6. They were dark-adapted for 15 min and exposed to the basic pattern: four consecutive exposures 15 min HL-15 min dark. The last two repeats were used in Figure 4.12d,e. Then followed 4 h of qE-activation (400 μmol(photons) $\cdot\, \mathrm{m}^{-2} \cdot \mathrm{s}^{-1}$, 470±10 nm), 45 min of low light to partly relax the photoinhibition (40 μmol(photons) $\cdot\, \mathrm{m}^{-2} \cdot \mathrm{s}^{-1}$, 470±10 nm), 15 min dark and another set of four consecutive exposures. The last two repeats were used for Figure 4.13b,c.

Evaluation of the cell-to-cell *vs* cell-to-population distances As the experiments are performed on the same sample with N algae, we can derive the couple positions in the dictionary learning NPQ space $((x_{3,i}, y_{3,i}, z_{3,i}), (x_{4,i}, y_{4,i}, z_{4,i})), i \in [1, N]$ corresponding to algae i for the third and fourth repeats. We introduce the distance $D_{i,j}$ as the distance of the point corresponding to algae i in the third repeat to the point corresponding to algae j in the fourth repeat:

$$D_{i,j} = \sqrt{(x_{4,j} - x_{3,i})^2 + (y_{4,j} - y_{3,i})^2 + (z_{4,j} - z_{3,i})^2} \tag{4.16}$$

for $(i, j) \in [1, N]^2$

Grid representation of the F_M traces in the NPQ space

To build Figure 4.13e,h we grouped the data points in a 8×8 grid and plotted the average F_M trace if there were more than three data points in a grid element. The traces from different point clouds are overlaid with the corresponding colors indicated in Figure 4.13d,g.

4.4.7 Contributions

I performed all the experiments except the validation of the reference dataset on the MacroSpeedZen (Figure 4.9d) performed by Marcelo Orlando. Discussions with Benjamin Bailleul, Francis-Andre Wollman and Sandrine Bujaldon led the choice of the biological populations. Discussions with David Colliaux led to the architecture of the Machine-Learning framework. Thomas Le Saux participated in the conception of the epi-fluorescence microscope hardware and Peter Hanappe in the conception of the software. I wrote the first draft of the manuscript, revised by David Colliaux and Benjamin Bailleul, with whom we designed the figures of the Main Text. I wrote the Supplementary Materials and made the corresponding figures. Ludovic Jullien and I worked on the revision of the Main Text and Supplementary materials to yield the current version. The work is still on-going.

4.5 Supplementary Materials

4.5.1 Description of the hardware of the fluorescence microscope

See Chapter 2 Section 2.4 for the presentation of the microscope.

Calibration of the illumination at the sample level

See Chapter 2 Section 2.5 for the characterization of the light sources.

Autofocus routine

In the protocols described in subsection 4.5.2, experiments last several hours and the sample can move under the microscope and lose focus. With a motor driving vertical motion of the microscope stage and controlled by an Arduino, we operated an autofocus routine at low light before each start of four consecutive basic pattern. The motor moves until the image captured presents a maximal Laplacian variance [103]. A detailed description is given in Section 5.6.4.

Image analysis of the single-cell Chlorophyll fluorescence movies

The algae in the video were segmented using local mathematical morphology operations described in *Chouket et al* [55] with the codes given in the corresponding Supplementary Materials [152] developed to segment fluorescent bacteria. As opposed to bacteria, algae are round and do not display a local maxima of fluorescence in the cell center. Instead, they show dark regions in the middle, corresponding to the part unoccupied by the fluorescent chloroplast. As a result, we changed the watershed source identification method: instead of locating local maxima of fluorescence, we locate the center of the algae. We begin by using a fill-holes operation to obtain only round and filled objects, which is not initially the case because of the dark areas. A simplified way to find the center of a disk with mathematical morphology operation is the following. Using a binary mask of the object, multiple consecutive erosions of one pixel are performed. After each erosion, a dilation is used to test if the center of the object has been reached. Since the disk is convex, an erosion followed by a dilation is fully reversible, except in one case. If the pixel is not reconstructed by the dilation, it means that the sphere has been completely eroded, and that the pixel was the furthest from the sphere boundaries, ie. the disk center. The number of steps it took to reach this non-return step is the distance of the center to the edge, here the radius of the algae in pixels. The results are displayed in Figure 4.15.

We manually annotated a single image in order to evaluate the performance of the segmentation. We notice that the algae out of focus are not identified by the segmentation, which is not a problem because in practice they would receive a different light intensity and emit a low fluorescence signal resulting in a poor signal-to-noise ratio. It resulted in an F1-score of 73%.[13] The F1-score could be improved with the current state-of-the art segmentation networks, with fine-tuning.

For long-lasting experiments as presented in Figure 4.17, the autofocus allows to keep the algae in the focal plane, but they can undergo horizontal shifts. It results in different positions of the algae between two videos. The algae are restored to their original position during the data processing by

[13]To compute the F1-score for segmentation, we first calculate the true positives (TP, pixels segmented as algae in the ground truth and predicted mask), false positives (FP - pixels segmented as algae that belong to background), and false negatives (FN - pixels segmented as background that are algae in the ground truth). These values can be derived from the overlapping regions between the predicted and ground truth masks. The precision (P) is defined as the ratio of true positives to the sum of true positives and false positives: precision = TP / (TP + FP). The recall (R) is defined as the ratio of true positives to the sum of true positives and false negatives: recall = TP / (TP + FN). The F1 score is then calculated as the harmonic mean of precision and recall: $F1 - score = 2\frac{P \times R}{P+R}$.

recovering the displacement vector between the two images. We recover it using a registration method based on the images cross-correlation [55].

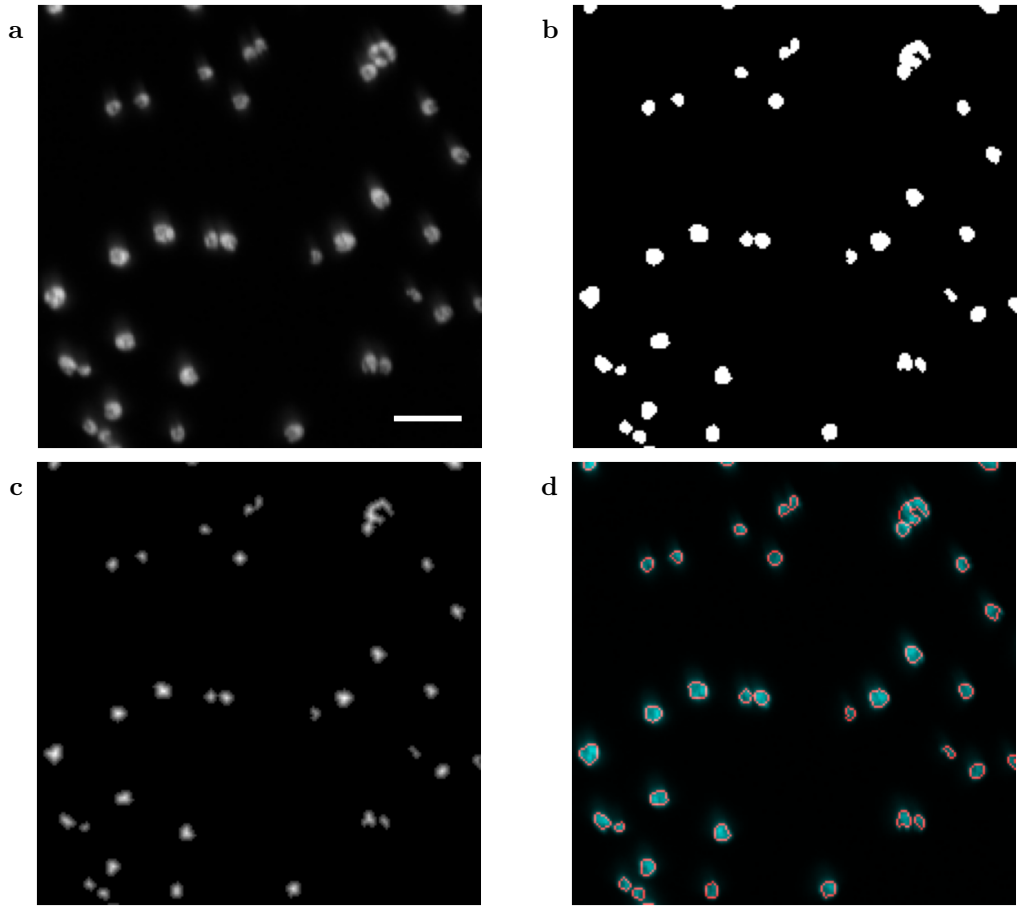

Figure 4.15: *Watershed segmentation of the fluorescence movies.* **a**: Grey-level image of the algae from a movie. Scale: 30 µm, cropped image; **b**: Intersubsection of the contrast mask and the auto-level mask, used as reference for the watershed segmentation; **c**: Distance map used to identify the local maxima; **d**: Contours of the segmented objects.

4.5.2 Illumination protocols

A whole illumination experiment lasts several hours. It involves a number of components designed to activate qE, qT and qI. The illumination involves a basic protocol pattern used to measure NPQ consisting in 15 min of high-light and 15 min of dark. It is supplemented by further illumination steps designed to reach a steady-state of qI, or to activate the qE. We summarize these different elements of the overall illumination protocol below.

Protocol inducing high-light stress and used to collect F_M (basic pattern)

The basic pattern allows to induce simultaneously qE, qI and qT by applying a high light (400 μmol(photons) $\cdot$ m^{-2} $\cdot$ s^{-1}, 470±10 nm) for 15 min and turning it off. This light is 10 times above the growth light (40 μmol(photons) $\cdot$ m^{-2} $\cdot$ s^{-1}, white LED) (therefore inducing an elevated light-stress), corresponding to levels commonly used in the literature [129].

Simultaneously to the stressing light, we apply a saturating pulse every 20 s (1300 μmol(photons) $\cdot$ m^{-2} $\cdot$ s^{-1}, 405±7 nm, 200 ms). The blue light is turned off when the saturating pulse is applied, this allows to remove the fluorescence contribution in response to the blue light. It allows to compare the fluorescence response to a saturating pulse during the light stress, but also in the dark when the blue light is turned off. The high-light exposure lasts 15 min and the following relaxation in the dark lasts 15 min as well. The relaxation is long enough to relax qE and qT but not qI which relaxes four times slower than it is induced [202]. **Dronpa-2** was used to calibrate the light intensity levels and an Arduino custom code was written to send digital signal to the LED controller and switch the LEDs at a millisecond precision. Figure 4.16 shows the time evolution of the light level in the field of view.

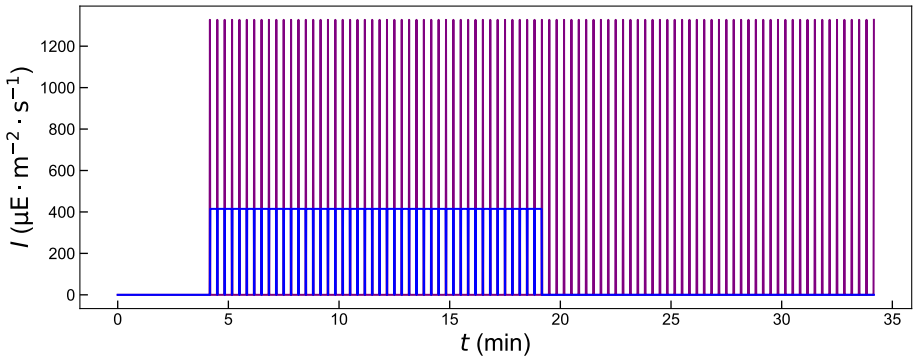

Figure 4.16: *Description of the basic pattern illumination.* The blue light induces the high-light stress (400 μmol(photons) $\cdot$ m^{-2} $\cdot$ s^{-1}, 470±10 nm), the purple light pulses (1300 μmol(photons) $\cdot$ m^{-2} $\cdot$ s^{-1}, 405±7 nm, 200 ms) saturate the photosynthetic chain to probe the fluorescence level under high-light and in the dark.

Protocol inducing a steady-state of photoinhibition (four patterns repeats)

When the algae are taken from the culture light and deposited on the pad, they are not photoinhibited. The basic pattern induces photoinhibition but the duration of the basic pattern approaches τ_{qI}. In order to discriminate qE and qT from qI, qI needs to reach a steady-state. After a single occurrence of the basic pattern, this steady-state is not reached. However, when the basic pattern is repeated consecutively multiple times, it eventually reaches the steady-state. This can be observed by comparing the fluorescence response of the first and last saturating pulses of a basic pattern. When they are equal, the syeady-state is reached. Figure 4.17b displays the fluorescence response to the complete light protocol. The basic pattern was repeated four times in a row before and after qE-activation to reach the steady-state. We see that is it reached after the third repeat for *stt*7 after

activation, and for *wt*4 before and after activation. We selected these three types of responses to collect the F_M traces of the populations $\boldsymbol{*stt7^i}$, $\boldsymbol{wt4^i}$ and $\boldsymbol{*wt4^i}$ respectively. For *stt*7 before activation, the exposure to the basic pattern induces rapidly qE, as seen by the decrease of fluorescence response between two first pulses at the onset of the basic pattern. In order to minimize the effect of qE in this population of the dataset which is expected to show no stress response ($\boldsymbol{stt7^i}$), we selected the third and not the fourth repeat of the basic pattern. The protocol consisting in repeating the basic pattern to reach a stead-state of photoinhibition is referred as: four patterns repeats.

Protocol inducing the LHCSR expression (qE-activation)

To induce the expression of LHCSR, we exposed the algae deposited on a pad to a high-light stress induced by the blue led (400 μmol(photons) $\cdot$ m^{-2} $\cdot$ s^{-1}, 470±10 nm) of the microscope for a long period (2-8 h). We performed the qE-activation after the four patterns repeats. After the qE-activation we applied a light level equivalent to the growth-light level (40 μmol(photons) $\cdot$ m^{-2} $\cdot$ s^{-1}, 470±10 nm) for 45 min to allow the stresses to relax (low-light relaxation). The latter protocol allows to read the fluorescence signal of individual algae before and after qE-activation on the same sample, and as a consequence to monitor the induction of the stress-response. Figure 4.17a shows the evolution of the blue light intensity received by the algae through the different steps, without the saturating pulses. There are no saturating pulses during the activation and the relaxation, only during the basic pattern.

Summary of the light protocols

The photoinhibition, qE-activation and fluorescence response are collected throughout one single experiment. Figure 4.17a shows the exposure to high-light stress (400 μmol(photons) $\cdot$ m^{-2} $\cdot$ s^{-1}, 470±10 nm) throughout the experiment. Figure 4.17b,c show the fluorescence response to the consecutive light protocols for the two strains investigated. The basic pattern fluorescence response used to build the canonical set as described in the Main Text are highlighted in the corresponding colors.

The light protocols are summarized in Table 4.2.

Table 4.2: Summary of the light protocols. The actinic light is a LED (470±10 nm), the saturating pulses are produced with a LED (1300 μmol(photons) $\cdot$ m^{-2} $\cdot$ s^{-1}, 405±7 nm, 200 ms) applied every 20 s.

Name	Duration	Actinic light levels (μmol(photons) $\cdot$ m^{-2} $\cdot$ s^{-1})	**SP**	Figure
dark adaptation	15 min	0	OFF	4.17
basic pattern	30 min	400	ON	4.16
four patterns repeats	2h	400	ON	4.17
qE-activation	1h30-8h	400	OFF	4.17
low-light relaxation	45	40	OFF	4.17

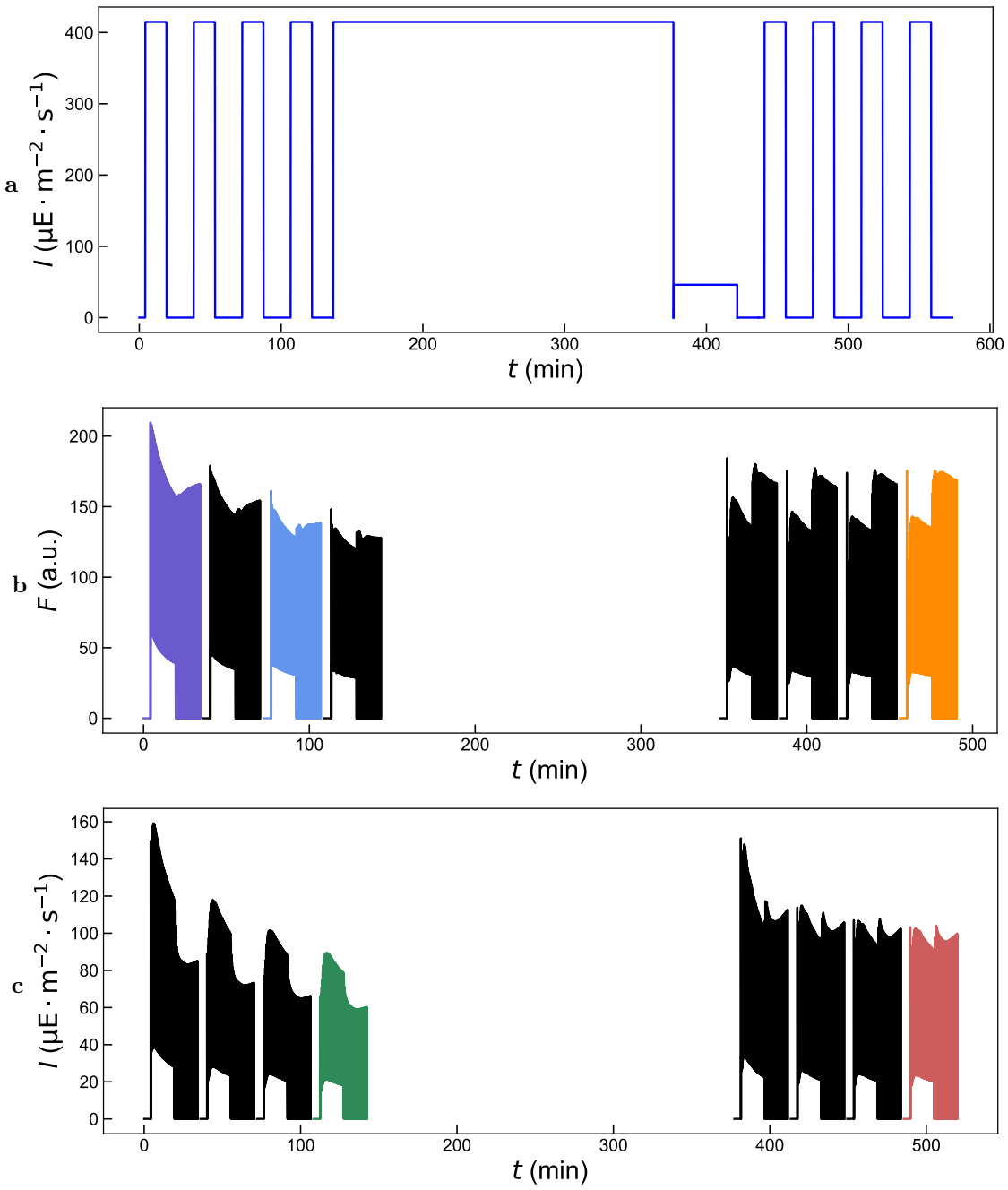

Figure 4.17: *Full excitation sequence allowing to probe qE, qI, qT, activate qE and reach a steady-state of photoinhibition.* **a**: Blue light inducting the high-light stress (saturating purple light pulses not displayed), the qE-activation and the photoinhibition; **b,c**: Response of *stt*7 (resp. *wt*4) to the full protocol, average over the fluorescence of the algae in the videos. The timescale does not correspond exactly to the theoretical pattern because the video processing is integrated in the experiment and one experiment needs to terminate before another starts. The colors correspond the the basic patterns response selected to build the dataset. Purple: ***stt7***, blue: ***stt7***^{i}, orange: ****stt7***^{i}, green: ***wt4***^{i}.

Evaluation of the quenching effect of the saturating pulses

In order to probe the fluorescence NPQ response under high-light and in the dark, we used a high saturating pulse frequency (1300 μmol(photons) $\cdot$ m^{-2} $\cdot$ s^{-1}, 405±7 nm, 200 ms) to have a better resolution of the stress-responses, at the risk of provoking a stress related to the saturating pulse. Although actinic light already saturates and provokes stress, we assessed if the saturating pulses significantly affected the fluorescence response by applying the basic pattern with actinic blue light set to zero (Figure 4.18a). We call this protocol SP assessment. Cells of wild type *wt4* were exposed to this sequence between the 15 min dark adaptation and the four patterns repeats. The time evolution of the fluorescence NPQ response to the SP assessment pattern is plotted in Figure 4.18c,d, overlaid with the response to the first repeat of the basic pattern that followed. The stress-response is much reacher with blue light on, demonstrating that the kinetics of ChlF response we observe mainly come from the light-stress provoked by the blue light, and not from the light-stress provoked by the saturating pulses.

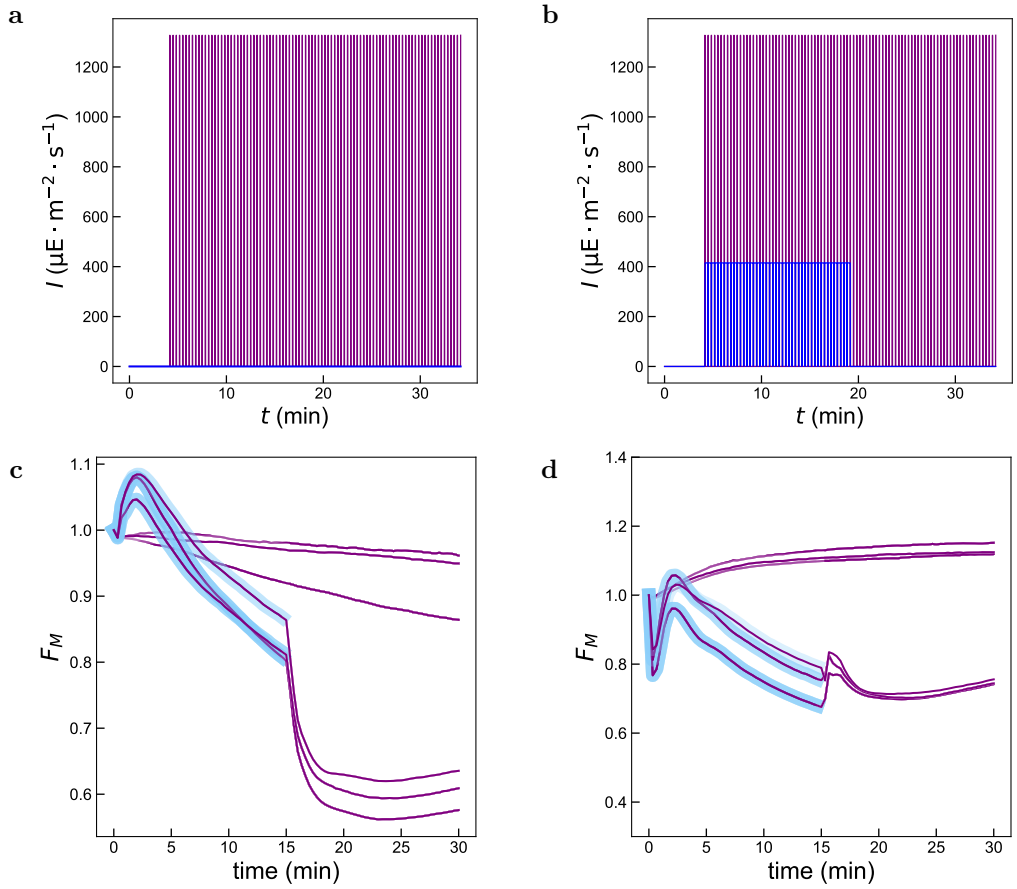

Figure 4.18: *Evaluation of the quenching effect of the saturating pulse.* **a**: Excitation sequence to investigate the light-stress induced by the saturating pulse when the blue light is turned off (SP assessment). **b**: Excitation sequence to investigate the light-stress induced by the saturating pulse when the blue light is turned on (basic pattern). **c**: F_M response of a *wt4* population after dark adaptation before qE-activation, to a SP assessment and to the basic pattern (highlighted in blue - 3 repeats). Equivalent to ***wt4***; **d**: F_M response of a *wt4* population after 2 h qE-activation, 45 min of low-light relaxation and 15 min of dark adaptation to a SP assessment and to the basic pattern (highlighted in blue - 3 repeats). Equivalent to ****wt4***.

Evidence of qE in *npq*4

The mutant *npq*4 lacks the LHCSR3 genes and it is commonly used in the literature as a negative control for qE. As displayed in Figure 4.19a, we noticed that the mutant *npq*4 exhibited an unexpected behavior after 4 h of qE-activation on the agarose pad. As shown in Figure 4.19 it shows a sharp drop in fluorescence at the light onset, characteristic of qE. This behavior has previously been identified in the literature and attributed to an over-expression of LHCSR1 to compensate for the absence of LHCSR3.[97, 211]

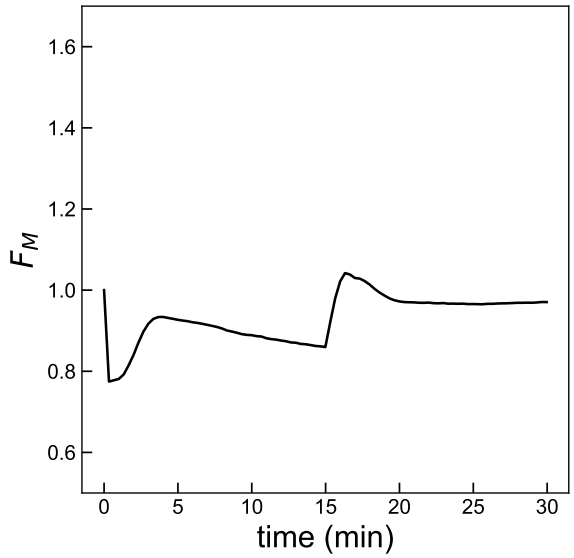

Figure 4.19: *Investigation of qE-activation in npq4 strain.* F_M response after 4 h of qE-activation on the agarose pad by the blue LED under the microscope.

Choice of the reference conditions to build the reference dataset

As a consequence of the observations made in Figure 4.19, we decided to discard *npq*4 from our library of training populations. As a negative control of qE, we used not-activated populations. The not-activated strains do not express qE and are not photoinhibited since they have not been exposed to activating light. Applying four consecutive times the basic pattern induces photoinhibition until a steady-state is reached, but does not induce the expression of qE. However, we observed that in some cultures, qE was expressed in *stt*7 not-activated strains. We attributed this to a compensation for the lack of state-transition.

We also estimated that the qI trait might have a too low expression level in the ***stt7*** population to allow high-quality results on the conclusions regarding qI.

4.5.3 Dataset of F_M traces

Generation of the Chlorophyll fluorescence traces of four reference populations

The reference dataset was generated by applying the full protocol described in 4.17a to the populations *stt*7 and *wt*4. The summary of these conditions is provided in Table 4.1 of the Main text. qT is present in wild-type *wt*4 and absent in the mutant *stt*7, qE is absent before qE-activation protocol and present after, and qI becomes stationary (considered absent) after the consecutive application of repeats of 15 min high-light (protocol: four patterns repeats).

We also acquired similar data with monoclonal populations that were not included in the dataset but used for validation and investigation of the origin of the distribution of the NPQ scores.

Finally, we also acquired data corresponding to various strains qE-activated and photoinhibited ${}^*x^i$, which we used to investigate the interactions between the NPQ components (Figure 4.13) and evaluate the performance of the Dictionary reconstruction on new data (Figure 4.14).

Data cleaning and pre-processing to obtain F_M

Prior to training the dataset, the outliers were removed. A KD-Tree [224] was built to represent the distance relationships between the inputs. An histogram of the average distance to the ten nearest neighbors was plotted. We manually set a threshold D to remove the points with all neighbors further than D. Among the 6803 points, we removed 31 points. We plotted the whole fluorescence traces corresponding to the outliers and they may correspond to fluorescence of algae that have moved during the acquisition (Figure 4.20a), noisy signal (Figure 4.20), or atypical behaviors (Figure 4.20c,d,e,f). Interestingly, in other experiments of strain selections that could be performed on the instrument, these outliers would be of special interest for they display traits of interest. In this scenario, they could enrich the dictionary and enable it to capture rare phenotypes with a low reconstruction error.

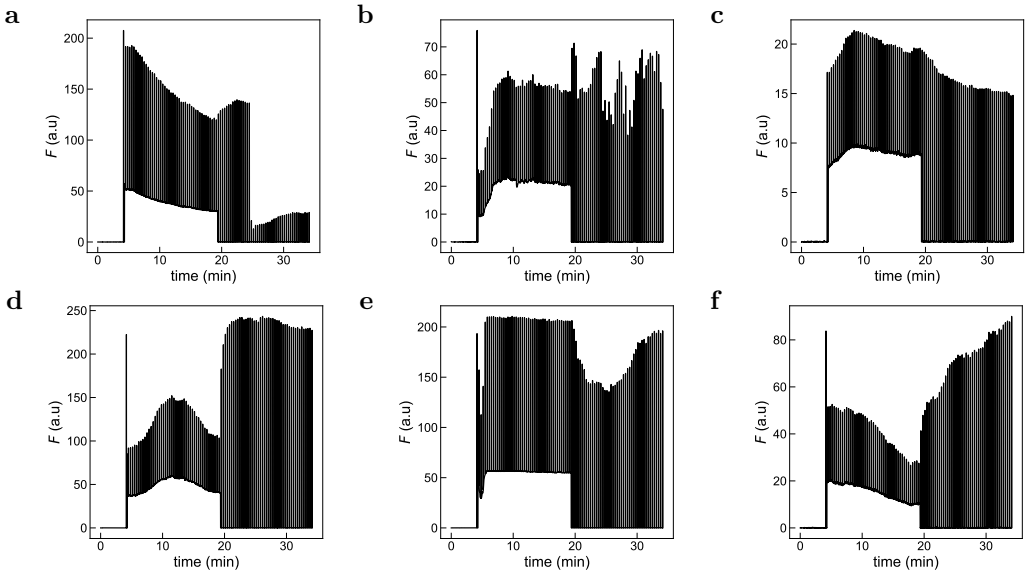

Figure 4.20: *Fluorescence responses identified as outliers.* Singular populations: **a**: ***stt7***; **b**: ****stt7**^{i}***; **c**: ***wt4**^{i}***; **d**: ****stt7**^{i}***; **e**: ****stt7**^{i}***; **f**: ****stt7**^{i}***.

For data processing, the F_M traces, response to saturating pulses only, were isolated from the whole fluorescence trace by selecting one in every 20 frames (framerate: 1 Hz, saturating pulse applied every 20 s). The data normalization is discussed in Section 4.5.4.

4.5.4 Dictionary learning to represent the F_M traces

Description of the Dictionary Learning hyperparameters

As presented in the Methods section, the dictionary learning aims at reconstructing a signal from a learned set of atoms. This set is learned by minimizing the loss function given in Eq.(4.17). The optimized metric is the reconstruction fidelity with a penalty on the sparsity level.

$$\min_{\mathbf{D},\mathbf{X}} \frac{1}{2}||\mathbf{Y} - \mathbf{DX}||_F^2 + \lambda||\mathbf{X}||_1, \tag{4.17}$$

Where:

- $\mathbf{Y}$ is the input data matrix of dimension 91$\times$ $n_{samples}$,
- $\mathbf{D}$ is the dictionary matrix with N_D atoms of dimension 91(normal matrix),
- $\mathbf{X}$ is the coefficient matrix of dimension N_D,
- $||\mathbf{Y} - \mathbf{DX}||_2^2$ is the squared Euclidean norm of the reconstruction error,
- $||\mathbf{X}||_1$ is the L1 norm (sum of absolute values) of the coefficients,
- λ is the regularization parameter that controls the sparsity level.

Investigation of the hyperparameter space

We explored several parameters, based on the analysis of the reconstruction error.

- **Normalization method**: We tried normalizing F_M by
  - the standard deviation $\sigma = \sqrt{\frac{1}{N-1}\sum_{i=1}^{N}(F_M(i) - \bar{F_M})^2}$, a classical reduction method;
  - the first pulse value $F_M(0)$ in reference to the NPQ formula;
  - the sum S $= \sum_{i=1}^{N} F_M(i)$ to obtain a probability law.
- **Dictionary Size** N_D: The size of the dictionary determines the number of atoms to be learned. The higher the size, the better the reconstruction. We explored sizes of dictionaries from 3 to 30 atoms.
- **Sparsity Level** λ: The sparsity enforces to learn to reconstruct the traces by combining a minimal number of atoms of the Dictionary. We explored sparsity constraints between 10^{-10} and 10^{-2}.
- **Training set size** $n_{samples}$: This parameter corresponds to the number of F_M traces representing each class in the training. We used a balance dataset, by selecting $n_{samples}$ in each class. To total training size is $4 \times n_{samples}$ because we have four classes. We tested training sizes from 3 to 300 (representative of the size of the smallest class in the reference dataset).

Several number of training-set sizes, number of atoms and sparsity levels were explored to see their influence on the reconstruction error. We began by a grid search, splitting the exploration space by chosing seven values each for N_D, λ and $n_{samples}$. Then, we refined the size of the search space around the optimum. We used as validation set the monoclonal populations of ***stt7***^{i}, ****stt7***^{i}, ***stt7*** and ***wt4***^{i} which were also used for the heterogeneity investigations displayed in Figure 4.12. These data resemble the training set but were not included in it during the training phase. More details on the validation are given in section 4.5.4.

We selected the normalization by S after observing that it systematically gave the lowest reconstruction error compared to the other normalization methods (Figure 4.21a). In the same Figure,

we identify that the reconstruction error decreases with the number of atoms in the dictionary. In practice, when using the normalization by the sum S, and a dictionary larger than 12 atoms, some atoms were never used in the reconstruction of the training set, and were therefore irrelevant to train the LDA. This was true for all the values of λ we investigated (10^{-10} to 10^{-2}). It is why the curve of the normalization by S stops at 12. The Figures 4.21b and 4.21c correspond to the results of the investigation limited to the normalization by S for clarity.

We investigated the impact of the size of the training set on the reconstruction error. Figure 4.21b shows that it is much less significant than the number of atoms. It shows that even a low amount of training data is sufficient to encompass the dynamics of the NPQ components in the dictionary. Therefore, the method could be generalized to studies at the population level with only a few repeats. Based on the curves, we selected 10 atoms for our dictionary, with a corresponding reconstruction error threshold of $2{\cdot}10^{-4}$.

Finally, we investigated the role of the parameter λ on the reconstruction, as shone in Figure 4.21c (normalization by S, number of atoms: 10). Given the span of the error axis, we can deduce that it is minimal. It does however play a role on the number of atoms used for the reconstruction as we observed experimentally. We selected $\lambda = 10^{-6}$ to give maximal weight to the sparsity constraint in the metric optimization.

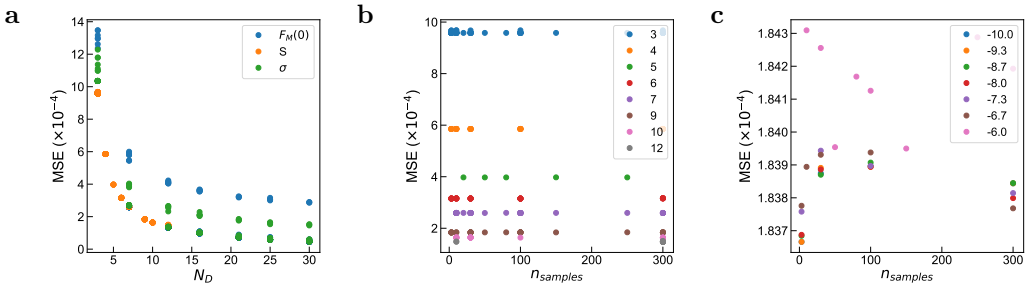

Figure 4.21: *Exploration of the role of the hyperparameters of the Dictionary Learning on the reconstruction error over a validation dataset.* The validation dataset consists in a set of populations prepared in the same conditions as the training set but not participating in the training phase. They correspond to the monoclonal experiments in Figure 4.12 of the Main Text. **a**: Impact of the normalization method and the number of atoms N_D on the reconstruction error. Legend: normalization method; **b**: Impact of the training set size $n_{samples}$ and the number of atoms N_D for dictionaries built using the normalization by S. Legend: number of samples per population (balanced dataset); **c**: Impact of the training set size $n_{samples}$ and the sparsity level λ for dictionaries built using the normalization by S and 10 atoms. Legend: $\log(\lambda)$.

Evaluation of the reconstruction threshold on a validation set

We evaluated the reconstruction accuracy of the selected dictionary on a validation dataset. It consisted in a set of traces from ***stt7***^{i}, ***stt7***, ****stt7***^{i} and ***wt4***^{i} populations prepared by the same conditioning as the training dataset and corresponding to the monoclonal strains used in Figure 4.12. We computed the Mean-Squared Error (MSE) between the traces and their reconstruction with the dictionary. We used the average of the reconstruction error of this dataset to investigate the influence of the hyperparameters in the previous section. Here we observe the distribution of the error for each population and find similar distributions, falling in the range of the error estimated in Figure 4.21c. We conclude that the dictionary performs well at reconstructing all the populations and encompasses well the distinct NPQ components (Figure 4.22a–f).

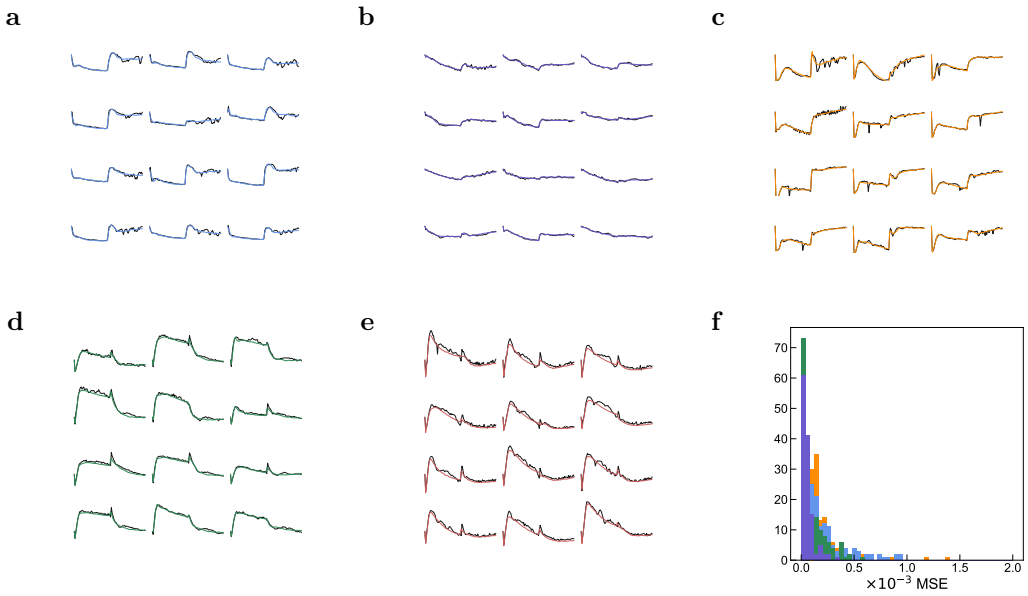

Figure 4.22: *Evaluation of the performance of the reconstruction of the Dictionary Learning on a validation set similar to the reference dataset except the populations are monoclonal.* **a-e**: F_M traces of monoclonal algae from ***stt7***^{i}, ***stt7***, ****stt7***^{i} and ***wt4***^{i} populations respectively (black) overlapped with the reconstruction by the dictionary learned on the reference dataset. The traces displayed are the twelve ones with the highest reconstruction error among all the algae from each experiment; **f**: distribution of the reconstruction error, the number of counts correspond to the number of algae. Means and SD ($\times 10^{-4}$): ***stt7***^{i} (blue): (2.5, 2.1); ***stt7*** (purple): (0.6, 0.5); ****stt7***^{i} (orange): (2.2, 3.0), ***wt4***^{i} (green): (1.0, 1.1).

4.5.5 Interpretation of the projection in the NPQ space

The results of the LDA projection are now interpreted. For each population, we first evaluated the span of the NPQ-scores on the axis corresponding to the stress they express (qT-0-0 for ***wt4***^{i}, 0-qE-0 for ****stt7***^{i} and 0-0-qI for ***stt7***). As the score increases along the axis, the patterns identified in the literature as signatures of qI, qE and qT respectively increase in ***stt7***, ****stt7***^{i} and ***wt4***^{i}: (i) The amplitude of *Phase V* increases when the qT-0-0 score increases (Q0 to Q2); (ii) The amplitude of *Phase I* increases when the 0-qE-0 score increases (Q0 to Q2); (iii) The loss of fluorescence between the beginning and the end of the experiment characteristic of photoinhibition increases when the 0-0-qI score increases. This result is much in line with the correlation observed between the NPQ scores and the *ad hoc* metrics of Figure 4.11. We then analyzed how the F_M traces evolve along each 3D-axis. We notice that the atom D_1 contributes to the average of the signal, with an always positive and high contribution. The atoms D_1 and D_2 can be used to describe the classes to which the algae belong. Overall, in the representation (D_1, D_2), the qI class corresponds to (+,0), qE to (+,+) and qT to (+,-). Then, the atom D_3 and D_4 contribute to the different amplitude of the stress expressed, and to a lesser extent D_2 as well.

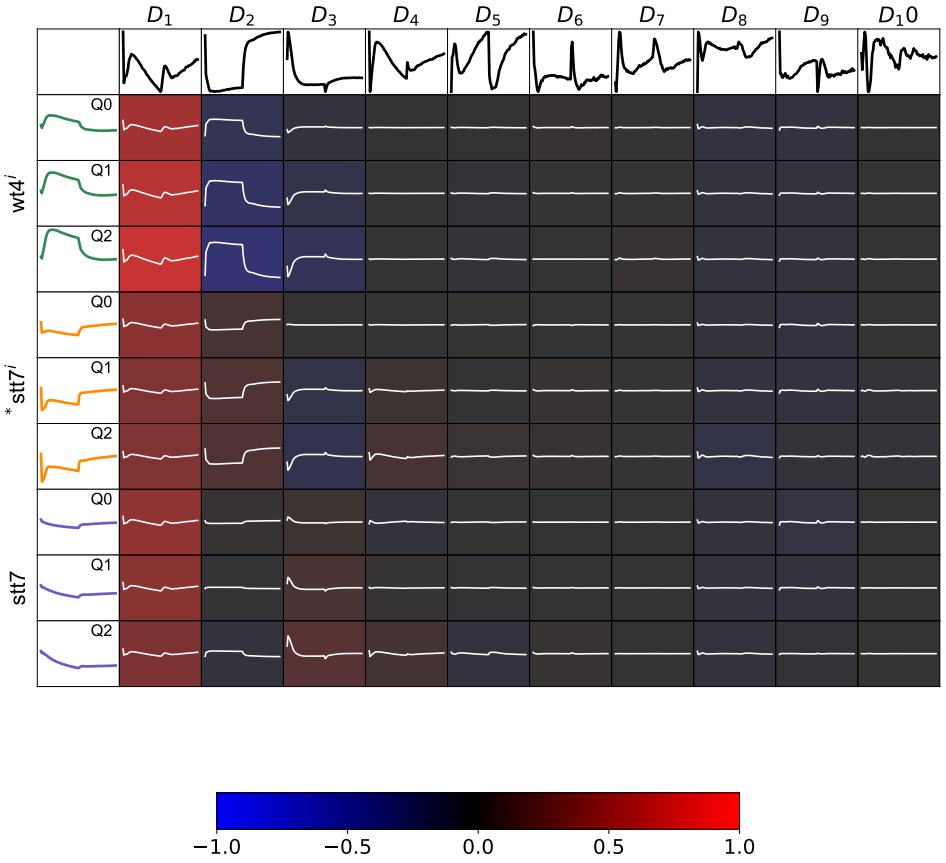

Figure 4.23: *Interpretation of the atom decomposition in terms of NPQ contribution.* Learned dictionary on the x entry, reference dataset on the y entry, (x,y): weighted atom y as it contributes in the reconstruction of the trace x. The background color represents the weight. Each population of the reference dataset is split into three groups. These groups have been established by segmenting the point cloud of a population along the axis representing its characteristic NPQ based on quantile boundaries: 20% and 80%. Example of $\boldsymbol{wt4}^i$: we split the span of the values along the axis qT-0-0 into three quantiles, to split the point cloud $\boldsymbol{wt4}^i$ into three groups of points. We call Q2 the group containing 20% of the points with the higher qT-0-0 scores, Q0 the group containing 20% of the points closer to the origin along the qT-0-0 axis, and the Q1 is the middle group with the remaining 60%. Similarly, the $\boldsymbol{*stt7}^i$ and $\boldsymbol{stt7}$ population are respectively split into 3 groups based on the qT (resp. qI) scores. The shape of the curves in the first column correspond to the average of the F_M traces of the points in each quantile.

.

4.5.6 Test of correlation between NPQ expression and light and size heterogeneity

In order to test the correlation between the heterogeneity of illumination of the algae and the level of expression of qE, qT, and qI , we first exploited the calibration of the light intensity in the field of view with **Dronpa-2** (Figure Section 2.5.2). We then measured the NPQ-score of the monoclonal culture wild type *wt4* qE-activated over four basic pattern repeats. As displayed in Figure 4.24a–c, no significant correlation appears.

In order to test the contribution of the size of the algae to the variance of the NPQ scores, we also extracted the projected surface of each alga exposed to the light as derived from the number of pixels corresponding to the segmented alga. As shown in Figure 4.24d–e, we did not evidence any significant correlation.

Eventually, we evaluated if the spatial position of the algae could affect their NPQ score. Indeed, they may have been differently exposed to gas exchange from the sides of the observation chamber. As displayed in Figure 4.24g–i, we did not evidence any specific spatial pattern of the NPQ score.

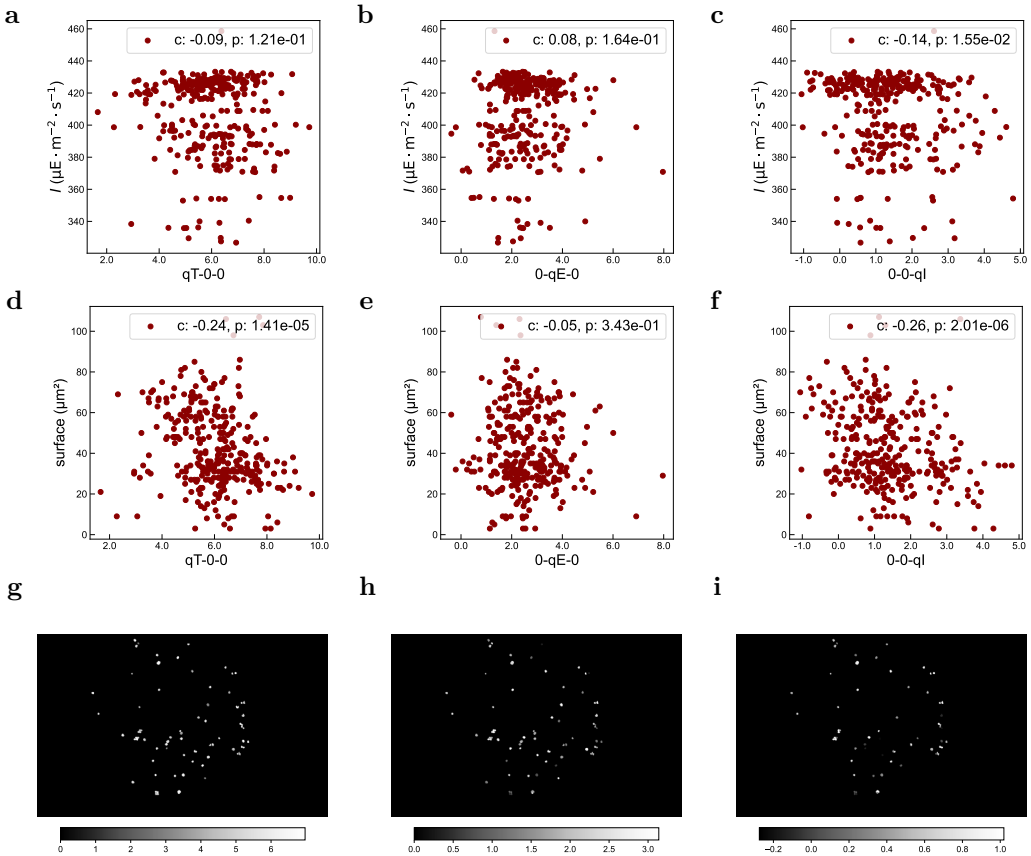

Figure 4.24: *Investigation of the correlation of the NPQ score with various parameters.* **a**–**c**: Dependence of the NPQ score (**a**: qT; **b**: qE; **c**: qI) on light intensity; **d**–**f**: Dependence of the NPQ score (**d**: qT; **e**: qE; **f**: qI) on the cell size; **g**–**i**: Dependence of the NPQ score (**g**: qT; **h**: qE; **i**: qI) on the cell position in the observation chamber. Strain: monoclonal *wt4, state: activated, overlap of the four consecutive basic pattern responses.

4.5.7 Statistical tests

Monoclonal experiments

In order to evaluate the reproducibility of the NPQ score, we performed a Mann-Whitney test on each couple of scores from two consecutive repeats on the monoclonal populations used in the experiments presented in Figures 4.12 and 4.14a–c of the Main Text. As displayed in Figure 4.25, the hypothesis of equality of the underlying distributions of the data was rejected for the 0-0-qI scores of $\boldsymbol{wt4}^i$ (p-value 10^{-6}) and $\boldsymbol{*wt4}^i$ (p-value 10^{-3}). For all the other samples, we failed to reject the equality hypothesis (p-values > 0.04). Therefore, we could use these experiments to study 0-qE-0 and qT-0-0 by identifying the repeats as identical.

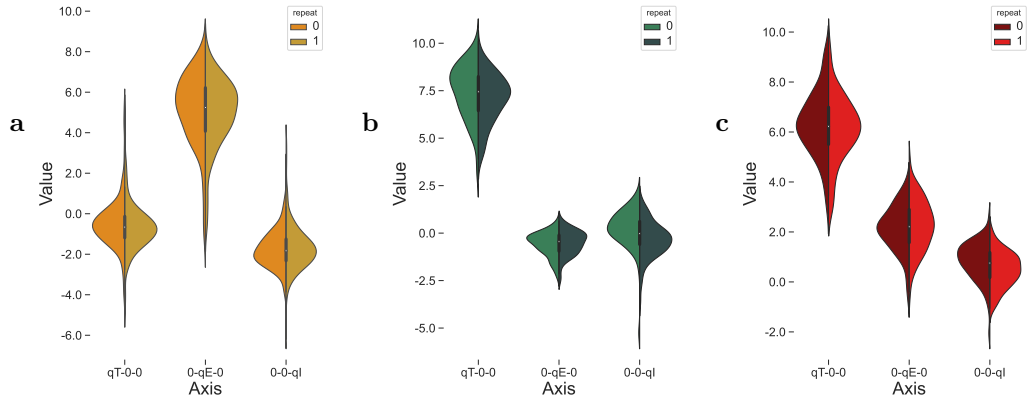

Figure 4.25: *Test of equality of the NPQ scores for the consecutive repeats of the experiments on monoclonal populations.* **a**: $\boldsymbol{*stt7}^i$monoclonal, two repeats – failed to reject equality ; **b**: $\boldsymbol{wt4}^i$monoclonal, two repeats – failed to reject equality except for 0-0-qI (p-value 10^{-6}); **c**: $\boldsymbol{*wt4}^i$monoclonal, two repeats – failed to reject equality except for 0-0-qI (p-value 10^{-3}).

Main text figures

The various statistical tests performed on the elements presented in the Main Text are presented in Table 4.3. The null-hypothesis is described along with the p-values and the conclusion. We performed normality tests on the data and report on the sample sizes. The data compared often share the same size, except when comparing $D_{i,i}$ and $D_{i,j}$. In the latter case, we used a bootstraping method, by performing the test on subsets of $D_{i,j}$ with sizes equal to $D_{i,i}$ (100 draws). The tests were performed in Python with the SciPy statistics library functions [212].

Figure	Population	Variable	Size	Null hypothesis	Samples compared	Test	p-value	Conclusion
3a	***stt7***^{i}, ***wt4***^{i}, ****stt7***^{i}, ***stt7***	NPQ(*Phase I*)	433,936 480,453	the central tendancy of the distribution of X is greater then Y's.	X: ***stt7***^{i}, ***wt4***^{i}, ***stt7*** Y: ****stt7***^{i}	Mann-Whitney	$<10^{-138}$	rejected
3b	***stt7***^{i}, ***wt4***^{i}, ****stt7***^{i}, ***stt7***	NPQ(*Phase V*)	433,936 480,453	the central tendancy of the distribution of X is greater then Y's.	X: ***stt7***^{i}, ****stt7***^{i}, ***stt7*** Y: ***wt4***^{i}	Mann-Whitney	$<10^{-194}$	rejected
3c	***stt7***^{i}, ***wt4***^{i}, ****stt7***^{i}, ***stt7***	0-qE-0	433,936 480,453	the central tendancy of the distribution of X is greater then Y's.	X: ***stt7***^{i}, ***wt4***^{i}, ***stt7*** Y: ****stt7***^{i}	Mann-Whitney	10^{-146}	rejected
3d	***stt7***^{i}, ***wt4***^{i}, ****stt7***^{i}, ***stt7***	qT-0-0	433,936 480,453	the central tendancy of the distribution of X is greater then Y's.	X: ***stt7***^{i}, ****stt7***^{i}, ***stt7*** Y: ***wt4***^{i}	Mann-Whitney	10^{-195}	rejected
3e	****stt7***^{i}	0-qE-0	480	the underlying distributions of 0-qE-0 and NPQ(*Phase I*) are uncorrelated	****stt7***^{i} 0-qE-0 and ****stt7***^{i} NPQ(*Phase I*)	Pearson	10^{-122}	rejected
		NPQ(*Phase I*)	480					
3f	***wt4***^{i}	qT-0-0	936	the underlying distributions of 0-qE-0 and NPQ(*Phase V*) are uncorrelated	***wt4***^{i} qT-0-0 and ***wt4***^{i} NPQ(*Phase V*)	Pearson	10^{-145}	rejected
		NPQ(*Phase V*)	936					
4a	****stt7***^{i} monoclonal	$D_{i,i}$	176	all input samples are from populations with equal variances	X = $D_{i,i}$ and Y = $D_{i,j}$	Levene bootstrap $D_{i,j}$	10^{-33}	rejected
		$D_{i,j}$	30976					
4d	***wt4***^{i} monoclonal	$D_{i,i}$	77	all input samples are from populations with equal variances	X = $D_{i,i}$ and Y = $D_{i,j}$	Levene bootstrap $D_{i,j}$	10^{-9}	rejected
		$D_{i,j}$	5929					
4b	repeat 0	0-qE-0	176	the underlying distributions of 0-qE-0 in the two repeats are equal	two consecutive repeats	Mann-Whitney	0.11	failed to reject
	repeat 1	0-qE-0	176					
4e	repeat 0	qT-0-0	77	the underlying distributions of qT-0-0 in the two repeats are equal	two consecutive repeats	Mann-Whitney	0.04	failed to reject
	repeat 1	qT-0-0	77					
4c	****stt7***^{i}	0-qE-0		all input samples are from populations with equal variances	3 non-monoclonal 2 monoclonal	Levene	0.99	failed to reject
4f	***wt4***^{i}	qT-0-0		all input samples are from populations with equal variances	4 non-monoclonal 1 monoclonal	Levene	10^{-9}	rejected
5a	****wt4***^{i} monoclonal	$D_{i,i}$	77	all input samples are from populations with equal variances	X = $D_{i,i}$ and Y = $D_{i,j}$	Levene bootstrap $D_{i,j}$	10^{-6}	rejected
		$D_{i,j}$	5929					
5b	repeat 0	qT-0-0	77	the underlying distributions of qT-0-0 in the two repeats are equal	two consecutive repeats	Mann-Whitney	0.4	failed to reject
	repeat 1	qT-0-0	77					
5c	repeat 0	0-qE-0	77	the underlying distributions of 0-qE-0 in the two repeats are equal	two consecutive repeats	Mann-Whitney	0.5	failed to reject
	repeat 1	0-qE-0	77					
5d	***wt4***^{i} to ****wt4***^{i}	0-qE-0	200-800	the underlying distributions of 0-qE-0 and qT-0-0 are uncorrelated	0-qE-0 and qT-0-0 for the total population	Pearson	$<10^{-250}$	rejected
		qT-0-0	200-800		0-qE-0 and qT-0-0 for individual sequentially activated populations		$<10^{-37}$	rejected
5g	cc124^i to *cc124^i	0-qE-0	200-800	the underlying distributions of 0-qE-0 and qT-0-0 are uncorrelated	0-qE-0 and qT-0-0 for the total population	Pearson	$<10^{-126}$	rejected
		qT-0-0	200-800		0-qE-0 and qT-0-0 for individual sequentially activated populations		$<10^{-7}$	rejected
6c	****wt4***^{i} and *M^i (unknown phenotype)	MSE		the distribution underlying X is stochastically greater than the one underlying Y	X = MSE(****wt4***^{i}), Y = MSE(*M^i)	Mann-Whitney	$<10^{-66}$	rejected

Table 4.3: Statistical tests performed on the elements presented in the Main Text. [1] the test was rejected due to the diversity of variance in the non-monoclonal strains, but the monoclonal variance is not an outlier.

4.5.8 Photoinhibition: evaluation of the relevance of the axis 0-0-qI

qI-score of the wild-types along qE-activation

We did not quantitatively analyze photoinhibition in the Main Text since this biological phenomenon is the hardest to control among the ones investigated and since no mutant strain exists. Accordingly, once we obtained the machine learning framework, we focused populations that had reached a steady-state of photoinhibition to avoid the contribution of qI.

Here we assess the projection of the traces from Figure 4.13d (qE-activation of *wt*4) and Figure 4.13g (qE-activation of *cc*124) on the 0-0-qI axis. The projections are plotted in Figure 4.26a,b. Before activation, qI is higher in $\boldsymbol{wt4}^i$ as initially observed in the training set. Throughout activation, it remains constant. In wild type *cc124*, it also remains stable. In both cases, the amplitude of the score is low, and convinced us we could neglect it.

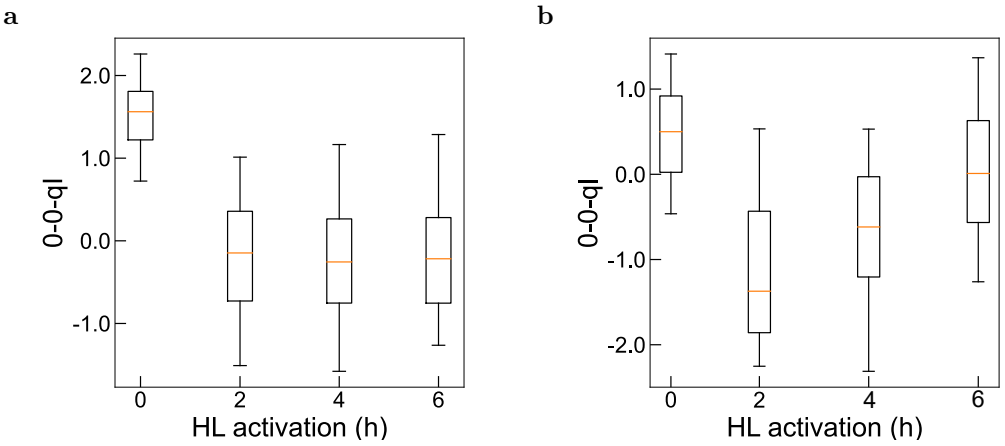

Figure 4.26: *Projection of the qE-activation process of wild-type strains along the 0-0-qI axis.* **a,b**: Projection of the NPQ scores of a *wt*4 (resp. *cc*124) population in response to a sequential qE-activation along the third dimension of the NPQ space, 0-0-qI; Data correspond to the same data as Figure 4.13d,g.

Evolution of the qI score under the four patterns repeats

As described in Section 4.5.2, applying the basic pattern on a population under growth light principally induces qI which relaxes slowly. Hence, repetitively applying the motif allows to reach a stationary regime of qI. Figure 4.27 displays the outcome of sequentially applying the basic pattern four times to a population of wild type *wt4* not activated (evolving from $\boldsymbol{wt4}$ to $\boldsymbol{wt4}^i$). In this Figure we evidence that the evolution of the point cloud along the 0-0-qI axis follows an exponential decay as reported in the literature [202].

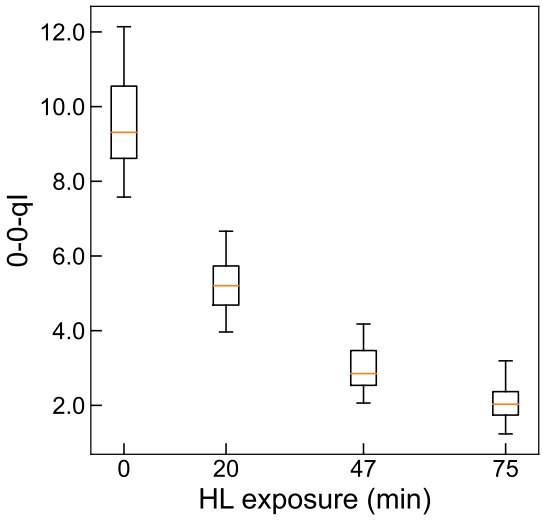

Figure 4.27: *Evolution of the 0-0-qI for a wild type wt4 strain exposed to the basic pattern four consecutive times.* Each basic pattern consists in 15 min of high-light exposure (400 μmol(photons) $\cdot$ m^{-2} $\cdot$ s^{-1}, 470$\pm$10 nm). Number of algae in the experiment: 157.

4.5.9 Alternative dimension reduction methods

With our dataset, we have tested what other approaches could have been used to reduce the dimension of the data. We compare qualitatively supervised and unsupervised methods, and linear and non-linear methods. In these tests, we did not use the intermediary Dictionary Learning step, in order to avoid any parameter selection. We used the functions provided in the library SciPy (v1.8.0) [212] with their default parameters. The aim of this section is also to investigate the need for labelled data when the objective is to retrieve biological meaning from the output of the dimension reduction.

Non-supervised, linear : Principal Component Analysis

We perform a Principal Component Analysis (PCA), using as input the F_M traces without the labels. It is a linear unsupervised method. Once the projection matrix is obtained, we perform the same alignment of the axis and redefine the origin as presented in the Methods section for the LDA. Then we color the point clouds with the known labels to investigate qualitatively the results. The PCA creates two clusters from the single ***stt7***^{i} class. Apart from the mixed half of the ***stt7***^{i} point cloud, the PCA manages to distinguish properly the classes in 3D. The evolution along the qT-0-0 axis seems to relate to the NPQ phenomena since only the ***wt4***^{i} population is spread along the axis. Both 0-qE-0 and 0-0-qI axis seems to mix qE and qI since both ***stt7***^{i} and ***stt7*** are spread along them. In conclusion the clustering performances of the PCA could be exploited for unlabeled data, but the biological meaning would be hard to interpret.

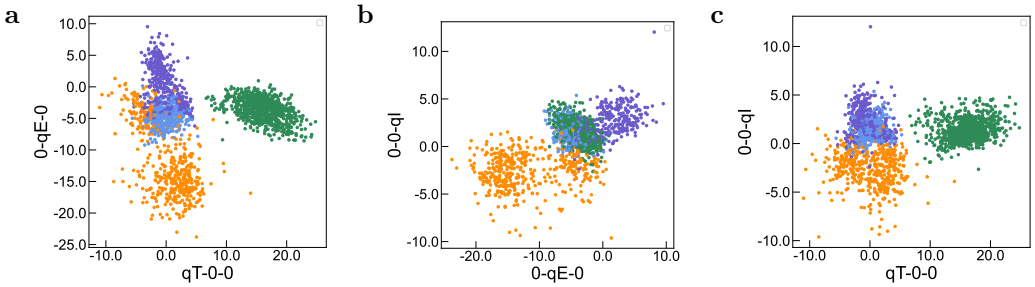

Figure 4.28: *PCA projection of the F_M traces of the reference dataset.* Orange :***stt7***^{i}, blue: ***stt7***^{i}, green: ***wt4***^{i}, purple: ***stt7***. **a**:(qT-0-0, 0-qE-0); **b**:(0-qE-0, 0-0-qI); **c**:(qT-0-0, 0-0-qI).

Supervised, linear: Linear Discriminant Analysis

We perform a Linear Discriminant Analysis (LDA), using as input the F_M traces without the labels and without the intermediary Dictionary Learning step presented in the Main Text. Once the projection matrix is obtained, we perform the same alignment of the axis and redefine the origin as presented in the Methods section. The results appear very similar to the results presented in the Main Text (Figure 4.29a and c appear similar). In Section 4.5.10 we compare the reconstruction of the F_M traces from the NPQ space corresponding to Figure 6 in the Main Text with and without the Dictionary Learning to underline the advantage to introduce a reconstruction step.

Non-supervised, non-linear: t-SNE/UMAP and K-means clustering

We compared two non-linear dimension reduction algorithms that are unsupervised, t-SNE and UMAP. The two methods take as input the F_M traces and project them onto a 2-dimensional space with the aim to cluster together projected points that come from traces that are similar (the similarity is defined within the metrics optimized by the algorithms). We begin by using the four training populations from the reference dataset. In order to evaluate the performance of the dimension reduction method in distinguishing the classes, we use the labels we already have from the dataset

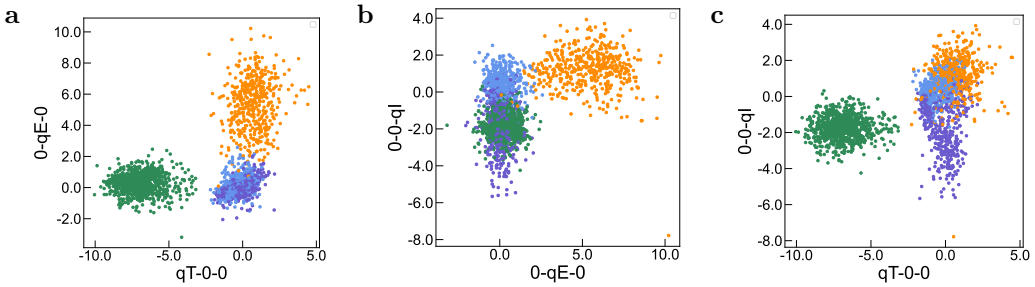

Figure 4.29: *LDA projection of the F_M traces of the reference dataset.* Orange : ***stt7**^{i}*, blue: ***stt7**^{i}*, green: ***wt4**^{i}*, purple: ***stt7***. **a**:(qT-0-0, 0-qE-0); **b**:(0-qE-0, 0-0-qI); **c**:(qT-0-0, 0-0-qI).

(Figure 4.30). On the one hand, we color the point clouds with the labels corresponding to the ground truth, and on the other hand we perform a K-means clustering algorithm. The K-means groups projected points together into clusters. The number K of expected point clouds has to be defined as input (the need to know the number of classes can be limiting when investigating a set of unlabelled samples).

There the prediction accuracy with t-SNE and UMAP is respectively 61% and 69%.

By construction the population ***stt7**^{i}* shares similarities with all the other classes, since it is expected to represent the origin of the NPQ space. We tried to remove it from the dataset and perform the K-means clustering with K=3 (Figure 4.31). In this case, the accuracy performances are higher (t-SNE: 79%, UMAP: 94%). We conclude that adding a set of traces with no stress response would not be suitable for non-linear investigations, as it makes the clustering of the projected data less accurate.

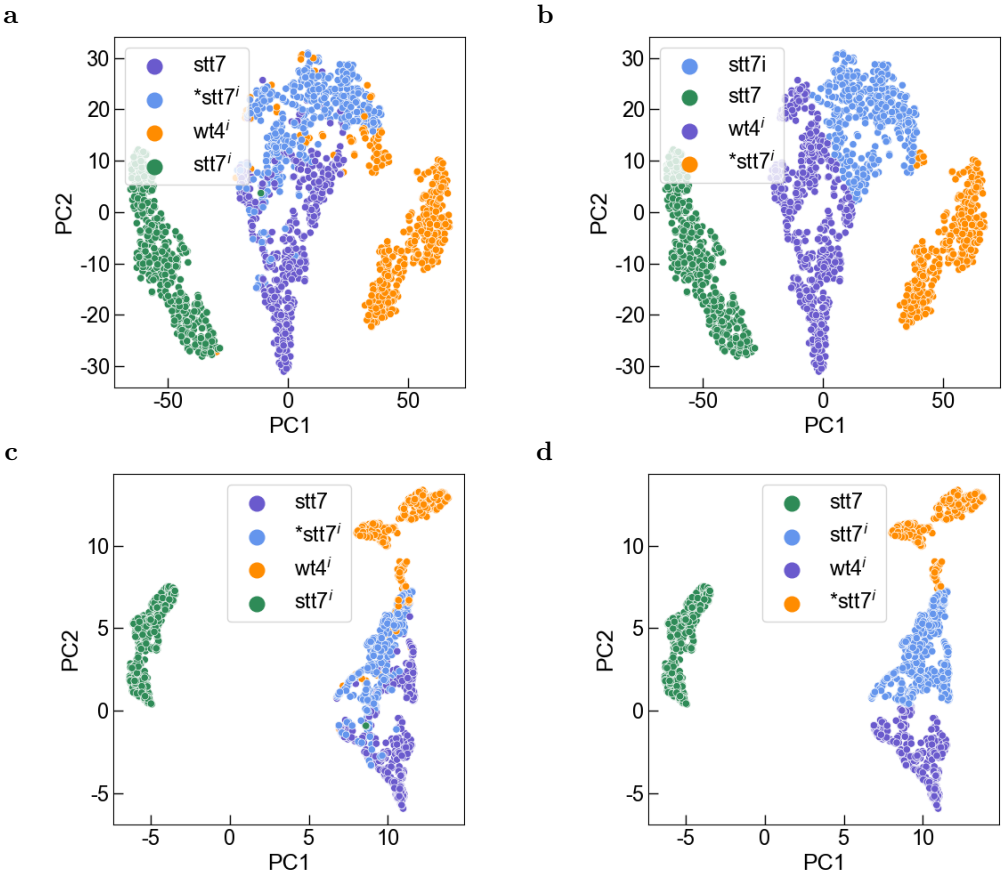

Figure 4.30: *Comparison between the ground truth labels and the labels attributed by K-Means clustering on the four populations of the reference dataset, unsupervised dimension reduction performed with UMAP and t-SNE.* **a,b**: t-SNE dimension reduction of the F_M traces of the four populations of the reference dataset, **a** ground truth, **b** K-Means clustering predictions; **c,d**: UMAP dimension reduction of the F_M traces of the four populations of the reference dataset, **c** ground truth, **d** K-Means clustering predictions.

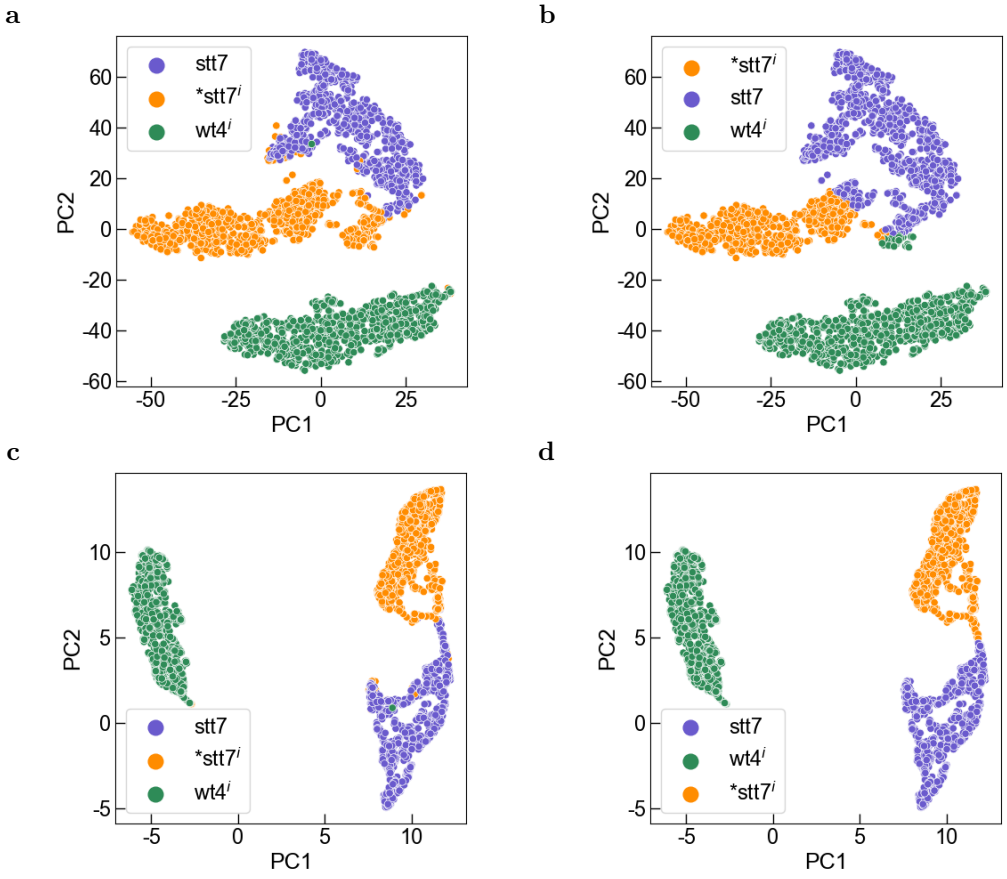

Figure 4.31: *Comparison between the ground truth labels and the labels attributed by K-Means clustering on the populations of the reference dataset presenting a stress response (qE, qT or qI), unsupervised dimension reduction performed with UMAP and t-SNE.* **a,b**: t-SNE dimension reduction of ***wt4***^{i}, ***stt7***^{i}, ****stt7***^{i} F_M traces from the reference dataset, **a** ground truth, **b** K-Means clustering predictions; **c,d**: UMAP dimension reduction of ***wt4***^{i}, ***stt7***^{i}, ****stt7***^{i} F_M traces from the reference dataset, **c** ground truth, **d** K-Means clustering predictions.

4.5.10 Atypical traits: role of the reconstruction optimization

In this section we compare the LDA dimension reduction with and without an intermediary reconstruction step by dictionary learning. We apply it to F_M traces not seen during the training phase. We use the strains presented in Figure 4.14e,h. The $\boldsymbol{*wt4}^i$ population is projected with an intermediary Dictionary Reconstruction step as presented in the Main Text (Figure 4.20a), or without (Figure 4.20b), following the method described in 4.5.9. We notice a more narrow distribution with the intermediary reconstruction. Then, we perform the same comparison with the atypical strain presented in the Main Text. The data project within the boundaries of the NPQ space defined throughout our analysis (Figures 4.20d,e). As such, they cannot be identified as outliers within this representation. The result in Figure 4.20d is not surprising considering how the Dictionary fails to reconstruct the traces properly. We conclude that an analysis only relying on the projection in the NPQ space could not allow to identify the critical difference of the original F_M traces to the expected behavior of a qE-activated wild-type. Here it stresses the necessity to ensure that the new data are compatible with the dimension reduction method. For this reason we have introduced a test on the Mean-Squared error to evaluate the reconstruction quality using a linear combination of the atoms described in the Main Text. With the dictionary learning reconstruction, we find an order of magnitude difference in the reconstruction quality between data compatible with the training set ($\boldsymbol{*wt4}^i$) and outlier data ($*\mathbf{M}^i$). This reconstruction in partly possible to perform when only the LDA is used. It is possible to use the pseudo-inverse of the projection matrix in order to recover the patterns that have been preserved in the dimension reduction. They represent the data identified as meaningful by the LDA to separate the data. Reconstructions using the pseudo-inverse of the LDA are presented for both populations in Figure 4.20c,f. As expected, the reconstructions are more noisy and less resembling the original traces than with the Dictionary Learning presented in the Main Text, since the LDA does not include a reconstruction metric. As a consequence, the comparison of the Mean-Squared error between the original F_M traces and their reconstruction is less discriminative to identify outlier populations (Figure 4.20g).

For data processing, the F_M traces were divided by the integral of the signal to yield a set of probability distributions.

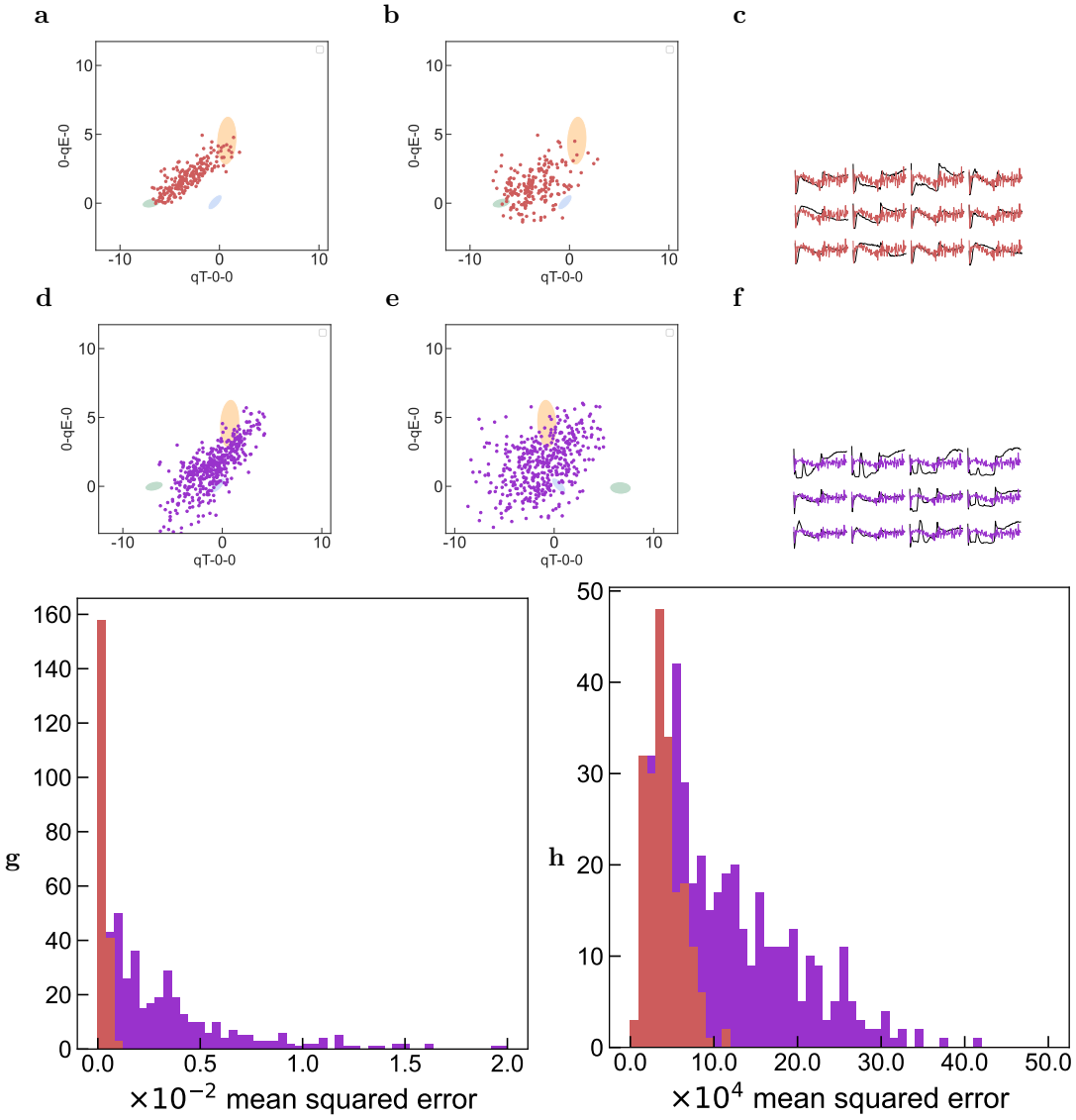

Figure 4.32: *Dimension reduction with LDA without introducing a reconstruction step, consequences on the identifications of outliers.* **a**: Projection of $\textit{*wt4}^i$ traces with Dictionary Learning + LDA in the NPQ space, the training populations centroids are indicated by shaded ellipses; **b**: Projection of $\textit{*wt4}^i$ traces with LDA only in the NPQ space, the training populations centroids are indicated by shaded ellipses; **c**: Pseudo-reconstruction of the traces from the projection of the F_m traces of $\textit{*wt4}^i$ directly to the NPQ space (LDA only). The traces with the highest reconstruction error are plotted. black: original F_M traces, red: pseudo-reconstruction; **d**: Projection of $^*\mathbf{M}^i$ traces with Dictionary Learning + LDA in the NPQ space, the training populations centroids are indicated by shaded ellipses; **e**: Projection of $^*\mathbf{M}^i$ traces with LDA only in the NPQ space, the training populations centroids are indicated by shaded ellipses; **f**: Pseudo-reconstruction of the traces from the projection of the F_m traces of $^*\mathbf{M}^i$ directly to the NPQ space (LDA only). The traces with the highest reconstruction error are plotted. black: original F_M traces, purple: pseudo-reconstruction; **g-h**: Distribution of the mean-squared error between the original F_M traces and the dictionary reconstruction (**g**) or the LDA pseudo-reconstruction (**h**). Red: $\textit{*wt4}^i$, purple: $^*\mathbf{M}^i$.

4.5.11 Mutant identification in non-linear clustering

We investigated whether non-linear dimension reduction algorithms were more performing at identifying outliers. We focused on UMAP since it builds a mapping between the input space and the low-dimension space that can be reused on new data, as opposed to t-SNE where the mapping is embedded in the algorithm.

We began by using the UMAP mapping obtained from Section 4.5.9 and applied the transformation to the traces corresponding to $\textbf{\textit{*wt4}}^i$ and $^*\mathbf{M}^i$. We observe that the $\textbf{\textit{*wt4}}^i$ populations projects onto the three training populations, and almost none on the rest of the projection space. Compared to the data presented in the Main Text, the notion of continuum that appears in the wild-type strains is absent. This representation could lead to believe that a wild-type strain will choose to express only one stress response among the three possibilities. However, from the analysis of the traces in Figure 4.13d,e,g,h, the stress responses are combined continuously in the NPQ space in wild-type strains. Therefore, the representation presented in Figure 4.33a does not match the underlying biology.

The $^*\mathbf{M}^i$ data are projected onto the same position as $\textbf{\textit{*stt7}}^i$ although the kinetics of the F_M traces are clearly distinct. The UMAP mapping has learned to project them onto the same cluster, which evidences a loss of information in the reduction dimension that can be critical when studying new data.

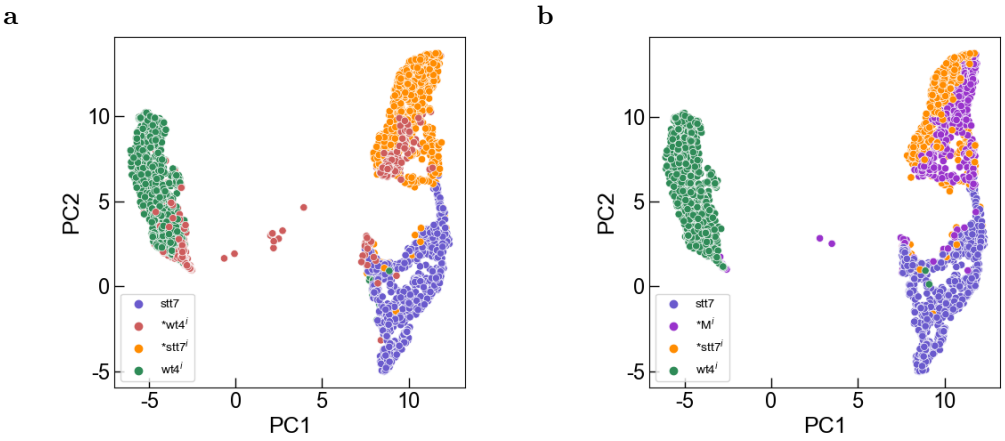

Figure 4.33: *Projection of* $\textbf{\textit{*wt4}}^i$ *(**a**) and* $^*\mathbf{M}^i$ *(**b**) using the UMAP mapping learned from* $\textbf{\textit{*stt7}}^i$, $\textbf{\textit{wt4}}^i$ *and* ***stt7****.*

Then we included the classes $\textbf{\textit{*wt4}}^i$ or $^*\mathbf{M}^i$ along with $\textbf{\textit{*stt7}}^i$, $\textbf{\textit{wt4}}^i$ and ***stt7*** in the non-linear dimension reduction in order to see how they would be distinguished (Figure 4.34). We performed the transformation with UMAP and t-SNE. Both algorithms perform better at distinguishing the atypical population $^*\mathbf{M}^i$ which resembles less the reference dataset than $\textbf{\textit{*wt4}}^i$.

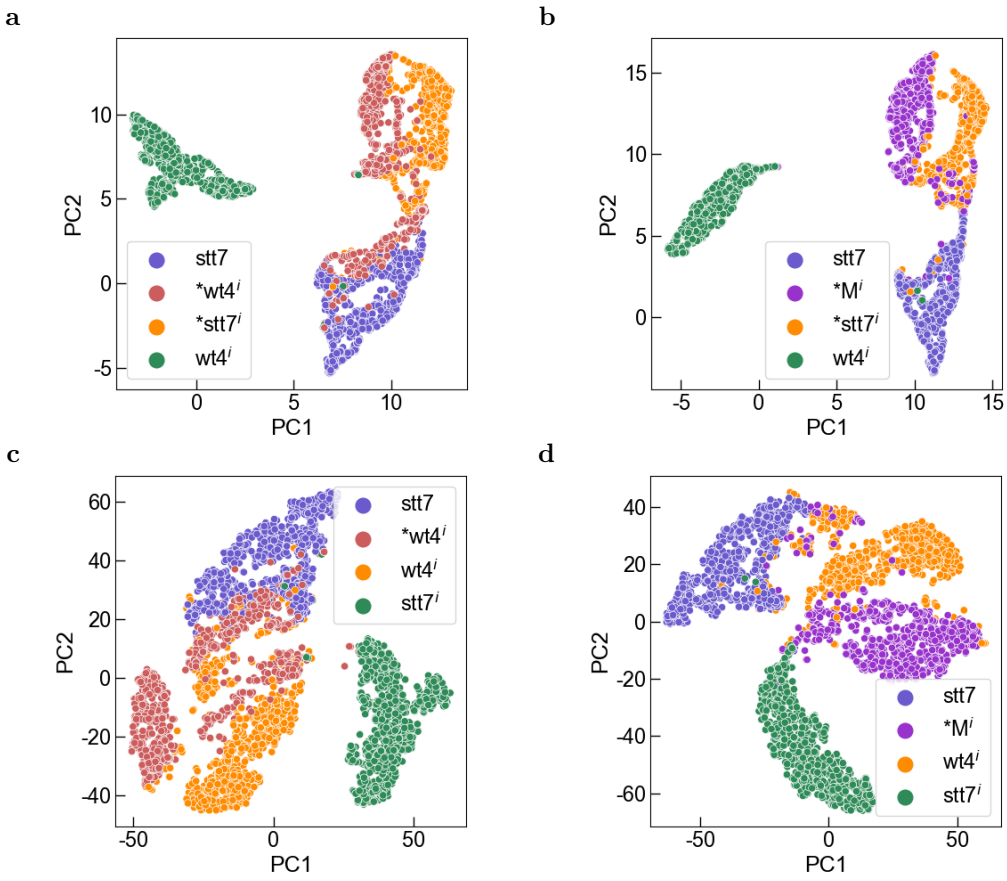

Figure 4.34: *Non-linear clustering of the database and the mutant.* **a**: UMAP, ground truth; **b**: UMAP, prediction; **c**: t-SNE, ground truth; **d**: t-SNE, prediction.

Chapter 5

Open Source microscopy

5.1 Introduction

In Chapter 2 I presented the epifluorescence microscope we built with Thorlabs equipment and automated with Python. As I spent a significant time designing the software in Open Source and making a replicable database system, I deemed consistent to make the hardware design open as well. In this chapter, I present how I reproduced the Thorlabs instrument described in Chapter 2 using an Open Source hardware optics library. I removed the proprietary hardware and controllers to make the whole instrument reproduction affordable and accessible. This approach was in line with the ROMI and the DREAM projects, as one of the project long-term deliverables is to define the specifications for a portable device, that could be used in particular in small-scale farms.

I then describe the software which is shared across both instruments, and the database system. In the midst of process, I successfully reproduced results of experiments described in Chapter 2 (light calibration) and Chapter 4 (NPQ score from fluorescence trace). It is worth underlining that, although the European Union requires a minimal level of Open Source in the funded projects, there is little recognition for the production and documentation efforts (at least at the academic level). I hope that persevering and discussing the advantages of working in openness can empirically contribute to changing this context. I begin the chapter with an introduction of the various aspects addressed to make the instrument open, and detail specific choices. Then I introduce a manuscript in the format of Journal of Open Hardware to present in details these contributions.

5.2 Open Source hardware

I had in mind to reproduce the instrument in an Open Source hardware version. Open Source hardware designates physical products or devices whose designs, specifications, and documentation are made available to the public, allowing anyone to study, modify, distribute, and manufacture them. I share the belief [225–227] that the development of Open Source hardware will play a significant role in smoothing the access to new state-of-the-art imaging techniques. As such, it has been recognized as an exciting new field of general interest, as evidenced by published articles in high-impact journals [228–232].

Since the motorized stage was already Open Source (Chapter 2), the main change at the automation level was to replace the LED controller (DC4104, Thorlabs, NJ) system. The alternative version uses a DC-DC converter (RDC 24/1.2, RECOM Power, Austria) powered by a direct current power supply and feeding current to the LED based on a digital, analog or pulse-width modulated input. The rise time of the LED controller was below the μs while the RECOM rises in 50 μs, which makes it more complex to measure OJIP (Chapter 3) but allows reproducing light calibration, pulse fluorescence experiments, and later modulated-light experiments.

I was also interested in replacing the main Thorlabs parts and modules, which can be very expensive. In the literature, two libraries mimicking Thorlabs parts were developed and published in 2018 with μCube [233] and 2019 with OpenUC2 [234]. Both libraries allow to reproduce a similar optomechanical framework using 3D printing. After meeting Benedict Diederich in a conference, we exchanged our Github pages and Benedict implemented our motorized stage (described in the following manuscript) in the UC2 library [235], while I reproduced the epifluorescence microscope setup with OpenUC2 as described in the manuscript below, with contributions from Thomas Le Saux, Peter Hanappe, Ian Coghill and Alec Cochard. I saw four advantages to this approach: the modularity offered by Thorlabs is preserved, the cost is low, the waiting time for parts is reduced because it is limited by 3D-printing and not ordering and shipping, and the design flexibility is increased because the parts can be modified using a 3D design software. The design flexibility, however, comes at the cost of a lower stability, especially for the alignement of the optics. Some parts of the final design, such as LED fiber holders, retain rings for filters, and optical tubes, were from Thorlabs but could have been 3D-printed.

5.3 Open Source software

Open Source software refers to computer software whose source code is freely available to the public. The term "Open Source" emphasizes the principles of transparency, collaboration, and community-driven development. Open Source software grants users the right to study, modify, distribute, and improve the software. I chose to write the codes in Python, a well-spread open-source programming language, to which anyone can contribute by writing libraries before distributing them online. Thanks to this highly collaborative framework, Python-based solutions have been developed in all the topics I needed to handle the project: instrument control, image analysis, machine learning, database systems, and more. Open Source is not widely prevalent in the context of experimental science. Instruments are usually provided with an Application Programming Interface (API) which describes the communication protocol with the hardware driver.[1] With the diversity of manufacturers comes a diversity of APIs, making coding hardware interfaces a complex task.

In recent times, there has been a notable surge of Python software being developed to control microscope with a unified system [236–239]. At the time I started developing the instrument, these works were neither published nor documented, which led me to develop my own system. It turns out I took a different direction, avoiding the use of a unified framework, which requires some level of maintenance and to be able to adapt the pipeline to the diversity of APIs. In fact, I decided to develop a set of modular tools that would be as independent of each other and of the manufacturers' APIs as possible, and could be used in multiple contexts. The pipeline is shown in Figure 5.1. The Arduino codes are borrowed or derived from the ROMI project.

For the motor and light source control, I took advantage of the possibility to control them with analogic or binary electric signals rather than a driver. For the motor, the Arduino controls a motor shield and sends electric signal to indicate the number of steps the motor should do and in which direction. The shield encrypts it and sends signals to generate magnetic fields in the motor's magnets through four wires. For the LED, the signal sets the current level in the LED circuit. I used the communication protocol between Python and Arduino developed in the ROMI project to describe the desired signals in Python and generate them with Arduino.

For the camera, I benefited from the framework of μManager [240]. μManager is a Java/C++ Open Source software which is used in multiple laboratories to control instruments, and has been combined with ImageJ and now DeepImageJ [241] to integrate imaging and image analysis with the possibility to use deep learning. μManager is so wide-spread that manufacturers frequently develop specific APIs that align with the μManager. I could have used μManager for the whole project. However, I had far more experience in Python than Java and C^{++}. Instead, I used the library *pymmcore* which binds μManager API with Python. That way, I could leverage the adaptation of

[1] The driver is a program that enables the computer to control the hardware device.

manufacturers' APIs to μManager and transfer them to Python. This allows to switch camera on a setup with minimal changes: only providing a file with the parameter names and values. The camera can be triggered externally by the Arduino that control the LEDs: the same type of signal can be used to control an LED or the camera, allowing to synchronize them.

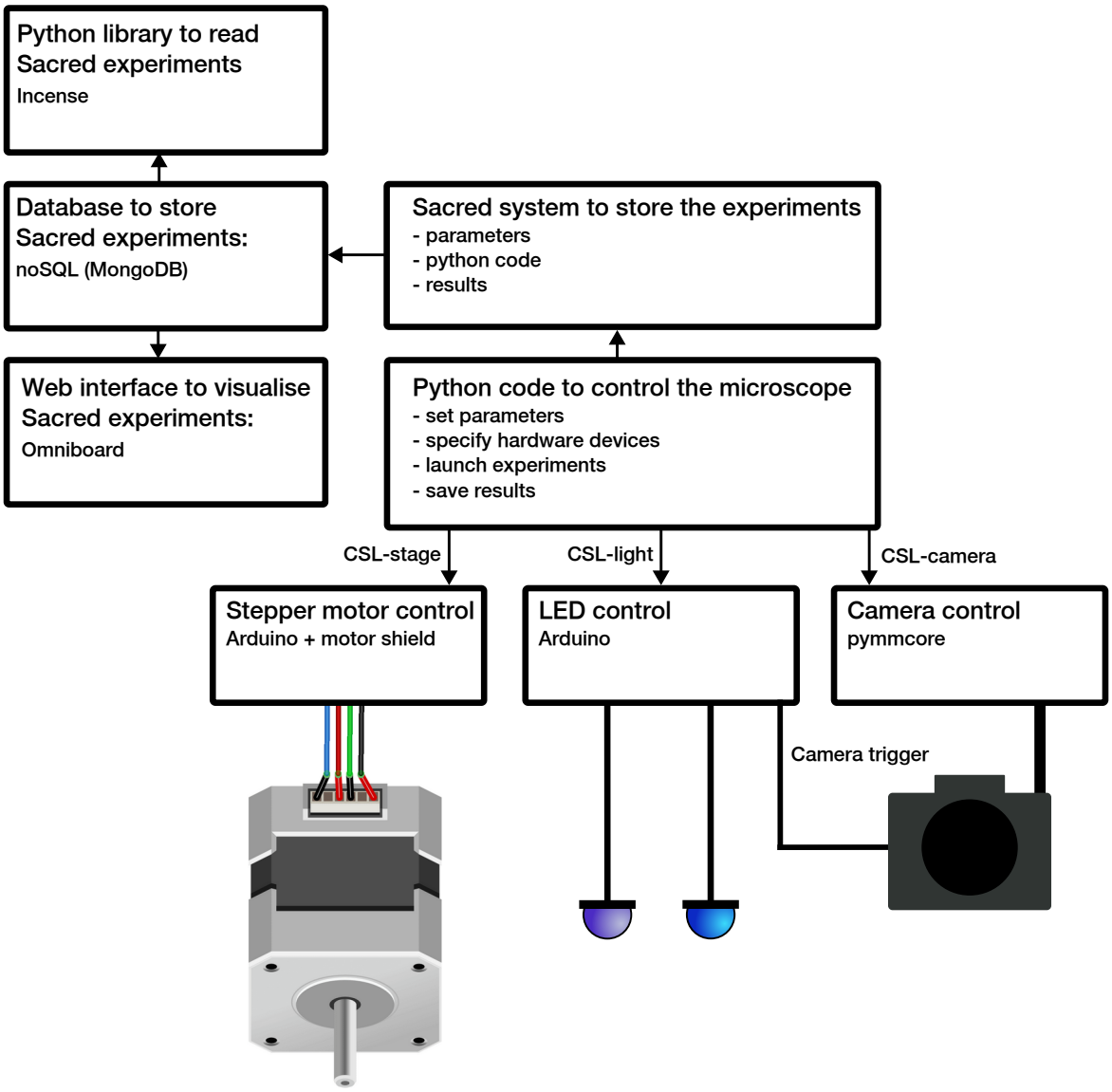

Figure 5.1: Scheme of the Software pipeline controlling the microscope parts (camera, light sources, motors) and collecting the experimental results.

5.4 Database system

Once the automation of the setup was implemented, it became obvious that data management would become critical. Here it is important to describe the landscape of database systems in microscopy, and in experimental research in general. Same as for the API, but less often, hardware

manufacturers may provide systems to store the experimental data, visualize them and eventually analyze them. An example is the LAS X platform developed by Leica compatible for all Leica microscopes, allowing to store data, metadata and perform analysis. Yet, the data formats are incompatible from one manufacturer to the other. To tackle this issue in microscopy, 20 years ago the Open Microscopy Environment (OME) consortium was created to produce open-source software and format standards in microscopy [242]. They introduced bio-formats, a Java library for reading and writing microscope images file formats and facilitating the exchange of data between instruments, analysis software, and partners. It converts the proprietary formats into the open OME data model, the standard introduced by OME. This format is bound to evolve in the next years under the OME-ZARR [243] format which allows storing x, y, z data, color channels, time evolution, and image transformations, and analyze and save the data with adapted interfaces.

The OME consortium also developed OMERO, a software platform to control, analyze, visualize and manage microscope experiments. It could have been adapted for us, but after reading the publications, investigating forums (often stating that a full-time data manager would be necessary), and realizing that at least four different programming languages are used in the current interface, we did not consider it. The other solution that was used in the ROMI project is to rely on a service provider. At the beginning of my PhD, there was no funded European project to justify such an expense, and by the time the DREAM project was accepted, I had already settled for the solution I describe below. The DREAM consortium was convinced by this solution and the various partners have started to implement it.

To manage the data, my experience in Machine Learning research guided me towards the use of dashboards. In Machine Learning, it is frequent to run multiple times the same code with small changes in the hyperparameters to reach an optimal result. To monitor the experiments, an extra-layer is added to the code to define the hyperparameters configuration and collect the outputs. It generates a file that stores the experiment's code and the output data and metadata. This file is usually visualized in a web interface. It can be seen as the equivalent of a laboratory notebook. The most commonly used library is Tensorboard, or the proprietary library Weights & Biases. By comparing multiple solutions, I found Sacred, which was very easy to implement. I detail Sacred in the following manuscript and give examples of the interface in the Supplementary Materials. We now aim to implement the system for the whole DREAM project, by writing small executable codes to transfer outputs from commercial instruments of our partners into the database, and adapt the outputs to the OME-ZARR format.

Since I implemented the database system three years ago, I count 19000 completed experiments and 21000 experiments in total. The experiments last between one second and two hours. The 2000 failed experiments are related to code development: an error forbids the complete execution of the experiment, the experiment is manually interrupted because one parameter was badly chosen, or a device was malfunctioning, or the mirror that sends the fluorescence to the camera or the photon counter was manually misplaced, etc. It is interesting to notice that less than 10% of the experiments correspond to development. It is an overall low cost because, once an experiment is developed, it can be ran again with minimal intervention: I count an average of 20 experiments per day since the database was implemented.

5.5 License

For the project I chose a GNU General Public License (GPLv3), introducing the concept of copyleft. This concept uses copyrights as means to grant rights and freedoms rather than impose restrictions. When someone distributes a project that is licensed under GPL and that they have modified, they must respect the license rights and forward them, to preserve the openness of the software. The GNU GPLv3 license gives the freedom to use the source both for commercial and non-commercial use, to modify the code (as long as the modifications are specified) and to redistribute copies. Each distribution must include the license and the modifications must equally be distributed

under the GPLv3 license. For the portable prototype of the DREAM project, we may consider selecting a wallet of license with different openness level for the hardware, software and interfaces. This is especially important when the project is aimed to be commercialized under open licenses. The level of openness of each license reflects the different levels of contribution and desire for engagement of the targeted user community. The interfaces, which are expected to be versatile and tunable by the users, will probably be more open than the hardware design. The latter needs to be consistent enough to properly integrate new developments of the software coming from diverse contributors. It is important to have a strong vision to guide the future developments of the Open project and ensure its viability over time, because a drawback of open contributions is the risk of losing consistency.

Our vision for the CSL-libraries presented in the following manuscript is to provide modules independent enough so that developments in one of them do not affect the other modules.

5.6 Manuscript: CSL-libraries for Modular Open Microscopy

5.6.1 Abstract

Microscopy is a vital experimental tool in life sciences. However, when attempting to reproduce or scale-up a published method, researchers often face difficulties implementing the specific protocols because they do not have full control over the hardware. To address these challenges, we present a modular Open Source hardware and software platform that integrates an automated microscope, a data processing pipeline, and a database management system. Our modular approach gives researchers the necessary tools to reproduce experimental setups and implement new protocols. It also provides a simple way to develop experiments with a persistent record of their configurations and results, even during the developmental stage. We provide comprehensive guidance on building and calibrating the microscope hardware, implementing automation, and data analysis and storage methods. Notably, our innovative communication protocol between Python and Arduino enables versatile control of light sources and motors. The highly modular Python software facilitates customization and reusability beyond microscopy, empowering researchers to adapt components for other scientific applications. Additionally, we integrate the pipeline with a flexible database management system, providing a user-friendly web interface for experiment visualization and data access.

5.6.2 Introduction

Microscopy is a vital experimental tool in life sciences for visualizing and analyzing biological structures and processes at the cellular and molecular scales. Its capabilities are continuously being extended by researchers who develop novel imaging protocols. One common problem, affecting the reproducibility and scalability of imaging systems and experimental results, is that the hardware and software design is not easily obtainable by users [228, 244]. Hohlbein *et al.* [245] describe how Open Microscopy can address these replication issues by making well-designed and well-documented hardware and software solutions openly available to a broad audience under an Open Source license [246]. In the recently established field of Open Microscopy, two avenues have been identified by Salido *et al* [247]: portable field microscopes (PFM), often based on smartphones, and multipurpose automated microscopes (MAM). While the first concentrates on accessibility, portability and low price, the second focuses on modularity and image quality. Both approaches have reached different development levels, from enabling replication to gathering a community (OpenFlexure [248], Foldscope [249], OpenUC2 [229]). Despite the comprehensive documentation available for the hardware design of existing projects, there has been somewhat less focus on the software and data management.

Independently, there have been multiple software solutions developed for instrument control. The most wide-spread is μManager [240] which is written in Java and C^{++} and allows for the control of several elements of a microscopy setup, including mechanical components (stages, shutter) and camera acquisition. Due to the popularity of μManager, several instrument manufacturers have adapted to its architecture and now provide tailored libraries. Hence, leveraging μManager resources

is a good strategy for developers wishing to program in another language. This is the concept of the PycroManager library [237], which gathers full control of a μManager instance using Python and the *pymmcore-plus* library. This library targets regular μManager users who are familiar with the more user-friendly Python. Along similar lines, a software known as Napari, an equivalent of ImageJ, and consequently of μManager, in Python [236], is being actively developed by a large community and will likely lead to significant improvements in microscopy software developments. Other libraries, also leveraging the tools of μManager and Napari, are developing rapidly [238, 239]. These libraries can be combined to create a unified modular environment for overall microscope instrument control. Unification is however a complex task, especially if some components are not compatible.

Another important aspect in relation to software is the management of data and metadata [250, 251]. It is essential to facilitate their analysis and enable efficient sharing of the information. The current gold-standard in microscopy research is the Open Microscopy Environment (OME [242]) that enables a full pipeline implementation from data acquisition, instrument specification and consistent monitoring throughout the analysis pipeline [252]. Due to its rich development, this platform can be hard to handle for a beginner.

In this work we present a highly modular microscope, with independent libraries for controlling each building block of the instrument (light sources, camera, motorized stage), as well as a Python-based software pipeline for experiment automation and data storage. We focus on ease of implementation and visualisation, so that our tools can be used as a laboratory notebook [253]. We detail (1) how to build and characterize the microscope, (2) how to implement experiments, (3) how to store experimental data. It should be noted that the system we introduce can be fabricated at low cost. The solution, with all components being controlled automatically, and with all settings and data being stored, is a step towards better replicability in microscopy research. As a form of validation, we replicated an experiment that was originally performed on a different, and more expensive higher-end, epi-fluorescence system.

5.6.3 (1) Overall implementation and design

Some of the modules were initially designed to control a more elaborate device that was built using mostly Thorlab components (see Chapter 2). This laboratory microscope was used to perform the experiments detailed in Chapter 4. In order to demonstrate the inter-operability of our design, we decided to build an affordable open-source open-hardware version based on the OpenUC2 library [229], and replicated the experiments. Both instruments also share the same software back-end. This dual setup has enabled us to conduct experiments concurrently, facilitating calibration and verification of the outcomes.

Hardware

The **OpenUC2-fluorescence microscope** houses the camera and optics to measure the fluorescence signal from the sample. A validated fluorescence microscope built with OpenUC2 is presented in [254]. Below we describe the modifications we made.

Our illumination system is decoupled from the imaging system. It consists in two high-power LEDs (470 nm and 405 nm) band-pass-filtered, collimated with a lens. Their beams are combined with a dichroïc filter. A low-cost microscope objective injects the light into an optical fiber. The output light is collimated by a lens and reflected by a dichroïc filter (cut-off wavelentgh 446 nm) through a second low-cost microscope objective onto the sample. To reach better image quality, a more sophisticated objective can be recommended, as in [254], but for our application a simpler one is sufficient. The fluorescence is collected by the same objective and transmitted by the dichroïc filter (560 nm) towards a tube lens and the camera. The fluoresced light is filtered by a green filter for light calibration with **Dronpa-2** (see Appendix 2.6) and a red filter for chlorophyll fluorescence (see Chapter 3). Low-cost band-pass filters show larger bandwidth for wavelength selection than high-quality ones. Therefore, we did not make cost compromises on the band-pass filters for excitation

and emission, which increases the cost of the instrument. However, low-cost high-pass filters were sufficient for the dichroic modules. Although using mirrors would have allowed to make the setup more compact, we decided to avoid them to limit the amount of manual alignment of the setup. Almost all the parts are 3D-printed, some coming from OpenUC2 library, but also some new designs for the lens-holding parts and the motor parts. Each part is easily removable to enforce modularity. The design and the optical parts are described on Github[2].

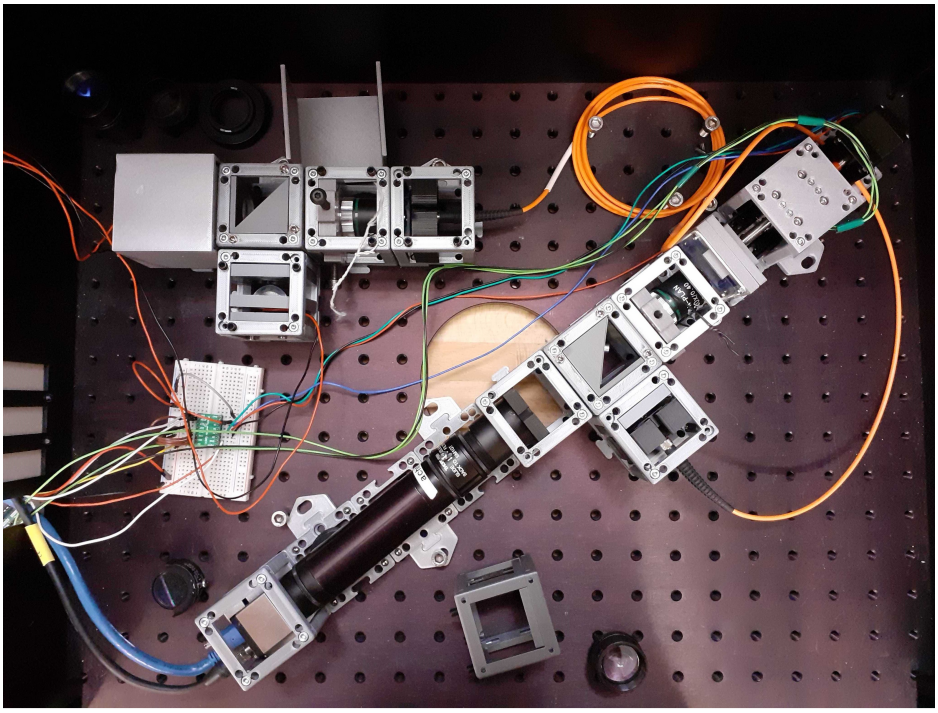

Figure 5.2: *OpenUC2 fluorescence microscope.*

Software

We introduce four software modules to interface with the hardware: CSL-serial, CSL-leds, CSL-stage, and CSL-camera.

CSL-serial allows communicating reliably between the main computer and the Arduino boards. The Python code allows sending commands to the firmware in a generic fashion using variadic functions. It implements a text-based, request–response message-passing system with additional error checking. The commands are serialized and wrapped into an "envelope" that adds a sequence number and an 8-bit cyclic redundancy check (CRC8). Both features allow detecting transmission errors and resend the command if necessary while avoiding duplicates. It also handles time-outs to avoid deadlocks in case of failure. The message size is limited to 58 bytes to avoid buffer overflows due to the limited capabilities of the serial implementation on some Arduino boards. This library is used in the libraries **CSL-leds** and **CSL-stage** (it is the only dependence between our libraries).

CSL-leds is a firmware for the Arduino Uno to generate trains of pulses to activate the light sources with frequencies of up to 500 Hz. An example code is provided in Figure 5.3a. The outputs of the Arduino should be connected to an LED driver that provides the necessary power to the LEDS. We control up to five LEDs synchronously (the practical limit is the number of pins available on the Arduino). The user can specify the start time (or delay), pulse duration, period and amplitude of

[2]SonyCSLParis/UC2_Fluorescence_microscope forked from openUC2/UC2_Fluorescence_microscope

the train of pulses (Figure 5.3b). This amplitude value corresponds to the duty-cycle of the PWM emitted during the "on" cycle of the pulses and is a means to control the light intensity of the LEDS. The time resolution is one millisecond with a maximum duration of 2^{15} seconds. The output can also be used as a trigger to synchronize image acquisition with a camera together with the light sources (Figure 5.3c).

a

```
from CSLlight import ControlLight
arduino_port = "COM5"
sec = 1000 #conversion ms to s
LED_param = {'pin':11,
             'offset':0.5*sec,
             'period': 5*sec,
             'duration': 2*sec,
             'analog_value': 255
             }

LEDs = ControlLight(port_arduino)
LEDs.add_digital_pulse(LED_param)
LEDs.start_measurement(100*sec)
LEDs.stop_measurement()
LEDs.reset() #optional
```

b

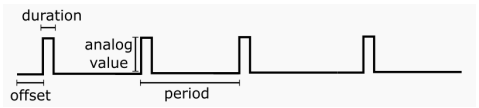

c

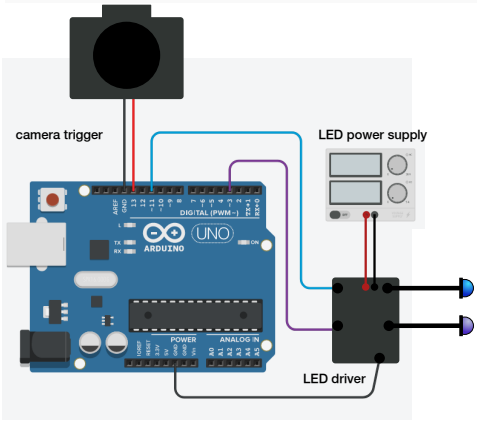

Figure 5.3: *Light source control module;* **a**: Example of code to control the LED **b**: Controllable parameters for each pin output of the Arduino. The output signal can be fed to a light source, a light source controller, or an instrument that takes a trigger signal as input; **c**: Scheme of the circuit to control an LED driver with an Arduino UNO (designed with Tinkercad [255]).

CSL-stage is a custom Arduino code allowing to control stepper motors through a motor shield (Figure 5.4c). We use standard stepper motor controllers that have a *step* and *direction* input. Up to three controllers, and thus three motors, can be driven simultaneously. The code takes into account relative and global displacement, stop switches, and can be disabled to allow manual control. The rotation speed can also be specified. The user can control the motors via the Arduino serial interface, via our Python library (Figure 5.4a), or via our simple graphical user interface (Figure 5.4b).

CSL-camera allows controlling cameras and set acquisition parameters, provided there exists an API to control them with μManager. The communication with the camera relies on *pymmcore-plus* library. The μManager's GUI application is used only once, to identify the camera parameters (Figure 5.5b). The camera configuration is then stored in a *.json* file and loaded by our Python library (Figure 5.5a). The configuration can be dynamically updated with Python.

Automated lab notebook

CSL-experiments module runs the experiments, analyzes the data, and provides persistent storage to duplicate the experiment. Experiments are coded in Python, with the help of the Sacred framework [101]. The adaptation of a Python code to a Sacred experiment is straightforward (Figure 5.6). The configuration parameters are loaded and can be updated by command-line interface for each experiment. The complete experimental environment (Python files, configurations, logs, outputs) is automatically saved in BSON format in a flexible noSQL database (MongoDB). This flexibility reduces the risk of breaking the code of older experiments when updates are made to the structure of the data. No specific implementation is needed to set up the automated code and parameters saving, and the "artifact" and "metric" properties are used to respectively save files and scalars. The operator can

a

```
from CSLstage.CSLstage import ControlStage

arduino_port = "COM6"
gears = [1,1,1]
stage = CSLstage(arduino_port, gears)
#gearbox ratio of X, Y and Z axis
stage.handle_enable(1)
stage.move_dx(10)
stage.handle_enable(0)
stage.reset()  #optional
```

b

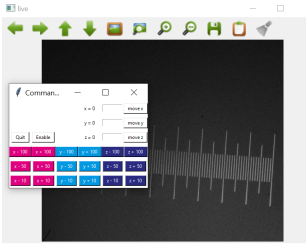

c

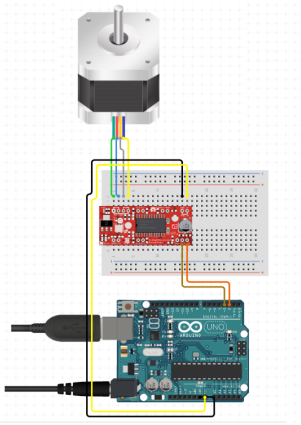

Figure 5.4: *Motor control module* **a**: Example of code to control the motors; **b**: Interface built on top of Python and Arduino to control the motors, example of focused image on the background; **c**: Example of circuit to control a Nema motor with an Easy Driver (designed with circuit.io [256].)

navigate the database using a web interface [102], use search filters, and visualize the experimental results. We provide in the Supplementary Materials screenshot examples of the database for the experiments used to generate Figure 5.7e. The database can also be accessed by queries through a Python library [257]. Finally, Plotly Dash [258] is a web application to build interactive data visualizations. Combined with a library that queries the database, it is possible to access the results of experiments but also perform post-processing and visualize the results on the go. An example of an interface is provided in Supplementary Materials.

5.6.4 (2) Quality control

Safety

CSL-leds The high-power LEDs diffuse heat when turned on for long experiments. To prevent the plastic cage from melting, we edited the 3D design and placed a copper plate in contact with the LED's PCB (See Figure 5.10 of the SI). The plate reaches an equilibrium temperature of 33^{o}C when the LED is powered with 1 W for 15 min (room temperature: 20^{o}C - see thermal image in Supplementary Materials). The glass-transition of our plastic (PLA) starts at 60^{o}C (See Figure 5.10 of the SI). High-power LEDs can also damage the eye when stared at. To avoid any risk, a 3D-printed cover was designed for the LED cubes. The complete microscope setup was also placed in an enclosure to minimize the interference of external light.

CSL-stage The 3D-printed part holding the motor is equipped with limit switches on both sides to avoid mechanical blocking.

OpenUC2-fluorescence microscope The platform is sensitive to vibrations, it should be placed on an isolated table.

CSL-experiments The Sacred framework requires to save the experimental results in local folders before copying them in the database. Temporary files can be used for this intermediary step, but saving the files in folders with names corresponding to the experiment ID is a straightforward back-up method. The database can also be copied and transferred using MongoDB CLI tools (mongodump, mongorestore).

Calibration

Light calibration

a

```
from CSLcamera import ControlCamera
cam_type = "MMConfig/UEye.json"
update_param = {"Exposure": 997,
                "Gain": 23}
downscale = 5 #downscale the image to save
cam = ControlCamera(cam_type, update_param, downscale)
N_im =  20
cam.snap_video(N_im)
video, timing = save_video(save_folder)
cam.reset()
```

b

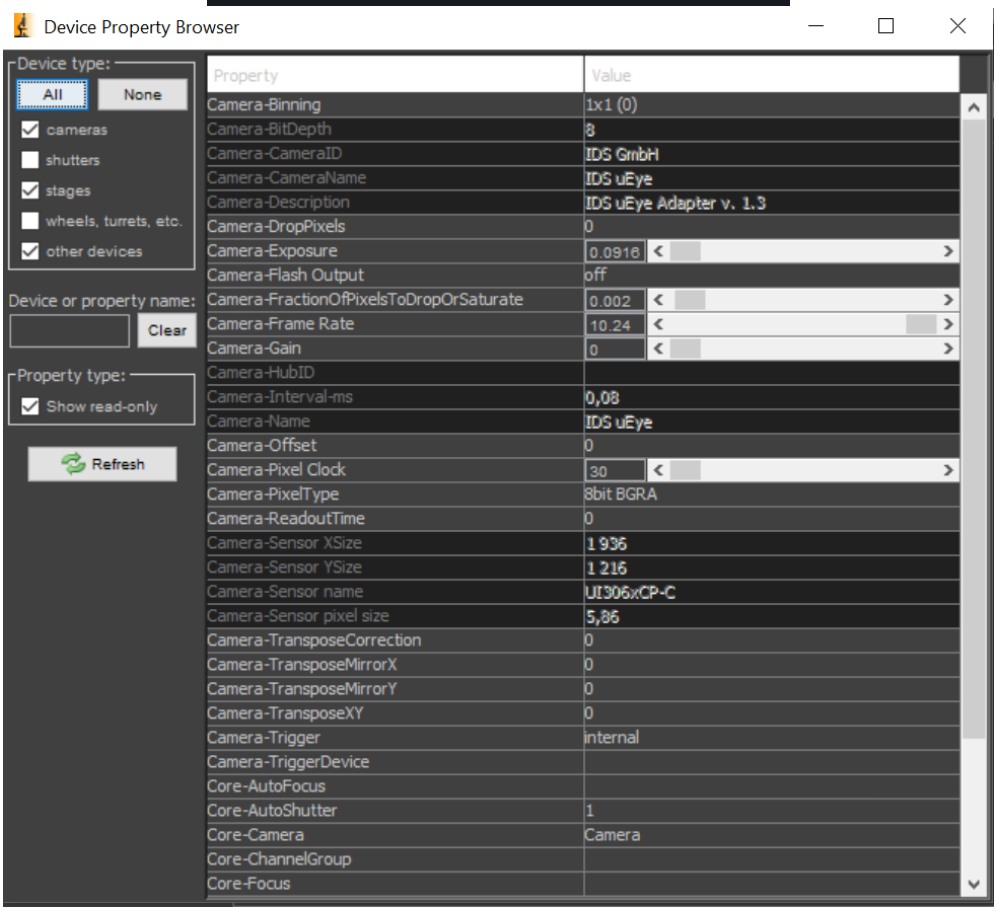

Figure 5.5: *Camera control module* **a**: Example of code to control the camera; **b**: Parameter names in μManager interface matching the manufacturer API.

The light intensity in the field of view was calibrated using the protein **Dronpa-2** as it was presented in Appendix 2.6. The protocol consists in sandwiching the protein solution between two microscope slides at the sample position. The blue light (filter 470 $\pm$ 7 nm) is turned on while the fluorescence is collected on the camera through a green filter (525 $\pm$ 36 nm). Good quality filters are required for this calibration otherwise the input light reflected or transmitted (depending on the setup configuration) will submerge the signal of interest. The fluorescence decay is fitted by a mono-

a

Script to control a camera

```
from CSLcamera import ControlCamera
cam_type = "MMConfig/UEye.json"
update_param = {"Exposure": 997,
                "Gain": 23}
downscale = 5 #downscale the image to save
cam = ControlCamera(cam_type, update_param, downscale)
N_im =  20
cam.snap_video(N_im)
video, timing = save_video(save_folder)
cam.reset()
```

The same script as Sacred experiment

```
from sacred.observers import MongoObserver
from sacred import Experiment
ex = Experiment('get_movie')
ex.observers.append(MongoObserver(db_name = "demo"))
from CSLcamera import ControlCamera

@ex.config
def config():
   cam_type = "MMConfig/UEye.json"
   update_param = {"Exposure": 997,
               "Gain": 23}

   downscale = 5 #downscale the image to save
   N_im =  20
@ex.capture
def get_camera():
   cam = ControlCamera(cam_type,
                       update_param,
                       downscale)

@ex.automain
def run(N_im):
   cam.snap_video(N_im)
   video, timing = save_video(save_folder, _run)
   #adding the _run parameter allows to save the
   #outputs in MongoDB.
```

b

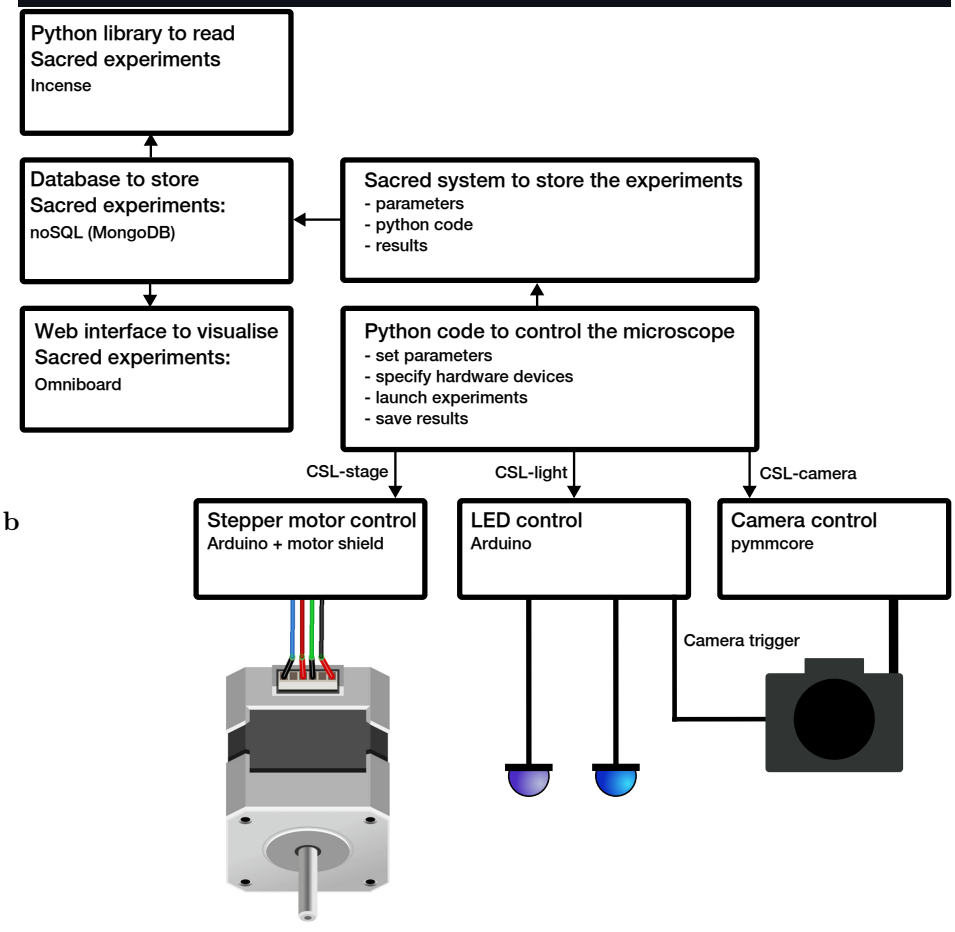

Figure 5.6: ***a****: Conversion of a Python code to a Sacred experiment;* ***b****: Instrument automation system.*

exponential function ($Ae^{-t/\tau} + B$), either pixel-by-pixel or over the mean of the images. The light

intensity can be retrieved from τ using the formula $1/I = \tau\sigma_{470}$. Then, to calibrate another LED, it is possible to use a powermeter. The first step is to record the power P_{470} of the blue LED by placing the powermeter in the position of the sample (for more details refer to Quarep-LiMi protocol: [259]). Then switch to the purple LED and collect P_{405} at the correct wavelength setting. Assuming the spot sizes to be equal, we have $I_{405} = I_{470}\frac{405\times P_{405}}{470\times P_{470}}$.

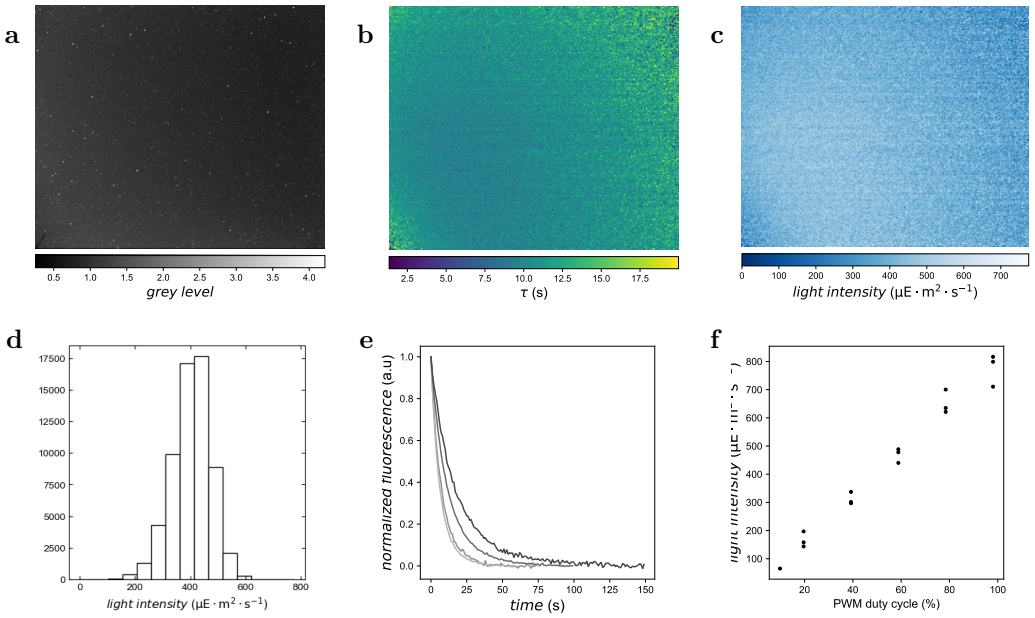

Figure 5.7: *Light calibration* **a**: Grey level image of **Dronpa-2** fluorescence in response to a blue light onset (first frame); **b**: Tau values extracted from the fluorescence kinetics allow to retrieve the light intensity using the formula I = $1/(\tau\sigma)$. Instrument: OpenUC2; **c**: Map of intensity in the field of view. PWM duty cycle: 50%. Instrument: OpenUC2; **d**: Distribution of the light intensity in the field of view. PWM duty cycle: 50%. Instrument: OpenUC2; **e**: Green fluorescence decay of **Dronpa-2** after a blue light onset (averaged over the image). The curves correspond to different PWM duty cycle which translate converted by the DC/DC converter to different intensity levels (from black to grey: 40%-60%-80%-100%. Instrument: OpenUC2); **f**: Calibration curve of the average light intensity for different PWM duty cycles; Instrument: OpenUC2.

Precision The displacement precision can be predicted from the stepper motor datasheet. For linear stepper motors, the travel per revolution L and the number of steps per revolution N are given, which allows to estimate the precision achievable. Note that if micro-stepping is possible, with a subdivision parameter S, it improves the theoretical precision to be $dL = L/(N \times S)$. In our case, the minimal theoretical displacement along the z-axis is $dL = 0.31\,\mu$m, with $L = 1.0\,$mm, $N = 200$, $S = 16$. It is possible to evaluate the practical precision by measuring with a ruler the displacement of the linear actuator over a given number of steps. While it is complex to evaluate the displacement precision of a motor in the z-direction using imaging, we demonstrate in Supplementary Materials how to evaluate it experimentally for an xy-stage. For the z-direction, more than the precision of the displacement, it is the ability to focus on a sample that is required (and described in 5.8).

Motor calibration The motor goes through a "homing" in order to move to a known absolute position. The motor moves away from the objective until it reaches the limit switch. This position is called "home" and corresponds to z=0.

When the motor changes direction, its movement can be delayed because of the clearance between the leadscrew driven by the motor and the nut that travels over the leadscrew. This backlash depends on the build quality of these components and it is therefore specific to each setup. To calibrate it on the z direction, the motor is moved in the positive (resp. negative) direction until the sample is in focus. We then move the motor with the manual interface until the image moves. The number of

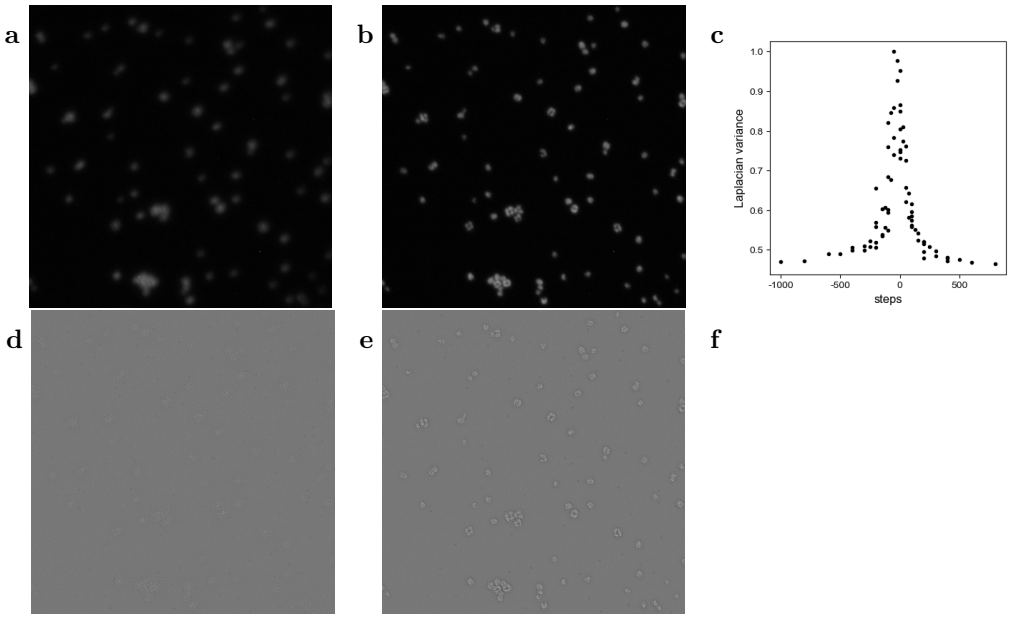

Figure 5.8: *Autofocus by moving the sample in the z-direction until the Laplacian variance of the image is maximal* **a**: Out-of-focus image (*Chlamydomonas reinhardtii* cells on an agarose pad); **b**: Focused image; **c**: Evolution of the Laplacian variance over the image as a function of the number of steps ran to acquire the image; **d**: Laplacian of the out-of-focus image; **e**: Laplacian of the focused image;

accumulated steps corresponds to the backlash, which needs to be calibrated only once. A routine could be implemented, and would resemble the autofocus described in the next section, leveraging simultaneously **CSL-camera**, **CSL-stage** and **CSL-leds**.

General testing

Autofocus

For experimental runs over several hours, it is necessary to frequently rectify the focus, particularly when the experiments are launched remotely. Our protocol begins by performing a "homing" and then moves the sample to the position that approximately corresponds to the focus, as previously established. Then, the sample is screened at different focal positions to iteratively identify the focal position with a pre-determined precision. An image is taken at each displacement. The position that maximizes the metric chosen to characterize the focus is identified, and the procedure is repeated with smaller steps around the maximum. The procedure stops when the step size has reached the desired precision. In Figure 5.8, the metric maximized is the Laplacian variance [103], corresponding to the second derivative of the image and emphasising the objects' edges.

5.6.5 (3) Use case

We present here a replication of a fluorescence microscopy experiment performed on algae to quantify their stress-response to high light. We demonstrate that, by collecting the stress response of a pre-conditionned population, we manage to correctly classify it based on its stress response, using data analysis tools trained on a dataset described in Chapter 4.

Principle

The objective of this work was to replicate the epifluorescence microscope described in Appendix 2.6 and Chapter 4. As part of a project shared between multiple collaborators, we wanted to provide a portable instrument easy to build for each partner. They can reproduce a shared set of experiments on their sample and ensure that the sample preparation is consistent before studying it with their other instruments. The initial instrument was built with Thorlabs and uses the software modules described above. The experimental results obtained with this instrument are presented in Chapter 4 that provides more information on the experiment and the data processing. The protocol consists in inducing light-stress response of algae and monitoring their response at the single-cell level. Then, using a reference dataset and machine learning algorithms, it is possible to quantitatively evaluate the stress-response level. We were able to successfully reproduce results from Figure 4.9c and 4.10c.

Methods

We used a culture of *Chlamydomonas reinhardtii* wild type *cc*124. The protocol under the microscope consists in sending high-light (400 μmol(photons) $\cdot\, \mathrm{m}^{-2} \cdot \mathrm{s}^{-1}$, 470±10 nm) for 15 min to induce stress-reponses. The signal of interest is the fluorescence response to pulses of saturating light (1300 μmol(photons) $\cdot\, \mathrm{m}^{-2} \cdot \mathrm{s}^{-1}$, 405±7 nm, 200 ms) sent every 20 s. This fluorescence trace is called F_M as a reference to the naming used in photosynthesis research (Fluorescence Maximum). We acquire a movie for the whole duration of the experiment, then we segment each alga (Figure 5.9a,d) and collect their individual fluorescence response (Figure 5.9b,e) using image segmentation with the code described in [55]. Then we categorized the responses according to the methodology we developed in Chapter 4. In brief, we applied the computational method we developed to project the F_M traces in a low-dimension space representing the different stress responses amplitudes (Figure 5.9c,f - see Chapter 4for additional details).

The wild-type population (*cc*124) adapted to growth-light was left in the dark from 15 minutes prior to the experiment. The measurement was repeated four times until the stationary level of photo-inhibition is reached. This strain is expected to show only one type of stress-response: qT, which translated into a large bump over the two first minutes and a fluorescence decay when the light is turned off.

Results

We found similar results as Chapter 4 (Figure 5.9c,f) as the point clouds are projected onto the same area. To supplement these results we trained a K-Means classifier on the original dataset and applied it to the population studied, which corresponds to the class $\mathbf{wt4}^i$. We used another wild-type strain than the one from the reference set that is expected to behave similarly (and that was used in Figure 4.13g of Chapter 4). Over two experiments amounting to 272 algae, we find an 92% prediction accuracy on this new strain for the class $\mathbf{wt4}^i$, which corresponds to the condition where qT is expressed and not qE, as expected from our strain. It allows to conclude that even if the experiments have been performed on two different wild-type strains (expected to behave similarly), one year apart, on two different instruments in two different rooms, we find the same quantitative results.

Reuse potential and adaptability

The modularity of the instrument and the generality of the modules allow them to be reused for other projects:

CSL-serial is application agnostic. It is usable for any project where a main computer has to communicate with Arduino firmware. We provides both Python and C^{++} classes.

CSL-leds was tested on circuit LEDs, on two types of Thorlabs LED controllers (*DC4100* and *T-cube LED driver*), and on a custom soldered circuit based on a DC-DC converter (*RECOM RCD*

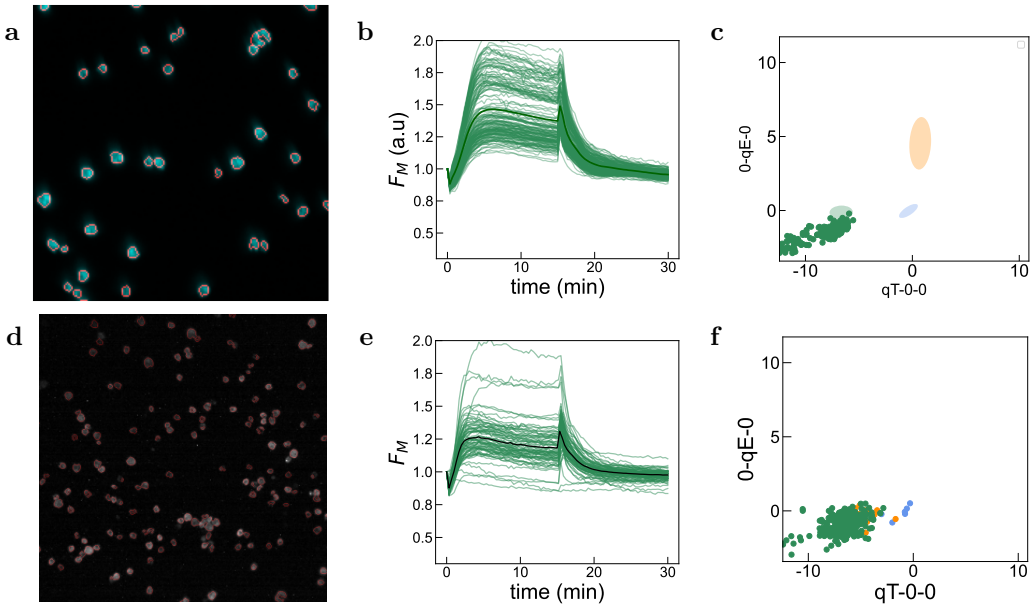

Figure 5.9: *Replication of monitoring of light induced stress in microalgae.* **a**: Cropped watershed segmentation of the algae under the Thorlabs microscope, average cell diameter: 9 μm; **b**: Fluorescence F_M response of all the algae of the WT population not activated, results from experiment described in Figure 4.9 of Chapter 4; **c**: Projection in the NPQ space using dictionary learning followed by linear discriminant analysis, results from Figure 4.10 of Chapter 4. **d**: Cropped watershed segmentation contours of the algae under the UC2 microscope, average cell diameter: 9 μm; **e**: Fluorescence F_M response of all the algae of the WT population not activated observed with the UC2 microscope; **f**: Projection in the NPQ space using dictionary learning followed by linear discriminant analysis of the traces in **d** and **e**. The colors correspond to the class predicted by a classifier trained on the dataset. Green: true positive (***wt4***^{i}– 92%), orange: ****stt7***^{i}, blue: ***stt7***^{i}.

24/1.2). We have used the module to trigger lights and cameras, but it can be used for any project that requires precise triggering with millisecond resolution.

CSL-stage has been used in three different scenarios. A manual stage was turned into a motorized one and controlled by the module as described in the Supplementary Materials and on GitHub [3]. The knobs initially used to manually move the platform are linked to motors via two belt-pulley systems (x and y displacements). One removable part of the platform is replaced by a 3D-printed part that allows to fix the two motors. The pulleys are also 3D-printed to fit on the knobs. The stage was replicated in the UC2 framework [260]. The 3D-printing of knobs was also used to increase the displacement range of a piezo-stage (KPZ101 - Thorlabs). The small displacements are controlled via piezo-control, and the larger displacements are controlled by the motor module. Finally, it was used to control the z-displacement of a sample in front of an objective to allow to change the focus, as described in the previous sections. The motor firmware is also used in Sony CSL's agricultural robot to precisely control the trajectories of the tools.

CSL-camera requires a camera with drivers installed and a corresponding API for μManager. It is important that the versions of μManager and *pymmcore-plus* match. We have tested the exposure, frame rate, frame size, and gain of four camera models (*UEye-3060CP* – IDS, *MER2-503-36U3C* – Daheng Imaging, *Orca Flash 4* – Hamamatsu and *iXon Ultra 897* – Andor).

CSL-experiments was implemented in five instruments of our laboratory, and we are aware of two more external users.

5.6.6 (4) Build details

- The build details for the **OpenUC2-fluorescence microscope** are available online at SonyCSL/UC2_Fluorescer forked from UC2 library.
- **CSL-stage** is available online at SonyCSL/Motorized-Stage
- For now, the libraries **CSL-serial**, **CSL-leds**, **CSL-camera** and **CSL-experiments** are stored together and documented in Alienor134/CSL-forge but will be isolated soon.

5.6.7 (5) Discussion

In this work, we demonstrate the seamless integration of the OpenUC2 open-hardware library [229] with our new modular Python libraries. We replicate a setup from the literature, automate it, and replicate associated results. We also show how to connect the automated instrument to a smart notebook to store the data and metadata in a database system.

In particular, we developed a robust protocol of communication between Python and Arduino via serial communication that can be adapted to many other use cases. It allows leveraging the control of instruments not through manufacturer's softwares, but by digital or Pulse-Width Modulated signals from Python through Arduino. This approach potentially allows for bypassing intricate interface layers. We built two libraries on top of it (**CSL-leds** and **CSL-stage**), and explain in the Github how to create new libraries based on **CSL-serial**. We use them to control light-sources, trigger cameras, and actuate motors. We have also presented how we leverage the extensive developments from μManager to control cameras easily. It allows switching the setup camera with only a few changes in the configurations.

The Python libraries to control hardware are highly modular with a low implementation barrier for a Python user. They were aimed to be easily reused independently: for instance, the light controller (**CSL-leds**) can be reused to control the light cycle of a plant growth chamber. The motor module (**CSL-stage**) used to control the autofocus or move the sample plate could be used also, for example, to stir a sample. In our experiments, the camera module (**CSL-camera**) acquires microscope images but it could be used also to monitor a macroscale chemical reaction.

[3] SonyCSLParis/Motorized-stage

The last novelty is the possibility to integrate the modules in a database management system. Often, experimental data are under-exploited because they are either not properly stored, not easy to access, or not properly documented. We suggest an approach to persistently record experimental parameters, results, intermediary data, and code that produced the experiment in a database. We have used the library Sacred [101] developed by the machine learning community where there is an increased tendency to automate experiment yet keep a full trace for future evaluations and comparisons. This level of automated data collection is still uncommon in biology research. The library is light-weight and requires little changes to an existing pipeline for integration.

All the required information to duplicate an experiment and all the corresponding output is stored in a flexible noSQL database hosted by MongoDB. The experiments are displayed in a web interface (Omniboard [102]) and can be accessed by the Python library Incense [257]. We believe that, thanks to the ease of implementation and flexibility, this library could be used for automated scientific experiments beyond microscopy and could use as a standard in Data Management Plans required for project fundings.

The main drawback of our hardware setup was the mechanical instability of the OpenUC2 cubes. Using injection molding as in [235] would improve the setup. Performing optical alignment was also complex, and designing simple 3D designs to ease it and make it more reliable would be needed. In order to make the LED control accessible, we have soldered the electric components to a plate. A next step will be to provide an LED controller PCB design that is easy to solder. Finally, we will also work on a new design integrating the lessons learned with this microscope to build a portable device that could be used to score plant stress as described in Chapter 4.

5.6.8 Contributions

- Paper writing: first draft Aliénor Lahlou
- Paper writing: final version and revisions: A.L., Peter Hanappe & Thomas Le Saux
- Use cases: A.L.
- Assembly: A.L., Ian Coghill, Ali Ruyer-Thompson, & T.L.S
- **OpenUC2-fluorescence microscope**: A.L., T.L.S, I.C. & Alec Cochard
- **CSL-experiments**: A.L.
- **CSL-camera**: A.L.
- **CSL-leds**: P.H. (Software, Documentation), A.L. (Design, Software, Documentation), Douglas Boari (Software), T.L.S. (Design)
- **CSL-stage**: A.L., A.R.T. & P.H. (Design, Software, Documentation)
- **CSL-serial**: P.H. (Software, Documentation)

5.7 Supplementary Materials

5.7.1 LED holder temperature

The LED holder is 3D printed but tends to warm-up and even melt when the light is kept on for tens of minutes. To avoid this we selected a 5 mm thick heat sink copper plate and drilled holes to allow the screw to tight the plate to the 3D part (Figure 5.10a). The LED was connected to the plate with thermal glue. With this configuration, the plastic did not melt even after several hours of

illumination at 1 W. We measured the temperature of the plate with a thermal camera after 10 min of illumination at 1 W and found 33^{o}C (Figure 5.10b). We noticed the wires got hotter, which could have been avoided with larger core wires.

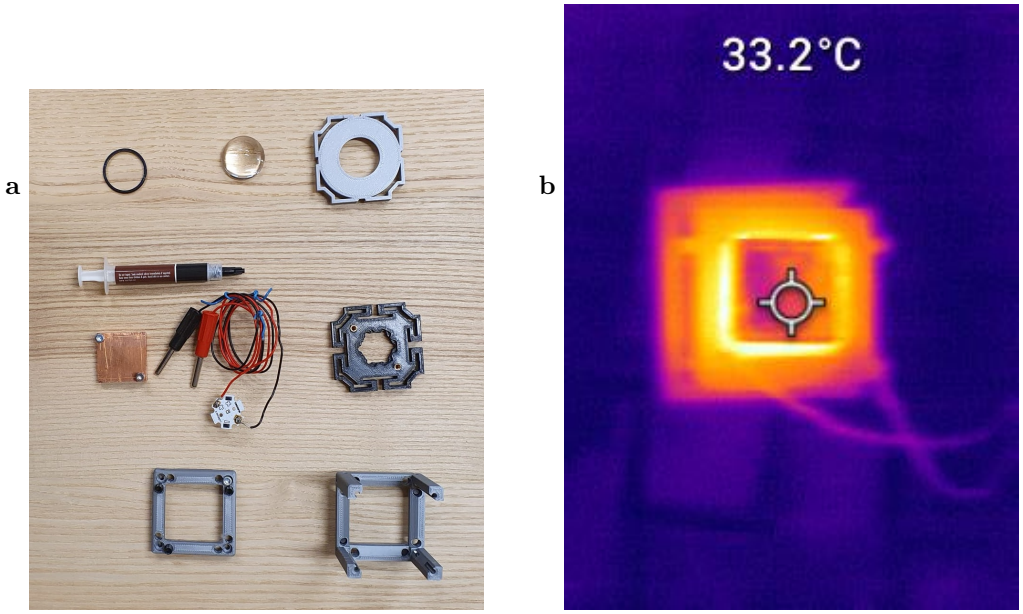

Figure 5.10: **a**: Parts of the LED: top: collimating lens and holders, middle: LED, LED holder, copper plate and thermal glue, bottom: base cube; **b**: Temperature image of the LED holder after 10 min illumination (1 W).

5.7.2 Motorized xy-stage

Presentation We automated an xy motorized stage and although it was not implemented in the set-up, it is worth sharing the design and calibration as a use-case for microscopy development. Our stage was integrated in the UC2 library and used in the publication of the OpenUC2 fluorescence microscope. The stage allows to move the sample perpendicular to the visual axis, enabling to screen a large sample. It relies on a stepper motor and a scalable 3D-printed pulley system [261]. When the motors are disabled, the stage can be controlled manually.

Precision

The precision of displacement can be derived theoretically or measured experimentally. We consider the pulley P_1 (with T_1 teeth) connected to the motor pulley P_2 (with T_2 teeth) screwed to a knob controlling a linear actuator (Figure 5.11a). The step angle α provides the angular displacement produced by a motor step. It can also be computed from the number of steps per revolution N: $\alpha = 360/N$. The linear movement L corresponds to the movement of the linear actuator for a full revolution of the knob (which can be measured with a ruler). Then, given the micro-stepping parameter S: $dL = L \cdot T_1/(T_2 \cdot N \cdot S)$. To further evaluate the actual precision of the displacement, it is possible to evaluate the displacement of an image with the camera between motor steps. A displacement in the (x,y) plane can be computed by using image registration. Image registration is a process that allows finding a spatial transformation between two images. In the case of movement in the (x,y) plane, it consists in computing the cross-correlation of the images. The position of the maximum of the cross-correlation map corresponds to the linear translation between the two images in pixels. The specifications of the microscope objectives normally provide their magnification factor. However, this magnification is specific to the manufacturer and corresponds to the couple (objective, tube lens). In our case, we selected the tube lenses that are in front of the camera based on our geometrical constraints rather than the manufacturer's recommendations. Therefore, a calibration of the scaling is necessary to convert the pixels in meters. It can be done using a patterned microscope slide. In the example of a manual staged converted into an automated one with pulleys fixed on manual knobs, we predict a shift of 5 µm per step in the x direction and 1.9 µm per step in the y direction (Figure 5.11a), and with the registration method relying on a patterned image (Figure 5.11b) we measure movements close to the predictions: an x-shift per step of 4.3 µm and a y-shift of 1.7 µm (Figure 5.11c). We also observe a non-linearity in the x movement which could be due to mechanical constraints.

Build details: The build details of our version can be found in [262].

5.7.3 Database system

Sacred provides a specific format to store data in a noSQL database, here MongoDB. A web interface [102] was developed to display the experiments following Sacred structure. It can be used to visualise the parameters of each experiment and browse experiments based on filters (Figure 5.12). It enables to visualise saved outputs, either as interactive graphs or through files (called artifacts) rendering (tables, images, movies). It is also possible to compare experiments: overlay results, compare configurations or compare source file differences as shown in Figures 5.13, 5.14 and 5.15 respectively

5.7.4 Example of Dash application

Dash Plotly is an open-source Python framework used for building interactive web applications for data visualization. It combines the functionalities of Plotly, a data visualization library, with Flask, a web framework, to create web-based dashboards, reports, and data-driven applications. In the work presented in Chapter 4, we combined the database system of Sacred with a Dash application to process and visualize the data (a screenshot is displayed in Figure 5.16). The experiments can be selected based on a predefined combination corresponding to a light-stress pre-conditioning. Then

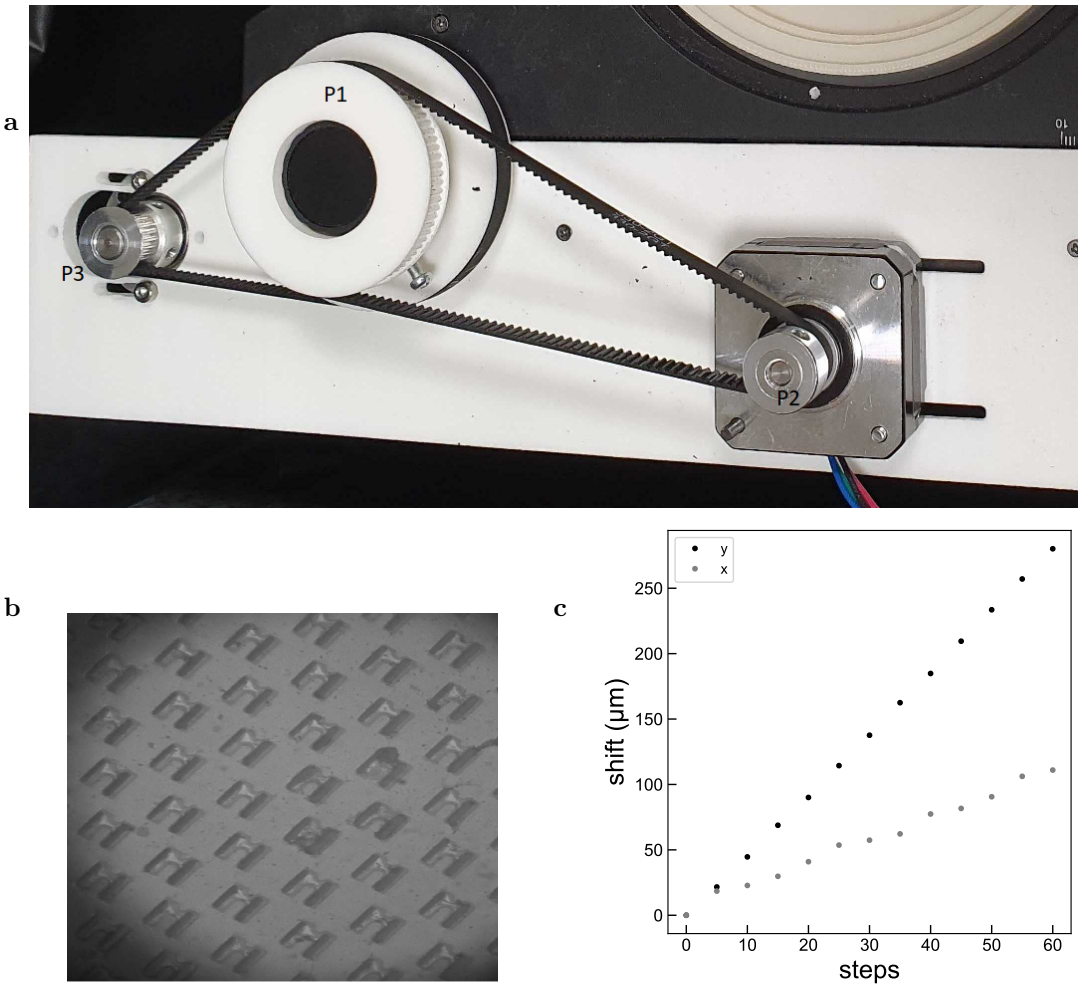

Figure 5.11: *Precision evaluation* **a**: Example of belt-pulley system with teeth to automate an xy-stage; **b**: Example of image used to compute the shift with image registration when the motor moves; **c**: Shift computed by image registration when the stage moves 5-by-5 steps in the x (grey) or y (black) direction.

the fluorescence data are projected into a 3D space using the selected projection algorithm. The user can select the 3D axis to be displayed. Each point corresponds to the NPQ scores of one alga. When the mouse is hovered over a datapoint, the corresponding fluorescence trace is displayed as well as the reference image from the movie, with the individual alga segmentation mask.

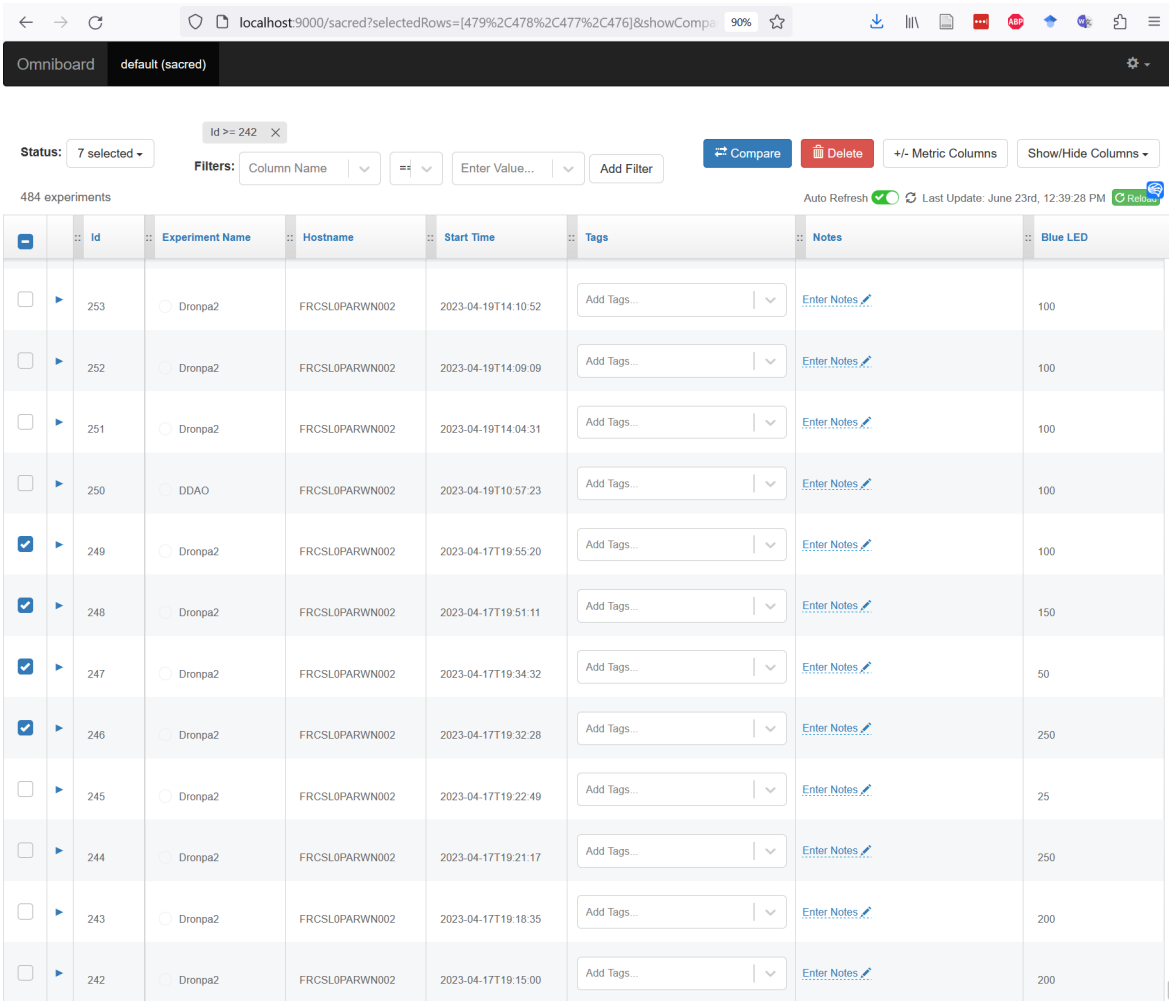

Figure 5.12: Web interface to visualize Sacred experiment results, source code, config, and saved files.

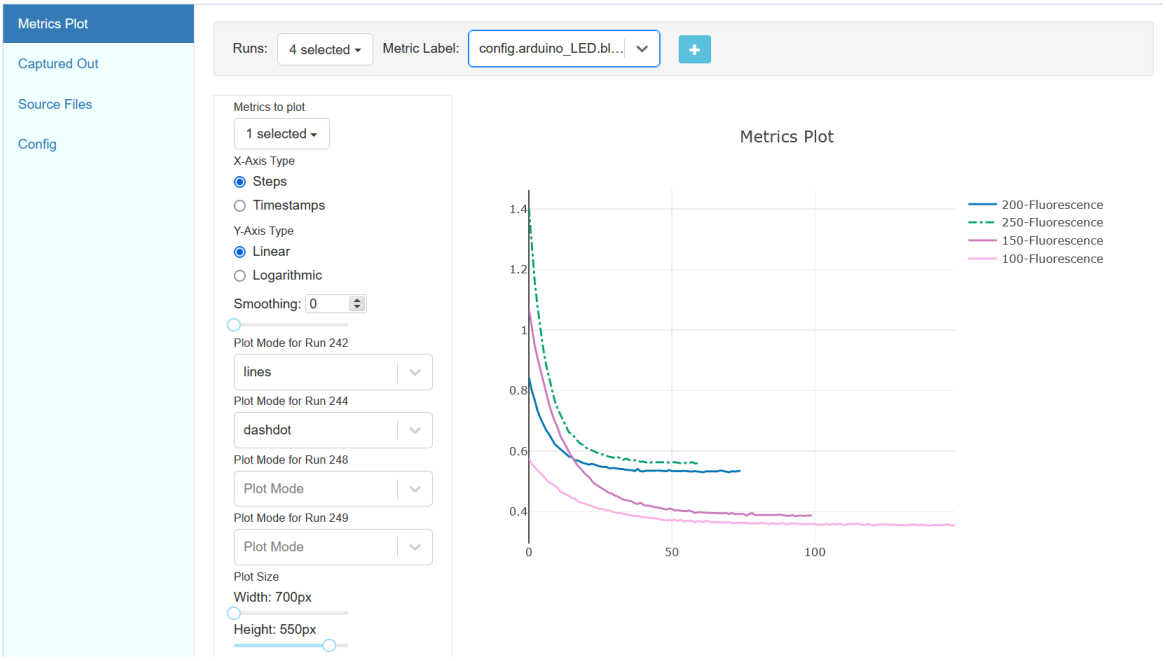

Figure 5.13: Graphical interface to monitor experimental results, overlay of four experiments used to generate Figure 5.7e,f.

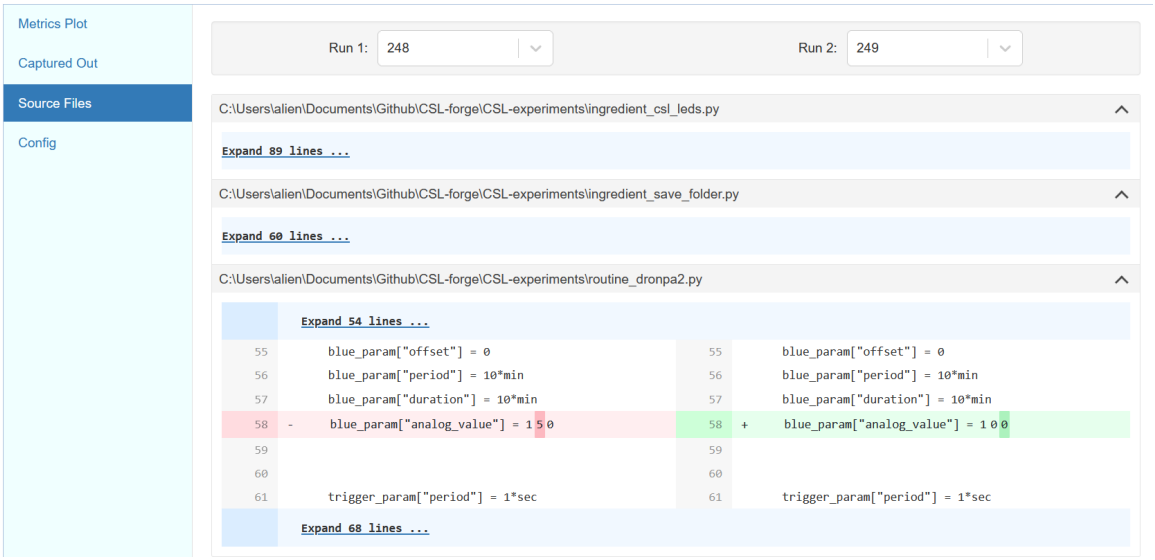

Figure 5.14: Dynamic display of source files differences between two experiments.

Figure 5.15: Display of configuration difference between two experiments.

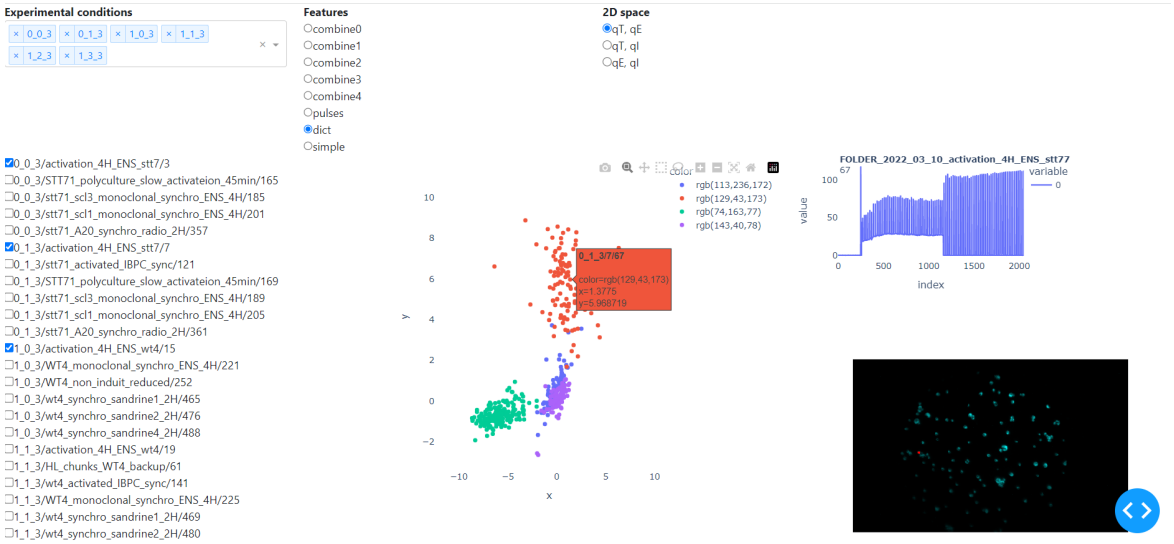

Figure 5.16: Example of Plotly Dash application developed to analyze the dataset described in Chapter 4.

Chapter 6

Conclusions

Monitoring plant metabolism to improve agriculture practices is a long road that requires novel sensing instruments and diagnosis methods. Furthermore, for operation at a large scale and in real-world conditions, such instruments and methods should be robust, easy to build and operate. Methods relying on chlorophyll fluorescence (ChlF) remote sensing have shone a great potential for probing plants' health status and identifying stress conditions before visible damages appear on the crops. In this manuscript, I have described several developments that contribute to advancing the state-of-the-art in several fields related to ChlF sensing.

Chapter 2 presents the requirements we derived to create a new instrument to probe ChlF of photosynthetic organisms. Following them, we designed a new epifluorescence microscope to monitor ChlF at the micrometer-scale. I made it modular and flexible enough to implement the protocols from the literature – which allowed me to validate the instrument in Chapter 3 – and to design new protocols to probe ChlF in Chapter 4. In particular, I wrote the entire software in Python, removing any limitation on the design of the excitation patterns: the user can design any sequence and send it to the light sources (up to 3 MHz). The specifications and the software guided the development of other instruments. I present one of them in Chapter 5. It is an open-source and open-hardware replication of the first microscope. I took the initiative to plan and design this Open project after being introduced to the OpenUC2 library by Benedict Diederich. I also guided and supervised the contributions of my co-authors to accomplish the project and write the manuscript included in Chapter 5.

Chapter 2 also introduces a method to calibrate light intensity over several orders of magnitude and over the whole visible spectrum. It is an important technique for photosynthesis research, where light is a key player, but also beyond. Indeed, a large community (Quarep-Limi[1]) was recently formed, focused on properly calibrating imaging instruments. The calibration methods were derived from years of research on fluorescent actinometers by the team of Ludovic Jullien and Thomas Le Saux. Recognizing their potential appeal to the diverse audience of Quarep-Limi, I suggested that we expand upon their work to deepen the calibration strategies and share accessible protocols to potential users. It resulted in the manuscript "Fluorescence to measure light intensity" (accepted in *Nature Methods*). We demonstrated the method's versatility by testing it on multiple instruments and configurations. In total, I tested the calibration method with **Dronpa-2** on eight set-ups in five different laboratories and wrote several codes to allow users to process their data easily.

Chapter 3 introduces another method to calibrate light intensity, this time using a leaf randomly picked up from a garden. Although I need to test it on a larger variety of species from the botanic garden of Jardin des Plantes, the method appears robust and generalizable among species, including

[1]Quality Assessment and Reproducibility for Instruments & Images in Light Microscopy

algae. To disseminate the method, I designed a Python application to allow any user able to measure the induction of ChlF to a light jump to retrieve their input light intensity.

Chapter 4 presents how the home-built microscope was used to introduce a new computational method that allows quantifying multi-stress responses embedded in a ChlF trace. The first step consists in creating a well-chosen dataset built by exploiting qualitative knowledge on the biological capacity of photosynthetic organisms. This dataset is then used to train a machine learning framework able to quantify the stress-response mechanisms.

More specifically, we studied at the single-cell level the response to light-stress in the species of microalgae *Chlamydomonas reinhardtii*. Light-stress provokes multiple mechanisms overlapping kinetically in the ChlF response. The dataset was built in order to acquire separately the kinetics representing the expression of a singular stress-response mechanism. It was achieved by using mutants, and specific pre-conditioning protocols were used to mitigate the stress-responses. To analyze the ChlF traces dataset, we introduced a two-step framework involving two different metric optimizations. The first step, Dictionary Learning, aims at decomposing the traces into a small set of basic traces (atoms) while at the same time minimizing the reconstruction error of traces in the dataset. The second step involves a linear dimension reduction which aims at separating the populations by projecting them in a space that has a dimension corresponding to the number of traits (NPQ-space with three NPQ components). Each axis represents a stress, the amplitude of which is given by the position on the axis. I showed that when analyzing the response of a wild-type strain, which expresses simultaneously multiple stress-responses, the framework is able to properly reconstruct the trace; this validates our approach. The framework is able to give scores to each component, allowing to derive conclusions on the possible interplay between the different components. It differs from the literature of remote sensing using machine learning, where developments usually allow classifying stress responses, but rarely allow quantifying them.

Chapter 5 presents the software I developed, now implemented completely or partially in five instruments. From discussions in conferences and workshops, I believe that the Sacred experiment database system I borrowed from the Machine Learning community is useful in many projects because there are few solutions that offer this level of versatility, either open or proprietary. Furthermore, it is aligned with the requirements of a Data Management Plan. I also believe that the CSL-libraries can be helpful to automate tasks beyond microscopy experiments thanks to their modularity and low implementation barrier. As a matter of fact, some of the libraries include Arduino codes initially developed for the ROMI rover by Peter Hanappe.

Taken together, these components bring a step closer to having a usable, portable device that can be used to measure the health status of plants. Such an instrument would play a key role in improving agriculture practices.

Chapter 7

Perspectives

The DREAM project is an EIC Pathfinder project initiated by Ludovic Jullien funded in 2021, and started 1^{st} April 2022. It officialized the collaboration that started in 2020 with my Cifre PhD between his team and Sony CSL, with the other actors we interacted with during my PhD work (Dr. Benjamin Bailleul, Dr. Ladislav Nedbal, Pr. Dusan Lazár and their respective teams). DREAM allowed to bring new partners and new skills, in particular in modeling and higher plants studies. The developments presented throughout this manuscript contributed to the DREAM project.

The DREAM project evokes the epifluorescence microscope, but also the design of a similar instrument for research experiments at the whole leaves level. In fact, two identical replicates of a macro-scale instrument were already built by Ian Coghill (ENS - DREAM project) to investigate leaves. Ian first got familiar with my developments by using the Open version of the microscope. Then he integrated the specifications derived in Chapter 2 as well as parts of the hardware choices described and the software developed.[1]

The Sacred database system is implemented and actively used in all the instruments derived from the epifluorescence microscope. The next step will be to write scripts to adapt the output of commercial instruments of the various partners of DREAM to deposit the data in a shared MongoDB database as a part of the Data Management Plan.

The Open version of the microscope was very useful to allow new members of the DREAM project to discover my developments and learn how to use and modify them. It also contributed to spreading the use of Python in the laboratory and the DREAM project. The Open version also gave insights for the design of a portable device for field analysis described in the DREAM project. In particular, we will consider 3D-printing to build it, and integrate the CSL-library codes to control it. We identified that the main constraint will be to find an affordable way to distinguish the excitation light from the measured fluorescence. Indeed, the minimal filtering requirements of the LEDs are met only by expensive optics. The solution will lie in changing the excitation light type, or in exploiting strategies based on modulated light analysis, such as the strategy employed in OPIOM to only recover the out-of-phase component [53].

Modulated light will be introduced in the DREAM project because it has additional advantages. However, in order to dig deeper into the possibilities of Fourier-based analysis, a method to eliminate the harmonic contributions from the excitation light will have to be introduced. One such method has already been presented in [54]. In fact, it has been introduced by Ian in the two replicates of the macro-instrument, and will be easy to implement back on the microscope since they share similar software.

[1] The macro-scale instrument and two experiments are presented in the supplementary materials of the manuscript “Fluorescence to measure light intensity”.

Chapter 2 describes the five LEDs implemented in the microscope. I predominantly used the blue and purple ones for the experiments, except when demonstrating the wide range of absorption of the photosynthetic apparatus and the dyes we presented in the manuscript "Fluorescence to measure light intensity". In the DREAM project they will be used to probe nanosensors fluorescence sensitive to O_2 and pH. It is possible to have access to the distribution of light in the field of view of the instruments for the blue and the purple light thanks to **Dronpa-2**. For the nanosensors, it could be possible to evaluate the spatial distribution of the other light sources in the field of view thanks to DDAO, the fluorescent dye that absorbs in the whole visible range and emits at a well-defined fluorescence wavelength.

The DREAM project's core is to identify new methods to generate ChlF signatures and retrieve a biophysically relevant information from photosynthetic organisms. One target is to qualify and quantify the current status of plants for crop management (e.g., water stress, disease). In this regard, the whole experimental framework and the underlying biological questions presented in Chapter 4 are relevant to the DREAM project. In particular, I discussed the design of the machine learning framework and the alternatives, as well as the number of experiments required. In the work presented in Chapter 4, we benefited from the rich literature on NPQ and compared the results to existing methods. A challenge for the DREAM project will be to probe the photosynthetic state automatically, which means with less biological knowledge, and using protocols that are not comparable to the literature. For this task, we will benefit from complementary tools, such as the introduction of new observables (nanosensors, ECS [263], etc...) and modeling strategies.

Such a diagnosis method could accompany the farmers towards more sustainable farming methods to reduce the impact of agriculture on the environment. The variables of a sustainable regenerative system include integration of biodiversity, landscape, soil, lightning, winds, humidity and other natural factors. This complicates the system and increases the risk of low crop yields or equally problematic, mental load for the farmer. By offering new tools to farmers (with the ROMI project and the DREAM project) we provide a frame and supporting means to the experimental process of turning a farm land into a regenerative farm. By leveraging innovative technologies and data analysis, the DREAM project will build upon my PhD project results and push them beyond, and contribute to optimizing resource allocation, minimizing environmental impact, and enhancing productivity in agriculture, thereby promoting sustainability and addressing key challenges in the agricultural sector.

Bibliography

[1] R. Ando, H. Mizuno, and A. Miyawaki. "Regulated Fast Nucleocytoplasmic Shuttling Observed by Reversible Protein Highlighting". In: *Science (New York, N.Y.)* 306 (2004), pp. 1370–1373.

[2] Intergovernmental Panel On Climate Change. *Climate Change and Land: IPCC Special Report on Climate Change, Desertification, Land Degradation, Sustainable Land Management, Food Security, and Greenhouse Gas Fluxes in Terrestrial Ecosystems*. 1st ed. Cambridge University Press, Dec. 2022. ISBN: 978-1-00-915798-8 978-1-00-915801-5. DOI: 10.1017/9781009157988.

[3] L. Danny Harvey. "A Guide to Global Warming Potentials (GWPs)". In: *Energy Policy* 21.1 (Jan. 1993), pp. 24–34. DOI: 10.1016/0301-4215(93)90205-T.

[4] S. Solomon, Intergovernmental Panel on Climate Change, and Intergovernmental Panel on Climate Change, eds. *Climate Change 2007: The Physical Science Basis: Contribution of Working Group I to the Fourth Assessment Report of the Intergovernmental Panel on Climate Change*. Cambridge ; New York: Cambridge University Press, 2007. ISBN: 978-0-521-88009-1 978-0-521-70596-7.

[5] FAO and UNEP. *The State of the World's Forests 2020: Forests, Biodiversity and People*. The State of the World's Forests (SOFO) 2020. Rome, Italy: FAO and UNEP, 2020. ISBN: 978-92-5-132419-6. DOI: 10.4060/ca8642en.

[6] *Greenhouse Gas Emissions from Agriculture in Europe*. https://www.eea.europa.eu/ims/greenhouse-gas-emissions-from-agriculture.

[7] S. E. Hook, A.-D. G. Wright, and B. W. McBride. "Methanogens: Methane Producers of the Rumen and Mitigation Strategies". In: *Archaea (Vancouver, B.C.)* 2010 (Dec. 2010), e945785. DOI: 10.1155/2010/945785.

[8] A. Patra et al. "Rumen Methanogens and Mitigation of Methane Emission by Anti-Methanogenic Compounds and Substances". In: *Journal of Animal Science and Biotechnology* 8.1 (Jan. 2017), p. 13. DOI: 10.1186/s40104-017-0145-9.

[9] C. Hénault and J. C. Germon. "Quantification de la dénitrification et des émissions de protoxyde d'azote (N2O) par les sols". In: *Agronomie* 15.6 (1995), pp. 321–355. DOI: 10.1051/agro:19950602.

[10] E. A. Davidson. "The Contribution of Manure and Fertilizer Nitrogen to Atmospheric Nitrous Oxide since 1860". In: *Nature Geoscience* 2.9 (Sept. 2009), pp. 659–662. DOI: 10.1038/ngeo608.

[11] A. J. Thomson et al. "Biological Sources and Sinks of Nitrous Oxide and Strategies to Mitigate Emissions". In: *Philosophical Transactions of the Royal Society B: Biological Sciences* 367 (2012), pp. 1157–1168.

[12] M. M. van Eerdt and P. K. N. Fong. "The Monitoring of Nitrogen Surpluses from Agriculture". In: *Nitrogen, the Confer-N-s*. Ed. by K. W. Van der Hoek et al. Amsterdam: Elsevier, Jan. 1998, pp. 227–233. ISBN: 978-0-08-043201-4. DOI: 10.1016/B978-0-08-043201-4.50035-6.

[13] P. M. Glibert et al. “The Haber Bosch-harmful Algal Bloom (HB-HAB) Link”. In: *Environmental Research Letters* 9 (Oct. 2014), p. 105001. DOI: 10.1088/1748-9326/9/10/105001.

[14] R. J. Diaz and R. Rosenberg. “Spreading Dead Zones and Consequences for Marine Ecosystems”. In: *Science (New York, N.Y.)* 321.5891 (Aug. 2008), pp. 926–929. DOI: 10.1126/science.1156401.

[15] Shukla, Priyadarshi et al. *IPCC, 2019: Climate Change and Land: An IPCC Special Report on Climate Change, Desertification, Land Degradation, Sustainable Land Management, Food Security, and Greenhouse Gas Fluxes in Terrestrial Ecosystems*. 2019.

[16] S. P. Slocombe et al. “Fixing the Broken Phosphorus Cycle: Wastewater Remediation by Microalgal Polyphosphates”. In: *Frontiers in Plant Science* 11 (2020).

[17] *Plate-forme microfluidique pour l'imagerie et la sélection de micro-algues à haut rendement en polyphosphates*. https://anr.fr/Projet-ANR-21-CE43-0021.

[18] H. J. M. van Grinsven et al. “Benchmarking Eco-Efficiency and Footprints of Dutch Agriculture in European Context and Implications for Policies for Climate and Environment”. In: *Frontiers in Sustainable Food Systems* 3 (2019).

[19] *The Netherlands 2020 – Analysis*. https://www.iea.org/reports/the-netherlands-2020.

[20] F. Bianchi, C. Booij, and T. Tscharntke. “Sustainable Pest Regulation in Agricultural Landscapes: A Review on Landscape Composition, Biodiversity and Natural Pest Control”. In: *Proceedings of the Royal Society B: Biological Sciences* 273.1595 (Apr. 2006), pp. 1715–1727. DOI: 10.1098/rspb.2006.3530.

[21] F. Magdoff. “Concept, Components, and Strategies of Soil Health in Agroecosystems”. In: *Journal of Nematology* 33.4 (Dec. 2001), pp. 169–172.

[22] Y.-C. Lu et al. “Cover Crops in Sustainable Food Production”. In: *Food Reviews International* 16.2 (May 2000), pp. 121–157. DOI: 10.1081/FRI-100100285.

[23] R. Lal. “Agroforestry Systems and Soil Surface Management of a Tropical Aifisol”. In: *Agroforestry systems* 8 (1989).

[24] R. Carson. *Silent Spring*. Boston: Houghton Mifflin, 2002.

[25] E. Commission. *Organic Production and Products*. 2023.

[26] D. Holmgren. *Permaculture : Principles and Pathways beyond Sustainability*. Hepburn, Victoria, Australia: Holmgren Design Services, 2002.

[27] B. Mollison. *Permaculture: A Designer's Manual*. Tyalgum, Australia: Tagari Publications, 1988.

[28] M. A. Altieri. *Agroecology: The Science of Sustainable Agriculture, Second Edition*. CRC Press, 1996.

[29] A. Wezel et al. “Agroecology as a Science, a Movement and a Practice. A Review.” In: *Agronomy for Sustainable Development* 29 (2009), pp. 503–515. DOI: 10.1051/agro/2009004.

[30] W. Rawls et al. “Effect of Soil Carbon on Soil Water Retention”. In: *Geoderma* 116 (Sept. 2003), pp. 61–76. DOI: 10.1016/S0016-7061(03)00094-6.

[31] S. Cueff et al. “Estimation of Soil Water Retention in Conservation Agriculture Using Published and New Pedotransfer Functions”. In: *Soil and Tillage Research* 209 (May 2021), p. 104967. DOI: 10.1016/j.still.2021.104967.

[32] P. Hobbs, K. Sayre, and R. Gupta. “The Role of Conservation Agriculture in Sustainable Agriculture”. In: *Philosophical transactions of the Royal Society of London. Series B, Biological sciences* 363 (July 2007), pp. 543–55. DOI: 10.1098/rstb.2007.2169.

[33] E. Coleman. *Four-Season Harvest*. Chelsea Green Publishing, 1999.

[34] *Associer Légumes et Arbres Fruitiers En Agroforesterie : Principes, Éléments Techniques et Points de Vigilance Pour Concevoir et Conduire Sa Parcelle*. Tech. rep. Avignon, France: Projet SMART, 2017.

[35] *Protéger Les Cultures En Augmentant La Diversité Végétale Des Espaces Agricoles. Rapport de l'Expertise Scientifique Collective.* Tech. rep. INRAE, 2022. DOI: https://dx.doi.org/10.17180/q7wm-q442.

[36] Biowallonie, ed. *Protection Des Cultures En Agriculture Biologique*. Feb. 2017.

[37] L. Tamm et al. "Use of Copper-Based Fungicides in Organic Agriculture in Twelve European Countries". In: *Agronomy* 12.3 (2022). DOI: 10.3390/agronomy12030673.

[38] R. W. Suatmadji. "Studies on the Effect of Tagetes Species on Plant Parasitic Nematodes". PhD thesis. Wageningen University, 1969.

[39] M. González-Chang et al. "Habitat Management for Pest Management: Limitations and Prospects". In: *Annals of the Entomological Society of America* 112 (May 2019), pp. 1–16. DOI: 10.1093/aesa/saz020.

[40] Y. Chiffoleau and D. Desclaux. "Participatory Plant Breeding: The Best Way to Breed for Sustainable Agriculture". In: *International Journal of Agricultural Sustainability* 4 (Jan. 2006). DOI: 10.1080/14735903.2006.9684795.

[41] A. Galieni et al. "Past and Future of Plant Stress Detection: An Overview from Remote Sensing to Positron Emission Tomography". In: *Frontiers in Plant Science* 11 (Jan. 2021), p. 609155. DOI: 10.3389/fpls.2020.609155.

[42] N. R. Baker and E. Rosenqvist. "Applications of Chlorophyll Fluorescence Can Improve Crop Production Strategies: An Examination of Future Possibilities". In: *Journal of Experimental Botany* 55.403 (Aug. 2004), pp. 1607–1621. DOI: 10.1093/jxb/erh196.

[43] L. Muneret et al. "Evidence That Organic Farming Promotes Pest Control". In: *Nature Sustainability* 1 (July 2018), pp. 361–368. DOI: 10.1038/s41893-018-0102-4.

[44] H. Kirchmann. "Why Organic Farming Is Not the Way Forward". In: *Outlook on Agriculture* 48 (Feb. 2019), p. 003072701983170. DOI: 10.1177/0030727019831702.

[45] J. Deguine et al. "Agroecological Crop Protection for Sustainable Agriculture". In: *Advances in Agronomy* 178 (Apr. 2023), pp. 1–59. DOI: 10.1016/bs.agron.2022.11.002.

[46] J. G. Moreau and J.-J. Daverne. *Manuel Pratique de La Culture Maraîchère de Paris*. Mme Ve Bouchard-Huzard, 1845.

[47] C. Carnavalet. *Le Maraîchage Sur Petite Surface - La French Method*. Terran Editions, 2020.

[48] M. Funabashi. "Synecological Farming: Theoretical Foundation on Biodiversity Responses of Plant Communities". In: *Plant Biotechnology* 33 (Apr. 2016). DOI: 10.5511/plantbiotechnology.16.0219a.

[49] M. Funabashi. "Augmentation of Plant Genetic Diversity in Synecoculture: Theory and Practice in Temperate and Tropical Zones". In: *Genetic Diversity in Horticultural Plants*. Ed. by D. Nandwani. Cham: Springer International Publishing, 2019, pp. 3–46. ISBN: 978-3-319-96454-6. DOI: 10.1007/978-3-319-96454-6_1.

[50] P. Hanappe. "Le permaculteur et son robot : les microfermes et la gouvernance des nouvelles technologies". In: *tic&société* Vol. 12, N° 1 (May 2018), pp. 229–253. DOI: 10.4000/ticetsociete.2452.

[51] D. Colliaux et al. "Computational Agroecology: Should We Bet the Microfarm on It?" In: *Eighth Workshop on Computing within Limits 2022*. LIMITS, June 2022. DOI: 10.21428/bf6fb269.5b8520b2.

[52] T. Wintz. "Automated Extraction of Phyllotactic Traits from Arabidopsis Thaliana". In: *CVPPP workshop ECCV* 6 (2018).

[53] J. Quérard et al. "Resonant Out-of-Phase Fluorescence Microscopy and Remote Imaging Overcome Spectral Limitations". In: *Nature Communications* 8.1 (Oct. 2017), p. 969. DOI: 10.1038/s41467-017-00847-3.

[54] A. Pellissier-Tanon et al. "Resonances at Fundamental and Harmonic Frequencies for Selective Imaging of Sine-Wave Illuminated Reversibly Photoactivatable Labels". In: *Chemphyschem : a European journal of chemical physics and physical chemistry* 23.23 (2022), e202200295. DOI: 10.1002/cphc.202200295.

[55] R. Chouket et al. "Extra Kinetic Dimensions for Label Discrimination". In: *Nature Communications* 13.1 (Mar. 2022), p. 1482. DOI: 10.1038/s41467-022-29172-0.

[56] R. Zhang. "Implementations and Applications of Out of Phase Imaging after Optical Modulation (OPIOM) in Fluorescence Macro-Imaging and Fluorescence Endomicroscopy". These de Doctorat. Sorbonne université, Dec. 2018.

[57] H. Kautsky and A. Hirsch. "Neue Versuche zur Kohlensäureassimilation". In: *Die Naturwissenschaften* 19.48 (Nov. 1931), pp. 964–964. DOI: 10.1007/BF01516164.

[58] M. Drusch et al. "The FLuorescence EXplorer Mission Concept—ESA's Earth Explorer 8". In: *IEEE Transactions on Geoscience and Remote Sensing* 55.3 (Mar. 2017), pp. 1273–1284. DOI: 10.1109/TGRS.2016.2621820.

[59] U. Schreiber. "Chlorophyll Fluorescence: New Instruments for Special Applications". In: *Photosynthesis: Mechanisms and Effects*. Ed. by G. Garab. Dordrecht: Springer Netherlands, 1998, pp. 4253–4258. ISBN: 978-0-7923-5547-2 978-94-011-3953-3. DOI: 10.1007/978-94-011-3953-3_984.

[60] A. Ač et al. "Meta-Analysis Assessing Potential of Steady-State Chlorophyll Fluorescence for Remote Sensing Detection of Plant Water, Temperature and Nitrogen Stress". In: *Remote Sensing of Environment* 168 (2015), pp. 420–436. DOI: 10.1016/j.rse.2015.07.022.

[61] A. Stirbet et al. "Chlorophyll a Fluorescence Induction: Can Just a One-Second Measurement Be Used to Quantify Abiotic Stress Responses?" In: *Photosynthetica* 56 (Mar. 2018), pp. 86–104. DOI: 10.1007/s11099-018-0770-3.

[62] M. Meroni et al. "Remote Sensing of Solar-Induced Chlorophyll Fluorescence: Review of Methods and Applications". In: *Remote Sensing of Environment* 113.10 (Oct. 2009), pp. 2037–2051. DOI: 10.1016/j.rse.2009.05.003.

[63] S. Bandopadhyay, A. Rastogi, and R. Juszczak. "Review of Top-of-Canopy Sun-Induced Fluorescence (SIF) Studies from Ground, UAV, Airborne to Spaceborne Observations". In: *Sensors* 20.4 (Jan. 2020), p. 1144. DOI: 10.3390/s20041144.

[64] L. Nedbal and V. Brezina. "Complex Metabolic Oscillations in Plants Forced by Harmonic Irradiance". In: *Biophysical Journal* 83.4 (Oct. 2002), pp. 2180–2189. DOI: 10.1016/S0006-3495(02)73978-7.

[65] D. Lazár. "Parameters of Photosynthetic Energy Partitioning". In: *Journal of Plant Physiology* 175 (2015), pp. 131–147. DOI: 10.1016/j.jplph.2014.10.021.

[66] B. Bailleul et al. "Electrochromism: A Useful Probe to Study Algal Photosynthesis". In: *Photosynthesis research* 106 (2010), pp. 179–189.

[67] D. Croteau, J. Alric, and B. Bailleul. "Chapter 18 - The Multiple Routes of Photosynthetic Electron Transfer in Chlamydomonas Reinhardtii". In: *The Chlamydomonas Sourcebook (Third Edition)*. Ed. by A. R. Grossman and F.-A. Wollman. London: Academic Press, Jan. 2023, pp. 591–613. ISBN: 978-0-12-821430-5. DOI: 10.1016/B978-0-12-821430-5.00001-8.

[68] E. H. Murchie et al. “Measuring the Dynamic Photosynthome”. In: *Annals of botany* 122.2 (2018), pp. 207–220.

[69] S. Eberhard, G. Finazzi, and F.-A. Wollman. “The Dynamics of Photosynthesis”. In: *Annual Review of Genetics* 42 (2008), pp. 463–515. DOI: 10.1146/annurev.genet.42.110807.091452.

[70] U. Rascher and L. Nedbal. “Dynamics of Photosynthesis in Fluctuating Light”. In: *Current Opinion in Plant Biology* 6.9 (2006), pp. 671–678. DOI: 10.1016/j.pbi.2006.09.012.

[71] *RIPE*. https://ripe.illinois.edu/.

[72] *Gain4crops*. https://gain4crops.eu/.

[73] S.-Y. Kwak et al. “Nanosensor Technology Applied to Living Plant Systems”. In: *Annual Review of Analytical Chemistry* 10.1 (2017), pp. 113–140. DOI: 10.1146/annurev-anchem-061516-045310.

[74] N. Wang, N. Zhang, and M. Wang. “Wireless Sensors in Agriculture and Food Industry—Recent Development and Future Perspective”. In: *Computers and Electronics in Agriculture* 50.1 (Jan. 2006), pp. 1–14. DOI: 10.1016/j.compag.2005.09.003.

[75] A. Yassine, S. Shirmohammadi, and V. Piuri. “IEEE CIVEMSA 2014 - Computational Intelligence and Virtual Environments for Measurement Systems and Applications [Conference Reports]”. In: *IEEE Computational Intelligence Magazine* 9.3 (Aug. 2014), pp. 10–11. DOI: 10.1109/MCI.2014.2326097.

[76] S. F. Ryan et al. “The Role of Citizen Science in Addressing Grand Challenges in Food and Agriculture Research”. In: *Proceedings of the Royal Society B: Biological Sciences* 285.1891 (Nov. 2018), p. 20181977. DOI: 10.1098/rspb.2018.1977.

[77] D. Iluz, I. Alexandrovich, and Z. Dubinsky. “The Enhancement of Photosynthesis by Fluctuating Light”. In: *Artificial Photosynthesis*. Ed. by M. Najafpour. InTech, Feb. 2012. ISBN: 978-953-307-966-0. DOI: 10.5772/31040.

[78] S. Shabala. “Oscillations in Plants”. In: *Communication in Plants: Neuronal Aspects of Plant Life*. Ed. by F. Baluška, S. Mancuso, and D. Volkmann. Berlin, Heidelberg: Springer, 2006, pp. 261–275. ISBN: 978-3-540-28516-8. DOI: 10.1007/978-3-540-28516-8_18.

[79] R. Yadav and R. G. Rinker. “The Efficacy of Concentration Forcing”. In: *Chemical Engineering Science* 44.10 (Jan. 1989), pp. 2191–2195. DOI: 10.1016/0009-2509(89)85153-X.

[80] A. Hjelmfelt, R. H. Harding, and J. Ross. “Optimization of Kinetic and Thermodynamic Properties in Irreversible Open Chemical and Thermal Engines”. In: *The Journal of Chemical Physics* 91.6 (Sept. 1989), pp. 3677–3684. DOI: 10.1063/1.456848.

[81] *Accueil ChlamyStation Database*. http://chlamystation.free.fr/.

[82] G. Nelson et al. “QUAREP-LiMi: A Community-Driven Initiative to Establish Guidelines for Quality Assessment and Reproducibility for Instruments and Images in Light Microscopy”. In: *Journal of Microscopy* 284.1 (Oct. 2021), pp. 56–73. DOI: 10.1111/jmi.13041.

[83] L. Nedbal et al. “Kinetic Imaging of Chlorophyll Fluorescence Using Modulated Light”. In: *Photosynthesis Research* 66.1 (2000), pp. 3–12.

[84] K. Oxborough. “Imaging of Chlorophyll a Fluorescence: Theoretical and Practical Aspects of an Emerging Technique for the Monitoring of Photosynthetic Performance”. In: *Journal of Experimental Botany* 55.400 (May 2004), pp. 1195–1205. DOI: 10.1093/jxb/erh145.

[85] E. Šetlíková et al. “The Photosynthesis of Individual Algal Cells during the Cell Cycle of Scenedesmus Quadricauda Studied by Chlorophyll Fluorescence Kinetic Microscopy”. In: *Photosynthesis Research* 84.1 (June 2005), pp. 113–120. DOI: 10.1007/s11120-005-0479-6.

[86] X. Johnson et al. "A New Setup for in Vivo Fluorescence Imaging of Photosynthetic Activity". In: *Photosynthesis Research* 102.1 (Oct. 2009), pp. 85–93. DOI: 10.1007/s11120-009-9487-2.

[87] E. Trampe et al. "Rapid Assessment of Different Oxygenic Phototrophs and Single-Cell Photosynthesis with Multicolour Variable Chlorophyll Fluorescence Imaging". In: *Marine Biology* 158 (July 2011), pp. 1667–1675. DOI: 10.1007/s00227-011-1663-1.

[88] E. Széles et al. "Microfluidic Platforms Designed for Morphological and Photosynthetic Investigations of Chlamydomonas Reinhardtii on a Single-Cell Level". In: *Cells* 11.2 (Jan. 2022), p. 285. DOI: 10.3390/cells11020285.

[89] U. Goodenough, ed. *The Chlamydomonas Sourcebook. Volume 1: Introduction to Chlamydomonas and Its Laboratory Use*. Third edition. London, UK San Diego, CA Cambridge, MA Oxford, UK: Academic Press, An imprint of Elsevier, 2023. ISBN: 978-0-12-822457-1.

[90] A. R. Grossmann and F.-A. Wollman, eds. *The Chlamydomonas Sourcebook. Volume 2: Organellar and Metabolic Processes*. Third edition. London, UK San Diego, CA Cambridge, MA Oxford, UK: Academic Press, An imprint of Elsevier, 2023. ISBN: 978-0-12-821430-5.

[91] H. Goëau et al. "PlantNet Mobile App". In: *Proceedings of the 21st ACM International Conference on Multimedia*. ACM, Oct. 2013. DOI: 10.1145/2502081.2502251.

[92] L. Taiz et al. "Plant Physiology and Development." In: *Plant physiology and development*. Ed. 6 (2015).

[93] R. Olson, H. Sosik, and A. Chekalyuk. "Photosynthetic Characteristics of Marine Phytoplankton from Pump-during-Probe Fluorometry of Individual Cells at Sea". In: *Cytometry* 37.1 (Sept. 1999), pp. 1–13. DOI: 10.1002/(SICI)1097-0320(19990901)37:1<1::AID-CYTO1>3.0.CO;2-C.

[94] S. Kuhlgert et al. "MultispeQ Beta: A Tool for Large-Scale Plant Phenotyping Connected to the Open PhotosynQ Network". In: *Royal Society Open Science* 3.10 (2016). DOI: 10.1098/rsos.160592.

[95] M. R. Krames et al. "Status and Future of High-Power Light-Emitting Diodes for Solid-State Lighting". In: *Journal of Display Technology* 3.2 (June 2007), pp. 160–175. DOI: 10.1109/JDT.2007.895339.

[96] J. T. Wessels, U. Pliquett, and F. S. Wouters. "Light-Emitting Diodes in Modern Microscopy—from David to Goliath?" In: *Cytometry Part A* 81A.3 (2012), pp. 188–197. DOI: 10.1002/cyto.a.22023.

[97] G. Peers et al. "An Ancient Light-Harvesting Protein Is Critical for the Regulation of Algal Photosynthesis". In: *Nature* 462.7272 (Nov. 2009), pp. 518–521. DOI: 10.1038/nature08587.

[98] M. W. Matthès et al. "Learning and Avoiding Disorder in Multimode Fibers". In: *Physical Review X* 11.2 (June 2021), p. 021060. DOI: 10.1103/PhysRevX.11.021060.

[99] H. Küpper et al. "A Microscope for Two-Dimensional Measurements of in Vivo Chlorophyll Fluorescence Kinetics Using Pulsed Measuring Radiation, Continuous Actinic Radiation, and Saturating Flashes". In: *Photosynthetica* 38.4 (2000), pp. 553–570.

[100] C. Westerwalbesloh et al. "A Microfluidic Photobioreactor for Simultaneous Observation and Cultivation of Single Microalgal Cells or Cell Aggregates". In: *PLOS ONE* 14.4 (Apr. 2019), e0216093. DOI: 10.1371/journal.pone.0216093.

[101] K. Greff et al. "The Sacred Infrastructure for Computational Research". In: *Proceedings of the 16th Python in Science Conference* (2017), pp. 49–56. DOI: 10.25080/shinma-7f4c6e7-008.

[102] V. R. Subramanian. *Omniboard*. Mar. 2023.

[103] J. Pech-Pacheco et al. "Diatom Autofocusing in Brightfield Microscopy: A Comparative Study". In: *Proceedings 15th International Conference on Pattern Recognition. ICPR-2000*. Vol. 3. Sept. 2000, 314–317 vol.3. DOI: 10.1109/ICPR.2000.903548.

[104] K. Sakai et al. "Design of a Comprehensive Microfluidic and Microscopic Toolbox for the Ultra-Wide Spatio-Temporal Study of Plant Protoplasts Development and Physiology". In: *Plant Methods* 15.1 (Dec. 2019), p. 79. DOI: 10.1186/s13007-019-0459-z.

[105] L. Pinon et al. "Phenotyping Polarization Dynamics of Immune Cells Using a Lipid Droplet-Cell Pairing Microfluidic Platform". In: *Cell Reports Methods* 2.11 (Nov. 2022), p. 100335. DOI: 10.1016/j.crmeth.2022.100335.

[106] L. W. Jong et al. "Cell Size for Commitment to Cell Division and Number of Successive Cell Divisions in Multicellular Volvocine Green Algae Tetrabaena Socialis and Gonium Pectorale". In: *Proceedings of the Japan Academy. Series B, Physical and Biological Sciences* 93.10 (Dec. 2017), pp. 832–840. DOI: 10.2183/pjab.93.052.

[107] S. P. Damodaran et al. "A Millifluidic Study of Cell-to-Cell Heterogeneity in Growth-Rate and Cell-Division Capability in Populations of Isogenic Cells of Chlamydomonas Reinhardtii". In: *PloS one* 10.3 (2015), e0118987.

[108] A. Sayegh. "Dérivation des électrons photosynthétiques par des quinones sur organisme entier : le cas de Chlamydomonas reinhardtii". PhD thesis. Doctoral dissertation, Sorbonne université, 2018.

[109] G. C. Papageorgiou, Govindjee, and Govindjee, eds. *Chlorophyll a Fluorescence: A Signature of Photosynthesis*. Vol. 19. Advances in Photosynthesis and Respiration. Dordrecht: Springer Netherlands, 2004. ISBN: 978-1-4020-3217-2 978-1-4020-3218-9. DOI: 10.1007/978-1-4020-3218-9.

[110] T. Mirkovic et al. "Light Absorption and Energy Transfer in the Antenna Complexes of Photosynthetic Organisms". In: *Chemical reviews* 117.2 (2017), pp. 249–293.

[111] P. Joliot. "Period-Four Oscillations of the Flash-Induced Oxygen Formation in Photosynthesis". In: *Discoveries in Photosynthesis*. Ed. by Govindjee et al. Vol. 20. Berlin/Heidelberg: Springer-Verlag, 2005, pp. 371–378. ISBN: 978-1-4020-3323-0. DOI: 10.1007/1-4020-3324-9_34.

[112] G. H. Krause and E. Weis. "Chlorophyll Fluorescence and Photosynthesis: The Basics". In: *Annual Review of Plant Physiology and Plant Molecular Biology* 42.1 (1991), pp. 313–349. DOI: 10.1146/annurev.pp.42.060191.001525.

[113] J. A. Bassham and M. Calvin. *The Path of Carbon in Photosynthesis*. Springer. 1960.

[114] J. N. Nishio and I. P. Ting. "Photosynthetic Characteristics of the Palisade Mesophyll and Spongy Mesophyll in the CAM/C4 Intermediate Plant, Peperomia Camptotricha*". In: *Botanica Acta* 106.2 (1993), pp. 120–125. DOI: 10.1111/j.1438-8677.1993.tb00347.x.

[115] T. C. Vogelmann and T. Han. "Measurement of Gradients of Absorbed Light in Spinach Leaves from Chlorophyll Fluorescence Profiles". In: *Plant, Cell & Environment* 23.12 (2000), pp. 1303–1311. DOI: 10.1046/j.1365-3040.2000.00649.x.

[116] G. C. Papageorgiou and Govindjee. "Photosystem II Fluorescence: Slow Changes – Scaling from the Past". In: *Journal of Photochemistry and Photobiology B: Biology* 104.1-2 (July 2011), pp. 258–270. DOI: 10.1016/j.jphotobiol.2011.03.008.

[117] M. Wada. "Chloroplast and Nuclear Photorelocation Movements". In: *Proceedings of the Japan Academy, Series B* 92.9 (2016), pp. 387–411.

[118] B. Baránková, D. Lazár, and J. Nauš. "Analysis of the Effect of Chloroplast Arrangement on Optical Properties of Green Tobacco Leaves". In: *Remote sensing of environment* 174 (2016), pp. 181–196.

[119] R. Emerson and E. Rabinowitch. "Red Drop and Role of Auxiliary Pigments in Photosynthesis". In: *Plant Physiology* 35.4 (July 1960), pp. 477–485.

[120] E. Wientjes et al. “Imaging the Photosystem I/Photosystem II Chlorophyll Ratio inside the Leaf”. In: *Biochimica et Biophysica Acta (BBA) - Bioenergetics* 1858.3 (Mar. 2017), pp. 259–265. DOI: 10.1016/j.bbabio.2017.01.008.

[121] H. K. Lichtenthaler et al. “Photosynthetic Activity, Chloroplast Ultrastructure, and Leaf Characteristics of High-Light and Low-Light Plants and of Sun and Shade Leaves”. In: *Photosynthesis Research* 2.2 (June 1981), pp. 115–141. DOI: 10.1007/BF00028752.

[122] K. Asada. “The Water-Water Cycle in Chloroplasts: Scavenging of Active Oxygens and Dissipation of Excess Photons”. In: *Annual Review of Plant Physiology and Plant Molecular Biology* 50.1 (June 1999), pp. 601–639. DOI: 10.1146/annurev.arplant.50.1.601.

[123] K. Acharya et al. “Primary Electron Donor(s) in Isolated Reaction Center of Photosystem II from Chlamydomonas Reinhardtii”. In: *The Journal of Physical Chemistry B* 116.16 (Apr. 2012), pp. 4860–4870. DOI: 10.1021/jp302849d.

[124] D. E. Budil and M. C. Thurnauer. “The Chlorophyll Triplet State as a Probe of Structure and Function in Photosynthesis”. In: *Biochimica et Biophysica Acta (BBA) - Bioenergetics* 1057.1 (Mar. 1991), pp. 1–41. DOI: 10.1016/S0005-2728(05)80081-7.

[125] W. Lubitz, F. Lendzian, and R. Bittl. “Radicals, Radical Pairs and Triplet States in Photosynthesis”. In: *Accounts of Chemical Research* 35.5 (May 2002), pp. 313–320. DOI: 10.1021/ar000084g.

[126] I. Vass et al. “Reversible and Irreversible Intermediates during Photoinhibition of Photosystem II: Stable Reduced QA Species Promote Chlorophyll Triplet Formation.” In: *Proceedings of the National Academy of Sciences* 89.4 (Feb. 1992), pp. 1408–1412. DOI: 10.1073/pnas.89.4.1408.

[127] E. Tyystjärvi et al. “Slow Degradation of the D1 Protein Is Related to the Susceptibility of Low-Light-Grown Pumpkin Plants to Photoinhibition”. In: *Plant Physiology* 100.3 (1992), pp. 1310–1317.

[128] U. Schreiber, U. Schliwa, and W. Bilger. “Continuous Recording of Photochemical and Non-Photochemical Chlorophyll Fluorescence Quenching with a New Type of Modulation Fluorometer”. In: *Photosynthesis research* 10.1 (1986), pp. 51–62.

[129] U. Schreiber. “Pulse-Amplitude-Modulation (PAM) Fluorometry and Saturation Pulse Method: An Overview”. In: *Chlorophyll a Fluorescence: A Signature of Photosynthesis*. Ed. by G. C. Papageorgiou and Govindjee. Advances in Photosynthesis and Respiration. Dordrecht: Springer Netherlands, 2004, pp. 279–319. ISBN: 978-1-4020-3218-9. DOI: 10.1007/978-1-4020-3218-9_11.

[130] *LI-6800 / Fluorometer Theory and Equation Summary.*

[131] K. Maxwell and G. N. Johnson. “Chlorophyll Fluorescence—a Practical Guide”. In: *Journal of experimental botany* 51.345 (2000), pp. 659–668.

[132] A. C. Ley and D. C. Mauzerall. “Absolute Absorption Cross-Sections for Photosystem II and the Minimum Quantum Requirement for Photosynthesis in Chlorella Vulgaris”. In: *Biochimica et Biophysica Acta (BBA) - Bioenergetics* 680.1 (Apr. 1982), pp. 95–106. DOI: 10.1016/0005-2728(82)90320-6.

[133] L. A. Staehelin. “Chloroplast Structure: From Chlorophyll Granules to Supra-Molecular Architecture of Thylakoid Membranes”. In: *Photosynthesis Research* 76.1-3 (2003), pp. 185–196. DOI: 10.1023/A:1024994525586.

[134] F. Rappaport et al. “On the Advantages of Using Green Light to Study Fluorescence Yield Changes in Leaves”. In: *Biochimica et Biophysica Acta (BBA) - Bioenergetics* 1767.1 (Jan. 2007), pp. 56–65. DOI: 10.1016/j.bbabio.2006.10.002.

[135] A. R. Holzwarth, D. Lenk, and P. Jahns. "On the Analysis of Non-Photochemical Chlorophyll Fluorescence Quenching Curves: I. Theoretical Considerations". In: *Biochimica et Biophysica Acta (BBA) - Bioenergetics* 1827.6 (June 2013), pp. 786–792. DOI: 10.1016/j.bbabio.2013.02.011.

[136] P. A. Salomé and S. S. Merchant. "A Series of Fortunate Events: Introducing Chlamydomonas as a Reference Organism." In: *The plant Cell* (2019).

[137] X.-P. Li et al. "A Pigment-Binding Protein Essential for Regulation of Photosynthetic Light Harvesting". In: *Nature* 403.6768 (2000), pp. 391–395.

[138] G. Allorent et al. "UV-B Photoreceptor-Mediated Protection of the Photosynthetic Machinery in Chlamydomonas Reinhardtii". In: *Proceedings of the National Academy of Sciences* 113.51 (Dec. 2016), pp. 14864–14869. DOI: 10.1073/pnas.1607695114.

[139] D. Petroutsos et al. "A Blue-Light Photoreceptor Mediates the Feedback Regulation of Photosynthesis". In: *Nature* 537.7621 (Sept. 2016), pp. 563–566. DOI: 10.1038/nature19358.

[140] N. Depège, S. Bellafiore, and J.-D. Rochaix. "Role of Chloroplast Protein Kinase Stt7 in LHCII Phosphorylation and State Transition in Chlamydomonas". In: *Science (New York, N.Y.)* 299.5612 (Mar. 2003), pp. 1572–1575. DOI: 10.1126/science.1081397.

[141] J. F. Allen. "State Transitions–a Question of Balance". In: *Science (New York, N.Y.)* (Mar. 2003). DOI: 10.1126/science.1082833.

[142] J. F. Allen. "Protein Phosphorylation in Regulation of Photosynthesis". In: *Biochimica et Biophysica Acta (BBA) - Bioenergetics* 1098.3 (Jan. 1992), pp. 275–335. DOI: 10.1016/S0005-2728(09)91014-3.

[143] R. Delosme, J. Olive, and F.-A. Wollman. "Changes in Light Energy Distribution upon State Transitions: An in Vivo Photoacoustic Study of the Wild Type and Photosynthesis Mutants from Chlamydomonas Reinhardtii". In: *Biochimica et Biophysica Acta (BBA) - Bioenergetics* 1273.2 (Feb. 1996), pp. 150–158. DOI: 10.1016/0005-2728(95)00143-3.

[144] M. Vink et al. "Light-Modulated Exposure of the Light-Harvesting Complex II (LHCII) to Protein Kinase(s) and State Transition in *Chlamydomonas Reinhardtii* Xanthophyll Mutants". In: *Biochemistry* 43.24 (June 2004), pp. 7824–7833. DOI: 10.1021/bi0302671.

[145] E. Rintamäki et al. "Cooperative Regulation of Light-Harvesting Complex II Phosphorylation via the Plastoquinol and Ferredoxin-Thioredoxin System in Chloroplasts". In: *Proceedings of the National Academy of Sciences* 97.21 (Oct. 2000), pp. 11644–11649. DOI: 10.1073/pnas.180054297.

[146] G. Allorent et al. "A Dual Strategy to Cope with High Light in Chlamydomonas Reinhardtii". In: *The Plant Cell* 25.2 (Feb. 2013), pp. 545–557. DOI: 10.1105/tpc.112.108274.

[147] K. J. van Wijk et al. "In Vitro Synthesis and Assembly of Photosystem II Core Proteins: The D1 Protein Can Be Incorporated into PSII in Isolated Chloroplasts and Thylakoids". In: *Journal of Biological Chemistry* 270.43 (Oct. 1995), pp. 25685–25695. DOI: 10.1074/jbc.270.43.25685.

[148] M. A. K. Jansen, A. K. Mattoo, and M. Edelman. "D1-D2 Protein Degradation in the Chloroplast". In: *European Journal of Biochemistry* 260.2 (1999), pp. 527–532. DOI: 10.1046/j.1432-1327.1999.00196.x.

[149] E. Tyystjärvi. "Photoinhibition of Photosystem II". In: *International Review of Cell and Molecular Biology*. Vol. 300. Elsevier, 2013, pp. 243–303. ISBN: 978-0-12-405210-9. DOI: 10.1016/B978-0-12-405210-9.00007-2.

[150] J. M. Troiano et al. "Identification of Distinct pH- and Zeaxanthin-Dependent Quenching in LHCSR3 from Chlamydomonas Reinhardtii". In: *eLife* 10 (Jan. 2021). Ed. by D. M. Kramer and C. S. Hardtke, e60383. DOI: 10.7554/eLife.60383.

[151] F. Wang et al. "The High Light Response and Redox Control of Thylakoid FtsH Protease in Chlamydomonas Reinhardtii". In: *Molecular Plant*. Dynamics of Photosynthesis 10.1 (Jan. 2017), pp. 99–114. DOI: 10.1016/j.molp.2016.09.012.

[152] Alienor134. *Alienor134/Image_segmentation:* Zenodo. Nov. 2021. DOI: 10.5281/zenodo.5684343.

[153] S. van der Walt et al. "Scikit-Image: Image Processing in Python". In: *PeerJ* 2 (June 2014), e453. DOI: 10.7717/peerj.453.

[154] E. Dougherty. *Mathematical Morphology in Image Processing*. CRC Press, Oct. 2018. ISBN: 978-1-351-83050-8.

[155] X. Xu et al. "Characteristic Analysis of Otsu Threshold and Its Applications". In: *Pattern Recognition Letters* 32.7 (May 2011), pp. 956–961. DOI: 10.1016/j.patrec.2011.01.021.

[156] U. Schmidt et al. "Cell Detection with Star-Convex Polygons". In: *Medical Image Computing and Computer Assisted Intervention – MICCAI 2018*. Ed. by A. F. Frangi et al. Lecture Notes in Computer Science. Cham: Springer International Publishing, 2018, pp. 265–273. ISBN: 978-3-030-00934-2. DOI: 10.1007/978-3-030-00934-2_30.

[157] A. Kirillov et al. *Segment Anything*. Apr. 2023. DOI: 10.48550/arXiv.2304.02643. arXiv: 2304.02643 [cs].

[158] Z. Miao et al. "Multi-Omics Integration in the Age of Million Single-Cell Data". In: *Nature Reviews Nephrology* 17.11 (Nov. 2021), pp. 710–724. DOI: 10.1038/s41581-021-00463-x.

[159] G.-J. Huizing et al. *Paired Single-Cell Multi-Omics Data Integration with Mowgli*. Preprint. Bioinformatics, Feb. 2023. DOI: 10.1101/2023.02.02.526825.

[160] L. van der Maaten and G. Hinton. "Visualizing Data Using T-SNE". In: *Journal of Machine Learning Research* 9 (2008), pp. 2579–2605.

[161] L. McInnes, J. Healy, and J. Melville. *UMAP: Uniform Manifold Approximation and Projection for Dimension Reduction*. Sept. 2020. DOI: 10.48550/arXiv.1802.03426. arXiv: 1802.03426 [cs, stat].

[162] R. O. Duda, P. E. Hart, and D. G. Stork. *Part 1: Pattern Classification and Scene Analysis*. New York etc. : J. Wiley & sons. Vol. 1. 1973. ISBN: 0-471-22361-1.

[163] M. Ester et al. "A Density-Based Algorithm for Discovering Clusters in Large Spatial Databases with Noise". In: (1996), pp. 226–231.

[164] C. R. Guadagno, A. Virzo De Santo, and N. D'Ambrosio. "A Revised Energy Partitioning Approach to Assess the Yields of Non-Photochemical Quenching Components". In: *Biochimica et Biophysica Acta (BBA) - Bioenergetics* 1797.5 (May 2010), pp. 525–530. DOI: 10.1016/j.bbabio.2010.01.016.

[165] C. J. Steen et al. "Interplay between LHCSR Proteins and State Transitions Governs the NPQ Response in Chlamydomonas during Light Fluctuations". In: *Plant, Cell & Environment* 45.8 (2022), pp. 2428–2445. DOI: 10.1111/pce.14372.

[166] A. Haar. "Zur Theorie der orthogonalen Funktionensysteme". In: *Mathematische Annalen* 71.1 (Mar. 1911), pp. 38–53. DOI: 10.1007/BF01456927.

[167] I. Daubechies. "The Wavelet Transform, Time-Frequency Localization and Signal Analysis". In: *IEEE Transactions on Information Theory* 36.5 (Sept. 1990), pp. 961–1005. DOI: 10.1109/18.57199.

[168] J. Mairal et al. "Online Dictionary Learning for Sparse Coding". In: *Proceedings of the 26th Annual International Conference on Machine Learning*. Montreal Quebec Canada: ACM, June 2009, pp. 689–696. ISBN: 978-1-60558-516-1. DOI: 10.1145/1553374.1553463.

[169] B. A. Olshausen and D. J. Field. "Sparse Coding with an Overcomplete Basis Set: A Strategy Employed by V1?" In: *Vision Research* 37.23 (Dec. 1997), pp. 3311–3325. DOI: 10.1016/S0042-6989(97)00169-7.

[170] R. A. Fisher. "The Use of Multiple Measurements in Taxonomic Problems". In: *Annals of Eugenics* 7.2 (1936), pp. 179–188. DOI: 10.1111/j.1469-1809.1936.tb02137.x.

[171] S. P. Long, A. Marshall-Colon, and X.-G. Zhu. "Meeting the Global Food Demand of the Future by Engineering Crop Photosynthesis and Yield Potential". In: *Cell* 161.1 (2015), pp. 56–66.

[172] B. Cole et al. "Plant Single-Cell Solutions for Energy and the Environment". In: *Communications biology* 4.1 (2021), pp. 1–12.

[173] B. F. Brehm-Stecher and E. A. Johnson. "Single-Cell Microbiology: Tools, Technologies, and Applications". In: *Microbiology and molecular biology reviews* 68.3 (2004), pp. 538–559.

[174] M. E. Lidstrom and M. C. Konopka. "The Role of Physiological Heterogeneity in Microbial Population Behavior". In: *Nature Chemical Biology* 6.10 (Oct. 2010), pp. 705–712. DOI: 10.1038/nchembio.436.

[175] J. F. H. Snel and H. H. A. Dassen. "Measurement of Light and pH Dependence of Single-Cell Photosynthesis by Fluorescence Microscopy". In: *Journal of Fluorescence* 10.3 (Sept. 2000), pp. 269–269. DOI: 10.1023/A:1009401211264.

[176] G. Konert et al. "Protein Arrangement Factor: A New Photosynthetic Parameter Characterizing the Organization of Thylakoid Membrane Proteins". In: *Physiologia plantarum* 166.1 (2019), pp. 264–277.

[177] L. Behrendt et al. "PhenoChip: A Single-Cell Phenomic Platform for High-Throughput Photophysiological Analyses of Microalgae". In: *Science advances* 6.36 (2020), eabb2754.

[178] M. Andersson et al. "A Microscopy-Compatible Temperature Regulation System for Single-Cell Phenotype Analysis–Demonstrated by Thermoresponse Mapping of Microalgae". In: *Lab on a Chip* 21.9 (2021), pp. 1694–1705.

[179] A. Herdean, D. L. Sutherland, and P. J. Ralph. "Phenoplate: An Innovative Method for Assessing Interacting Effects of Temperature and Light on Non-Photochemical Quenching in Microalgae under Chemical Stress". In: *New Biotechnology* 66 (2022), pp. 89–96.

[180] K. Matsumura, T. Yagi, and K. Yasuda. "Role of Timer and Sizer in Regulation of Chlamydomonas Cell Cycle". In: *Biochemical and biophysical research communications* 306.4 (2003), pp. 1042–1049.

[181] A. Garz et al. "Cell-to-Cell Diversity in a Synchronized Chlamydomonas Culture as Revealed by Single-Cell Analyses". In: *Biophysical journal* 103.5 (2012), pp. 1078–1086.

[182] W. Mohr et al. "Resolution of Conflicting Signals at the Single-Cell Level in the Regulation of Cyanobacterial Photosynthesis and Nitrogen Fixation". In: *PLOS one* 8.6 (2013), e66060.

[183] T. Rühle, B. Reiter, and D. Leister. "Chlorophyll Fluorescence Video Imaging: A Versatile Tool for Identifying Factors Related to Photosynthesis". In: *Frontiers in plant science* 9 (2018), p. 55.

[184] G. H. Krause and E. Weis. "Chlorophyll Fluorescence as a Tool in Plant Physiology: II. Interpretation of Fluorescence Signals". In: *Photosynthesis Research* 5.2 (1984), pp. 139–157. DOI: 10.1007/BF00028527.

[185] M. Á. Ruiz-Sola and D. Petroutsos. "A Toolkit for the Characterization of the Photoprotective Capacity of Green Algae". In: *Plastids*. Ed. by E. Maréchal. Vol. 1829. New York, NY: Springer US, 2018, pp. 315–323. ISBN: 978-1-4939-8653-8 978-1-4939-8654-5. DOI: 10.1007/978-1-4939-8654-5_21.

[186] S. Tietz et al. "NPQ(T): A Chlorophyll Fluorescence Parameter for Rapid Estimation and Imaging of Non-Photochemical Quenching of Excitons in Photosystem-II-associated Antenna Complexes". In: *Plant, Cell & Environment* 40.8 (2017), pp. 1243–1255. DOI: 10.1111/pce.12924.

[187] M. Nilkens et al. "Identification of a Slowly Inducible Zeaxanthin-Dependent Component of Non-Photochemical Quenching of Chlorophyll Fluorescence Generated under Steady-State Conditions in Arabidopsis". In: *Biochimica et Biophysica Acta (BBA) - Bioenergetics* 1797.4 (Apr. 2010), pp. 466–475. DOI: 10.1016/j.bbabio.2010.01.001.

[188] R. W. Pearcy. "Sunflecks and Photosynthesis in Plant Canopies". In: *Annual review of plant biology* 41.1 (1990), pp. 421–453.

[189] E. Erickson, S. Wakao, and K. K. Niyogi. "Light Stress and Photoprotection in Chlamydomonas Reinhardtii". In: *The Plant Journal* 82.3 (2015), pp. 449–465. DOI: 10.1111/tpj.12825.

[190] J. Minagawa and R. Tokutsu. "Dynamic Regulation of Photosynthesis in Chlamydomonas Reinhardtii". In: *The Plant Journal* 82.3 (2015), pp. 413–428.

[191] A. V. Ruban. "Nonphotochemical Chlorophyll Fluorescence Quenching: Mechanism and Effectiveness in Protecting Plants from Photodamage". In: *Plant physiology* 170.4 (2016), pp. 1903–1916.

[192] J. Kromdijk et al. "Improving Photosynthesis and Crop Productivity by Accelerating Recovery from Photoprotection". In: *Science (New York, N.Y.)* 354.6314 (2016), pp. 857–861.

[193] E. Kaiser, A. Morales, and J. Harbinson. "Fluctuating Light Takes Crop Photosynthesis on a Rollercoaster Ride". In: *Plant Physiology* 176.2 (2018), pp. 977–989.

[194] D. Ghosh, S. Mohapatra, and V. Dogra. "Improving Photosynthetic Efficiency by Modulating Non-Photochemical Quenching". In: *Trends in Plant Science* (2022).

[195] A. P. De Souza et al. "Soybean Photosynthesis and Crop Yield Are Improved by Accelerating Recovery from Photoprotection". In: *Science* 377.6608 (Aug. 2022), pp. 851–854. DOI: 10.1126/science.adc9831.

[196] T. Sinclair et al. "Comment on "Soybean Photosynthesis and Crop Yield Are Improved by Accelerating Recovery from Photoprotection"". In: *Science* 379.6634 (Feb. 2023), eade8506. DOI: 10.1126/science.ade8506.

[197] E. H. Harris. "Chlamydomonas as a Model Organism". In: *Annual Review of Plant Physiology and Plant Molecular Biology* 52.1 (2001), pp. 363–406. DOI: 10.1146/annurev.arplant.52.1.363.

[198] P. Müller, X.-P. Li, and K. K. Niyogi. "Non-Photochemical Quenching. A Response to Excess Light Energy1". In: *Plant Physiology* 125.4 (Apr. 2001), pp. 1558–1566. DOI: 10.1104/pp.125.4.1558.

[199] F.-A. Wollman. "State Transitions Reveal the Dynamics and Fexibility of the Photosynthetic Apparatus". In: *The EMBO Journal* 20.14 (July 2001), pp. 3623–3630. DOI: 10.1093/emboj/20.14.3623.

[200] S. V. Bergner et al. "STT7-Dependent Phosphorylation Is Modulated by Changing Environmental Conditions, and Its Absence Triggers Remodeling of Photosynthetic Protein Complexes". In: *Plant Physiology* 168.2 (June 2015), pp. 615–634. DOI: 10.1104/pp.15.00072.

[201] E. Tyystjärvi and E.-M. Aro. "The Rate Constant of Photoinhibition, Measured in Lincomycin-Treated Leaves, Is Directly Proportional to Light Intensity". In: *Proceedings of the National Academy of Sciences of the United States of America* 93 (Apr. 1996), pp. 2213–8. DOI: 10.1073/pnas.93.5.2213.

[202] E. Tyystjärvi. "Chapter Seven - Photoinhibition of Photosystem II". In: *International Review of Cell and Molecular Biology*. Ed. by K. W. Jeon. Vol. 300. International Review of Cell and Molecular Biology. Academic Press, Jan. 2013, pp. 243–303. DOI: 10.1016/B978-0-12-405210-9.00007-2.

[203] C. Goh, U. Schreiber, and R. Hedrich. "New Approach of Monitoring Changes in Chlorophyll a Fluorescence of Single Guard Cells and Protoplasts in Response to Physiological Stimuli". In: *Plant, Cell and Environment* 22.9 (1999), pp. 1057–1070. DOI: 10.1046/J.1365-3040.1999.00475.X.

[204] C. M. M. Gachon et al. "Single-Cell Chlorophyll Fluorescence Kinetic Microscopy of Pylaiella Littoralis (Phaeophyceae) Infected by Chytridium Polysiphoniae (Chytridiomycota)". In: *European Journal of Phycology* 41.4 (Nov. 2006), pp. 395–403. DOI: 10.1080/09670260600960918.

[205] R. Endo and K. Omasa. "Chlorophyll Fluorescence Imaging of Individual Algal Cells: Effects of Herbicide on Spirogyra Distenta at Different Growth Stages". In: *Environmental science and technology* 38.15 (), pp. 4165–4168.

[206] G. M. Cooper. "Chloroplasts and Other Plastids". In: *The Cell: A Molecular Approach. 2nd Edition*. Sinauer Associates, 2000.

[207] T. Roach and C. S. Na. "LHCSR3 Affects De-Coupling and Re-Coupling of LHCII to PSII during State Transitions in Chlamydomonas Reinhardtii". In: *Scientific Reports* 7.1 (Mar. 2017), p. 43145. DOI: 10.1038/srep43145.

[208] T. Hastie, R. Tibshirani, and J. Friedman. *The Elements of Statistical Learning*. Springer Series in Statistics. New York, NY: Springer, 2009. ISBN: 978-0-387-84857-0 978-0-387-84858-7. DOI: 10.1007/978-0-387-84858-7.

[209] W. J. Nawrocki, X. Liu, and R. Croce. "Chlamydomonas Reinhardtii Exhibits De Facto Constitutive NPQ Capacity in Physiologically Relevant Conditions". In: *Plant Physiology* 182.1 (Jan. 2020), pp. 472–479. DOI: 10.1104/pp.19.00658.

[210] G. Bonente et al. "Analysis of LhcSR3, a Protein Essential for Feedback De-Excitation in the Green Alga Chlamydomonas Reinhardtii". In: *PLOS Biology* 9.1 (Jan. 2011), e1000577. DOI: 10.1371/journal.pbio.1000577.

[211] L. Girolomoni et al. "LHCSR3 Is a Nonphotochemical Quencher of Both Photosystems in Chlamydomonas Reinhardtii". In: *Proceedings of the National Academy of Sciences* 116.10 (Mar. 2019), pp. 4212–4217. DOI: 10.1073/pnas.1809812116.

[212] P. Virtanen et al. "SciPy 1.0: Fundamental Algorithms for Scientific Computing in Python". In: *Nature Methods* 17.3 (Mar. 2020), pp. 261–272. DOI: 10.1038/s41592-019-0686-2.

[213] L. van der Maaten and G. Hinton. "Visualizing Data Using T-SNE". In: *Journal of Machine Learning Research* 9.86 (2008), pp. 2579–2605.

[214] L. McInnes et al. "UMAP: Uniform Manifold Approximation and Projection". In: *Journal of Open Source Software* 3.29 (Sept. 2018), p. 861. DOI: 10.21105/joss.00861.

[215] M. E. Malerba et al. "Cell Size, Photosynthesis and the Package Effect: An Artificial Selection Approach". In: *New Phytologist* 219.1 (2018), pp. 449–461.

[216] H. H. McAdams and A. Arkin. "Stochastic Mechanisms in Gene Expression". In: *Proceedings of the National Academy of Sciences* 94.3 (Feb. 1997), pp. 814–819. DOI: 10.1073/pnas.94.3.814.

[217] M. B. Elowitz et al. "Stochastic Gene Expression in a Single Cell". In: *Science (New York, N.Y.)* 297.5584 (Aug. 2002), pp. 1183–1186. DOI: 10.1126/science.1070919.

[218] E. H. Simpson. "The Interpretation of Interaction in Contingency Tables". In: *Journal of the Royal Statistical Society: Series B (Methodological)* 13.2 (1951), pp. 238–241. DOI: 10.1111/j.2517-6161.1951.tb00088.x.

[219] M. Scholz et al. “Light-dependent N-terminal Phosphorylation of LHCSR3 and LHCB4 Are Interlinked in Chlamydomonas Reinhardtii”. In: *The Plant Journal* 99.5 (Sept. 2019), pp. 877–894. DOI: 10.1111/tpj.14368.

[220] R. Zhang et al. “Macroscale Fluorescence Imaging against Autofluorescence under Ambient Light”. In: *Light: Science & Applications* 7.1 (Nov. 2018), p. 97. DOI: 10.1038/s41377-018-0098-6.

[221] D. S. Gorman and R. P. Levine. “Cytochrome f and Plastocyanin: Their Sequence in the Photosynthetic Electron Transport Chain of Chlamydomonas Reinhardi.” In: *Proceedings of the National Academy of Sciences* 54.6 (Dec. 1965), pp. 1665–1669. DOI: 10.1073/pnas.54.6.1665.

[222] F. Pedregosa et al. “Scikit-Learn: Machine Learning in Python”. In: *Journal of Machine Learning Research* 12.85 (2011), pp. 2825–2830.

[223] D. Katz. “The Streak Plate Protocol”. In: *Microbe Library* (2008).

[224] J. L. Bentley. “Multidimensional Binary Search Trees Used for Associative Searching”. In: *Communications of the ACM* 18.9 (Sept. 1975), pp. 509–517. DOI: 10.1145/361002.361007.

[225] J. M. Pearce. “Building Research Equipment with Free, Open-Source Hardware”. In: *Science* 337.6100 (Sept. 2012), pp. 1303–1304. DOI: 10.1126/science.1228183.

[226] J. M. Pearce. “Return on Investment for Open Source Scientific Hardware Development”. In: *Science and Public Policy* 43.2 (Apr. 2016), pp. 192–195. DOI: 10.1093/scipol/scv034.

[227] J. Willinsky. *The Unacknowledged Convergence of Open Source, Open Access, and Open Science*. https://firstmonday.org/ojs/index.php/fm/article/download/1265/1185?inline=1. Text. Aug. 2005.

[228] T. Wenzel. “Open Hardware: From DIY Trend to Global Transformation in Access to Laboratory Equipment”. In: *PLOS Biology* 21.1 (Jan. 2023), e3001931. DOI: 10.1371/journal.pbio.3001931.

[229] B. Diederich et al. “A Versatile and Customizable Low-Cost 3D-printed Open Standard for Microscopic Imaging”. In: *Nature Communications* 11.1 (Nov. 2020), p. 5979. DOI: 10.1038/s41467-020-19447-9.

[230] P. G. Pitrone et al. “OpenSPIM: An Open-Access Light-Sheet Microscopy Platform”. In: *Nature Methods* 10.7 (July 2013), pp. 598–599. DOI: 10.1038/nmeth.2507.

[231] K. J. A. Martens et al. “Visualisation of dCas9 Target Search in Vivo Using an Open-Microscopy Framework”. In: *Nature Communications* 10.1 (Aug. 2019), p. 3552. DOI: 10.1038/s41467-019-11514-0.

[232] J. S. H. Danial et al. “Constructing a Cost-Efficient, High-Throughput and High-Quality Single-Molecule Localization Microscope for Super-Resolution Imaging”. In: *Nature Protocols* 17.11 (Nov. 2022), pp. 2570–2619. DOI: 10.1038/s41596-022-00730-6.

[233] M. Delmans and J. Haseloff. “µCube: A Framework for 3D Printable Optomechanics”. In: *Journal of Open Hardware* 2.1 (May 2018), p. 2. DOI: 10.5334/joh.8.

[234] B. Diederich et al. “UC2 – A 3D-printed General-Purpose Optical Toolbox for Microscopic Imaging”. In: *Imaging and Applied Optics 2019 (COSI, IS, MATH, pcAOP)*. Munich: OSA, 2019, ITh3B.5. ISBN: 978-1-943580-63-7. DOI: 10.1364/ISA.2019.ITh3B.5.

[235] A. C. Zehrer et al. *An Open-Source, High Resolution, Automated Fluorescence Microscope*. May 2023. DOI: 10.1101/2023.05.31.542706.

[236] N. Sofroniew et al. *Napari: A Multi-Dimensional Image Viewer for Python*. Zenodo. Nov. 2022. DOI: 10.5281/zenodo.7276432.

[237] H. Pinkard et al. "Pycro-Manager: Open-source Software for Customized and Reproducible Microscope Control". In: *Nature methods* 18.3 (Mar. 2021), pp. 226–228. DOI: 10.1038/s41592-021-01087-6.

[238] D. M. Susano Pinto et al. "Python-Microscope – a New Open-Source Python Library for the Control of Microscopes". In: *Journal of Cell Science* 134.19 (Oct. 2021), jcs258955. DOI: 10.1242/jcs.258955.

[239] X. C. Moreno et al. "ImSwitch: Generalizing Microscope Control in Python". In: *Journal of Open Source Software* 6.64 (Aug. 2021), p. 3394. DOI: 10.21105/joss.03394.

[240] A. D. Edelstein et al. "Advanced Methods of Microscope Control Using μManager Software". In: *Journal of Biological Methods* 1.2 (Nov. 2014), e10. DOI: 10.14440/jbm.2014.36.

[241] E. Gómez-de-Mariscal et al. "DeepImageJ: A User-Friendly Environment to Run Deep Learning Models in ImageJ". In: *Nature Methods* 18.10 (Oct. 2021), pp. 1192–1195. DOI: 10.1038/s41592-021-01262-9.

[242] I. G. Goldberg et al. "The Open Microscopy Environment (OME) Data Model and XML File: Open Tools for Informatics and Quantitative Analysis in Biological Imaging". In: *Genome Biology* 6.5 (2005), R47. DOI: 10.1186/gb-2005-6-5-r47.

[243] J. Moore et al. *OME-Zarr: A Cloud-Optimized Bioimaging File Format with International Community Support*. Feb. 2023. DOI: 10.1101/2023.02.17.528834.

[244] A. M. Chagas. "Haves and Have Nots Must Find a Better Way: The Case for Open Scientific Hardware". In: *PLOS Biology* 16.9 (Sept. 2018), e3000014. DOI: 10.1371/journal.pbio.3000014.

[245] J. Hohlbein et al. "Open Microscopy in the Life Sciences: Quo Vadis?" In: *Nature Methods* 19.9 (Sept. 2022), pp. 1020–1025. DOI: 10.1038/s41592-022-01602-3.

[246] *The Open Source Definition (Annotated)*. July 2006.

[247] J. Salido et al. "A Review on Low-Cost Microscopes for Open Science". In: *Microscopy Research and Technique* 85.10 (2022), pp. 3270–3283. DOI: 10.1002/jemt.24200.

[248] J. T. Collins et al. "Robotic Microscopy for Everyone: The OpenFlexure Microscope". In: *Biomedical Optics Express* 11.5 (May 2020), pp. 2447–2460. DOI: 10.1364/BOE.385729.

[249] J. S. Cybulski, J. Clements, and M. Prakash. "Foldscope: Origami-Based Paper Microscope". In: *PLOS ONE* 9.6 (June 2014), e98781. DOI: 10.1371/journal.pone.0098781.

[250] P. N. Edwards et al. "Science Friction: Data, Metadata, and Collaboration". In: *Social Studies of Science* 41.5 (2011), pp. 667–690.

[251] C. L. Borgman. *Research Data: Who Will Share What, with Whom, When, and Why?* SSRN Scholarly Paper. Rochester, NY, Oct. 2010. DOI: 10.2139/ssrn.1714427.

[252] C. Allan et al. "OME Remote Objects (OMERO): A Flexible, Model-Driven Data Management System for Experimental Biology". In: *Nature methods* 9.3 (Feb. 2012), pp. 245–253. DOI: 10.1038/nmeth.1896.

[253] Gray, J. et al. "Scientific Data Management in the Coming Decade | ACM SIGMOD Record". In: 34(4) (), pp. 34–41.

[254] A. C. Zehrer et al. *An Open-Source, High Resolution, Automated Fluorescence Microscope*. Preprint. Cell Biology, May 2023. DOI: 10.1101/2023.05.31.542706.

[255] *Tinkercad | From Mind to Design in Minutes*. https://www.tinkercad.com/dashboard.

[256] *Circuit Design App for Makers- Circuito.Io*. https://www.circuito.io/app?components=9238,9442,11021.

[257] R. Busche. *JarnoRFB/Incense*. Feb. 2023.

[258] P. T. Inc. *Collaborative Data Science*. Montreal, QC, 2015.

[259] N. Gaudreault et al. "Illumination Power, Stability, and Linearity Measurements for Confocal and Widefield Microscopes". In: *protocols.io* (2023).

[260] B. Diederich. *openUC2/UC2-Motorized-XY-Table: This Repository Explains How to Turn a Manual Microscope Stage into a Motorized One.*

[261] Thingiverse.com. *GT2 Timing Pulley (Scalable FreeCAD Model) by Manueaswn.*

[262] A. Ruyer-Thompson, P. Hanappe, and A. Lahlou. *CSL-stage*. https://github.com/SonyCSLParis/Motorized-stage. Apr. 2023.

[263] B. Bailleul et al. "Electrochromism: A Useful Probe to Study Algal Photosynthesis". In: *Photosynthesis Research* 106.1-2 (Nov. 2010), pp. 179–189. DOI: 10.1007/s11120-010-9579-z.

Appendix A

Appendix

A.1 Supplementary Materials for "Fluorescence to measure light intensity"

Fluorescence to measure light intensity

Aliénor Lahlou,[1,2,*] Hessam Sepasi Tehrani,[1] Ian Coghill,[1] Mrinal Mandal,[1] Yuriy Shpinov,[1]

Marie-Aude Plamont,[1] Isabelle Aujard,[1] Thomas Le Saux,[1,*] Ludovic Jullien[1,*]

Yuxi Niu,[3] Ladislav Nedbal[3,4] Dusan Lazár[4]

Pierre Mahou,[5] Willy Supatto,[5] Emmanuel Beaurepaire[5]

Isabelle Eisenmann,[6,7] Nicolas Desprat,[6,7] Vincent Croquette,[6,7] Raphaël Jeanneret[6,7]

[1]PASTEUR, Département de chimie, École normale supérieure,
PSL University, Sorbonne Université, CNRS, Paris, France
[2]Sony Computer Science Laboratories, Paris, France
[3]Institute of Bio- and Geosciences/Plant Sciences, Forschungszentrum Jülich, Jülich, Germany
[4]Department of Biophysics, Faculty of Science, Palacký University, Olomouc, Czech Republic
[5]Laboratory for Optics and Biosciences, Ecole polytechnique, CNRS, INSERM, IP Paris, Palaiseau, France
[6]Laboratoire de Physique de l'École normale supérieure,
ENS, Université PSL, CNRS, Sorbonne Université, Université Paris Cité, F-75005 Paris, France
[7]Institut de Biologie de l'ENS (IBENS), École Normale Supérieure,
CNRS, INSERM, PSL University, Paris, France

[*]To whom correspondence should be addressed; E-mail:
Alienor.Lahlou@ens.psl.eu, on leave to Alienor.Lahlou@sony.com,
Thomas.Lesaux@ens.psl.eu,
Ludovic.Jullien@ens.psl.eu.

2023-07-16

The Supporting Information is divided in two parts:

- The three sections 1–3 are dedicated to end-users, who are willing to implement the reported fluorescent actinometers;
- The Appendix has six sections A–F, which contain more advanced information as well as the complete validation of the reported fluorescent actinometers.

The following list indicates the references of the sections and subsections associated with the calls "See Supporting Information" of the Main Text:

- Conversion of units of light intensity: Section A;
- Theoretical derivation of the time evolution of the fluorescence signal associated with the photoconversion of the fluorescent actinometers: Section B, subsections B.1 and B.2;
- Data processing for retrieving the characteristic time τ from the time evolution of the fluorescence signal associated with the photoconversion of the fluorescent actinometers: Theoretical rational in Section B, subsections B.1 and B.2, and Fitting protocol in subsection 2.1;
- Range of light intensity I in which its derivation obeys the simple equation given in Figure 1a of the Main Text: Section B, subsections B.1.1 and B.2.1, and Eq.S62;
- General estimate of the achievable measurement uncertainty on light intensity I: Section D
- Information on the fluorescent actinometers:
  - **Cin**: Synthesis: Subsection 1.2.1, Protocol for implementation: Subsection 2.1.3, Validation: Subsection D.4.1;
  - **Nit**: Synthesis: Subsection 1.2.2, Protocol for implementation: Subsection 2.1.3, Validation: Subsection D.5.1;
  - **DASA**: Synthesis: Subsection 1.2.3, Protocol for implementation: Subsection 2.1.3, Validation: Subsection D.4.3;
  - **Dronpa-2**: Production: Subsection 1.3, Protocol for implementation: Subsection 2.1.3, Validation: Subsection D.4.2;
  - **PA**: Production: Subsection 1.4, Protocol for implementation: Subsection 2.1.3, Validation: Subsection D.4.4;
- Reporting with fluorescence on the time evolution of the absorbance (which follows reaction extent) at the excitation wavelength by the inner filter effect: Subsection B.1.2;

- A second protocol to measure light intensity : Subsection B.3.1;
- **DDAO** as a suitable photochemically inert light intensity-transferring fluorophore: Subsection D.6.3;
- Molecular diffusion generates blurring when it occurs at the time scale of **Dronpa-2** photoconversion: Subsection 2.1.4;
- Original optical setup for fluorescence macroimaging: Subsection D.3.2;
- Optical simulation of illumination in the original optical setup for fluorescence macroimaging: Subsection E.1;
- Interference of molecular diffusion of the fluorescent actinometer in confocal microscopy: Subsection 2.3.3;
- Consistency of the light intensities extracted in confocal microscopy with a fluorescent actinometer and with a power meter: Subsection E.2;
- Experiments and validations performed using a confocal microscope equipped with a continuous laser: Subsections 2.3.3 and E.2;
- Analysis of the **PA** fluorescence kinetics of a dark-acclimated suspension of microalgae exposed to its illumination light at 625 nm: Subsections B.2 and 2.4.3;
- Measurement of the emission spectrum of a light source with a spectrophotometer: Subsection D.2.2;
- Retrieval of information on a light source in the form of spectral light intensity: Subsections: 2.5;
- Characterization of the illumination from purple and red-orange Light Emitting Diodes (LEDs): Subsections: 2.5;
- Retrieval of information on a white LED in the form of spectral light intensity by using **DDAO**: Subsections: 2.2, 2.5, and B.3;
- Imaging of a Petri dish containing a solution of **Dronpa-2** being illuminated by a surrounding radial array of LEDs: Section: F.

Table S1 indicates the subsections providing the theoretical background (Theory), the sample preparation (Sample), the instrumental description (Instrument), the implementation protocol (Protocol), and the protocol validation (Validation) associated to the Figures of the Main Text.

Table S2 complement the metadata, statistical parameter and image processing of the figures of the Main Text. The metadata can be found in the "imaging_metadata" folder of the online repository (10.281/zenodo.7665939). Precision on image analysis: since the exponential fitting parameters are not restricted by boundaries, the fits can output outliers. Effects of misfits can be seen on the borders of Figure 2i. To limit the outlier influence on the display of the content of interest, a uniform mask computed with the library *skimage.filters.thresholding*[1] from the grey-level image is used on the

tau maps and intensity maps to avoid fitting noise on the dark areas and reduce computation costs. The unmasked values are clipped between specified histogram quantiles of tau maps and intensity maps to remove misfit-related outliers. Note that a Gaussian smoothing (*skimage.filter.gaussan*[1]($\sigma = 1$)) was used after processing of the intensity map to build Figure 3h.

Table S1: Supporting Information related to the Figures of the Main Text.

	Theory	**Sample**	**Instrument**	**Protocol**	**Validation**
Figure 1a,b	B.1–B.2	1	D.2–D.3	2.1	D.4
Figure 1c,d	B.3	2.2	D.2–D.3	2.2	D.6.3
Figure 2a–i	B.2	B.2.1	D.3.1	2.3.3	D.4.2
Figure 2j–l	B.2	B.2.1	S23	E.1	E.1
Figure 3	S90–B.2	B.2.1	D.3.3	MT–2.3.3	E.2.3
Figure 4a	S90	B.2.1	D.3.3	2.3.3	E.2.2
Figure 4b	D.4.4	1.4	D.3.1–D.3.4	2.4.3	D.4.4
figure 5a–c	B.3	2.2	D.3.1	2.5	D.6.3

Table S2: Complementary data for the figures in the main text

Figure	Metadata	τ	$CI_{95\%}$	threshold	quantile clip
1c	refer to table S1	**Nit**: 157 s **Cin**: 2160 s **Dronpa-2**: 15 s **DASA**: 51 s **PA**: 71 µs	$\pm$ 4.2%[a] $\pm$ 1.5%[a] $\pm$ 1.5%[a] $\pm$ 4.1%[a] $\pm$ 9.0%[b]	N/A	N/A
2a-i	metadata_epifluo	0.63 s	$\pm$ 0.9%	minimum	[0.01, 0.995]
2j-l	metadata_macroscope	N/A	N/A	triangle	[0.01, 0.995]
3a-f	metadata_pulse_confocal metadata_confocal_cell	nucleus: 1.87 µs liquid: 2.08 µs	$\pm$ 0.5 %[b] $\pm$ 6.1%[b]	li	[0.01, 0.95]
3h	metadata_pulse_confocal metadata_confocal_bacteria	N/A	N/A	li	[0.01, 0.95]
4a	metadata_pulse_confocal metadata_confocal_calib	[1.26, 16.29] µs	max: $\pm$ 0.6%[b]	li	N/A
4b	metadata_OJIP_PSI FL6000 fluorometer PSI	[0.26,2.3] ms	max: $\pm$ 11%[b]	N/A	N/A

[a] The confidence interval was computed with Igor Pro.
[b] The confidence interval was computed with the python library lmfit.[2]

Table S3: Complements to the legends of the Figures in the Main Text.

Figure	Complements
Figure 1b	*Five fluorescent actinometers covering the UV-Vis range in action.* Monoexponential fit of the time evolution of the normalized fluorescence signal $F(t)/F(0)$ provides τ (in s: 157, 2160, 15, 51, 71.10^{-6}), which yields I in μE.m^{-2}.s^{-1} (W.m^{-2}): 5.3 (1.7) at 380 nm,2.5 (0.7) at 405 nm, 270 (69) at 480 nm, 15 (2.9) at 632 nm, 7800 (2000) at 470 nm with **Nit**, **Cin**, **Dronpa-2**, **DASA**, and **PA** respectively.
Figure 3c–f	Maps of the characteristic time τ (**c**) and light intensity (**e**), and corresponding histograms (**d**,**f**; a 3×3 binning is applied to the initial video sequence to improve fitting accuracy).

Contents

1 Materials

The following subsections report on (i) the characterization of the commercially available fluorophores and (ii) the production of the materials, which have been used to implement and validate the protocols for measuring light reported in this manuscript.

1.1 Characterization of the commercially available fluorophores

Two commercially available fluorophores have been used in the following: Rhodamine B (**RhB**) and 7-hydroxy-9H-(1,3-dichloro-9,9-dimethylacridin-2-one) (**DDAO**). To enable the end-users to control the quality of their sample of those fluorophores, we provide below two series of analytical characterizations:

- Their absorption, fluorescence excitation, and fluorescence emission spectra (Figure S2a,b);

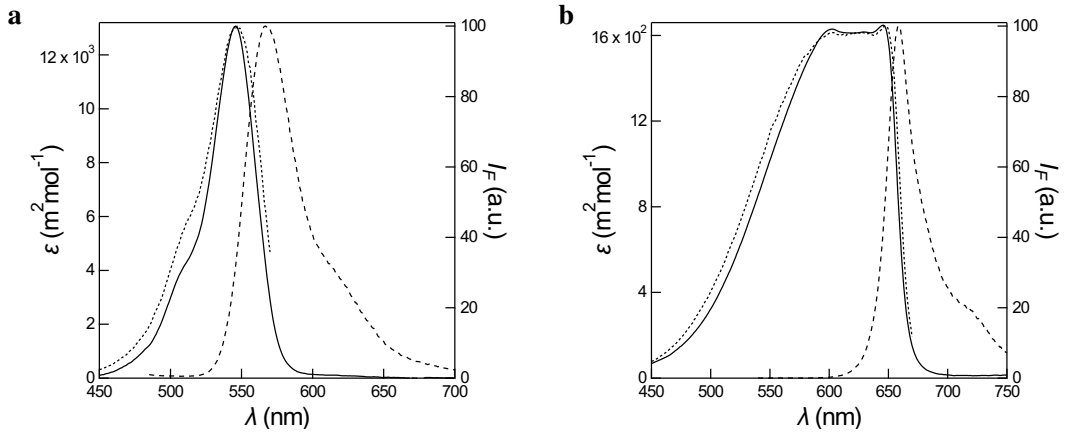

Figure S1: Absorption (solid line), fluorescence excitation (dotted line), and fluorescence emission (dashed line) spectra of 0.8 μM Rhodamine B (**a**; **RhB**; Solvent: Ethanol; $\lambda_{\mathrm{em}} = 574$ nm and $\lambda_{\mathrm{exc}} = 480$ nm for the excitation and emission spectra respectively) and 7.4 μM 7-hydroxy-9H-(1,3-dichloro-9,9-dimethylacridin-2-one) (**b**; **DDAO**; Solvent: pH = 7.9 HEPES buffer (100 mM NaCl, 5 mM NaOH, 10 mM HEPES); $\lambda_{\mathrm{em}} = 675$ nm and $\lambda_{\mathrm{exc}} = 520$ nm for the excitation and emission spectra respectively). $T = 298$ K.

- Their chromatography in HPLC. The experiments were carried out using 2.6 μM Rhodamine B (**RhB**) and 10 μM **DDAO** solutions in H_2O. They have been analyzed by high-pressure liquid chromatography using a C18 column (4.6×50 mm, particle size 2.7 μm; Poroshell 120) operating at 1.0 mL/min and thermostated at 25 $^{\mathrm{o}}$C. The detection of **RhB** and **DDAO** was performed at 565 nm and 450 nm respectively. 15 μL of **RhB** or **DDAO** solutions were injected in the chromatographic system. **RhB** was eluted with a mobile phase composed of two solvents A (methanol) and B (water) whereas **DDAO** was eluted with two solvents A (methanol) and C (0.1% formic acid in H_2O). A gradient was used to optimize the separation of the analytes:
  - For **RhB**, the gradient used was as follow: Initially, the column was equilibrated with a mobile phase consisting of 50% A and 50% B. Six minutes after the injection, the proportion of A was linearly increased to 80%

and continued at 80% A for another 2 minutes. After this step, the composition of the mobile phase was set to initial condition within 1 min and the column was equilibrated for 6 min prior to next injection. The retention time for **RhB** was $t_R = 6.1$ min in these experimental conditions.

– For **DDAO**, the gradient used was as follow: Initially, the column was equilibrated with a mobile phase consisting of 50% A and 50% C. Seven minutes after the injection, the proportion of A was linearly increased to 90% and continued at 90% A for another 1 min. After this step, composition of the mobile phase was set to initial condition within 1 min and the column was equilibrated for 6 min prior to next injection. The retention time for **DDAO** was $t_R = 5.3$ min in these experimental conditions.

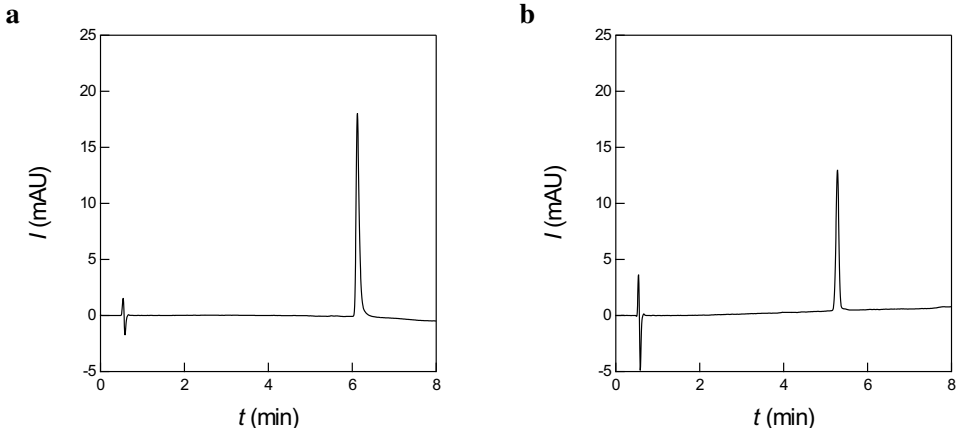

Figure S2: HPLC Chromatography of 2.6 μM Rhodamine B (**a**; **RhB**) and 10 μM 7-hydroxy-9H-(1,3-dichloro-9,9-dimethylacridin-2-one) (**b**; **DDAO**). See Text. $T = 298$ K.

1.2 Syntheses

1.2.1 *(E)*-3-(3,5-Dibromo-2,4-dihydroxyphenyl) acrylic acid ethyl ester (Cin)[3]

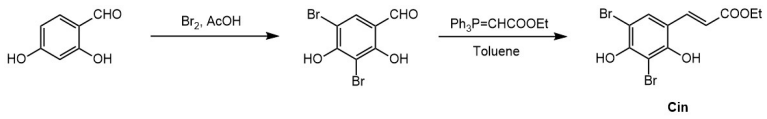

Figure S3: Synthetic pathway of **Cin**.

3,5-Dibromo-2,4-dihydroxybenzaldehyde Bromine (2.32 g, 0.74 mL, 14.5 mmol; 2 eq) was added dropwise to a solution of 2,4-dihydroxybenzaldehyde (1.00 g, 7.25 mmol) in acetic acid (10 mL) over 30 min at room temperature. The resulting mixture was vigorously stirred for 2 h at room temperature. After addition of water (20 mL), the precipitate was filtered, washed with water and dried. 3,5-dibromo-2,4-dihydroxybenzaldehyde was obtained as pale orange crystals after recrystallization of the crude residue in ethanol (1.20 g, 55% yield). m.p: 200 ^{o}C; ^{1}H-NMR (ppm, 250 MHz, $CDCl_3$, 298

K) δ 9.68 (s, 1 H), 7.70 (s, 1 H), 6.60 (s, 1 H); ^{13}C-NMR (ppm, 62.8 MHz, $CDCl_3$, 298 K) δ 193.5, 158.6, 157.1, 135.6, 114.9, 99.9, 97.8.

1-Carboethoxymethylidene triphenyl phosphorane Ethyl bromoacetate (5.75 g, 34.5 mmol) was added to a solution of triphenylphosphine (10.0 g, 38 mmol; 1.15 eq) in toluene (40 mL). The mixture was vigorously refluxed for 10 h under stirring. The white precipitate was filtered off, washed with toluene and dried. The addition at 5 °C of 1 M NaOH (50 mL) to a solution of white solid (10 g) in water (200 mL) gave a white and gummy solid that was filtered, washed with water and dried to yield 1-carboxymethylidene triphenyl phosphorane as a white solid (8.0 g, 60% yield).

***(E)*-3-(3,5-Dibromo-2,4-dihydroxyphenyl) acrylic acid ethyl ester (Cin)** A mixture of 3,5-dibromo-2,4-dihydroxybenzaldehyde and 1-carboethoxymethylidene triphenyl phosphorane (1.5 eq) in toluene (10 mL for 1 mmol of aldehyde) was heated at 60 °C under argon upon protecting from light. The course of the reaction was followed by TLC (cyclohexane/AcOEt). After 2 to 4 h, the reaction was completed. After cooling to room temperature, toluene was removed in a vacuum. The crude residue was purified by flash chromatography on silica gel (mixtures of ethyl acetate and cyclohexane as eluent) to give *(E)*-3-(3,5-dibromo-2,4-dihydroxyphenyl) acrylic acid ethyl ester (**Cin**) in 40 to 60% yield. m.p. 118–118.5 °C; ^{1}H-NMR (ppm, 250 MHz, $CDCl_3$, 298 K) δ 7.81 (d, 1 H, *J*=16.1 Hz), 7.60 (s, 1 H), 6.47 (d, 1 H, *J*=16.1 Hz), 6.07 (bs, 2 H), 4.22 (q, 2 H, *J*=7.0 Hz), 1.33 (t, 3 H, *J*=7.0 Hz); ^{13}C-NMR (ppm, 62.8 MHz, CD_3COCD_3, 298 K) δ 167.3, 154.2, 153.7, 138.7, 131.6, 118.8, 117.8, 102.1, 101.8, 60.7, 14.6; Elemental Analysis: (%) for $C_{11}H_{10}O_4Br_2$(365.9): C 36.10, H 2.75; found : C 36.06, H 2.63; Mass spectrometry: MS (CI, CH_4): *m/z* 367 [*M*+1]; MS (CI, CH_4, HR): *m/z* 364.9024, 366.9006 and 368.8992 (calcd mass for $C_{11}H_{10}O_4Br_2$: 364.9024, 366.9004 and 368.8985).

1.2.2 α-(4- Diethylamino)phenyl)-N-phenylnitrone (Nit)[4]

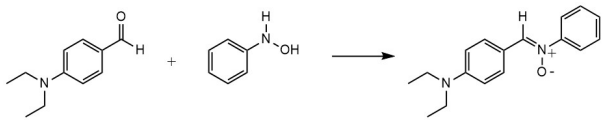

Figure S4: Synthetic pathway of **Nit**.

4-(Diethylamino)benzaldehyde (1.5 g, 8.5 mmol) and phenylhydroxylamine (0.925 g, 8.5 mmol) were stirred in glacial acetic acid (8 mL) for 2 h. The reaction mixture was then poured into water and extracted with ether. The ether extracts were washed with saturated aqueous sodium bicarbonate and with brine, dried on sodium sulfate and concentrated under a vacuum. After recrystallization in cyclohexane /toluene, the nitrone (**Nit**) was obtained as orange needles (1.70 g, 6.4 mmol, 75%). ^{1}H NMR ($CDC1_3$, 300 MHz, δ) 8.30 (d, 2H, $J = 9$ Hz); 7.79-7.76 (m, 3H), 7.48-7.37 (m, 3H), 6.71 (d, 2H, $J = 9$ Hz), 3.43 (q, 4H, $J = 7$ Hz), 1.22 (t, 6H, $J = 7$ Hz).

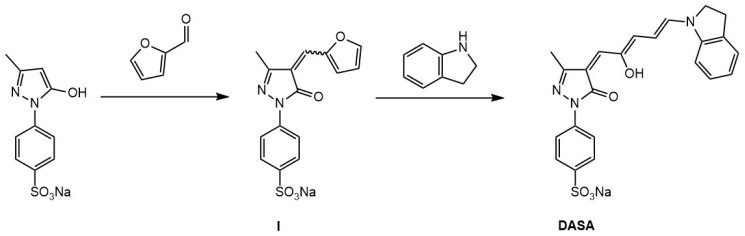

Figure S5: Synthetic pathway of **DASA**.

1.2.3 Sodium 4-(4-((2Z,4E)-2-hydroxy-5-(indolin-1-yl)penta-2,4-dien-1-ylidene)-3-methyl-5-oxo-4,5-dihydro-1H-pyra-zol-1-yl)benzenesulfonate (DASA)[5]

3-Methyl-1-(4-sulfophenyl)-5-pyrazolone (1.97 mmol, 500 mg) was suspended in water (5 mL) and carefully neutralized to pH 7 with 1 M sodium bicarbonate. To this, furfural (1.97 mmol, 189 mg) was added and the reaction mixture stirred at 20 ^{o}C for 16 h. The solvent was then evaporated under reduced pressure to give the sodium 4-(4-(furan-2-ylmethylene)-3-methyl-5-oxo-4,5-dihydro-1H-pyrazol-1-yl)benzenesulfonate intermediate (**I**) as a red solid (494 mg, 76% yield). The product is a mixture of Z and E isomers (2:1). ^{1}H NMR (300 MHz, Deuterium Oxide) δ 8.09 (d, J = 3.8 Hz, 1H), 7.83 (d, J = 1.6 Hz, 1H), 7.80 – 7.61 (m, 7H), 7.33 (s, 1H), 7.18 (d, J = 3.5 Hz, 0.5H), 7.16 (s, 0.5H), 6.68 (dd, J = 3.7, 1.6 Hz, 1H), 6.61 (dd, J = 3.6, 1.7 Hz, 0.5H), 2.32 (s, 1.5H), 2.11 (s, 3H). ^{13}C NMR (75 MHz, DMSO) δ 164.32, 161.54, 150.90, 150.76, 150.26, 150.11, 149.51, 148.12, 144.35, 138.07, 130.29, 127.36, 127.22, 126.24, 126.18, 124.65, 121.29, 120.10, 116.91, 116.62, 114.84, 114.45, 17.39, 12.64; HRMS (ESI+) m/z calcd. For [$C_{15}H_{11}N_2O_5S$] [M–H+]: 331.039; found: 331.040.

I (0.565 mmol, 200 mg) and indoline (0.565 mmol, 67 mg) were dissolved in methanol (2 mL) and stirred at 20 ^{o}C for 1 h. Then this solution was diluted in 10 mL ethyl ether, the precipitate filtered and washed with 3×5 mL of ethyl ether to yield **DASA** as a dark blue powder (165 mg, 62% yield). ^{1}H NMR (300 MHz, Deuterium Oxide) δ 8.01 (dd, J = 6.0, 1.9 Hz, 1H), 7.95 (d, J = 8.4 Hz, 2H), 7.76 (d, J = 8.6 Hz, 2H), 7.27 (d, J = 7.6 Hz, 1H), 7.05 (t, J = 7.6 Hz, 1H), 6.86 (t, J = 7.3 Hz, 1H), 6.67 – 6.56 (m, 2H), 5.37 (d, J = 1.5 Hz, 1H), 3.76 (d, J = 3.2 Hz, 1H), 3.48 – 3.37 (m, 2H), 3.15 – 2.97 (m, 2H), 1.80 (s, 3H). ^{13}C NMR (75 MHz, DMSO) δ 202.51, 163.24, 162.70, 150.52, 149.47, 144.27, 137.06, 134.63, 129.83, 126.99, 126.28, 124.53, 117.63, 116.97, 107.38, 103.62, 61.04, 47.83, 43.50, 27.78, 10.58. Additional small peaks due to the presence of the keto isomer on the pyrazole. HRMS (ESI-) m/z calcd. For [$C_{23}H_{20}N_3O_5S$] [M-]: 450.11; found: 450.11.

1.3 Production of Dronpa-2-containing samples

1.3.1 Plasmids

The plasmids for bacterial expression of **Dronpa-2** carrying an N-terminal hexahistidine tag and for mammalian expression of **Dronpa-2** fused at the C-terminal of the histone H2B (H2B-Dronpa-2) were previously described.[6,7]

1.3.2 Production of Dronpa-2-labeled *Escherichia coli*

Escherichia coli cells from the TOP10 strain were transformed with the **Dronpa-2** plasmid by electroporation. The transformed *E. coli* cells were grown at 37 °C in LB broth. When the optical density at 600 nm reached 0.2, expression was induced by addition of isopropyl β-*D*-1-thio-galactopyranoside (IPTG) to a final concentration of 1 mM. After 4 h of expression at 30 °C, 1 mL aliquots were taken and cells were centrifuged at 8000 rpm for 5 min. After centrifugation, the supernatant was removed and the *E. coli* cells were washed once with 1 ml of PBS (pH 7.4, 50 mM sodium phosphate, 150 mM NaCl) and then resuspended in 250 μL of PBS buffer.

This suspension of *Escherichia coli* was used to prepare a monolayer of bacterial cells deposited on an agarose pad as follows. 125 uL of a 2% pad of low-melting agarose in PBS was sandwiched between two circular glass slides separated by 250 μm by spacers (Gene Frames AB0578; Thermo Scientific). After the agarose became solid, the top cover slide was removed and 2 μL of the bacterial suspension was deposited on the surface of the agar pad. After 15 min, the top cover slide was replaced to seal the sample.

1.3.3 Production and purification of Dronpa-2

The **Dronpa-2** plasmid with an N-terminal hexahistidine tag was transformed in *E. coli* BL21 strain. Cells were grown in Terrific Broth (TB) at 37 ^{o}C. The expression was induced at 30 ^{o}C or 16 ^{o}C by addition of isopropyl β-*D*-1-thio-galactopyranoside (IPTG) to a final concentration of 1 mM at OD(600)=0.6. The cells were harvested after 16 h of expression and lysed by sonication in lysis buffer (50 mM PBS with 150 mM NaCl at pH 7.4, 1 mg/ml DNAse, 5 mM $MgCl_2$ and 1 mM phenylmethylsulfonyl fluoride (PMSF), and a cocktail of protease inhibitors (Sigma Aldrich; S8830)). After lysis, the mixture was incubated on ice for 2 h for DNA digestion. The insoluble material was removed by centrifugation and the supernatant was incubated overnight with Ni-NTA agarose beads (Thermo Fisher) at 4 ^{o}C in a rotator-mixer. The protein loaded Ni-NTA column was washed with 20 column volumes of N1 buffer (50 mM PBS, 150 mM NaCl, 20 mM imidazole, pH 7.4) and 5 column volumes of N2 buffer (50 mM PBS, 150 mM NaCl, 40 mM imidazole, pH 7.4). The bound protein was eluted with N3 buffer (50 mM PBS, 150 mM NaCl, 0,5 M imidazole, pH 7.4). The protein fractions were eventually dialyzed with cassette Slide-A-Lyzer Dialysis Cassettes (Thermo Fisher) against 50 mM PBS, 150 mM NaCl pH 7.4.

1.3.4 Production of Dronpa-2-labeled mammalian cells

U-2 OS cells were grown at 37 ^{o}C in 5% CO_2 in air atmosphere in McCoy's 5A Medium complemented with 10% fetal bovine serum (FBS). Cells were transiently transfected with Genejuice (Merck) according to the manufacturer's protocol then washed with Dulbecco's phosphate buffered saline (DPBS; 2.7 mM KCl, 138 mM NaCl, 1.5 mM KH_2PO_4, 8.1 mM Na_2HPO_4, Thermofisher) and fixed with 2% paraformaldehyde (PFA) solution in DPBS.

1.4 Production of PA-containing samples

The algae strain used were wild type CC124 and WT4 of *Chlamydomonas reinhardtii* provided by IBPC.[1] The algae were grown in heterotrophic media TAP [2] under constant 5-10 μE.m^2.s^{-1} white LED and agitation at 25 ^{o}C. The population was diluted to the tenth the day before the experiment to ensure that the culture observed is in exponential phase.

2 Protocols of implementation of the fluorescent systems for measuring light intensity

2.1 Measurements of light intensity with the fluorescent actinometers

2.1.1 Reagents

- Fluorescent actinometer among **Cin**, **Nit** and Rhodamine B **RhB**, **Dronpa-2**, **DASA**, or **PA**
- Solvent to produce the solution of the fluorescent actinometer:
  - 20 mM Tris pH 7 100 mM NaCl buffer for **Cin**
  - Spectrograde ethanol for **Nit**
  - DPBS pH 7.4 buffer (2.7 mM KCl, 138 mM NaCl, 1.5 mM KH_2PO_4, 8.1 mM Na_2HPO_4) or Tris buffer pH 7.4 (50 mM Tris, 150 mM NaCl) for **Dronpa-2**
  - Spectrograde DMSO and spectrograde acetonitrile for **DASA**
  - Heterotrophic media TAP [3] for **PA**

2.1.2 Equipments

- Balance to prepare the solutions
- Brown glassware or Aluminium foil to keep the solutions in the darkness
- Spectral data available online $\mathrm{https://chart-studio.plotly.com/\sim Alienor134/\#/}$
- Fluorimeter or any optical instrument, which can measure and record the time evolution of the fluorescence signal from the fluorescent actinometer
- Quartz cuvette or glass microscope slides with a 100 μm spacer to build a chamber
- Software for fitting the time evolution of the fluorescence response to illumination

[1] http://www.ibpc.fr/UMR7141/en/home/
[2] https://www.chlamycollection.org/methods/media-recipes/tap-and-tris-minimal/
[3] https://www.chlamycollection.org/methods/media-recipes/tap-and-tris-minimal/

2.1.3 Procedure

Figure S6: *Fluorescence reporting for retrieving light intensity with a fluorescent actinometer.* A jump of constant light I is applied onto the actinometer. The time evolution of its fluorescence signal F is recorded and fit with a mono-exponential curve to extract its characteristic time τ. I is retrieved from τ by using the photoconversion cross section σ of the actinometer.

Generic protocol (Figure S6)

1. Have a solution of the fluorescent actinometer (liquid or solid), which exhibits an absorbance lower than 0.15 along the optical path;

2. Suddenly expose the solution of the fluorescent actinometer to illumination, set at the level of light intensity I to be measured;

3. Collect the time evolution of the fluorescence emission signal;

4. Except for the **PA** actinometer (see below), process the time evolution of the fluorescence emission signal $F\left(\lambda_{\mathrm{exc}}, \lambda_{\mathrm{em}}, t\right)$ (or $F\left(\lambda_{\mathrm{exc}}, \lambda_{\mathrm{em}}, \overrightarrow{r}, t\right)$ in fluorescence imaging) by the fitting of a mono-exponential curve given in Eq.(S1), to enable the retrieval of the associated characteristic time τ (or $\tau\left(\overrightarrow{r}\right)$ in fluorescence imaging).

$$F\left(\lambda_{\mathrm{exc}}, \lambda_{\mathrm{em}}, t\right) = F\left(\lambda_{\mathrm{exc}}, \lambda_{\mathrm{em}}, \infty\right) + \left[F\left(\lambda_{\mathrm{exc}}, \lambda_{\mathrm{em}}, 0\right) - F\left(\lambda_{\mathrm{exc}}, \lambda_{\mathrm{em}}, \infty\right)\right] \exp\left(-\frac{t}{\tau}\right) \tag{S1}$$

   First apply the unsupervised monoexponential fitting function given in Eq.(S1) over the whole acquisition window to extract a first guess of the characteristic time τ_1. Then restrict the time window to [0, $5\tau_1$] and extract a second value τ_2 using the same monoexponential fitting function. This last τ value is used for the next step.

5. Compute the level of light intensity I as $I = \frac{1}{\sigma\tau}$ where σ is the photoconversion cross section tabulated below.

6. Check that the computed level of light intensity I is within the appropriate range of light intensity I tabulated below.

7. The preceding computation yields the level of light intensity I in E.m^{-2}.s^{-1}. Denoting its values in E.m^{-2}.s^{-1} and W.m^{-2} as $I(\lambda_{\mathrm{exc}}, \mathrm{E.m^{-2}.s^{-1}})$ and $I(\lambda_{\mathrm{exc}}, \mathrm{W.m^{-2}})$ respectively, the relation between $I(\lambda_{\mathrm{exc}}, \mathrm{E.m^{-2}.s^{-1}})$ and $I(\lambda_{\mathrm{exc}}, \mathrm{W.m^{-2}})$ is given in Eq.(S12)

$$I(\lambda_{\mathrm{exc}}, \mathrm{W.m^{-2}}) \;=\; \frac{hcN_A}{\lambda_{\mathrm{exc}}} \times I(\lambda_{\mathrm{exc}}, \mathrm{E.m^{-2}.s^{-1}}) \approx 0.12 \times \frac{\mathrm{I}(\lambda_{\mathrm{exc}}, \mathrm{E.m^{-2}.s^{-1}})}{\lambda_{\mathrm{exc}}\,(\mathrm{m})} \tag{S2}$$

   with the Planck constant $h = 6.63\ 10^{-34}$ m^2.kg.s^{-1}, speed of light in a vacuum $c = 3.00\ 10^{8}$ m.s^{-1}, the Avogadro number $N_A = 6.02\ 10^{23}$ mol^{-1}, and where λ_{exc} is in m.

Description of five fluorescent actinometers covering the entire UV-Vis wavelength range The following specific protocols exploit five fluorescent actinometers covering the entire UV-Vis wavelength range for measurement of light intensity (Figure S7):

Figure S7: *Five fluorescent actinometers covering the UV-Vis range in action*. Monoexponential fit of the time evolution of the normalized fluorescence signal $F(t)/F(0)$ provides τ.

- Two actinometers for the UV A wavelength range (relevant for decontamination of materials, evaluation of environmental radiation, photoactivation of many caged molecules in optogenetics, photocatalysis with metal complexes, etc): (i) The dark (E)-3-(3,5-dibromo-2,4-dihydroxyphenyl) acrylic acid ethyl ester (**Cin**), which irreversibly converts under illumination between 350 and 420 nm into the bright 6,8-dibromo-7-hydroxycoumarin fluorescing between 400 and 550 nm in Tris pH 7 buffer (Figure S8a); (ii) The dark α-(4-diethylamino)phenyl)-N-phenylnitrone (**Nit**), which irreversibly converts under illumination between 320 and 430 nm into the dark N-(p-dimethylaminophenyl)formanilide in ethanol (Figure S8b). The photochemically inert rhodamine B (**RhB**) emitting fluorescence between 550 and 650 nm is used here for reporting on **Nit** photoconversion with fluorescence;

- One actinometer for the blue wavelength range (important in optogenetics for photoactivating opsins, FAD CRY, FAD BLUF, and FMN LOV systems, or driving photosynthesis): A bright reversibly photoswitchable fluorescent protein **Dronpa-2** (or M159T), contained within Escherichia coli or eucaryotic cells, or in buffered solution or polyacrylamide gel, emitting fluorescence between 500 and 600 nm, which reversibly converts into a dark photoisomerized state under illumination between 400 and 550 nm (Figure S8c);

- One actinometer for the green to red wavelength range (important for photoactivating opsins or bilin PHY3 in optogenetics, or driving photosynthesis): In acetonitrile, the donor-acceptor Stenhouse dye **DASA** emitting fluorescence extending up to 675 nm reversibly converts into a dark state under illumination between 530 and 670 nm (Figure S8d);

- Since the width of the absorption band of the preceding fluorescent actinometers is limited which necessitates to have several of them to cover the whole range of wavelengths, we eventually report on the last fluorescent actinometer, the photosynthetic apparatus of algae (denoted **PA**), which can provide an estimate of light intensity for the entire visible range of wavelengths. In oxygenic photosynthetic organisms, a few percent of collected sunlight energy is released as fluorescence in the 650-800 nm range. When exposed to constant light at sun-like light intensity, the fluorescence of dark-adapted photosynthetic organisms rises in less than 1 s from a minimum to a maximum via intermediate steps (Figure S8e). The rate constant of the fastest step linearly depends on the light intensity. Usefully, its value does not significantly depend on the type of photosynthetic organism.

These fluorescent actinometers are easily accessible to different communities of end users either via syntheses (for **Cin**, **Nit**, **DASA**) or as protein (**Dronpa-2**) and microorganisms (**Dronpa-2**, **PA**) for end users with access to biological techniques.

Specific protocols

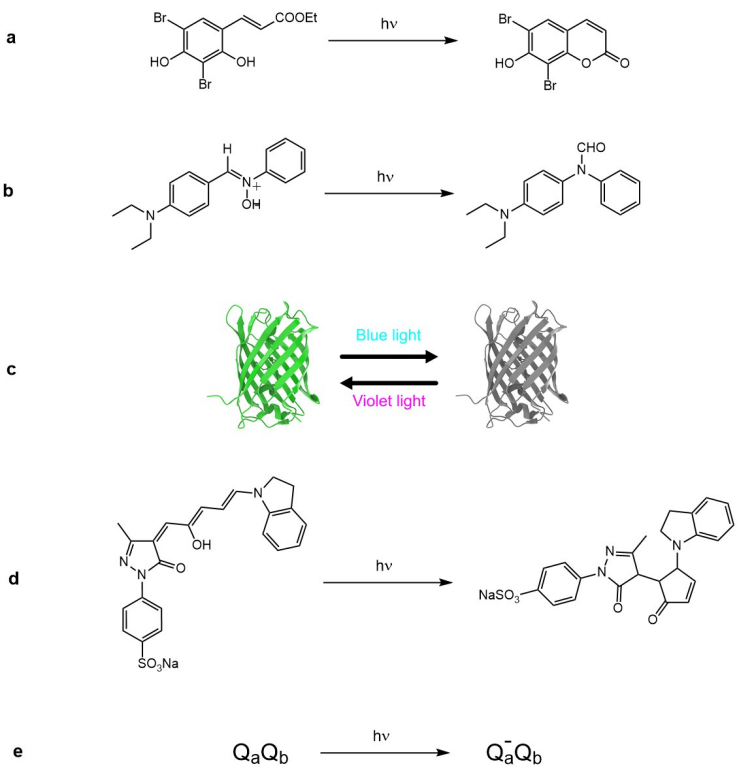

Figure S8: *Photoconversion of the fluorescent actinometers:* **Cin** (**a**), **Nit** (**b**), **Dronpa-2** (**c**), **DASA** (**d**), **PA** (**e**).

Cin to measure light intensity in the 350–420 nm range

1. Prepare a 10 mM stock solution of **Cin** (MW: 365.9 g.mol^{-1}) by dissolving 3.8 mg of **Cin** powder in 1 mL of spectrograde DMSO.

2. Dilute the 10 mM stock solution in 20 mM Tris pH 7 100 mM NaCl buffer to yield a final solution with absorbance equal to 0.15 along the optical path ℓ of the investigated sample. For instance, it yields [**Cin**] $\simeq$ 6 μM for the $\ell = 1$ cm representatives containers used in photocatalysis or [**Cin**] = 0.6 mM for a solution sandwiched between two glass slides with a 100 μm-thick spacer for measuring light intensity in microscopy applications of optogenetics. This solution can be kept at 4 ^{o}C for a week under the protection from ambient light (e.g. by using a brown glassware enveloped in an Aluminium foil). The reference absorption and fluorescence emission spectra of **Cin**, as well as the list of its molar absorption coefficient at various wavelengths is provided online (see also Figure S24 and Table S4).

3. Fill the container with the final solution.

4. Expose the container to time constant monochromatic light at wavelength λ_{exc} in the [350 nm;420 nm] wavelength range.

5. Record the fluorescence intensity at 456 nm,[4] $F(\lambda_{\text{exc}}$,456 nm,$t)$, as a function of time (Figure S9). If illumination of interest and fluorescence measurements are performed on a same instrument, $F(\lambda_{\text{exc}}$,456 nm,$t)$ can be recorded continuously upon illumination at the targeted excitation wavelength. Otherwise, the excitation can be performed in one instrument, and the fluorescence read in another. In this case the excitation has to be performed stepwise by recording each exposure duration to account for the time scale. The fluorescence should be measured between each step, and will be optimal when exciting at 368 nm, which is the maximum of absorption wavelength of the photogenerated 6,8-dibromo-7-hydroxycoumarin.

6. Process the time evolution of the gathered fluorescence signal with the monoexponential fitting equation given in Eq.(S1) to retrieve the relaxation time τ (Figure S9).

7. Extract the light intensity I as $I = \frac{1}{\sigma\tau}$ by using the relevant value of the cross section of **Cin** photoconversion $\sigma(\lambda_{\text{exc}})$ given in Table S4.

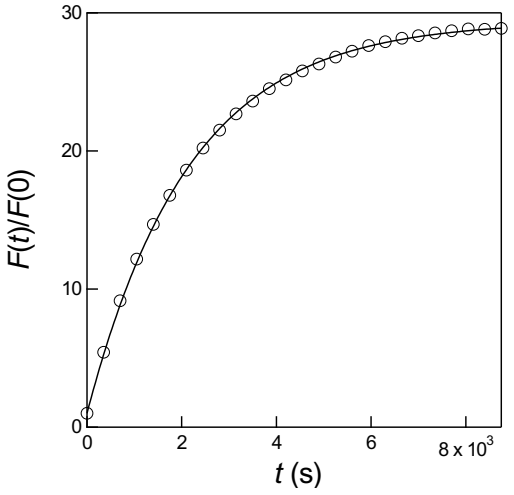

Figure S9: *Representative time evolution of the fluorescence signal with the **Cin** actinometer.* Time dependence of the normalized fluorescence emission at 456 nm of a 5.6 μM **Cin** solution in 20 mM Tris pH 7 100 mM NaCl buffer contained in a 1×1 cm^2 quartz cuvette upon illumination at constant light intensity at $\lambda_{\text{exc}} = 405$ nm. Markers: Experimental data; solid lines: Monoexponential fit with Eq.(S1). Using data provided in Table S4, the characteristic time $\tau = 2160$ s retrieved from the fit yields $I(\lambda_{\text{exc}}) = 2.5$ μE.m^{-2}.s^{-1} (0.7 W.m^{-2}). $T = 293$ K.

Nit to measure light intensity in the 320–430 nm range

1. Prepare stock solutions of **Nit** (MW: 240 g.mol^{-1}; 3.0 mg/ml; 12.5 mM) and **RhB** (MW: 479 g.mol^{-1}; 2.9 mg/mL; 6 mM) in spectrograde ethanol.

2. Dilute the **Nit** stock solution in spectrograde ethanol to produce the final solutions upon taking care to exhibit an absorbance lower or equal to 0.15 at the absorption maximum along the optical path ℓ of the investigated sample.

[4]This wavelength corresponds to the maximum of fluorescence emission and it is given here as an example. Any wavelength between 400 and 550 nm can be used with fluorescence reporting, albeit with a lower fluorescence signal.

For instance, it yields [**Nit**] = 5.8 μM for the $\ell = 1$ cm representatives containers used in photocatalysis or [**Nit**] = 0.58 mM for a solution sandwiched between two glass slides with a 100 μm-thick spacer for measuring light intensity in microscopy applications of optogenetics.

3. Dilute the **RhB** stock solution in the preceding **Nit** solution in ethanol to produce a solution further containing Rhodamine B (**RhB**) at [**RhB**] = 1 μM. This solution can be kept at 4 ^{o}C for a week under the protection from ambient light (e.g. by using a brown glassware enveloped in an Aluminium foil). The reference absorption and fluorescence emission spectra of **Nit**, as well as the list of its molar absorption coefficient at various wavelengths is provided online (see also Figure S38 and Table S8).

4. Fill the container with the final solution.

5. Expose the container to time constant monochromatic light at wavelength λ_{exc} in the [320 nm;430 nm] wavelength range.

6. Record the fluorescence intensity at 574 nm,[5] $F(\lambda_{\text{exc}}$,574 nm,$t)$, as a function of time (Figure S10). If illumination of interest and fluorescence measurements are performed on a same instrument, $F(\lambda_{\text{exc}}$,574 nm,$t)$ can be recorded continuously upon illumination at the targeted excitation wavelength. Otherwise, the excitation can be performed in one instrument, and the fluorescence read in another. In this case the excitation has to be performed stepwise by recording each exposure duration to account for the time scale. The fluorescence should be measured between each step, and will be optimal when exciting at 555 nm, which is the maximum of absorption wavelength of **RhB**.

7. Process the time evolution of the gathered fluorescence signal with the monoexponential fitting equation given in Eq.(S1) to retrieve the relaxation time τ (Figure S10).

8. Extract the light intensity I as $I = \frac{1}{\sigma\tau}$ by using the relevant value of the cross section of **Nit** photoconversion $\sigma(\lambda_{\text{exc}})$ given in Table S8.

Dronpa-2 to measure light intensity in the 440–500 nm range

1. Dilute the **Dronpa-2**-labeled *Escherichia coli* cells and **Dronpa-2** solution in DPBS pH 7.4 buffer (2.7 mM KCl, 138 mM NaCl, 1.5 mM KH_2PO_4, 8.1 mM Na_2HPO_4, Thermofischer) or in Tris buffer pH 7.4 (50 mM Tris, 150 mM NaCl) to get final solutions, which exhibit an absorbance lower than 0.15 at 488 nm along the optical path ℓ. These solutions can be kept at 4 ^{o}C for weeks under the protection from ambient light (e.g. by using a brown glassware enveloped in an Aluminium foil). The reference absorption and fluorescence emission spectra of **Dronpa-2**, as well as the list of its molar absorption coefficient at various wavelengths is provided online (see also Figure S27 and

[5]This wavelength corresponds to the maximum of fluorescence emission of **RhB** and it is given here as an example. Any wavelength between 550 and 650 nm can be used with fluorescence reporting, albeit with a lower fluorescence signal.

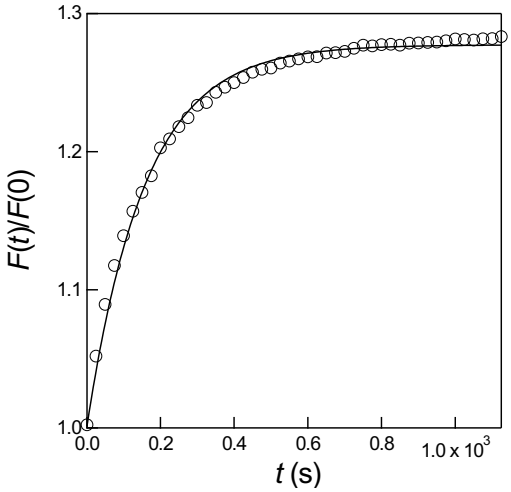

Figure S10: *Representative time evolution of the fluorescence signal with the **Nit** actinometer.* Time dependence of the normalized fluorescence emission at 574 nm of a 5.8 μM **Nit** and 1μM **RhB** solution in spectroscopy grade ethanol contained in a 1×1 cm^2 quartz cuvette upon illumination at constant light intensity at $\lambda_{\text{exc}} = 380$ nm. Markers: Experimental data; solid lines: Monoexponential fit with Eq.(S1). Using data provided in Table S8, the characteristic time $\tau = 157$ s retrieved from the fit yields $I(\lambda_{\text{exc}}) = 5.3$ μE.m^{-2}.s^{-1} (1.7 W.m^{-2}). $T = 293$ K.

Table S5). The **Dronpa-2**-labeled eucaryotic cells are directly used after fixation (see subsection 1.3.4). They can be kept for at least a week at 4 $^{\text{o}}$C in the dark.

2. Fill the container with the final **Dronpa-2**-labeled *Escherichia coli* cells and **Dronpa-2** solution.

3. Expose the container (in the case of the **Dronpa-2**-labeled *Escherichia coli* cells and **Dronpa-2** solution) or the **Dronpa-2**-labeled eucaryotic cells to time constant monochromatic light at wavelength λ_{exc} in the [445 nm;500 nm] wavelength range.

4. Record the fluorescence intensity at 515 nm,[6] $F(\lambda_{\text{exc}}$,515 nm,$t)$, as a function of time (Figure S11). If illumination of interest and fluorescence measurements are performed on a same instrument, $F(\lambda_{\text{exc}}$,515 nm,$t)$ can be recorded continuously upon illumination at the targeted excitation wavelength. Otherwise, the excitation can be performed in one instrument, and the fluorescence read in another. In this case the excitation has to be performed stepwise by recording each exposure duration to account for the time scale. The fluorescence should be measured between each step, and will be optimal when exciting at 488 nm, which is the maximum of absorption wavelength of **Dronpa-2**.

5. Process the time evolution of the gathered fluorescence signal with the monoexponential fitting equation given in Eq.(S1) to retrieve the relaxation time τ (Figure S11).[7]

6. Extract the light intensity I as $I = \frac{1}{\sigma\tau}$ by using the relevant value of the cross section of **Dronpa-2** photoconversion $\sigma(\lambda_{\text{exc}})$ given in Table S5.

[6]This wavelength corresponds to the maximum of fluorescence emission of **Dronpa-2** and it is given here as an example. Any wavelength between 500 and 600 nm can be used with fluorescence reporting, albeit with a lower fluorescence signal.

[7]A Jupyter notebook Notebooks/Dronpa2_video.ipynb is available to perform the corresponding computations online with Binder.

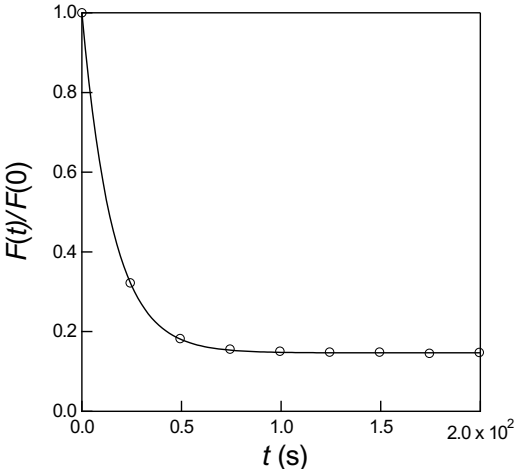

Figure S11: *Representative time evolution of the fluorescence signal with the **Dronpa-2** actinometer.* Time dependence of the normalized fluorescence emission at 515 nm from **Dronpa-2**-labeled bacteria in DPBS $1\times$ pH 7.4 buffer in 3 mm optical path cuvette upon illumination at constant light intensity at $\lambda_{\rm exc} = 480$ nm. Markers: Experimental data; solid lines: Monoexponential fit with Eq.(S1). Using data provided in Table S5, the characteristic time $\tau = 15$ s retrieved from the fit yields $I(\lambda_{\rm exc}) = 270$ μE.m^{-2}.s^{-1} (69 W.m^{-2}). $T = 293$ K.

DASA to measure light intensity in the 530–670 nm range

1. Prepare a stock solution of **DASA** (MW: 450 g.mol^{-1}) in spectrograde DMSO in order to yield a stock solution at about 1 mg.mL^{-1}.

2. Dilute the **DASA** stock solution in spectrograde acetonitrile to generate a final solution with absorbance equal to 0.15 along the optical path ℓ of the investigated sample. As a representative example for applications in photochemistry, we adopt $\ell = 0.3$ cm and [**DASA**] = 40 μM. As a representative example for applications in optogenetics and fluorescence microscopy, [**DASA**] = 100 μM for a **DASA** solution sandwiched between to glass slides with a $\ell = 200$ μm-thick spacer. The **DASA** solutions have to be equilibrated at room temperature under the protection from ambient light (e.g. by using a brown glassware enveloped in an Aluminium foil) for 2 h after preparation, and used no later than a day after their production. The reference absorption and fluorescence emission spectra of **DASA**, as well as the list of its molar absorption coefficient at various wavelengths is provided online (see also Figure S31 and Table S6).

3. Fill the container with the final solution.

4. Expose the container to time constant monochromatic light at wavelength $\lambda_{\rm exc}$ in the [530 nm; 670 nm] wavelength range.

5. Record the fluorescence intensity in the [650 nm; 675 nm] wavelength range $F(\lambda_{\rm exc},\lambda_{\rm em},t)$, as a function of time (Figure S12). If illumination of interest and fluorescence measurements are performed on a same instrument,

$F(\lambda_{\mathrm{exc}},\lambda_{\mathrm{em}},t)$ can be recorded continuously upon illumination at the targeted excitation wavelength. Otherwise, the excitation can be performed in one instrument, and the fluorescence read in another. In this case the excitation has to be performed stepwise by recording each exposure duration to account for the time scale and the fluorescence should be measured between each step.

6. Process the time evolution of the gathered fluorescence signal with the monoexponential fitting equation given in Eq.(S1) to retrieve the relaxation time τ (Figure S12).

7. Extract the light intensity I as $I = \frac{1}{\sigma\tau}$ by using the relevant value of the cross section of **DASA** photoconversion $\sigma(\lambda_{\mathrm{exc}})$ given in Table S6).

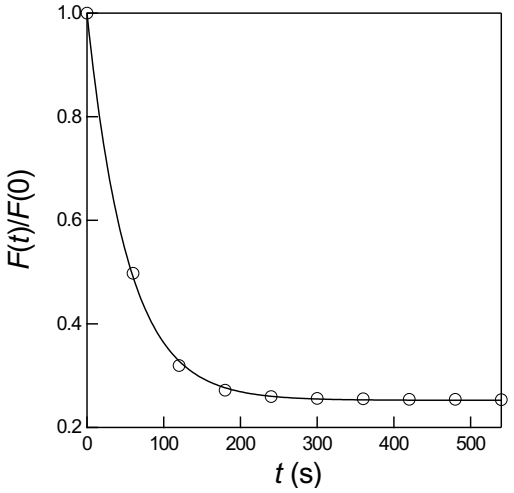

Figure S12: *Representative time evolution of the fluorescence signal with the **DASA** actinometer.* Time dependence of the normalized fluorescence emission of a 20 μM **DASA** solution in a 1:100 (v/v) mixture of spectroscopy grade DMSO and acetonitrile in a 3 mm light path quartz cuvette upon illumination at constant light intensity at $\lambda_{\mathrm{exc}} = 632$ nm. Markers: Experimental data; solid lines: Monoexponential fit with Eq.(S1). Using data provided in Table S6), the characteristic time $\tau = 52$ s retrieved from the fit yields $I(\lambda_{\mathrm{exc}}) = 15$ μE.m^{-2}.s^{-1} (2.9 W.m^{-2}). $T = 293$ K.

PA to measure light intensity in the 400–650 nm range

1. Prepare the microalgae solution according to the subsection 1.4.

2. Dilute the microalgae solution to generate a final solution with absorbance equal to 0.15 along the optical path ℓ of the investigated sample.

3. Fill the container with the final solution.

4. Expose the container to time constant monochromatic light at wavelength λ_{exc} in the [400 nm; 650 nm] wavelength range.

5. Record the time evolution of the fluorescence intensity at 690 nm,[8] $F(t)$, over 1 s at 3 MHz sampling frequency by using a fast photodetector (e.g. photodiode, MPPC, oscilloscope; see subsection D.4.4) (Figure S13).

6. The time evolution of the fluorescence signal retrieved from applying constant illumination on the **PA** actinometer is more complex than the one of the other fluorescent actinometers[9] and it deserves a specific fitting protocol. Process the time evolution of the fluorescence signal with the following iterative fitting method to retrieve the relaxation time τ:[10]

   - In a first step, apply an unsupervised fit with Eq.(S3)

$$F(t) = F(0) + A_{OJ}\left(1 - e^{-t/\tau_{OJ}}\right)^{s_{OJ}} + A_{JI}\left(1 - e^{-t/\tau_{JI}}\right)^{s_{JI}} + A_{IP}\left(1 - e^{-t/\tau_{IP}}\right)^{s_{IP}} \quad \text{(S3)}$$

     in order to retrieve a first estimate of the value of the characteristic time τ_{OJ} associated to the of the initial step of **PA** fluorescence rise ;

   - In a second step, restrict the time window to [0;3τ_{OJ}] and apply the fit given in Eq.(S4) to the time evolution of the fluorescence emission

$$F(t) = F(0) + A\left(1 - e^{-t/\tau}\right)^{s} \quad \text{(S4)}$$

     upon fixing $s = 1.24$[8] in order to retrieve a second estimate of the value of the characteristic time τ associated to the initial step of **PA** fluorescence rise ;

   - In the last step, restrict the time window to [0;5τ], apply the fit given in Eq.(S4) to the time evolution of the fluorescence emission upon adopting the values of parameters extracted during the second step as starting values, and retrieve the final value of the characteristic time τ associated to the initial step of **PA** fluorescence rise .

7. Extract the light intensity I as $I = \frac{1}{\sigma\tau}$ by using the relevant value of the cross section of **PA** photoconversion $\sigma(\lambda_{\text{exc}})$ given in Table S7.

2.1.4 Troubleshooting

General

- No time evolution of the fluorescence signal from the final solution of fluorescent actinometer under constant illumination: Check that the final solution has been kept at 4 ^{o}C under the protection from ambient light.

[8] This wavelength corresponds to the maximum of fluorescence emission of **PA** and it is given here as an example. Any wavelength between 650 and 750 nm can be used with fluorescence reporting, albeit with a lower fluorescence signal.

[9] For more details on the origin of the light-limited step of **PA**, refer to section D.4.4.

[10] A Jupyter notebook Notebooks/PA_OJIP_rise_fit.ipynb is available to perform the corresponding computations online with Binder.

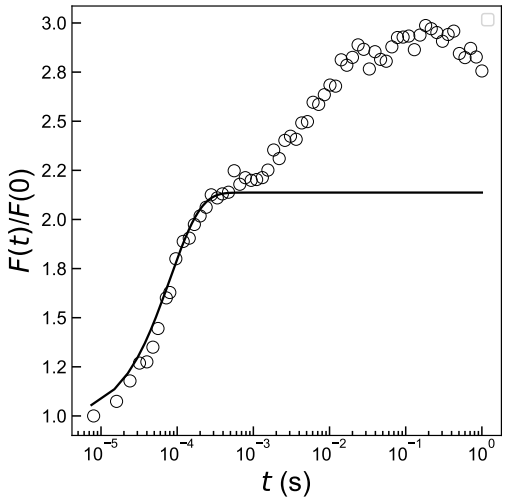

Figure S13: *Representative time evolution of the fluorescence signal with the **PA** actinometer.* Time dependence of the normalized fluorescence emission of *Chlamydomonas reinhardtii* (CC 124) in exponential growth phase upon illumination at constant light intensity at $\lambda_{\text{exc}} = 470$ nm. Markers: Experimental data; solid lines: Monoexponential fit with Eq.(S1). Using data provided in Table S7, the characteristic time $\tau = 71$ μs retrieved from the fit yields $I(\lambda_{\text{exc}}) = 7.8\, m\text{E.m}^{-2}\text{.s}^{-1}$ (2.0 kW.m^{-2}). $T = 293$ K.

- If the cross section σ at an excitation wavelength belonging to the wavelength range of relevance for a given fluorescent actinometer is not tabulated in the reported Table, a good estimate can be retrieved from linear interpolation by exploiting the cross sections at the two closest tabulated values.

- With **Dronpa-2** and **DASA** which are reversibly photoswitchable fluorescent actinometers, the light intensity I obeys Eq.(S8)

$$I\left(\lambda_{\text{exc}}\right) \quad = \quad \frac{1 - k^{\Delta}\tau}{\sigma\tau} \tag{S5}$$

where k^{Δ} is the rate constant associated to thermal relaxation after photoconversion (expressed in s^{-1}). Hence, using Eq.(S6)

$$I \quad = \quad \frac{1}{\sigma\tau} \tag{S6}$$

for retrieving I implies that $k^{\Delta}\tau \ll 1$, which has to be checked. k^{Δ} is respectively equal to 0.02 and 0.002 s^{-1} for **Dronpa-2**[9] and **DASA**[5] around room temperature.

- For calibration of light intensity in fluorescence imaging, Eq.(S1) becomes Eq.(S7)

$$F\left(\lambda_{\text{exc}}, \lambda_{\text{em}}, \overrightarrow{r}, t\right) = F\left(\lambda_{\text{exc}}, \lambda_{\text{em}}, \overrightarrow{r}, \infty\right) + \left[F\left(\lambda_{\text{exc}}, \lambda_{\text{em}}, \overrightarrow{r}, 0\right) - F\left(\lambda_{\text{exc}}, \lambda_{\text{em}}, \overrightarrow{r}, \infty\right)\right] \exp\left(-\frac{t}{\tau\left(\overrightarrow{r}\right)}\right) \tag{S7}$$

which yields the map $I\left(\overrightarrow{r}\right)$ sought for from Eq.(S8)

$$I\left(\overrightarrow{r}\right) \quad = \quad \frac{1}{\sigma\tau\left(\overrightarrow{r}\right)} \tag{S8}$$

Eqs.(S7,S8) are strictly valid when the actinometer molecules do not move. However, when they can diffuse (diffusion coefficient D), Eqs.(S1,S8) can still be used but the spatial resolution of the $I(\overrightarrow{r})$ is then limited to $\sqrt{D\tau(\overrightarrow{r})}$:[9] The faster the photoconversion, the higher the spatial resolution. At the limit of homogenization (e.g. upon stirring), the spatial information of the illumination profile is lost and one can retrieve the overall amount of light intensity I received by the actinometer solution from the measured overall relaxation time τ with Eq.(S6).

Specific

DASA

- The time evolution of the fluorescence signal from the DASA fluorescent actinometer does not conform to the observation in Figure S12: Check that the **DASA** solutions have been equilibrated at room temperature under the protection from ambient light for 2 h after preparation, and used no later than a day after their production.

PA

- The fluorescence rise starts decaying after reaching the maximum. The tri-exponential fit must be stopped at the maximum for better accuracy.
- When calibrating a red light source, make sure to exclude the excitation light from the detected light by using a narrow fluorescence filter (for example, a 700 nm filter to calibrate a 650 nm LED).
- Make sure that the observed rise time of the **PA** fluorescence signal is not driven by the rise time of your light source (e.g. due to heating in LEDs; generally in the μs range[9]) or of your photodetector by preliminarily analyzing the rise time of the fluorescence signal from a photochemically inert fluorophore (**DDAO** for instance) upon turning on light.[9]

2.1.5 Time taken

The duration of the overall measurement is evaluated to 2 h:

1. Preparation of the final solution of a fluorescent actinometer: 75 min
2. Collection of the time evolution of the fluorescence emission under constant illumination: 30 min as an order of magnitude (depending on the actinometer and light intensity)
3. Data processing: 15 min

2.1.6 Anticipated results

A general estimate of the achievable measurement uncertainty on I is 20%. Where photoconversion occurs rapidly, on a timescale where molecular motion is minimal, it is possible to retrieve a map of the spatial distribution of light intensity. However, if the molecules can visit the whole irradiated area at the timescale of the actinometer photoconversion, only mean light intensity values can be obtained.

2.1.7 References

- About actinometry: H. J. Kuhn, S. E. Braslavsky, and R. Schmidt, Chemical Actinometry (IUPAC Technical Report), *Pure Appl. Chem.*, **2004**, *76*, 2105–2146.
- About fluorescence: B. Valeur, M.-N. Berberan-Santos, Molecular Fluorescence: Principles and Applications 2$^{\text{nd}}$ Edition, Wiley, **2012**.
- About **Cin**: **1**. N. Gagey, P. Neveu, and L. Jullien. Reporting two-photon uncaging with the efficient 3,5-dibromo-2,4-dihydroxycinnamic caging group, *Angew. Chem. Intl. Ed.*, **2007**, *46*, 2467–2469.; **2**. N. Gagey, P. Neveu, C. Benbrahim, B. Goetz, I. Aujard, J. - B. Baudin, L. Jullien, Two-photon uncaging with fluorescence reporting: Evaluation of the o-hydroxycinnamic platform, *J. Am. Chem. Soc.*, **2007**, *129*, 9986–9998.
- About **Nit**: **1**. P. F. Wang, L. Jullien, B. Valeur, J.-S. Filhol, J. Canceill, J.-M. Lehn, Multichromophoric Cyclodextrins. 5. Antenna-induced Unimolecular Photoreactions. Photoisomerization of a Nitrone, *New J. Chem.*, **1996**, *20*, 895–907; **2**. M. Emond, T. Le Saux, S. Maurin, J.-B. Baudin, R. Plasson, L. Jullien, 2-Hydroxy-Azobenzenes to Tailor pH Pulses and Oscillations with Light, *Chem. Eur. J.*, **2010**, *16*, 8822–8831.
- About **Dronpa-2**: **1**. R. Chouket, A. Pellissier-Tanon, A. Lahlou, R. Zhang, D. Kim, M.-A. Plamont, M. Zhang, X. Zhang, P. Xu, N. Desprat, D. Bourgeois, A. Espagne, A. Lemarchand, T. Le Saux, L. Jullien, Extra kinetic dimensions for label discrimination, *Nat. Commun.*, **2022**, *13*, 1482; **2**. J. Quérard, R. Zhang, Z. Kelemen, M.-A. Plamont, X. Xie, R. Chouket, I. Roemgens, Y. Korepina, S. Albright, E. Ipendey, M. Volovitch, H. L. Sladitschek, P. Neveu, L. Gissot, A. Gautier, J.-D. Faure, V. Croquette, T. Le Saux, L. Jullien, Resonant out-of-phase fluorescence microscopy and remote imaging overcome spectral limitations, *Nat. Commun.*, **2017**, *8*, 969.
- About **DASA**: Y Shpinov, A Schlichter, P Pelupessy, T Le Saux, L Jullien, B Adelizzi, Unexpected acid-triggered formation of reversibly photoswitchable Stenhouse salts from Donor-acceptor Stenhouse adducts, *Chem. Eur. J.*, **2022**, *28*, e202200497.
- About **PA**: **1**. Maxwell, K., and Johnson, G. N., Chlorophyll fluorescence – a practical guide, J. Exp. Bot, **2000**, *51*, 659–668; **2**. D. Lazar, The polyphasic chlorophyll a fluorescence rise measured under high intensity of exciting light, *Funct. Plant Biol.*, **2006**, *33*, 9 – 30.

- About data processing: **1**. Mechanistic reduction leading to monoexponential fit of the time evolution of the fluorescence signal: R. Chouket, A. Pellissier-Tanon, A. Lahlou, R. Zhang, D. Kim, M.-A. Plamont, M. Zhang, X. Zhang, P. Xu, N. Desprat, D. Bourgeois, A. Espagne, A. Lemarchand, T. Le Saux, L. Jullien, Extra kinetic dimensions for label discrimination, *Nat. Commun.*, **2022**, *13*, 1482; **2**. About **PA** data processing: D. Joly, R. Carpentier, Sigmoidal reduction kinetics of the photosystem II acceptor side in intact photosynthetic materials during fluorescence induction, *Photochem. Photobiol. Sci.*, **2009**, *8*, 167–173.

2.2 A reporting fluorophore to transfer information on light intensity from one wavelength to another

2.2.1 Reagents

- 7-Hydroxy-9H-(1,3-dichloro-9,9-dimethylacridin-2-one) (**DDAO**)
- Solvent to produce the **DDAO** solution:
  - Spectrograde DMSO
  - Aqueous HEPES pH 7.9 buffer (100 mM NaCl, 5 mM NaOH, 10 mM HEPES)

2.2.2 Equipments

- Balance to prepare the **DDAO** solution
- Brown glassware or Aluminium foil to keep the solutions in the darkness
- Fluorimeter or any optical instrument, which can measure and record the fluorescence signal
- Quartz cuvette or glass microscope slides with a 100 μm spacer to build a chamber

2.2.3 Procedure

1. Dissolve **DDAO** (MW: 308 g.mol^{-1}) in spectrograde DMSO in order to yield a stock solution at about 50 mM concentration.
2. Dilute the preceding stock solution in an aqueous HEPES pH 7.9 buffer (100 mM NaCl, 5 mM NaOH, 10 mM HEPES) to produce a final solution at **DDAO** concentration in the few μM range. The reference absorption and fluorescence emission spectra of **DDAO**, as well as the list of its molar absorption coefficient[11] at various wavelengths is provided online (see also Figure S42 and Table S9).

[11] In **DDAO**, the molar absorption coefficient $\varepsilon\left(\lambda_{\mathrm{exc}}\right)$ and the scaled excitation coefficient $\epsilon\left(\lambda_{\mathrm{exc}}\right)$ are identical.

3. Submit the final solution of **DDAO** to illumination at two wavelengths $\lambda_{\mathrm{exc},1}$ (with known intensity $I\left(\lambda_{\mathrm{exc},1}\right)$ measured with one actinometer reported above) and $\lambda_{\mathrm{exc},2}$ (with intensity $I(\lambda_{\mathrm{exc},2})$ to be measured).

4. Collect the corresponding intensities of its fluorescence emission at a same emission wavelength between 640 and 700 nm.

5. Use Eq.(S9)

$$I(\lambda_{\mathrm{exc},2}) = \frac{\varepsilon\left(\lambda_{\mathrm{exc},1}\right) F\left(\lambda_{\mathrm{exc},2}, \lambda_{\mathrm{em}}\right)}{\varepsilon\left(\lambda_{\mathrm{exc},2}\right) F\left(\lambda_{\mathrm{exc},1}, \lambda_{\mathrm{em}}\right)} I\left(\lambda_{\mathrm{exc},1}\right). \tag{S9}$$

to extract the light intensity sought for by using the list of its molar absorption coefficient at various wavelengths provided online and in Table S9.

2.2.4 Troubleshooting

- If the absorption coefficient ε at an excitation wavelength belonging to the wavelength range of light absorption by **DDAO** is not tabulated in Table S9, a good estimate can be retrieved from linear interpolation by exploiting the absorption coefficients at the two closest tabulated values.

2.2.5 Time taken

The duration of the overall measurement is evaluated to 2 h:

1. Preparation of the final solution of **DDAO**: 75 min

2. Collection of the **DDAO** fluorescence emission at two wavelengths: 30 min

3. Data processing with Eq.(S9): 15 min

2.2.6 Anticipated results

A general estimate of the achievable measurement uncertainty on I is 20%.

2.2.7 References

About **DDAO** as a dye:

- **1**. D. Warther, F. Bolze, J. Lonéard, S. Gug, A. Specht, D. Puliti, X.- H. Sun, P. Kessler, Y. Lutz, J.-L. Vonesch, B. Winsor, J.-F. Nicoud, M. Goeldner, Live-Cell One- and Two-Photon Uncaging of a Far-Red Emitting Acridinone Fluorophore, *J. Am. Chem. Soc.*, **2010**, *132*, 2585–2590; **2**. R. Labruère, A. Alouane, T. Le Saux, I. Aujard, P. Pelupessy, A. Gautier, S. Dubruille, F. Schmidt, L. Jullien, Self-immolation for uncaging with fluorescence reporting, *Angew. Chem. Int. Ed.*, **2012**, *51*, 9344–9347.

2.3 Measurement of the light intensity at 488 nm at the focal plane of fluorescence microscopes

2.3.1 Reagents

- Either fixed **Dronpa-2**-labeled *Escherichia coli* or eucaryotic cells at the nucleus, or 5–10 μM **Dronpa-2** solutions either in Tris buffer pH 7.4 (50 mM Tris, 150 mM NaCl) or in DPBS $1\times$ pH 7.4 buffer (2.7 mM KCl, 138 mM NaCl, 1.5 mM KH_2PO_4, 8.1 mM Na_2HPO_4).

2.3.2 Equipments

- Fluorescence microscope
- Software for fitting the time evolution of the fluorescence response to illumination

2.3.3 Procedure

Epifluorescence microscope

1. Sandwich a **Dronpa-2** aqueous solution between two glass-slides with a 100 μm-thick spacer. Alternatively, you can use **Dronpa-2**-labeled *Escherichia coli* or eucaryotic cells.
2. Expose the sample to a pulse of constant 470 nm light. Alternatively, expose the sample to a train of four 30 s-long 470 nm light pulses separated by 2 min of darkness in order to benefit from additional data.[12]
3. Collect the fluorescence images at 550 nm.[13]
4. Apply monoexponential fits to the time evolution of the fluorescence signal at each pixel with Eq.(S1) to extract the map of characteristic time $\tau\,(\overrightarrow{r})$ (averaged over the successive light ON-light OFF cycle when using a train of light pulses).
5. Compute the light intensity at each pixel $I(470\text{ nm},\vec{r})$ by using Eq.(S8) and the cross section σ at 488 nm provided in Table S5. A simplified version of the code is given in an online Jupyter notebook in Notebooks/Dronpa2_video.ipynb.

[12] It has been demonstrated that the kinetics of the time evolution of the fluorescence decay is similar in the successive pulses.[9]

[13] We typically used a camera set to 3 Hz over 10 min. Before further processing, the acquired video images can be downsized by a 3×3 averaging kernel to improve the signal-to-noise ratio. A mask of the illuminated area was evaluated by exploiting a threshold of the intensity from the average fluorescence image and all the following operations were performed on the unmasked pixels only.

Confocal microscope equipped with a continuous 488 nm laser

1. Acquire 100 square images of the **Dronpa-2** containing sample (**Dronpa-2**-labeled *Escherichia coli* or eucaryotic cells, or a **Dronpa-2** solution sandwiched between two glass-slides with a 80-100 μm-thick spacer) in the raster scanning mode (128×128 pixel^2; pixel size: 0.4 μm; dwell time τ_{dt}: 3.4 μs; $\lambda_{\rm exc}$ = 488 nm; 500 nm $\leq \lambda_{\rm em} \leq$ 600 nm) with the focused 488 nm laser of the confocal microscope. The image of fixed **Dronpa-2**-labeled cells at the nucleus displayed in Figure S14a has been obtained with an objective Plan-NeoFluar 20×, NA 0.5; over a 53×53 μm^2 square at 5% light power associated to 1.76 μW measured in the focal plane of the objective with the powermeter.

2. Average the fluorescence signal over square zone of interest located in the center of the collected images (typically a 3×3 μm^2 zone when using the **Dronpa-2** solution or the cell nucleus for the **Dronpa-2**-labeled cells at the nucleus displayed in Figure S14a respectively).

3. Plot the dependence of the averaged fluorescence signal as a function of time, which was extracted from the image rank n as $n\tau_{dt}$. Figure S14b displays the average drop over the nucleus. It also shows that the **Dronpa-2** aqueous solution sandwiched between two glass-slides yields a similar kinetic signature upon properly restricting analysis to a central portion of the overall image, which avoids molecular diffusion to interfere with the **Dronpa-2** photoconversion.

4. Extract the maps of the characteristic time τ (Figure S14c) and light intensity at 488 nm delivered by the focused laser beam at the focal plane of the confocal microscope (Figure S14d) upon exploiting Eq.(S8) and the relevant parameters for **Dronpa-2** in Table S5. Representative histograms in the field of view are displayed in Figures S14e and f respectively.

5. To calibrate the overall scale of light intensities, reproduce the protocol described above at different settings of the instrument to be calibrated.

Confocal microscope equipped with a pulsed 488 nm laser Same as paragraph 2.3.3 upon acquiring 50–100 square images of the **Dronpa-2** containing sample (**Dronpa-2**-labeled *Escherichia coli* or eucaryotic cells, or a **Dronpa-2** solution sandwiched between two glass-slides with a 80-100 μm-thick spacer) in the raster scanning mode (512×512 pixel^2; pixel size: from 0.057 to 0.569 μm; dwell time τ_{dt}: 1.2 μs; $\lambda_{\rm exc}$ = 488 nm; 500 nm $\leq \lambda_{\rm em} \leq$ 600 nm) with the focused 488 nm laser of the confocal microscope. The image of fixed **Dronpa-2**-labeled cells at the nucleus displayed in Figure S14a has been obtained with an objective HC PL APO CS2; Leica 40×, NA 1.1; over a 29.12×29.12 μm^2 to 291.19×291.19 μm^2 square at 2% light power associated to 18.5 μW measured in the focal plane of the objective with the powermeter.

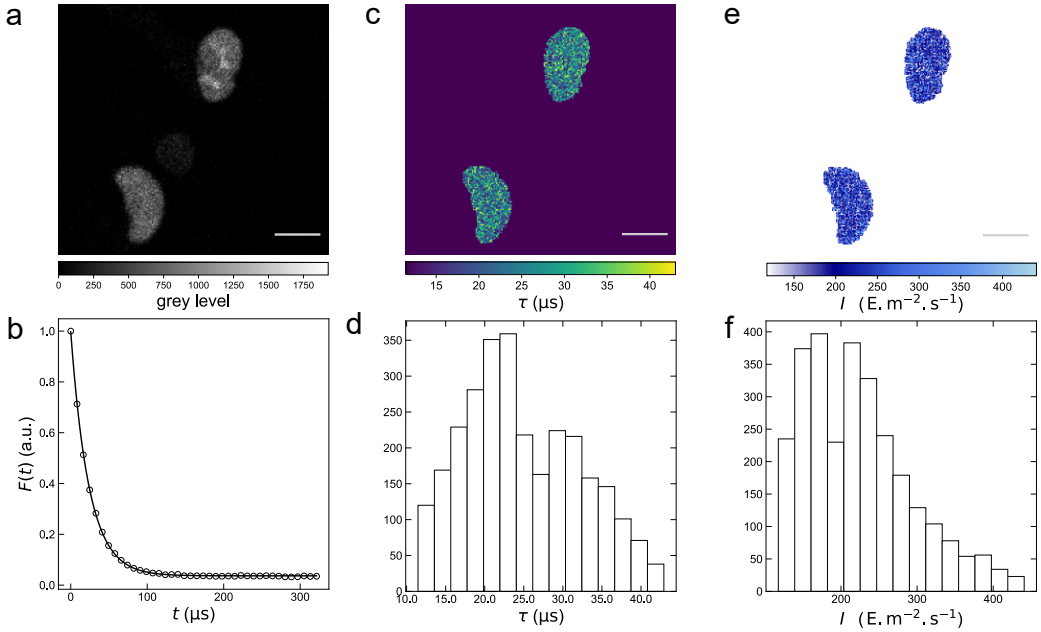

Figure S14: ***Dronpa-2*** *for characterization of the spatial distribution of the light intensity of a confocal microscope equipped with a continuous laser.* **a**,**b**: **Dronpa-2**-labeled nucleus of a fixed UO2S cell imaged with a confocal microscope in the raster scanning mode (λ_{exc} = 488 nm; 500 nm $\leq \lambda_{\text{em}} \leq$ 600 nm). Initial image (**a**); Time evolution of the averaged fluorescence over the whole nucleus (**b**; triangles: experimental data; solid line: monoexponential fit wit Eq.(S1). The corresponding evolution from a central portion of the overall image of a 10 μM **Dronpa-2** solution sandwiched between two glass-slides is shown with circles); **c**–**f**: Maps of the characteristic time τ (**c**) and light intensity (**d**), and corresponding histograms (**e**,**f**; a 3×3 binning is applied to the initial video sequence to improve fitting accuracy). Solvent: Tris buffer pH 7.4 (50 mM Tris, 150 mM NaCl); Pixel size: 0.33μm; Laser power 10%; T = 293 K.

2.3.4 Troubleshooting

General

- No fluorescence decay is observed: Light intensity at 488 nm is too low or the **Dronpa-2** sample is already photoswitched. In the first case, increase light intensity at 488 nm. In the second case, refresh the **Dronpa-2** sample in darkness for half an hour.

- For calibration of light intensity in fluorescence imaging, Eq.(S1) becomes Eq.(S10)

$$F\left(\lambda_{\text{exc}}, \lambda_{\text{em}}, \overrightarrow{r}, t\right) = F\left(\lambda_{\text{exc}}, \lambda_{\text{em}}, \overrightarrow{r}, \infty\right) + \left[F\left(\lambda_{\text{exc}}, \lambda_{\text{em}}, \overrightarrow{r}, 0\right) - F\left(\lambda_{\text{exc}}, \lambda_{\text{em}}, \overrightarrow{r}, \infty\right)\right] \exp\left(-\frac{t}{\tau\left(\overrightarrow{r}\right)}\right) \quad \text{(S10)}$$

  which yields the map $I\left(\overrightarrow{r}\right)$ sought for from Eq.(S11)

$$I\left(\overrightarrow{r}\right) = \frac{1}{\sigma\tau\left(\overrightarrow{r}\right)} \quad \text{(S11)}$$

  Eqs.(S10,S11) are strictly valid when the actinometer molecules do not move. However, when they can diffuse (diffusion coefficient D), Eqs.(S10,S11) can still be used but the spatial resolution of the $I\left(\overrightarrow{r}\right)$ is then limited to $\sqrt{D\tau\left(\overrightarrow{r}\right)}$:[9] The faster the photoconversion, the higher the spatial resolution. At the limit of homogenization (e.g.

upon stirring), the spatial information of the illumination profile is lost and one can retrieve the overall amount of light intensity I received by the actinometer solution from the measured overall relaxation time τ with Eq.(S6).

Epifluorescence microscope

- The fluorescence decays are not similar when using a train of light pulses to benefit from additional data: Check that the delay between two light pulses is long enough to yield significant recovery of the bright state of **Dronpa-2** after light-driven photoswitching.[14]

Confocal microscopy

- Figure S14b evidences the similarity of the characteristic times, which have been retrieved by using both **Dronpa-2** containing samples. This observation was anticipated from the previous observations pointing on similar cross sections for photoisomerization of **Dronpa-2** at 488 nm in solution and in fixed cells.[9] However, it also validated the choice of the acquisition parameters, which limited the interference of molecular diffusion for retrieving the characteristic time of **Dronpa-2** photoconversion. Indeed, whereas the **Dronpa-2** molecules do not move in the fixed cell, they can freely diffuse in the **Dronpa-2** solution. Hence, in the latter case, the square imaged surface has to be chosen large enough in order to keep a central zone where the interference of molecular diffusion can be neglected for retrieving the characteristic time of **Dronpa-2** photoconversion from the light-induced decay of fluorescence signal upon illumination.[9] For building Figure S14b, we recorded 100 scans with a delay of 56 ms between two scans at a same pixel, which yielded 5.6 s for the total duration of the acquisition. During that time, the typical distance randomly visited by the **Dronpa-2** molecule was about 20 μm,[15] which is to be compared with the 53 μm-long side of the imaged square surface so as to reduce the analyzed surface not experiencing any interference from diffusion in the (x,y) plane to a 3×3 μm^2 square zone of interest located in the center of the collected images.[16] As shown in Figure S15, an analysis performed over the whole acquired image evidences the interference of **Dronpa-2** diffusion, which can be observed by the departure from a monoexponential decay at the longest times.[9] Nevertheless, the monoexponential fit still provides a satisfactory order of magnitude of the light intensity. Hence 39 μs was extracted for the characteristic time τ from the latter analysis whereas 34 μs was retrieved from the analysis on a 3×3 μm^2 square zone of interest located in the center of the collected images.

2.3.5 Time taken

Once the **Dronpa-2** sample is available, the duration of the overall measurement is evaluated to less than 1 h:

[14] The relaxation time for thermal recovery of the bright state of **Dronpa-2** in the dark is 50 s at 25 ^{o}C.

[15] We here used the 9 10^{-11} m^2.s^{-1} value of the diffusion coefficient of EGFP to derive an estimate (available on the Bionumber web site).

[16] At the corresponding timescale, we did not notice any interference that could originate from diffusion along the z axis in the inhomogeneous light profile generated with the microscope objective.

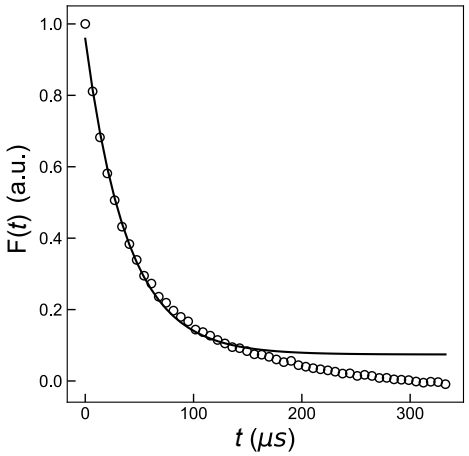

Figure S15: *Evidence for the interference of molecular diffusion in the decay of fluorescence emission from a 5 μM **Dronpa-2** solution in DPBS $1\times$ pH 7.4 buffer submitted to 488 nm illumination.* The series of 100 images has been acquired over a 53×53 μm^2 square in 6 s in the raster scanning mode (Objective $20\times$, NA 0.5; 128×128 pixel^2; pixel size: 0.4 μm; dwell time τ_{dt}: 3.4 μs) with the focused 488 nm laser of the confocal microscope (5% light power associated to 1.76 μW measured in the focal plane of the objective with the powermeter). The dependence of the fluorescence signal averaged over the whole 53×53 μm^2 square field of view is plotted as a function of time, which was extracted from the image rank n as $n\tau_{dt}$. Markers: Experimental data; solid line: Monoexponential fit with Eq.(S1) of the Main Text. $T = 293$ K.

1. Collection of the time evolution of the fluorescence emission: 30 min as an order of magnitude (depending on the light intensity)

2. Data processing: 15 min

2.3.6 Anticipated results

The output image of the light of intensity $I(470$ nm,$\vec{r})$ in the field of view of the microscope from which one can subsequently retrieve the histogram of the spatial distribution of the light at 470 nm in the field of view of the microscope. The estimate of the achievable measurement uncertainty on I is 20%.

2.3.7 References

- About actinometry: H. J. Kuhn, S. E. Braslavsky, and R. Schmidt, Chemical Actinometry (IUPAC Technical Report), *Pure Appl. Chem.*, **2004**, *76*, 2105–2146.

- About fluorescence: B. Valeur, M.-N. Berberan-Santos, Molecular Fluorescence: Principles and Applications 2$^{\text{nd}}$ Edition, Wiley, **2012**.

- About **Dronpa-2**: **1**. R. Chouket, A. Pellissier-Tanon, A. Lahlou, R. Zhang, D. Kim, M.-A. Plamont, M. Zhang, X. Zhang, P. Xu, N. Desprat, D. Bourgeois, A. Espagne, A. Lemarchand, T. Le Saux, L. Jullien, Extra kinetic

dimensions for label discrimination, *Nat. Commun.*, **2022**, *13*, 1482; **2**. J. Quérard, R. Zhang, Z. Kelemen, M.-A. Plamont, X. Xie, R. Chouket, I. Roemgens, Y. Korepina, S. Albright, E. Ipendey, M. Volovitch, H. L. Sladitschek, P. Neveu, L. Gissot, A. Gautier, J.-D. Faure, V. Croquette, T. Le Saux, L. Jullien, Resonant out-of-phase fluorescence microscopy and remote imaging overcome spectral limitations, *Nat. Commun*., **2017**, *8*, 969.

- About data processing: Mechanistic reduction leading to monoexponential fit of the time evolution of the fluorescence signal: R. Chouket, A. Pellissier-Tanon, A. Lahlou, R. Zhang, D. Kim, M.-A. Plamont, M. Zhang, X. Zhang, P. Xu, N. Desprat, D. Bourgeois, A. Espagne, A. Lemarchand, T. Le Saux, L. Jullien, Extra kinetic dimensions for label discrimination, *Nat. Commun.*, **2022**, *13*, 1482.

2.4 Quantitation of non-monochromatic light sources with a fluorescent actinometer

2.4.1 Reagents

- Fluorescent actinometer. In the reported examples, we adopted **Nit** and **PA**
- Solvent to produce the solution of the fluorescent actinometer:
  - Spectrograde ethanol for **Nit**
  - Heterotrophic media TAP [17] for **PA**

2.4.2 Equipments

- Balance to prepare the solutions
- Brown glassware or Aluminium foil to keep the solutions in the darkness
- Spectral data available online $\mathrm{https://chart-studio.plotly.com/\sim Alienor134/\#/}$
- Fluorimeter or any optical instrument, which can measure and record the time evolution of the fluorescence signal from the fluorescent actinometer
- Quartz cuvette or glass microscope slides with a 100 μm spacer to build a chamber
- Software for fitting the time evolution of the fluorescence response to illumination

[17] https://www.chlamycollection.org/methods/media-recipes/tap-and-tris-minimal/

2.4.3 Procedure

Quantitation of a purple LED emitting at 405 nm We first report an example of such a measurement by using the combination of α-(p-dimethylaminophenyl)-N-phenylnitrone (**Nit**) and Rhodamine B (**RhB**) in ethanol as a fluorescent actinometer to characterize the emission spectrum of a Light Emitting Diode (LED) at 405 nm.

1. Acquire the LED emission spectrum, either as a reference from the purchaser or after a measurement with a spectrophotometer in which the the light emitted from the LED is sent into the emission pathway of a fluorometer with reduced slits opening. Figure S16a displays the unscaled emission spectrum $S(\lambda)$ of a Light Emitting Diode (LHUV-0405, Lumileds, NL), which emits at 405$\pm$15 nm.

2. Divide the curve $S(\lambda)$ by its integral S calculated over the wavelength range of LED emission to yield the normalized emission spectrum $j(\lambda) = S(\lambda)/S$ (Figure S16b).

3. The flux of photons arriving at the sample at each wavelength λ which is sought for, $I(\lambda)$, is proportional to $j(\lambda)$ but the proportionality factor S_I is unknown (see Eq.S38). To measure S_I, first compute the integral of the action spectrum AS of the LED on **Nit** in ethanol (see Eq.S40) by multiplying the absorption spectrum of the nitrone **Nit**, $\varepsilon(\lambda)$ (Figure S16c) by the normalized emission spectrum $j(\lambda)$ (Figure S16d) upon further using $\varphi = 0.17$ as an average over the concerned wavelength range (see Table S8).

4. On the other hand, submit a 12 μM **Nit** and 1 μM **RhB** solution in ethanol to illumination in a 3 mm optical path cuvette.

5. Record the rise of the fluorescence emission at 574 nm as a function of time.

6. Retrieve the relaxation time τ of the photoreaction from monoexponential fitting of the data (see Figure S16e).

7. Exploit the values of τ and AS to retrieve the scaling parameter $S_I = 1/(\tau AS)$.

8. Retrieve the scaled emission spectrum of the LED from $I(\lambda) = S_I \times j(\lambda)$ (see Figure S16f).

Quantitation of a red-orange LED emitting at 625 nm We then report an example of measurement by using the **PA** fluorescent actinometer to calibrate the emission spectrum of a Light Emitting Diode (LED) at 625 nm mounted on the FL 6000 fluorometer from Photon Systems Instruments (PSI; Drasov, Czech Republic) (LXML-PH01 LED, which belongs to the LUXEON Rebel Color Line from LUMILEDS). The following protocol has been reproduced for various percentages of light power of the PSI instrument, which led us to build the calibration curve displayed in Figure 4 of the Main Text.

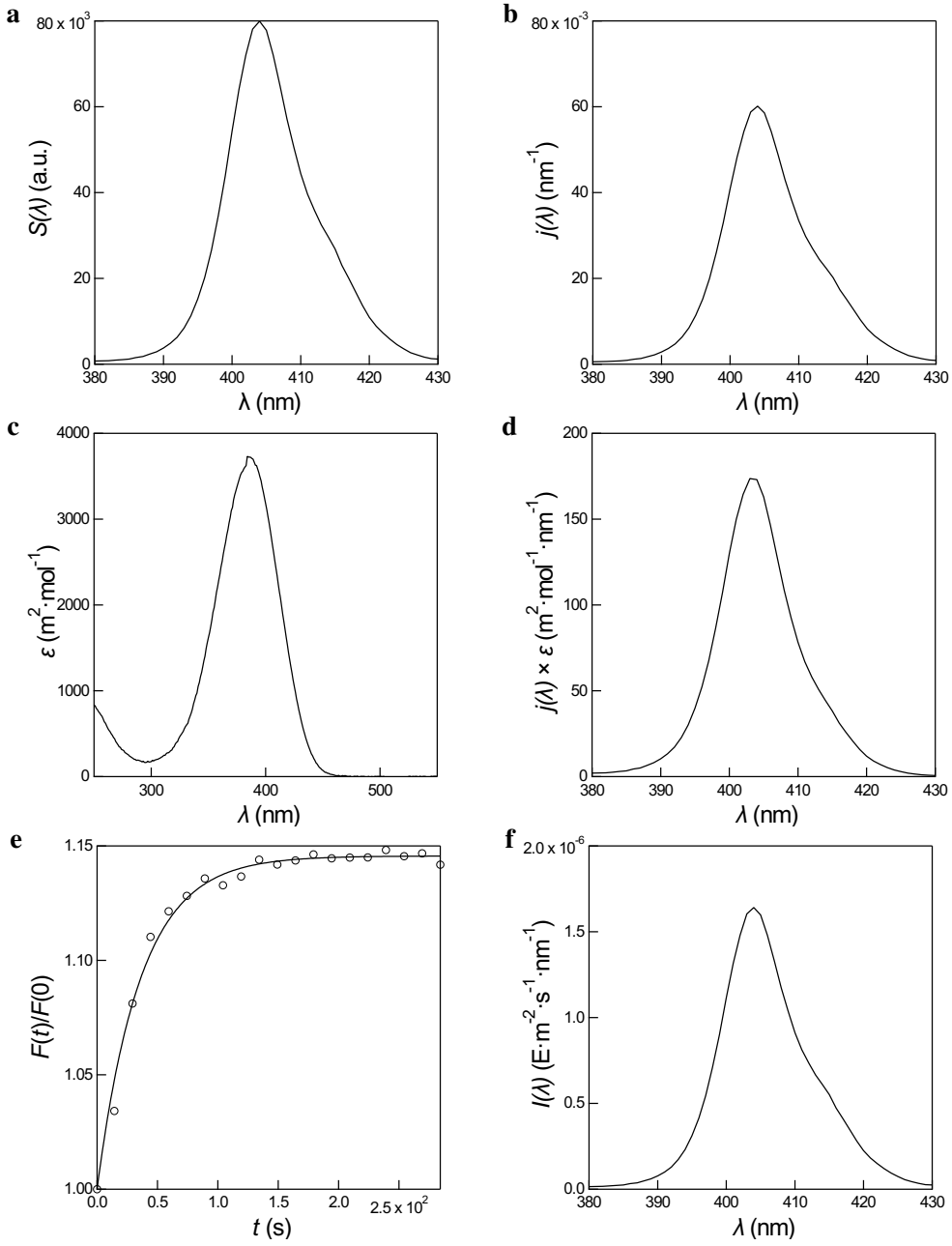

Figure S16: *Quantitation of a purple LED emitting at 405 nm*. Non-normalized ($S(\lambda)$; **a**) and normalized ($S(\lambda)/S$; **b**) emission spectrum of the LED at 405 nm; **c**: Absorption spectrum of **Nit** $\varepsilon(\lambda)$; **d**: Action spectrum of the LED on **Nit** in ethanol; **e**: Rise of the fluorescence emission of a 12 μM **Nit** and 1 μM **RhB** solution in ethanol at 574 nm as a function of time. Markers: experimental data; solid line: monoexponential fit. From the fit, we retrieved $\tau = 38.3$ s for the relaxation time. $T = 293$ K; **f**: Scaled emission spectrum of the LED.

1. Acquire the LED emission spectrum.

2. Divide the curve $S(\lambda)$ by its integral S calculated over the wavelength range of LED emission to yield the normalized emission spectrum $j(\lambda) = S(\lambda)/S$ (Figure S17a).

3. Multiply the scaled excitation spectrum of **PA**, $\sigma_{\mathrm{mic}}(\lambda)$ (Figure S17b), by the normalized emission spectrum $j(\lambda)$

to generate the action spectrum of the LED on **PA**, $\sigma_{\mathrm{mic}}(\lambda) \times j(\lambda)$ (Figure S17c).

4. Compute the integral AS of the action spectrum of the LED on **PA**.
5. On the other hand, submit a sample of *Chlamydomonas reinhardtii* to LED illumination in the fluorometer.
6. Record the rise of the fluorescence emission at 625 nm as a function of time (see Figure S17d).
7. Retrieve the relaxation time τ of the **PA** photoactivation from the fitting protocol reported in paragraph 2.1.3.
8. Exploit the values of τ and AS to retrieve the scaling parameter $S_I = 1/(\tau AS)$.
9. Retrieve the scaled emission spectrum of the LED from $I(\lambda) = S_I \times j(\lambda)$ (see Figure S17e).

2.4.4 Troubleshooting

Make sure that the suspension of algae is not sedimented.

2.4.5 Time taken

The duration of the overall measurement is evaluated to 2 h:

1. Collection of the unscaled LED spectrum: 30 min
2. Collection of the time evolution of the fluorescence emission under constant illumination: 30 min as an order of magnitude (depending on the light intensity)
3. Data processing: 60 min

2.4.6 Anticipated results

A quantitative spectral measurement of light intensity with achievable measurement uncertainty equal to 20% with **Nit** and 70% with **PA**.

2.4.7 References

- About actinometry: H. J. Kuhn, S. E. Braslavsky, and R. Schmidt, Chemical Actinometry (IUPAC Technical Report), *Pure Appl. Chem.*, **2004**, *76*, 2105–2146.
- About fluorescence: B. Valeur, M.-N. Berberan-Santos, Molecular Fluorescence: Principles and Applications 2$^{\mathrm{nd}}$ Edition, Wiley, **2012**.

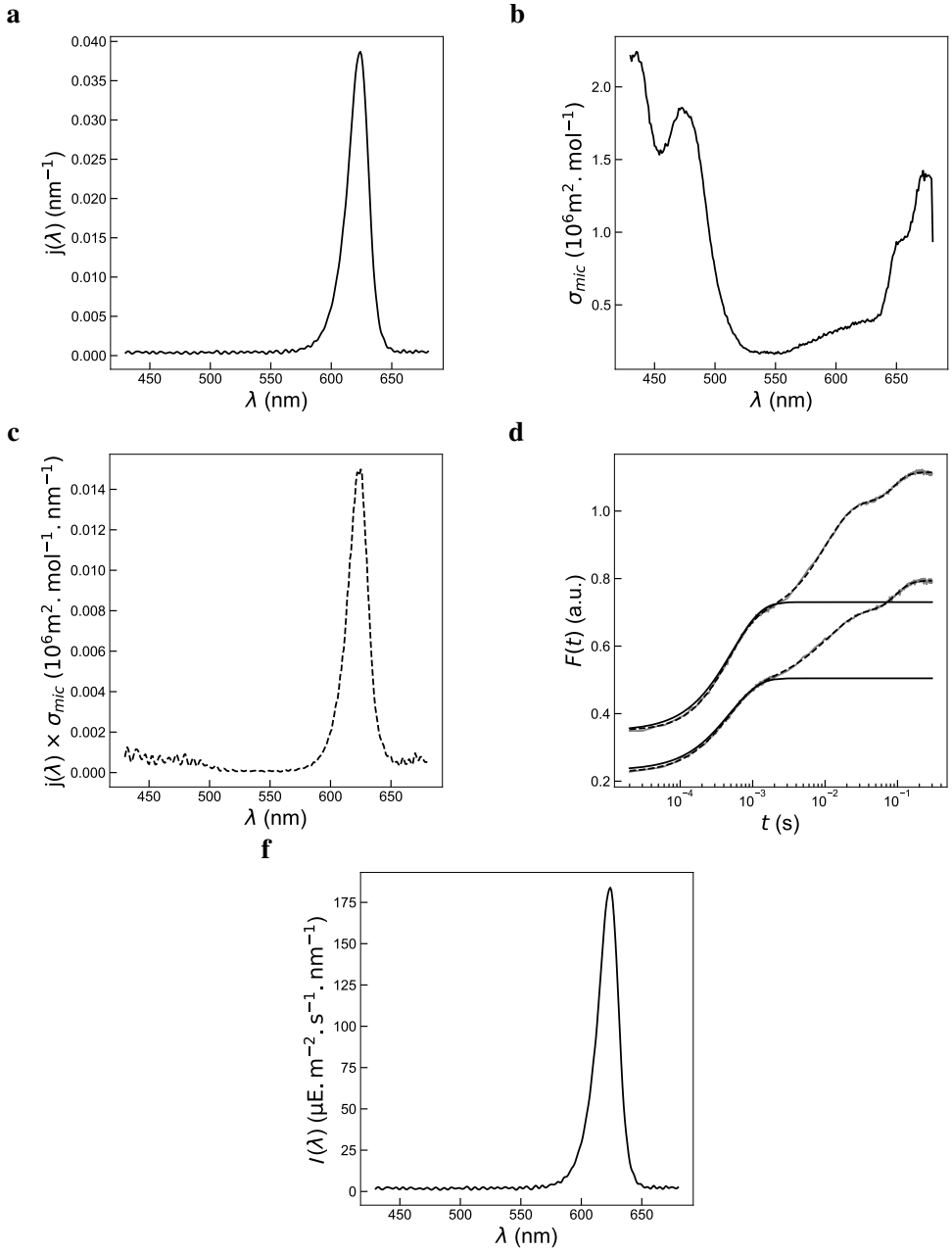

Figure S17: *Quantitation of a red-orange LED emitting at 625 nm.* **a**: Normalized emission spectrum ($j(\lambda) = S(\lambda)/S$) of the LED at 625 nm; **b b**: Scaled fluorescence excitation spectrum $\sigma_{\mathrm{mic}}(\lambda)$ of **PA** in *Chlamydomonas reinhardtii (CC_124)* in exponential phase in minimal media ($\lambda_{\mathrm{em}} = 470$ nm); **c**: Action spectrum of the LED at 625 nm on **PA** in *Chlamydomonas reinhardtii (CC_124)*; **d**: Time evolution of the **PA** fluorescence emission under constant illumination at 625 nm for the power setting 60% on the PSI instrument (2 repeats). The experimental data (grey markers) have been fitted with Eqs.(S3) (dashed lines) and (S4) (solid lines) to retrieve $\tau = 427$ μs and $\tau = 460$ μs for the characteristic time τ associated to the initial step of **PA** fluorescence rise ; **e**: Scaled emission spectrum of the LED at 625 nm. $T = 293$ K.

- About **Nit**: **1**. P. F. Wang, L. Jullien, B. Valeur, J.-S. Filhol, J. Canceill, J.-M. Lehn, Multichromophoric Cyclodextrins. 5. Antenna-induced Unimolecular Photoreactions. Photoisomerization of a Nitrone, *New J. Chem.*, **1996**, *20*, 895–907; **2**. M. Emond, T. Le Saux, S. Maurin, J.-B. Baudin, R. Plasson, L. Jullien, 2-Hydroxy-Azobenzenes to

Tailor pH Pulses and Oscillations with Light, *Chem. Eur. J.*, **2010**, *16*, 8822–8831.

- About **PA**: **1**. Maxwell, K., and Johnson, G. N., Chlorophyll fluorescence – a practical guide, J. Exp. Bot, **2000**, *51*, 659–668; **2**. D. Lazar, The polyphasic chlorophyll a fluorescence rise measured under high intensity of exciting light, *Funct. Plant Biol.*, **2006**, *33*, 9 – 30.

- About data processing: **1**. Mechanistic reduction leading to monoexponential fit of the time evolution of the fluorescence signal: R. Chouket, A. Pellissier-Tanon, A. Lahlou, R. Zhang, D. Kim, M.-A. Plamont, M. Zhang, X. Zhang, P. Xu, N. Desprat, D. Bourgeois, A. Espagne, A. Lemarchand, T. Le Saux, L. Jullien, Extra kinetic dimensions for label discrimination, *Nat. Commun.*, **2022**, *13*, 1482; **2**. About **PA** data processing: D. Joly, R. Carpentier, Sigmoidal reduction kinetics of the photosystem II acceptor side in intact photosynthetic materials during fluorescence induction, *Photochem. Photobiol. Sci.*, **2009**, *8*, 167–173.

2.5 Quantitation of non-monochromatic light sources with a photochemically inert fluorophore

2.5.1 Reagents

- 7-Hydroxy-9H-(1,3-dichloro-9,9-dimethylacridin-2-one) (**DDAO**)
- Solvent to produce the **DDAO** solution:
  - Spectrograde DMSO
  - Aqueous HEPES pH 7.9 buffer (100 mM NaCl, 5 mM NaOH, 10 mM HEPES)

2.5.2 Equipments

- Balance to prepare the **DDAO** solution
- Brown glassware or Aluminium foil to keep the solutions in the darkness
- Spectral data available online $\mathrm{https://chart-studio.plotly.com/\sim Alienor134/\#/}$
- Fluorimeter or any optical instrument, which can measure and record the fluorescence signal
- Quartz cuvette or glass microscope slides with a 100 μm spacer to build a chamber

2.5.3 Procedure

- Record the emission spectrum $S(\lambda)$ of the white LED by following the protocol reported in the paragraph D.2 upon using appropriate filters to avoid spectral overlaps with the fluorescence emission of **DDAO**. To perform this calibration with the epifluorescence microscope, we filtered the LED light before the sample with the same filters as for the spectrum measurement: a short-pass 694 filter (694/SP, AHF, FR) and a fluorescence dichroic 665 nm beamsplitter (FF665-Di02-25x36, Semrock, NY) to eliminate any contribution from the white LED signal that could overlap with **DDAO** fluorescence.

- Normalize the emission spectrum $S(\lambda)$ by its integral to yield the normalized emission spectrum $j(\lambda) = S(\lambda)/S$ (Figure S18a).

- Build the action spectrum of the white LED on **DDAO** from exploiting the excitation spectrum of the latter identical to its absorption spectrum (Figure S18b).

- Use Eq.(S79) to compute its integral AS_{abs}.

- On the other hand, collect the fluorescence signal from the same **DDAO** solution by using a band-pass 775/140 filter (775/140 single band-pass, Semrock, US) under two illuminations:

  - 470$\pm$10 nm LED of the epifluorescence microscope calibrated in intensity with **Dronpa-2** at various light intensities to investigate the linear dependence of the fluorescence level of **DDAO** $F\left(\lambda_{exc,1}\right)$ on the light intensity $I\left(\lambda_{\mathrm{exc},1}\right)$ at 470 nm (Figure S18c).
  - White LED at various feeding currents to record the dependence of its fluorescence level $F\left(\lambda_{\min};\lambda_{\max}\right)$ on the LED-feeding current.

  Equipped with the molar absorption coefficient of **DDAO** at $\lambda_{\mathrm{exc},1}$, use Eq. (S77) to compute the $S_{I,0}$ value at various currents feeding the white LED. The resulting dependence of the scaled spectral light intensity of the white LED is displayed in Figure S18d.

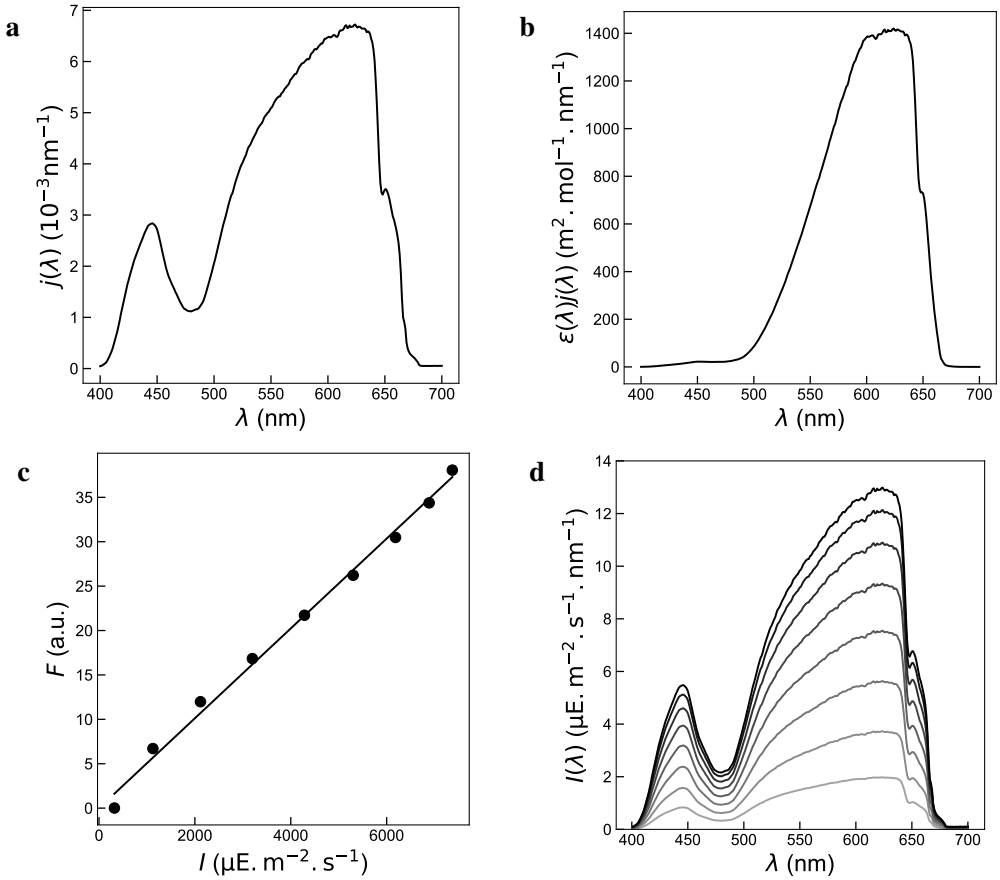

Figure S18: *Quantitation of a white LED with **DDAO***. **a**: Emission spectrum of the white LED normalized by its integral $j(\lambda) = S(\lambda)/S$; **b**: Action spectrum of the white LED on **DDAO** $\epsilon(\lambda)j(\lambda)$; **c**: Dependence of the fluorescence level of 10 μM **DDAO** in aqueous HEPES pH 7.9 buffer (100 mM NaCl, 5 mM NaOH, 10 mM HEPES) sandwiched between two microscope slides $F\left(\lambda_{\mathrm{exc},1}\right)$ on the light intensity $I\left(\lambda_{\mathrm{exc},1}\right)$ at 470 nm. Squares: experimental data from averaging the fluorescence collected by the camera, solid line: linear fit; **d**: Scaled spectral photon flux of the white LED for current levels feeding the white LED ranging from 55, 111, 166, 222, 277, 333, 388, 444 mA (light to dark). $T = 293$ K.

2.5.4 Troubleshooting

- Make sure that the same filter is used for the spectrum measurement of the light source and the set-up;
- Make sure the excitation light is properly filtered and not received by the detector for the two light sources used.

2.5.5 Time taken

The duration of the overall measurement is evaluated to 2 h:

1. Collection of the unscaled LED spectrum: 30 min
2. Acquisition of the DDAO fluorescence signals: 30 min

3. Data processing: 60 min

2.5.6 Anticipated results

A quantitative spectral measurement of light intensity with 20% achievable measurement uncertainty.

2.5.7 References

About **DDAO** as a dye:

- **1**. D. Warther, F. Bolze, J. Lonéard, S. Gug, A. Specht, D. Puliti, X.- H. Sun, P. Kessler, Y. Lutz, J.-L. Vonesch, B. Winsor, J.-F. Nicoud, M. Goeldner, Live-Cell One- and Two-Photon Uncaging of a Far-Red Emitting Acridinone Fluorophore, *J. Am. Chem. Soc.*, **2010**, *132*, 2585–2590; **2**. R. Labruère, A. Alouane, T. Le Saux, I. Aujard, P. Pelupessy, A. Gautier, S. Dubruille, F. Schmidt, L. Jullien, Self-immolation for uncaging with fluorescence reporting, *Angew. Chem. Int. Ed.*, **2012**, *51*, 9344–9347.

3 Glossary

- Actinometer: An actinometer is a system which can be used to directly measure light intensity by knowing the quantum yield of its photo-conversion, and following the time-course of the reaction extent on the application of light.
- Characteristic time (or relaxation time): Time retrieved by the fitting of a mono-exponential curve from the time evolution of the fluorescence emission signal, which reports on the actinometer photoconversion extent.
- Cross section of photoconversion: Measure of the molecular surface leading to the actinometer photoconversion after light absorption (often expressed in $m^2.mol^{-1}$).
- Fluorescence emission spectrum: A fluorescence emission spectrum is recorded by fixing the excitation wavelength and scanning the emission wavelength. Hence, it results in a plot of fluorescence intensity vs. emission wavelength.
- Fluorescence excitation spectrum: A fluorescence excitation spectrum is recorded by fixing the emission wavelength and scanning the excitation monochromator wavelength. Hence, the fluorescence excitation spectrum gives information about the wavelengths at which a sample absorbs light so as to emit at the single emission wavelength chosen for observation.
- Inner filter effect: The inner filter effect manifests itself in samples exhibiting an absorbance along the optical path typically exceeding 0.15. It results in a decay of the intensity of the excitation light in the sample. As a consequence, the fluorescence signal is attenuated and dominated by the sample surface. In addition, if the excitation and emission

fluorescence spectra significantly overlap, the fluorescence emission can be reabsorbed by the sample itself, which results in spectral distortion and even in some cases complete loss of the fluorescence signal.

- Irradiance: Irradiance is the light flux received by a surface per unit area. The SI unit of irradiance is the watt per square metre. Alternatively, it is denominated photon flux density with mole of photon per unit of time per square metre (See Eq.(S12) for the energy conversion) units, which is wavelength independent. Irradiance is often called light intensity. Spectral irradiance is the irradiance of a surface per unit wavelength, which is commonly measured in watts per square metre per nanometre or in mole of photon per unit of time per square metre per nanometre as done in the Main Text.

- Quantum yield of fluorescence: The fluorescence quantum yield gives the probability of the excited state being deactivated by fluorescence rather than by another, non-radiative mechanism.

- Quantum yield of photoconversion: The quantum yield of photoconversion gives the probability of the excited state being deactivated by photoconversion rather than by another mechanism.

A Conversion of energy units

In this manuscript, we provide the values of the light intensities in E.m^{-2}.s^{-1} (or mol. of photons.m^{-2}.s^{-1}). This unit is currently used in actinometry. However, it is not often used in other fields such as optical microscopy, in which the researchers prefer to adopt W.m^{-2}. We provide below the conversion between both units.

We consider a monochromatic light of wavelength λ_{exc}. Its values in E.m^{-2}.s^{-1} and W.m^{-2} are respectively denoted as $I(\lambda_{\text{exc}}, \text{E.m}^{-2}\text{.s}^{-1})$ and $I(\lambda_{\text{exc}}, \text{W.m}^{-2})$. The relation between $I(\lambda_{\text{exc}}, \text{E.m}^{-2}\text{.s}^{-1})$ and $I(\lambda_{\text{exc}}, \text{W.m}^{-2})$ is given in Eq.(S12)

$$I(\lambda_{\text{exc}}, \text{W.m}^{-2}) \quad = \quad \frac{hcN_A}{\lambda_{\text{exc}}} \times I(\lambda_{\text{exc}}, \text{E.m}^{-2}\text{.s}^{-1}) \approx 0.12 \times \frac{\text{I}(\lambda_{\text{exc}}, \text{E.m}^{-2}\text{.s}^{-1})}{\lambda_{\text{exc}}\,(\text{m})} \tag{S12}$$

with the Planck constant $h = 6.63\ 10^{-34}$ m^2.kg.s^{-1}, speed of light in a vacuum $c = 3.00\ 10^{8}$ m.s^{-1}, the Avogadro number $N_A = 6.02\ 10^{23}$ mol^{-1}, and where λ_{exc} is in m.

B Theoretical derivation of the expressions for retrieving light intensity

B.1 First protocol: Kinetic analysis of an actinometer engaged in an irreversible photochemical reaction

We first perform the kinetic analysis of an actinometer engaged in an irreversible photochemical reaction, which is relevant of the **Cin**, **Nit**, and **PA**[18] actinometers.

B.1.1 The model

We consider mechanisms of light-driven conversions, which can be reduced to the irreversible photochemical reaction displayed in Figure S19.

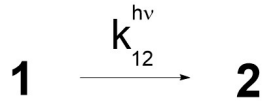

Figure S19: Reduced mechanism accounting for the photoactivation of an actinometer **1** leading to the irreversible formation of the product **2**.

Since most such light-driven conversions involve multiple steps, this assumption implies that the light intensity is low enough to make the photochemical activation step rate-limiting.

We here consider that the irreversible photochemical reaction is performed in a closed system (overall volume V).

Two asymptotic cases are considered:

- *Case 1*. The actinometer molecules do not diffuse and one can access the spatial profile of photon flux $\mathcal{I}(x, y, z)$ at coordinates (x, y, z) (given in mole of photons – or E – per unit of time) assumed to be constant in time;

[18] In fact, the kinetic model of the **PA** actinometer is more complex than the one developed below. However, we used Eq.(S24) to retrieve the cross section associated to the **PA** photoconversion.

- *Case 2*. The system can be considered homogeneous at any time of its evolution. This situation can result from either (i) homogeneously illuminating the whole system, (ii) stirring the sample content, or (iii) applying a non-homogeneous illumination profile on a small enough system such that molecular motion leading to homogeneous concentrations (by diffusion, convection,...) can be considered realized at any time of the photochemically-driven evolution of the whole system.[19] The whole system can then be considered to be submitted to an integrated photon flux (given in mole of photons – or E – per unit of time) constant in time and equal to $\mathcal{I} = \int_V \mathcal{I}(x,y,z)$.

Analyses of the temporal evolution of the concentration profiles in **1** and **2** with other boundary conditions can be found elsewhere.[9–11]

In the following, in a purpose of simplification, we adopt a unique notation, which has to be interpreted as accounting for the local (Case 1) or global (Case 2) time evolution of the concentrations and observables. Hence we rely on the mechanism displayed in Figure S19 to write Eq.(S13) describing the evolution of the concentrations :

$$\frac{d1}{dt} = -\frac{d2}{dt} = -k_{12}\ 1 \tag{S13}$$

where we can make explicit the photochemical contribution to the rate constant by writing

$$k_{12} = k_{12}^{h\nu}. \tag{S14}$$

We first derive the theoretical expressions of the concentrations in **1** and **2** (denoted 1 and 2 respectively) upon applying a light jump and establish the relation existing between the illumination time associated to the photochemical reaction and the photophysical and photochemical parameters associated to the photo-activation step. Then we analyze the time evolution of the absorbance and intrinsic/extrinsic fluorescence emission of the actinometer under illumination.

B.1.2 Light-jump experiments with monochromatic illumination

Expression of the concentrations We consider that the system initially contains the actinometer **1** at concentration $S_{\rm tot}$. The system is "suddenly"[20] illuminated, so that the incident photon flux varies from 0 to $\mathcal{I}(x,y,z)$ (Case 1), or from 0 to $\mathcal{I}$ (Case 2). The rate constant $k_{12} = k_{12}^{h\nu}$ can be considered constant. Upon writing $S_{\rm tot} = 1 + 2$, Eq.(S13) yields:

$$1 = S_{\rm tot} \exp\left(-\frac{t}{\tau}\right) \tag{S15}$$

$$2 = S_{\rm tot}\left[1 - \exp\left(-\frac{t}{\tau}\right)\right] \tag{S16}$$

where

$$\tau = \frac{1}{k_{12}} \tag{S17}$$

[19] This condition is fulfilled when $\tau_V \ll \tau$ where τ_V and τ respectively designate the time associated to molecular motion and the photochemical reaction over the whole system volume V.

[20] Note that "suddenly" here refers to a time interval such that Eq.(S13) can be considered valid.

designates the local (Case 1) or global (Case 2) relaxation time associated to the photochemical reaction in the presence of light at constant photon flux $\mathcal{I}(x,y,z)$ (Case 1) or $\mathcal{I}$ (Case 2).

The reaction rate for the photo-consumption of the actinometer **1** is proportional to the local (Case 1) or global (Case 2) photon flux of the monochromatic excitation light absorbed by **1** at the excitation wavelength – written in both cases as, $\mathcal{I}_{\rm abs}(\lambda_{\rm exc})$, and to the unitless photo-consumption cross section, φ_{12}, which measures the probability of **1** photoactivation leading to **2** production after **1** light absorption:

$$-\frac{d1}{dt} = \frac{\mathcal{I}_{\rm abs}(\lambda_{\rm exc})\varphi_{12}}{V} \tag{S18}$$

where V is the irradiated volume (expressed in L or dm^3) and $\mathcal{I}_{\rm abs}(\lambda_{\rm exc})$ is expressed in E per unit of time.

$\mathcal{I}_{\rm abs}(\lambda_{\rm exc})$ is given by Eq.(S19)

$$\mathcal{I}_{\rm abs}(\lambda_{\rm exc}) \quad = \quad \frac{A_1(\lambda_{\rm exc})}{A_{\rm tot}(\lambda_{\rm exc})}\mathcal{I}(\lambda_{\rm exc}) \tag{S19}$$

where $A_1(\lambda_{\rm exc})$ is the absorbance of **1**, $A_{\rm tot}(\lambda_{\rm exc})$ is the total absorbance, and $\mathcal{I}(\lambda_{\rm exc})$ is the photon flux absorbed by the solution at the excitation wavelength. According to the Beer-Lambert law, the latter can be written

$$\mathcal{I}(\lambda_{\rm exc}) \quad = \quad \mathcal{I}_0(\lambda_{\rm exc})\left[1-\exp\left(-2.3A_{\rm tot}(\lambda_{\rm exc})\right)\right] \tag{S20}$$

where $\mathcal{I}_0(\lambda_{\rm exc})$ is the photon flux of the incident beam at the excitation wavelength.

We further consider that an actinometer is illuminated with a light source that perpendicularly illuminates a cuvette filled with its solution. Upon introducing the length of the optical pathlength ℓ and the scaled molar excitation (leading to light absorption by the actinometer[21]) coefficient $\epsilon_1(\lambda_{\rm exc})$ (expressed in m^2.mol^{-1}) at the excitation wavelength,[22] Eq.(S18) yields

$$-\frac{d1}{dt} \quad = \quad \epsilon_1(\lambda_{\rm exc})\mathcal{I}_0(\lambda_{\rm exc})\varphi_{12}\ell\frac{1-exp\left(-2.3A_{\rm tot}(\lambda_{\rm exc})\right)}{A_{\rm tot}(\lambda_{\rm exc})V}1. \tag{S21}$$

If the total absorbance $A_{\rm tot}(\lambda_{\rm exc})$ is lower than 0.15, the kinetics is first order (at first order[12]) with a rate constant k_{12} given in Eq.(S22)

$$k_{12} \quad = \quad 2.3\epsilon_1(\lambda_{\rm exc})\varphi_{12}\frac{\mathcal{I}_0(\lambda_{\rm exc})\ell}{V} = 2.3\epsilon_1(\lambda_{\rm exc})\varphi_{12}I_0(\lambda_{\rm exc}) \tag{S22}$$

upon introducing the incident light intensity $I_0(\lambda_{\rm exc})$ (expressed in E.m^{-2}.s^{-1}).

Eq. (S22) can be alternatively written by introducing the cross section for the photochemical reaction $\sigma_{12}(\lambda_{\rm exc})$

$$\sigma_{12}(\lambda_{\rm exc}) = 2.3\epsilon_1(\lambda_{\rm exc})\varphi_{12} \tag{S23}$$

[21] When energy transfer can occur from a light-collecting antenna towards the actinometer chromophore (like in the actinometer **PA**), the molar absorption coefficient $\varepsilon_1(\lambda_{\rm exc})$ has to be replaced by the excitation coefficient $\epsilon_1(\lambda_{\rm exc})$, which take into account the contribution of the antenna towards light absorption. For a sake of simplicity, we have only retained the notation $\epsilon_1(\lambda_{\rm exc})$ in the derivation.

[22] Note that the unit of $\varepsilon(\lambda)$ is in m^2.mol^{-1}. One has: $\varepsilon(\lambda)$(m^2.mol^{-1})=0.1$\times\varepsilon(\lambda)$(mol.L^{-1}.cm^{-1}).

which yields

$$k_{12} = \frac{1}{\tau} = \sigma_{12}(\lambda_{\rm exc}) I_0(\lambda_{\rm exc}). \tag{S24}$$

Eq.(S22) shows that the rate constant k_{12} can be evaluated from the knowledge of the photophysical and photochemical parameters, $\epsilon_1(\lambda_{\rm exc})$ and φ_{12} or $\sigma_{12}(\lambda_{\rm exc})$, as soon as $I_0(\lambda_{\rm exc})$ is known. Conversely, $I_0(\lambda_{\rm exc})$ can be retrieved from Eq.(S25) from the knowledge of $\epsilon_1(\lambda_{\rm exc})$ and φ_{12} or $\sigma_{12}(\lambda_{\rm exc})$, and the relaxation time of the photochemical reaction τ.

$$I_0(\lambda_{\rm exc}) = \frac{k_{12}}{2.3\epsilon_1(\lambda_{\rm exc})\varphi_{12}} = \frac{1}{2.3\epsilon_1(\lambda_{\rm exc})\varphi_{12}\tau} = \frac{1}{\sigma_{12}(\lambda_{\rm exc})\tau} \tag{S25}$$

In order to simplify the notations, we identified $I_0(\lambda_{\rm exc})$ to $I(\lambda_{\rm exc})$ and $\sigma_{12}(\lambda_{\rm exc})$ to $\sigma(\lambda_{\rm exc})$ for the actinometers engaged in an irreversible photoconversion in the Main Text.

When the monochromatic illumination is focussed such that photo-activation occurs only within a sub-volume $V_{\rm exc}$ of the total volume V and provided that molecular motion over the whole system volume is fast at the time scale of its photoconversion, one has:

$$k_{12} = \frac{V_{\rm exc}}{V} k_{\rm V_{exc}} \tag{S26}$$

where $k_{\rm V_{exc}}$ designates the rate constant associated to photoactivation within the volume $V_{\rm exc}$.

Expression of the absorbance The time evolution of the absorbance $A(\lambda_{\rm exc})$ at the excitation wavelength $\lambda_{\rm exc}$ is expressed in Eq.(S27)

$$A(\lambda_{\rm exc}) \;=\; [\varepsilon_1(\lambda_{\rm exc})1 + \varepsilon_2(\lambda_{\rm exc})2]\,\ell = \left\{ [\varepsilon_1(\lambda_{\rm exc}) - \varepsilon_2(\lambda_{\rm exc})] \exp\left(-\frac{t}{\tau}\right) + \varepsilon_2(\lambda_{\rm exc}) \right\} S_{\rm tot}\ell \tag{S27}$$

where $\varepsilon_1(\lambda_{\rm exc})$ and $\varepsilon_2(\lambda_{\rm exc})$ designate the molar absorption coefficients of **1** and **2** respectively and ℓ is the optical pathlength.

In particular, when $\varepsilon_2(\lambda_{\rm exc})$ is vanishing (as with the nitrone actinometer), Eq.(S27) yields

$$A(\lambda_{\rm exc}) \;=\; \varepsilon_1(\lambda_{\rm exc}) S_{\rm tot}\ell \exp\left(-\frac{t}{\tau}\right). \tag{S28}$$

As shown in Eqs.(S27,S28), the relaxation time τ can be simply extracted from a robust monoexponential fit of the temporal evolution of the absorbance signal.

Expression of the fluorescence We consider two cases where fluorescence can be used to report on the time evolution of the illuminated actinometer:

- We first consider the case of bright states **1** and **2**;
- We then consider the case of adding a fluorophore, which reports on the time evolution of the illuminated actinometer by the inner filter effect (see below).

Intrinsic fluorescence reporting When **1** and **2** are intrinsically bright, the temporal dependence of the fluorescence emission $F(t)$ originates from summing the individual contributions of **1** and **2**. Denoting $Q_i = \epsilon_{\rm i}(\lambda_{\rm exc})\varphi_{\rm F,i}$ for the molecular brightness ($\varphi_{\rm F,i}$ designate the quantum yield of fluorescence of the species **i**), one has

$$F(t) \;\; = \;\; (Q_1 1 + Q_2 2)\, I = \left[(Q_1 - Q_2)\, S_{\rm tot} \exp\left(-\frac{t}{\tau}\right) + Q_2 S_{\rm tot} \right] I. \tag{S29}$$

Then, as shown in Eq.(S29), the relaxation time τ can be simply extracted from a robust monoexponential fit of the temporal evolution of the fluorescence signal.

Extrinsic fluorescence reporting When **1** and **2** are not fluorescent, one can add a fluorophore to report with fluorescence on the time evolution of the absorbance driven by the time evolution of the illuminated actinometer. To illustrate the corresponding principle of inner filter effect, we analyze the following model.

We consider that a light beam of wavelength $\lambda_{\rm exc}$ and intensity $I(\lambda_{\rm exc})$ perpendicularly illuminates a pathlength ℓ. At the abscissa x, the excitation light intensity is equal to $I(\lambda_{\rm exc}) \exp\left[-2.3 A_{\rm tot}(\lambda_{\rm exc}) x/\ell\right]$ where $A_{\rm tot}(\lambda_{\rm exc})$ is the total absorbance of the sample along the pathlength ℓ. The light absorbed by the reporting fluorophore **F** in a thin slice of thickness dx is $1 - \exp\left[-2.3 A_{\mathbf{F}}(\lambda_{\rm exc}) dx/\ell\right] \approx 2.3 A_{\mathbf{F}}(\lambda_{\rm exc}) dx/\ell$ with $A_{\mathbf{F}}$ the fluorophore absorbance of the cuvette which is assumed to be small. Then the total fluorescence emission from the reporting fluorophore collected at the wavelength λ_F at the detecting element can be written

$$F(\lambda_{\rm exc}, \lambda_F) = \int_0^\ell \alpha(x) F(\lambda_F) \times I(\lambda_{\rm exc}) \exp\left[-2.3 A_{\rm tot}(\lambda_{\rm exc}) x/\ell\right] \times 2.3 A_{\mathbf{F}}(\lambda_{\rm exc}) dx/\ell \tag{S30}$$

where $\alpha(x)$ is a collecting factor and $F(\lambda_F)$ the fluorescence intensity per absorbed photon at the wavelength λ_F. Assuming that $\alpha(x)$ only weakly depends on x in the considered geometry, we finally derive

$$F(\lambda_{\rm exc}, \lambda_F) = C \frac{1 - \exp\left(-2.3 A_{\rm tot}(\lambda_{\rm exc})\right)}{2.3 A_{\rm tot}(\lambda_{\rm exc})} \tag{S31}$$

where

$$C = 2.3 \alpha F(\lambda_F) I(\lambda_{\rm exc}) A_{\mathbf{F}}(\lambda_{\rm exc}) \tag{S32}$$

which is a constant during a given experiment.

When $A_{\rm tot}(\lambda_{\rm exc}) < 0.15$, we develop the exponential term in Eq.(S31) at the second order around zero and obtain Eq.(S33)

$$F(\lambda_{\rm exc}, \lambda_F) = C \left(1 - \frac{2.3 A_{\rm tot}(\lambda_{\rm exc})}{2}\right) \tag{S33}$$

When $A_{\mathbf{F}} \ll A_{\rm tot}(\lambda_{\rm exc})$, we use Eq.(S27) and derive Eq.(S34)

$$F(\lambda_{\rm exc}, \lambda_F) = C \left[1 - \frac{2.3}{2} \left(\left[\varepsilon_1(\lambda_{\rm exc}) - \varepsilon_2(\lambda_{\rm exc})\right] S_{\rm tot} \exp\left(-\frac{t}{\tau}\right) + \varepsilon_2(\lambda_{\rm exc}) S_{\rm tot} \right) \ell \right] \tag{S34}$$

reducing to Eq.(S35)

$$F(\lambda_{\rm exc}, \lambda_F) = C \left[1 - \frac{2.3}{2} \left(\varepsilon_1(\lambda_{\rm exc}) S_{\rm tot} \exp\left(-\frac{t}{\tau}\right) \right) \ell \right] \tag{S35}$$

when $\varepsilon_2(\lambda_{\rm exc})$ is vanishing (as with the nitrone actinometer).

Eqs.(S34,S35) demonstrates that τ can then be retrieved from analyzing the time evolution fluorescence of the reporting fluorophore **F**.

B.1.3 Light-jump experiments with non-monochromatic illumination

We now consider a light source associated with a spectral light intensity $I(\lambda)$ (expressed in E.m^{-2}.s^{-1}.nm^{-1}) spread over [$\lambda_{\rm min}$;$\lambda_{\rm max}$] (with the wavelength expressed in nm). It perpendicularly illuminates a cuvette filled with an actinometer associated to a scaled excitation spectrum leading to its light absorption $\epsilon_1(\lambda)$ (expressed in m^2.mol^{-1}). Following from Eqs.(S22–S24), the rate constant k_{12} for the actinometer photoconversion as well as the associated characteristic time τ obey Eq.(S36)

$$k_{12} = \frac{1}{\tau} = 2.3 \int_{\lambda_{\rm min}}^{\lambda_{\rm max}} \epsilon_1(\lambda)\phi_{12}(\lambda)I(\lambda)d(\lambda) = \int_{\lambda_{\rm min}}^{\lambda_{\rm max}} \sigma_{12}(\lambda)I(\lambda)d(\lambda) \tag{S36}$$

where $\phi_{12}(\lambda)$ and $\sigma_{12}(\lambda)$ designate the quantum yield and the cross section associated with the photoconversion.

We introduce the normalized emission spectrum $j(\lambda) = I(\lambda)/S_I$, where S_I designates the integral of $I(\lambda)$ over [$\lambda_{\rm min}$;$\lambda_{\rm max}$] (Eq.(S38))

$$\int_{\lambda_{\rm min}}^{\lambda_{\rm max}} I(\lambda)d(\lambda) \quad = \quad S_I \tag{S37}$$

and the integral of $j(\lambda)$ over the same wavelength range is equal to one (Eq.(S38))

$$\int_{\lambda_{\rm min}}^{\lambda_{\rm max}} j(\lambda)d(\lambda) \quad = \quad 1 \tag{S38}$$

Eq.(S36) yields Eq.(S39)

$$k_{12} = \frac{1}{\tau} = 2.3 S_I \int_{\lambda_{\rm min}}^{\lambda_{\rm max}} \epsilon_1(\lambda)\phi(\lambda)j(\lambda)d(\lambda) = S_I \int_{\lambda_{\rm min}}^{\lambda_{\rm max}} \sigma_{12}(\lambda)j(\lambda)d(\lambda) \tag{S39}$$

From computing the integral of the action spectrum AS of the light source given in Eq. (S40)

$$AS = \int_{\lambda_{\rm min}}^{\lambda_{\rm max}} \sigma_{12}(\lambda)j(\lambda)d(\lambda) \tag{S40}$$

and measuring the characteristic time τ, one can extract the integral $S_I = 1/(\tau AS)$ and retrieve the scaled spectral light intensity $I(\lambda) = S_I \times j(\lambda)$ sought for given in Eq.(S71)

$$I(\lambda) = \frac{1}{\left(\int_{\lambda_{\rm min}}^{\lambda_{\rm max}} \sigma_{12}(\lambda)j(\lambda)d(\lambda)\right) \times \tau} j(\lambda) \tag{S41}$$

Eq.(S71) bears much similarity to Eq.(S25) except for a convolution of the cross section with the spectral light intensity.

In practice, one has the dependence of $\epsilon_1(\lambda)\phi(\lambda)$ or $\sigma_{12}(\lambda)$ on the wavelength and an unscaled emission spectrum of the light source $S(\lambda)$ (expressed in arbitrary unit) and the goal is to scale it to retrieve the spectral light intensity $I(\lambda)$

(expressed in E.m^{-2}.s^{-1}.nm^{-1}) at the sample. The scaling step first involves the normalization of the unscaled emission spectrum $S(\lambda)$ by its integral S (Eq.(S42))

$$\int_{\lambda_{\min}}^{\lambda_{\max}} S(\lambda) d(\lambda) = S \tag{S42}$$

to yield the normalized emission spectrum $j(\lambda) = S(\lambda)/S$. Then one proceeds as reported above to first compute the integral of the action spectrum AS of the light source given in Eq.(S40), and then retrieve the scaled spectral light intensity $I(\lambda) = S_I \times j(\lambda)$ sought for from the measured characteristic time τ and the integral $S_I = 1/(\tau AS)$.

B.2 First protocol: Kinetic analysis of an actinometer engaged in a reversible photochemical reaction

The actinometers engaged in an irreversible photochemical reaction benefit from simple kinetic laws. However, they can be used only once. Hence, we additionally performed the kinetic analysis of an actinometer engaged in a reversible photochemical reaction, which is relevant of the **Dronpa-2** and **DASA** actinometers.

B.2.1 The model

We now consider relaxation mechanisms, which can be reduced to the reversible photochemical reaction displayed in Figure S20. In particular this model is often relevant to account for the behavior of reversibly photoswitchable actinometers such as the reversibly photoswitchable fluorescent proteins or synthetic photochromes.

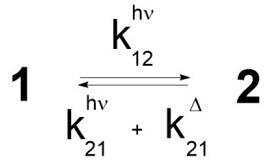

Figure S20: Reduced mechanism accounting for the photochemical behavior of a reversibly photoswitchable actinometer. The most stable state of the actinometer is assumed to be **1**, which can switch to the less stable state **2** by photoisomerization. Back reaction from **2** to **1** can occur either by photoisomerization or thermally-driven exchange.

The frame of assumptions is the same as the one exposed in the preceding section. Relying on the mechanism displayed in Figure S20, we write Eqs.(S43–S44) describing the concentration evolutions:

$$\frac{d1}{dt} = -k_{12}\, 1 + k_{21}\, 2 \tag{S43}$$

$$\frac{d2}{dt} = k_{12}\, 1 - k_{21}\, 2 \tag{S44}$$

where we make explicit the photochemical and thermal contributions to the rate constants by writing

$$k_{12} = k_{12}^{h\nu} \tag{S45}$$

$$k_{21} = k_{21}^{h\nu} + k_{21}^{\Delta} \tag{S46}$$

where the exponent indicates the nature of the contribution.

In the following, we derive the theoretical expressions of the concentrations in **1** and **2** and the intrinsic/extrinsic fluorescence intensity upon applying a light jump.

B.2.2 Light-jump experiments

Expression of the concentrations We consider that the system initially contains the actinometer **1** at concentration $S_{\rm tot}$. The system is "suddenly"[23] illuminated so that the incident light intensity varies from 0 to $I(x,y,z)$ (Case 1), or from 0 to I (Case 2). The rate constant $k_{12} = k_{12}^{h\nu}$ and $k_{21} = k_{21}^{h\nu} + k_{21}^{\Delta}$ can be considered constant. Upon introducing the total concentration in actinometer $S_{\rm tot} = 1 + 2$, Eqs.(S43,S44) yield:

$$-\frac{d\left(2-2^{\infty}\right)}{dt} = \left(k_{12}+k_{21}\right)\left(2-2^{\infty}\right) \tag{S47}$$

from which we derive

$$2-2^{\infty} = 1^{\infty}-1 = -2^{\infty}\exp\left(-\frac{t}{\tau}\right) \tag{S48}$$

where

$$2^{\infty} = \frac{K_{12}}{1+K_{12}}S_{\rm tot} \tag{S49}$$

$$1^{\infty} = \frac{1}{1+K_{12}}S_{\rm tot} \tag{S50}$$

$$\tau = \frac{1}{k_{12}+k_{21}} \tag{S51}$$

$$K_{12} = \frac{k_{12}}{k_{21}} \tag{S52}$$

In Eqs.(S48–S52), 2^{∞}, 1^{∞}, τ, and K_{12} respectively denote the steady-state value of the concentrations in **2** and **1**, the relaxation time associated to the reversible exchange between the states **1** and **2**,[24] and the photoisomerization constant of the actinometer in the presence of light constant in time, which has to be interpreted either locally (Case 1) or globally (Case 2) in relation to the presence of light at constant light intensity $I(x,y,z)$ (Case 1) or I (Case 2).

Upon keeping the notations and the assumptions introduced above in the model of irreversible two-state exchange, we derive at first order

$$k_{12} = 2.3\epsilon_1(\lambda_{\rm exc})\varphi_{12}I_0(\lambda_{\rm exc}) \tag{S53}$$

$$k_{21} = 2.3\epsilon_2(\lambda_{\rm exc})\varphi_{21}I_0(\lambda_{\rm exc}) + k_{21}^{\Delta} \tag{S54}$$

where $\epsilon_1(\lambda_{\rm exc})$ and $\epsilon_2(\lambda_{\rm exc})$ are the scaled molar excitation coefficients for photoisomerization of **1** and **2** at the excitation wavelength, and φ_{12} and φ_{21} are the quantum yields associated to photoisomerization of **1** into **2** and of **2** into **1** respectively. Eqs. (S53,S54) can be alternatively written by introducing the cross sections for the photochemical reaction $\sigma_{12}(\lambda_{\rm exc})$ and $\sigma_{21}(\lambda_{\rm exc})$

$$\sigma_{12}(\lambda_{\rm exc}) = 2.3\epsilon_1(\lambda_{\rm exc})\varphi_{12} \tag{S55}$$

$$\sigma_{21}(\lambda_{\rm exc}) = 2.3\epsilon_2(\lambda_{\rm exc})\varphi_{21} \tag{S56}$$

[23] Note that "suddenly" here refers to a time interval such that Eqs.(S43,S44) can be considered valid.

[24] Note that the expression given in Eq.(S51) is independent on the initial composition of the system.

which yields

$$k_{12} = \sigma_{12}(\lambda_{\rm exc})I_0(\lambda_{\rm exc}) \tag{S57}$$

$$k_{21} = \sigma_{21}(\lambda_{\rm exc})I_0(\lambda_{\rm exc}) + k_{21}^{\Delta}. \tag{S58}$$

Eqs.(S53,S54) show that the rate constants k_{12} and k_{21} can be evaluated from the knowledge of the photophysical and photochemical parameters, $\epsilon_1(\lambda_{\rm exc})$, $\epsilon_2(\lambda_{\rm exc})$, φ_{12} and φ_{21}, as soon as $I_0(\lambda_{\rm exc})$ is known. Conversely, $I_0(\lambda_{\rm exc})$ can be retrieved with Eq.(S59) retrieved from Eq.(S53,S54,S57,S58) from the knowledge of $\epsilon_1(\lambda_{\rm exc})$, $\epsilon_2(\lambda_{\rm exc})$, φ_{12} or $\sigma_{12}(\lambda_{\rm exc})$, φ_{21} or $\sigma_{21}(\lambda_{\rm exc})$, and the relaxation time of the photochemical reaction τ.

$$I_0(\lambda_{\rm exc}) = \frac{k_{12} + k_{21} - k_{21}^{\Delta}}{2.3\left(\epsilon_1(\lambda_{\rm exc})\varphi_{12} + \epsilon_2(\lambda_{\rm exc})\varphi_{21}\right)} = \frac{\left(1 - k_{21}^{\Delta}\tau\right)}{\left(\sigma_{12}(\lambda_{\rm exc}) + \sigma_{21}(\lambda_{\rm exc})\right)\tau} \tag{S59}$$

When

$$I(\lambda_{\rm exc}) \geq 10 \times \frac{k_{21}^{\Delta}}{\sigma(\lambda_{\rm exc})}, \tag{S60}$$

$$k_{21}^{\Delta}\tau \ll 1, \tag{S61}$$

and Eq.(S59) can be simplified to yield Eq.(S62)

$$I = \frac{1}{\sigma(\lambda_{\rm exc})\tau} \tag{S62}$$

where we simplified the notations by identifying $I_0(\lambda_{\rm exc})$ to $I(\lambda_{\rm exc})$ and $[\sigma_{12}(\lambda_{\rm exc}) + \sigma_{21}(\lambda_{\rm exc})]$ to $\sigma(\lambda_{\rm exc})$ as done in the Main Text.

When the illumination is focussed, Eq.(S26) is valid with a similar analysis to the one exposed above.

Expression of the absorbance The time evolution of the absorbance $A(\lambda_{\rm exc})$ at the excitation wavelength $\lambda_{\rm exc}$ is expressed in Eq.(S63)

$$A(\lambda_{\rm exc}) = \left[\varepsilon_1(\lambda_{\rm exc})1 + \varepsilon_2(\lambda_{\rm exc})2\right]\ell = A(\lambda_{\rm exc})^{\infty} + \left\{\left[\varepsilon_1(\lambda_{\rm exc}) - \varepsilon_2(\lambda_{\rm exc})\right]\exp\left(-\frac{t}{\tau}\right)\right\}2^{\infty}\ell \tag{S63}$$

where $\varepsilon_1(\lambda_{\rm exc})$ and $\varepsilon_2(\lambda_{\rm exc})$ designate the molar absorption coefficients of **1** and **2** respectively, $A(\lambda_{\rm exc})^{\infty} = \varepsilon_1(\lambda_{\rm exc})1^{\infty} + \varepsilon_2(\lambda_{\rm exc})2^{\infty}$, and ℓ is the optical pathlength. As shown in Eq.(S63), the relaxation time τ can be simply extracted from a robust monoexponential fit of the temporal evolution of the absorbance signal.

Expression of the fluorescence We consider two cases where fluorescence can be used to report on the time evolution of the illuminated actinometer:

- We first consider the case of bright states **1** and **2**;
- We then consider the case of adding a fluorophore, which reports on the time evolution of the illuminated actinometer by the inner filter effect.

Intrinsic fluorescence reporting When **1** and **2** are intrinsically bright, the temporal dependence of the fluorescence emission $F(t)$ originates from summing the individual contributions of **1** and **2**. Denoting $Q_i = \epsilon_{\rm i}(\lambda_{\rm exc})\varphi_{\rm F,i}$ for the molecular brightness ($\varphi_{\rm F,i}$ designate the quantum yield of fluorescence of the species **i**), one has

$$F(t) \quad = \quad (Q_1 1 + Q_2 2)\, I = F^{\infty} + (Q_1 - Q_2)\, 2^{\infty} I \exp\left(-\frac{t}{\tau}\right) \tag{S64}$$

where $F^{\infty} = Q_1 1^{\infty} + Q_2 2^{\infty}$. Then, as shown in Eq.(S64), the relaxation time τ can be simply extracted from a robust monoexponential fit of the temporal evolution of the fluorescence signal.

Extrinsic fluorescence reporting When **1** and **2** are not fluorescent, one can add a fluorophore to report on the time evolution of the absorbance driven by the the time evolution of the illuminated actinometer. The equations (S31,S32) derived above are still valid and when $A_{\rm tot}(\lambda_{\rm exc}) < 0.15$, we develop the exponential term in Eq.(S31) at the second order around zero and obtain Eq.(S33), which demonstrates that τ can be retrieved from analyzing the time evolution fluorescence of the reporting fluorophore **F**.

B.3 Second protocol: Transfer of information on light intensity from a wavelength to another with a photochemically inert fluorophore

B.3.1 Illumination with monochromatic illumination

We consider a fluorophore illuminated with a light source (incident photon flux $\mathcal{I}_0(\lambda_{\rm exc})$) that perpendicularly illuminates a cuvette filled with its solution. The reaction rate for its conversion to its excited state **E** is proportional to the photon flux absorbed by its ground state **G** at the monochromatic excitation wavelength $\mathcal{I}_G(\lambda_{\rm exc})$ (expressed in E.s^{-1}). Then the time evolution of the concentration G in **G** obeys Eq.(S65)

$$-\frac{dG}{dt} \quad = \quad \frac{\mathcal{I}_G(\lambda_{\rm exc})}{V} \tag{S65}$$

where V designates the illuminated volume of the fluorophore solution.

$\mathcal{I}_G(\lambda_{\rm exc})$ is given by Eq.(S66)

$$\mathcal{I}_G(\lambda_{\rm exc}) \quad = \quad \frac{A_G(\lambda_{\rm exc})}{A_{\rm tot}(\lambda_{\rm exc})}\mathcal{I}(\lambda_{\rm exc}) \tag{S66}$$

where $A_G(\lambda_{\rm exc})$ is the absorbance of **G**, $A_{\rm tot}(\lambda_{\rm exc})$ is the total absorbance, and $\mathcal{I}(\lambda_{\rm exc})$ is the photon flux absorbed by the solution at the excitation wavelength. The latter is given in Eq.(S20).

Upon introducing the length of the optical pathlength ℓ and the known molar absorption coefficient $\varepsilon_G(\lambda_{\rm exc})$ (expressed in m^2.mol^{-1}) of the fluorophore at the excitation wavelength, Eq.(S65) yields

$$-\frac{dG}{dt} \quad = \quad \varepsilon_G(\lambda_{\rm exc})\mathcal{I}_0(\lambda_{\rm exc})\ell\frac{1 - exp\left(-2.3A_{\rm tot}(\lambda_{\rm exc})\right)}{A_{\rm tot}(\lambda_{\rm exc})V}G. \tag{S67}$$

If the total absorbance $A_{\rm tot}(\lambda_{\rm exc})$ is lower than 0.15, the kinetics of light absorption is first order (at first order) with a rate constant $k_{\rm abs}$ given in Eq.(S68)

$$k_{\rm abs} \quad = \quad 2.3\varepsilon_G(\lambda_{\rm exc})\frac{\mathcal{I}_0(\lambda_{\rm exc})\ell}{V} = 2.3\varepsilon_G(\lambda_{\rm exc})I_0(\lambda_{\rm exc}) \tag{S68}$$

upon introducing the incident light intensity $I_0(\lambda_{\rm exc})$ (expressed in E.m^{-2}.s^{-1}).

We introduce the total concentration of the fluorophore as $F_{\rm tot}$. Far from the saturation of the excited state of the fluorophore, the fluorophore population in its excited state is given by $E = k_{\rm abs}\tau_E F_{\rm tot}$ where τ_E designates the lifetime of the excited state. Then the fluorescence signal $F\left(\lambda_{\rm exc}, \lambda_{\rm em}\right)$ collected from the fluorophore at a wavelength $\lambda_{\rm em}$ upon exciting at $\lambda_{\rm exc}$ is given in Eq.(S69)

$$F\left(\lambda_{\rm exc}, \lambda_{\rm em}\right) = k_F E = k_F k_{\rm abs}\tau_E F_{\rm tot} = 2.3 k_F \tau_E F_{\rm tot}\varepsilon_G(\lambda_{\rm exc})I_0(\lambda_{\rm exc}) \tag{S69}$$

where k_F designates the rate constant associated to the radiative deexcitation of the excited state by fluorescence emission.

Most of the fluorophores obey the Kasha's rule, which states that photon emission (termed fluorescence in the case of a singlet S state) is expected in appreciable yield only from the lowest excited state, S_1. Since only one state is expected to yield emission, an equivalent statement of the rule is that the wavelength and the quantum yield of fluorescence emission are independent of the excitation wavelength. Then the ratio $F\left(\lambda_{\rm exc}, \lambda_{\rm em}\right)/\varepsilon_G(\lambda_{\rm exc})I_0(\lambda_{\rm exc})$ is a constant and the fluorescence signals $F\left(\lambda_{{\rm exc},1}, \lambda_{\rm em}\right)$ and $F\left(\lambda_{{\rm exc},2}, \lambda_{\rm em}\right)$ recorded at a same emission wavelength $\lambda_{\rm em}$ from a same fluorophore solution upon exciting at the wavelengths $\lambda_{{\rm exc},1}$ (with a known light intensity $I_0(\lambda_{{\rm exc},1})$) and $\lambda_{{\rm exc},2}$ (with light intensity $I_0(\lambda_{{\rm exc},2})$ to be measured) respectively are linked with Eq.(S70), which is given in Figure 1b of the Main Text upon identifying $I_0(\lambda_{\rm exc})$ to $I(\lambda_{\rm exc})$ in order to simplify the notations

$$I_0(\lambda_{{\rm exc},2}) = \frac{\varepsilon_G\left(\lambda_{{\rm exc},1}\right) F\left(\lambda_{{\rm exc},2}, \lambda_{\rm em}\right)}{\varepsilon_G\left(\lambda_{{\rm exc},2}\right) F\left(\lambda_{{\rm exc},1}, \lambda_{\rm em}\right)} I_0\left(\lambda_{{\rm exc},1}\right). \tag{S70}$$

B.3.2 Illumination with non-monochromatic illumination

We now consider a light source associated to a spectral light intensity $I_0(\lambda)$ (expressed in E.m^{-2}.s^{-1}.nm^{-1}) spread over [$\lambda_{\rm min}$;$\lambda_{\rm max}$] (with the wavelength expressed in nm). Then the rate constant $k_{\rm abs}$ for light absorption by the fluorophore obeys Eq.(S71)

$$k_{\rm abs} = 2.3 \int_{\lambda_{\rm min}}^{\lambda_{\rm max}} \varepsilon_G(\lambda) I_0(\lambda) d(\lambda) \tag{S71}$$

and

$$F\left([\lambda_{\rm min}; \lambda_{\rm max}], \lambda_{\rm em}\right) = k_F E = k_F k_{\rm abs}\tau_E F_{\rm tot} = 2.3 k_F \tau_E F_{\rm tot} \int_{\lambda_{\rm min}}^{\lambda_{\rm max}} \varepsilon_G(\lambda) I_0(\lambda) d(\lambda). \tag{S72}$$

The application of the Kasha's rule now yields the ratio $F\left([\lambda_{\rm min}; \lambda_{\rm max}], \lambda_{\rm em}\right) / \int_{\lambda_{\rm min}}^{\lambda_{\rm max}} \varepsilon_G(\lambda) I_0(\lambda) d(\lambda)$ to be a constant and the relation Eq.(S72) yields Eq.(S73)

$$\int_{\lambda_{\rm min}}^{\lambda_{\rm max}} \varepsilon_G(\lambda) I_0(\lambda) d(\lambda) = \frac{\varepsilon_G\left(\lambda_{{\rm exc},1}\right) F\left([\lambda_{\rm min}; \lambda_{\rm max}], \lambda_{\rm em}\right)}{F\left(\lambda_{{\rm exc},1}, \lambda_{\rm em}\right)} I_0\left(\lambda_{{\rm exc},1}\right) \tag{S73}$$

by assuming that the light source delivering emission at $\lambda_{{\rm exc},1}$ is monochromatic (see section C).

We introduce the normalized emission spectrum $j(\lambda) = I_0(\lambda)/S_{I,0}$, where $S_{I,0}$ designates the integral of $I(\lambda)$ over [$\lambda_{\rm min}$;$\lambda_{\rm max}$] (Eq.(S74))

$$\int_{\lambda_{\rm min}}^{\lambda_{\rm max}} I_0(\lambda) d(\lambda) \quad = \quad S_{I,0} \tag{S74}$$

and the integral of $j(\lambda)$ over the same wavelength range is equal to one (see Eq.(S38)). Then Eq.(S73) yields Eq.(S75)

$$S_{I,0}\int_{\lambda_{\min}}^{\lambda_{\max}}\varepsilon_G(\lambda)j(\lambda)d(\lambda)=\frac{\varepsilon_G\left(\lambda_{\text{exc},1}\right)F\left([\lambda_{\min};\lambda_{\max}],\lambda_{\text{em}}\right)}{F\left(\lambda_{\text{exc},1}\right)}I_0\left(\lambda_{\text{exc},1}\right) \tag{S75}$$

Hence, the computation of the integral of the action spectrum AS_{abs} of the light source given in Eq.(S79)

$$AS_{\text{abs}}=\int_{\lambda_{\min}}^{\lambda_{\max}}\varepsilon_G(\lambda)j(\lambda)d(\lambda) \tag{S76}$$

together with the acquisition of $F\left([\lambda_{\min};\lambda_{\max}],\lambda_{\text{em}}\right)$ and $F\left(\lambda_{\text{exc},1}\right)$ measured with a light source emitting at $\lambda_{\text{exc},1}$ with intensity $I_0\left(\lambda_{\text{exc},1}\right)$ yields the integral

$$S_{I,0}=\frac{\varepsilon_G\left(\lambda_{\text{exc},1}\right)F\left([\lambda_{\min};\lambda_{\max}],\lambda_{\text{em}}\right)}{AS_{\text{abs}}F\left(\lambda_{\text{exc},1}\right)}I_0\left(\lambda_{\text{exc},1}\right) \tag{S77}$$

which can be alternatively written

$$S_{I,0}=\frac{F\left([\lambda_{\min};\lambda_{\max}],\lambda_{\text{em}}\right)}{AS_{\text{abs,norm}}F\left(\lambda_{\text{exc},1}\right)}I_0\left(\lambda_{\text{exc},1}\right) \tag{S78}$$

by introducing the integral of the normalized action spectrum $AS_{\text{abs,norm}}$ of the light source given in Eq.(S79)

$$AS_{\text{abs,norm}}=\int_{\lambda_{\min}}^{\lambda_{\max}}\frac{\varepsilon_G(\lambda)}{\varepsilon_G\left(\lambda_{\text{exc},1}\right)}j(\lambda)d(\lambda) \tag{S79}$$

It becomes then possible to retrieve the scaled spectral light intensity $I_0(\lambda)=S_{I,0}\times j(\lambda)$ sought for given in Eq.(S80)

$$I_0(\lambda)=\frac{\varepsilon_G\left(\lambda_{\text{exc},1}\right)F\left([\lambda_{\min};\lambda_{\max}],\lambda_{\text{em}}\right)}{\left(\int_{\lambda_{\min}}^{\lambda_{\max}}\varepsilon_G(\lambda)j(\lambda)d(\lambda)\right)F\left(\lambda_{\text{exc},1}\right)}I_0\left(\lambda_{\text{exc},1}\right)j(\lambda)=\frac{F\left([\lambda_{\min};\lambda_{\max}],\lambda_{\text{em}}\right)}{AS_{\text{abs,norm}}F\left(\lambda_{\text{exc},1}\right)}I_0\left(\lambda_{\text{exc},1}\right)j(\lambda) \tag{S80}$$

Eq.(S80) bears much similarity to Eq.(S70) except for a convolution of the molar absorption coefficient of the fluorophore with the spectral light intensity.

In practice, one has the dependence of the absorption molar coefficient $\varepsilon_G(\lambda)$ on the wavelength and an unscaled emission spectrum of the light source $S(\lambda)$ (expressed in arbitrary unit) and the goal is to scale it to retrieve the spectral light intensity $I_0(\lambda)$ (expressed in E.m^{-2}.s^{-1}.nm^{-1}) at the sample. The scaling step first involves the normalization of the unscaled emission spectrum $S(\lambda)$ by its integral S (see Eq.(S42)) to yield the normalized emission spectrum $j(\lambda)=S(\lambda)/S$. Then one proceeds as reported above to first compute the integral of the action spectrum AS_{abs} of the light source given in Eq.(S79), and then retrieve the scaled spectral light intensity $I_0(\lambda)=S_{I,0}\times j(\lambda)$ sought for after determining $S_{I,0}$ with Eq.(S77) from the acquisition of $F\left([\lambda_{\min};\lambda_{\max}],\lambda_{\text{em}}\right)$ and $F\left(\lambda_{\text{exc},1}\right)$ measured with a light source emitting at $\lambda_{\text{exc},1}$ with intensity $I_0\left(\lambda_{\text{exc},1}\right)$.

In order to simplify the notations, we identified $I_0(\lambda_{\text{exc}})$ to $I(\lambda_{\text{exc}})$ and $S_{I,0}$ to S_I in the Main Text.

C Assumption of monochromatic vs polychromatic light for retrieving cross sections of light absorption

In this account, we used filtered LEDs (for the experiments in cuvettes and in epifluorescence microscopy) and a Xe lamp (for the experiments in cuvettes) as light sources. Although they exhibit a limited bandwidth – less than 2-3 and 10

nm with the filtered Xe lamp and LEDs respectively, we have been concerned with the level of error, which result from considering them as strictly monochromatic for retrieving both the cross sections associated to the photoconversion (for the actinometers) and the fluorescence intensity (for **DDAO**) at a given wavelength λ_{exc}.

We consider a light source associated to a spectral light intensity $I(\lambda)$ (expressed in E.m^{-2}.s^{-1}.nm^{-1}) spread over [$\lambda_{\min}$;$\lambda_{\max}$] (with the wavelength expressed in nm). It perpendicularly illuminates a cuvette filled with an actinometer or a photochemically inert fluorophore associated to a scaled excitation spectrum leading to its light absorption $\epsilon(\lambda)$ (expressed in m^2.mol^{-1}). Then the rate constant for light absorption by the actinometer or the fluorophore obeys Eq.(S81)

$$k_{\text{abs,poly}} = 2.3 \int_{\lambda_{\min}}^{\lambda_{\max}} \epsilon(\lambda) I(\lambda) d(\lambda). \tag{S81}$$

$k_{\text{abs,poly}}$ determines the value of the fluorescence intensity of the fluorophore but it also determines the rate constant of the photoconversion of the actinometer k_{12} when its associated quantum yield φ_{12} does not depend on the excitation wavelength (see Eqs.(S23,S24)).

In the polychromatic approximation, we consider $I(\lambda)$ to be a Gaussian distribution (bandwidth 2σ) with its integral $I_{\lambda_{\text{exc}}}$ peaking at λ_{exc} and extending over the wavelength range [$\lambda_{\text{exc}} - 3\sigma$; $\lambda_{\text{exc}} + 3\sigma$]. Then Eq.(S81) yields Eq.(S82)

$$k_{\text{abs,poly}} = 2.3 \int_{\lambda_{\text{exc}}-3\sigma}^{\lambda_{\text{exc}}+3\sigma} \epsilon(\lambda) \frac{I_{\lambda_{\text{exc}}}}{\sigma\sqrt{2\pi}} e^{\frac{-(\lambda-\lambda_{\text{exc}})^2}{2\sigma^2}} d\lambda. \tag{S82}$$

In the monochromatic approximation, $I(\lambda) = I_{\lambda_{\text{exc}}} \delta(\lambda - \lambda_{\text{exc}})$ and Eq.(S81) reduces to Eq.(S83)

$$k_{\text{abs,mono}} = 2.3 \times \epsilon(\lambda_{\text{exc}}) \times I_{\lambda_{\text{exc}}}. \tag{S83}$$

To assess the relevance of the monochromatic approximation for retrieving both the cross sections associated to the photoconversion (for the actinometers) and the fluorescence intensity (for **DDAO**) at a given wavelength λ_{exc}, we generated a simulated arbitrary spectrum $\epsilon(\lambda)$ (Figure S21a) and computed the deviation ($\frac{|k_{\text{abs,poly}} - k_{\text{abs,mono}}|}{max(k_{\text{abs,poly}}, k_{\text{abs,mono}})}$) for various values of λ_{exc} (position in the spectrum) and σ (half bandwidth of the light source) (Figure S21b). For $\sigma = 20$ nm (larger than the half bandwidth of our LEDs) and whatever λ_{exc}, the error remains below 20%, which is the error estimated for our evaluations of light intensity. In fact, the bandwidths of all the light-sources we used for calibration were below $\sigma = 10$ nm so that the error is closer to 5%, which validates our exploitation of the monochromatic approximation for retrieving both the cross sections associated to the photoconversion (for the actinometers) and the fluorescence intensity (for **DDAO**) at a given wavelength λ_{exc}.

D Characterization of the fluorescent systems for measuring light intensity

This section details the Materials and Methods, and the thorough characterization of the fluorescent systems, which we report to measure light intensity. It also details the experiments, which have been performed for their validation.

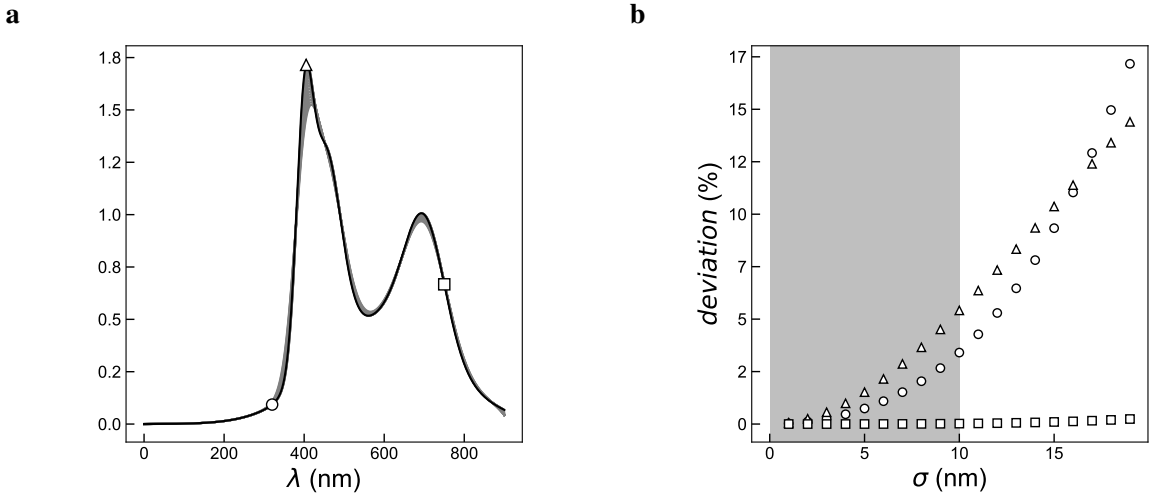

Figure S21: *Evaluation of the assumption of monochromatic vs polychromatic light for retrieving cross sections of light absorption*. **a** Arbitrary excitation spectrum $\epsilon(\lambda)$ (solid black line). This spectrum has been blurred by its convolution with a gaussian kernel with increasing standard deviation (from 1 to 20 nm) representing the emission spectra of light sources with various bandwidths (grey lines) in order to give an insight of how the bandwidth of the light source affects the spectrum values; **b** Evolution of the deviation between $k_{\mathrm{abs,poly}}$ and $k_{\mathrm{abs,mono}}$ computed for various values of λ_{exc} (circles: 320 nm, triangles: 405 nm, squares: 750 nm) and σ for the spectrum $\epsilon(\lambda)$ given in **a**. The grey area represents the range of bandwidths of the various light sources used in this manuscript.

D.1 Materials

The materials were produced as reported in subsections B.1.1, B.2.1, and 1.4. For the syntheses, the reagents were obtained from Sigma-Aldrich or TCI and used without purification. Solvents were obtained from VWR. Flash chromatography silica (high purity, 6 nm pore size, 40-63 μm particle size) was obtained from Sigma-Aldrich and was used to perform purifications in manual column chromatography. NMR measurements were recorded using a Bruker Ultrashield 300 MHz NMR. ^{1}H-NMR chemical shifts are reported using the residual protons of the deuterated solvents as references. ^{13}C chemical shifts are reported using the signal from the solvents as references. The NMR spectra were processed using the Mnova Mestrelab software. Mass spectra were recorded using a Bruker UHR-Q-TOF MaXis system with ESI ionization method at the High-resolution Mass Spectroscopy Platform at Orleans University.

D.2 UV/Vis absorption and fluorescence spectrometers

D.2.1 Instruments

UV/Vis absorption spectra were recorded on a UV/Vis spectrophotometer (Cary 300 UV-Vis, Agilent Technologies, Santa Clara, CA) at 20 °C equipped with a Peltier 1×1 thermostatic cell holder (Agilent Technologies). Samples were contained either in 1 cm × 1 cm (3 mL; the cuvette content was stirred) or in 0.3 cm × 0.3 cm (45 μL; the cuvette content was not stirred) quartz cuvettes (Hellma Optics, Jena, Germany). Fluorescence measurements were acquired on a LPS 220 spectrofluorometer (PTI, Monmouth Junction, NJ), equipped with a TLC50 cuvette holder (Quantum Northwest, Liberty Lake, WA) thermoregulated at 25 °C.

D.2.2 Light sources

The constant illumination applied to generate the time evolution of the fluorescence signal from the chemical actinometers has been obtained by using:

- LEDs for the photoconversion experiments performed at various light intensities. The lights from high power LEDs (NCSU033B, Nichia Corp, JP; LHUV-405, LXZ1-PB01, Lumileds, NL, LXML-PWN1-0080, Lumileds, NL) driven by a 4-channel current driver (DC4104, Thorlabs, NJ) were collimated by high-NA condenser (ACL25416UA, $f = 16$ mm, Thorlabs, NJ) and filtered (BP ZET 365/20x, Chroma Technology, BP ET405/20x; Chroma Technology, VT, BP FF01-479/40-25, Semrock, NY and SP 694/SP, AHF, FR combined with a 665 dichroïc filter FF665-Di02-25x36, Semrock, NY). The quasi-parallel beams were combined with dichroic mirrors (ZT375rdc, T425LPXR, Chroma Technology, VT) and sent on the 3×3 mm^2 aperture of the sample cuvette;
- the Xenon lamp of the LPS 220 spectrofluorometer (PTI, Monmouth Junction, NJ) for the photoconversion experiments performed at various excitation wavelengths.

The emission spectra of the LEDs have been recorded by sending the light emitted from the LEDs into the emission pathway of the fluorometer with reduced slits opening.

D.2.3 Measurement of the light intensity with a powermeter

A powermeter (PM100A, Thorlabs, NJ; *S130C* probe, Thorlabs, NJ) has been used to report on the light intensity applied on the cuvettes. In a first experiment, we analyzed the time recovery of the fluorescence signal from 488 nm-photoswitched **Dronpa-2** upon illumination at 405 nm[7,9] in order to calibrate at 405 nm the geometrical factor linking the indication provided by the powermeter with the light intensity applied on the cuvette. Subsequently keeping constant the position of the powermeter probe in the following experiments, we neglected the dispersion of the refractive index over the investigated wavelength range and retained the value of this geometrical factor to convert the indication of the powermeter (in W) into the light intensity (in E.s^{-1}.m^{-2}; see Section A) at the excitation wavelength.[25]

D.3 Optical setups

D.3.1 Epifluorescence microscope

Description Several photoconversion experiments (on photosynthetic organisms, **Dronpa-2**, **DASA**, **DDAO**) have been performed on a home-built inverted epifluorescence microscope (Figure S22). To illuminate the samples, the lights from high power LEDs (LXZ1-PB01, LHUV-405, LXZ1-PX01, LXM3-PD01; Lumileds, NL) are collimated by high-NA condensers (ACL25416U-A, $f = 16$ mm, Thorlabs, NJ) and filtered by band pass filters (ET405/20x, ET550/15x; Chroma

[25] In our setup, the LEDs deliver homogeneous illumination on the 0.3 cm $\times$ 0.3 cm cuvette and the light intensity retrieved from the measurement with the powermeter corresponds to the applied illumination in this case. In contrast, the measurement with the powermeter only provides an equivalent light intensity assuming homogeneous illumination of the whole cuvette content when illumination is performed with the Xe lamp – delivering heterogeneous illumination – or when using a partially illuminated a 1 cm $\times$ 1 cm cuvette in which only part of the stirred content is illuminated.

Technology, VT and FF01-479/40-25, FF01-650/13, Semrock, US) to avoid spectral overlaps. The quasi-parallel beams are combined with dichroic mirrors (T425LPXR, T505LPXR Chroma Technology, VT and FF01 560 Di01, Semrock, NY) and injected in a 400 μm-core optical fiber using a 20$\times$ objective (Nikon, NA = 0.75) to further homogenize the light beams. Light at the output of the fiber is collimated with a 10$\times$ objective (Olympus, NA = 0.5) and focused with $f = 150$ mm lens (AC254-150-A Thorlabs, NJ) at the back focal plane of a 10$\times$ imaging objective (Zeiss, NA = 0.5) after being reflected by a dichroic mirror (Di-FF506, Semrock, US). The LEDs are powered by an LED driver (DC4104, Thorlabs, NJ) controlled by an Arduino Uno card or a DAQ card (SCB68A with PCI 6374, National Instruments, US) depending on the applications. The DAQ card also collects the output signals from detectors at 3 MHz maximum. The fluorescence signal can either be collected by a photodetector (MPPC C13366 Hamamatsu, JP) or a camera (UEye 3060CT-M - IDS, DE). Another photodetector (MPPC C13366 Hamamatsu, JP) is used to collect the light excitation before it reaches the sample. The photodetector was used in subsections 2.1.3, 2.4.3, D.4.4 dealing with experiments on **PA**, **DASA**, and **DDAO** (Fluorescence images at wavelength 690/8 nm – FF01 690/8 Semrock), whereas the camera was used in subsections 2.5, D.4.3, D.6 for the **Dronpa-2** experiments (Fluorescence images at 525/30 nm – FF525-30, Semrock, US). The videos were acquired at 3 or 5 Hz.

In order to evidence the effect of diffusion on the determination of the light intensity in the sample (see Figure 2g–i of the Main Text), we patterned the light in the focal plane by inserting a silver film for camera with a black and white imprinted picture on the conjugated plan of the objective.

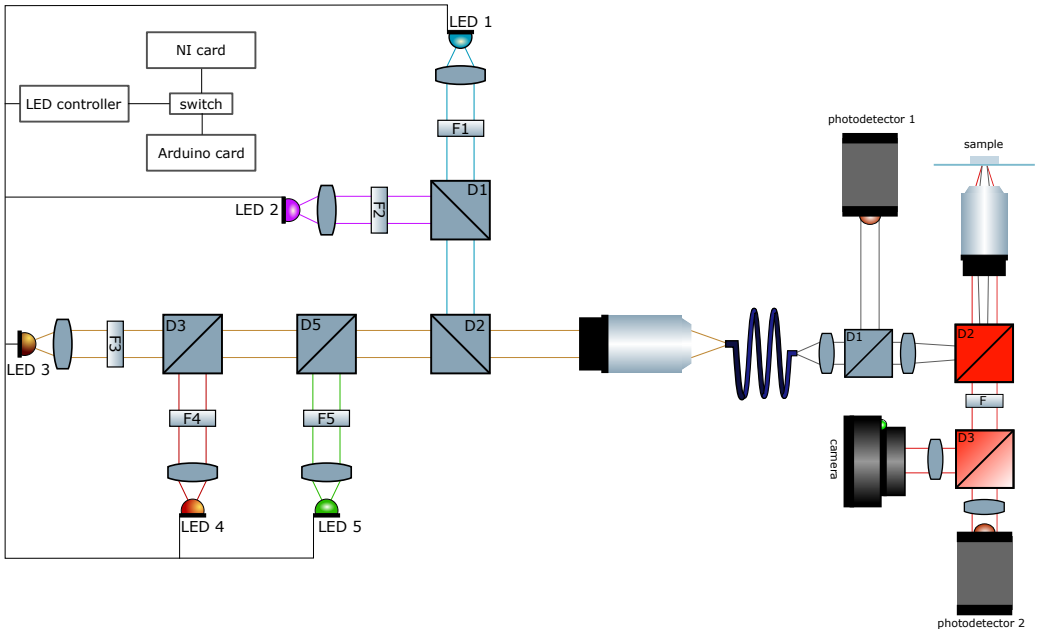

Figure S22: Schematic representation of the epifluorescence microscope.

Measurement of the light intensity at the focal plane with a powermeter The light intensity at the focal plane of this microscope has been estimated with a powermeter (PM100A, Thorlabs, NJ). Its probe (*S170C* Thorlabs, NJ) was

placed at the position of the sample and the excitation wavelength was selected. The collected output is given in Watt. To estimate the surfacic power (W/m^2), we further recorded a scaled image of the illumination spot at the sample position to measure the spot surface (0.25 mm^2 in our configuration where the illumination was narrowed by a diaphragm; see Figure 2a of the Main Text).

D.3.2 Fluorescence macroimager

Images of a CAD model representation of the physical setup, created in Rhinoceros 3D (Robert McNeel & Associates, Seattle, WA, US), are shown in Figure S23. The setup consists of separated imaging and illumination paths. The two views provided of the model show how the angle of the optical axes of both, which are shown in red, differ. Looking at the macroscope from the front, the illumination axis is offset from vertical by 28.6°, and from the side, 11.2°. The imaging path consists of a macroscope objective (1X/WF, Nikon, Tokyo, Japan), to collimate the light originating from the sample plane; an emission filter (550 nm CWL, 100 nm FWHM; 33-331, Edmund Optics Inc., Barrington, NJ, US), to pass as much of only the fluoresced light as possible; and a camera objective (AF Nikkor 50 mm f/1.8D, Nikon, Tokyo, Japan), to focus the collimated light onto the image sensor of a greyscale global-shutter camera (UI-3060CP-M-GL, IDS Imaging Development Systems GmbH, Obersulm, Germany). The illumination path consists of a condenser lens (ACL25416U, Thorlabs Inc., Newton, NJ, US) to collect the light from a blue LED (L1RX-BLU1000000000, Lumileds, San Jose, CA, USA) and collimate it for passing through an excitation filter (ET470/40×, Chroma Technology Corp., Bellows Falls, VT, US). Following the filter, the collimated light is injected into the entrance of a lightpipe (65-840, Edmund Optics Inc., Barrington, NJ, US) using a plano convex lens (LA1422-A, Thorlabs Inc., Newton, NJ, US). The lightpipe is used to homogenize the input light, providing homogeneous light at the pipe's exit. The exit end of the lightpipe is conjugated to the sample plane through the use of a matched achromatic doublet pair (MAP1040100-A, Thorlabs Inc., Newton, NJ, US). Images, or a description, of the optomechanical components used to hold the optical components in place are not described here. The distance between the components in the imaging path is such that the macroscope objective forms collimated light at its output, and the camera objective takes the collimated light and focuses it onto the sensor. The distance between the two objectives was approximately 65 mm, with the emission filter being placed about 20 mm above the macroscope objective. The distances between the components in the illumination path are introduced in the following section on the setup of the simulation.

In relation to the electronics, the LED was connected to an LED driver (DC4104, Thorlabs Inc., Newton, NJ, US) to power it, and the camera to a custom-built PC running Windows 10 (Microsoft Corp., Redmond, WA, US) to accept images from it. The cameras frames were triggered using an Elegoo Uno R3 board (Elegoo, Shenzhen, China).

The experiment was carried out using a 4 μM **Dronpa-2** solution sandwiched between two round 40 mm microscope cover slips (Thermo Fisher Scientific, Waltham, MA, US), using a 17 × 28 mm Gene Frame (Thermo Fisher Scientific, Waltham, MA, US) to maintain the separation between the slides at approximately 0.25 mm and hold the solution in place. The sandwich was placed flat, relative to the imaging optical axis, on the sample plane, and at the

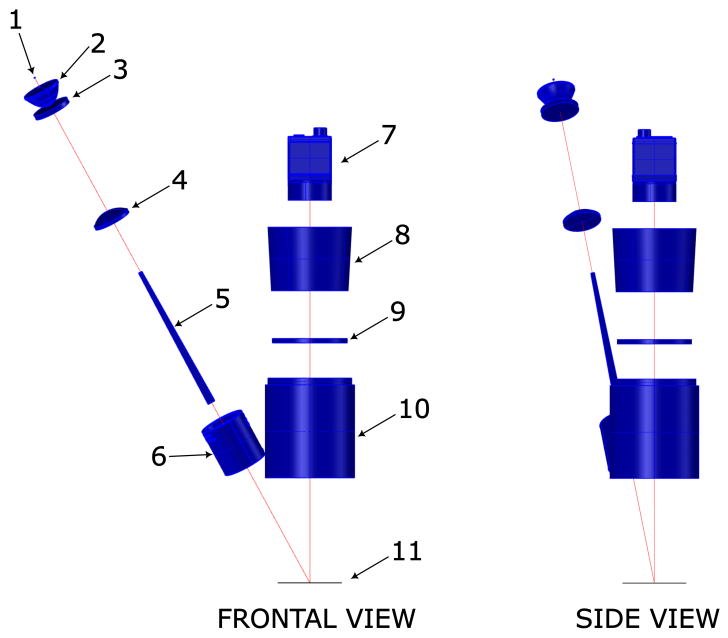

Figure S23: *Fluorescence macroimager*. CAD rendered diagrams of the optical elements composing the macroscope; LEFT – Frontal view, RIGHT –Side view. 1 – LED, 2 – Condenser, 3 – Excitation Filter, 4 – Condenser, 5 – Lightpipe, 6 – Matched Achromatic Doublets, 7 – Camera, 8 – Camera Objective, 9 – Emission Filter, 10 – Macroscope Objective, 11 – Sample.

focal distance of the macroscope objective. The experiment involved acquiring images, at a frequency of 6 Hz, for 30 seconds, while, at a time point shortly after the camera was started, the LED was driven with a current of 1000 mA. The video and data corresponding to the final intensity image output is provided (Macroscope/MACRO_video.tiff and Macroscope/MACRO_ExperimentalData.npy, respectively).

D.3.3 Confocal microscopy

Several photoconversion experiments on **Dronpa-2** have been performed on confocal microscopes. The confocal micrographs were acquired on a Zeiss LSM 710 Laser Scanning Microscope equipped with continuous laser lines at 405 and 488 nm and a Plan NeoFluar 20×/0.5 objective, or on a Leica TCS SP8 confocal microscope equipped with a HC PL APO CS2 40x/1.10 water immersion objective, a continuous laser line delivering light at 405 nm and a white light laser (WLL) source delivering 200-300 ps light pulses at 488 nm every 13.6 ns. ZEN software from Zeiss or LAS X software from Leica were used to collect the data. The images were analyzed with Fiji and Python.

D.3.4 Fluorometer for acquisition of the fast OJIP transient fluorescence response to PA illumination

Besides the corresponding measurements which have been performed with the epifluorescence microscope equipped with the MPPC photodetector, we used the FL 6000 fluorometer from Photon Systems Instruments (PSI; Drásov, Czech Republic) to record the fast OJIP transient fluorescence response to illumination of microalgae.

The LED mounted on this PSI instrument is the LXML-PH01 LED, which belongs to the LUXEON Rebel Color Line

from LUMILEDS. Its unscaled emission spectrum $S(\lambda)$ was measured with a portable spectrophotometer (SpectraPen Mini - PSI, CZ).

D.3.5 Fluorescence Correlation Spectroscopy

The one-photon excitation FCS setup consisted of a laser source, a home built microscope and two avalanche photodiodes (APD). The laser source was a 488 nm laser (LBX-488, Oxxius, Lannion, FR). The laser beam was expanded 3 times at the entrance of the microscope using pairs of converging lenses (AC254-030-A and AC254-075-A, Thorlabs, NJ) to reach a diameter of 8 mm and sent with a dichroic mirror (FF506-Di03, Semrock, NJ) at the back aperture of a water-immersion objective (60×/1.2, UPlanApo, Olympus, JP). The fluorescence was collected through the same objective and filtered with a bandpass filter (ET525/30m, Chroma VT; FF01-650/13 Semrock, NY) before being focused at the entrance of a 50 µm core optical fiber (M14L02, Thorlabs, NJ) with a $f = 200$ mm lens (AC254-200-A, Thorlabs, NJ). Light at the exit the fiber was re-collimated with a 50 mm lens and separated by a cube beam splitter with a 1:1 ratio and then focused on the 200 μm^2 working surfaces of the two APDs (SPCM-AQR-14, Excelitas Technologies, MA). The signal outputs of the APD modules (TTL pulses) were acquired by a digital autocorrelator module (ALV-6000, ALV-Gmbh, DE) which computed online the cross-correlation function of the fluorescence fluctuations. Ten runs of 60 s were averaged to yield the final data including the associated standard deviations at the different lag times.

D.4 Intrinsically fluorescent actinometers

D.4.1 Cin

This actinometer has been thoroughly investigated by Jullien et al.[3,13] It has been shown to irreversibly convert into 6,8-dibromo-7-hydroxycoumarin in water[13] and in water–acetonitrile mixtures[3] under illumination in the UV A wavelength range.

Preparation of the Cin solutions The synthesis of the *(E)*-3-(3,5-dibromo-2,4-dihydroxyphenyl) acrylic acid ethyl ester (**Cin**) actinometer is reported in the subsection 1.2.1. The **Cin** solution was produced in two steps. A first 10 mM stock solution was made by dissolving 3.8 mg **Cin** powder in 1 mL of spectrograde DMSO. This stock solution was subsequently diluted in 20 mM Tris pH 7 100 mM NaCl buffer to get the final solutions used for the fluorometric investigations at 5.6 or 16.8 μM concentration. In these solutions, the volumetric DMSO/Buffer ratio is 0.05 and 0.16 % respectively. These solutions can be kept under the protection of ambient light (container covered with an Aluminium foil) at 20 ^{o}C for up to a day.

Absorption spectrum of Cin and emission spectrum of its coumarin photoproduct **Cin** exhibits a significant light absorption between 300 and 430 nm solution in 20 mM Tris pH 7 100 mM NaCl buffer (see Figure S24). Its photoproduct, 6,8-dibromo-7-hydroxycoumarin, emits fluorescence between 400 and 600 nm in the same solvent (see Figure S24).

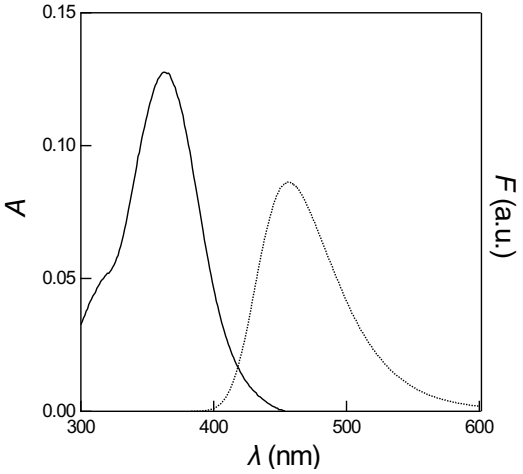

Figure S24: Absorption spectrum of 5.6 μM **Cin** solution (solid line) and fluorescence emission spectrum of its photoproduct, 6,8-dibromo-7-hydroxycoumarin (dotted line; $\lambda_{\rm exc} = 368$ nm) in 20 mM Tris pH 7 100 mM NaCl buffer recorded in a 1×1 cm^2 quartz cuvette. $T = 293$ K.

Determination of the quantum yield of Cin photoconversion in pH 7 Tris buffer at 405 nm The quantum yield of the **Cin** photoconversion is 0.05 at 350 nm in acetonitrile/20 mM Tris pH 7 100 mM NaCl buffer 1/1 (v/v).[3] In this manuscript, we evaluated its value at 405 nm in pure 20 mM Tris pH 7 100 mM NaCl buffer. We also examined any possible upper range of light intensity beyond which the photochemical step is not anymore rate-limiting in the **Cin** light-driven conversion in pH 7 Tris buffer.

Figure S25a displays the time dependence of the fluorescence emission of 16.8 μM **Cin** in 20 mM Tris pH 7 100 mM NaCl buffer at 456 nm upon irradiation at various light intensities at 405$\pm$20 nm, which have been measured by using the **Nit** actinometer (see below). Then we applied the monoexponential fitting function given in Eq.(S1) to the temporal rises of the normalized fluorescence in order to retrieve the characteristic times of the photoconversion τ. As displayed in Figure S25b, the inverse of the characteristic times of the photoconversion linearly depends on the light intensity. This behavior demonstrates that the rate limiting step of **Cin** photoconversion in 20 mM Tris pH 7 100 mM NaCl buffer is photochemical at least up to 6 10^{-4} E.m^{-2}.s^{-1} light intensity. However, despite the observed linearity of the inverse of the characteristic time of the **Cin** photoconversion on the light intensity, one notices that the photoproduced 6,8-dibromo-7-hydroxycoumarin experiences significant photobleaching (see Figure S25a), which may reduce the amplitude of the observable fluorescence rise. Hence it is suggested to restrict the use of the fluorescent actinometer to light measurements below 5 10^{-5} E.m^{-2}.s^{-1} light intensity at 405 nm.

Eq.(S24) was used to retrieve $\sigma = 184 \pm 2$ m^2.mol^{-1} from the slope of the dependence of the inverse of the characteristic time of the photoconversion on the light intensity. Equipped with the latter value of the cross section for the photoconversion and the value of the molar absorption coefficient of **Cin** at 405 nm (0.7 10^4 M^{-1}.cm^{-1} = 0.7 10^3 m^2.mol^{-1}), we used Eq.(S23) to extract $\varphi_F = 0.13 \pm 0.02$ as the value of the quantum yield of the **Cin** photoconversion at 405 nm in 20 mM Tris pH 7 100 mM NaCl buffer.

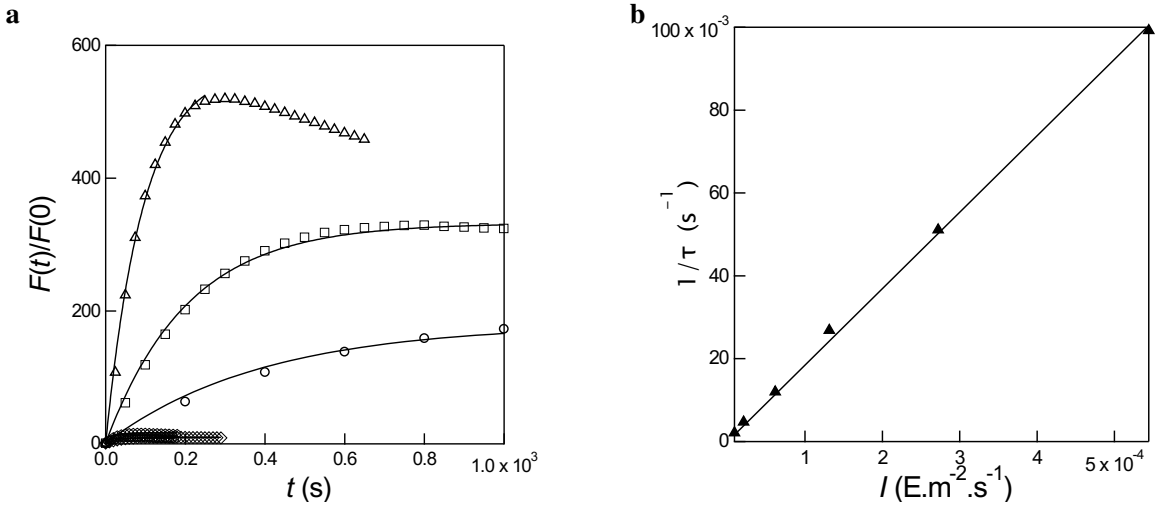

Figure S25: *Determination of the cross section for the photoconversion of (E)-3-(3,5-dibromo-2,4-dihydroxyphenyl) acrylic acid ethyl ester (**Cin**) in pH 7 Tris buffer at 405 nm.* **a**: Time evolution of the normalized fluorescence emission at 456 nm from a 16.8 μM **Cin** in 20 mM Tris pH 7 100 mM NaCl buffer contained in a 3 mm optical path quartz cuvette upon irradiation at various constant light intensity at 405 nm (in 10^{-5} E.m^{-2}.s^{-1}): 0.88 (circles), 2.0 (squares), 6.1 (triangles), 13 (diamonds), 27 (disks), and 54 (hexagons). Markers: Experimental data; Solid lines: Monoexponential fit with Eq.(S1); **b**: Dependence of the inverse of the characteristic time τ retrieved in **a** from the monoexponential fit on the light intensity. Markers: Experimental data; Solid line: Linear fit. The extracted slope is 184 ± 2 m^2.mol^{-1}. $T = 293$ K.

Dependence of the quantum yield of the Cin photoconversion on the excitation wavelength Then we studied the dependence of the quantum yield of the **Cin** photoconversion on the excitation wavelength. Figure S26 displays the time dependence of the fluorescence emission of a 5.6 μM **Cin** in 20 mM Tris pH 7 100 mM NaCl buffer upon irradiation at constant light intensity at 350, 365, 380, 405, and 420 nm, which have been measured from recording the light power transmitted through the 1 cm light path quartz cuvette. Then we applied the monoexponential fitting function given in Eq.(S1) to the temporal rises of the normalized fluorescence at 456 nm in order to retrieve the rate constants of the photoconversion upon exciting at various wavelengths (Figure S26). Equipped with the rate constants of the photoconversion and the light intensities (retrieved from the light powers) measured at all the excitation wavelengths, and the dependence of the molar absorption coefficient of **Cin** on the wavelength, we used Eq.(S23) to extract the dependence of the quantum yield of the **Cin** photoconversion on the excitation wavelength upon fixing the value of the quantum yield of the **Cin** photoconversion to 0.13 at 405 nm. The results are displayed in Table S4. The quantum yield of the **Cin** photoconversion is essentially constant and equal to 0.22 ± 0.02 from 350 to 380 nm but seems to drop on the red edge of its absorption band.

Estimate of the achievable measurement uncertainty on light intensity I Considering the uncertainty in the parameters (σ and τ), we estimate that the achievable measurement uncertainty on light intensity I is 20% by using **Cin**.

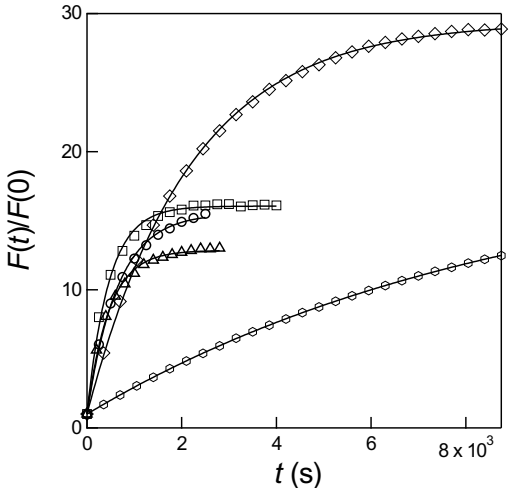

Figure S26: *Dependence of the quantum yield of the* ***Cin*** *photoconversion on the excitation wavelength.* Time dependence of the normalized fluorescence emission at 456 nm of a 5.6 μM **Cin** in 20 mM Tris pH 7 100 mM NaCl buffer contained in a 1×1 cm^2 quartz cuvette upon illumination at constant light intensity at 350 (circles), 365 (squares), 380 nm (triangles), 405 (diamonds), and 420 (hexagons) nm. Markers: Experimental data; solid lines: Monoexponential fit with Eq.(S86). $T = 293$ K.

Table S4: Photoconversion parameters of *(E)*-3-(3,5-dibromo-2,4-dihydroxyphenyl) acrylic acid ethyl ester (**Cin**) in 20 mM Tris pH 7 100 mM NaCl buffer. The quantum yield of photoconversion φ_F has been extracted from analyzing the rise of the fluorescence emission at 456 nm of a 5.6 μM **Cin** in 20 mM Tris pH 7 100 mM NaCl buffer under monochromatic illumination at 350, 365, 380, 405, and 420 nm as representatives of 350 nm – 420 nm range. The molar absorption coefficients $\varepsilon(\lambda_{\rm exc})$ were extracted from the **Cin** absorption spectrum by using the Beer-Lambert law. The cross section $\sigma(\lambda_{\rm exc})$ was evaluated with Eq.(S23). $I_{\rm sup}(\lambda_{\rm exc})$ indicates the upper light intensity tested and relevant for a reliable measurement.

$\lambda_{\rm exc}$ (nm)	$10^3 \times \varepsilon(\lambda_{\rm exc})$ ($\pm10\%$; M^{-1}cm^{-1})	$\sigma(\lambda_{\rm exc})$ ($\pm10\%$; m^{2}mol^{-1})	φ_F (±0.02)	$I_{\rm sup}(\lambda_{\rm exc})$ (E.m^{-2}.$^{-1}$ (W.m^2))
350	20	940	0.20	1.6 10^{-5}(5.5)^a
365	23	1200	0.23	1.4 10^{-5}(4.6)^a
380	19	1000	0.24	1.7 10^{-5}(5.3)^a
405	6.4	184	0.13	5.0 10^{-5}(15)^a
420	2.5	49	0.09	1.3 10^{-4}(37)^a

^{a} Extracted from the value of $I_{\rm sup}(\lambda_{\rm exc})$ by using $I_{\rm sup}(\lambda_{\rm exc}) = I_{\rm sup}(\lambda_{\rm exc,ref}) \times \frac{\varepsilon(\lambda_{\rm exc,ref})}{\varepsilon(\lambda_{\rm exc})}$ where $\lambda_{\rm exc,ref}$ designates the wavelength at which the extraction of the cross section of photoconversion has been performed ($\lambda_{\rm exc,ref} = 405$ nm for **Cin**).

D.4.2 Dronpa-2

The reversibly photoswitchable fluorescent proteins (RSFPs)[14] are favorable endogenously fluorescent actinometers, when access to biological techniques is available. Indeed, they are genetically-encoded and can be easily introduced in various live and fixed biological samples (e.g. bacteria, eucaryotic cells from animals and plants, leaves and roots of live plants) or produced as solutes in a buffer solution. Moreover, their cross sections for photoisomerization span a wide range (over two orders of magnitude[9]) in the 450-500 nm range, which opens a road to measure light intensity over a wide range of values. In this manuscript, we illustrate this series of fluorescent actinometers with **Dronpa-2** (or

M159T).[15] This variant of the reversibly photoswitchable green fluorescent protein Dronpa[16] benefits from an appropriate characteristic time close to the minute associated to its thermal return after photoconversion, which makes it appropriate for repeated use without generating a too demanding lower limit of the reliably measurable light intensity. However, the proposed methodology will be relevant as well for the other RSFPs.

In aqueous solution at neutral pH, **Dronpa-2** exhibits a broad absorption band spanning the 420-520 nm range. Under blue light around 480 nm, **Dronpa-2** photoswitches from a bright to a dark state (negative photochromism). In contrast, it photoswitches from a dark to a bright state under violet light (around 405 nm). The quantitative analysis of the kinetics of **Dronpa-2** photoswitching has been thoroughly investigated by Le Saux, Jullien, et al.[7,9] The time evolution of its fluorescence emission upon constant illumination at 480 nm and 405 nm obeys a simple two-state kinetic model at time scales longer than a few ms, which enables to measure light intensity up to 10 E.m^{-2}.s^{-1} (3×10^{6} W.m^{-2}).[9]

Preparation of the Dronpa-2 samples Three **Dronpa-2**-based actinometers are proposed for measuring light intensity in the 440-500 nm wavelength range: a **Dronpa-2** solution, **Dronpa-2**-labeled *Escherichia coli* cells, and fixed U-2 OS eucaryotic cells **Dronpa-2**-labeled at their nucleus.

The production of those actinometers is reported in the subsections 1.3.2, 1.3.3, and 1.3.4.

The concentration of the solutions of **Dronpa-2** purified protein, i.e. **Dronpa-2** solution, and **Dronpa-2** labeled bacteria were fixed as follows. The absorption spectrum of the original samples were recorded over the 200 nm – 800 nm wavelength range. The original solutions were subsequently diluted in DPBS $1\times$ pH 7.4 buffer (2.7 mM KCl, 138 mM NaCl, 1.5 mM KH_2PO_4, 8.1 mM Na_2HPO_4) such that their absorbance at 488 nm was in the 0.15 range.

The **Dronpa-2** solution and **Dronpa-2**-labeled *Escherichia coli* cells can be kept under the protection of ambient light (container covered with an Aluminium foil) at - 20 °C for up to two weeks. The fixed U-2 OS eucaryotic cells **Dronpa-2**-labeled at their nucleus remain functional for several weeks when kept at +4°C.

Absorption and emission spectra of Dronpa-2 At neutral pH, the **Dronpa-2** solution exhibits a significant light absorption between 440 nm and 500 nm and emits fluorescence peaking at 512 nm (see Figure S27).

Determination of the cross sections of photoconversion of Dronpa-2 in bacteria at 480 and 405 nm We already evidenced that the **Dronpa-2** photoconversion can be reliably modeled as a two-state exchange up to a threshold of light intensity in the 10 E.m^{-2}.s^{-1} with values of the cross sections of photoconversion of **Dronpa-2** in aqueous solution at pH 7.4, which are respectively equal to 198 and 415 m^2.mol^{-1} at 480 and 405 nm.[9] We also analyzed the **Dronpa-2** photoconversion in fixed eucaryotic cells **Dronpa-2**-labeled at the nucleus and did not notice any significant departure of the photoconversion kinetics with respect to the solution (see Supplementary Table 6 in the Supporting Information of the reference[7]). In this subsection, we measured the values of the corresponding cross sections of photoconversion of **Dronpa-2** in **Dronpa-2** labeled bacteria.

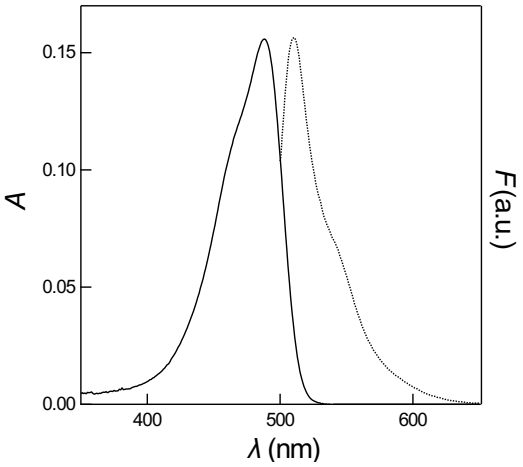

Figure S27: Absorption (solid line) and emission (dotted line; $\lambda_{\rm exc} = 480$ nm) spectra of 2.1 μM **Dronpa-2** solution in DPBS $1\times$ pH 7.4 buffer recorded in a 1×1 cm^2 quartz cuvette. $T = 293$ K.

Figures S28a,c display the time dependence of the fluorescence emission of the suspension of **Dronpa-2** labeled bacteria in DPBS $1\times$ pH 7.4 buffer contained in a 3 mm light path quartz cuvette upon irradiation at various combinations of light intensities, which have been calibrated from analyzing the time evolution of the fluorescence signal from the **Dronpa-2** pH 7.4 aqueous solution upon illumination at 480 or 405 nm.[7,9] Figure S28a displays the time decay of the fluorescence emission of the suspension of **Dronpa-2** labeled bacteria upon illumination at several light intensities at 480 nm under constant light intensity at 405 nm whereas Figure S28c displays the time rise of the fluorescence emission of the suspension of 480 nm-phoswitched **Dronpa-2** labeled bacteria upon illumination at several light intensities at 405 nm under constant light intensity at 480 nm. Then we applied the monoexponential fitting function given in Eq.(S1) to the temporal evolutions of the normalized fluorescence at 515 nm in order to retrieve the characteristic times of the photoconversion τ under the various conditions of illumination. As displayed in Figures S28b,d the inverses of the characteristic times of the photoconversion linearly depend on the light intensity. This behavior demonstrates that the rate limiting step of the **Dronpa-2** photoconversion in **Dronpa-2** labeled bacteria is photochemical at least up to 2 10^{-3} E.m^{-2}.s^{-1} light intensity. Eq.(S24) was used to retrieve $\sigma(480) = 251 \pm 7$ m^2.mol^{-1} and $\sigma(405) = 370 \pm 2$ m^2.mol^{-1} from the observed slopes.

Comparison of the cross sections of photoconversion of Dronpa-2 at 480 nm in solution and in a polyacrylamide gel In order to account for the impact of molecular diffusion on the determination of the light intensity in the focal plane of the epifluorescence microscope, we compared the kinetics of the photoconversion of **Dronpa-2** on a selected homogeneous region of interest (100×100 pixels; see Figure S29a) in solution and in a polyacrylamide gel (prepared by adding 20 μL of **Dronpa-2** stock solution to 20 μL of 40% acrylamide/bis-acrylamide (37.5:1 ratio, Merck), 1 μL of 10% N,N,N',N'-Tetramethylethylenediamine (TEMED) in water and 1 μL of 10 % ammonium persulfate in water. The blue light was turned on and the decays of the fluorescence were collected on the camera at 3 Hz (see Figure S29b). The

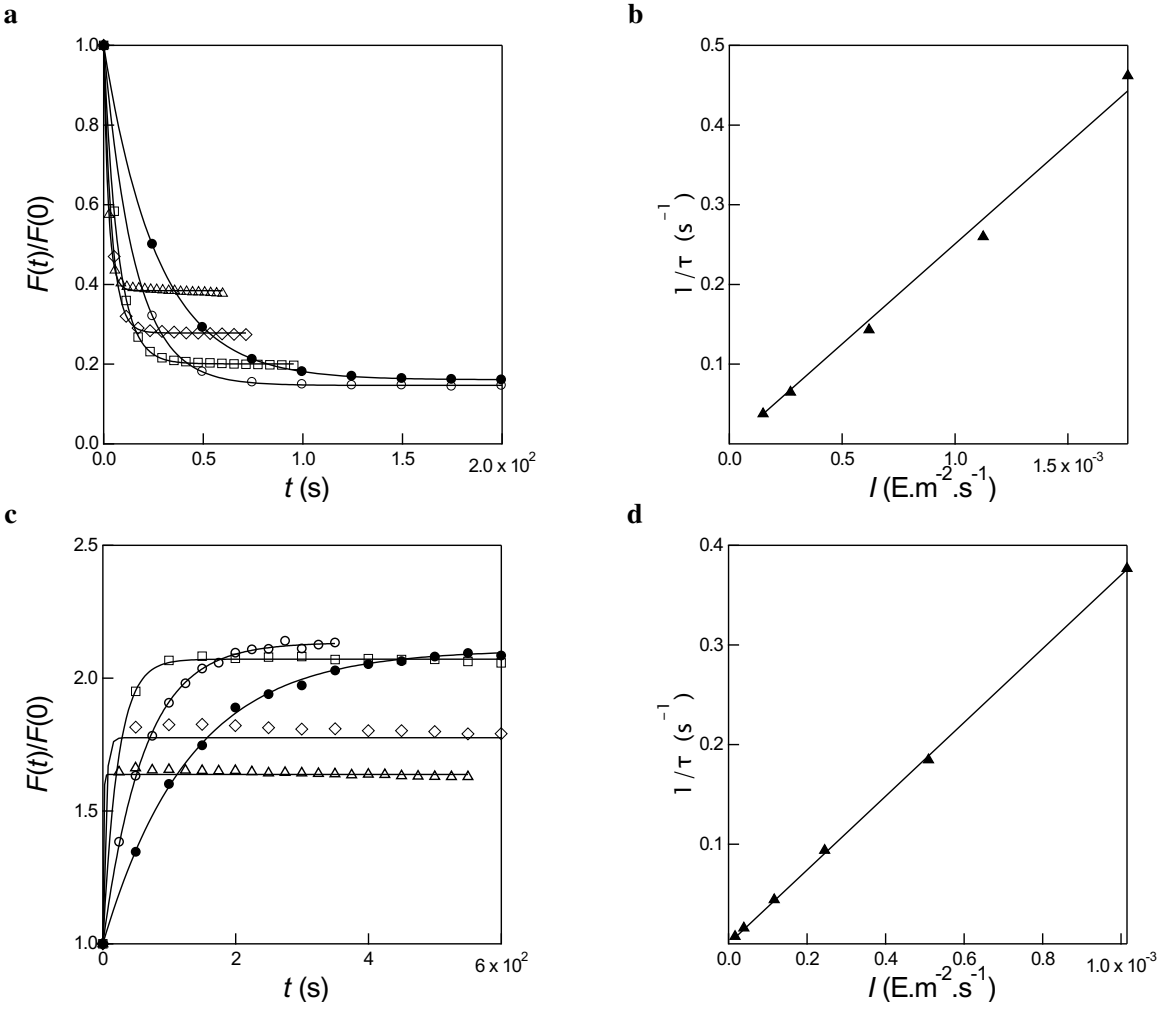

Figure S28: *Determination of the cross section of photoconversion of* ***Dronpa-2*** *in* ***Dronpa-2*** *labeled bacteria at 480 and 405 nm.* **a**: Time evolution of the normalized fluorescence emission at 515 nm from **Dronpa-2** labeled bacteria in DPBS $1\times$ pH 7.4 buffer in 3 mm optical path cuvette upon irradiation at various constant light intensities at 480 nm (in 10^{-4} E.m^{-2}.s^{-1}; disks: 1.5; circles: 2.7; squares: 6.2; diamonds: 11.2; triangles: 17.7) and constant light intensity at 405 nm equal to 3.9 10^{-5} E.m^{-2}.s^{-1}. Markers: Experimental data; Solid lines: Monoexponential fit with Eq.(S1); **b**: Dependence of the inverse of the characteristic time τ retrieved in **a** from the monoexponential fit on the light intensity. Markers: Experimental data; Solid line: Linear fit. The extracted slope is 251 ± 7 m^2.mol^{-1}; **c**: Time evolution of the normalized fluorescence emission at 515 nm from **Dronpa-2** labeled bacteria in 3 mm optical path cuvette upon irradiation at various constant light intensities at 405 nm (in 10^{-5} E.m^{-2}.s^{-1}; disks: 1.7; circles: 3.9; squares: 11.6; diamonds: 24.5; triangles: 51.0) and constant light intensity at 480 nm equal to 6.2 10^{-4} E.m^{-2}.s^{-1}. Markers: Experimental data; Solid lines: Monoexponential fit with Eq.(S1); **d**: Dependence of the inverse of the characteristic time τ retrieved in **c** from the monoexponential fit on the light intensity. Markers: Experimental data; Solid line: Linear fit. The extracted slope is 370 ± 2 m^2.mol^{-1}.

retrieved characteristic times τ decays were found similar in the solution ($\tau = 0.91$ s) and in the gel ($\tau = 1.03$ s) so as to support that the cross sections of photoconversion of **Dronpa-2** in solution and in a polyacrylamide gel are essentially identical under these experimental conditions.

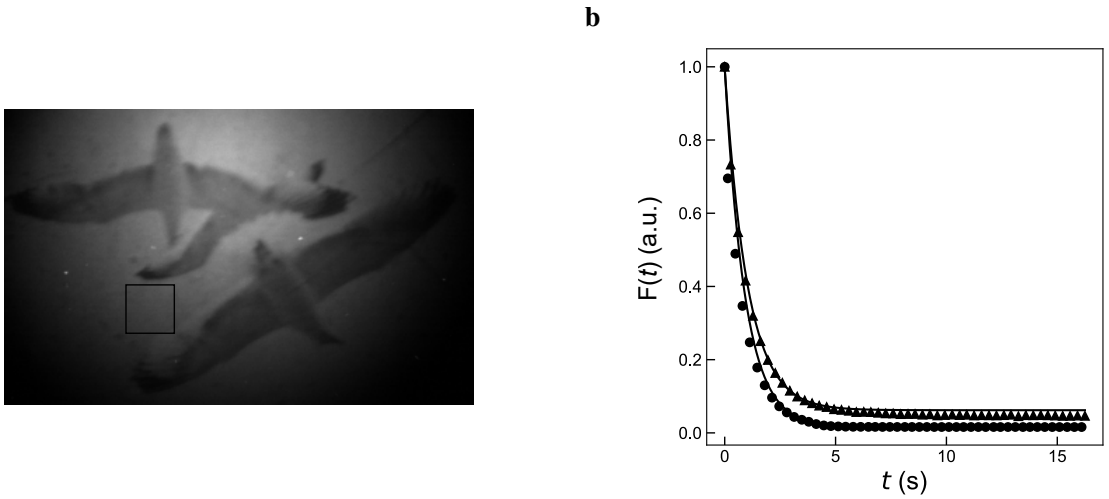

Figure S29: *Comparison of the fluorescence decay associated to the photoconversion of* ***Dronpa-2*** *in solution and in a polyacrylamide gel*. **a**: 100×100 pixels region of interest selected for analysis in the image generated in the polyacrylamide gel; **b**: Averaged decays of the fluorescence signal over the selected area. Experimental data: disk (solution) triangles (gel); monoexponential fits: solid lines (solution: $\tau = 0.91$ s, polyacrylamide gel: $\tau = 1.03$ s).

Dependence of the cross sections of the Dronpa-2 photoconversion on the excitation wavelength Then we studied the dependence of the cross sections of photoconversion of **Dronpa-2** in **Dronpa-2** solution and in **Dronpa-2** labeled bacteria on the excitation wavelength.

Figures S30a,b display the time dependence of the fluorescence emission of a 8.8 μM **Dronpa-2** solution (Figure S30a) and of **Dronpa-2** labeled bacteria (Figure S30b) in DPBS 1× pH 7.4 buffer upon irradiation at constant light intensity at 445, 480, and 500 nm in a 3 mm optical path quartz cuvette. Then we applied the monoexponential fitting function given in Eq.(S1) to the temporal rises of the normalized fluorescence at 515 nm in order to retrieve the rate constants of the photoconversion upon exciting at various wavelengths. Equipped with the rate constants of the photoconversion and the light intensities (retrieved from the light powers) measured at all the excitation wavelengths, we used Eq.(S23) to extract the dependence of the cross sections of photoconversion of **Dronpa-2** in the **Dronpa-2** solution and in **Dronpa-2** labeled bacteria on the excitation wavelength upon fixing their values to 198 and 251 $\text{m}^2.\text{mol}^{-1}$ at 480 nm respectively. The results are displayed in Table S5. By further using the dependence of the molar absorption coefficient of **Dronpa-2** in in DPBS 1× pH 7.4 buffer on the wavelength, we extracted the quantum yield associated to **Dronpa-2** photoswitching at 445, 480, and 500 nm in **Dronpa-2** solution and in **Dronpa-2** labeled bacteria respectively. As displayed in Table S5, the extracted values are all in the $1\text{–}2\times10^{-2}$ range and do not considerably depend on the excitation wavelength.

Estimate of the achievable measurement uncertainty on light intensity I Considering the uncertainty in the parameters (σ and τ), we estimate that the achievable measurement uncertainty on light intensity I is 20% by using **Dronpa-2**.

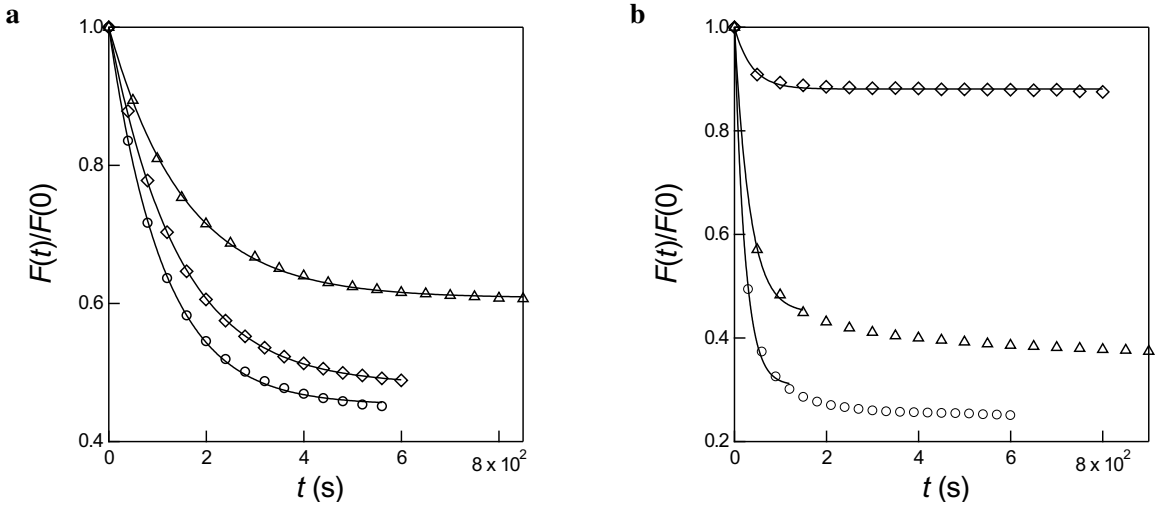

Figure S30: *Dependence of the cross sections of photoconversion of* ***Dronpa-2*** *on the excitation wavelength from analyzing the decay of the* ***Dronpa-2*** *fluorescence under illumination*. Time dependence of the normalized fluorescence emission at 515 nm of a 8.8 μM **Dronpa-2** solution (**a**) and **Dronpa-2** labeled bacteria (**b**) in DPBS $1\times$ pH 7.4 buffer in 3 mm optical path cuvette upon illumination at constant light intensity at 445 (triangles), 480 nm (circles), and 500 (diamonds) nm. Markers: Experimental data; solid lines: Monoexponential fit with Eq.(S1). $T = 293$ K.

Table S5: Photoconversion parameters of **Dronpa-2** in **Dronpa-2** solution and in **Dronpa-2** labeled bacteria in DPBS $1\times$ pH 7.4 buffer. The cross sections of photoconversion, $\sigma_{\rm sol}(\lambda_{\rm exc})$ and $\sigma_{\rm bac}(\lambda_{\rm exc})$, have been extracted from analyzing the decay of the fluorescence emission at 515 nm of a 8.8 μM **Dronpa-2** solution and **Dronpa-2** labeled bacteria respectively, under monochromatic illumination at 445, 480, and 500 nm upon adopting the value at 480 nm (which was measured in subsection D.4.2) and under fixing the rate constant associated to thermal return k_{21}^{Δ} (3.2 10^{-3} s^{-1} in the **Dronpa-2** solution and in the **Dronpa-2** labeled bacteria respectively). The molar absorption coefficients $\varepsilon(\lambda_{\rm exc})$ were extracted from the **Dronpa-2** absorption spectrum in **Dronpa-2** solution in DPBS $1\times$ pH 7.4 buffer by using the Beer-Lambert law. The quantum yields of **Dronpa-2** photoconversion in **Dronpa-2** solution and of **Dronpa-2** labeled bacteria, $\varphi_{\rm sol}$ and $\varphi_{\rm bac}$ respectively, were evaluated from the cross sections of photoconversion with Eq.(S23). $[I(\lambda_{\rm exc})]$ indicates the range of reliably measurable light intensity associated to the actinometer photoconversion at $\lambda_{\rm exc}$.

$\lambda_{\rm exc}$ (nm)	$10^4\varepsilon_{\rm sol}(\lambda_{\rm exc})$ (±0.1; $M^{-1}cm^{-1}$)	$\sigma_{\rm sol}(\lambda_{\rm exc})$ ($\pm10\%$; m^2mol^{-1})	$10^2\varphi_{\rm sol}$ (±0.2)	$\sigma_{\rm bac}(\lambda_{\rm exc})$ ($\pm10\%$; m^2mol^{-1})	$10^2\varphi_{\rm bac}$ (±0.2)	$[I(\lambda_{\rm exc})]^a$ ($E.m^{-2}.s^{-1}$ ($W.m^2$))
445	3.8	140	1.6	192	2.2	[3 10^{-4}–18] ([80–4.8 10^6])
480	7.0	198	1.2	251	1.6	[2 10^{-4}–10] ([50–2.5 10^6])
500	5.3	128	1.0	151	1.3	[3 10^{-4}–13] ([72–1.0 10^6])

[a] The lower range of $I(\lambda_{\rm exc})$ has been computed from Eq.(S60) upon using the values of k_{21}^{Δ} and $\sigma_{\rm sol}(\lambda_{\rm exc})$. The upper range of $I(\lambda_{\rm exc})$ has been retrieved from the value of $I_1^{\rm c}(480\ {\rm nm})$ given in Supplementary Table 3 of the reference[9] by using $I_{\rm sup}(\lambda_{\rm exc}) = I_1^{\rm c}(480\ {\rm nm}) \times \frac{\varepsilon(480\ {\rm nm})}{\varepsilon(\lambda_{\rm exc})}$.

D.4.3 DASA

Photochromic dyes provide attractive reusable actinometers since they reversibly change of color upon photoreaction.[17] Yet, only a few of them absorb up to the red wavelength range. Donor-acceptor Stenhouse dyes reversibly photoswitch between an open conjugated state absorbing above 500 nm, and a cyclic non-conjugated state that absorbs below 300 nm.[18] We recently introduced such a photochromic dye – subsequently denoted **DASA**, which has been thoroughly investigated by Jullien, Adelizzi et al.[5] In acetonitrile, it exhibits a broad absorption band spanning the 530-670 nm range, which is

associated to an open form. It encounters a reversible two-step light-triggered conversion under illumination at 595 nm: A Z/E photoisomerization is followed by a thermally-driven cyclization resulting in the cyclic colorless form.

Preparation of the DASA solution The synthesis of the sodium 4-(4-((2Z,4E)-2-hydroxy-5-(indolin-1-yl)penta-2,4-dien-1-ylidene)-3-methyl-5-oxo-4,5-dihydro-1H-pyra-zol-1-yl)benzenesulfonate (**DASA**) actinometer is reported in the subsection 1.2.3. The preparation of the **DASA** solution is performed in two steps. A first 0.2 mM mother **DASA** solution is prepared in spectroscopy grade DMSO. It can be kept under the protection of ambient light (container covered with an Aluminium foil) at 20 °C for up to a week. The mother solution is then diluted in spectroscopy grade acetonitrile to yield a final 40 μM **DASA** in a 1:50 (v/v) (or 20 μM **DASA** in a 1:100 (v/v)) mixture of spectroscopy grade DMSO and acetonitrile. This solution has to be freshly prepared and equilibrated for 2 h before immediate use.

Absorption and emission spectra of DASA In acetonitrile, the **DASA** open state absorbs light between 530 and 670 nm and emits fluorescence emission, which peaks at 650 nm and extends up to 675 nm (see Figure S31).

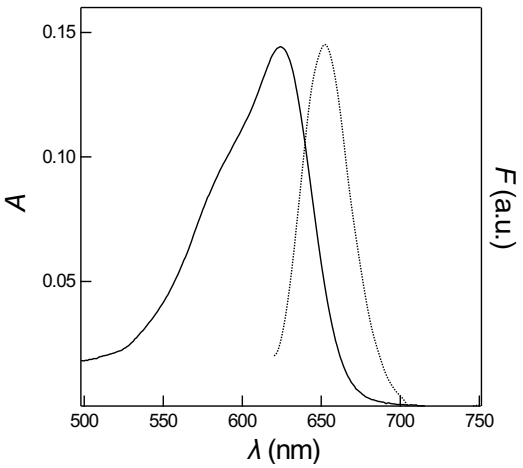

Figure S31: Absorption (solid line) and emission (dotted line; $\lambda_{\text{exc}} = 600$ nm) spectra of 30 μM **DASA** solution in a 1:50 (v/v) mixture of spectroscopy grade DMSO and acetonitrile recorded in a 3 mm quartz cuvette. $T = 293$ K.

Determination of the quantum yield of DASA photoconversion in acetonitrile at 632 nm We evaluated the quantum yield of **DASA** photoconversion in acetonitrile at 632 nm and examined whether there is a possible upper range of light intensity beyond which the photochemical step is not anymore rate-limiting in the **DASA** light-driven conversion.

Figure S32a displays the time evolution of the fluorescence emission of 40 μM **DASA** in a 1:50 (v/v) mixture of spectroscopy grade DMSO and acetonitrile contained in a 3 mm optical path cuvette upon illumination at various light intensities at 632 nm measured with a powermeter. The monoexponential fitting function given in Eq.(S1) was applied to the temporal decays of the normalized fluorescence emission at 675 nm in order to retrieve the characteristic times of the photoconversion τ upon exciting at various light intensities. As displayed in Figure S32b, the inverse of the characteristic

times of the photoconversion linearly depends on the light intensity. This behavior demonstrates that the rate limiting step of **DASA** photoconversion in acetonitrile is photochemical at least up to 6 10^{-4} E.m^{-2}.s^{-1} light intensity. Eq.(S24) was used to retrieve $\sigma = 1135 \pm 50$ m^2.mol^{-1} from the slope.

This experiment was reproduced on a microscopy setup with MPPC detection of the emitted fluorescence. 40 and 100 μM **DASA** in a 1:35 (v/v) mixture of spectroscopy grade DMSO and acetonitrile contained in a 200 μm-high glass slide chamber were exposed to illumination at various light intensities at 630 ± 7 nm (measured with a powermeter) and their emission was collected at 690 ± 8 nm. As displayed in Figure S32c, very similar results have been obtained with σ values ranging from 1128 ± 40 to 1136 ± 50 m^2.mol^{-1}.

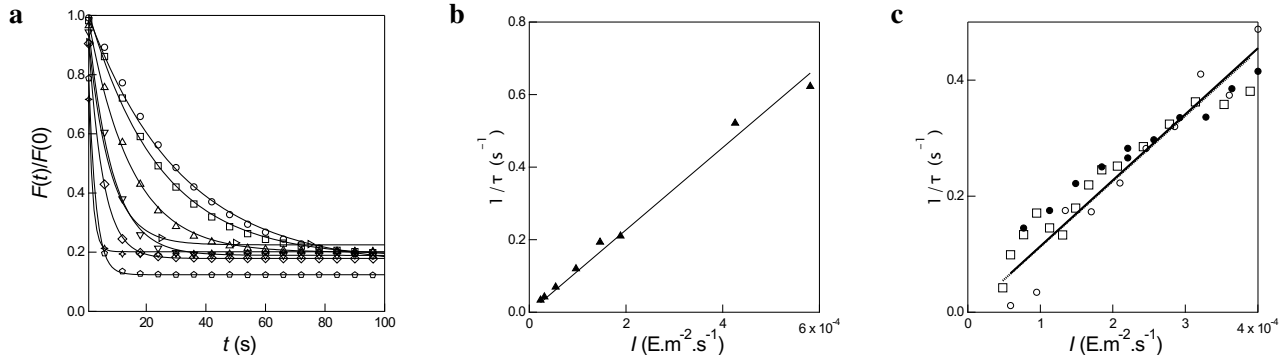

Figure S32: *Determination of the quantum yield of photoconversion of sodium 4-(4-((2Z,4E)-2-hydroxy-5-(indolin-1-yl)penta-2,4-dien-1-ylidene)-3-methyl-5-oxo-4,5-dihydro-1H-pyra-zol-1-yl)benzenesulfonate (**DASA**)*. **a**: Time evolution of the normalized fluorescence emission at 675 nm from a 40 μM **DASA** solution in a 1:50 (v/v) mixture of spectroscopy grade DMSO and acetonitrile contained in a 3 mm optical path cuvette upon illumination at various light intensities at 632 nm (in $10^{-5}\times$ E.m^{-2}.s^{-1}: 2.3, 3.1, 5.5, 9.7, 15, 19, 43, and 58). Markers: Experimental data; Solid lines: Monoexponential fit with Eq.(S1); **b**: Dependence of the inverse of the characteristic time τ retrieved in **a** from the monoexponential fit on the light intensity. Markers: Experimental data; Solid line: Linear fit. The extracted slope is 1135 m^2.mol^{-1} **c**: Dependence of the inverse of the characteristic time τ retrieved in the experiments performed on **DASA** solutions in a 1:35 (v/v) mixture of spectroscopy grade DMSO and acetonitrile contained in a 200 μm-high glass slide chamber upon illumination at various light intensities with a microscopy setup equipped with MPPC detection of the emitted fluorescence. Excitation wavelength: 630 ± 7 nm; emission wavelength: 690 ± 8 nm. Markers: The disks and the circles are associated to two series of experiments on 40 μM **DASA** solution and the squares have been recorded on a 100 μM **DASA** solution. The solid and dotted lines result from the monoexponential fit on the light intensity of the data gathered on 40 and 100 μM **DASA** solutions respectively. The extracted slopes are 1135 ± 50 and 1128 ± 40 m^2.mol^{-1} respectively.

Dependence of the quantum yield of the DASA photoconversion on the excitation wavelength Then we studied the dependence of the quantum yield of the **DASA** photoconversion on the excitation wavelength. Two different protocols have been implemented.

Decay of the DASA absorbance under illumination Figure S33a displays a representative time dependence of the absorption spectrum of 40 μM **DASA** in a 1:50 (v/v) mixture of spectroscopy grade DMSO and acetonitrile upon irradiation at constant light intensity at 632 nm. This experiment has been reproduced upon exciting at various wavelengths

while recording the light power transmitted through the 3 mm light path quartz cuvette. Then we applied the monoexponential fitting function given in Eq.(S1) to the temporal decays of the normalized absorbance at 632 nm in order to retrieve the rate constants of the photoconversion upon exciting at various wavelengths (Figure S33b). Equipped with the rate constants of the photoconversion and the light intensities (retrieved from measuring the light powers with a powermeter) measured at all the excitation wavelengths, we used Eq.(S23) to extract the dependence of the cross section of the **DASA** photoconversion on the excitation wavelength upon fixing its value to 1135 $m^2.mol^{-1}$ at 632 nm. The results are displayed in Table S6. The quantum yield of the **DASA** photoconversion is demonstrated to be essentially constant over the whole range of investigated wavelengths.

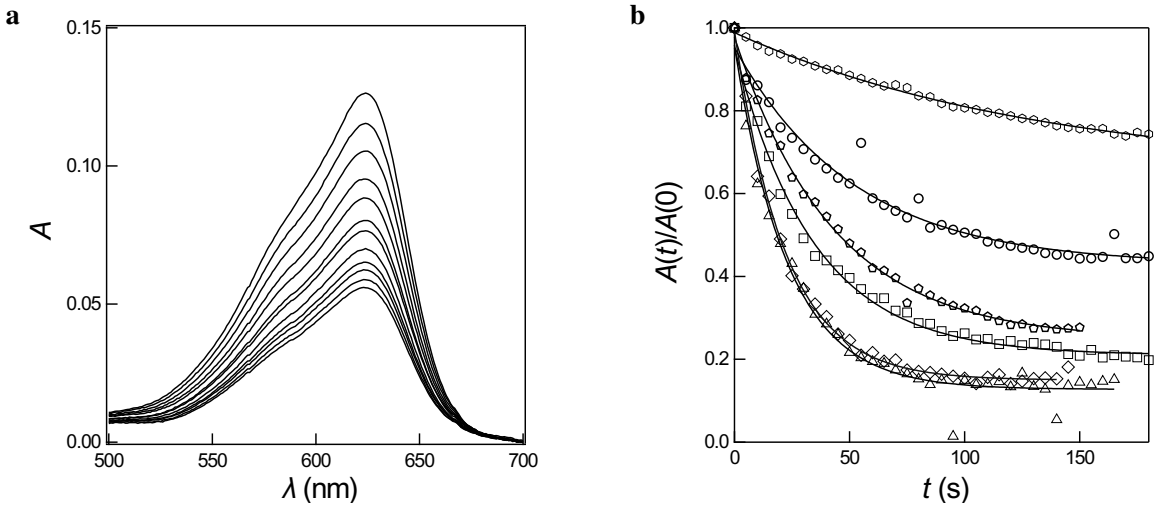

Figure S33: *Dependence of the cross section of the **DASA** photoconversion on the excitation wavelength from analyzing the decay of the **DASA** absorbance under illumination*. **a**: Time dependence of the absorption spectrum of 40 μM **DASA** in a 1:50 (v/v) mixture of spectroscopy grade DMSO and acetonitrile in a 3 mm light path quartz cuvette upon irradiation at constant light intensity at 632 nm in 5 s increments from the initial time; **b**: Time dependence of the normalized absorbance at 632 nm of 40 μM **DASA** solution in a 1:50 (v/v) mixture of spectroscopy grade DMSO and acetonitrile upon illumination at constant light intensity at 530 (circles), 560 nm (squares), 600 (triangles), 632 (diamonds), 650 (pentagons), and 670 (hexagons) nm. Markers: Experimental data; Solid lines: Monoexponential fit with Eq.(S1). $T = 293$ K.

Decay of the DASA fluorescence under illumination Figure S34 displays the time dependence of the fluorescence emission of 20 μM **DASA** in a 1:100 (v/v) mixture of spectroscopy grade DMSO and acetonitrile upon irradiation at constant light intensity at 530, 560, 600, 632, 650, and 670 nm, which have been measured from recording the light power transmitted through the 3 mm light path quartz cuvette. Then we applied the monoexponential fitting function given in Eq.(S1) to the temporal decays of the normalized fluorescence in order to retrieve the rate constants of the photoconversion upon exciting at various wavelengths. Equipped with the rate constants of the photoconversion and the light intensities (retrieved from the light powers) measured at all the excitation wavelengths, we used Eq.(S23) to extract the dependence of the cross section of the **DASA** photoconversion on the excitation wavelength upon fixing the value of the cross section of the **DASA** photoconversion to 1135 $m^2.mol^{-1}$ at 632 nm. The results are displayed in Table

S6. Again, the quantum yield of the **DASA** photoconversion is essentially constant over the whole range of investigated wavelengths. Hence, the value of the cross section for the **DASA** photoconversion can be reliably computed from the dependence of its molar absorption coefficient on the wavelength given in Eq.(S23).

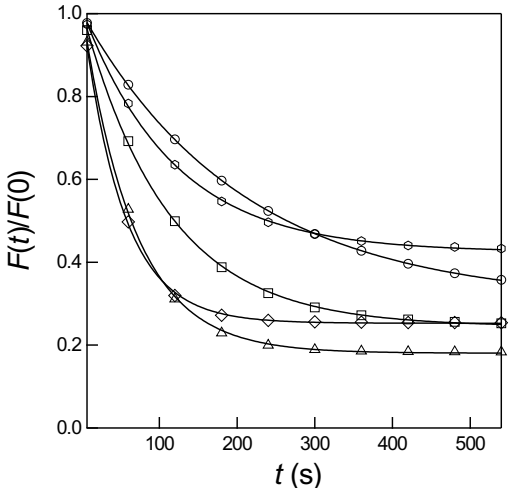

Figure S34: *Dependence of the cross section of the **DASA** photoconversion on the excitation wavelength from analyzing the drop of endogeneous fluorescence under illumination*. Time dependence of the normalized fluorescence emission of a 20 μM **DASA** solution in a 1:100 (v/v) mixture of spectroscopy grade DMSO and acetonitrile in a 3 mm light path quartz cuvette upon illumination at constant light intensity at 530 (circles), 560 nm (squares), 600 (triangles), 632 (diamonds), and 650 (hexagons) nm. Emission wavelength: 650 nm for illumination at 530, 560, 600, and 632 nm; 670 nm for 650 nm excitation; 685 nm for excitation at 670 nm. Markers: Experimental data; solid lines: Monoexponential fit with Eq.(S1). $T = 293$ K.

Estimate of the achievable measurement uncertainty on light intensity I Considering the uncertainty in the parameters (σ and τ), we estimate that the achievable measurement uncertainty on light intensity I is 20% by using **DASA**.

D.4.4 Photosynthetic apparatus (PA)

The preceding chemical actinometers provide accurate values of light intensity. However, they are effective in a rather narrow range of wavelengths, which necessitates to use several actinometers to measure light intensity over a wide range of wavelengths. We have been interested to exploit the photosynthetic apparatus as an intrinsically fluorescent actinometer, which can provide two to three orders of magnitude of light intensity over the whole 400–650 nm range.

In oxygenic photosynthetic organisms, sunlight is collected with an efficient antenna absorbing light in the whole visible wavelength range.[19] The absorbed energy is conveyed to the photosystem II and photosystem I, where it drives a charge separation accompanied by water splitting leading to oxygen evolution, followed by assimilation of carbon dioxide to produce sugars. However, a small part of the absorbed energy (a few percent) is released as fluorescence emission (mostly by chlorophylls, Chl) spanning the 650–800 nm range with an emission maximum around 680 nm at room temperature. When dark-adapted photosynthetic samples are exposed to continuous constant light, the Chl a fluorescence intensity shows characteristic changes called fluorescence transient or OJIP rise. Primarily reporting on the

Table S6: Photoconversion parameters of sodium 4-(4-((2Z,4E)-2-hydroxy-5-(indolin-1-yl)penta-2,4-dien-1-ylidene)-3-methyl-5-oxo-4,5-dihydro-1H-pyra-zol-1-yl)benzenesulfonate (**DASA**) in mixtures of spectroscopy grade DMSO and acetonitrile. The quantum yields of photoconversion, φ_A and φ_F have been respectively extracted from analyzing the decay of the absorbance at 632 nm of a 40 μM **DASA** 1:50 (v/v) DMSO:acetonitrile solution, and the decay of the fluorescence emission of a 20 μM **DASA** in 1:100 (v/v) DMSO:acetonitrile solution under monochromatic illumination at 530, 560, 600, 632, 650, and 670 nm as representatives of 530 nm – 670 nm range. φ is the mean value of φ_A and φ_F. The molar absorption coefficients $\varepsilon(\lambda_{\text{exc}})$ were extracted from the **DASA** absorption spectrum by fixing $\varepsilon(632\text{ nm}) = 87\times10^3$ $\text{M}^{-1}\text{cm}^{-1}$.[5] The cross section $\sigma(\lambda_{\text{exc}})$ was evaluated with Eq.(S23). $[I(\lambda_{\text{exc}})]$ indicates the range of reliably measurable light intensity associated to the actinometer photoconversion at λ_{exc}.

λ_{exc} (nm)	$10^4 \times \varepsilon(\lambda_{\text{exc}})$ (±0.1; $\text{M}^{-1}\text{cm}^{-1}$)	φ_F (±0.01)	φ_A (±0.01)	φ (±0.01)	$\sigma(\lambda_{\text{exc}})$ ($\pm10\%$; $\text{m}^2\text{mol}^{-1}$)	$[I(\lambda_{\text{exc}})]^a$ ($\text{E.m}^{-2}\text{.s}^{-1}$ (W.m^2))
530	1.8	0.05	0.07	0.06	255	[8-290] 10^{-5}([18-660])
560	3.5	0.05	0.08	0.07	530	[4-150] 10^{-5}([9-320])
600	7.2	0.05	0.06	0.05	885	[2-72] 10^{-5}([4-140])
632	8.7	0.06	0.06	0.06	1135	[2-60] 10^{-5}([4-110])
650	3.8	0.06	0.07	0.07	575	[3-140] 10^{-5}([6-260])
670	0.6	–[b]	0.14[c]	0.14[c]	210[c]	–

[a] The lower range of $I(\lambda_{\text{exc}})$ has been computed from Eq.(S60) upon using the values of k_{21}^{Δ} from reference[5] and $\sigma_{\text{sol}}(\lambda_{\text{exc}})$. The upper range of $I(\lambda_{\text{exc}})$ has been retrieved from using $I_{\text{sup}}(\lambda_{\text{exc}}) = I_{\text{sup}}(\lambda_{\text{exc,ref}}) \times \frac{\varepsilon(\lambda_{\text{exc,ref}})}{\varepsilon(\lambda_{\text{exc}})}$ where $\lambda_{\text{exc,ref}}$ designates the wavelength at which the extraction of the cross section of photoconversion has been performed ($\lambda_{\text{exc,ref}} = 632$ nm for **DASA**).
[b] Too slow a relaxation to be reliably measured.
[c] The slow relaxation induced a higher error on the extraction of φ_A (and subsequently of φ and $\sigma(670\text{ nm})$).

successive reduction of the electron acceptors of the photosynthetic electron transport chain, the chlorophyll fluorescence intensity rises in less than 1 s from a minimum level (the O level) to a maximum level (P). Depending on the light level and the experimental conditions, the curve displays one, two or three intermediate steps identified as local maxima labeled K, J and I, and subsequently decays over a few minutes.[20] The first step systematically reflects the light-limited reaction (reduction of the electron acceptor Qa). This so-called photochemical phase, linearly depends on the intensity of the exciting light.[21,22] Moreover, its value does not significantly depend on the nature of the photosynthetic organism,[8] so as to facilitating getting samples for light measurement.

Conditioning of the PA-containing samples The production of the **PA**-containing samples is reported in subsection 1.4. All the samples have been submitted to darkness for 15 min before starting the illumination experiments.

Fluorescence excitation and emission spectra of PA Photosynthetic organisms collect sunlight over the whole visible wavelength range by means of an antenna integrating multiple chromophores. The associated energy is subsequently funneled to the reaction center, where the charge separation governing photosynthesis occurs. Considering that fluorescence emission is a side-product of the light-driven process of charge separation driving the initial step of **PA** fluorescence rise under constant illumination, we recorded the fluorescence excitation spectrum of a culture of *Chlamydomonas reinhardtii (CC_124)* in exponential growth phase (Figure S35). It exhibits strong values in the purple-blue and red wavelength ranges and a minimum at green wavelengths.

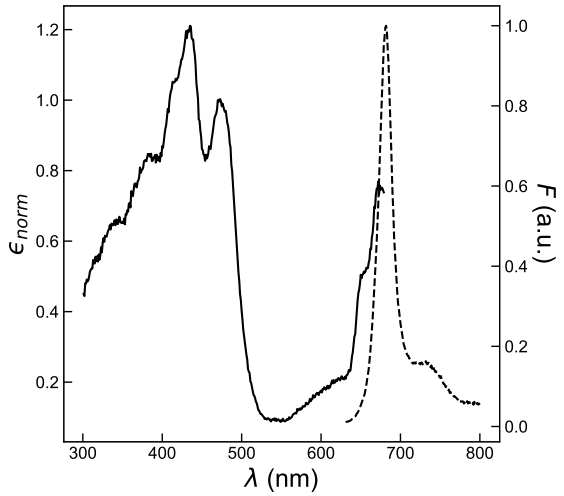

Figure S35: *Fluorescence excitation and emission spectra of **PA***. Normalized fluorescence excitation $\epsilon_{\rm norm}$ (solid line; $\lambda_{\rm em} = 690 \pm 2$ nm, normalized at 470 nm) and emission $F_{\rm norm}$ (dotted line; $\lambda_{\rm exc} = 470 \pm 2$ nm) spectra of a culture of *Chlamydomonas reinhardtii (CC_124)* in exponential growth phase. $T = 293$ K. The excitation spectrum has been normalized at 470 nm.

Determination of the cross section of PA photoconversion at 470 nm We then evaluated the cross section of **PA** photoconversion associated to the initial step of **PA** fluorescence rise from dark acclimated cells of *Chlamydomonas reinhardtii (CC_124)* (in exponential phase in minimal media) upon applying a 0.3–1 s-long[26] pulse of constant light at 470±10 nm. Figure S36a displays representative time evolutions of the normalized fluorescence emission at 470±10 nm from the dark acclimated cells observed with the photodetector under the epifluorescence microscope.[27]

After setting time zero to fluorescence crossing a threshold above zero corresponding to the light turning on and logarithmically subsampling the data to allow us for faster fitting, the fit of the time evolutions of the normalized fluorescence emission was performed stepwise:

- In a first step, we followed the analysis reported in reference[8] and applied an unsupervised fit with Eq.(S84)

$$F(t) \;=\; F(0) + A_{\rm OJ}\left(1 - e^{-t/\tau_{\rm OJ}}\right)^{s_{\rm OJ}} + A_{\rm JI}\left(1 - e^{-t/\tau_{\rm JI}}\right)^{s_{\rm JI}} + A_{\rm IP}\left(1 - e^{-t/\tau_{\rm IP}}\right)^{s_{\rm IP}} \qquad \text{(S84)}$$

  in order to retrieve a first estimate of the value of the characteristic time $\tau_{\rm OJ}$ associated to the initial step of **PA** fluorescence rise ;

- In a second step, we restricted the time window to [0;3$\tau_{\rm OJ}$] and applied the fit given in Eq.(S85) to the time evolution of the fluorescence emission

$$F(t) \;=\; F(0) + A\left(1 - e^{-t/\tau}\right)^{s} \qquad \text{(S85)}$$

[26] Depending on the light level.

[27] Recording started 10 ms before the LED was turned on. The rise-time of the LED is always faster than 1 μs while the dynamics of the initial step of **PA** fluorescence rise is in the tenths of microseconds range. Therefore the rise time of the LED does not interfere with the recording of the fluorescence rise dynamics.

upon fixing $s = 1.24$[8] in order to retrieve a second estimate of the value of the characteristic time τ associated to the intial rise of the **PA** fluorescence;

- In the last step, we restricted the time window to [0;5τ], applied the fit given in Eq.(S85) to the time evolution of the fluorescence emission upon adopting the values of parameters extracted during the second step as starting values, and retrieved the final value of the characteristic time τ associated to the initial step of **PA** fluorescence rise .

This fitting protocol was found relevant as displayed in Figures S36a,b. Moreover it was typically found accurate above 50 μE.m^{-2}.s^{-1} under blue illumination.

As displayed in Figure S36c, the inverse of the characteristic time of the photoconversion associated to the initial step of **PA** fluorescence rise linearly depends on the light intensity. This behavior demonstrates that the process driving the initial step of **PA** fluorescence rise evolution is photochemical at least up to 10^{-2} E.m^{-2}.s^{-1} light intensity. It also enabled us to retrieve $(1.8 \pm 0.1)\times10^6$ m^2.mol^{-1} as the cross section of **PA** photoconversion associated to the initial step of **PA** fluorescence rise from the slope.

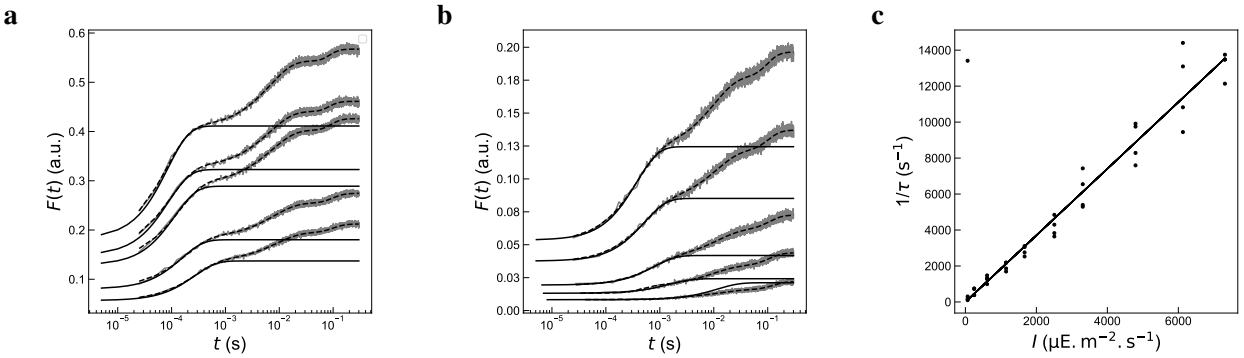

Figure S36: *Determination of the cross section associated with the initial step of **PA** fluorescence rise from dark acclimated microalgae (Chlamydomonas reinhardtii (CC_124) in exponential phase in minimal media) cells upon constant illumination at 470±10 nm.* **a,b**: Time evolution of the **PA** fluorescence emission under constant illumination at 470 nm in the epifluorescence microscope at various light intensities (previously calibrated with **Dronpa-2**) in the field of view. **a**: 7300, 6100, 4800, 3300, 2500 μE.m^{-2}.s^{-1}; **b**: 1700, 600, 250, 60 μE.m^{-2}.s^{-1}. A moving average was applied on the experimental data (grey markers) before subsampling with window sizes of 50 and 10 for the fits given in Eq.(S84) (dashed lines) and (S85) (solid lines) respectively to retrieve the characteristic time $\tau(\mu s)$= 74, 76, 100, 134, 232, 327, 455, 676, 1320, 11000 associated to the initial step of **PA** fluorescence rise ; **c**: Light intensity-dependence of the inverse of the characteristic time τ associated to the initial step of **PA** fluorescence rise , which was retrieved from the monoexponential fit on the light intensity in the range 60–7300 μE.m^{-2}.s^{-1} by using the 470±10 nm LED of the epifluorescence microscope. Markers: experimental data, solid line: linear fit (slope $\sigma(470) = (1.8 \pm 0.1)\times10^6$ m^2.mol^{-1}).

Dependence of the cross section of the PA photoconversion on the excitation wavelength The dependence of the cross section of the **PA** photoconversion on the excitation wavelength has been further investigated with the epifluorescence setup at two other wavelengths from two different LEDs (6 repeats: 3 with the strain CC_124 and 3 with the strain $WT4A$):

- A purple LED emitting at 405±7 nm. It was calibrated with a **Dronpa-2** solution as an actinometer[9] and used in the range 250–4000 μE.m^{-2}.s^{-1} (80–1200 W.m^{-2});
- A red-orange LED emitting at 650 nm. It was calibrated with the powermeter and used in the range 200–6500 μE.m^{-2}.s^{-1} (40–1200 W.m^{-2});

with collection of emitted fluorescence at 690 nm.

From the dependence of the inverse of the characteristic time on the light intensity (data not shown), we obtained (2.0± 0.06)×10^6 m^2.mol^{-1} and (1.0± 0.02)×10^6 m^2.mol^{-1} associated to the purple and and red-orange lights respectively.

Upon fixing the value of the cross section of the **PA** photoconversion to 2.0×10^6 m^2.mol^{-1} at 470 nm as a reference, we could scale the fluorescence excitation spectrum displayed in Figure S35 in order to generate the scaled fluorescence excitation spectrum $\sigma_{\mathrm{mic}}(\lambda)$ (see Figure S37). Figure S37 further displays the set of cross sections that have been directly measured in the preceding experiments. The fair observed agreement between the prediction from the scaled fluorescence excitation spectrum and the experimental values suggests the former to be relevant for retrieving the cross section of the **PA** photoconversion in the [400 nm; 650 nm] wavelength range.

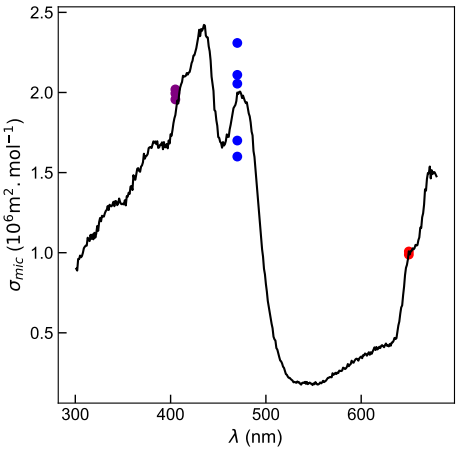

Figure S37: *Fluorescence excitation spectrum* $\sigma_{\mathrm{mic}}(\lambda_{\mathrm{exc}})$ *of* ***PA*** *in Chlamydomonas reinhardtii (CC_124)* ($\lambda_{\mathrm{em}} = 690$ nm). Scaling reference: $\sigma(470)$ = 2.0 ×10^6 m^2.mol^{-1}. The color markers represent the $\sigma(\lambda_{exc})$ measured experimentally using three LEDs.

Table S7 sums up the relevant parameters which have to be used for measuring the light intensity at various wavelengths with the **PA** actinometer.

Estimate of the achievable measurement uncertainty on light intensity I Considering the uncertainty in the parameters (σ and τ) and the specific nature of the fitting function applied to the time evolution of the fluorescence signal, we estimate that the achievable measurement uncertainty on light intensity I is 70% by using **PA**.

Table S7: *Photoconversion parameters associated to the initial step of **PA** fluorescence rise* . The normalized excitation coefficient $\epsilon_{\rm norm}(\lambda_{\rm exc})$ was extracted from the **PA** fluorescence excitation spectrum displayed in Figure S35. The cross sections $\sigma(\lambda_{\rm exc})$ and $\sigma_{\rm mic}(\lambda_{\rm exc})$ have respectively been measured (see Figure S37) and computed at 405 and 650 nm from using the excitation spectra of the dark acclimated *Chlamydomonas reinhardtii (CC_124)* cells (in exponential phase in minimal media) upon fixing the value of the cross section of the **PA** photoconversion to 2.0 $\times 10^6$ $\rm m^2.mol^{-1}$ at 470 nm. $I_{\rm sup}(\lambda_{\rm exc})$ indicates the upper light intensity tested and relevant for a reliable measurement.

$\lambda_{\rm exc}$ (nm)	$\epsilon_{\rm norm}(\lambda_{\rm exc})$	$\sigma(\lambda_{\rm exc})$ ($10^6 \rm m^2 mol^{-1}$)	$\sigma_{\rm mic}(\lambda_{\rm exc})$ ($10^6 \rm m^2 mol^{-1}$)	$I_{\rm sup}(\lambda_{\rm exc})$ ($\rm E.m^{-2}.s^{-1}$ ($\rm W.m^2$))
405	1.0 ± 0.05	2.0 ± 0.06	2.0 ± 0.4^a	$10^{-2}(3000)^b$
470	1.0 ± 0.05	2.0 ± 0.4	2.0 ± 0.4^a	$10^{-2}(2600)^b$
650	0.55 ± 0.05	1.0 ± 0.02	1.1 ± 0.4^a	$10^{-2}(1900)^b$

[a] Estimated from 6 repeats at 470 nm on two different *Chlamydomonas reinhardtii* strains.

[b] Extracted from the value of $I_{\rm sup}(\lambda_{\rm exc})$ by using $I_{\rm sup}(\lambda_{\rm exc}) = I_{\rm sup}(\lambda_{\rm exc,ref}) \times \frac{\epsilon(\lambda_{\rm exc,ref})}{\epsilon(\lambda_{\rm exc})}$ where $\lambda_{\rm exc,ref}$ designates the wavelength at which the extraction of the cross section of photoconversion has been performed ($\lambda_{\rm exc,ref} = 470$ nm for **PA**).

D.5 Combination of a non-fluorescent actinometer with a fluorescent reporter

D.5.1 α-(4-Diethylamino)phenyl)-N-phenylnitrone (Nit)

This actinometer has been thoroughly investigated.[12,23] It has been shown to irreversibly convert into N-(p-dimethylamino-phenyl)formanilide in ethanol under illumination in the UV A wavelength range.

Preparation of the Nit solutions The synthesis of α-(4-diethylamino)phenyl)-N-phenylnitrone (**Nit**) actinometer is reported in the subsection 1.2.2. Stock solutions of α-(4-diethylamino)phenyl)-N-phenylnitrone (3.0 mg/ml; 12.5 mM) and Rhodamine B (2.9 mg/mL; 6 mM) were produced in spectrograde ethanol. They can be kept under the protection of ambient light (container covered with an Aluminium foil) at -20 $^{\rm o}$C for up to two weeks. They were subsequently diluted in spectrograde ethanol to produce the final solutions upon taking care to exhibit an absorbance at the absorption maximum lower or equal to 0.15.

Absorption and emission spectra of Nit In ethanol, the **Nit** open state absorbs light between 320 and 430 nm. Rhodamine B emits fluorescence emission, which peaks at 574 nm and extends from 550 up to 650 nm (see Figure S38).

Determination of the quantum yield of Nit photoconversion in ethanol at 405 nm The value of the quantum yield of the **Nit** photoconversion has been already measured to be 0.16 at 365 nm.[23] In this manuscript, we independently evaluated this value at 405 nm. We also examined whether there is a possible upper range of light intensity beyond which the photochemical step is not anymore rate-limiting in the light-driven **Nit** conversion into N-(p-dimethylaminophenyl)formanilide in ethanol.

Figure S39a displays the time dependence of the fluorescence emission of 14 μM **Nit** and 1.0 μM **RhB** in spectroscopy grade ethanol upon irradiation at various light intensities at 405 nm, which have been measured from analyzing the time

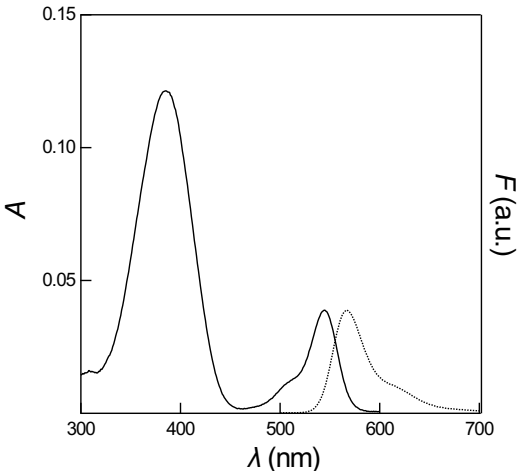

Figure S38: Absorption (solid line) and emission (dotted line; $\lambda_{\rm exc} = 384$ nm) spectra of 14 μM **Nit** and 1 μM **RhB** solution in EtOH recorded in a 1×1 cm^2 quartz cuvette. $T = 293$ K.

recovery of the fluorescence signal from 488 nm-photoswitched **Dronpa-2** upon illumination at 405 nm.[7,9] Then we applied the monoexponential fitting function given in Eq.(S1) to the temporal rises of the normalized fluorescence at 574 nm in order to retrieve the characteristic times of the photoconversion τ upon exciting at various light intensities. As displayed in Figure S39b, the inverse of the characteristic times of the photoconversion linearly depends on the light intensity. This behavior demonstrates that the rate limiting step of **Nit** photoconversion in ethanol is photochemical at least up to 7 10^{-4} E.m^{-2}.s^{-1} light intensity. Eq.(S23) was used to retrieve $\sigma = 1005 \pm 30$ m^2.mol^{-1} from the slope. Equipped with the latter value of the cross section for the photoconversion and the value of the molar absorption coefficient of **Nit** at 405 nm (3.1 10^4 M^{-1}.cm^{-1} = 3.1 10^3 m^2.mol^{-1}), we used Eq.(S23) to extract $\varphi_F = 0.14 \pm 0.02$ as the value of the quantum yield of the **Nit** photoconversion at 405 nm.

Dependence of the quantum yield of the Nit photoconversion on the excitation wavelength Then we studied the dependence of the quantum yield of the **Nit** photoconversion on the excitation wavelength. Two different protocols have been implemented.

Decay of the Nit absorbance under illumination Figure S40a displays a representative time dependence of the absorption spectrum of 5.8 μM **Nit** in spectroscopy grade ethanol upon irradiation at constant light intensity at 365 nm. This experiment has been reproduced upon exciting at various wavelengths while recording the light power transmitted through the 1 cm light path quartz cuvette. Then we applied the monoexponential fitting function given in Eq.(S86)

$$\frac{A(\lambda_{\rm exc},t)}{A(\lambda_{\rm exc},0)} = \frac{A(\lambda_{\rm exc},\infty)}{A(\lambda_{\rm exc},0)} + \left[1 - \frac{A(\lambda_{\rm exc},\infty)}{A(\lambda_{\rm exc},0)}\right] \exp(-t/\tau) \tag{S86}$$

to the temporal decays of the normalized absorbance at 383 nm in order to retrieve the rate constants of the photoconversion upon exciting at various wavelengths (Figure S40b). Equipped with the rate constants of the photoconversion and the light intensities (retrieved from the light powers) measured at all the excitation wavelengths, and the dependence of the

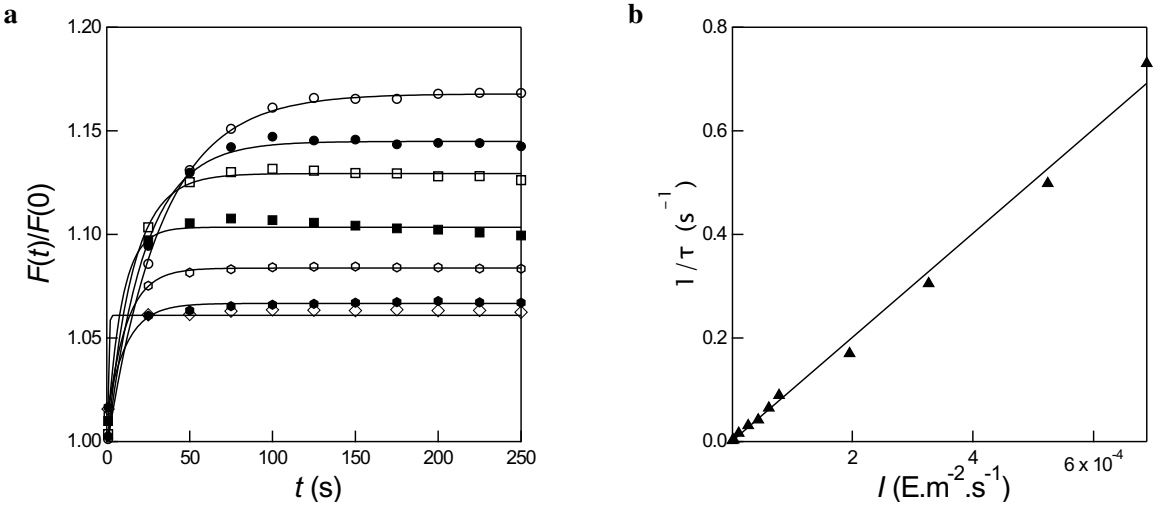

Figure S39: *Determination of the cross section for the photoconversion of α-(4-diethylamino)phenyl)-N-phenylnitrone (**Nit**) into N-(p-dimethylaminophenyl)formanilide in ethanol at 405 nm.* **a**: Time evolution of the normalized fluorescence emission at 574 nm from a 14 μM **Nit** and 1.0 μM **RhB** in spectroscopy grade ethanol contained in a 1×1 cm^2 quartz cuvette upon irradiation at constant light intensity at 405 nm at various light intensities (in 10^{-5} E.m^{-2}.s^{-1}): 2.7 (circles), 4.4 (disks), 6.2 (empty squares), 7.9 (filled squares), 33 (empty hexagons), 52 (diamonds), and 69 (filled hexagons). Markers: Experimental data; Solid lines: Monoexponential fit with Eq.(S1); **b**: Dependence of the inverse of the characteristic time τ retrieved in **a** from the monoexponential fit on the light intensity. Markers: Experimental data; Solid line: Linear fit. The extracted slope is 1005 ± 30 m^2.mol^{-1}.

molar absorption coefficient of **Nit** on the wavelength, we used Eq.(S23) to extract the dependence of the quantum yield of the **Nit** photoconversion on the excitation wavelength upon fixing the value of the quantum yield of the **Nit** photoconversion to 0.14 at 405 nm. The results are displayed in Table S8. The 0.15 value measured at 365 nm is in fair agreement with the 0.16 reported value at the same wavelength.[23] Moreover, the quantum yield of the **Nit** photoconversion is essentially constant over the whole range of investigated wavelengths.

Rise of the RhB fluorescence under illumination Figure S41 displays the time dependence of the fluorescence emission of 5.8 μM **Nit** and 1.0 μM **RhB** in spectroscopy grade ethanol upon irradiation at constant light intensity at 365, 380, 400, and 420 nm, which have been measured from recording the light power transmitted through the 1 cm light path quartz cuvette. Then we applied the monoexponential fitting function given in Eq.(S1) to the temporal rises of the normalized fluorescence at 574 nm in order to retrieve the rate constants of the photoconversion upon exciting at various wavelengths (Figure S41). Equipped with the rate constants of the photoconversion and the light intensities (retrieved from the light powers) measured at all the excitation wavelengths, and the dependence of the molar absorption coefficient of **Nit** on the wavelength, we used Eq.(S23) to extract the dependence of the quantum yield of the **Nit** photoconversion on the excitation wavelength upon fixing the value of the quantum yield of the **Nit** photoconversion to 0.14 at 405 nm. The results are displayed in Table S8. The 0.19 value measured at 365 nm is in fair agreement with the 0.16 reported value at the same wavelength.[23] Moreover, the quantum yield of the **Nit** photoconversion is again essentially constant over the whole range of investigated wavelengths.

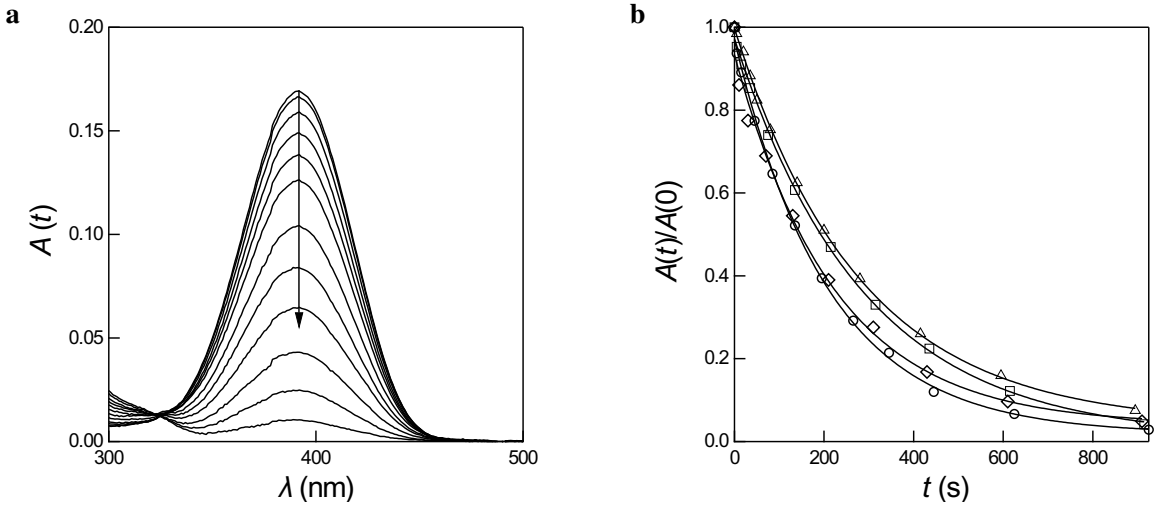

Figure S40: *Dependence of the quantum yield of the **Nit** photoconversion on the excitation wavelength from analyzing the decay of the **Nit** absorbance under illumination*. **a**: Time dependence of the absorption spectrum of 5.8 μM **Nit** in spectroscopy grade ethanol through the 1 cm light path quartz cuvette upon irradiation at constant light intensity at 365 nm. t(s): 0, 5, 20, 35, 50, 80, 140, 200, 280, 415, 595, and 895; **b**: Time dependence of the normalized absorbance at 383 nm of 5.8 μM α-(4-Diethylamino)phenyl)-N-phenylnitrone (**Nit**) in spectroscopy grade ethanol upon illumination at constant light intensity at 365 (diamonds), 380 nm (disks), 400 (diamonds) and 430 (squares) nm. Markers: Experimental data; solid lines: Monoexponential fit with Eq.(S86). $T = 293$ K

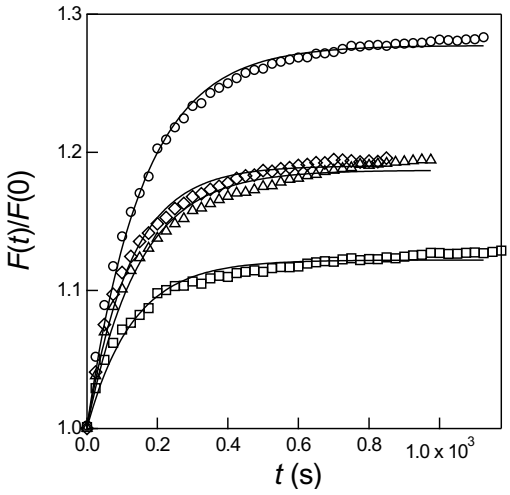

Figure S41: *Dependence of the quantum yield of the **Nit** photoconversion on the excitation wavelength from analyzing the rise of the **RhB** fluorescence under illumination*. Time dependence of the normalized fluorescence emission at 574 nm of a 5.8 μM **Nit** and 1μM **RhB** solution in spectroscopy grade ethanol through the 1 cm light path quartz cuvette upon illumination at constant light intensity at 365 (triangles), 380 nm (circles), 400 (diamonds) and 420 (squares) nm. Markers: Experimental data; solid lines: Monoexponential fit with Eq.(S86). $T = 293$ K.

Estimate of the achievable measurement uncertainty on light intensity I Considering the uncertainty in the parameters (σ and τ), we estimate that the achievable measurement uncertainty on light intensity I is 20% by using **Nit**.

Table S8: Photoconversion parameters of α-(4-diethylamino)phenyl)-N-phenylnitrone (**Nit**) in ethanol. The quantum yields of photoconversion, φ_A and φ_F have been respectively extracted from analyzing the decay of the absorbance at 383 nm of a 5.8 μM **Nit** solution in ethanol, and the rise of the fluorescence emission at 574 nm of a 5.8 μM **Nit** and 1μM **RhB** solution in ethanol under monochromatic illumination at 365, 380, 400, and 420 nm as representatives of 320 nm – 430 nm range. φ is the mean value of φ_A and φ_F. The molar absorption coefficients $\varepsilon(\lambda_{\rm exc})$ were extracted from the **Nit** absorption spectrum by using the Beer-Lambert law. The cross section $\sigma(\lambda_{\rm exc})$ was evaluated with Eq.(S23). $I_{\rm sup}(\lambda_{\rm exc})$ indicates the upper light intensity tested and relevant for a reliable measurement .

$\lambda_{\rm exc}$ (nm)	$10^4 \times \varepsilon(\lambda_{\rm exc})$ ($\pm$0.1; $M^{-1}cm^{-1}$)	φ_F ($\pm$0.02)	φ_A ($\pm$0.02)	φ ($\pm$0.02)	$\sigma(\lambda_{\rm exc})$ ($\pm$10%; m^2mol^{-1})	$I_{\rm sup}(\lambda_{\rm exc})$ ($E.m^{-2}.s^{-1}$($W.m^{-2}$))
365	2.2	0.24	0.15	0.19	960	11 10^{-4}(360)[a]
380	3.4	0.13	0.18	0.15	1200	7.2 10^{-4}(230)[a]
400	3.5	0.14	0.14	0.14	1100	7.0 10^{-4}(200)[a]
420	2.0	0.20	0.20	0.20	850	12 10^{-4}(340)[a]

[a] Extracted from the value of $I_{\rm sup}(\lambda_{\rm exc})$ by using $I_{\rm sup}(\lambda_{\rm exc}) = I_{\rm sup}(\lambda_{\rm exc,ref}) \times \frac{\varepsilon(\lambda_{\rm exc,ref})}{\varepsilon(\lambda_{\rm exc})}$ where $\lambda_{\rm exc,ref}$ designates the wavelength at which the extraction of the cross section of photoconversion has been performed ($\lambda_{\rm exc,ref} = 405$ nm for **Nit**).

D.6 DDAO for transferring information on light intensity from a wavelength to another

One current operation on an optical setup is to transfer available information on light intensity from a wavelength to another. This is especially attractive in the orange and red wavelength range, where fluorescent actinometers are scarce and often exhibit a poor quantum yield of fluorescence. **DDAO** [7-hydroxy-9H-(1,3-dichloro-9,9-dimethylacridin-2-one)][24,25] is here an attractive fluorophore for transferring information on light intensity from a wavelength to another along the principle exposed in the Main Text. It is commercially available and exhibits a broad absorption band essentially covering the whole visible wavelength range after ionization of its phenol group obtained at pH$\geq$6.[25]

D.6.1 Preparation of the DDAO solutions

In a first step, we produced a 52 mM **DDAO** solution in DMSO by dissolving 0.8 mg of DDAO in 55 μg of spectrograde DMSO.[25] This mother solution was then diluted in an aqueous HEPES pH 7.9 buffer (100 mM NaCl, 5 mM NaOH, 10 mM HEPES) to reach 9 μM (see Figure S42).

D.6.2 Absorption and fluorescence emission spectra of DDAO

DDAO exhibits a broad absorption band between 450 and 650 nm and strongly emits fluorescence between 640 and 700 nm in HEPES pH 7.4 buffer. Table S9 reports on the dependence of the molar absorption coefficient of **DDAO** on the wavelength.

D.6.3 Validation of DDAO as light intensity-transferring fluorophore

We first checked that the quantum yield of fluorescence of **DDAO** did not depend on the excitation wavelength in its absorption band in the visible wavelength range as evidenced by the similarity of its absorption and normalized fluorescence excitation spectra (see Figure S2b). Hence, **DDAO** was shown to obey the Kasha's rule, which enables us to exploit

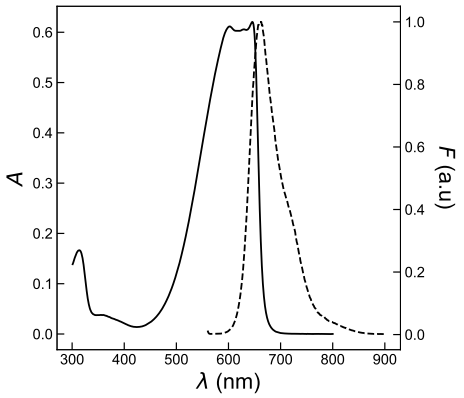

Figure S42: Absorption (solid line) and emission (dotted line; $\lambda_{\text{exc}} = 600$ nm) spectra of 9 μM **DDAO** in an aqueous pH 7.9 HEPES buffer (100 mM NaCl, 5 mM NaOH, 10 mM HEPES) recorded in a 1×1 cm^2 quartz cuvette. $T = 293$ K.

Table S9: Dependence of the molar absorption coefficient $\varepsilon(\lambda_{\text{exc}})$ of **DDAO** on the wavelength. Solvent: Aqueous HEPES pH 7.9 buffer (100 mM NaCl, 5 mM NaOH, 10 mM HEPES).

λ_{exc} (nm)	$10^{-4} \times \varepsilon(\lambda_{\text{exc}})$ ($\text{M}^{-1}\text{cm}^{-1}$)
450	0.09 ± 0.01
470	0.18 ± 0.02
490	0.34 ± 0.04
510	0.60 ± 0.08
530	0.98 ± 0.13
550	1.44 ± 0.19
570	1.89 ± 0.24
590	2.24 ± 0.29
610	2.31 ± 0.30
630	2.31 ± 0.30
650	2.27 ± 0.30
670	0.21 ± 0.03

Eq.(S70) to transfer information on light intensity from one wavelength to another.

Then two series of experiments have been further performed in different regimes of light intensity to validate the relevance of **DDAO** as light intensity-transferring fluorophore.

Regime of low light intensity This series of experiments has been performed on the epifluorescence microscope by measuring the dependence of the **DDAO** fluorescence collected by the camera with a 775/140 band-pass filter on the light intensity from LEDs at 405$\pm$7 nm, 470$\pm$10 nm, 550$\pm$6 nm, and 630$\pm$9 nm evaluated by the current applied to feed the LEDs using the LED driver (DC4104, Thorlabs, NJ).

We first used the LED emitting at 405$\pm$7 nm (Figure S43a). For each applied voltage, we

- linked the **DDAO** fluorescence intensity to the light intensity, which was measured with the **Dronpa-2** actinometer;
- further measured the light intensity with the powermeter by using the protocol reported in subsection D.3.1.

Then we turned to the LEDs emitting at 470±10 nm (Figure S43b), 550±6 nm (Figure S43c), and 630±9 nm (Figure S43d). For each applied voltage, we

- measured the **DDAO** fluorescence intensity and used Eq.(S70) to retrieve the light intensity;
- further measured the light intensity with the powermeter and an actinometer (**Dronpa-2** at 470±10 nm and **DASA** at 630±9 nm).

From examining Figures S43a–d, we concluded that:

- the light intensity linearly depends on the applied voltage for all the investigated LEDs;
- the **DDAO** fluorescence intensity provides consistent values of the light intensity with the measurements made with the fluorescent actinometers and the powermeter thereby validating its relevance.

Regime of high light intensity In a second series of experiments, we established the dependence of the fluorescence intensity at 650 nm from a 10 nM **DDAO** solution in 50 mM CHES buffer pH 9.3 on the light intensity of the focused 488 nm laser of our photoswitchometer,[9] which was measured with the powermeter.

In a first step, we measured the beam waist of the focused 488 nm laser by Fluorescence Correlation Spectroscopy (FCS). The time dependence of the autocorrelation function extracted from a 3.4 nM Fluorescein solution in 50 mM CHES buffer pH 9.3 is displayed in Figure S44a. It was fitted with the theoretical expression of the autocorrelation function involving 2D diffusion and the formation of the triplet state given in Eq.(S87) in which τ_D, τ_T, and A_T designate the diffusion time through the beam waist, the relaxation time of the fluorophore triplet state, and an amplitude fitting parameter.

$$G(\tau) \quad = \quad G(0) \times \left(1 + \frac{\tau}{\tau_D}\right)^{-1} \times \left[1 + A_T \exp\left(-\frac{\tau}{\tau_T}\right)\right] \tag{S87}$$

By using $D_{\rm Fluo} = 4.25\ 10^{-10}$ m^2.s^{-1} for the value of the diffusion coefficient of Fluorescein in water at 298 K,[26] we extracted the lateral extension of the beam waist $\omega_{\rm xy} = 2\,(D_{\rm Fluo}\tau_D)^{0.5} = 0.26$ μm from the $\tau_D = 40$ μs value retrieved from the fit. Equipped with the $\omega_{\rm xy}$ value, we recorded the time dependence of the autocorrelation function extracted from a 10 nM DDAO solution in 50 mM CHES buffer pH 9.3 (see Figure S44b). No significant formation of a triplet state could be observed and we fitted experimental data with Eq.(S88).

$$G(\tau) \quad = \quad G(0) \times \left(1 + \frac{\tau}{\tau_D}\right)^{-1} \tag{S88}$$

From the retrieved diffusion time $\tau_D = 29$ μs value and the knowledge of $\omega_{\rm xy} = 0.26$ μm, we extracted $D_{\rm DDAO} = 5.8$ 10^{-10} m^2.s^{-1} for the value of the diffusion coefficient of **DDAO** in water at 293 K.

Equipped with the surface of the laser beam at the beam waist, we could investigate the dependence of the **DDAO** fluorescence signal on the light intensity of the laser measured with the powermeter. As displayed in Figure S45, the

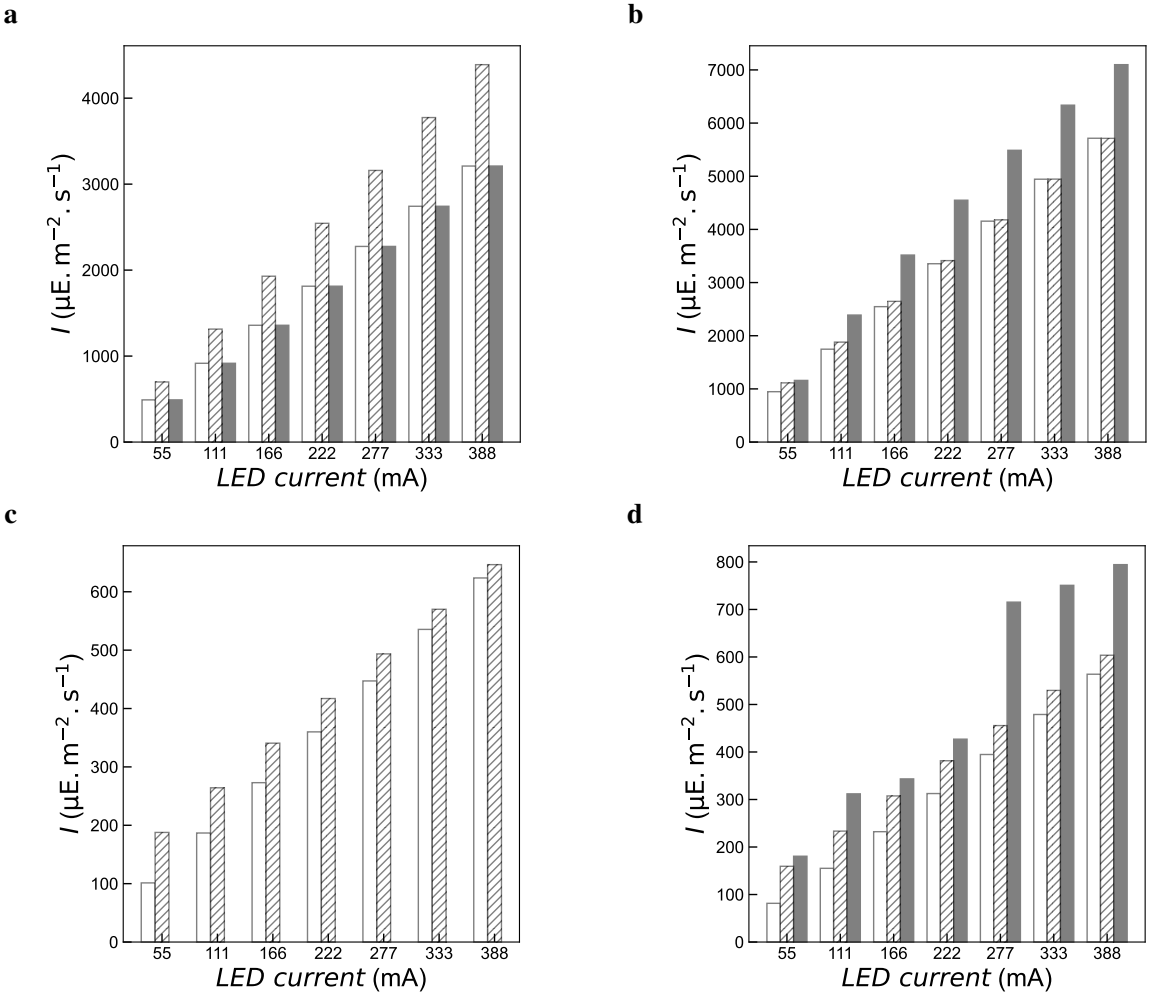

Figure S43: *Validation of **DDAO** as light intensity-transferring fluorophore in a regime of low light intensity*. Dependence of the light intensity from LEDs at 405±7 nm (**a**), 470±10 nm (**b**), 550±6 nm (**c**), and 630±9 nm (**d**) on the voltage applied to feed the LEDs as retrieved from using the **DDAO** fluorescence intensity (**a**–**d**, white bar), actinometers (**Dronpa-2** in **a** and **b**, **DASA** in **d**, black bar), and the powermeter (**a**–**d**, striped bar), using the protocol described in subsection D.3.1. $T = 293$ K.

observed dependence is linear up to 1500 kW.cm^{-2} (6 10^4 E.m^{-2}.s^{-1}) and then saturates. Such a threshold is higher than the maximal light flux generated on a regular confocal microscope.

As a conclusion, **DDAO** is validated as light intensity-transferring fluorophore for most current microscopy setups with one-photon excitation.

Estimate of the achievable measurement uncertainty on light intensity I Considering the uncertainty in the parameters (σ and τ) exploited to acquire light intensity at a reference wavelength by using a fluorescent actinometer, we estimate that the achievable measurement uncertainty on light intensity I is 20% by using **DDAO**.

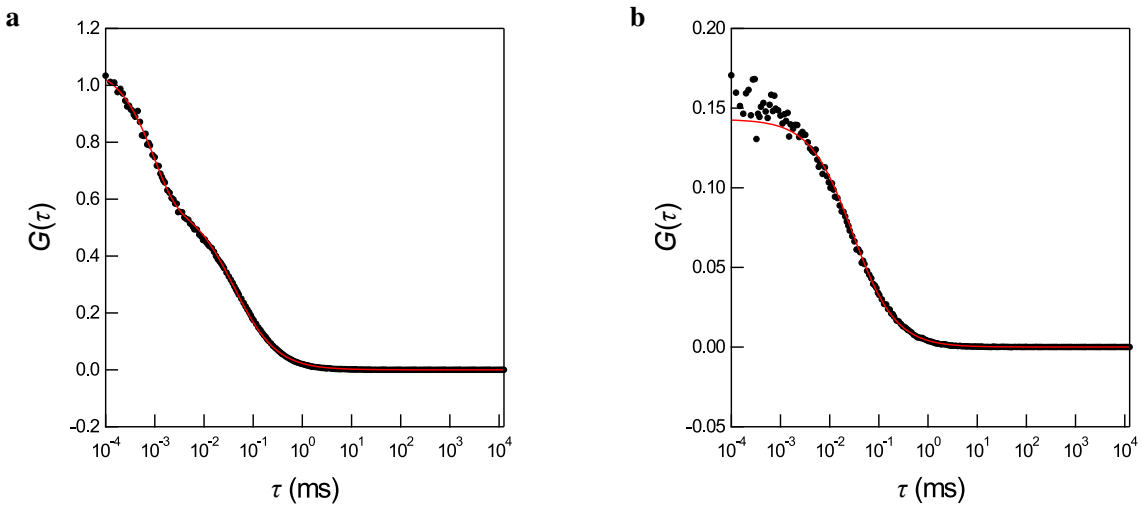

Figure S44: *FCS autocorrelation curves recorded at 293 K from 3.4 nM Fluorescein (**a**) and 10 nM **DDAO** (**b**)*. Markers: Experimental data; Lines: Fits according to Eqs.(S87,S88) for Fluorescein and **DDAO** respectively, which yield $G(0) = 0.59$, $\tau_D = 40$ μs, $\tau_T = 1.0$ μs, and $A_T = 0.8$ for Fluorescein, and $G(0) = 0.14$ and $\tau_D = 29$ μs for **DDAO**. Solvent: 50 mM CHES buffer pH 9.3. $T = 293$ K.

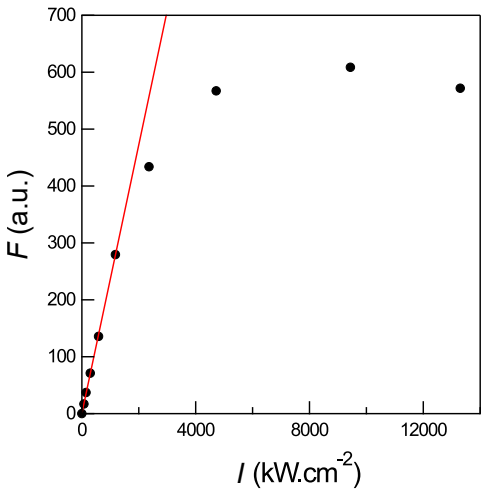

Figure S45: *Validation of **DDAO** as light intensity-transferring fluorophore in a regime of high light intensity*. Dependence of the fluorescence intensity at 650 nm from a 10 nM **DDAO** solution in 50 mM CHES buffer pH 9.3 on the light intensity of the 488 nm laser, which was measured with the powermeter. Markers: Experimental data; solid line: Linear fit. $T = 293$ K.

E Validation of the extraction of the light intensity in fluorescence imaging

E.1 Fluorescence macroimager

The first protocol for light intensity measurement was validated in wide-field imaging by applying it in the case of a macroscope setup described in subsection D.3.2 whose illumination comes in from an angle, causing an intensity gradient at the sample, and comparing the obtained results to ones obtained through an optical simulation combined with a power

meter reading.

A model of the illumination system was created and run using the optical design software package Optic Studio 18.9 (Zemax LLC, Kirkland, WA, US). The file corresponding to this is provided in Figure S46. A 3D view of the model within the software is shown at the top of Figure S46, while a CAD model, created in Rhinocerous 3D, is provided at the bottom of the same figure – to provide information on the relative spacing between the components. The corresponding Optic Studio (or Zemax) file is additionally provided (Macroscope/MACRO_Zemax.zmx). The optical components modelled are detailed in the subsection D.3.2. In this case however, an excitation filter was not implemented, and instead the source wavelength was set to the appropriate wavelength of 470 nm. The LED was modelled using the "Source Radial" object, whereby the radial intensity profile was entered according to data provided by the manufacturer. An aperture was placed at the position of the achromatic doublets in order to prevent stray light, passing over the lenses, from reaching the detector placed at the sample plane. Its aperture was set to the diameter of the lenses. The sample plane was set at the appropriate angle according to the angle of illumination axis relative to the imaging axis.

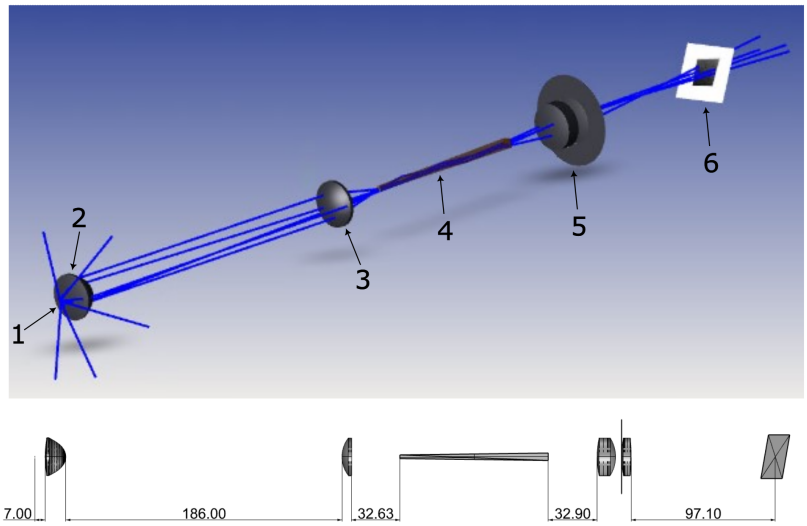

Figure S46: *3D view of the optical model of the fluorescence macroimager within the Optic Studio 18.9 software.* 1 – LED, 2 – Condenser, 3 – Plano-Convex Lens, 4 – Lightpipe, 5 – Matched Achromatic Doublet Pair and Aperture, 6 – Sample.

The simulation was run with 50,000,000 rays with the settings "Use Polarization" and "Split NSC Rays" selected. Following this, the incoherent irradiance data, provided (Macroscope/MACRO_SimulationData.npy), was saved for further processing. A jupyter python notebook, containing the code which carries out the calculations described in the remainder of this section, is provided (Macroscope/MACRO_Code.ipynb). The simulation provided the irradiance information in units of $W.cm^{-2}$. This was converted to units of $\mu E.m^{-2}.s^{-1}$, and the resulting image scaled and cropped such that the image was of the same size, and the relevant features in the same location, compared with the images obtained in the physical experiment. The power value attributed to the LED in the simulation was set to be a reasonable, but not the exact, value. As such, the homogeneity information is accurate, but the overall power still required scaling. In order to

do so, the power values from the simulation were integrated over the area of the illumination, to first obtain the overall power (P_{Total}):

$$P_{\mathrm{Total}} = \sum_{1}^{x}\sum_{1}^{y} I\left(x,y\right) \times A_{\mathrm{pixel}} \tag{S89}$$

where $I\left(x,y\right)$ is the intensity within a pixel with the image coordinates (x,y), and A_{pixel} the area that one pixel corresponds to at the sample plane. The scale factor between the overall power calculated from the simulation, and that obtained using a powermeter according to section D.2.3 with a squared sensor (S170C, Thorlabs Inc., Newton, NJ, US) with a neutral density filter (to expand the sensor's maximum), was determined and applied to the intensity values of the simulated intensity image. This operation provided a corresponding simulated intensity image, which could be directly compared with the experimentally obtained intensity image.

As a way to compare the results, the angle of the light gradient direction was determined for both the simulated and experimentally obtained image. In order to do so, data were extracted along a straight line within the illuminated area, and a line fit made on the intensity data along such line, providing gradient information. This was carried out repeatedly on the image at different rotational positions. The rotation angle corresponding to the highest gradient corresponded to the direction of the gradient. The angle between the directions found for the computed and experimental gradients is $3.2°$, which accounts for a fair agreement between the data and the simulation.

E.2 Confocal microscopes

E.2.1 Theory

The measurement of light intensity in confocal microscopy exhibits several differences with respect to the measurement in wide-field microscopy:

- Illumination is not homogeneous over the field of view as in epifluorescence microscopy. Introducing the cartesian coordinates (x,y,z), we consider that illumination results from a focused laser beam assumed to adopt a radially and axially Gaussian intensity profile given in Eq.(S90)

$$I\left(x,y,z\right) = I_0 \exp\left[-2\left(\frac{x^2+y^2}{w_0^2}\right)\right] \exp\left[-2\left(\frac{z^2}{z_0^2}\right)\right] \tag{S90}$$

  where I_0, w_0, and z_0 designate the light intensity at coordinates $(0,0,0)$, the waist radius in the focal plane, and the radial resolution z_0 respectively (see Figure S47).[28]

- In order to build an image, the focus of the laser scans the sample according to a chosen pixel size Δy, as displayed in Figure S48.

In relation with estimating the light intensity in confocal microscopy, we are interested in the time evolution of the overall fluorescence signal arising from the molecules of fluorescent actinometer, which are assumed to be spatially fixed.

[28] As a consequence, Eq. S90 is valid only for lenses of relatively low NA (which have a cylindrical illumination profile).

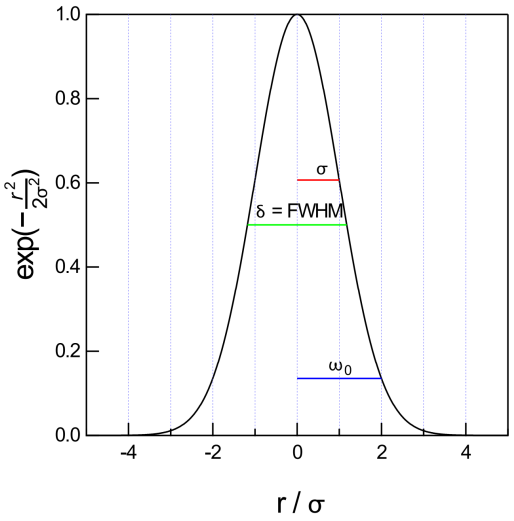

Figure S47: *Cross-section of the gaussian beam for* $z = z_0$. $\omega_0 = 2\sigma$ and I_0 corresponds to the maximum.

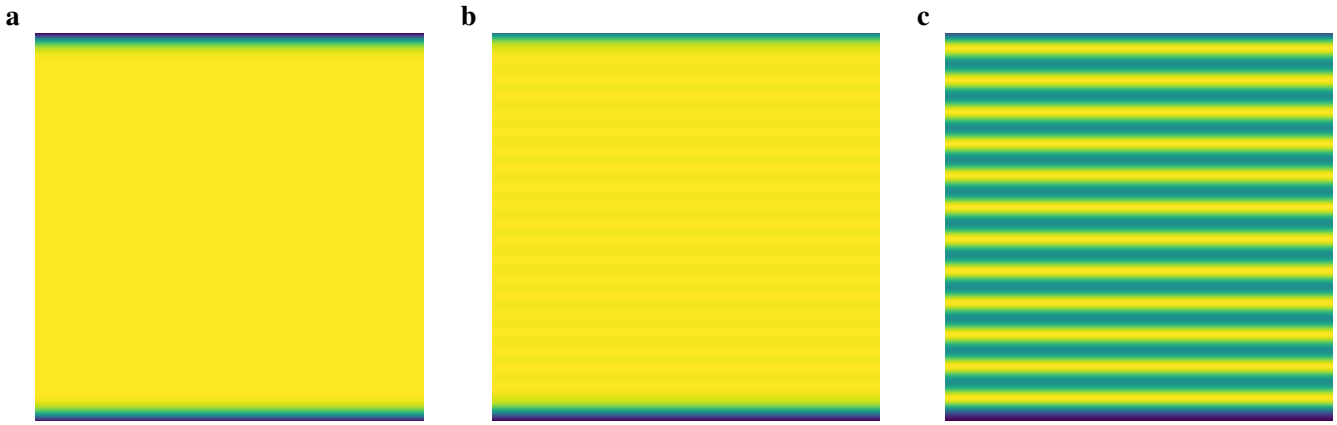

Figure S48: *Simulation of the integrated light path of the laser for different values of the pixel size* Δy. The simulations were performed by convolving a Gaussian kernel representing the beam of the laser with horizontal lines representing the path of the laser. $\omega_0 = 0.3$ and $\Delta y = 0.08$, 0.29 and 0.5 in **a**, **b** and **c** respectively.

The concentration of fluorescent actinometer $C(x, y, z, t)$ is submitted to Eq.(S91)

$$\frac{\partial C\left(x,y,z,t\right)}{\partial t} \quad = \quad -\sigma I\left(x\left(t\right),y\left(t\right),z\left(t\right)\right)C\left(x,y,z,t\right) \tag{S91}$$

by assuming the photoconversion to be irreversible.[29]

Photoconversion along a line Following Braeckmans et al,[27,28] we first consider the laser beam to scan along a single line expressed by $y = Y$ with a constant scanning speed v and take the x-axis to be parallel with the scanning direction. We first estimate the overall fluorescence signal arising from the molecules of fluorescent actinometer when the scan of the line segment has been completed.

[29] When photoconversion is reversible, Eq.(S91) reports on the distance of the concentration $C\left(x,y,z,t\right)$ to its steady-state.

Due to scanning, the x-coordinate of the light intensity profile is a function of time: $I\left(x-x\left(t\right),y-Y,z\right)$. We consider scanning to start at $x=-\ell/2$ and end up at $x=\ell/2$ with $x\left(t\right)=vt-\ell/2$ and T to be the time it takes for the scanning beam to cross the line with length ℓ at constant scanning speed $v=\ell/T$. We denote $C_0\left(x,y,z\right)$ the concentration of fluorescent actinometer before starting to record the first frame. Then the fluorescence signal $F_{1,1}\left(x,y,z\right)$ at position (x,y,z) after time T is given in Eq.(S92)

$$F_{1,1}\left(x,y,z,T\right)=C_0\left(x,y,z\right)e^{\left[-\sigma\int_0^T L(x(t),Y,z)I(x-x(t),y-Y,z)dt\right]}\times\int_0^T L\left(x\left(t\right),Y,z\right)I\left(x-x\left(t\right),y-Y,z\right)dt \quad \text{(S92)}$$

where $L\left(x\left(t\right),Y,z\right)$ is the function that describes the modulation of the light intensity and has value 0 when the laser is switched off and 1 when the laser is turned on.

Expressing t in terms of $x\left(t\right)$ and renaming $x\left(t\right)$ as x', Eq.(S92) yields Eq.(S93)

$$F_{1,1}\left(x,y,z,T\right) \;=\; C_0\left(x,y,z\right)e^{\left[-\frac{\sigma}{v}\int_{-\ell/2}^{\ell/2}I(x-x',y-Y,z)dx'\right]}\times\int_{-\ell/2}^{\ell/2}I\left(x-x',y-Y,z\right)dx' \quad \text{(S93)}$$

which yields Eq.(S94)

$$\begin{aligned}F_{1,1}\left(x,y,z,T\right)=C_0\left(x,y,z\right)e^{-\sqrt{\frac{\pi}{8}}\frac{\sigma w_0}{v}I_0e^{-2\frac{(y-Y)^2}{w_0^2}}e^{-2\frac{z^2}{z_0^2}}\left\{\mathrm{erf}\left[\frac{\sqrt{2}}{w_0}\left(x+\frac{\ell}{2}\right)\right]-\mathrm{erf}\left[\frac{\sqrt{2}}{w_0}\left(x-\frac{\ell}{2}\right)\right]\right\}} \\ \times\sqrt{\frac{\pi}{8}}\frac{w_0}{v}I_0e^{-2\frac{(y-Y)^2}{w_0^2}}e^{-2\frac{z^2}{z_0^2}}\left\{\mathrm{erf}\left[\frac{\sqrt{2}}{w_0}\left(x+\frac{\ell}{2}\right)\right]-\mathrm{erf}\left[\frac{\sqrt{2}}{w_0}\left(x-\frac{\ell}{2}\right)\right]\right\}\end{aligned} \quad \text{(S94)}$$

after the variable change $X=\frac{\sqrt{2}}{w_0}\left(x-x'\right)$.

Provided that $\ell\gg w_0$ and $-\frac{\ell}{2}\ll x\ll\frac{\ell}{2}$, Eq.(S94) yields Eq.(S95)

$$F_{1,1}\left(x,y,z,T\right)=C_0\left(x,y,z\right)e^{-\sqrt{\frac{\pi}{2}}\frac{\sigma w_0}{v}I_0e^{-2\frac{(y-Y)^2}{w_0^2}}e^{-2\frac{z^2}{z_0^2}}}\times\sqrt{\frac{\pi}{2}}\frac{w_0}{v}I_0e^{-2\frac{(y-Y)^2}{w_0^2}}e^{-2\frac{z^2}{z_0^2}} \quad \text{(S95)}$$

Photoconversion of a square A 2D square geometry is subsequently photoconverted by scanning N line segments at regular interline spacing Δy. Following Braeckmans et al,[27,28] we consider the case associated to $\Delta y\leq w_0$. In such a situation, the molecules of fluorescent actinometer experience photoconversion during several scans and the fluorescence signal $F_{1,N}\left(x,y,z,T\right)$ obtained after scanning N lines is computed by integrating $F_{1,1}\left(x,y,z,T\right)$ over y from $y=-\ell/2$ to $y=\ell/2$. Hence, Eq.(S95) first yields Eq.(S96)

$$F_{1,N}\left(x,y,z,T\right)=C_0\left(x,y,z\right)e^{-\sqrt{\frac{\pi}{2}}\frac{\sigma w_0}{v\Delta y}I_0e^{-2\frac{z^2}{z_0^2}}\int_{-\ell/2}^{\ell/2}e^{-2\frac{(y-y')^2}{w_0^2}}dy'}\times\sqrt{\frac{\pi}{2}}\frac{w_0}{v\Delta y}I_0e^{-2\frac{z^2}{z_0^2}}\int_{-\ell/2}^{\ell/2}e^{-2\frac{(y-y')^2}{w_0^2}}dy', \quad \text{(S96)}$$

which gives Eq.(S97)

$$\begin{aligned}F_{1,N}\left(x,y,z,T\right)=C_0\left(x,y,z\right)e^{-\sqrt{\frac{\pi}{2}}\frac{\sigma w_0}{v\Delta y}I_0e^{-2\frac{z^2}{z_0^2}}\int_{\frac{\sqrt{2}}{w_0}\left(y-\frac{\ell}{2}\right)}^{\frac{\sqrt{2}}{w_0}\left(y+\frac{\ell}{2}\right)}\frac{w_0}{\sqrt{2}}e^{-X^2}dX} \\ \times\sqrt{\frac{\pi}{2}}\frac{w_0}{v\Delta y}I_0e^{-2\frac{z^2}{z_0^2}}\int_{\frac{\sqrt{2}}{w_0}\left(y-\frac{\ell}{2}\right)}^{\frac{\sqrt{2}}{w_0}\left(y+\frac{\ell}{2}\right)}\frac{w_0}{\sqrt{2}}e^{-X^2}dX\end{aligned} \quad \text{(S97)}$$

after the variable change $X = \frac{\sqrt{2}}{w_0}(y - y')$. Eq.(S97) eventually yields Eq.(S98)

$$F_{1,N}(x,y,z,T) = C_0(x,y,z)\, e^{-\sigma \frac{\pi w_0^2}{2v\Delta y} I_0 e^{-2\frac{z^2}{z_0^2}}} \times \frac{\pi}{2}\frac{w_0^2}{v\Delta y} I_0 e^{-2\frac{z^2}{z_0^2}} \tag{S98}$$

upon considering that $\ell \gg w_0$. In the limit of recovering the fluorescence signal from the focal plane only, one finally obtains Eq.(S99)

$$F_{1,N}(x,y,0,T) = C_0(x,y,0)\, e^{-\sigma \frac{\pi w_0^2}{2\Delta y^2} I_0 d} \times \frac{\pi w_0^2}{2\Delta y^2} I_0 d \tag{S99}$$

upon introducing the dwell time $d = \frac{\Delta y}{v}$.

Interestingly, $C_0(x,y,0)\, e^{-\sigma \frac{\pi w_0^2}{2\Delta y^2} I_0 d}$ provides the final distribution of the concentration of the fluorescent actinometer after scanning N line segments to build the first frame, which acts as the initial distribution to build the second frame. Then, one reproduces the calculation above and it writes Eq.(S100)

$$F_{2,N}(x,y,0,T) = C_1(x,y,0)\, e^{-\sigma \frac{\pi w_0^2}{2\Delta y^2} I_0 d} = C_0(x,y,0)\, e^{-\sigma \frac{\pi w_0^2}{2\Delta y^2} I_0 2d} \times \frac{\pi w_0^2}{2\Delta y^2} I_0 d \tag{S100}$$

After acquiring n frames, one eventually obtains Eq.(S101)

$$F_{n,N}(x,y,0,T) = C_0(x,y,0)\, e^{-\sigma \frac{\pi w_0^2}{2\Delta y^2} I_0 nd} \times \frac{\pi w_0^2}{2\Delta y^2} I_0 d = C_0(x,y,0)\, I d e^{-\frac{nd}{\tau}} \tag{S101}$$

with

$$I = \frac{\pi w_0^2}{2\Delta y^2} I_0 \tag{S102}$$

and

$$\frac{1}{\tau} = \sigma I = \sigma \frac{\pi w_0^2}{2\Delta y^2} I_0, \tag{S103}$$

which designate the integral light intensity at the laser focus divided by the pixel surface, and the inverse of the characteristic time associated to the photoconversion of the fluorescent actinometer at light intensity I.

Hence, the extraction of the characteristic time τ from the decay of the fluorescence signal of the fluorescent actinometer on the number of frames multiplied by the dwell time (which amounts to a time t) provides an average of the light intensity I experienced by the sample during image acquisition.

E.2.2 Confocal microscopy equipped with a continuous laser

Measurement of the radial waist of the laser beam To validate the relevance of the evaluation of the light intensity by using the **Dronpa-2** actinometer, we first implemented Raster image correlation spectroscopy (RICS) on a suspension of Fluorescein-labeled 0.04 μm beads (FluoSpheres F8795, Thermo Fischer Scientific, MA) for determining the radial waist of the laser beam of the confocal microscope ω_0.[29,30]

In a first step, we measured the hydrodynamic radius of the fluorescent beads by FCS. We measured the beam waist of the focused 488 nm laser by recording the time dependence of the autocorrelation function extracted from a 10 nM Fluorescein solution in 50 mM CHES pH 9.3 (Figure S49a). It was fitted with the theoretical expression of the autocorrelation function involving 2D diffusion and the formation of the triplet state given in Eq. (S87). By using $D_{\mathrm{Fluo}} = 4.25\ 10^{-10}$ $\mathrm{m}^2.\mathrm{s}^{-1}$ for the value of the diffusion coefficient of Fluorescein in water at 298 K,[26] we extracted the lateral extension of the beam waist $\omega_0 = 2\left(D_{\mathrm{Fluo}}\tau_D\right)^{0.5} = 0.28$ μm from the $\tau_D = 45$ μs value retrieved from the fit. We recorded the time dependence of the autocorrelation function extracted from a suspension of Fluorescein-labeled beads in 50 mM CHES pH 9.3 (see Figure S49b) and we fitted experimental data with Eq.(S88). From the retrieved diffusion time $\tau_D = 4.4$ ms value and the knowledge of $\omega_0 = 0.28$ μm, we extracted $D_{\mathrm{beads}} = 4.25\ 10^{-12}$ $\mathrm{m}^2.\mathrm{s}^{-1}$ for the value of the diffusion coefficient of the Fluorescein-labeled beads in water at 293 K.

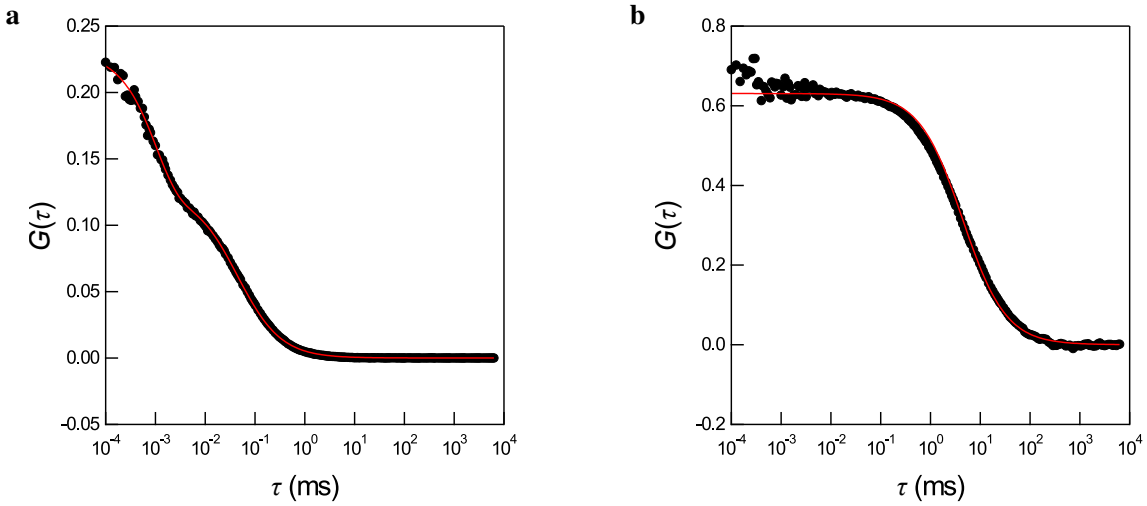

Figure S49: *FCS autocorrelation curves recorded at 293 K from 10 nM Fluorescein (**a**) and 3 nM Fluorospheres beads (**b**).* Markers: Experimental data; Lines: Fits according to Eqs.(S87,S88) for Fluorescein and Fluorescein-labeled beads respectively, which yield $G(0) = 0.12$, $\tau_D = 44$ μs, $\tau_T = 1.0$ μs, and $A_T = 0.9$ for Fluorescein, and $G(0) = 0.63$ and $\tau_D = 4.4$ ms for the Fluorescein-labeled beads. Solvent: 50 mM CHES buffer pH 9.3. $T = 293$ K.

Equipped with the diffusion coefficient of the Fluorescein-labeled beads, a series of 30 images of their suspension at 3 nM concentration in 50 mM CHES pH 9.3 sandwiched between two glass-slides with a 80 μm-thick spacer was acquired over a 10.6×10.6 $\mu\mathrm{m}^2$ square in the raster scanning mode (Objective 20×, NA 0.5; 256×256 pixel^2; pixel size: 0.042 μm; dwell time τ_{dt}: 8.275 μs) with the focused 488 nm laser of the confocal microscope (5% light power associated to 1.76 μW measured in the focal plane of the objective with the powermeter). The data have been processed with the Globals software for Images SimFCS, which is kindly available from https://www.lfd.uci.edu/globals/ (Figure S50). Hence, we retrieved $\omega_0 = 0.44$ μm from analyzing the whole set of data.

Measurement of the light intensity with the fluorescent actinometer The theoretical analysis reported in subsection E.2.1 established the dependence of the characteristic time τ associated to the photoconversion of the fluorescent acti-

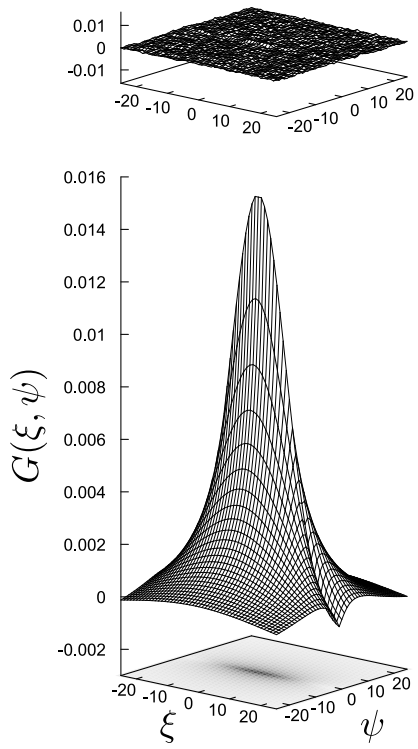

Figure S50: *Fit and difference of the correlation of the image of Fluorescein-labeled beads in water at 293 K obtained at 488 nm with the confocal microscope equipped with the continuous laser*. In the fit plotted in three dimensions, the height of the plot corresponds to the magnitude of the function (color code). The horizontal axis is the horizontal correlation shift, ξ. The vertical axis is the vertical correlation shift, ψ. The image correlation was calculated at a region of interest of 128 $\times$ 128 pixel^2 placed in the center of the original series of images and the correlation function was calculated for half the size of the region of interest in the original image (64$\times$64 pixels^2).

nometer on the light intensity I experienced by the sample during image acquisition and the tabulated cross section σ of the actinometer photoconversion. In a first step, we validated the relevance of the corresponding Eq.(S103) by plotting the dependence of $1/\tau$ on the square of the pixel size Δy^2.

As shown in Figure S51, τ linearly depends on the square of the pixel size Δy^2 up to ω_0^2 as anticipated from Eq.(S103). Hence, the measurement of the characteristic time τ together with the tabulated cross section σ of the actinometer photoconversion make possible to extract I experienced by the sample during image acquisition, and subsequently $I_0 = \frac{2\Delta y^2}{\sigma\pi w_0^2\tau}$ from the knowledge of w_0 and Δy.

Measurement of the light intensity with the powermeter At the same time, a powermeter spatially integrates light intensity over all its detecting element and delivers $\frac{1}{2}I_0\pi w_0^2$ (obtained by 2D integration of the Gaussian beam). With the present confocal microscope, scanning is performed at constant speed along the x-axis and light application effectively occurs only during a fraction γ of the period of the sinusoidal motion of the focal point.[30] Hence, the $power$ experienced

[30]To evaluate the fraction γ, the sensitive element of a fast photodiode (PD10A, Thorlabs, NJ) was placed at the focal plane of the imaging objective during acquisition of a series of 30 images. The output signal from the photodiode was digitized by a 300 MHz oscilloscope (RTB2004, Rhode and Schwarz, Munich, Germany) and we measured $\gamma = 0.4$, indicating that the laser excitation is turned off when the beam returns to the initial x position between line scans to reduce photo-damage to the sample.

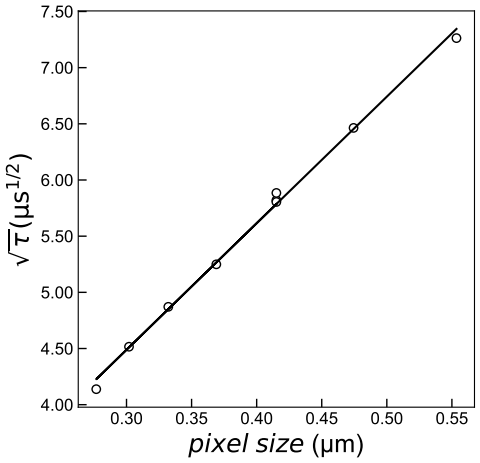

Figure S51: *Dependence of the square root of the characteristic time τ retrieved from the decay of the fluorescence signal of **Dronpa-2** on the pixel size Δy.* The dependence has been established by averaging the fluorescence signal over segmented 256×256 images of **Dronpa-2**-labeled fixed U-2 OS cells scanned with the confocal microscope equipped with a continuous laser with 8.24 μs dwell time and 10 % laser power at 488 nm.

by the sensor during scanning is $P = \frac{\gamma}{2} I_0 \pi w_0^2$.

Equipped with the value of w_0 measured with Raster image correlation spectroscopy and the γ parameter, it subsequently becomes possible to retrieve the $I_0 = \frac{2}{\gamma \pi w_0^2} P$ value from the light power measured with the powermeter.

Conclusion We used the preceding results to evaluate the consistency of the measurement of the light intensity delivered by the focused laser beam at the focal plane of the confocal microscope at $\lambda = 488$ nm as retrieved with the **Dronpa-2** actinometer and with the powermeter:

- Exploiting the **Dronpa-2** actinometer in the nucleus of fixed cells, we extracted $\tau = 19$ μs for the characteristic time associated to the photoconversion at 10% light power measured in the scanning mode at 1.7 μs dwell time over a 128×128 pixels^2 image with 0.415 μm pixel size and $\omega_0 = 0.44$ μm. Using $\sigma = 198$ m^2.mol^{-1}, we retrieved $I_0 = 150 \pm 30$ E.m^{-2}.s^{-1};

- Exploiting the associated measurement of the powermeter in the focal plane of the objective (3.65 μW; 1.45 10^{-11} E.s^{-1}), the value of w_0 measured with Raster image correlation spectroscopy ($\omega_0 = 0.44$ μm), and the $\gamma = 0.4$ parameter, we extracted $I_0 = 120 \pm 25$ E.m^{-2}.s^{-1}.

The fair agreement between both derivations underlines the relevance of the fluorescent actinometers to estimate the light intensity in confocal microscopy.

E.2.3 Confocal microscopy equipped with a pulsed laser

Measurement of the radial waist of the laser beam

Measurement from Raster image correlation spectroscopy (RICS) To measure the radial waist of the laser beam, we first proceeded as reported above with the confocal microscope equipped with a continuous laser. We applied Raster image correlation spectroscopy (RICS) on a suspension of Fluorescein-labeled 0.04 μm beads (FluoSpheres F8795, Thermo Fischer Scientific, MA) for determining the radial waist of the laser beam of the confocal microscope ω_0.[29,30]

Equipped with the $D_{\mathrm{beads}} = 4.25\ 10^{-12}$ m^2.s^{-1} diffusion coefficient of the Fluorescein-labeled beads in water at 293 K, we acquired a series of 50 images of their suspension at 3 nM concentration in 50 mM CHES pH 9.3 sandwiched between two glass-slides with a 120 μm-thick spacer over a 6.05×6.05 μm^2 square in the raster scanning mode (Objective HC PL APO CS2 40×, NA 1.1; 256×256 pixel^2; pixel size: 0.024 μm; dwell time τ_{dt}: 4.9 μs) with the focused 488 nm laser of the confocal microscope. The data have been then processed with the Globals software for Images SimFCS, which is kindly available from https://www.lfd.uci.edu/globals/ (Figure S52). Hence, we retrieved $\omega_0 = 0.32$ μm from analyzing the whole set of data.

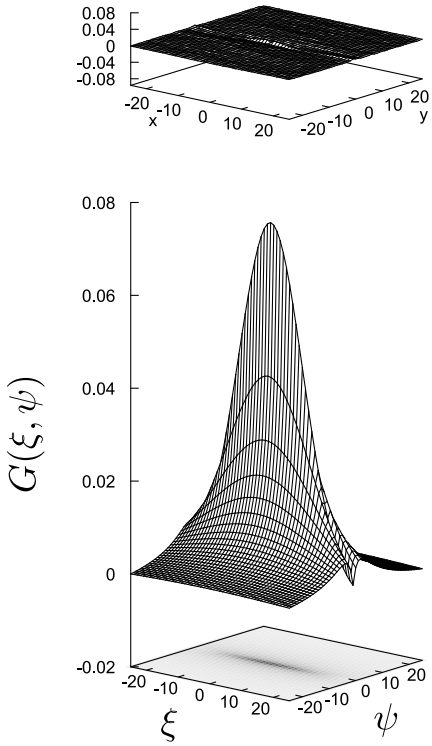

Figure S52: *Fit and difference of the correlation of the image of Fluorescein-labeled beads in water at 293 K obtained at 488 nm with the confocal microscope equipped with the pulsed laser*. In the fit plotted in three dimensions, the height of the plot corresponds to the magnitude of the function (color code). The horizontal axis is the horizontal correlation shift, ξ. The vertical axis is the vertical correlation shift, ψ. The image correlation was calculated at a region of interest of 128×128 pixel^2 placed at the center of the original series of images and the correlation function was half the size of the original image, 64×64 pixels^2.

Measurement from collecting the point spread function We also characterized the beam waist of the pulsed laser at 488 nm on the confocal microscope by recording a z-stack of (x,y) images of a 100 μm Green-Yellow-labeled bead (Fluospheres, ThermoFischer).[31] We both processed the images in 2D (by Gaussian fit of the image of the z-stack associated to the highest average value; Figure S53) and 3D (by using the software MetroloJ[32]) and extracted $\omega_0 = 0.28$ μm and $\omega_0 = 0.26$ μm respectively.

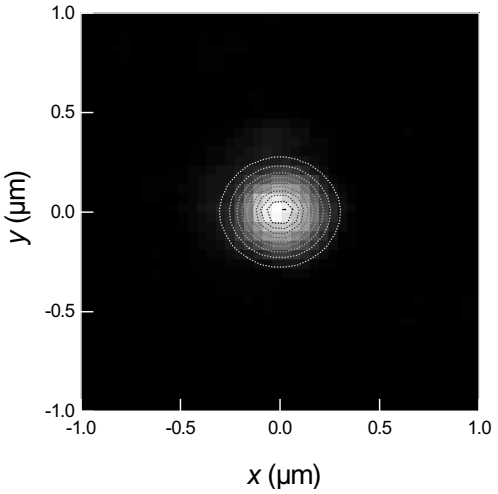

Figure S53: *Two-dimensional curve fitting of a 100 nm Green-Yellow-labeled polystyrene bead imaged with the confocal microscope equipped with the 488 nm pulsed laser.* Dotted contour lines from white to black correspond to increase in intensity by steps of 10% of the fitted maximum value.

Measurement of the light intensity with the fluorescent actinometer The principle of the validation reported above for the confocal microscope equipped with the continuous laser remains valid. Thus, we again evaluated the relevance of Eq.(S103) by plotting the dependence of $\sqrt{\tau}$ on the pixel size Δy.

As shown in Figure S54, τ linearly depends on the square of the pixel size Δy^2 up to ω_0^2 as anticipated from Eq.(S103). Hence, the measurement of τ together with the tabulated cross section σ of the actinometer photoconversion make possible to extract I experienced by the sample during image acquisition, and subsequently $I_0 = \frac{2\Delta y^2}{\sigma\pi w_0^2\tau}$ from the knowledge of w_0 and Δy.

At that step, it is important to notice that the tabulated cross section σ of the **Dronpa-2** photoconversion reported in Table 1 of the Main Text refers to photoconversions, which have been investigated in a regime of light intensities not covering the ones presently reached with the pulsed laser at 488 nm.

Measurement of the light intensity with the powermeter The expressions derived above for the measurement of the light intensity with the powermeter are still applicable. Equipped with the value of w_0 measured with Raster image correlation spectroscopy and the γ parameter (equal to $\gamma = 1$ in the exploited bleaching mode), the I_0 value retrieved from the light power P measured with the powermeter is equal to $I_0 = \frac{2}{\gamma\pi w_0^2}P$.

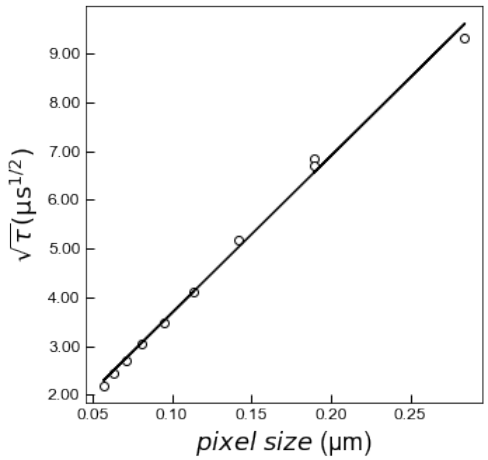

Figure S54: *Dependence of the square root of the characteristic time τ retrieved from the decay of the fluorescence signal of **Dronpa-2** on the pixel size Δy.* The dependence has been established by averaging the fluorescence signal over a segmented 512×512 images of **Dronpa-2**-labeled fixed U-2 OS cells scanned with the confocal microscope equipped with a pulsed laser with 1.2 μs dwell time and 0.2 % laser power at 488 nm.

Conclusion We used the preceding results to compare the measurements of the light intensity delivered by the focused laser beam at the focal plane of the confocal microscope at $\lambda = 488$ nm as retrieved with the **Dronpa-2** actinometer and with the powermeter from exploiting the value of the beam waist:

- Exploiting the **Dronpa-2** actinometer in the nucleus of fixed cells, we extracted $\tau = 1.2$ μs for the characteristic time associated to the photoconversion at 2% light power measured in the scanning mode at 1.2 μs dwell time over a 512×512 pixels^2 image with 0.114 μm pixel size and $\omega_0 = 0.3$ μm. Using $\sigma = 198$ m^2.mol^{-1}, we retrieved $I_0 = 390 \pm 80$ E.m^{-2}.s^{-1};

- Exploiting the associated measurement of the powermeter in the focal plane of the objective (17.3 μW; 6.9 10^{-11} E.s^{-1}), the value of w_0 measured with Raster image correlation spectroscopy ($\omega_0 = 0.3$ μm), and the $\gamma = 1$ parameter, we extracted $I_0 = 490 \pm 100$ E.m^{-2}.s^{-1}.

The fair agreement between both derivations suggests that using $\sigma = 198$ m^2.mol^{-1} is relevant for the measurement of the light intensity delivered by the focused laser beam at the focal plane of the confocal microscope.

F Measurement of light intensity from a LED array

Here, we present a case demonstrating a limitation of the first protocol for measuring light intensity: retrieving 3D intensity distribution information in a non-homogeneous light intensity profile. In order to evaluate and demonstrate this limitation, an experiment was conducted whereby our protocol was applied to the situation of a Petri dish, containing a solution of the **Dronpa-2** fluorescent actinometer, being illuminated by a surrounding radial array of LEDs and being imaged from above; and the results compared to those obtained through an optical simulation.

F.1 Experimental Setup

An image and CAD rendered views of the setup, with the Petri dish and **Dronpa-2** solution sectioned, created in Rhinoceros 3D (Robert McNeel & Associates, Seattle, WA, US), of the setup are provided in Figure S55. The setup consists of an LED strip light (ZFS-85000HD-B, JKL Components Corporation, Los Angeles, CA, US), which contains 460 nm LEDs (L1SP-RYL0002800000, Lumileds, San Jose, CA, USA), stuck to the inside of a large 100 mm diameter plastic Petri dish (Corning Incorporated, Corning, NY, US), and a small 35 mm diameter plastic petri dish (Thermo Fisher Scientific, Waltham, MA, US), containing 1.6 mL of 4 μM **Dronpa-2** solution, placed inside it at its center. In order to have the solution at approximately the same height as the LEDs, a base was printed in black PLA/PHA plastic (ColorFabb B.V, Belfeld, Netherlands) on the Ultimaker 2+ Connect 3D printer (Ultimaker B.V., Utrecht, Netherlands), for the small Petri dish to sit on. In order to simplify the situation, and therefore the simulation, the bottom of the large Petri dish was covered with paper painted with highly absorbent black paint (Musou Black, Koyo Orient Japan Co., Ltd., Saitama, Japan) in order to eliminate any reflections, which could reach the **Dronpa-2** solution, meaning it could be ignored in the simulation (Figure S55). The CAD images do not show the large Petri dish for this reason. In Figure S55, the CAD models show the **Dronpa-2** solution in place, with a meniscus shape, based on the meniscus shape of water in a Petri dish as seen in reference.[33] A scale bar is provided for the final CAD model, which is a 2D frontal sectioned view, allowing the size and position of the different components to be recovered.

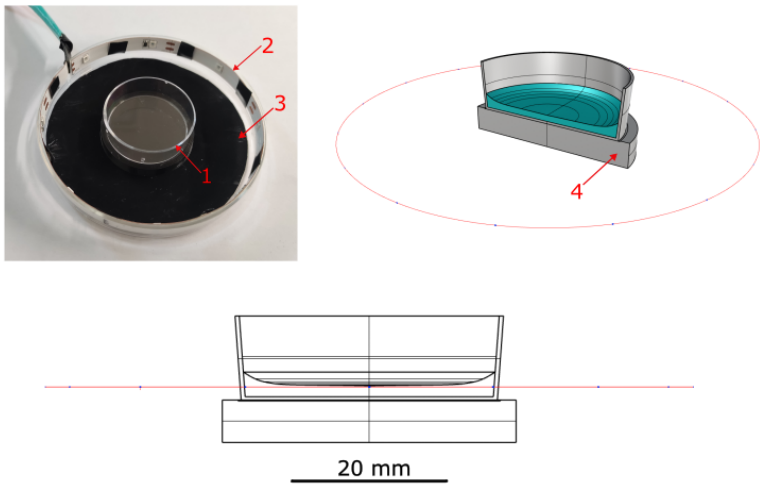

Figure S55: *Photo (top left), CAD perspective sectioned view (top right) and CAD front sectioned view (bottom) of the Petri dish LED array setup.* 1 – Small Petri Dish (where the **Dronpa-2** solution is held), 2 – LED Array (460 nm), 3 – Large Petri Dish with Blackened Bottom, 4 – 3D Printed Base. The large Petri dish is omitted in the CAD views since it is not implemented in the simulation. The 20 mm scale bar applies only to the bottom image. In the CAD drawings, the LEDs are shown in blue.

The setup was imaged from above using a greyscale global-shutter camera (UI-3060CP-M-GL, IDS Imaging Development Systems GmbH, Obersulm, Germany), with a Nikon camera objective (AF Nikkor 50 mm f/1.8D, Nikon, Tokyo,

Japan), and with an emission filter (550 nm CWL, 100 nm FWHM; 33-331, Edmund Optics Inc., Barrington, NJ, US), placed after the objective, to pass as much of only the fluorescence light as possible. In relation to the electronics, the LED was connected to an LED driver (LEDD1B, Thorlabs Inc., Newton, NJ, US) to power it, and the camera to a custom-built PC running Windows 10 (Microsoft Corp., Redmond, WA, US) to accept images from it. The cameras frames were triggered using an Elegoo Uno R3 board (Elegoo, Shenzhen, China). The experiment involved acquiring images, at a frequency of 6 Hz, for 70 s, while, at a time point shortly after the camera was started, the LED array was driven at the maximum current possible with the LED driver used. In this case, only 8 of the LEDs, of equal spacing, were used. In order to make this possible, black tape was placed over the relevant LEDs to block the light emitted from them. The data corresponding to the video and final intensity image output are provided (LED Array/LEDArray_ExperimentVideo.tiff).

F.2 Simulation Setup and Protocol

A model of the system was created and run using the optical design software package Optic Studio 18.9 (Zemax LLC, Kirkland, WA, US). The file corresponding to this is provided (LED Array/LEDArray_Simulation.zmx). A 3D view of the model within the software is shown at the top of Figure S56. The LEDs were modelled using the "Source Radial" object, whereby the radial intensity profile was entered according to data provided by the manufacturer. The Petri dish was modeled as a volume object with a refractive index of 1.59, corresponding to that of polycarbonate, with no absorption. The **Dronpa-2** solution was modelled as a volume object with the material "WATER" selected. The CAD files for these two objects have been provided (LED Array/Liquid.stp, LED Array/PetriDish.stp). The software does not contain the transmission data of the **Dronpa-2** solution, and so it was entered manually as 71 % for 30 mm of optical path distance. In order to be able to measure the profile of absorbed light flux within the solution, a detector volume, 20 $\times$ 20 $\times$ 3.228 mm, containing 200 $\times$ 200 $\times$ 20 voxels, was set up fully covering the solution. The simulation was run with 1,000,000 rays with the settings "Use Polarization" and "Split NSC Rays" selected. Following this, the absorbed light flux for each slice, provided (LED Array/LEDArray_Intensity2DSLices.npy), was saved for further processing. A jupyter python notebook, containing the code which carries out the calculations described in the remainder of this section, is provided (LED Array/LEDArry_Code.ipynb).

F.3 Results and Discussion

F.3.1 Simulated 3D-distribution of absorbed light flux

The 2D image slices obtained from the simulation are provided in Figure S57. It can be seen that the light intensity distribution varies along the z-axis, with a bright central region being apparent in the lower slices and not the top. It is likely that the cause is related to reflection phenomena occurring at the bottom of the dish.

F.3.2 Simulated 2D-maps of the characteristic times of Dronpa-2 photoconversion and light intensity

Theoretical derivation The conversion of the simulated steady 3D-spatial distribution of light intensity $I\left(r,z\right)$ into a 2D map of characteristic time $\tau\left(r,z\right)$ is required to compare the simulation with the experimental observation.

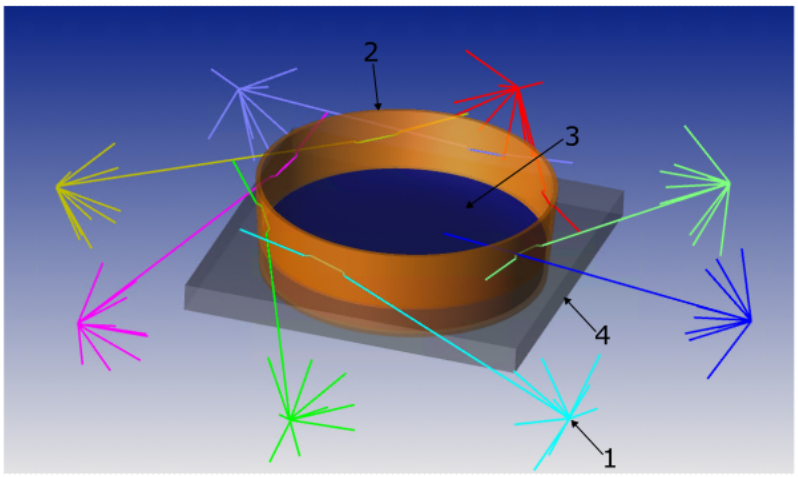

Figure S56: *3D view of the optical model of the Petri dish LED array setup within the Optic Studio 18.9 software*. 1 – LED, 2 – 35 mm Petri Dish, 3 – **Dronpa-2** solution, 4 – Detector Volume.

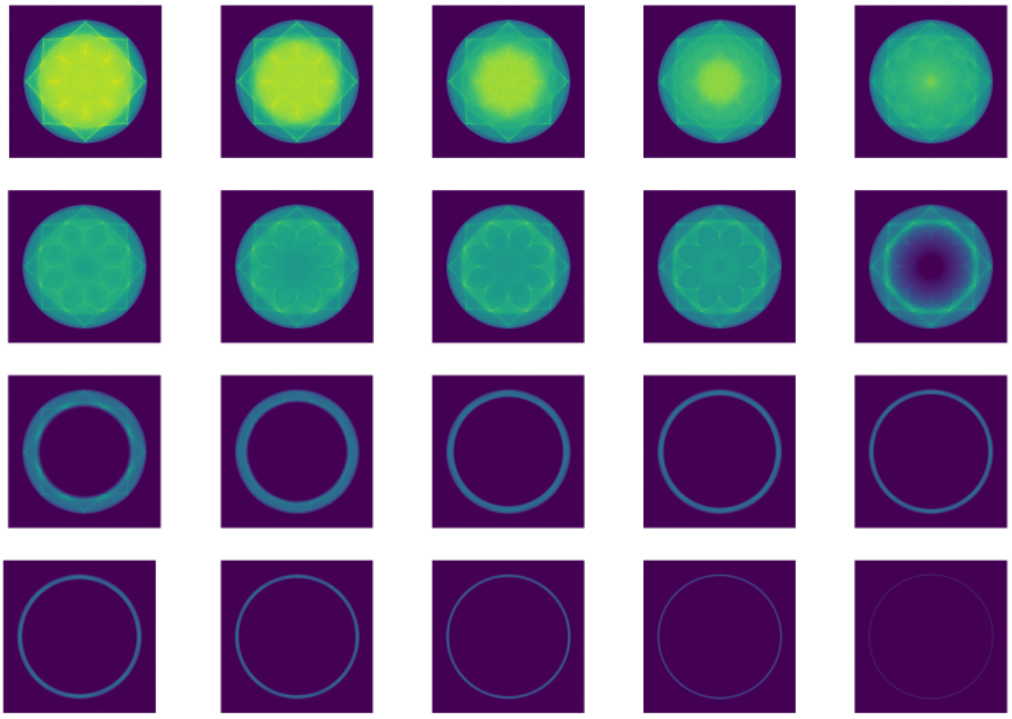

Figure S57: *2D images of the absorbed light flux at each of the 20 z-axis locations within the detection volume*. The first image corresponds to the **Dronpa-2** solution space adjacent to the bottom of the petri dish, and the following images, going left to right, and down, in a raster fashion, correspond to image slices progressively closer to the fluid surface. Since this work did not consider the absolute light intensity, but rather the distribution, a color scale is omitted.

The **Dronpa-2** solution contained in the Petri dish is divided in voxels, which are assumed to contain **Dronpa-2** at identical concentration. Furthermore, we consider large enough voxels to neglect diffusion effects involving transfer of the bright and dark states of **Dronpa-2** between voxels experiencing distinct light intensities. Under such conditions, the

conversion is performed as follows:

- In each voxel i, the time dependence of the fluorescence signal from **Dronpa-2** $F_i(r,z,t)$ obeys:

$$F_i(r,z,t) = F_i(r,z,\infty) + a_i(r,z)\, I_i(r,z) \exp\left[-\sigma I_i(r,z)\, t\right] \tag{S104}$$

  where $F_i(r,z,\infty)$ designates the final value of the fluorescence signal;

- One calculates the sums of the time dependences of the fluorescence signal from **Dronpa-2** along the optical axis $F(r,t)$

$$F(r,t) = \sum_{i=1}^{i=n} F_i(r,z,\infty) + \sum_{i=1}^{i=n} a_i(r,z)\, I_i(r,z) \exp\left[-\sigma I_i(r,z)\, t\right] \tag{S105}$$

  where the voxels along the optical axis are numbered from 1 to n;

- We assume $a_i(r,z) = a$ to be independent on r and z in the considered regime of light intensity. Then the sums of the time dependences of the fluorescence signal from **Dronpa-2** along the optical axis becomes

$$F(r,t) = \sum_{i=1}^{i=n} F_i(r,z,\infty) + a \sum_{i=1}^{i=n} I_i(r,z) \exp\left[-\sigma I_i(r,z)\, t\right] \tag{S106}$$

- Although multiexponentially decreasing, $F(r,t)$ is fitted with a monoexponential fitting function

$$F(r,t) = F(r,\infty) + b(r) \exp\left[-\sigma \langle I(r)\rangle t\right] \tag{S107}$$

  which provides the 2D-map of light intensity $\langle I(r)\rangle$.

- The 2D-map of $\tau(r)$ is eventually extracted as

$$\tau(r) = \frac{1}{\sigma \langle I(r)\rangle}. \tag{S108}$$

Results and discussion Maps of the characteristic times τ of **Dronpa-2** photoconversion, and light intensity I, for both the experimental and simulation cases, are provided in Figure S58. It can be seen visually that, although not an exact match, the results of both cases fairly agree with each other. More precisely, the eight-fold symmetry of the distribution is conveniently accounted for on both maps. One possible explanation for the small discrepancy arising from the weaker flower motif observed in the experimental maps is that the surface roughness, which could have impacted upon the reflections taking place, was not modelled for the simulation. Another possible factor causing differences could have been some inaccuracy in positioning between the plane of the LED array and the fluid. Despite the slight differences, this experiment demonstrates that the technique is able to extract information, closely matching that from a simulation. However, recovering information on light intensity in fully 3D cannot be retrieved from the integral image of light intensity displayed in Figure S58, which is a limit of this protocol.

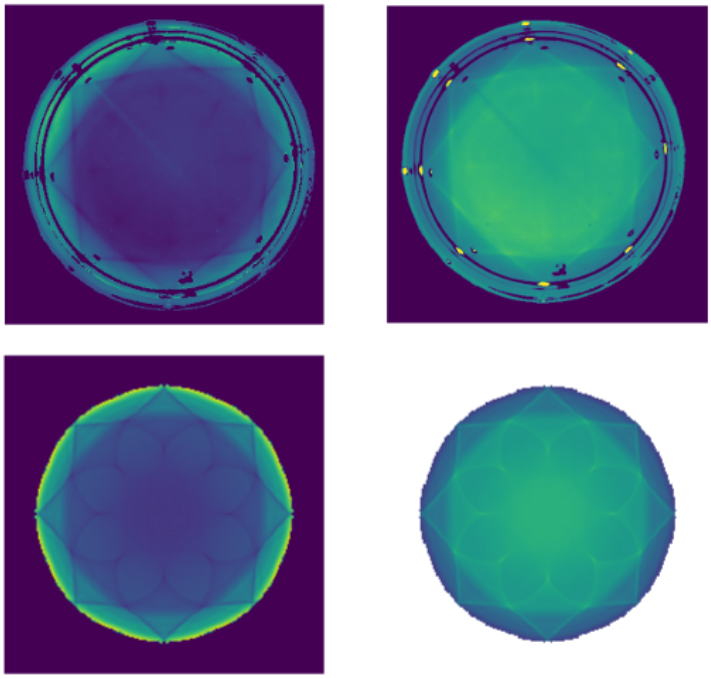

Figure S58: *τ (left) and light intensity (right) maps of the experimental (top) and simulation (bottom) situation.* Since this work did not consider the absolute light intensity, but rather the distribution, a color scale is omitted.

References

[1] Stéfan van der Walt, Johannes L. Schönberger, Juan Nunez-Iglesias, François Boulogne, Joshua D. Warner, Neil Yager, Emmanuelle Gouillart, Tony Yu, and the scikit-image contributors. scikit-image: image processing in Python. *PeerJ*, 2:e453, 6 2014.

[2] Matthew Newville, Till Stensitzki, Daniel B. Allen, and Antonino Ingargiola. LMFIT: Non-Linear Least-Square Minimization and Curve-Fitting for Python, September 2014.

[3] N. Gagey, P. Neveu, C. Benbrahim, B. Goetz, I. Aujard, J.-B. Baudin, and L. Jullien. Two-photon uncaging with fluorescence reporting: evaluation of the o-hydroxycinnamic platform. *Journal of the American Chemical Society*, 129(32):9986–9998, 2007.

[4] P. West and G. Davis. The synthesis of diarylnitrones. *The Journal of Organic Chemistry*, 54(21):5176–5180, 1989.

[5] Y. Shpinov, A. Schlichter, P. Pelupessy, T. Le Saux, L. Jullien, and B. Adelizzi. Unexpected acid-triggered formation of reversibly photoswitchable stenhouse salts from donor-acceptor stenhouse adducts. *Chemistry–A European Journal*, 2022.

[6] J. Querard, T.-Z. Markus, M.-A. Plamont, C. Gauron, P. Wang, A. Espagne, M. Volovitch, S. Vriz, V. Croquette, A. Gautier, T. Le Saux, and L. Jullien. Photoswitching kinetics and phase-sensitive detection add discriminative dimensions for selective fluorescence imaging. *Angewandte Chemie*, 127(9):2671–2675, 2015.

[7] J. Quérard, R. Zhang, Z. Kelemen, M.-A. Plamont, X. Xie, R. Chouket, I. Roemgens, Y. Korepina, S. Albright, E. Ipendey, M. Volovitch, H. L. Sladitschek, P. Neveu, L. Gissot, A. Gautier, J.-D. Faure, V. Croquette, T. Le Saux, and L. Jullien. Resonant out-of-phase fluorescence microscopy and remote imaging overcome spectral limitations. *Nat. Comm.*, 8:969, 2017.

[8] D. Joly and R. Carpentier. Sigmoidal reduction kinetics of the photosystem ii acceptor side in intact photosynthetic materials during fluorescence induction. *Photochemical & Photobiological Sciences*, 8(2):167–173, 2009.

[9] R. Chouket, A. Pellissier-Tanon, A. Lahlou, R. Zhang, D. Kim, M.-A. Plamont, M. Zhang, X. Zhang, P. Xu, N. Desprat, D. Bourgeois, A. Espagne, A. Lemarchand, T. Le Saux, and L. Jullien. Extra kinetic dimensions for label discrimination. *Nature communications*, 13(1):1–8, 2022.

[10] N. Kiskin and D. Ogden. Two-photon excitation and photolysis by pulsed laser illumination modelled by spatially non-uniform reactions with simultaneous diffusion. *Eur. Biophys. J.*, 30:571–587, 2002.

[11] N. Kiskin, R. Chillingworth, J. McCray, D. Piston, and D. Ogden. The efficiency of two-photon photolysis of a "caged" fluorophore, o-1-(2-nitrophenyl)ethylpyranine, in relation to photodamage of synaptic terminals. *Eur. Biophys. J.*, 30:588–604, 2002.

[12] P. Wang, L. Jullien, B. Valeur, J.-S. Filhol, J. Canceill, and J.-M. Lehn. Multichromophoric cyclodextrins. 5. antenna-induced unimolecular photoreactions. photoisomerization of a nitrone. *New journal of chemistry*, 20(7-8):895–907, 1996.

[13] N. Gagey, P. Neveu, and L. Jullien. Reporting two-photon uncaging with the efficient 3,5-dibromo-2,4-dihydroxycinnamic caging group. *Angew. Chem. Intl. Ed.*, 46:2467–2469, 2007.

[14] D. Bourgeois and V. Adam. Reversible photoswitching in fluorescent proteins: a mechanistic view. *IUBMB life*, 64(6):482–491, 2012.

[15] A. Stiel, S. Trowitzsch, G. Weber, M. Andresen, C. Eggeling, S. Hell, S. Jakobs, and M. Wahl. 1.8 å bright-state structure of the reversibly switchable fluorescent protein Dronpa guides the generation of fast switching variants. *Biochem. J.*, 402:35–42, 2007.

[16] R. Ando, H. Mizuno, and A. Miyawaki. Regulated fast nucleocytoplasmic shuttling observed by reversible protein highlighting. *Science*, 306:1370–1373, 2004.

[17] H. Dürr and H. Bouas-Laurent. *Photochromism: molecules and systems, Elsevier*. Elsevier, 2003.

[18] M. Lerch, W. Szymanski, and B. Feringa. The (photo)chemistry of stenhouse photoswitches: guiding principles and system design. *Chem. Soc. Rev.*, 47:1910–1937, 2018.

[19] T. Mirkovic, E. Ostroumov, J. Anna, R. Van Grondelle, and G. Scholes. Light absorption and energy transfer in the antenna complexes of photosynthetic organisms. *Chemical reviews*, 117(2):249–293, 2017.

[20] A. Stirbet and Govindjee. On the relation between the kautsky effect (chlorophyll a fluorescence induction) and photosystem ii: basics and applications of the ojip fluorescence transient. *Journal of Photochemistry and Photobiology B: Biology*, 104(1-2):236–257, 2011.

[21] R. Delosme. Etude de l'induction de fluorescence des algues vertes et des chloroplastes au début d'une illumination intense. *Biochimica et Biophysica Acta (BBA)-Bioenergetics*, 143(1):108–128, 1967.

[22] R. Strasserf and A. Srivastava. Polyphasic chlorophyll a fluorescence transient in plants and cyanobacteria. *Photochemistry and photobiology*, 61(1):32–42, 1995.

[23] K. Koyano, H. Suzuki, Y. Mori, and I. Tanaka. Quantum yield of photo-rearrangement of nitrones. *Bulletin of the Chemical Society of Japan*, 43(11):3582–3587, 1970.

[24] P. Corey, R. Trimmer, and W. Biddlecom. A new chromogenic β-galactosidase substrate: 7-β-d-galactopyranosyloxy-9, 9-dimethyl-9h-acridin-2-one. *Angewandte Chemie International Edition in English*, 30(12):1646–1648, 1991.

[25] D. Warther, F. Bolze, J. Léonard, S. Gug, A. Specht, D. Puliti, X.-H. Sun, P. Kessler, Y. Lutz, J.-L. Vonesch, B. Winsor, J.-F. Nicoud, and M. Goeldner. Live-cell one-and two-photon uncaging of a far-red emitting acridinone fluorophore. *Journal of the American Chemical Society*, 132(8):2585–2590, 2010.

[26] C. Culbertson, S. Jacobson, and J. Ramsey. Diffusion coefficient measurements in microfluidic devices. *Talanta*, 56(2):365–373, 2002.

[27] K. Braeckmans, L. Peeters, N. Sanders, S. De Smedt, and J. Demeester. Three-dimensional fluorescence recovery after photobleaching with the confocal scanning laser microscope. *Biophysical journal*, 85(4):2240–2252, 2003.

[28] K. Braeckmans. Photobleaching with the confocal laser scanning microscope for mobility measurements and the encoding of microbeads. *Thesis submitted in fulfillment of the requirements for the degree of Doctor in Pharmaceutical Sciences, Ghent University*, 2004.

[29] M. Digman, C. Brown, P. Sengupta, P. Wiseman, A. Horwitz, and E. Gratton. Measuring fast dynamics in solutions and cells with a laser scanning microscope. *Biophysical journal*, 89(2):1317–1327, 2005.

[30] C. Brown, R. Dalal, B. Hebert, M. Digman, A. Horwitz, and E. Gratton. Raster image correlation spectroscopy (rics) for measuring fast protein dynamics and concentrations with a commercial laser scanning confocal microscope. *Journal of microscopy*, 229(1):78–91, 2008.

[31] R. Cole, T. Jinadasa, and C. Brown. Measuring and interpreting point spread functions to determine confocal microscope resolution and ensure quality control. *Nature protocols*, 6(12):1929–1941, 2011.

[32] C. Matthews and F. Cordeliéres. Metroloj: an imagej plugin to help monitor microscopes' health. In *ImageJ User & Developper Conference*, 2010.

[33] A. Paffi, M. Liberti, F. Apollonio, A. Sheppard, and Q. Balzano. In vitro exposure: Linear and non-linear thermodynamic events in petri dishes. *Bioelectromagnetics*, 36(7):527–537, 2015.

A.2 Publications

Published

Extra kinetic dimensions for label discrimination. Chouket R., Pellissier-Tanon A., Lahlou A. Zhang R., Kim D., Plamont M.-A., Zhang M., Zhang X., Xu P., Desprat N., Bourgeois D., Espagne A., Lemarchand A., Le Saux T., Jullien L.
Nat Commun 13, 1482 (2022).

Resonances at Fundamental and Harmonic Frequencies for Selective Imaging of Sine-Wave Illuminated Reversibly Photoactivatable Labels. Pellissier-Tanon A., Chouket R. Zhang, R., Lahlou A., Espagne A., Lemarchand A., Croquette V., Jullien L. & Le Saux T.
ChemPhysChem, 23(23), e202200295, 2023.

Accepted

Fluorescence to measure light intensity. Lahlou, A., Sepasi Tehrani H., Coghill I., Shpinov Y., Mandal M., Plamont M.-A., Aujard I., Niu Y., Nedbal L., Lazár D., Mahou P., Supatto W., Beaurepaire E., Eisenmann E., Desprat N., Croquette V., Jeanneret R., Le Saux T., Jullien L.
Nat Meth, 2023.

Under preparation

Leaves to measure light intensity. Lahlou A., Lazar D., Le Saux T., Jullien L.

A machine learning framework for single-cell scoring of NPQ components in *Chlamydomonas reinhardtii*. Lahlou A., Bujaldon S., Orlando M., Israelievitch E., Hanappe P., Le Saux T., Jullien L., Bailleul B. & Colliaux D. (to be defined).

CSL-libraries for modular Open Microscopy. Lahlou A., Ruyer-Thompson A., Coghill I, Le Saux T., & Hanappe P. (to be defined)

Collective photoprotection through light-induced phase separation in a phototactic micro-algae. Eisenmann I., Lhomme A., Lahlou A., Bujaldon S., Le Saux T., Bailleul B., Desprat N., Jeanneret R.